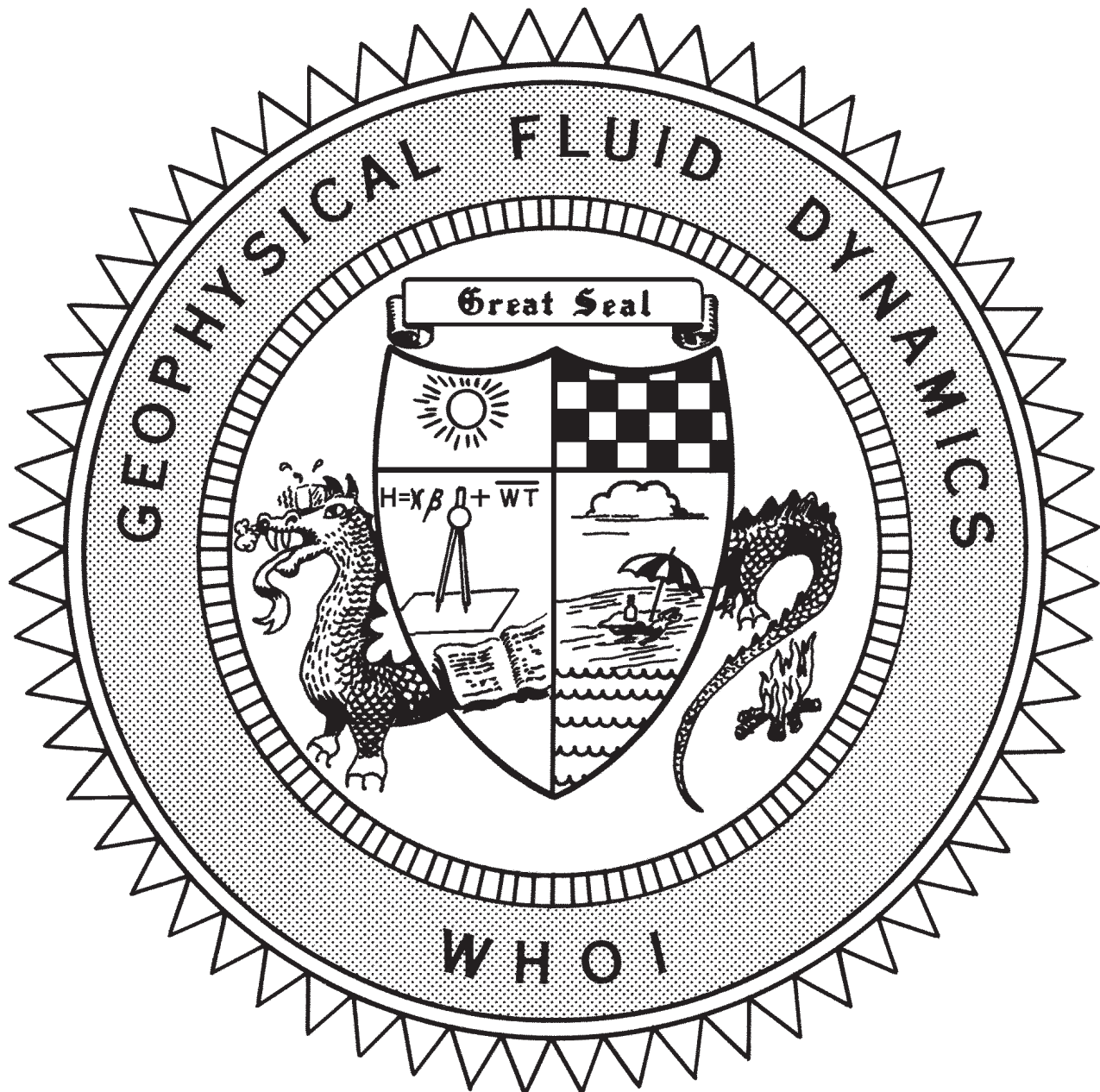


***2012 Program of Study:
Coherent Structures***



**Course Lectures
Fellows Project Reports**

WHOI-2013-07

2012 Program of Study: Coherent Structures

by

Colm-cille Caulfield and Charles Doering

Woods Hole Oceanographic Institution
Woods Hole, Massachusetts 02543

November 2013

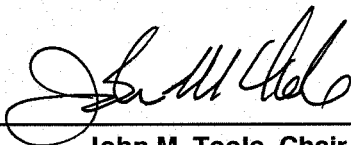
Technical Report

Funding was provided by the Office of Naval Research under Grant No. N00014-09-10844 and the National Science Foundation under Contract No. OCE-0824636.

Reproduction in whole or in part is permitted for any purpose of the United States Government. This report should be cited as Woods Hole Oceanographic Institution Technical Report, WHOI-2013-07.

Approved for public release; distribution unlimited.

Approved for Distribution:

A handwritten signature in black ink, appearing to read 'John M. Toole', is written over a horizontal line.

John M. Toole, Chair

Department of Physical Oceanography

Preface

The 2012 GFD Program theme was *Coherent structures* with Professors Jeffrey Weiss of the University of Colorado at Boulder and Edgar Knobloch of the University of California at Berkeley serving as principal lecturers. Together they introduced the audience in the cottage and on the porch to a fascinating mixture of models, mathematics and applications. Deep insights snaked through the whole summer, as the principal lecturers stayed on to participate in the traditional debates and contributed stoutly to the supervision of the fellows. The first ten chapters of this volume document these lectures, each prepared by pairs of the summer’s GFD fellows. Following the principal lecture notes are the written reports of the fellows’ own research projects. This summer’s fellows were:

- Cédric Beaume, IMFT, Toulouse
- Vamsi Chalamalla, University of California, San Diego
- Felicity Graham, University of Tasmania
- Yuan Guo, New York University
- Pedram Hassanzadeh, University of California, Berkeley
- Duncan Hewitt, University of Cambridge
- Bevin Maulsby, University of North Carolina
- Rosalind Oglethorpe, University of Cambridge
- Alban Sauret, IRPHE, Marseille
- Srikanth Toppaladoddi, Yale University

In 2012, the Sears Public Lecture was delivered by Professor Howard Bluestein, of the University of Oklahoma on the topic of “Probing tornadoes with mobile doppler radars”. The topic was particularly suitable for the summer’s theme: a tornado is a special examples of a vortex, perhaps the mother of all coherent structures in fluid dynamics. Howie “Cb” showed how modern and innovative measurement techniques can yield valuable information about the formation and evolution of tornadoes, as well as truly amazing images. Over a hundred listeners filed into Redfield for the occasion, and then enjoyed refreshments in the evening air afterwards outside the auditorium.

Charlie Doering and Oliver Bühler initially acted as the co-directors for the summer, with Colm-cille Caulfield ably stepping in to replace Oliver after he had to bow out. A large number of long-term staff members ensured that the fellows never lacked for guidance, and the seminar series was filled by a steady stream of visitors, talking about topics as diverse as how sharks smell and how to slice symmetry. Anders Jensen worked his usual magic in the Lab, dealing inventively with aquarium sand, bentonite and ketchup as well as with more traditional experimental fluids, and Janet Fields and Jeanne Fleming kept the program running smoothly behind the scenes.

TABLE OF CONTENTS

PREFACE	i
TABLE OF CONTENTS.....	ii
PARTICIPANTS	iv
LECTURE SCHEDULE.....	viii
PRINCIPAL LECTURES	
Jeffrey Weiss, University of Colorado, Boulder	
Edgar Knobloch, University of California, Berkeley	
Lecture 1	
<i>Dynamics of coherent structures and the impact on transport and predictability</i>	
Jeffrey Weiss.....	1
Lecture 2	
<i>Coherent structures in 2D fluid dynamics</i>	
Jeffrey Weiss	9
Lecture 3	
<i>Coherent structures in 2D fluid dynamics and structures in 3D quasi-geostrophic fluid dynamics</i>	
Jeffrey Weiss.....	20
Lecture 4	
<i>Part I: Structures in 3D quasi-geostrophic flows</i>	
Jeffrey Weiss.....	36
<i>Part II: Rapidly rotating convection</i>	
Jeffrey Weiss.....	47
Lecture 5	
<i>Applications of coherent structures to the study of weather and climate</i>	
Jeffrey Weiss.....	55
Lecture 6	
<i>Introduction to spatially localized structures</i>	
Edgar Knobloch	67
Lecture 7	
<i>The Swift-Hohenberg equation in one spatial dimension</i>	
Edgar Knobloch	88

Lecture 8	
<i>Pinning and depinning in one and two dimensions</i>	
Edgar Knobloch	106
Lecture 9	
<i>Spatially localized structures in fluid flows</i>	
Edgar Knobloch	129
Lecture 10	
<i>More applications</i>	
Edgar Knobloch	151
FELLOWS' REPORTS	
<i>Thixotropic gravity currents</i>	
Duncan R. Hewitt, Cambridge University	168
<i>Smoothing out sandpiles: rotational bulldozing of granular material</i>	
Alban Sauret, Aix-Marseille University & IRPHE.....	198
<i>Spin down of a stellar interior</i>	
Rosalind Oglethorpe, Cambridge University.....	224
<i>Slender swimmers in Stokes flow</i>	
Srikanth Toppaladoddi, Yale University	249
<i>Scattering of internal waves over random topography</i>	
Yuan Guo, New York University	267
<i>The effect of upwelling and downwelling on turbulent entrainment in a surface stress-driven flow</i>	
Vamsi Chalamalla, University of California, San Diego.....	287
<i>Equatorial quasi-geostrophy</i>	
Felicity Graham, University of Tasmania.....	307
<i>2:1 Spatial resonance in Langmuir circulation</i>	
Bevin Maultsby, University of North Carolina.....	334
<i>Optimal transport from wall to wall</i>	
Pedram Hassanzadeh, University of California, Berkeley.....	362
<i>A reduced model for exact coherent states in high Reynolds number shear flows</i>	
Cedric Beaume, Universite de Toulouse	406

2012 GFD Fellows, Staff and Visitors

Fellows

Cedric Beaume	Universite de Toulouse
Vamsi Krishna Chalamalla	University of California, San Diego
Felicity Graham	University of Tasmania
Yuan Guo	New York University
Pedram Hassanzadeh	University of California, Berkeley
Duncan Hewitt	Cambridge University
Bevin Maultsby	University of North Carolina
Rosalind Oglethorpe	University of Cambridge
Alban Sauret	Aix-Marseille University & IRPHE
Srikanth Toppaladoddi	Yale University

Staff and Visitors

James Anderson	Stevens Institute of Technology
Gualtiero Badin	University of Hamburg
Neil Balmforth	University of British Columbia
Helmut Baumert	IAMARIS e.V. - Applied Water Research
Javier Beron-Vera	RSMAS, University of Miami
Howard Bluestein	University of Oklahoma
Onno Bokhove	University of Twente
Oliver Buhler	Courant Institute of Mathematical Sciences
Colm-cille Caulfield	University of Cambridge
Matthew Chantry	University of Bristol
Sergei Chernyshenko	Imperial College London
Greg Chini	University of New Hampshire
Predrag Cvitanovic	Georgia Institute of Technology
Robert Deegan	University of Michigan
Diego Del-Castillo-Negrete	Oak Ridge National Laboratory
Navid Dianati-Maleki	University of Michigan
Charles Doering	University of Michigan
Francesco Fedele	Georgia Institute of Technology
Raffaele Ferrari	Massachusetts Institute of Technology
Pascale Garaud	University of California, Santa Cruz
John Gibson	Imperial College London
David Goluskin	Columbia University
Nicolas Grisouard	Courant Institute of Mathematical Sciences
George Hagstrom	New York University

George Haller
Miranda Holmes-Cerfon
Keith Julien
Joseph Keller
Richard Kerswell
Edgar Knobloch
Norman Lebovitz
Stefan Linz
Alireza Mashayekhi
Philip Morrison
Josefina Olascoaga
Michael Proctor
Matthew Salewski
Tobias Schneider

Tiffany Shaw
Edward Spiegel
Wenbo Tang
Anthony Thornton
Jacques Vanneste
Geoffrey Vasil
George Veronis
Jeffrey Weiss
John Whitehead
Djoko Wirosoetisno

McGill University
Harvard University
University of Colorado, Boulder
Stanford University
University of Bristol
University of California, Berkeley
University of Chicago
Institut fuer Theoretische Physik
University of Toronto
University of Texas, Austin
RSMAS, University of Miami
University of Cambridge
Philips University Marburg
Max Planck Institute for Dynamics and Self-Organization
Lamont Doherty Earth Observatory
Columbia University
Arizona State University
University of Twente
University of Edinburgh
Canadian Inst. for Theoretical Astrophysics (CITA)
Yale University
University of Colorado, Boulder
Woods Hole Oceanographic Institution
Durham University

2012 Principal Lecturers



Edgar Knobloch



Jeffrey Weiss



2012 Geophysical Fluid Dynamics Participants

First row (seated on ground): David Goluskin, Vamsi Challamalla, Srikanth Toppaladoddi, Alban Sauret, Pedram Hassanzadeh, Cedric Beaume, Felicity Graham, Duncan Hewitt, Rosalind Oglethorpe, Bevin Maltsby, Yuan Guo

Second row (seated): Charles Doering, Norman Lebovitz, unknown, Philip Morrison, Joseph Keller, George Veronis, Jeffrey Weiss, Edgar Knobloch, Ali Mashayekhi, Pascale Garaud, Claudia Cenedese, Oliver Buhler, Matthew Chantry

Third row: Edward Spiegel (standing), Tiffany Shaw, Greg Chini, Colm Caulfield, unknown, Shreyas Mandre, Tobias Schneider, Georgy Manucharyan, James Anderson, Neil Balmforth, Robert Deegan, Matthew Salewski

Fourth row: Raffaele Ferrari, Woosok Moon (hidden), Glenn Flierl, John Gibson, unknown, Michael Proctor, Stefan Linz, Gualtiero Badin, Nicolas Grisouard, L. Mahadevan, Rich Kerswell, Keith Julien, Onno Bokhove

Not pictured: Helmut Baumert, Javier Beron-Viera, Howard Bluestein, Sergei Chernyshenko, Predrag Cvitanovic, Diego Del-Castillo-Negrete, Navid Dianati-Maleki, Francesco Fedele, George Hagstrom, George Haller, Miranda Holmes-Cerfon, Josefina Olascoaga, Wenbo Tang, Anthony Thornton, Geoffrey Vasil, Djoko Wirosoetisno

**GFD Lecture Schedule
June 18 – August 24**

June 18 – June 22 – Principal Lectures - 10:00 AM

Dynamics of Coherent Structures and their Impact on Transport and Predictability
Jeffrey Weiss, University of Colorado

June 25 – June 29 – Principal Lectures - 10:00 AM

Spatially Localized Structures: Theory and Applications
Edgar Knobloch, University of California, Berkeley

Beginning July 2 lectures will be at 10:30 AM unless otherwise noted

July 2

Exchange Flows and the Principle of Maximum Flux
Rich Kerswell, Bristol University

July 3

Summer Subtropical Anticyclones and their Role in the General Circulation of the Atmosphere
Tiffany Shaw, Lamont Doherty Earth Observatory

July 4

HOLIDAY – no lectures

July 5

Convection, Stability, Coherent Structures and Turbulence
Charlie Doering, University of Michigan
Greg Chini, University of New Hampshire

July 6

Odor Dispersal in the Sea and the Physiological and Behavioral Responses of Sharks and Lobsters to Find Food by Smell
Jelle Atema, Boston University

Monday, July 9

10:00 AM

A Unified Theory of LCS as Transport Barriers

George Haller, McGill University

11:00 AM

Elliptic LCS in the Ocean: Geodesic Detection of Mesoscale Eddies

Francisco J. Beron-Vera, RSMAS, University of Miami

2:00 PM

Hyperbolic LCS in the Ocean: Forecasting Oil Spill Movement

M. Josefina Olascoaga, RSMAS, University of Miami

Tuesday, July 10

Scalar Dispersion in the Large-Deviation Regime

Jacques Vanneste, University of Edinburgh

Wednesday, July 11

Timestepping Schemes - Global Stability and Convergence

Djoko Wirosoetisno, Durham University

Thursday, July 12

Geostrophic Turbulence in the Upper Ocean

Joern Callies, MIT

Friday, July 13

Down-welling in Basins Subject to Buoyancy Loss

Claudia Cenedese, WHOI

Monday, July 16

Wall-localized Convection and Multiple-Scale Dynamics

Geoff Vasil, CITA, Toronto

Tuesday, July 17

Double-Diffusive Convection

Pascale Garaud, University of California, Santa Cruz

Wednesday, July 18

Universal Equations and Constants of (3D) Turbulent Motions

Helmet Baumert, ISMARIS, Hamburg

Thursday, July 19

From the Luzon Strait to the Lab: Modeling the Internal Tides

Matthieu Mercier, MIT

Friday, July 20

Undercompressive Shocks on Ion-Bombarded Surfaces

Miranda Holmes-Cerfon, New York University

Monday, July 23

Boundary Layers and Mixing in Abyssal Canyons

Rebecca Walsh-Dell, MIT/WHOI

Tuesday, July 24

Conservative Water Wave Model with Full Wave Dispersion and Horizontal Circulation

Onno Bokhove, University of Twente

Wednesday, July 25

Chaotic Stirring in an Idealized 3D Eddy

Larry Pratt, Woods Hole Oceanographic Institution

Thursday, July 26

Linear Stability of Non-Autonomous Systems

Shreyas Mandre, Brown University

Friday, July 27

Dynamical Systems, Kinetic Theory, Fluid Equations and All That

Ed Spiegel, Columbia University

Monday, July 30

Eddy Diffusion in Lagrangian Coherent Structures

Wenbo Tang, Arizona State University

Tuesday, July 31

Non-local Models of Anomalous Transport in the Presence of Coherent Structures

Diego Del-Castillo Negrete, Oakridge National Laboratory

Wednesday, August 1

Modeling Particle Size Segregation and its Applications to Geophysics Granular Flows

Anthony Thornton, University of Twente

Thursday, August 2

Generalized Linear Models for Networks of Spiking Neurons

Sara Solla, Northwestern University

Friday, August 3

The Solar Tachocline - Rotating, Stratified, Magnetized Turbulence

Toby Wood, University of California, Santa Cruz

Monday, August 6

The Structure and Dynamics of Tornadoes: A Review

Howard Bluestein, University of Oklahoma

Tuesday, August 7

Spontaneous Generation of Near-Inertial Internal Waves from an Oceanic Front

Amala Mahadevan, WHOI

PUBLIC LECTURE, 5:00 PM, Redfield Auditorium

Probing Tornadoes with Mobile Doppler Radars

Professor Howard Bluestein, University of Oklahoma

Wednesday, August 8

10:30

Zonal Flow Formation and Convection Structures in Spherical Quasigeostrophic Models at Low Prandtl Number

Celine Guervilly, University of California, Santa Cruz

2:30 PM

Got Symmetry? Here is how you slice it

Predrag Cvitanovic, Georgia Tech

Thursday, August 9

10:30

Water Wave Production by Oscillating Bodies

Joe Keller, Stanford University

2:30 PM

From Oceanic Sea States, Wave Spectra and Dispersion to Traveling Waves in Navier-Stokes

Francesco Fedele, Georgia Institute of Technology

Friday, August 10

Jamming

L. Mahadevan, Harvard University

AUGUST 13-17

QUIET WEEK – NO LECTURES

August 20-23

Fellows' Presentations

Monday, August 20

10:15 to 11:15

Thixotropic Gravity Currents and the Ketchup Question

Duncan Hewitt, Cambridge University

11:30 to 12:30

Smoothing Out Sandpiles: Rotational Bulldozing of Granular Material

Alban Sauret, IRPHE

Tuesday, August 21

10:15 to 11:15

Spin Down of a Stellar Interior

Rosalind Oglethorpe, Cambridge University

11:30 to 12:30

Swimming Slender Rods in Stokes Flow

Srikanth Toppaladoddi, Yale University

2:30 to 3:30

Scattering of Internal Waves Over Random Topography

Yuan Guo, New York University

Wednesday, August 22

10:15 to 11:15

What Goes Up Doesn't Come Down: The Effect of Upwelling and Downwelling on Turbulent Entrainment in a Surface Stress-Driven Flow

Vamsi Chalamalla, University of California, San Diego

11:30 to 12:30

Equatorial Quasi-Geostrophy

Felicity Graham, University of Tasmania

2:30 to 3:30

A 2-Dimensional, 3-Component Model of Langmuir Circulation

Bevin Maulsby, University of North Carolina

Thursday, August 23

10:15 to 11:15

Optimal Transport: Wall to Wall

Pedram Hassanzadeh, University of California, Berkeley

11:30 to 12:30

A Reduced Model for Exact Coherent Structures in High Reynolds Shear Flows

Cedric Beaume, IMFT

GFD 2012 Lecture 1: Dynamics of Coherent Structures and their Impact on Transport and Predictability

Jeffrey B. Weiss; notes by Duncan Hewitt and Pedram Hassanzadeh

June 18, 2012

1 Introduction

1.1 What is a Coherent Structure?

Structures are ubiquitous in planetary atmospheres, oceans, and stars (figure 1). These structures are of great interest because some of them have significant *direct* human impact (e.g. hurricanes, storms, Jet Stream). In addition, studying structures can provide insight into understanding and modeling other high-impact phenomena such as climate and weather. For example, sub-gridscale parametrization is an important part of ocean modeling; however, it has been observed that increasing resolution (and hence the accessible Reynolds number) drastically changes the flow field and results in an ‘explosion’ in the population of coherent vortices (figure 2).

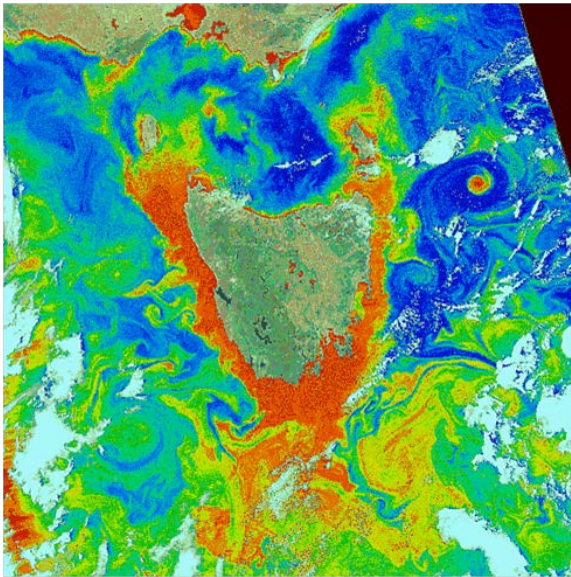
There is no rigorous definition of a coherent structure. In general, the best way to categorize them is based on the human brain, and employing the principle of ‘you know one when you see one’. On the whole, structures *cannot* be derived from the underlying partial differential equations: some conclusions can be drawn from these governing equations, but in general we need experimental and numerical observations to guide a theoretical study of structures.

In general, simple systems provide a road map for more complex physical systems on a planetary scale, such as oceans and atmospheres. Therefore, the overall approach is to seek the generic properties of these planetary fluids, and study simplified systems. We then extrapolate these simple systems back to the more complex large-scale physical systems of interest.

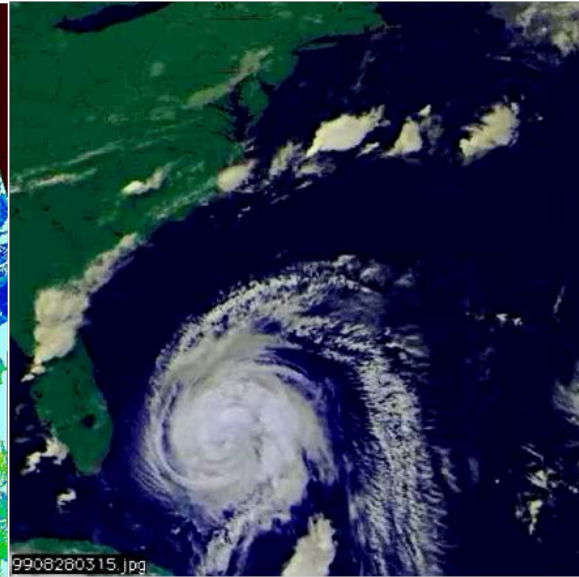
1.2 Properties of Coherent Structures

The term ‘coherent structure’ was first coined by [1] for vortices in a free shear layer. Below we give some properties of coherent structures, following [2]. It should be noted that the properties listed here are suggestions, and are probably both incomplete and overly exclusive, such that some things we would like to include as structures are either not included or are ruled out.

- Coherent structures are recurrent.



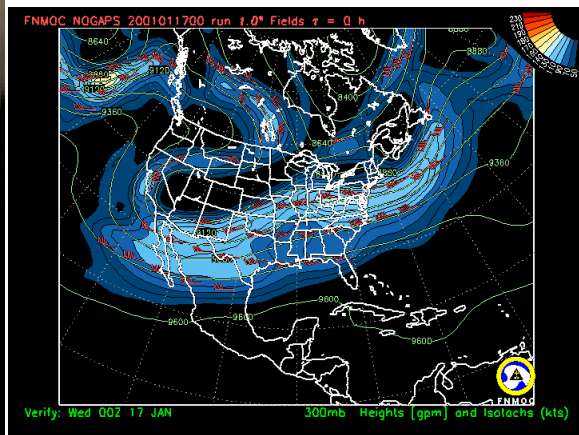
(a) An oceanic eddy off the coast of Tasmania



(b) Hurricane Dennis off the coast of Florida



(c) The Great Red Spot of Jupiter



(d) The Jet Stream over North America

Figure 1: Examples of structures in planetary atmospheres and oceans.

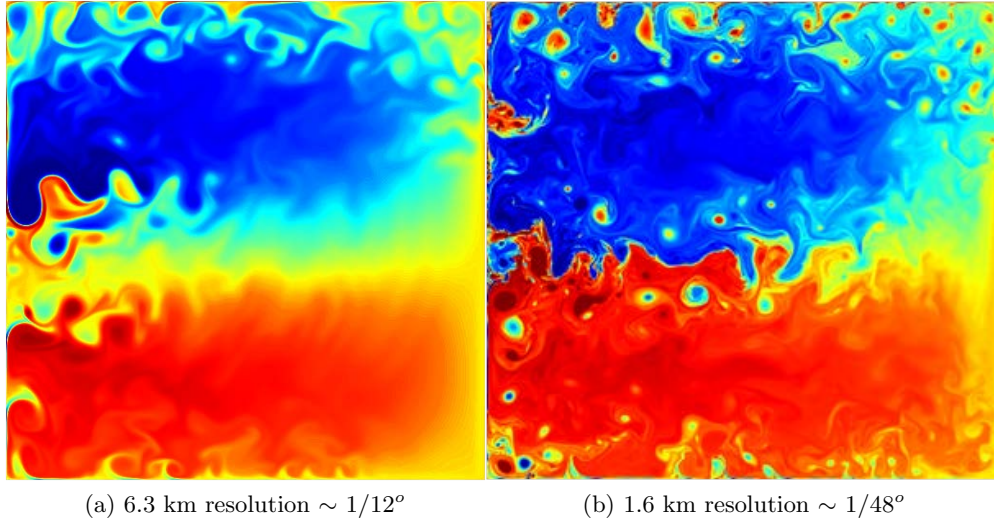


Figure 2: The effect of increasing numerical resolution in a simulation of ocean gyre, taken from [3].

- Coherent structures are spatially localized and isolated, as opposed to waves with a single Fourier mode, which are not. Solitary waves, which are localized and contain many Fourier modes are an example of a coherent structure.
- Coherent structures are a preferred state of the nonlinear dynamics: they are either close to stationary flow configurations, or self-similarly evolving states, which are robust to perturbations.
- Coherent structures are dynamically self-organizing, and thus not characteristic of any forcing.
- Coherent structures are long-lived in a Lagrangian frame, meaning that the time scale over which the structure decays is much longer than the typical Eulerian time scales of the flow (e.g. the Eulerian rotation period of the vortex). Structures are therefore weakly dissipative on Eulerian timescales.

1.2.1 Coherent Structures and Turbulence Theory

In traditional theories of turbulence, flows are treated as random, and a random phase approximation in (Fourier) wavenumber space is typically used to analyze them. However, coherent structures, as defined above, are *local* in physical space, and therefore a random phase approximation will destroy the physical localization. For example, a step function in physical space has a wide spectrum in Fourier space (Heisenberg’s uncertainty principle).

1.2.2 Recognition Algorithms

Structures can be identified by a number of different techniques. The most common approach is using subjective automated algorithms. These algorithms work by taking prede-

defined criteria and thresholds for the various properties outlined above. Such a method has an inherent subjectivity. A good recognition algorithm will be robust to small changes in the criteria such as the specific values of the thresholds. Other methods include human identification by eye, Lagrangian coherent structure theory, wavelet theory, and various statistical procedures.

2 Two-Dimensional Fluid Dynamics

The large-scale dynamics of planetary and oceanic flows are dominated by rotation and stable density stratification. Such flows are characterized with velocity scale V , length scales L (horizontal) and H (vertical), Coriolis parameter $f = 2\Omega \sin \theta$ (where Ω is the frequency of rotation and θ is the latitude), and Brunt-Väisälä frequency N . The Brunt-Väisälä frequency describes the frequency of oscillation of a displaced parcel of fluid in a stable stratified density field $\rho(z)$, and is given by $N^2 = (-g/\rho) \partial\rho/\partial z$, where g is the gravitational acceleration.

The effects of rotation are described by the Rossby number Ro , which can be thought of as a ratio of the timescales for rotation and advection, and is given by

$$Ro = \frac{U}{Lf}. \quad (1)$$

If $Ro \ll 1$, then the rotation timescale $1/f$ is much shorter than the advection timescale L/U , and the effects of rotation dominate.

The effects of stable stratification are described by the Froude number F , which can be thought of as a ratio of the timescales for oscillation in the background stratification and advection, and is given by

$$F = \frac{U}{HN}. \quad (2)$$

If $F \ll 1$, then the stratification is strong.

In the limits $Ro \ll 1$ and $F \ll 1$, the system is marked by rapid rotation and strong stable stratification, which results in significant (spatial) anisotropy in the flow. In particular, the vertical velocity w is smaller than the horizontal ones (i.e. $w \ll u, v$). In the extreme limit of $w = 0$, we can consider the system as two-dimensional in the $x - y$ plane.

2.1 2D Fluid Equations

We assume that the flow $\mathbf{u}(x, y, t) = (u, v)$ is incompressible

$$\nabla \cdot \mathbf{u} = 0, \quad (3)$$

and that the density ρ is constant. Without loss of generality, we set $\rho = 1$. The flow satisfies the Navier-Stokes momentum equation,

$$\frac{D\mathbf{u}}{Dt} = \frac{\partial\mathbf{u}}{\partial t} + (\mathbf{u} \cdot \nabla) \mathbf{u} = -\nabla p + \nu \nabla^2 \mathbf{u}, \quad (4)$$

where p is the pressure, ν is the viscosity, and rotation is ignored for now (i.e. $f = 0$). We define the vorticity $\boldsymbol{\omega}$ to be

$$\boldsymbol{\omega} = \nabla \wedge \mathbf{u} = \omega \hat{\mathbf{z}}, \quad (5)$$

Due to incompressibility (3) the flow can be described by a streamfunction $\psi(x, y, t)$ as $(u, v) = (-\partial\psi/\partial y, \partial\psi/\partial x)$. With respect to this streamfunction, the vorticity is given by

$$\omega = \nabla^2 \psi. \quad (6)$$

Taking the curl of (4) gives the vorticity equation,

$$\frac{D\omega}{Dt} = \frac{\partial\omega}{\partial t} + J[\psi, \omega] = \nu \nabla^2 \omega, \quad (7)$$

where the Jacobean J is given by

$$J[\psi, \omega] = \frac{\partial\psi}{\partial x} \frac{\partial\omega}{\partial y} - \frac{\partial\psi}{\partial y} \frac{\partial\omega}{\partial x}. \quad (8)$$

In the inviscid limit, $\nu \rightarrow 0$, (7) reduces to

$$\frac{D\omega}{Dt} = 0, \quad (9)$$

and vorticity is conserved following the flow.

In general, the flow is described by the vorticity equation (7) and the equation relating vorticity to the streamfunction (6). Often, in more situations beyond pure 2d flows, conservation equations for ‘potential vorticity’ can be derived that are analogous to (7), but the relationship between potential vorticity and velocity will be different to (6) (e.g. see 2.1.1).

Finally, we define the circulation Γ_C around a closed curve C to be

$$\Gamma_C = \oint_C \mathbf{u} \cdot d\mathbf{l} = \int_S \boldsymbol{\omega} \cdot d\mathbf{S}, \quad (10)$$

where the closed curve C , with line element $d\mathbf{l}$, contains an area S , with area element $d\mathbf{S}$.

2.1.1 Effect of Rotation

In 2D fluid dynamics, if the Coriolis parameter f is a constant (the ‘ f -plane approximation’), then it can be absorbed into a modified pressure p in (4), because the Coriolis term $f(\mathbf{u} \wedge \hat{\mathbf{z}})$ can be written as a perfect gradient $f\nabla\psi$. In this case, the flow is still described by (6) and (7). However, if f varies by latitude, e.g. as $f(y) = f(y_o) + \beta y$ where $\beta = (\partial f / \partial y)_{y_o}$ (β -plane approximation), then (7) will be replaced with an equation conserving *potential* vorticity $q = \omega + \beta y$ (i.e. $Dq/Dt = 0$).

2.2 Steady Inviscid Solutions

On an f -plane, if the flow is steady and inviscid, then (7) reduces to

$$J[\psi, \omega] = 0. \quad (11)$$

Therefore, any parallel flow, in which the streamfunction is a function of x or y only, is a solution of the equations. For example, zonal or meridional jets are solutions.

Note, however, that under a β -plane approximation (described above), meridional jets ($\psi = \psi(x)$) are no longer solutions of the equations. To the degree that coherent structures are steady-solutions of the inviscid equations, this explains why coherent jets tend to zonal rather than meridional.

2.3 Vortices

In polar coordinates (r, θ) , the steady inviscid governing equation (11) and the vorticity (6) can be written as

$$J[\psi, \omega] = \frac{1}{r} \left(\frac{\partial \psi}{\partial r} \frac{\partial \omega}{\partial \theta} - \frac{\partial \psi}{\partial \theta} \frac{\partial \omega}{\partial r} \right) = 0, \quad (12)$$

$$\omega = \nabla^2 \psi = \frac{1}{r} \frac{\partial}{\partial r} \left(r \frac{\partial \psi}{\partial r} \right) + \frac{1}{r^2} \frac{\partial^2 \psi}{\partial \theta^2}. \quad (13)$$

Therefore, any axisymmetric flow $\psi = \psi(r)$ satisfies the steady inviscid equations (12) and (13). Again, to the degree that coherent structures are steady-solutions of the inviscid equations, we expect to see axisymmetric vortices.

2.3.1 Gaussian vortex

Consider the axisymmetric vortex given by

$$\omega(r) = \frac{\Gamma}{2\pi r_0^2} e^{-r^2/2r_0^2}, \quad (14)$$

which is described by two constant parameters: the circulation Γ ; and the size r_0 . The velocity field is purely azimuthal $\mathbf{u} = u_\theta \mathbf{e}_\theta$, and can be found from inverting the curl (13) (analogous to the Biot-Savart law in electromagnetism). This operation gives a constant of integration, which is chosen to ensure that the velocity is bounded at the origin. The velocity is therefore given by

$$u_\theta(r) = \frac{\Gamma}{2\pi r} \left[1 - e^{-r^2/2r_0^2} \right]. \quad (15)$$

Note that, with vortices, we often define a vorticity ω , and infer the velocity u_θ . Equation (15) shows that the velocity is zero at the origin and increases initially linearly with r . The velocity is maximum at r_0 , and then decays like $1/r$.

2.3.2 Point Vortex

In the limit $r_0 \rightarrow 0$, we can consider the Gaussian vortex to be a point vortex, with vorticity ω given by

$$\omega(\mathbf{x}) = \Gamma \delta(\mathbf{x}). \quad (16)$$

The corresponding velocity is given by

$$u_\theta(r) = \begin{cases} \Gamma/2\pi r & r \neq 0 \\ 0 & r = 0 \end{cases} \quad (17)$$

Suppose we have N point vortices, each with circulation Γ_i and location \mathbf{x}_i . Then the vorticity at position \mathbf{x} is obtained from the superposition of ω_i

$$\omega(\mathbf{x}) = \sum_i^N \Gamma_i \delta(\mathbf{x} - \mathbf{x}_i), \quad (18)$$



Figure 3: Schematic showing point vortex pairs: (a) two vortices of equal and opposite circulation, translate without changing their separation; (b) two vortices of equal circulation, rotate without changing their separation.

and the corresponding velocity field outside all point vortices is given by

$$\mathbf{u}(x, y) = \sum_i^N \frac{\Gamma_i}{2\pi} \left[\frac{-(y - y_i) \hat{\mathbf{x}} + (x - x_i) \hat{\mathbf{y}}}{(x - x_i)^2 + (y - y_i)^2} \right], \quad (x, y) \neq (x_i, y_i) \quad (19)$$

and the velocity at point vortex j is given by

$$\mathbf{u}(x_j, y_j) = \sum_{i \neq j}^N \frac{\Gamma_i}{2\pi} \left[\frac{-(y - y_i) \hat{\mathbf{x}} + (x - x_i) \hat{\mathbf{y}}}{(x - x_i)^2 + (y - y_i)^2} \right]. \quad (20)$$

Consider now the inviscid time-dependent governing equation,

$$\frac{\partial \omega}{\partial t} + J[\psi, \omega] = 0. \quad (21)$$

Inserting (18) into (21), and balancing terms, gives

$$\frac{\partial \Gamma_i}{\partial t} = 0, \quad \text{and} \quad \frac{D\mathbf{x}_i}{Dt} = \mathbf{u}(\mathbf{x}_i), \quad (22)$$

which shows that the circulation of each vortex remains constant, and each vortex moves with the velocity that is induced from the other vortices at that point.

Examples of the motion of two point vortices are given in figure 3. A pair of point vortices with equal but opposite circulation separated by a distance d translates at the speed of $\Gamma/2\pi d$ without changing the separation. The direction of translation can be easily inferred by finding the direction of velocity induced by one vortex on the other one. On the other hand, a pair of vortices with equal circulation of the same sign rotates around their centre of vorticity with a period of $2\pi^2 d^2/\Gamma$.

References

- [1] G. BROWN AND A. ROSHKO, *On density effects and large structure in turbulent mixing layers*, J. Fluid Mech., 64 (1974), pp. 775–816.
- [2] J. MCWILLIAMS AND J. WEISS, *Anisotropic geophysical vortices*, Chaos, 4 (1994), pp. 305–312.

- [3] A. SIEGEL, J. WEISS, J. TOOMRE, J. MCWILLIAMS, P. BERLOFF, AND I. YAVNEH,
Eddies and vortices in ocean basin dynamics, Geophys. Res. Lett., 28 (2001), pp. 3183
– 3186.

GFD 2012 Lecture 2: Coherent Structures in 2D Fluid Dynamics

Jeffrey B. Weiss; notes by Yuan Guo and Bevin Maultsby

June 19, 2012

1 Introduction

Structures in the atmosphere and ocean such as hurricanes, storms and the path of jet streams that have large human impact like They provide insight into better sub-grid-scale parameterization. Most structures cannot be derived from underlying PDE's and to learn about their details requires observations and numerical simulations. There are several interesting and important structures present in two-dimensional fluid dynamics. One major motivation for examining such 2D fluid dynamics is to further understand the anisotropy that is present in atmosphere and ocean. These lecture notes are organized as follows:

In section 2, we introduce the point vortex model. This idealized model provides mathematical and physical insight. The equations for point vortex dynamics define a Hamiltonian system. However, their singular nature gives no insight into the dynamics of vortex shape, and filters out processes that depend on the shape dynamics.

Thus in section 3, we present a model of compact and well-separated vortex. The vortex moments are defined and the equations of the motion of the centroid are given. Asymptotic analysis leads to an infinite system of coupled ordinary differential equations for physical-space moments of the individual regions. If truncated to a finite number of moments, a self-consistent closed model is obtained at any order. Nonzero 2nd order moments yields the "elliptical moment model".

In section 4, we examine an important process in fluid mechanics: same-sign vortex merger. A threshold for the merger of equal-sized vortices is given. We also discuss the situation when diffusion is present, as well as the interesting phenomenon of the onset of chaotic motion in the elliptical moment model. Statistical mechanics give some predictions, but there are some constraints in actual fluids that prevent vortices from exploring the phase space as described by statistical mechanics.

In section 5, we briefly introduce the cascade theory of turbulence, focusing on 2D turbulence. We describe four different types of vortex interactions in 2d decaying turbulence: two-vortex merger, dipole propagation, vortex scattering, and tripole merger. The conservation laws of energy and enstrophy are crucial in the study of cascade theory. We also examine the relationship of cascade and vortex merger and the role of energy and enstrophy fluxes.

In section 6, we look into structure-based temporal scaling theory, which is quite different from traditional cascade theory. Our goal is to construct scaling theory guided by vortex

statistics from numerical simulations. We make several assumptions in the theory resulting in relationships between the exponents of the power law evolution of vortex properties.

2 Point Vortices

First we will examine point vortices in greater detail; the setting here is inviscid dynamics. A point vortex system is closed: the vorticity of the system will always remain concentrated at the point vortices. This no longer holds, however, with the addition of viscosity, which causes the vorticity to spread out across the system. We will examine this case later.

Recall, the vorticity evolution equations

$$\begin{aligned}\partial_t \omega + J[\psi, \omega] &= \nu \nabla^2 \omega \\ \omega &= \nabla^2 \psi,\end{aligned}$$

while the definition of a point vortex is

$$\omega(\vec{x}) = \sum_{i=1}^N \Gamma_i \delta(\vec{x} - \vec{x}_i).$$

This expression may depend on time t . From the above, we obtain

$$\frac{D\omega_t}{Dt} = \sum_{i=1}^N [\partial_t \Gamma_i \delta(\vec{x} - \vec{x}_i) - \Gamma_i \nabla \delta(\vec{x} - \vec{x}_i) \cdot \dot{\vec{x}}_i] + \sum_{i=1}^N \vec{U} \cdot \nabla (\Gamma_i \delta(\vec{x} - \vec{x}_i)) = 0.$$

The gradient of a delta-function is infinite. Reinterpreting these equations for a small but finite-size Gaussian vortex of size r_0 renders these terms $O(1/r_0)$. Considering only the order one term yields

$$\partial_t \Gamma_i = 0,$$

while the $O(1/r_0)$ term gives

$$\dot{\vec{x}}_i = \vec{U}(\vec{x}_i),$$

and the point vortex is advected by the velocity field.

Another important fact to observe is that a collection of point vortices is Hamiltonian. Denoting the Hamiltonian by H , we can write

$$H = - \sum_{i \neq j} \frac{\Gamma_i \Gamma_j}{4\pi} \ln |\vec{x}_i - \vec{x}_j|.$$

(In the above, the natural logarithm is a result of Green's function for the Laplacian in two dimensions.) The equations of motion for this system are

$$\Gamma_i \begin{pmatrix} \dot{x}_i \\ \dot{y}_i \end{pmatrix} = \begin{pmatrix} -\frac{\partial H}{\partial y_i} \\ \frac{\partial H}{\partial x_i} \end{pmatrix}.$$

A physical interpretation of the Hamiltonian is that of the “interaction energy for an infinite domain.”

As this is a Hamiltonian system, we can observe both regular and chaotic dynamics. Depending on the boundary conditions, there may be other invariants as well, such as translation symmetries that yield linear momentum conservation, and rotation symmetries that yield angular momentum conservation. Exploration in this direction reveals that a system on an infinite domain with three vortices is regular, while a system with four is chaotic.

3 Elliptical vortices

Elliptical vortices exhibit particular interesting behavior, and there is a lot of literature on this subject. One of the first papers on the subject is the 1986 paper on vortex interactions by Melander, Zabusky and Styczek [1].

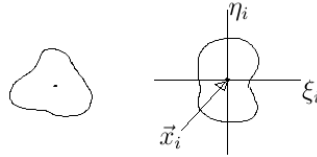


Figure 1: Two compact, separated vortices.

In this setting we are considering compact, well separated vortices, such as the two vortices above. In such systems, the vorticity is zero outside of these compact structures. Each vortex has its own constant vorticity ω_i , area A_i , and circulation Γ_i , defined by

$$\Gamma_i := \omega_i A_i.$$

As shown in the elliptical vortex on the right in the above illustration, we can put local coordinates (ξ_i, η_i) on each vortex. The centroid \vec{x}_i of each vortex is then given by

$$A_i \vec{x}_i = \int_{\text{vortex } i} \vec{x} d\xi_i d\eta_i$$

Each vortex also has moments, which are given by

$$J_i^{(m,n)} = \int_{\text{vortex } i} \xi_i^m \eta_i^n d\xi_i d\eta_i.$$

We can glean various bits of information by choosing m and n in specific ways. For example, setting $m = n = 0$ yields the area of the vortex. If $m = 1$ and $n = 0$, we obtain the x component of the centroid, while if $m = 0$ and $n = 1$, we obtain the y component of the centroid. If $m = 2$ and $n = 0$, we obtain the variance in ξ of the size of the vortex, while if $m + n = 2$ then we obtain the covariance matrix for the size of the vortex. The sum $m + n$ defines the order of moments.

There are a couple of assumptions which are key to the development of these ideas. In particular, we have a small parameter

$$\varepsilon = \frac{\text{size of a vortex}}{\text{separation between vortices}} \ll 1.$$

In other words, we assume that the separation between vortices is $O(1)$, with the size of each vortex much smaller. As the size of each vortex is small, the moments bring in power of ε :

$$J^{(m,n)} \sim O(\varepsilon^{m+n+2}),$$

where the additional 2 in the exponent comes from the integration in the definition of J_i . Therefore, each higher moment is higher order in ε than lower order moments.

The above definitions are focused on a single vortex within the system. We have not yet addressed the interaction of the vortices. It is important to note that we do not need any assumption that vortices maintain the same shape; instead we describe vortices in terms of their moments.

Since the area A_i is constant, the motion of the centroids is given by

$$\begin{aligned} A_i \dot{\vec{x}}_i &= \frac{d}{dt} \int_{\text{vortex } i} \vec{x} d\xi_i d\eta_i \\ &= \int_{\text{vortex } i} \vec{U}(\vec{x}) d\xi_i d\eta_i. \end{aligned}$$

The velocity $\vec{U}(\vec{x})$ is the velocity induced by all of the other vortices, which we recall are far away from our basic assumption on the separation distance between vortices. Asymptotic analysis can show that in the same way that point vortices do not have any self advection, the centroid position does not have any self advection.

We can now Taylor expand the velocity $\vec{U}(\vec{x})$ around the centroid of a vortex. Here \vec{x}_i is in vortex i , and its velocity induced by vortex j becomes

$$\dot{\vec{x}}_i = \frac{1}{A_i} \sum_{q=0}^{\infty} \sum_{p=0}^q \frac{1}{p!(q-p)!} J_i^{(p,q-p)} \frac{\partial^p}{\partial x^p} \frac{\partial^{q-p}}{\partial y^{q-p}} \vec{U} \Big|_{\vec{x}_i}.$$

Recall that

$$U(\vec{x}) = \sum_j U_j(\vec{x}),$$

where $U_j(\vec{x})$ is the velocity induced by vortex j at \vec{x} .

One can repeat similar steps to get an equation for $\frac{\partial}{\partial t} J_i^{(m,n)}$, from which one can perform asymptotic analysis. We do not go into details here, see Melander *et al.* 1986 [1] for more information.

A result of this analysis is that we can truncate at any order and get a closed system. In other words, if we keep all moments through the k^{th} order in the initial condition, then the time evolution of those moments up through the k^{th} order will not generate moments of order greater than k .

If we keep only the centroid, then this is exactly the point vortex model. The first order moment is zero by definition. For the second order moments, we need $m + n = 2$. In other words, we set the pair (m, n) to be $(2, 0)$, $(1, 1)$, and $(0, 2)$.

Here we can get a good idea of what it means for a system of point vortices to be closed. If we truncate at order two, then closure implies that all higher order moments depend completely on the 2nd order moments. As long as the second order moments are nonzero, this yields an ellipse, called the “elliptical moment model.” In addition to the position and location parameters we have already seen, the elliptical model yields two additional parameters, illustrated below.

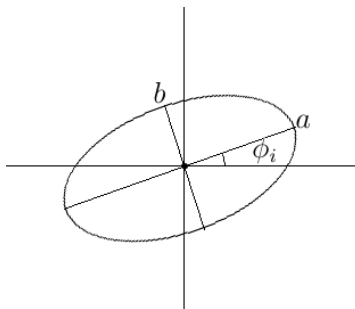


Figure 2: Two additional parameters for the elliptical moment model.

One of the additional parameter is the angle ϕ_i , while the other parameter is the ellipticity ratio $\frac{a}{b}$ of lengths of the major and minor axes. These parameters completely describe the ellipse. The result is a Hamiltonian dynamical system with four degrees of freedom (as the area is fixed).

4 Same-sign vortex merger

Same-sign point vortices co-rotate. We will see that two finite-size vortices with the same sign which are “close enough” will merge together. Such same-sign merger can be illustrated with numerical simulations and observed in laboratory experiments.

There is a threshold for merger which can make this notion of “close enough” more precise. In general, if the separation between two vortices of equal size is larger than 3.3 times the radius of those vortices, then they will rotate around each other for all t and never merge. However, their behavior changes dramatically once the separation distance is less than 3.3 times their radius; in this case, they will merge quite quickly.

If there is diffusion present in the system, then vortices will always merge. This behavior happens because the radii will grow slowly on a diffusive time scale. As a result, the ratio between their radii and the separation is eventually small enough to cross the threshold.

One interesting phenomenon is the onset of chaos in an elliptical model. If a system begins with two elliptical vortices whose separation is above the threshold, as expected they rotate around each other. Visually, they appear to wiggle as their ellipticity rotates, and they become essentially circular. If however, their separation is below the threshold, the distance between their centers quickly collapses. As a result, the ellipticity of the system

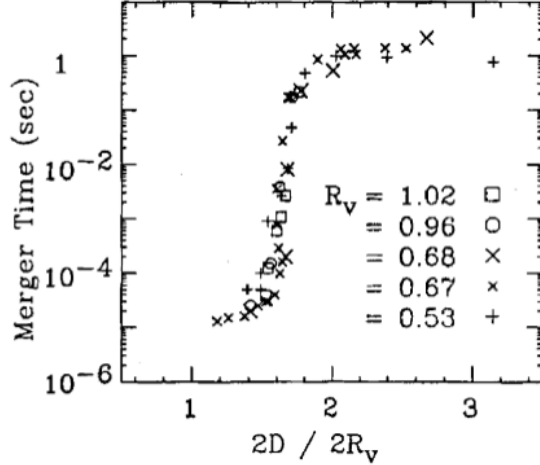


Figure 3: Measured two-vortex merger time as a function of separation $2D$ normalized to vortex diameter $2R_v$, by C. F. Driscoll, *et al.* 1991 [4].

becomes infinite. As the equation for the model has a term of $\frac{1}{r}$, where r denotes the separation between the vortices, the model blows up. This singular behavior is analogous to vortex merger.

There are several theories that give *correlations* with merger, yet do not seem to fully explain the threshold. One can argue that the threshold is still something of a mystery. It is interesting to note that statistical mechanics predicts that vortices always merge if the system is allowed to fully explore the phase space. According to this prediction, a system with an initial condition of two vortices will always result in a single vortex as the most probable state. However, there are constraints in the actual fluid dynamics that prevent vortices from exploring the phase space as described by statistical mechanics. But if the fluid dynamics allows the vortices to merge, then statistical mechanics calculations give the correct predictions.

We can connect the ideas of the last three sections with the following observation. Point vortices do not exhibit merger at all, whereas the elliptical moment model, which allows shape oscillations gives the signature for vortex merger. Hence the elliptical model is the simplest inviscid model that provides information about this important dissipative process.

5 Cascade Theory

5.1 2d turbulence cascades

We now give a brief overview of two-dimensional turbulence cascades. First we note that fluids in this context have small viscosity ν , and large dimensionless Reynolds number given

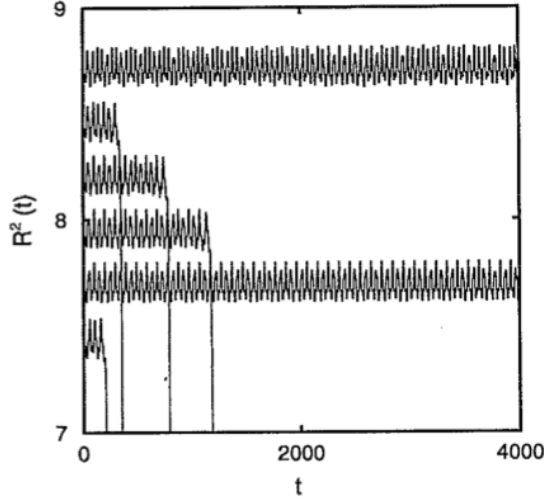


Figure 4: Vortex separation squared $R^2(t)$ from the elliptical-moment model for initially circular vortices with $\Gamma_1 = \pi/4$, $\Gamma_2 = \pi$ and initial separations $R_0 = 2.746 - 2.751$ in steps of 0.001. The trajectories are successively offset by $\Delta R^2 = 0.25$, by J. B. Weiss and J. C. McWilliams, 1993 [2].

by

$$\text{Re} = \frac{UL}{\nu} \gg 1,$$

where U is the velocity and L is the length scale. From the Laplacian dissipation, we get a term of

$$-\frac{k^2}{\text{Re}},$$

in wavenumber space, where k is the wavenumber.

Classical cascade theories are based on physical models of how energy flows through wavenumber space coupled with dimensional analysis of Navier-Stokes equations. There are a few typical assumptions for cascade theory. The first is to assume that a system has some forcing concentrated along a particular forcing scale, k_f . Due to the form of the dissipation operator, dissipation occurs at large wavenumbers. There is an inertial range (perhaps more than one inertial range, in fact) determined by values of k where forcing and dissipation are both small. Lastly, the fundamental concept of local cascade theory is that energy is transferred locally in scale.

5.2 3D Cascades

When we consider 3d homogeneous isotropic turbulence, we assume that we have forcing at large scales and dissipation at small scales.

Let ε represent the energy flux of the system. If we assume that we are in a statistically steady state, then ε moves from large scales to small scales. In a statistically steady state

ε for a turbulent cascade must be constant in inertial range as there is no large forcing or dissipation terms. Dimensional analysis yields the Kolmogorov scaling relation

$$E(k) \sim k^{-5/3},$$

which represents a direct transfer from large scales to small scales.

5.3 2D Cascades

5.3.1 Conservation of Energy and Enstrophy

Two-dimensional homogeneous isotropic turbulence is different from the 3D case because there is conservation of enstrophy. Denote enstrophy by Z , then

$$Z = \frac{1}{2} \int d^2\vec{x} |\vec{\omega}|^2.$$

Statistically, enstrophy represents the mean square of the vorticity. It can also be seen though as analogous to the kinetic energy of the system.

Now let us examine the role that energy conservation plays. First, note that the time derivative of energy E depends on the enstrophy:

$$\frac{dE}{dt} = -2\nu Z.$$

A fact about 3d turbulence is that the energy dissipation is constant as the viscosity goes to zero because the enstrophy of the system grows. The resulting vortex stretching is crucial in 3D. The major difference when we switch to 2D is the lack of a vortex stretching term. (Later, we will see quasigeostrophic dynamics in 3D that will resemble 2D as there is a similar lack of vortex stretching.)

The time derivative of the enstrophy is

$$\frac{dZ}{dt} = \left\langle \omega_i \omega_j \frac{\partial U_i}{\partial x_j} \right\rangle - 2\nu P,$$

where $\omega_i \omega_j$ is the vortex stretching term, and P is the “palinstrophy” given by

$$P = \frac{1}{2} \int dx |\nabla \times \vec{\omega}|^2.$$

One may wonder why the vortex stretching term $\omega_i \omega_j$ is zero in two dimensions. This is due to the fact that the vorticity and the velocity are always in perpendicular directions, which prevents vortex stretching. As a result, the enstrophy time derivative is always negative. Taking the limit as viscosity vanishes, we see that the enstrophy cannot grow. Hence the energy is conserved in 2D.

5.3.2 Cascade Theory and Mergers

Now we examine what happens if we add energy and enstrophy fluxes to the system. Due to the conservation of energy, there are separate energy and enstrophy cascade regimes with cascades in opposite directions. Energy cascades to large scales, while enstrophy cascades to small scales, where it then dissipates. Dimensional analysis gives the slope of spectrum in these cascades, and the inverse energy cascade results in large scale structures.

Several typical numerical simulations of decaying 2d turbulence have shown that in relatively short times periods, individual vortices self organize into a collection of coherent vortices. Afterwards, the vortices advect each other around, and same-sign vortices merge, whence there are fewer vortices. After a much longer period of time, the system ends with a dipole which slowly decays through diffusion.

The dominant dissipative mechanism in decaying 2d turbulence is vortex merger. Most merger events are two-vortex mergers, which are often catalyzed by a third vortex, but occasionally three-vortex mergers occur. Conservative vortex interactions include dipole propagation and vortex scattering. The idea of scattering is illustrated in the following example: imagine two dipoles, A translating with opposite sign vortex A' , and B translating with opposite-sign vortex B' , and the dipoles propagate to bring them close together. When A and B are close together, they may be near an unstable co-rotating periodic state. Then they will “switch partners” so that A is now rotating with B , and A' is rotating with B' . The trajectories of these new pairs depart near unstable manifolds of the are near unstable orbits of the periodic state. Varying the impact parameters, which governs how the pairs approach, changes how close the incoming dipoles are the stable manifold of the periodic orbit. The closer the dipoles approach the periodic orbit, the longer they remain in its vicinity, and the more they co-rotate before leaving its neighborhood. In this case, the angle at which they exit becomes sensitive to the impact parameter and is unpredictable. This example is a case of “chaotic scattering.”

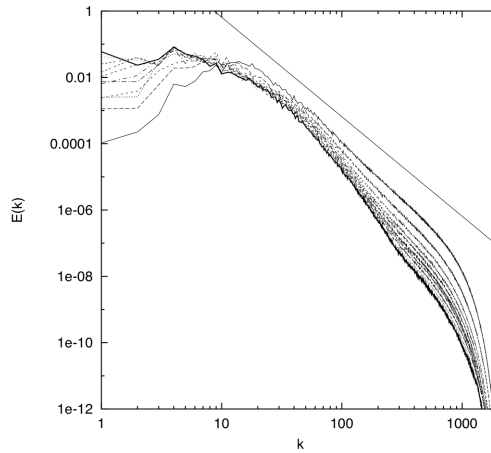


Figure 5: Energy spectra for the solution at high Re for times $t=1,2,\dots,11$. Solid line shows the k^{-3} classical prediction, by A. Bracco *et al.* 2000 [4].

6 Structure-Based Temporal Scaling Theory

Structure-based scaling theory address the properties of the vortex population, as well as the global quantities like energy and enstrophy. This differs from traditional cascade theory which ignores the coherent structures. Simulations of 2d decaying turbulence exhibit spectra that are steeper and an enstrophy time decay that is slower than cascade theory predicts.

In numerical simulations, we see three phases: vortex formation, vortex interaction, and the final dipole. The first phase is poorly understood compared to the vortex interaction phase. The goal here is to construct a scaling theory guided by vortex statistics from numerical simulations. First, however, we must measure vortex statistics, which is inevitably based on a subjective census algorithm (as there is no entirely precise definition of a vortex). The output this census is the number of vortices and the distribution of their properties, such as vortex size and enstrophy, over the course of the simulation.

6.1 Vortex Scaling Theory

For scaling theory we have a few assumptions. The first assumption, based on inviscid dynamics, is that energy is conserved. Let ω_p denote the peak vorticity, as illustrated below.

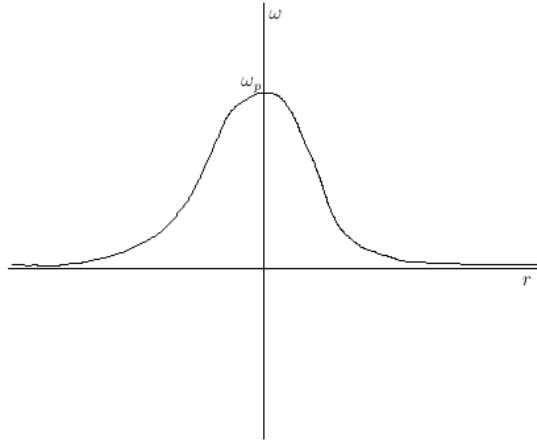


Figure 6: Typical vortex shape indicating the peak vorticity.

The second assumption, also based on inviscid dynamics, is that ω_p is conserved. Moreover, we assume that all of the vorticity is inside the coherent, well-formed vortices and the vorticity outside these vortices is zero.

Observations from numerical simulations show that the number of vortices N decays with a power law:

$$N \sim t^{-\xi}, \quad \xi \approx 0.72.$$

Each individual vortex is characterized by a location \vec{x}_i , a size r_i (the notion of size can be made precise), and a vorticity ω_i . The population of vortices is then characterized by a

probability density function

$$p(r, \omega, t),$$

which represents the probability of finding a vortex of size r and with vorticity ω at time t .

For convenience we assume that r and ω are independent. With this assumption we can write

$$p(r, \omega, t) = p_r(r, t)p_\omega(\omega, t).$$

In fact this assumption is not necessary, but it simplifies the following equations, as we reduce the number of variables from two to one.

The final assumption is that the probability density functions evolve self-similarly. In other words, the time dependence of the pdf depends only on the time dependence of the average

$$\langle r \rangle(t).$$

Thus if we define a new variable

$$X := \frac{r}{\langle r \rangle(t)},$$

then the assumption is that $p(X)$ is independent of time. (This could be done for the joint distribution as well.)

The assumption of self-similarity allows one to write the moments of the pdf in terms of the average. In particular, the average of the n^{th} power of the radius is equal to the n^{th} power of the average multiplied by a constant depending on n :

$$\langle r^n \rangle(t) = c_n \langle r \rangle^n(t).$$

Thus the time dependence of all moments can be related to the time dependence of the average.

References

- [1] M. V. Melander, N. J. Zabusky and A. S. Styczek, 1986. A moment model for vortex interactions of the two-dimensional Euler equations. Part 1. Computational validation of a Hamiltonian elliptical representation. *J. Fluid Mech.* 167, pp 95-115.
- [2] J. B. Weiss and J. C. McWilliams, 1993. Temporal Scaling Behavior of Decaying Two-Dimensional Turbulence. *Phys. Fluids A*, Vol. 5, No. 3, 608.
- [3] G. F. Carnevale, J. C. McWilliams, Y. Pomeau, J. B. Weiss, and W. R. Young, 1991. Evolution of Vortex Statistics in Two-Dimensional Turbulence. *Physical Review Letters*, 66, 2735.
- [4] A. Bracco, J. C. McWilliams, G. Murante, A. Provenzale and J. B. Weiss, 2000. Revisiting 2D Turbulence at Millennial Resolution. *Physics of Fluids*, 12, 2931-2941.
- [5] K. S. Fine, C. F. Driscoll, J. H. Malmberg, and T. B. Mitchell, 1991. Measurements of Symmetric Vortex Merger. *Physical Review Letters*, 67, 588-591.

GFD 2012 Lecture 3: Coherent Structures in 2D Fluid Dynamics and Structures in 3D Quasi-Geostrophic Fluid Dynamics

Jeffrey Weiss; notes by Rosalind Oglethorpe and Felicity Graham

June 20, 2012

1 Structure based scaling theory

In this lecture, we revisit the structure based temporal scaling theory for two-dimensional turbulent fluids. Scaling theory involves characterising the vortex population in terms of some of its properties; here, the total number of vortices N , vorticity ω , and vortex radius r are considered. The scaling behaviour of other vortex properties can be defined in terms of these quantities. We relate the three quantities to the scaling exponent ξ . Our assumptions from yesterday are that both energy and peak vorticity is conserved over the domain (note that this is only expected to be valid as $\text{Re} \rightarrow \infty$), that all vorticity is contained within the vortices themselves, and that the probability distribution functions (PDFs) of the vortex properties evolve self-similarly. Note that the latter assumption implies that averages of powers of quantities scale the same as powers of averages, for example:

$$\langle r^n \rangle(t) = c_n \langle r \rangle^n(t), \quad (1)$$

where c_n is independent of time and $\langle . \rangle$ denotes an averaged quantity.

1.1 Scaling of vortex properties

1.1.1 Circulation

Circulation Γ can be expressed in the following form

$$\Gamma_i = \int_{\text{vortex } i} \omega \, d^2\mathbf{x} \sim \omega_i r_i^2, \quad (2)$$

where constant relating Γ_i to $\omega_i r_i^2$ depends on the specific shape of the vortex. Hence, the evolution of the average circulation can be expressed as follows

$$\langle |\Gamma| \rangle \sim \langle \omega \rangle \langle r \rangle^2. \quad (3)$$

1.1.2 Energy

In 2D fluids, energy can be expressed in the following form

$$E = \frac{1}{2} \int |\mathbf{u}|^2 d^2\mathbf{x} = \frac{1}{2} \int |\nabla\psi|^2 d^2\mathbf{x}. \quad (4)$$

We integrate the above expression by parts, and since

$$\omega = \nabla^2\psi, \quad (5)$$

the energy can be expressed as

$$E = -\frac{1}{2} \int \omega\psi d^2\mathbf{x}. \quad (6)$$

Here, we've assumed that either ψ goes to 0 at infinity, for an infinite domain, or that the domain has periodic boundaries.

By inverting $\omega = \nabla^2\psi$, the streamfunction becomes

$$\psi(\mathbf{x}) = \frac{1}{2\pi} \int \omega(\mathbf{x}') \ln |\mathbf{x} - \mathbf{x}'| d^2\mathbf{x}'. \quad (7)$$

It is important to recognise that the vorticity generates the streamfunction; the streamfunction is not a locally derived property, but rather depends on the vorticity at near and far scales.

Substituting (7) into (6), we obtain

$$E = -\frac{1}{4\pi} \int \omega(\mathbf{x})\omega(\mathbf{x}') \ln |\mathbf{x} - \mathbf{x}'| d^2\mathbf{x} d^2\mathbf{x}'. \quad (8)$$

Now, considering isolated vortices, we sum over the domain to obtain

$$\begin{aligned} E = & -\frac{1}{4\pi} \left[\sum_{i=1}^N \int_{vortex\ i} \omega(\mathbf{x})\omega(\mathbf{x}') \ln |\mathbf{x} - \mathbf{x}'| d^2\mathbf{x} d^2\mathbf{x}' \right. \\ & \left. + \sum_{i \neq j} \int_{vortex\ i} d^2\mathbf{x} \int_{vortex\ j} \omega(\mathbf{x})\omega(\mathbf{x}') \ln |\mathbf{x} - \mathbf{x}'| d^2\mathbf{x}' \right]. \end{aligned} \quad (9)$$

The first part of equation (9) describes the energy induced by self-interactions and the second part of the equation describes the energy induced by vortex-vortex interactions. The logarithmic term is the Green's function. For the purposes of scaling E , in what follows logarithmic corrections are ignored. Further details regarding the accuracy of this omission are discussed in [1].

From the interaction energy part of equation (9), it might be assumed that the energy of interaction scales like $N^2\Gamma^2$; however, this result disagrees with turbulence simulations [2]. To derive the scaling expression for E , we consider the numbers of same-sign and opposite-sign interactions between pairs of vortices from equation (9) above. The total vorticity is

zero so that we have an equal number of vortices with positive and negative vorticity (note that we assume that all vortices have approximately the same magnitude of vorticity)

$$\text{number of same-sign pairs} = 2 \frac{N}{2} \left(\frac{N}{2} - 1 \right), \quad (10)$$

$$\text{number of opposite-sign pairs} = 2 \left(\frac{N}{2} \right)^2. \quad (11)$$

It is clear that we get cancellation from the contribution of same-sign and opposite-sign pairs, so that E scales like the number of vortices rather than the number of pairs, i.e.

$$E_{\text{interaction}} \sim E_{\text{self}} \sim N < \Gamma >^2. \quad (12)$$

This scaling now represents the combined effect of all vortices, rather than including them one at a time.

1.1.3 Enstrophy

The enstrophy equation can be expressed in the following form

$$Z = \frac{1}{2} \int |\omega|^2 d^2 \mathbf{x}, \quad (13)$$

from which, the scaling $Z \sim N < \omega >^2 < r >^2$ is obtained.

1.1.4 Final scalings

We have derived the scaling of Γ , E and Z as follows

$$< \Gamma > \sim < \omega > < r >^2, \quad (14)$$

$$E \sim N < \Gamma >^2, \quad (15)$$

$$Z \sim N < \omega >^2 < r >^2. \quad (16)$$

Using these three quantities it is possible to express the scaling behaviour of the other vortex properties of the fluid field.

Now, our underlying assumptions that E and ω are conserved properties, namely

$$E \sim t^0, \text{ and} \quad (17)$$

$$< \omega > \sim t^0, \quad (18)$$

along with the evolution of the vortex number N observed in turbulence solutions

$$N(t) = N(T_0) \left(\frac{t}{t_0} \right)^{-\xi}, \quad (19)$$

provide the necessary closure to the theory. Empirically, we find that $N \sim t^{-\xi}$, where $\xi \sim 0.72$.

It is possible to express the time-evolution of all quantities in terms of scaling exponent ξ . For example,

$$E \sim t^0 \sim N < \Gamma >^2, \quad (20)$$

$$< \Gamma > \sim N^{-1/2} \sim t^{\xi/2}, \quad (21)$$

$$< r > \sim t^{\xi/4}. \quad (22)$$

Experimental studies have employed a range of numerical techniques to evaluate the evolution of vortex properties, as proposed by the scaling theory, and the value of the exponent ξ . These include direct numerical simulations (DNS) of 2D turbulence, point vortex models and laboratory experiments (e.g., that examine electrically excited vortices in a thin electrolyte). There is reasonable agreement between most experimental studies on the robustness of the scaling relationships and most studies estimate a value of ξ close to 0.7 [3, 4]. For example, Bracco et. al. [9] found good agreement between numerical simulations of decaying 2d turbulence and scaling theory for the vortex properties N , r , ω , Γ and the scaling exponent ξ (figure 1). These agreements are relatively consistent between low and high resolution simulations (figure 2). However, some studies estimate slower or faster decays (table 1 from [3]). These differences may be due to the choice of analysis technique used, lateral dissipation and initial conditions such as the initial number of vortices (for example, all of the studies estimating a value of ξ much different to 0.7 had less than 100 vortices initially, which decreases the statistical significance of the results [3]). Whether experiments were run for a sufficient period of time to resolve the scaling regime has also been questioned [3]. Finally, despite reasonable agreement with experimental studies, there remains no convincing theory for the value of ξ .

2 Point-vortex model of 2D decaying turbulence

One of the primary goals of the point-vortex model was to construct the simplest model capturing the scaling regime of two-dimensional decaying turbulence [1]. In this model, 2D decaying turbulence is described by a “vortex gas” with circulations that determine the velocity field. Vortex same-sign merger is the dominant dissipative mechanism. The point-vortices are Hamiltonian, and hence, conservative, and each vortex has a position and circulation. Under this framework, same-sign pairs rotate without merger. However, given that when two point-vortices approach, the dissipation becomes important, we require a modification of the dynamics: when two same-sign vortices approach within a critical merger distance, they merge instantaneously, and are replaced by a single new vortex. The Hamiltonian dynamics then continues with this new vortex set. So, the new point-vortex dynamics is conservative everywhere in time except for a set of measure zero. This is a new class of dynamical system, which has been called punctuated Hamiltonian dynamics, and is neither conservative nor smoothly dissipative. This class of dynamical systems captures the intermittency of high Reynolds number turbulence.

2.1 Merger rules

When two same-sign vortices approach within a critical merger distance, determined to be less than approximately 3.3 times the vortex radius, the Hamiltonian dynamics are

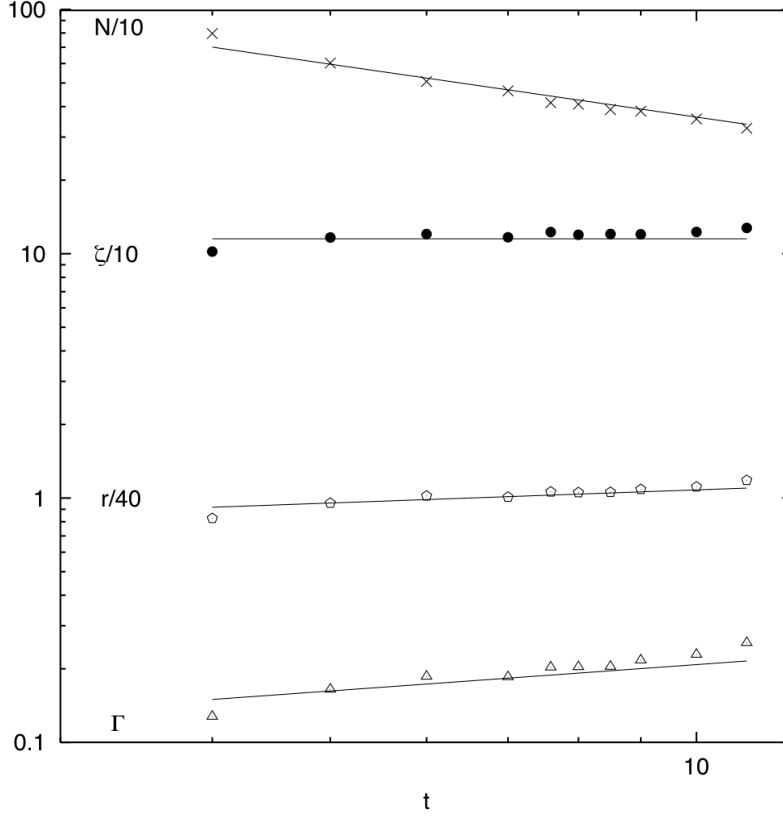


Figure 1: A comparison of average vortex number $N(t)$, vortex radius $r(t)$, vortex circulation magnitude $\Gamma(t)$, and peak vorticity ω (denoted by ζ in the figure) from a 2d decaying turbulence simulation (symbols) and scaling theory (solid lines) with $\xi = 0.72$. The model was of 4096^2 resolution. Each of the quantities has been multiplied by a suitable constant for graphical representation purposes. Note the logarithmic x- and y-axes. From [9].

interrupted and the two vortices merge into one new vortex. To capture this merger, we must modify our point-vortex model so that each vortex carries a dynamically inactive size. During the merger, the energy and peak vorticity are conserved, as in scaling theory. We further assume that the initial vortices have uniform peak vorticity, $\omega_i = \pm\omega_a$ for all i , and that the newly formed vortex also has the same vorticity (i.e. $\omega_{new} = \omega_1 = \omega_2$). Furthermore, we derive the following rules for the size and circulation of the new vortex based on the conservation of E

$$\Gamma_{new}^2 = \Gamma_1^2 + \Gamma_2^2, \quad (23)$$

$$r_{new}^4 = r_1^4 + r_2^4. \quad (24)$$

An interesting experiment would be to trace the linear momentum as two vortices merge. Since the circulation of the new vortex is not identical to the sum of the circulations of the

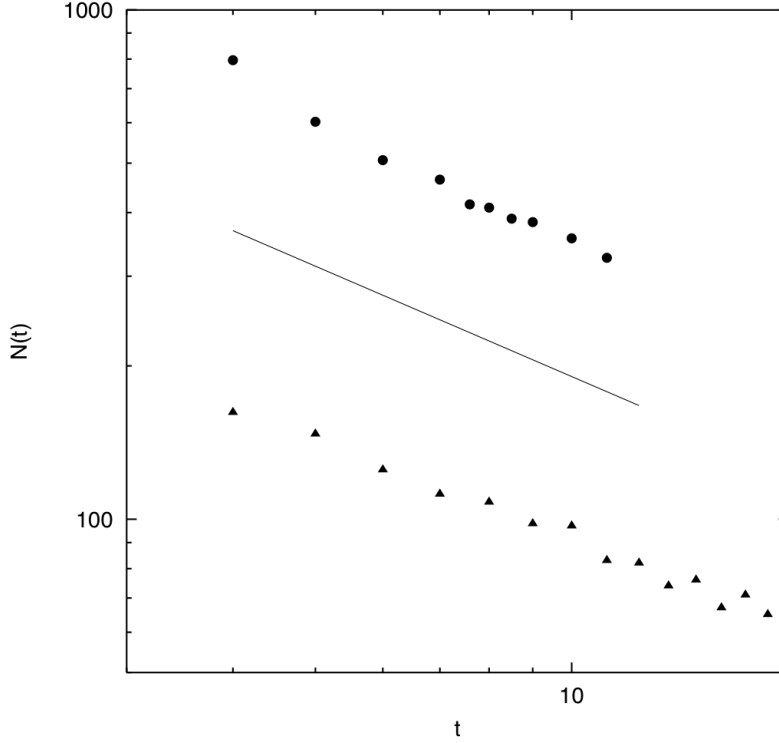


Figure 2: A comparison of average vortex number $N(t)$ estimated from decaying 2d turbulence simulations at high resolution (circles) and low resolution (triangles). Evolution predicted by scaling theory with $\xi = 0.72$ is represented by the solid line. Note the logarithmic x- and y-axes. From [9].

merging vortices, we would expect a change in linear momentum over the simulation.

2.2 Results of Punctuated model

Long integrations of the punctuated point-vortex model are obtained through renormalization, whereby the final state of an integration is used to initialise a new simulation with many more vortices, allowing us to reach the asymptotic scaling regime more quickly and to obtain sufficient data to reduce the sampling error. The model reproduces the vortex number N , vortex radius r_a , circulation magnitude Γ , enstrophy Z and kurtosis K_a predicted from scaling theory very well (figure 4). Figure 5 shows that the punctuated model produces scaled distributions that, within sampling variability, are constant in time and hence evolve self-similarly, although the model contains a higher number of small vortices than the turbulence solution.

3 Forced 2D turbulence

Forcing can be included in the 2D Navier-Stokes equations as follows

TABLE I. 2D turbulence experiments in which the vortex density decay rate was determined. The type of experiment is listed, as is an estimate of the initial number of vortices and the density decay exponent, χ . The second estimate from Bracco *et al.* (Ref. 17) (in parentheses) is for a subset of “strong” vortices.

Authors	Type	N_0	χ
McWilliams, 1990 ^a	DNS	500	0.71
Tabeling <i>et al.</i> , 1991 ^b	Lab	36–100	0.7 ± 0.1
Benzi <i>et al.</i> , 1992 ^c	Pt. vortex	300	0.6 ± 0.05
Weiss and McWilliams, 1993 ^d	Pt. vortex	400	0.72 ± 0.02
Cardoso <i>et al.</i> , 1994 ^e	Lab	50	0.44 ± 0.1
Hansen <i>et al.</i> , 1998 ^f	Lab	64	0.7 ± 0.1
Bracco <i>et al.</i> , 2000 ^g	DNS	800	0.76 ± 0.03 (0.67 ± 0.02)
Trizac, 1998 ^h	Molecular	50000	0.71 ± 0.01
Clercx and Nielsen, 2000 ⁱ	DNS	100	1.0 ± 0.1
Sire and Chavanis, 2000 ^j	Pt. vortex	50	1
Clercx <i>et al.</i> , 2003 ^k	Lab./DNS	100	0.7 ± 0.1
van Bokhoven <i>et al.</i> , 2007 ^l	DNS	64	$0.63\text{--}0.93$

Figure 3: table from [3]

$$\partial_t \mathbf{u} + \mathbf{u} \cdot \nabla \mathbf{u} = -\nabla p + \nu \nabla^2 \mathbf{u} - \alpha \mathbf{u} + \mathbf{f}, \quad (25)$$

where ∂_t denotes a partial derivative with respect to time, \mathbf{u} is the 2D fluid velocity, p is pressure, ν is the viscosity, α is a linear frictional damping term and \mathbf{f} is the forcing term [5]. The evolution of fluid properties (e.g. energy, enstrophy, vorticity) depends on the details of the forcing. The forced state produces an inverse energy cascade to larger scales, which arises primarily from the interaction of strain and vortices of different sizes, without requiring vortex merger or growth as in the non-forced simulations [5]. Forced 2D turbulence also produces a direct enstrophy cascade to smaller scales. We direct readers to [5] for a more comprehensive review of forced 2D turbulence.

4 Summary of 2D

We have considered the properties and evolution of coherent structures under decaying and forced 2D turbulence. 2D vortex dynamics can be modelled by both point vortices and elliptical vortices, where decaying turbulence acts like a “vortex gas”. By implementing structure based scaling theory, we can represent all vortex properties in terms of a few quantities, such as vortex number N , vortex radius r and vorticity ω . Furthermore, the time-evolution of all vortex properties can be expressed in terms of the vortex exponent ξ . Numerical and experimental studies show a reasonable agreement of values of the exponent; disagreements on the value of ξ can be attributed to different lateral dissipations or initial conditions. The punctuated point vortex model is a Hamiltonian point vortex model that

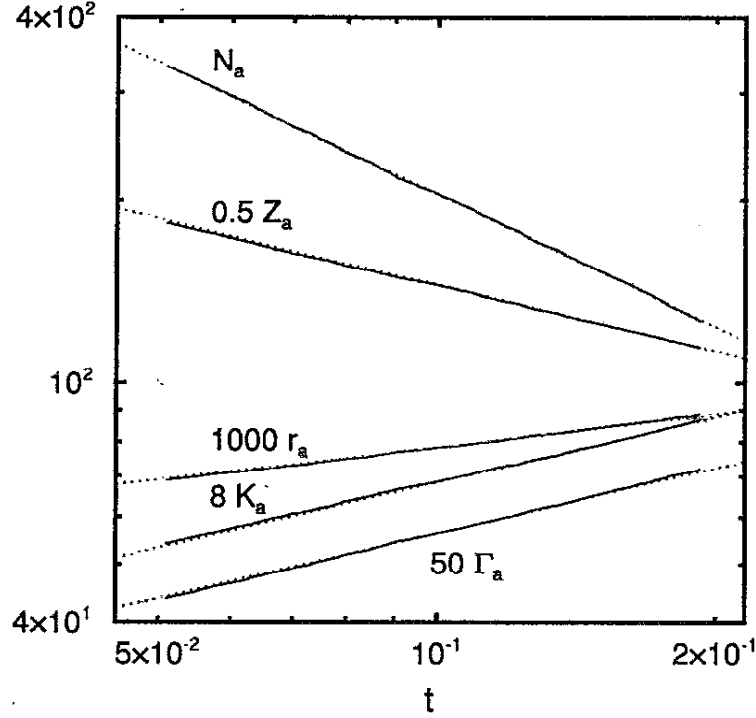


Figure 4: A comparison of average vortex number $N_a(t)$, vortex radius $r_a(t)$, vortex circulation magnitude $\Gamma_a(t)$, enstrophy $Z_a(t)$, and kurtosis $K_a(t)$ from the modified point-vortex model (solid lines) and scaling theory (dotted lines). In the model, $t_0 \leq t \leq t_0 + t'_{\text{end}}$, where $t_0 = 0.050$ and $t'_{\text{end}} \approx 0.14$ is the earliest time for one of the 30 cycles to reach $N = 100$. From [1].

has been modified such that vortices carry a size that is dynamically-inactive except during close approaches, when dissipative vortex merger occurs. This modified model captures the main features of 2D decaying turbulence well. According to [4],

Concerning the decay problem, we are thus left at the present time with an elegant phenomenological theory (“universal decay theory”), which turns out to represent consistent sets of numerical and experimental observations.

However, there remains disagreement, particularly observable at Walsh Cottage, whether decay theory is truly “universal” and whether the numerical and experimental observations that underlie the theory are truly “consistent”. Finally, it is possible to observe inverse energy cascades in forced 2D turbulence, although the properties and evolution of the coherent structures in this framework will depend on the mechanism of forcing.

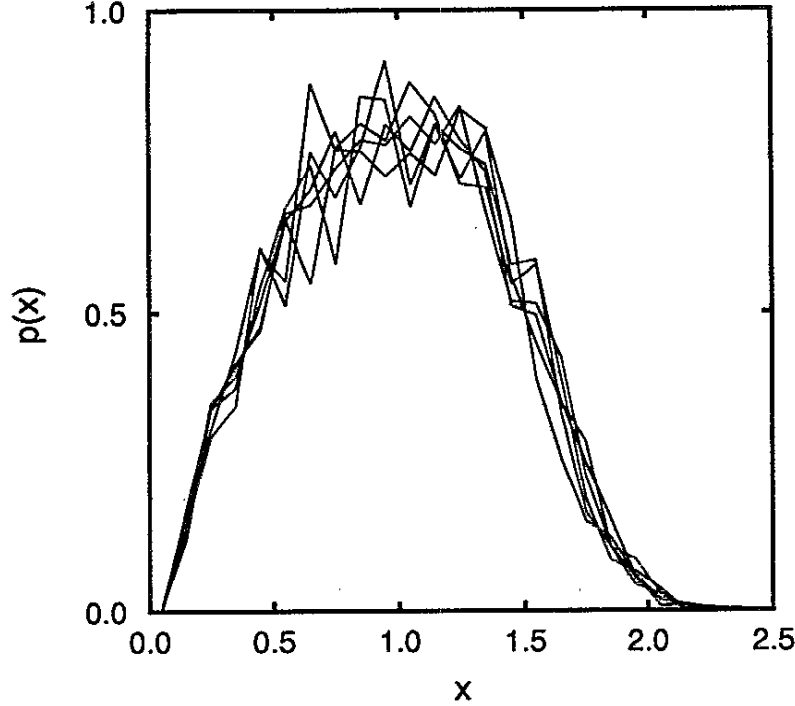


Figure 5: Probability distribution functions $p(x)$ at six different times from the punctuated point-vortex model calculated by averaging over 30 cycles. From [1].

5 Structures in 3D Quasigeostrophic Fluid Dynamics

5.1 Quasigeostrophic equations

We relax the 2D assumption and again consider the case of $Ro \ll 1$ (rapid rotation, i.e. scales slower than a day) and $F \ll 1$ (strong stratification). We assume the system is hydrostatic,

$$\frac{\partial p}{\partial z} + \rho g = 0, \quad (26)$$

so vertical gravity is balanced by the vertical pressure gradient, and that the fluid is thin, so the vertical dimension is much smaller than the horizontal dimensions. The 3D momentum equation is

$$\frac{\partial \mathbf{u}}{\partial t} + (\mathbf{u} \cdot \nabla) \mathbf{u} = -\nabla p + \nu \nabla^2 \mathbf{u} - \mathbf{f} \times \mathbf{u}, \quad (27)$$

and the fluid is incompressible

$$\nabla \cdot \mathbf{u} = 0. \quad (28)$$

The equation for conservation of mass is

$$\frac{\partial \rho}{\partial t} + (\mathbf{u} \cdot \nabla) \rho = 0, \quad (29)$$

and the vertical density gradient is given by

$$\frac{\partial \rho}{\partial z} = -\frac{N^2}{g}, \quad (30)$$

where $N = N(z)$ is the buoyancy frequency, which we assume to be horizontally uniform. An asymptotic analysis of the 3D equations, with $Ro \ll 1$, results in the quasigeostrophic equations.

At lowest order in Ro , we obtain

$$\mathbf{0} = -\nabla p - \mathbf{f} \times \mathbf{u}, \quad (31)$$

where the leading order velocity field is

$$\mathbf{u}(x, y, z, t) = (u, v, 0), \quad (32)$$

and \mathbf{f} is the Coriolis parameter defined in lecture 1. Therefore, to leading order, the Coriolis force balances the horizontal pressure gradient. This is called geostrophy. The leading order velocity field is called the geostrophic velocity. The geostrophic velocity is 2D, so using incompressibility we can write the geostrophic velocity in terms of a streamfunction ψ :

$$(u, v) = \left(-\frac{\partial \psi}{\partial y}, \frac{\partial \psi}{\partial x} \right). \quad (33)$$

The next order in the asymptotic analysis gives the time dependence of \mathbf{u} and the vertical velocity. Taking the curl of the next order of the momentum equation (27) and using incompressibility gives

$$\frac{D\omega}{Dt} - f \frac{\partial w}{\partial z} = \nu \nabla^2 \omega, \quad (34)$$

where we define the material derivative as

$$\frac{D}{Dt} \equiv \frac{\partial}{\partial t} + \mathbf{u} \cdot \nabla. \quad (35)$$

Using (29) and (30) we find an equation for the vertical velocity

$$w = -\frac{f}{N^2} \frac{D}{Dt} \frac{\partial \psi}{\partial z}. \quad (36)$$

We then combine this with (34) to obtain

$$\frac{D}{Dt} \left(\omega + \frac{\partial}{\partial z} \left(\frac{f^2}{N^2} \frac{\partial \psi}{\partial z} \right) \right) = \nu \nabla^2 \omega, \quad (37)$$

or

$$\frac{Dq}{Dt} = \nu \nabla^2 q, \quad (38)$$

to leading order, where q is the potential vorticity

$$q = \omega + \frac{\partial}{\partial z} \left(\frac{f^2}{N^2} \frac{\partial \psi}{\partial z} \right). \quad (39)$$

The first term in this equation is the relative vorticity obtained from the curl of the geostrophic velocity, $\omega = \nabla \times \mathbf{u} = \nabla_{2D}^2 \psi$, and the second is the ‘stretching term’. The vertical velocity causes stretching, which causes ω to change over time.

If N is constant, $N \neq N(z)$, then let $z' = Nz/f$, and the potential vorticity is given by the isotropic 3D Laplacian,

$$q = \nabla_{3D}^2 \psi. \quad (40)$$

Equations (38) and (40) are the 3D quasigeostrophic (QG) equations for constant N . The 3D Laplacian in (40) indicates that the velocity field depends on the global 3D vorticity distribution.

We can compare the 3D QG equations with constant N to the 2D equations found previously:

	2D	3D QG, constant N
Inviscid vorticity equation:	$\frac{D\omega}{Dt} = 0$	$\frac{Dq}{Dt} = 0$
$q - \psi$ relationship:	$\omega = \nabla_{2D}^2 \psi$	$q = \nabla_{3D}^2 \psi$

The similarity of the QG equations to the 2D vorticity equations leads to the same turbulent cascade theory as 2D. If $\nu = 0$, the potential vorticity q is invariant, so as in 2D there is no stretching of potential vorticity in QG. The energy

$$E = -\frac{1}{2} \int q(x)\psi(x)d^3\mathbf{x} \quad (41)$$

is conserved, as in 2D, although there is now a contribution from potential energy. Thus the analysis of the 2D equations gives some insight into a fully 3D, asymptotic ($Ro \ll 1$, $F \ll 1$) regime.

5.2 QG decaying turbulence

Isotropy of the $q - \psi$ relation ($q = \nabla^2 \psi$) and Taylor-Proudman ideas led to predictions of 3D isotropic spectra [7] and vertical barotropic (depth-independent) columns. However, numerical simulations (320^3 resolution) by [6] with random homogeneous and isotropic initial conditions show otherwise. The simulations use the dynamical QG equation

$$\frac{Dq}{Dt} = -\mathcal{D}, \quad (42)$$

with q defined in (39). The dissipation operator $\mathcal{D} = \nu \nabla^4 q$ represents the effects of the smaller scales of motion (ν is a small hyperviscosity). Figure 6 shows results of the simulations at four different times. The simulations show the formation of roughly spherical vortices (in stretched coordinates $z' = Nz/f$). The vortices are advected by the velocity field caused by the other vortices. The two primary interaction mechanisms that transform the vortex population are between same sign vortices: nearly horizontal merger, as we have already seen in 2D, and vertical vortex alignment, which is a new phenomenon to QG. Unlike vortex merger, the vertical alignment process is at least partly reversible (in that aligned vortices can move out of alignment) and the vortices remain distinct. The number

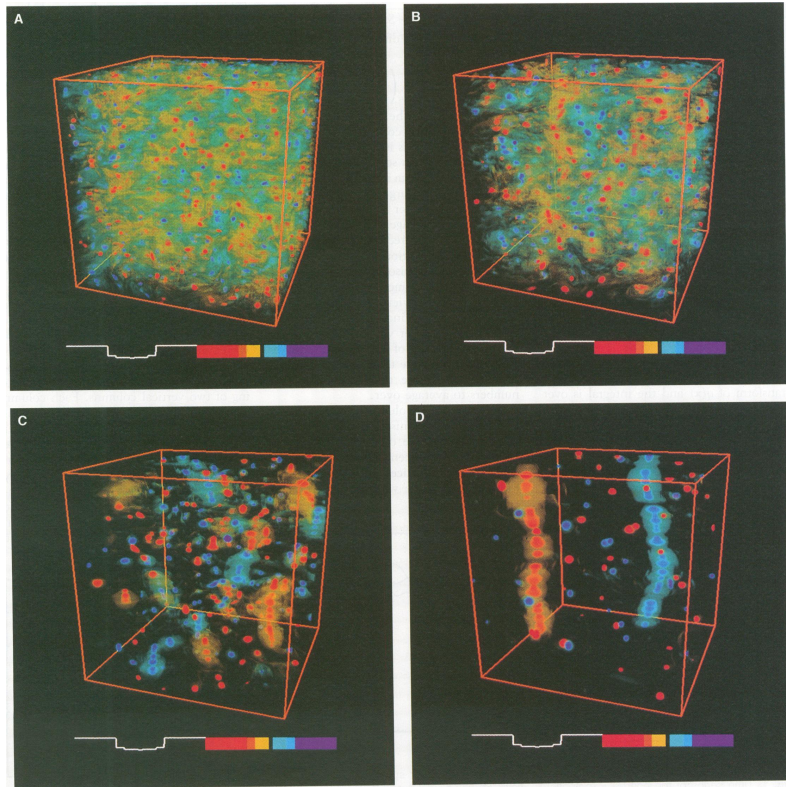


Figure 6: Potential vorticity $q(x, y, z')$ at (A) $t = 5.0$, (B) $t = 10.0$, (C) $t = 25.6$, and (D) $t = 72.1$. Taken from [6].

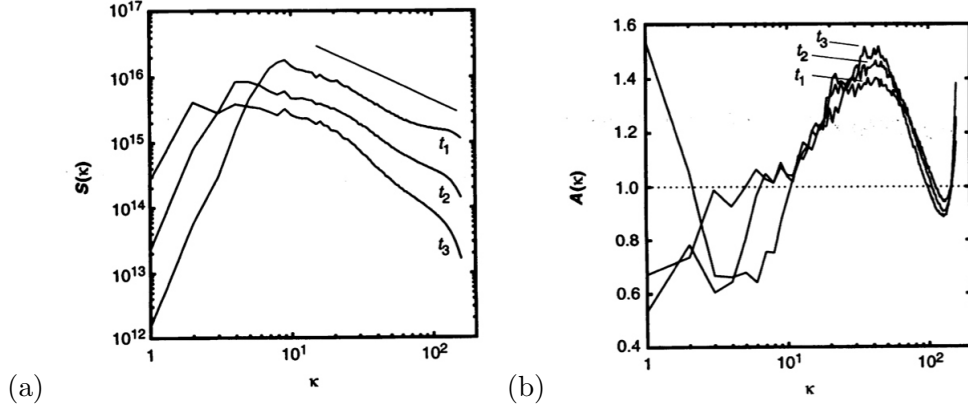


Figure 7: (a) Wavenumber spectra of potential vorticity $S(\kappa)$ at $t_1 = 2.2$, $t_2 = 5.0$, and $t_3 = 10.0$. (b) Spectrum anisotropy $A(\kappa)$ at t_1, t_2 , and t_3 . Taken from [6].

of vortices decreases with time due to vortex merger, and the end result is of two columns of vertically aligned same-sign vortices, with the appearance of ‘beads on a string’. This two column system is an analogue of the final vortex dipole in 2D. Similarly to 2D, the spectra are steeper than cascade theory predicts. In addition, there is significant spectral anisotropy,

$$A(\kappa) = \frac{3S_{z'}(\kappa)}{S_x(\kappa) + S_y(\kappa) + S_{z'}(\kappa)} \neq 1, \quad (43)$$

where $S_i(\kappa)$ are the directionally weighted wavenumber spectra of q

$$S_i(\kappa) = \int_{|\boldsymbol{\kappa}|=\kappa} \left(\frac{\kappa_i}{\kappa} \right)^2 |\hat{q}|^2 d\boldsymbol{\kappa}, \quad (44)$$

$i = x, y, z'$, $\hat{q}(\boldsymbol{\kappa})$ is the 3D Fourier transform of $q(\mathbf{x})$, and $\kappa = |\boldsymbol{\kappa}|$ is the magnitude of the 3D wavenumber. Note that $\sum_i S_i = S(\kappa)$ which is the spectrum of \hat{q} averaged over a shell of constant κ . Graphs of $S(\kappa)$ and $A(\kappa)$ are shown in figure 7. $A(\kappa) \neq 1$ indicates an anisotropic potential vorticity distribution at wave number κ . Due to this anisotropy (which is perhaps not surprising since D/Dt is not isotropic), the vortices are broader in the horizontal than the vertical.

5.3 QG vortex census ([8])

With the idea that ‘geostrophic turbulence is controlled by the self-, pair-, and collective-dynamics of its coherent vortices’, [8] did a vortex based statistical analysis of the results from the numerical simulations described above. This describes the structure and evolution of the vortex population in QG turbulence. A subjective automated algorithm is used to perform a vortex census to identify vortices and to measure their size, strength and shape. The result of this census is that the number of vortices decreases over time, which is expected from vortex merger. The mean enstrophy and mean circulation both increase over time. The mean of the peak vorticity, q_p , is approximately constant after an initial time (when the number of weak vortices appears to decrease faster than the number of strong

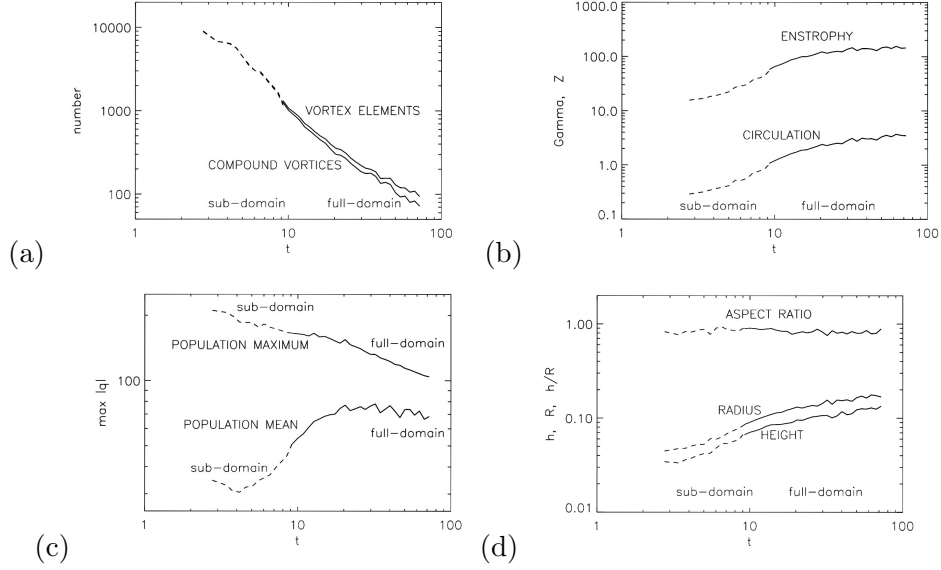


Figure 8: Graphs of the QG vortex census results: (a) number of vortices; (b) Γ and Z ; (c) maximum of q_p and mean of q_p ; (d) height h , radius R and aspect ratio. Taken from [8])

vortices), while the maximum of q_p decreases due to dissipative effects. The mean radius and height both increase over time, but the aspect ratio remains approximately constant (≈ 0.8). However, this constancy is not yet well understood. All these quantities appear to be described relatively well by power laws in t (see figure 8), which indicates the possibility of a scaling theory. Since there are no vertical velocity dynamics in the potential vorticity q , which is only advected horizontally, a scaling theory for QG can be derived in a similar way to the 2D scaling theory above.

5.4 QG scaling theory

The scaling theory is derived similarly to 2D (see section 1), with an additional empirical constant of the vortex aspect ratio. The assumptions are

- $q_p \sim \text{constant}$
- Aspect ratio $\sim \text{constant}$
- $N \sim t^{-\xi}$
- E conserved
- All vorticity is within vortices (this assumption turns out to be less valid than in 2D, because there are more background vorticity effects)

Following the same arguments as in the 2D scaling, we find scaling exponents for the different quantities in terms of a single exponent ξ . Empirically, from the results of the vortex census, $\xi \approx 1.25$, which is higher than for 2D. Therefore the number of coherent

vortices decreases more rapidly in 3D QG than in 2D. The assumption of constant aspect ratio gives

$$\langle h \rangle \sim \langle R \rangle, \quad (45)$$

where $\langle h \rangle$ is the average vortex height and $\langle R \rangle$ is the average vortex radius. Similarly to 2D, the circulation and enstrophy scale as

$$\langle \Gamma \rangle \sim \langle q \rangle \langle R \rangle^2, \quad \langle Z \rangle \sim \langle q \rangle^2 \langle R \rangle^2, \quad (46)$$

where q is potential vorticity (39). The energy is given by

$$E \sim \int d^3 \mathbf{x} \int d^3 \mathbf{x}' q(\mathbf{x}) q(\mathbf{x}') G(\mathbf{x}, \mathbf{x}'), \quad (47)$$

where G is a Green's function. In 2D, the Green's function $\sim \ln |\mathbf{x} - \mathbf{x}'|$, and we ignored the log terms in the scaling theory (see section 1.1.2). However, in 3D QG, the Green's function $\sim 1/|\mathbf{x} - \mathbf{x}'|$, so we must pick a length scale $L \sim |\mathbf{x} - \mathbf{x}'|$. This introduces some ambiguity. Considering the interaction energy between vortices, we choose $L \sim N^{-1/3}$, which is the typical vortex pair separation distance. This gives scalings of

$$\langle R \rangle \sim \langle h \rangle \sim t^{2\xi/9} = t^{0.28}, \quad (48)$$

$$\langle \Gamma \rangle \sim \langle Z \rangle \sim t^{4\xi/9} = t^{0.55}. \quad (49)$$

Considering the self-interaction energy, we choose $L \sim R$, which is the vortex size. This gives scalings of

$$\langle R \rangle \sim \langle h \rangle \sim t^{\xi/5} = t^{0.25}, \quad (50)$$

$$\langle \Gamma \rangle \sim \langle Z \rangle \sim t^{2\xi/5} = t^{0.50}. \quad (51)$$

For both choices of L , the scalings of $\langle R \rangle$, $\langle h \rangle$ and $\langle \Gamma \rangle$ agree well with the vortex census results ($\langle R \rangle \sim t^{0.29 \pm 0.05}$, $\langle h \rangle \sim t^{0.28 \pm 0.05}$, $\langle \Gamma \rangle \sim t^{0.45 \pm 0.10}$). There is more discrepancy in the exponent of $\langle Z \rangle$, which is smaller in the vortex census results ($\langle Z \rangle \sim t^{0.34 \pm 0.10}$) than in the scaling theory. This indicates that there is greater dissipation of vorticity q within the vortices in the numerical simulation than assumed in the scaling theory.

5.4.1 QG column waves

Another interesting observation from the numerical simulations in [6] is the appearance of vertical helical and planar waves on the vortex columns. These are shown in figure 9, but have not yet been studied.

References

- [1] Weiss, J.B., McWilliams J.C. 1993. Temporal scaling behavior of decaying two-dimensional turbulence. *Phys. Fluids A*, 5(3), 608-621.

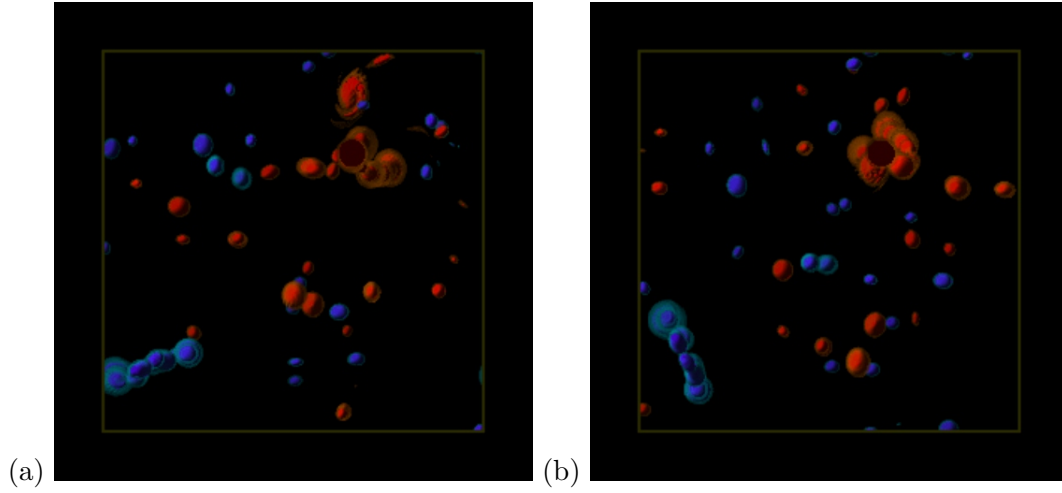


Figure 9: Top view of the simulation results [6] at two different times, showing a planar wave (blue vortex column, positive vorticity) and a helical wave (red vortex column, negative vorticity).

- [2] Carnevale, G.F., McWilliams, J.C., Pomeau, Y., Weiss, J.B., Young, W.R. 1991. Evolution of vortex statistics in two-dimensional turbulence. *Phys. Rev. Lett.*, 6(21), 2735-2737.
- [3] LaCasce, J.H. 2008. The vortex merger rate in freely decaying, two-dimensional turbulence. *Phys. Fluids*, 20, DOI: 10.1063/1.2957020.
- [4] Tabeling P. 2002. Two-dimensional turbulence: a physicist approach. *Phys. Rep.*, 362, 1-62.
- [5] Boffetta, G., Ecke, R.E. 2012. Two-dimensional turbulence. *Annu. Rev. Fluid Mech.*, 427-451, DOI:10.1146/annurev-fluid-120710-101240.
- [6] McWilliams, J. C., Weiss, J. B., Yavney, I., 1994. Anisotropy and Coherent Vortex Structures in Planetary Turbulence. *Science*, 264, 410-413.
- [7] Charney, J. G. 1971. Geostrophic Turbulence. *J. Atm. Sci.*, 28, 1087-1095.
- [8] McWilliams, J. C., Weiss, J. B., Yavneh, I. 1999. The vortices of homogeneous geostrophic turbulence. *J. Fluid Mech.*, 401, 1-26.
- [9] Bracco, A., McWilliams, J.C., Giuseppe, M., Provenzale, A., Weiss, J.B. 2000. Revisiting 2D Turbulence at Millenial Resolution, *Physics of Fluids*, 12, 2931-2941.

GFD 2012 Lecture 4 Part I: Structures in 3D quasi-geostrophic flows

Jeffrey B. Weiss; notes by Alban Sauret and Vamsi Krishna Chalamalla

June 21, 2012

1 Introduction

Geostrophic fluid dynamics describes a flow in which the force due to pressure gradient balances the Coriolis force. The large-scale flows in the atmosphere and ocean are approximately in geostrophic balance. Many studies show that the QG decaying turbulence self-organizes into roughly spherical vortices. Dynamical evolution of these vortices such as merging and alignment processes are interesting. Results of numerical investigations which studied the evolution processes such as merging and alignment are discussed in the following sections [1, 2].

2 Vortex merging

Similar to the two-dimensional decaying turbulence, quasi-geostrophic three-dimensional turbulence leads to same sign vortex merging, which is an important mechanism in determining the flow evolution.

2.1 Numerical method and initial condition

Numerical simulations are performed to study the dynamics of vortex merging process and also the effects of varying the aspect ratio on the merging process [1]. The following equation for potential vorticity has been solved numerically.

$$\frac{\partial q}{\partial t} + J(\psi, q) = \mathfrak{D}, \quad (1)$$

where

$$J(\psi, q) = \frac{\partial \psi}{\partial x} \frac{\partial q}{\partial y} - \frac{\partial \psi}{\partial y} \frac{\partial q}{\partial x}, \quad (2)$$

is the Jacobian operator, ψ is the stream function and the potential vorticity q is defined as

$$q = \frac{\partial^2 \psi}{\partial x^2} + \frac{\partial^2 \psi}{\partial y^2} + \frac{\partial^2 \psi}{\partial z'^2}, \quad (3)$$

where z' is the rescaled vertical coordinate, $z' = (N/f)z$. \mathfrak{D} on the right hand side of the potential vorticity equation represents the dissipation term, which is assumed to be

small compared to the other terms. Simulations are performed in a domain of size 2π in the horizontal directions and D in the vertical direction, where $D=2\pi$ in all simulations except those with the smallest aspect ratio $H/R=0.16$ where $D=\pi/2$. Periodic boundary conditions are used in all the three directions. The initial condition for potential vorticity is given by two ellipsoidal distributions with circular horizontal cross-sections of radius R and half-height H . Figure 1 shows the initial potential vorticity distribution. The vorticity field is symmetric with respect to the mid-plane $z'_c = D/2$.

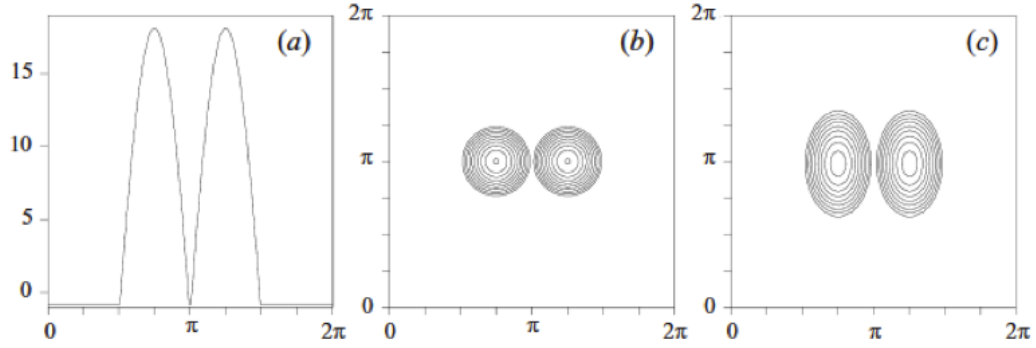


Figure 1: Initial potential vorticity distribution (a) the cosine profile of the vortices (b) horizontal PV section on the mid-plane (c) vertical PV section on the plane (x,z).

2.2 Results

Figure 2 shows the time evolution of the vorticity field for one of the simulated case with aspect ratio $H/R = 1.5$. Figure 2(a) shows the potential vorticity field at a horizontal section $z'_c = D/2$. Figure 2(b) shows PV distribution at $z'_1 = z'_c + 3H/4$, whereas figure 2(c) shows the PV distribution at a vertical section $y = \pi$. The horizontal section of PV distribution at $z'_c = D/2$ shows the vortices merging to form a core with thin filaments around the core. Vertical section of PV distribution shows that these filaments are actually an ensemble of 'PV sheets' which enclose the merging vortices. Horizontal section of PV distribution at z'_1 shows that there is no definite core at this vertical level and the vorticity has been elongated to form spiral like shape. Overall, the evolution leads to an increase in the final radius and decrease in the vortex height thus reducing the aspect ratio. Another interesting dynamics of the vortex cores is that they elongate to form a flattened core before merging. Figure 3 shows the three-dimensional volume rendering of the PV field at different time instances.

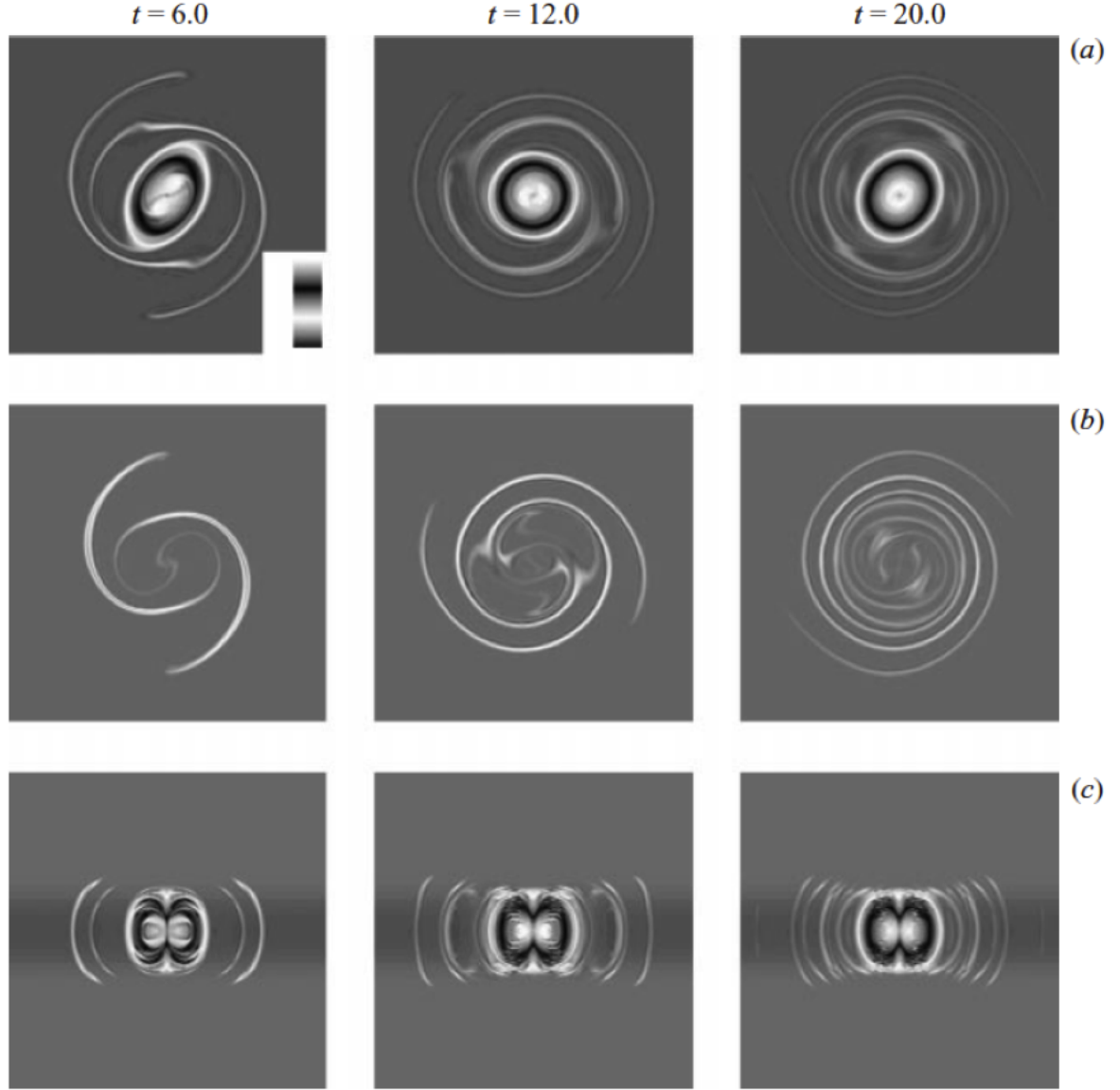


Figure 2: Potential vorticity distribution for baroclinic merging with vertical aspect ratio $H/R=1.5$ at times $t=6, 12, 20$. (a) Horizontal sections of potential vorticity on the mid-plane $z'_c = D/2$ (b) horizontal sections of potential vorticity on the plane $z'_1 = D/2 + 3H/4$ (c) vertical sections of potential vorticity on the plane (x,z) .

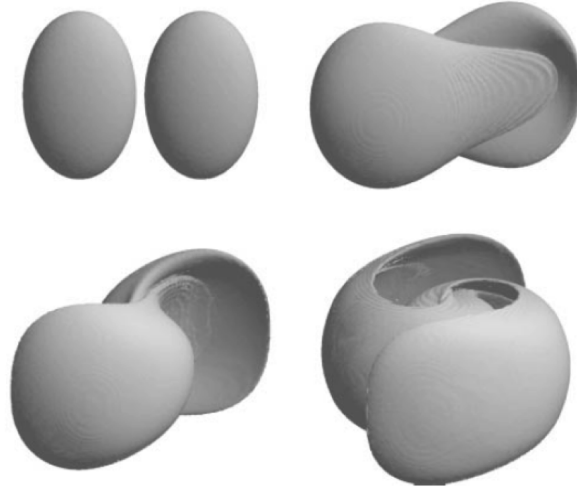


Figure 3: Volume rendering of potential vorticity at time $t=0, 1, 2, 4$ for baroclinic merging with $H/R = 1.5$.

At larger aspect ratio ($H/R = 2.5$), there is not much difference in the structures and the merging dynamics when compared with the case when $H/R = 1.5$. However, at low aspect ratios some interesting new features are observed in the outer filaments. Figure 4 shows the (a) horizontal (b) vertical sections of PV field at 3 different time instances. The aspect ratio H/R is 0.66 in this case. A horizontal section at $z_c' = D/2$ shows the merging of vortices forming a central core along with the shedding of thin filaments. At a later time, these vortex filaments develop secondary instabilities forming small vortices along the filaments. A vertical section of the PV field shows the curvature similar to the large aspect ratio result. The vortices formed by the secondary instability of the filaments are also visible in the vertical section.

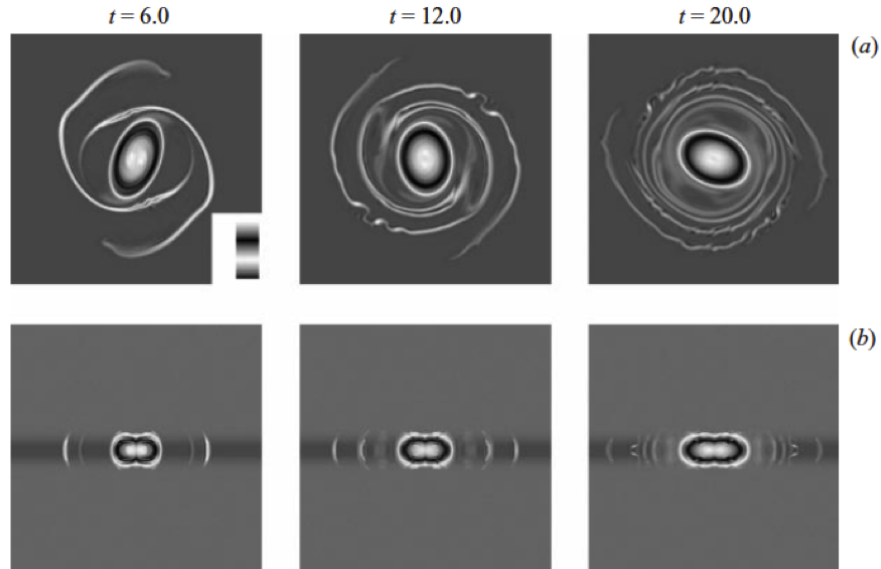


Figure 4: Potential vorticity distribution for baroclinic merging with vertical aspect ratio $H/R = 0.66$ at times $t=6, 12, 20$ (a) Horizontal sections of potential vorticity on the mid-plane $z_c' = D/2$ (b) vertical sections of potential vorticity on the plane (x,z) .

Next, still lower aspect ratio $H/R = 0.16$ is considered. The secondary instabilities are very prominent in the outer filaments. Figure 5 shows the horizontal section ($z_c' = D/2$) of PV field at 3 different times. The PV field shows that the filaments are almost destroyed and the newly formed vortices are prominently seen in the outer region.

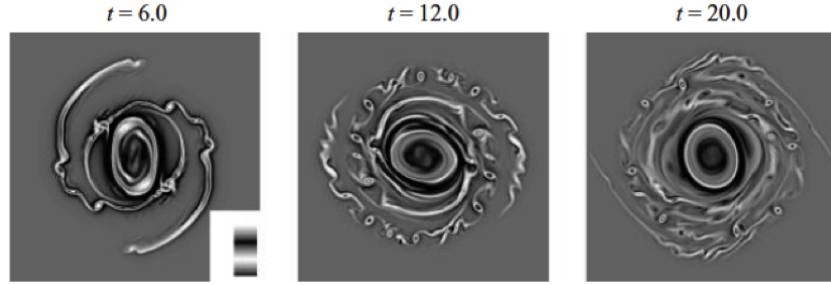


Figure 5: Potential vorticity distribution for baroclinic merging with vertical aspect ratio $H/R = 0.16$. The panels show horizontal sections of potential vorticity on the mid-plane $z_c' = D/2$ at times $t=6, 12, 20$.

2.3 Lagrangian analysis

Lagrangian analysis provides a good picture of the dynamical evolution of vortex core. The source of fluid particles in the final core (merged) is studied by seeding the tracer particles at two horizontal sections $z_c' = D/2$ and $z_1' = z_c' + 3H/4$. The grey scale in the inset of figures 6(a) and 6(b) indicates the final distance of particles at the end of merging process. At $z_c' = D/2$, figure 6 shows that the fluid particles forming the core of the final vortex are originating mainly from the cores of the merging vortices. Outer layers of each vortex move far from the core forming the thin filaments, as discussed before. However at z_1' , there is no definite core and the particles inside the individual vortices do not play a significant role. Most of the vorticity is distributed in the outer spiral-shaped filaments.

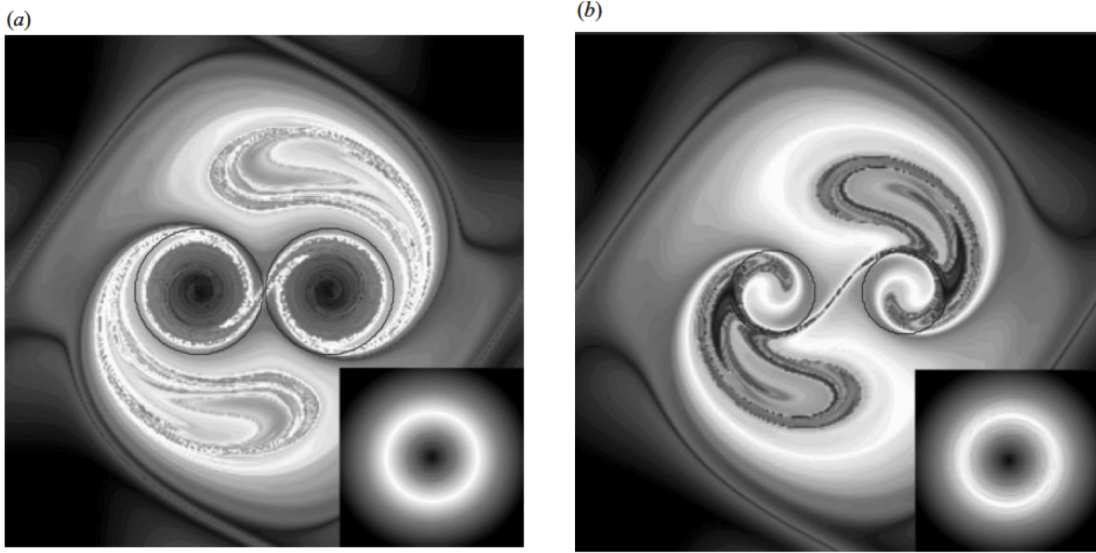


Figure 6: Initial tracer distribution for an aspect ratio $H/R = 1.5$. The grey scale indicates the final distance from the center of the domain that the particles will achieve at the end of the merging process, as depicted in the smaller panel inset. (a) $z'_c = D/2$, (b) $z'_1 = z'_c + 3H/4$.

2.4 Critical merging distance

Similar to two-dimensional vortex merging, we expect there to be a critical merging distance between the merging vortices. The dependence of this merging distance on the aspect ratio is presented here. Tracer particles are introduced into the flow with certain number of particles inside each vortex. Merging is considered to be done, when the total number of particles in the suitably defined central region reaches a threshold value which is taken as 99% of the total particles seeded in the flow. Figure 7 shows the graph of critical merging distance as a function of the aspect ratio. Results show that the critical merger distance is influenced strongly by the baroclinicity in the flow. At low vertical aspect ratio, interactions are more local and the critical merging distance is low. For example when $H/R = 0.66$, critical merging distance is observed to be $2.1 R$. As the aspect ratio (H/R) increases the critical merging distance increases rapidly. At very higher values of H/R , the critical merging distance exceeds that of barotropic vortex merger. Since the vortices here are constrained to have initial conditions which decay in z , they are never barotropic which could explain this apparent contradiction.

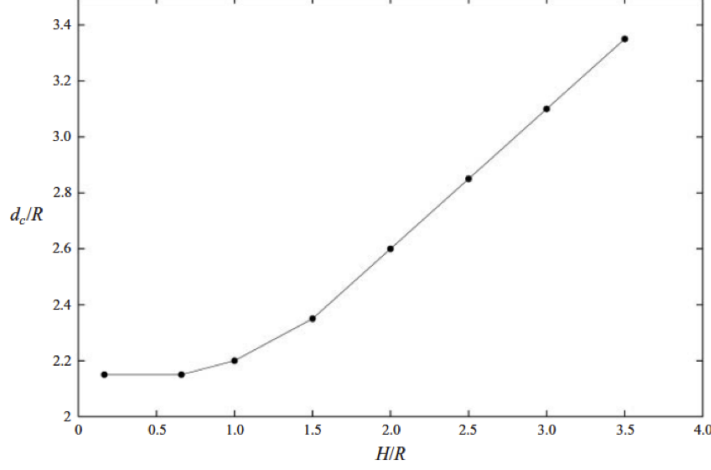


Figure 7: Critical merging distance d_c/R as a function of the initial vertical aspect ratio H/R .

3 Vortex alignment and merger

Interactions between the ellipsoidal vortices in the three-dimensional quasi-geostrophic turbulence has been studied using the ellipsoidal moment model and the results compared to the numerical simulations [2]. First, we establish the governing equations for the potential vorticity for three-dimensional QG turbulence.

3.1 Ellipsoidal moment model

The equation for the evolution of the potential vorticity q is

$$\frac{\partial q}{\partial t} + J(\psi, q) = \mathcal{D}, \quad (4)$$

where

$$J(\psi, q) = \frac{\partial \psi}{\partial x} \frac{\partial q}{\partial y} - \frac{\partial \psi}{\partial y} \frac{\partial q}{\partial x}, \quad (5)$$

is the Jacobian operator, ψ is the stream function and the potential vorticity q is defined as

$$q = -\nabla^2 \psi = -\left(\frac{\partial^2 \psi}{\partial x^2} + \frac{\partial^2 \psi}{\partial y^2} + \frac{\partial^2 \psi}{\partial z^2} \right), \quad (6)$$

The process of Hamiltonian moment reduction [3] is applied to the three-dimensional QG equations. The equations and the details of this reduction can be found in the appendix section of [2]. The ellipsoid moment model is used to study the interaction of the symmetric vortices. Initial vortex size has been chosen as a spheroid with the aspect ratio of 0.8, which is relevant to the recent QG turbulent simulations [4, 5]. Figure 8 shows the initial positions of the two vortices. The trajectories of the vortices were tracked using an adaptive Runge-Kutta method. Figure 9 shows the trajectories of one of the vortices with two different initial positions.

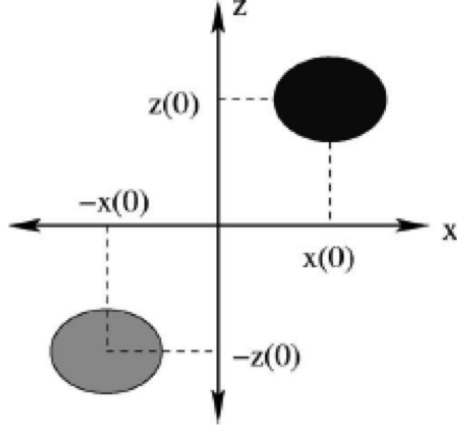


Figure 8: Schematic diagram of the initial positions of the two vortices and the coordinate system used.

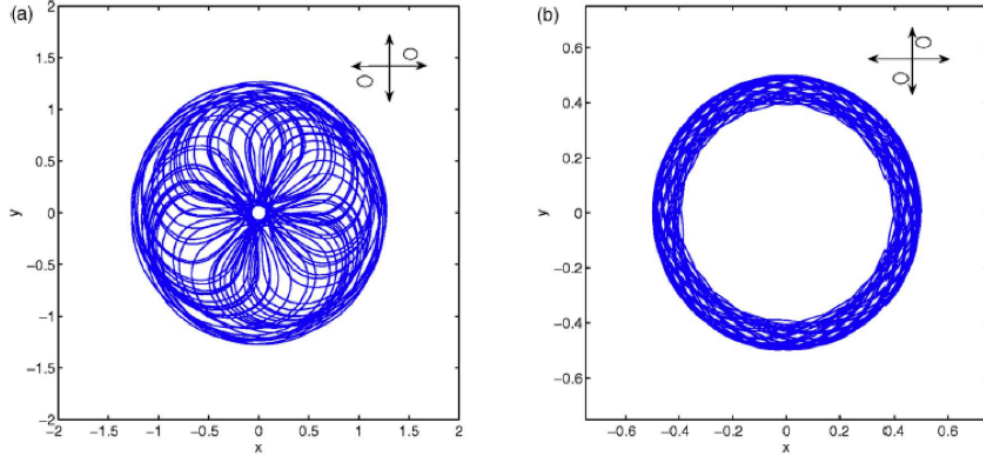


Figure 9: Trajectories projected into the $x - y$ plane for vortices with initial positions (a) $x_1(0) = 1.275$, $z_1(0) = 0.175$ and (b) $x_1(0) = 0.5$, $z_1(0) = 2.0$ as shown schematically in the insets.

3.2 Characteristics of merger/alignment

In two dimensions, when the centers of two vortices coincide, the Hamiltonian becomes singular. However, in three-dimensions the centers of vortices never coincide unless they lie on same horizontal plane initially. Based on the trajectories of the ellipsoid moment model, the horizontal separation $r_h(t) = 2\sqrt{x_1(t)^2 + y_1(t)^2}$, between the centers of vortices has been considered as the criteria for vortex merging/alignment. The minimum value of horizontal separation $\mathcal{R} = \min(r_h(t)/r_h(0))$ for different initial positions is shown in figure 10. For larger vertical separations, no sharp transition between merging/non-merging is

observed. In conclusion, there is a sharp transition between merging and non-merging but a smooth transition between alignment and non-alignment.

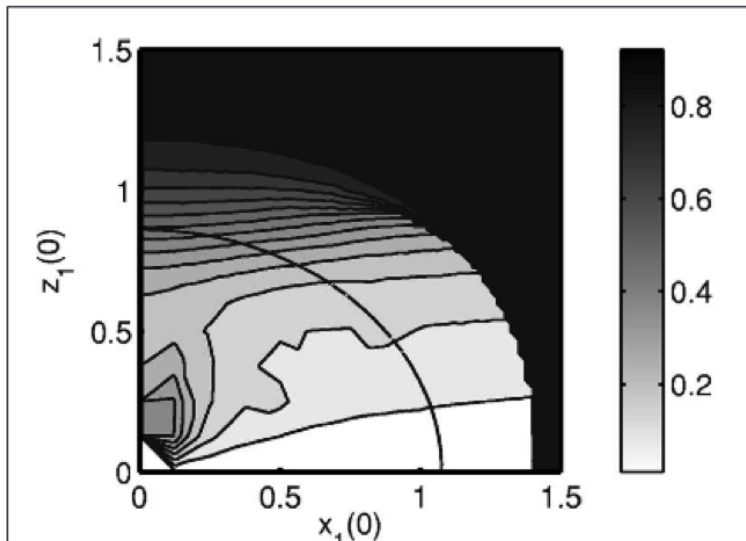


Figure 10: Contours of $\mathcal{R} = \min_t(r_h(t)/r_h(0))$ for varying initial positions $[x_1(0), z_1(0)]$. The solid line is the curve of initial positions that result in two vortices that are initially touching.

3.3 Three-dimensional QG simulations

Numerical simulations are performed integrating the three-dimensional QG equations using a fully pseudo-spectral model. Dissipation is included to obtain well behaved numerical solutions. The domain is periodic in all the three directions. Initial conditions for vorticity are chosen such that it matches with the ellipsoidal moment model simulations described above. Vortex merging is observed with small vertical separation and certain critical horizontal separation. Figure 11 shows the evolution of vortex merging in the $x - y$ plane at different time. Each vortex is seen to have developed a handle which move towards the other vortex along with the formations of filaments. The filaments here dissipate rather quickly because of the non-zero dissipation term. But the total dissipation is not severe, since the the maximum value of the potential vorticity falls to 93% of the initial value at $t = 500$. The predictions by the ellipsoidal moment model for the range of initial positions resulting in vortex merging agree well the QG simulation results. The three-dimensional structure of vortices has been investigated in the alignment region to learn about the inviscid behavior of vortices in the alignment region. The evolution of two aligning vortices in a high resolution simulation shows traveling wave-like structures that move up and down the vortex. These waves appear in most of the simulations in the alignment region, which are speculated to be related to the alignment process.

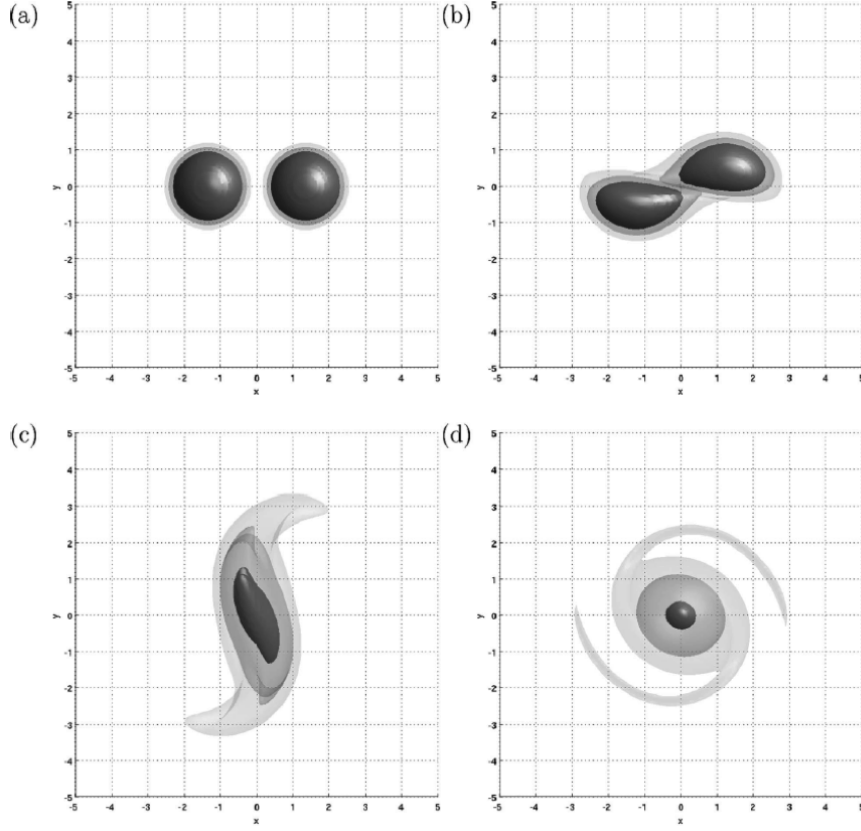


Figure 11: Snapshots of the evolution with $x_0 = 1.35$ and $z_0 = 0.3$ at (a) $t = 0$ (b) $t = 50$ (c) $t = 200$, and (d) $t = 500$. The isosurfaces are at 90%, 50%, and 10% of the maximum potential vorticity at that time. The view is looking down the z axis onto the $x - y$ plane.

4 Conclusion

Numerical studies show that the vortex merging in three-dimensional QG turbulence involves more complex dynamics when compared with the two-dimensional turbulence. The ellipsoid moment model has been used to study the merger and alignment of interacting vortices. Numerical simulations of the QG equations show a good agreement with the ellipsoid moment model regarding the range of initial positions which will result in merging or alignment. Higher resolution simulations and further study of ellipsoid moment model is required to improve the understanding of three-dimensional vortex merging and alignment.

References

- [1] von Hardenberg, J., McWilliams, J.C., Provenzale, A., Shchepetkin, A. and Weiss, J.B. (1999) Vortex merging in quasigeostrophic flows. *J. Fluid Mech.*, **412**, 331-353.

- [2] Martinsen-Burrell, N., Julien, K. Petersen, M.R. and Weiss, J.B. (2006) Merger and alignment in a reduced model for three dimensional quasigeostrophic ellipsoidal vortices, *Phys. Fluids*, **18**, 057,101114.
- [3] Meacham, S.P., Morrison, P.J. and Flierl, G.R. (1997) Hamiltonian moment reduction for describing vortices in shear, *Phys. Fluids*, **9**, 2310.
- [4] McWilliams, J.C., Weiss, J.B. and Yavneh, I. (1999) The vortices of homogeneous geostrophic turbulence, *J. Fluid Mech*, **401**, 1.
- [5] Reinaud, J.N., Dritschel, D.G. and Koudella, C.R. (2003) The shape of vortices in quasi-geostrophic turbulence, *J. Fluid Mech.*, **474**, 175.

GFD 2012 Lecture 4 Part II: Rapidly rotating convection

Jeffrey B. Weiss; notes by Alban Sauret and Vamsi Krishna Chalamalla

June 21, 2012

1 Introduction

Rapidly rotating convection constitutes an interesting mathematical system, and is relevant in geophysics and oceanography, for example, in the phenomenon of ocean deep convection. However, the rapid rotation and strong thermal forcing found in natural systems is inaccessible to numerical simulations of the underlying Boussinesq equation. By applying an asymptotic expansion one obtains reduced equations for non-hydrostatic quasi-geostrophic dynamics that allows one to reach regimes of rapid rotation and strong thermal forcing. Some results of numerical simulations and a model to describe those results will be presented, in particular the regime where coherent convective plumes are obtained.

1.1 Ocean deep convection

Figure 1.a presents the global thermohaline circulation on Earth. Sinking water is present in the Atlantic, in the Antarctic that creates a global overturning which circulates around the globe. It also raises the question of how the water gets to the top or to the bottom of the ocean. Note that the timescale of this motion is roughly 1000 years. The intermittent sinking takes place on very small scales and is relatively fast. Therefore, different time and length scales are present in this problem which makes it difficult to simulate. Figure 1.b shows zones where deep and bottom or intermediate waters form and sink and the major broad scale upwelling zone. This circulation of waters, has a large impact on the global climate and therefore constitutes an important topic.

1.2 Phases of deep convection

The phenomenon of deep convection [1] shows three major phases: a preconditioning phase where a cyclonic gyre of length scales $L \sim 100$ km domes isopycnals making the density more uniform; then, there is a deep convecting phase where cooling events trigger deep plumes of length scales $L \sim 1$ km; finally these plumes organize and creating geostrophic eddies that have scales about $L \sim 10$ km. In the following discussion, plumes of length scales $L \sim 1$ km are considered.

1.3 Rotation and deep convection

Before going further, it is important to notice that the deep convection is influenced by rotation. Indeed, it occurs in polar latitude where the Coriolis parameter f is large. Thus,

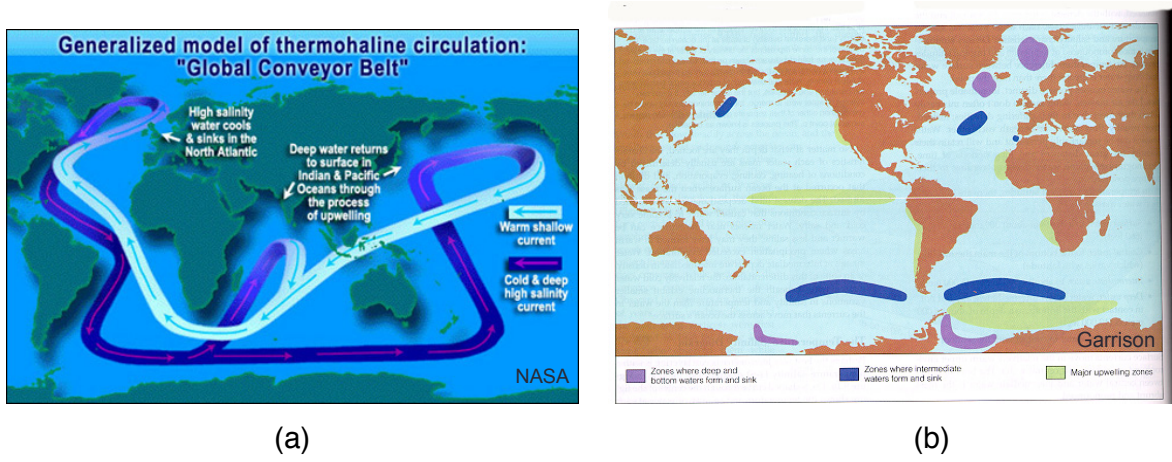


Figure 1: (a) Schematic of a generalized model of thermohaline circulation showing the Global Conveyor Belt. (b) Schematic of the principal zones where deep and bottom (in purple) or intermediate waters (in blue) form and sink and the major upwelling zone (in green).

we can define a natural Rossby number R_0^* such that

$$R_0^* = \frac{L_{rot}}{H} = \sqrt{\frac{B}{f^3 H^2}} \quad (1)$$

where L_{rot} is the horizontal rotational scale, H the height, and B the buoyancy flux. Observations show that $R_0^* \sim 0.1 - 0.4$.

2 Non-hydrostatic quasi-geostrophic model

The traditional quasigeostrophic approximations result from assuming rapid rotation, strong stable stratification, hydrostatic balance (vertical pressure gradients are balanced by gravity), and geostrophy (horizontal pressure gradients are balanced by the Coriolis force). This results in a diagnostic relation for the geostrophic velocity. By going to higher order, one obtains a prognostic equation for the time evolution.

Here, a non-hydrostatic quasi-geostrophic model [2, 3] is considered. We start with Boussinesq equations in a rapidly rotating regime, i.e. the Rossby number is small, $R_0 = \epsilon \ll 1$. Usually structures in ocean and atmosphere have a large horizontal scale and a small vertical scale. But if we now consider structures such as convective plumes, they are tall and thin which imply $A_z = H/L = 1/\epsilon \gg 1$.

Then, a multiscale asymptotic expansion is done, assuming a large vertical scale $Z = z/A_z = \epsilon z$. It also requires a slow time T defined by $T = \epsilon^2 t$. Then, using asymptotic expansions, the partial derivatives in the vertical direction and time become

$$\partial/\partial z \rightarrow \partial/\partial z + \epsilon \partial/\partial Z \quad \text{and} \quad \partial/\partial t \rightarrow \partial/\partial t + \epsilon^2 \partial/\partial T. \quad (2)$$

Considering a Reynolds decomposition where averaging is done over the fast space and fast time results in mean equations for the slow vertical scale and slow time

$$\bar{\mathbf{u}}(Z, T) = \int dx dy dz dt \mathbf{u}(x, y, z, t, Z, T). \quad (3)$$

Define the velocity fluctuation as $\mathbf{u}' = \mathbf{u} - \bar{\mathbf{u}}(Z, T)$. Using asymptotic analysis both the mean velocity and the fluctuation term are expanded in powers of ϵ :

$$\bar{\mathbf{u}} = \bar{\mathbf{u}}_0 + \epsilon \bar{\mathbf{u}}_1 + \dots \quad \text{and} \quad \mathbf{u}' = \mathbf{u}'_0 + \epsilon \mathbf{u}'_1 + \dots \quad (4)$$

The vertical momentum equation gives the leading balances for the first-order terms:

$$\frac{\partial \bar{p}_0}{\partial Z} = \Gamma \bar{\theta}_0 \quad (5)$$

which says that the mean state hydrostatic at lower order, where p is the pressure, θ is the temperature, Γ the non-dimensional buoyancy frequency defined by: $\Gamma = B L/U^2$. The horizontal momentum equation to lowest order is

$$\bar{\mathbf{u}}_0 = \mathbf{0} \quad \text{and} \quad \hat{\mathbf{z}} \times \mathbf{u}'_0 = -\nabla p'_1. \quad (6)$$

Therefore, at lowest order, the mean velocity is zero and the fluctuation of the velocity field is in geostrophic balance.

These lowest order equations lead to some implications. Geostrophy implies horizontal non-divergence, $\nabla_{\perp} \cdot \mathbf{u}'_{0\perp} = 0$ and then the vertical velocity is independent of z , $\partial w'_0 / \partial z = 0$. In a traditional QG model, this leads to $w'_0 = 0$ since layer is thin and $w_0 = 0$ on boundaries. But here, because of the multiple length scales, we just have no fast z derivatives, so $w'_0 \neq 0$ remains possible provided it only depends on slow Z . Thus, the lowest order velocity can have a slow vertical scale dependence: $w'_0 = w'_0(x, y, Z)$. As a results, the first order fluctuations are non-hydrostatic.

To write the equations of motion, we use the usual toroidal and poloidal decomposition through the streamfunctions Ψ and ϕ which are defined by

$$\mathbf{u}' = -\nabla \times \Psi \hat{\mathbf{z}} - \nabla \times \nabla \times \phi \hat{\mathbf{z}}. \quad (7)$$

We therefore can write

$$\mathbf{u}'_0 = \begin{pmatrix} -\partial \Psi_0 / \partial y \\ \partial \Psi_0 / \partial x \\ \nabla_{\perp}^2 \phi_0 \end{pmatrix} \quad (8)$$

where $\phi_0 = \phi_0(x, y, Z)$ and has no fast z variation. The first two terms are given by the function Ψ in the usual way and the last terms, $\nabla_{\perp}^2 \phi_0$ gives a non-hydrostatic vertical velocity that shows the difference with the classical quasi-geostrophic model.

3 Rotating Rayleigh-Bénard convection

3.1 Non-dimensional parameters

The length scale is chosen such that the Reynolds number is unity, $Re = 1$. The remaining parameters describing the problem are the scaled Rayleigh number: $\tilde{Ra} = E^{4/3} Ra$, which defines the strength of the buoyancy frequency, where E is the Ekman number defined by $E = \nu/(2\Omega H^2)$, and the Prandtl number σ which represents the ratio of momentum to heat diffusion. This scaling of E and Ra is based on the critical Rayleigh number for the initial instability in the presence of rotation. In the following sections, numbers indicating order are dropped but the lowest order in all cases are kept.

3.2 Reduced equation

The vertical velocity equation is:

$$\frac{\partial w}{\partial t} + J(\Psi, w) + \frac{\partial \Psi}{\partial Z} = \frac{\tilde{Ra}}{\sigma} \theta' + \nabla_{\perp}^2 w \quad (9)$$

where θ' is the temperature fluctuation, and J is the Jacobian defined by

$$J(A, B) = \frac{\partial A}{\partial x} \frac{\partial B}{\partial y} - \frac{\partial A}{\partial y} \frac{\partial B}{\partial x}. \quad (10)$$

In this equation, $\partial w/\partial t$ is the vertical velocity tendency, $J(\Psi, w)$ represents the horizontal advection of vertical velocity. Note that there is no vertical advection. The term $\partial \Psi/\partial Z$ is the unbalanced vertical pressure gradient which forces vertical velocity, $\tilde{Ra} \theta'/\sigma$ is the buoyancy forcing term and finally $\nabla_{\perp}^2 w$ is the horizontal dissipation.

The equation for the vertical vorticity defined by $\omega = \nabla_{\perp}^2 \Psi$ is:

$$\frac{\partial \omega}{\partial t} + J(\Psi, \omega) - \frac{\partial w}{\partial Z} = \nabla_{\perp}^2 \omega \quad (11)$$

Here, $\partial \omega/\partial t$ is the vertical vorticity tendency, $J(\Psi, \omega)$ the usual horizontal advection of vertical vorticity, $-\partial \omega/\partial Z$ represents a stretching term where vertical velocity gradients on large scales spin up vorticity and implies an ageostrophic horizontal divergence, and lastly $\nabla_{\perp}^2 \omega$ stands for the horizontal dissipation.

We can also write the temperature fluctuation equation:

$$\frac{\partial \theta'}{\partial t} + J(\Psi, \theta') + \omega \frac{\partial \bar{\theta}}{\partial Z} = \frac{1}{\sigma} \nabla_{\perp}^2 \theta \quad (12)$$

where $\partial \theta'/\partial t$ is the temperature fluctuation tendency, $J(\Psi, \theta')$ is the horizontal advection of temperature, $\omega \partial \bar{\theta}/\partial Z$ is the vertical advection of the mean temperature gradient (this is the only mean quantity which comes into this equation) and $1/\sigma \nabla_{\perp}^2 \theta$ is the horizontal diffusion of temperature fluctuation.

Finally, the mean temperature evolves on a slow time:

$$\frac{\partial \bar{\theta}}{\partial T} + \frac{\partial \overline{\theta' \omega'}}{\partial Z} = \frac{1}{\sigma} \frac{\partial^2 \bar{\theta}}{\partial Z^2} \quad (13)$$

where $\partial\bar{\theta}/\partial T$ represents the mean temperature tendency on the slow time, $\partial\overline{\theta'\omega'}/\partial Z$ is the large scale divergence of the eddy temperature flux and the overline denotes the horizontal average and average over fast time. Finally $1/\sigma \partial^2\bar{\theta}/\partial Z^2$ is the dissipation.

4 Numerical simulations

Numerical simulations [3, 4] have been performed with periodic boundary conditions using the Galerkin-Fourier approach in (x, y) direction and Chebyshev polynomials in the vertical direction z . The simulations have been done for a range of scaled Rayleigh numbers \tilde{Ra} and Prandtl numbers σ . The resolution has been varied with the scaled Rayleigh number \tilde{Ra} . A semi-implicit Runge-Kutta time stepping is used. The boundary conditions are impenetrable, fixed temperature, stress-free boundaries. Mathematically, it can be written as $\bar{\theta} = 1$ at $z = 0$, $\bar{\theta} = 0$ at $z = 1$, and $w = 0$, $\partial_z\Psi = 0$, $\theta' = 0$ at $z = 0$ and $z = 1$.

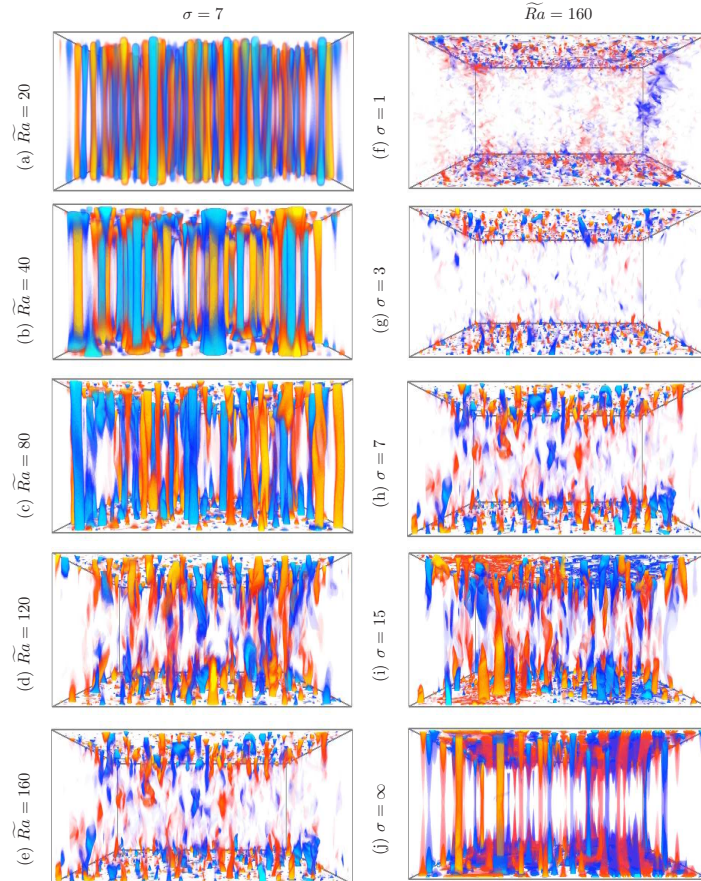


Figure 1. Volume renders of θ for $\sigma = 7$ and varying \tilde{Ra} (left) and $\tilde{Ra} = 160$ and varying σ (right).

Figure 2: Temperature fluctuations for various Rayleigh numbers and Prandtl numbers. From [4].

4.1 Observations

Figure 2 shows snapshot of the simulations for various Rayleigh and Prandtl numbers. The left column is for Prandtl number $\sigma = 7$ and the Rayleigh numbers increases from top to bottom. We see that we first have the presence of columns at low Rayleigh number, $\tilde{Ra} = 20$, here we are going to focus on this regime. Then, the Rayleigh number \tilde{Ra} increases and the columns start breaking up leading to a more turbulent regime. The right columns shows a fixed Rayleigh number, $\tilde{Ra} = 160$, with increasing Prandtl number going down. We see that increasing the Prandtl number leads to the appearance of columns. Note that there is no exact correspondence between varying the Prandtl and the Rayleigh number.

In summary, for rotating convection, columns are present for small Rayleigh number and/or large Prandtl number. In the following we are going to focus on this particular regime.

4.2 Convective Taylor Column regime

We consider the regime of convective Taylor columns. The simulation parameters are $\tilde{Ra} = E^{4/3} Ra = 40$, $\sigma = 7$ and the grid resolution in this case is $192 \times 192 \times 97$. Starting with arbitrary initial conditions, the temperature fluctuations relatively quickly organize into 2D convective columns. Hot plumes and cold plumes are present and the columns have nearly zero circulation. As a result they don't significantly advect each other in the horizontal direction. Moreover, the vorticity shows that fluid flows in opposite directions at the top and bottom with ring of vorticity around the center of the column. Also note that vorticity goes to zero at the mid-plane owing to symmetry.

4.3 Model of convective Taylor columns

To build a model of this convective Taylor columns, we seek steady nonlinear solution with axisymmetric structures [5]. It is also assumed that all the heat flux is carried by columns (this can be relaxed). Then we define c_f as the number of columns per units area and the Nusselt number by $Nu = -\partial_z \bar{\theta}(z = 0)$. Then, the set of equations for a single column become

$$\frac{\partial^2 \phi}{\partial Z^2} + \nabla_r^2 \left(\tilde{Ra} \frac{\partial \bar{\theta}}{\partial Z} + \nabla_r^4 \right) \phi = 0 \quad (14)$$

$$\frac{\partial \bar{\theta}}{\partial Z} + \frac{Nu}{1 + c_f \sigma < (\partial_r \phi)^2 >} = 0 \quad (15)$$

where $< >$ denotes the horizontal integral over column and ∇_r^2 is the radial component of the Laplacian.

4.4 Convective Taylor columns

The simplest solution of the set of equations (14)-(15) is a separable solution between the vertical and horizontal directions. First, consider horizontal Bessel function of first kind, $\phi(r, Z) = \hat{\phi}(Z) J_0(kr)$. The problem with this first solution is that there is an infinite heat flux and infinite circulation, we therefore need a cutoff. Moreover, another problem is that

this model fails to match numerical solution as the radial decay is too slow compared to the numerical simulations.

Therefore, we can improve the model by looking at Hankel functions, which are complex Bessel function defined by $H_0(kr) = J_0(kr) + i Y_0(kr)$. Then the solution can be written as

$$\phi(r, Z) = \left(\frac{\pi}{8 \sigma^2 c_f} \right)^{1/2} \phi(Z) H_0(kr) + c.c \quad (16)$$

where $c.c.$ denotes the complex conjugate. In this case the integral quantities (mass flux, heat flux, circulation) are finite, although there is a singularity at $r = 0$ which will be neglected because the integrated physical quantities are finite. If we take this ansatz in the equations (14)-(15), the vertical amplitude function $\phi(Z)$ is solution of an eigenvalue problem.

We can compare the analytical solutions to numerical simulations (see figure 3). We see that the solution based on Bessel functions (red curve) oscillates long after the actual structures goes to zero. The solution based on Hankel functions (blue curve) matches well with the numerical results for the radial solution. However for the axial profile, the Bessel functions gives a better results than Hankel functions. The horizontal oscillation is better captured by the Hankel solution than the Bessel functions.

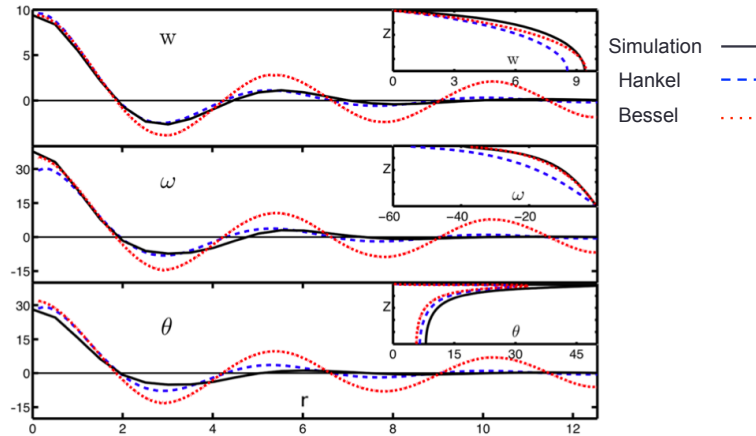


Figure 3: Radial and vertical (inset) profiles of the vertical velocity $w(z = 1/2, r)$, the vorticity $\omega(z = 1/96, r)$ and the temperature fluctuation $\theta(z = 1/96, r)$ solid line are the results of numerical simulations, blue dashed line is the solution based on Hankel function, and red dotted line the solution based on Bessel function. Note that the logarithmic singularity is present but nearly invisible. From [5].

5 Conclusion

We have seen that the non-hydrostatic quasi-geostrophic equations describe rapidly rotating convection. The numerical simulations show that there are several regimes of rotating

convection. Here, the focus is on the moderate forcing regime which has convective Taylor columns. The horizontal structure of these columns is well-described by an analytical model based on Hankel functions.

Ongoing work on the topic include the study of the turbulent regime and understanding the Lagrangian transport, which has implications for how tracers such as CO_2 are transported from surface to the deep ocean, and to construct a census to measure the population statistics of the columns.

References

- [1] Marshall, J. & Schott, F. 1999. Open-ocean convection: observations, theory and models. *Rev. Geophys.*, 37, 1-64.
- [2] Julien, K., Knobloch E., Milliff, R. and J. Werne, J. 2006. Generalized Quasi-Geostrophy for Spatially Anisotropic Rotationally Constrained Flows . *J. Fluid Mech.*, 555, 233-274.
- [3] Sprague, M., Julien, K., Knobloch, E. & Werne, J. 2006. Numerical Simulations of an Asymptotically Reduced System for Rotationally Constrained Convection. *J. Fluid Mech.*, 551, 141-174.
- [4] Julien, K., Rubio, A., Grooms, I. and Knobloch, E. Statistical and physical balances in low Rossby number Rayleigh-Benard convection. *Geophysical and Astrophysical Fluid Dynamics*, 2012, in press.
- [5] Grooms, I., Julien, K., Weiss, J.B. & Knobloch, E. 2010. A Model of Convective Taylor Columns in Rotating Rayleigh-Bénard Convection. *Phys. Rev. Lett.*, 104, 224501.

GFD 2012 Lecture 5: Applications of coherent structures to the study of weather and climate

Jeffrey B. Weiss; notes by Srikanth Toppaladoddi & Cédric Beaume

June 22, 2012

1 History of computational weather forecasting

Weather forecast plays an important role in preventing disasters. Weather and climate modeling started approximately one century ago, in 1922 with L. F. Richardson. He divided a region into a grid of cells and did 6 weeks of hand calculations to try and model the pressure. The use of computers in weather prediction started only in 1950, when J. G. Charney and his group completed a two-dimensional weather model and ran it on the Electronic Numerical Integrator And Computer (ENIAC). This early work paved way for the founding of the Geophysical Fluid Dynamics Laboratory (GFDL) in the National Oceanic and Atmospheric Administration (NOAA) to study the physical processes that govern the behavior of the atmosphere and the oceans as complex fluid systems. Computers enhanced numerical modeling of the atmosphere and in 1956 N. Phillips developed a mathematical model to depict monthly and seasonal patterns in the troposphere [2]. This model became the first realistic and successful climate model. In 1963, motivated by the study of atmospheric convection, E. N. Lorenz derived simplified equations of convection rolls and implemented them in a simple program. Computations of the resulting equations led to the discovery of chaotic dynamics [3]. Climate modeling has improved a lot since then, and in 1974 S. H. Schneider & R. E. Dickinson reviewed the advances in the field, stating “climate modeling has possibly now reached a threshold where further progress will lead to potential human benefits” [4].

2 Coherent structures in weather and climate

Despite the progress made since the 70’s, weather forecast is an extremely difficult task to do accurately. The dynamics of most flows in the atmosphere and oceans is chaotic and even small perturbations can cause large changes. An idea to improve current forecasts is to use coherent structures as the backbone for geophysical turbulent flows. Although being subjective, these structures can be used to reduce variable description of turbulence. Here, we give an example of such coherent structures and their use in numerical weather prediction.

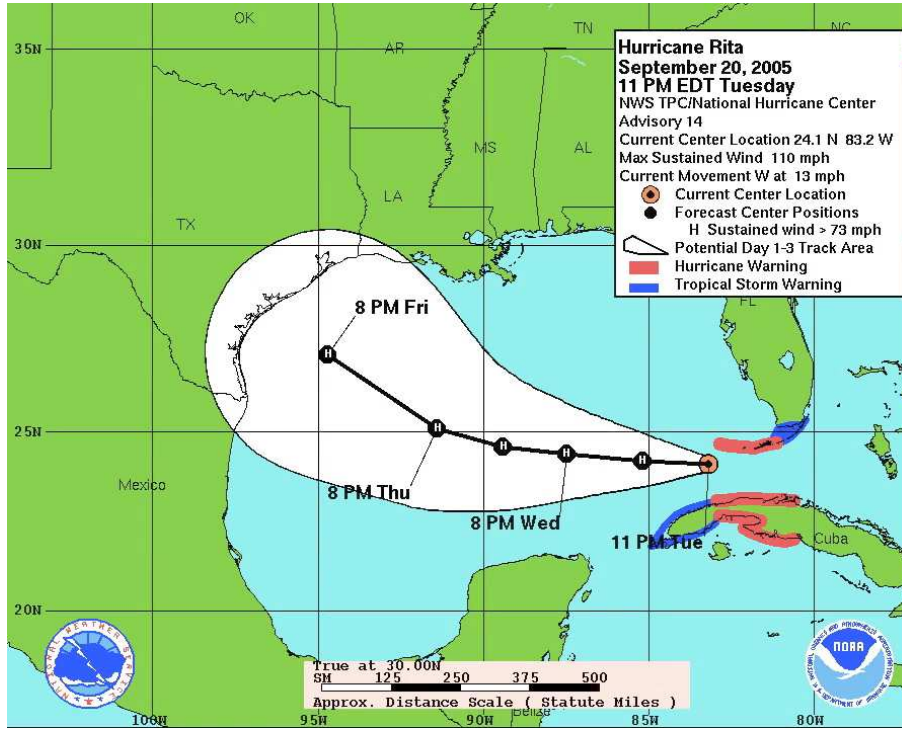


Figure 1: Initial prediction on September 20, 2005 by NWS TPC/National Hurricane Center. Rita is at the tip of Florida and heads west. The black line indicates prediction and the white cone the error. After [1].

2.1 Coherent structures: hurricane Rita

On September 18, 2005 hurricane Rita formed near the Bahamas and became the fourth most intense Atlantic hurricane ever recorded. The potential danger of such an event motivated weather forecasters to predict Rita's trajectory and prompted mass evacuation in coastal Texas. Approximately 3 million people fled prior to Rita's landfall, and the losses were heavy: approximately 100 people died and the damage cost was evaluated at \$ 12 billion. Predictions are reported in figure 1. The predictions contain a large error cone indicating the prediction uncertainty, and are to be compared with Rita's actual trajectory, reported in figure 2. The hurricane finally hit the US at the boundary between Texas and Louisiana 4 days after the initial prediction in figure 1. Rita's trajectory is located within the large cone of errors but very close to its boundary which led to inappropriate decisions in several areas. Although the predictions were rather good, there is room for improvement which translates in more security and less damage.

2.2 Climatic variations: El Niño

Climate and local events are influenced by many variations occurring on different timescales. Among these variations one can cite the North Atlantic Oscillation which consists of atmo-

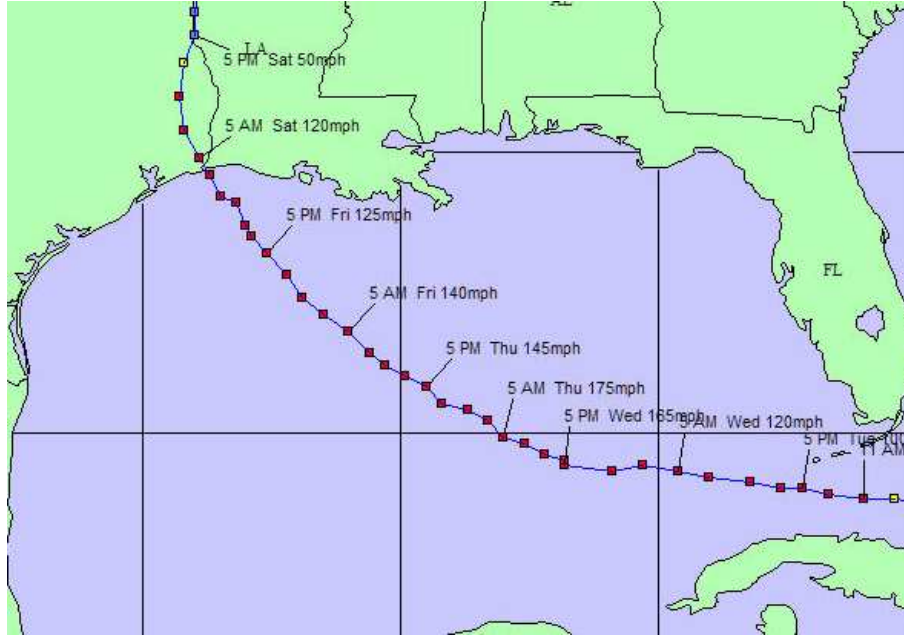


Figure 2: Rita's trajectory. Blue dots indicate low speed ($>39\text{mph}$), yellow medium speed ($>58\text{mph}$) and red fast speed ($>74\text{mph}$). Rita finally hit the boundary between Texas and Louisiana, slightly to the right of the initial predictions 4 days later. After [1].

spheric surface pressure oscillations between the Icelandic low and the Azores high. Another important example of climate variability is given by El-Niño. It is a coupled atmosphere/ocean phenomenon characterized by unusually warm ocean temperatures in the equatorial Pacific that has important consequences on the weather around the globe. This phenomenon can be identified in Pacific Sea Surface Temperature (SST) representations. In figure 3 are reported Pacific SST from 1986 to 2007, time increasing downwards. Indonesia is towards the left of the figure while South America is towards the right. The blue areas on the right of the first plot indicate cool water. The temperature of the water in these areas varies seasonally, being warmest in the northern hemisphere springtime and coolest in the northern hemisphere fall. The red areas on the left indicate hot water, usually seen in the western Pacific. El Niño is an exaggeration of the usual seasonal cycle and can easily be identified in the anomalies on the right figure. Indeed, several El Niños can be seen, for example, in 1986–1987, in 1991–1992 and in 1997–1998. These climate patterns cause extreme weather in many regions of the world such as floods and droughts that can affect many countries.

3 Using coherent structures to improve forecasts

In this part, we discuss traditional methods to predict climate change and weather forecast, and introduce how coherent structures could be used to improve forecasts.

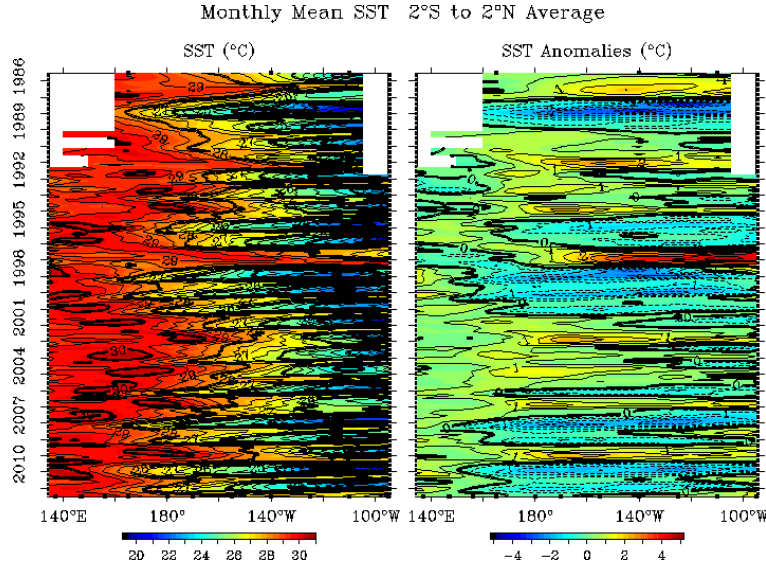


Figure 3: Left: Plot of the tropical Pacific Sea Surface Temperature (SST) in the horizontal, Indonesia is towards the left and South America towards the left. Time is increasing from top to bottom. Red areas indicate hot water while blue ones indicate cool water. Right: Same type of plot but SST anomalies are plotted instead of SST. The anomalies are the difference between the SST and the average for each month.

3.1 Traditional method

The basic method used in numerical weather prediction can be divided into the following steps. A preliminary step consists in covering the area in which the weather is to be predicted with an appropriate model grid. Then, we need to gather information about the current state of the atmosphere (temperature, pressure, wind velocity, humidity, precipitation, etc.). This information is then used to describe the initial condition of the model through a data assimilation scheme which merges the observations with previous model forecasts. As we obtain more observations the initial condition becomes more accurate. Once the initial condition is set, the simulation is run forward to the forecast time. For subsequent forecasts, former predictions are compared to the corresponding observations to verify the model did a good job. Corrections and improvements can then be undertaken. In practice, about half of the cost of numerical weather prediction comes from obtaining observations and the other half comes from running models.

3.1.1 Observation

The first major step in predicting weather is observation. This is done using different kinds of instruments to measure the state of the nature. Ground stations are stationary and are used to measure local quantities such as temperature, pressure, wind velocity, precipitation, humidity, etc. Ground stations are often well equipped and very reliable. Observations are also obtained from other instruments such as balloons, satellites, radar, ships or aircraft.

Observations are not typically taken at the same locations as model gridpoints and can be at different times than model timesteps. Data assimilation is used merge these observations onto the model grid.

3.1.2 Data assimilation

Data assimilation is a mature field with much previous work and a sometimes dense nomenclature (see, e.g., [5, 6]). Different types of data assimilation algorithms are available such as sequential ones (nudging, optimal interpolation, or Kalman filtering), variational ones (minimizing a cost function or 3D variational assimilation) and hybrid ones that combine both methods. Let us introduce a nomenclature of the main state vectors that we will use in the following:

- the true state of the atmosphere \mathbf{x}_t . This is a quantity we cannot access.
- the background state \mathbf{x}_b which results from a previous model forecast.
- the observations taken from measurements of the true state \mathbf{y} . This quantity is a post-processing of the data collected during observation.
- the analysis \mathbf{x}_a . This is the best estimate of the true state obtained by data assimilation.

We give now the example of a 3D variational assimilation (3Dvar). Let us define the observational operator H so that $H(\mathbf{x})$ is the observation obtained from state \mathbf{x} . Then we define two error covariance matrices: the error in the background state,

$$B = \langle (\mathbf{x}_b - \mathbf{x}_t)(\mathbf{x}_b - \mathbf{x}_t)^T \rangle, \quad (1)$$

and the error in observations,

$$R = \langle (\mathbf{y} - H(\mathbf{x}_t))(\mathbf{y} - H(\mathbf{x}_t))^T \rangle, \quad (2)$$

where $\langle \cdot \rangle$ denotes time averaging and T denotes the transpose. Note that these error matrices are difficult to estimate because they involve \mathbf{x}_t which is the unknown true state of the atmosphere. It is commonly assumed that H is a linear operator, $H(\mathbf{x}) = \mathbf{H}\mathbf{x}$ with \mathbf{H} the corresponding matrix. We also make the assumptions that the error is unbiased (the mean is zero) and that the observations and background errors are uncorrelated. We define then a cost function

$$J(\mathbf{x}) = (\mathbf{x}_b - \mathbf{x})^T B^{-1} (\mathbf{x}_b - \mathbf{x}) + (\mathbf{y} - \mathbf{H}\mathbf{x})^T R^{-1} (\mathbf{y} - \mathbf{H}\mathbf{x}). \quad (3)$$

The analysis state \mathbf{x}_a is then by definition the solution that minimizes J , given by

$$\mathbf{x}_a = \mathbf{x}_b + \mathbf{K}(\mathbf{y} - \mathbf{H}\mathbf{x}_b), \quad \mathbf{K} = \mathbf{B}\mathbf{H}^T(\mathbf{H}\mathbf{B}\mathbf{H}^T + \mathbf{R})^{-1}. \quad (4)$$

Implementing this solution is difficult for two main reasons. First, as mentioned above, obtaining estimates of B and R are difficult. Second, the vectors are very high dimensional (often 10^7 -d for \mathbf{x} and 10^5 -d for \mathbf{y}) making the computations expensive. There are many strategies for dealing with these issues which will not be discussed here.

While numerical weather prediction has seen significant improvements over the decades, there are still failures. Often the failures involve errors in prediction the location of structures such as storms, hurricanes, or the jet stream [7].

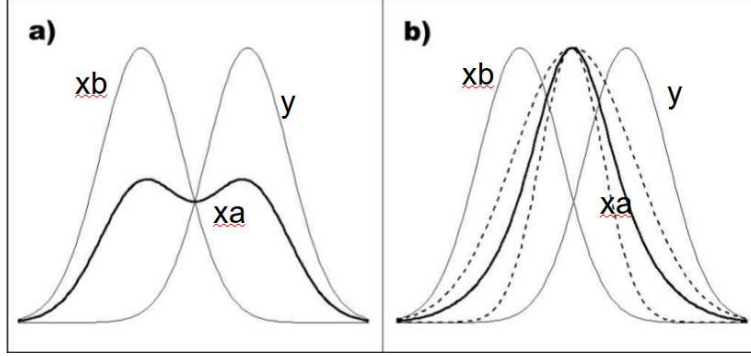


Figure 4: Depiction of a standard assimilation technique applied to a structure with different locations in the observations y and background x_b (a) and a suggested improvement (b). The simplified assimilation technique consists of taking the average between the background and the observation which smears the original structure. The proposed improvement consists of constructing a structure at the mean location of the background structure and the observed structure.

3.2 Improving data assimilation

One drawback of standard assimilation techniques is that they do not preserve the coherence of physically localized structures. As a simple example, imagine an assimilation scheme that takes the average between the observation y and the background x_b . Application of such an algorithm is depicted in figure 4.a. It consists in setting the analysis x_a as the average between the observation y and the background x_b . As the figure shows it, such an algorithm leads to a structure that does not possess the same properties as the observed or background ones: its amplitude is low, its center is no longer a maximum and it can possess two local maxima depending on the position of y and x_b .

To avoid such issues, we desire techniques that can work in many scenarios and applicable to a variety of structures. We refer to methods that explicitly include properties of structures in the data assimilation as “structure assimilation”. We build this type of methods in three modular steps.

First, structures need to be identified. This can be done using a variety of existing techniques including those based on wavelets, manifolds, a subjective technique. Once identified, state variables such as the position, size and strength of the structure are defined. The identification is applied to both the background and observations, resulting in background and observed structure variables.

The second step of the method consists in assimilating the structure variables. One can use any of the various data assimilation methods for this step. The result is an analyzed structure that is the best estimate based on the observed and background structure. For example, if the assimilation scheme is a simple average, then the center of the analyzed structure x_a^0 is then given by

$$x_a^0 = \frac{x_b^0 + y^0}{2} \quad (5)$$

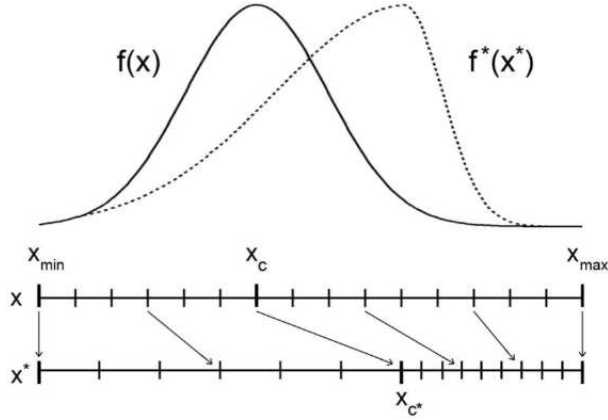


Figure 5: Depiction of a 1D grid morphing technique from a structure f to f^* . The starting structure lies on the grid x . Segments of the grid are stretched or compressed to obtain the grid x^* . The displacement of the meshpoints provides a new structure $f^*(x^*)$.

with x_b^0 being the center of the background structure and y^0 that of the observed one. This type of method is depicted in figure 4.b.

Finally, the last step is the computation of the analysis field on the model grid. While the first two steps implement on well developed techniques, this step has not been previously explored. We propose using the technique of grid morphing to map the structure variables back onto the model grid. Grid morphing is attractive because it has been studied for image processing in the field of computer science. An example of 1D grid morphing is shown in figure 5. The idea of grid morphing is to displace some meshpoints and conserve the value of the field at these points as they are displaced. The resulting shape is then deformed to fit the desired one.

Preliminary numerical simulations using structure assimilation show significant improvements in forecast error [8]. The method was tested using a two-layer QG channel model. Figure 6 compares the errors made by traditional assimilation and structure assimilation. One can see that the error curve for structure assimilation is significantly below that of traditional assimilation. This trend is strengthened by the standard deviation which is smaller for structure assimilation than for traditional assimilation. It follows that structure assimilation can improve forecasts and lead to more reliable results.

4 Climate variability

Climate dynamics is a topic that has assumed importance in recent times due to anthropogenic greenhouse gas emissions leading to climate change. The climate system is a highly nonlinear and a highly coupled system with many feedback mechanisms. Studying the climate system thus requires a hierarchy of models, from highly simplified energy balance models to complex Global Climate Models (GCMs). GCMs include as much of the essential physics as is computationally feasible, and parameterize many processes to reduce their computational cost.

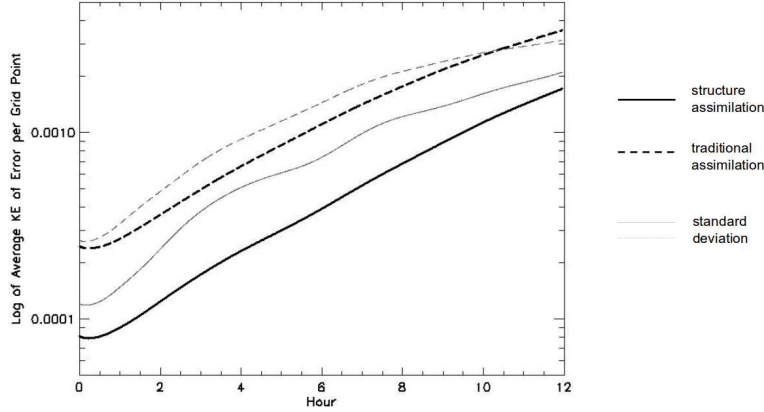


Figure 6: Average kinetic energy of error per grid point as a function of hour after 10,000 forecasts. The straight bold line represents structure assimilation while the dashed bold line represent traditional assimilation. Standard deviations are shown in straight and dashed lines respectively for structure assimilation and traditional assimilation.

In this section, we use stochastic dynamical systems and non-equilibrium statistical mechanics to explore the natural variability of the climate system.

The Earth's climate system has processes whose governing timescales vary from a day to thousands of years, and these nonlinear processes are highly coupled. The natural variability of the climate system takes the form of spatio-temporal patterns which are often difficult to predict. Examples of spatio-temporal patterns include El Niño and the North Atlantic Oscillations.

5 Non-equilibrium Thermodynamics

Non-equilibrium thermodynamics deals with systems which are far from thermodynamic equilibrium. Such systems sustain heat fluxes and produce entropy. A non-equilibrium steady state (NSS) is a statistically steady-state that is kept away from equilibrium by external forcing. One of the simplest examples of this forcing is a system connected to thermal reservoirs at two different temperatures. The NSS then carries a heat from the hot reservoir to the cold reservoir.

A NSS sustains statistically stationary fluctuations about its mean state. Associated with these fluctuations is an entropy production, which can be either positive (entropy producing) or negative (entropy reducing). The Fluctuation Theorem (FT) gives the ratio of the probability of finding fluctuations which increase or decrease entropy. If the probability of a finite time fluctuation changing entropy by S is $P(S)$, and the probability of it changing by the opposite amount is $P(-S)$, then the FT tells us that:

$$\frac{P(S)}{P(-S)} = e^{St}. \quad (6)$$

Equation (6) means that, for a given positive entropy production $|S|$, the probability of a

system having an entropy reducing fluctuation is exponentially smaller than the probability of having an entropy producing fluctuation. Because the second law of thermodynamics says that entropy must increase on average, we only expect to see negative entropy fluctuations in thermodynamically small systems on thermodynamically short timescales.

6 Linear Gaussian models

Linear Gaussian stochastic models are some of the simplest models that capture a nonequilibrium steady-state. They also have been effectively used to model a number of phenomena in the climate system. These models take the form

$$\frac{d\vec{X}}{dt} = A\vec{X} + F\vec{\zeta}, \quad (7)$$

where \vec{X} represents the state space of the system. The first term on the right hand side is the linear deterministic dynamics and for the model to remain finite the matrix A must be stable, i.e. the real parts of its eigenvalues are all negative. The second term on the right hand side is additive Gaussian noise where $\vec{\zeta}$ is Gaussian white noise with

$$\langle \vec{\zeta}(t)\vec{\zeta}^T(t') \rangle = I\delta(t - t'), \quad (8)$$

where T denotes the matrix transpose and I is the identity matrix. The diffusion matrix which characterizes the noise process is $D = FF^T/2$.

The most common approach for constructing linear Gaussian models for climate phenomena is to build empirical models. In this approach one fits the matrices A and D to data from either observations or numerical models. The data is typically reduced to $O(10 - 50)$ degrees of freedom through the use of empirical orthogonal functions (EOF). For example, to study El-Niño one uses observations of sea surface temperature and the state space \vec{X} represents the amplitudes of the EOF patterns.

These simple stochastic models often perform surprisingly well when compared to complex dynamical systems models as can be seen from figure 7. However, it is still unclear why the models perform well for some phenomena and not for others.

Much of the recent work on stochastic models in the climate system has focused on the non-normality of the deterministic operator and the amplification of the noise. The property of non-normality is unsatisfying in that the matrix A can be made normal by a suitable coordinate transformation. However, there is a related coordinate invariant property of the system: the violation of detailed balance. Thermodynamically, systems in thermal equilibrium satisfy detailed balance, while systems in a NSS violate detailed balance. A linear Gaussian model violates detailed balance when $AD - DA^T \neq 0$, and produces noise amplification regardless of the coordinate system.

To analyze the time series data, we make use of the stochastic entropy production which is defined as:

$$S = \ln \left(\frac{P(X)}{P(X')} \right), \quad (9)$$

where X is a finite time trajectory segment, X' is the time reversed trajectory segment, and $P(X)$ is the probability of finding the segment in a long time series. The stochastic

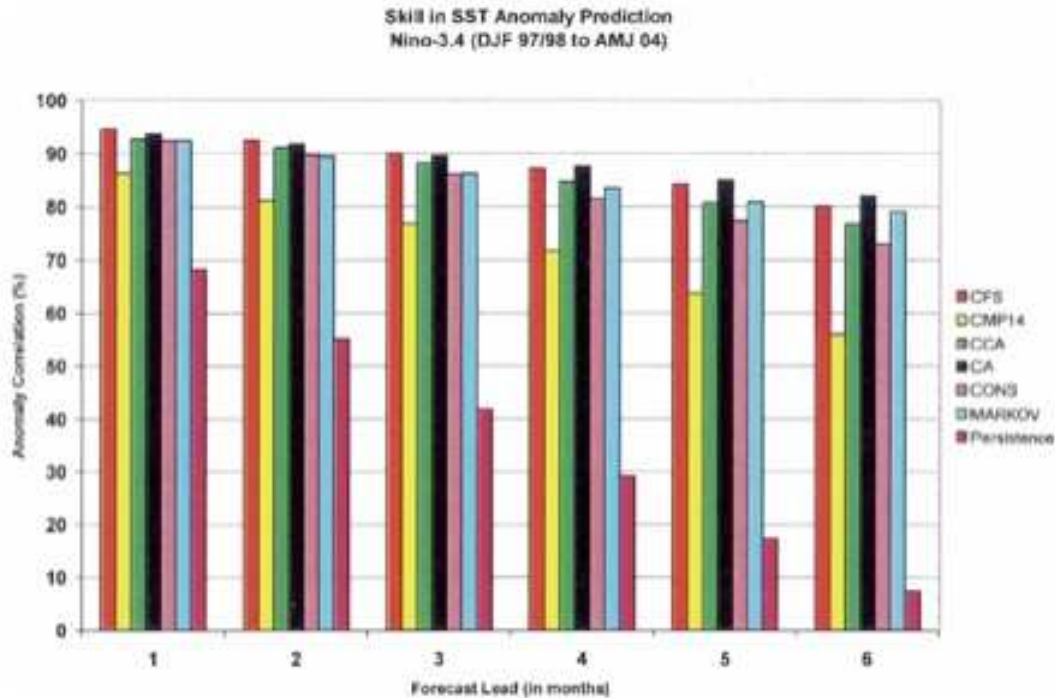


Figure 7: Comparison of different models used to forecast the Nino-3.4 sea surface temperature anomaly. The blue bar is from a stochastic model. From [9]

entropy production requires the trajectory segment over all times between the endpoints of the segment. To apply this to discrete-time climate data, we use a coarse grained entropy, based only on the state vector at the endpoints of the trajectory segment, the endpoint entropy production. The calculations are done with two different methods: the theoretical method which is based on an analysis of the Equation 7, and the direct method, which is based on constructing a pdf of the entropy production of the individual trajectory segments in the data. Agreement between the two methods demonstrates the self-consistency of the linear Gaussian model applied to the data. Computation of the entropy production in a linear Gaussian model of tropical SST shows that we observe negative entropy producing fluctuations on timescales of months (Figure 8). This demonstrates that tropical SST dynamics on monthly timescales is a thermodynamically small system.

In summary, many aspects of natural climate variability takes the form of well-defined patterns. Natural climate variability has a large human impact, and is often poorly captured by GCMs. Climate variability can be modeled as fluctuations about a nonequilibrium steady state in a thermodynamically small system. This suggests that improved understanding of nonequilibrium steady states could have a significant impact on understanding the climate system.

References

- [1] <http://www.nws.noaa.gov/rita>.

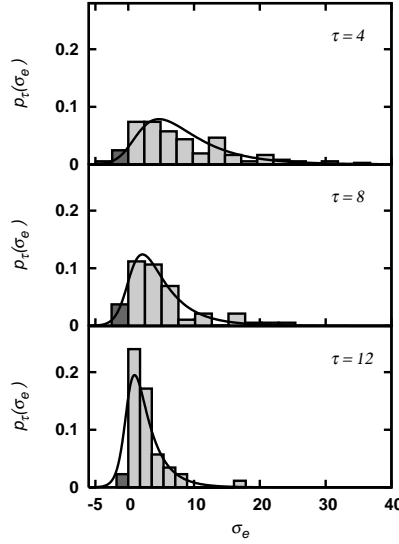


Figure 8: Probability distribution function of the endpoint entropy production. The solid curve is the distribution from the theoretical method and the binned distribution is calculated using the direct method. The darker shaded bins show trajectory segments with negative entropy production. From [10]

- [2] N. A. Phillips, *The general circulation of the atmosphere: a numerical experiment*, Royal Meteorological Society **82** (352): 123–154, 1956.
- [3] E. N. Lorenz, *Deterministic nonperiodic flow*, Journal of Atmospheric Sciences 20: 130–141, 1963.
- [4] S. H. Schneider & R. E. Dickinson, *Climate modeling*, Reviews of Geophysics and Space Physics 12: 447–493, 1974.
- [5] F. Bouttier & P. Courtier, *Data assimilation concepts and methods*, Meteorological Training Course Lecture Series, 1999.
- [6] E. Kalnay, *Atmospheric Modeling, Data Assimilation and Predictability*, Cambridge University Press, 2003.
- [7] E. Kalnay, S.J. Lord, R.D. McPherson, Maturity of Operational Numerical Weather Prediction: Medium Range, *Bulletin of the American Meteorological Society* 79, 2753–2769, 1998.
- [8] Brad E. Beechler, Jeffrey B. Weiss, Gregory S. Duane, and Joseph Tribbia, Jet Alignment in a 2 Layer Quasi-Geostrophic Channel Using One-Dimensional Grid Warping, *The Journal of the Atmospheric Sciences*, doi: 10.1175/2009JAS3263.1., 2010.
- [9] Saha, S., S. Nadiga, C. Thiaw, J. Wang, W. Wang, Q. Zhang, H. M. Van den Dool, H.-L. Pan, S. Moorthi, D. Behringer, D. Stokes, M. Peña, S. Lord, G. White, W. Ebisuzaki,

- P. Peng, P. Xie, 2006: The NCEP Climate Forecast System. *J. Climate*, 19, 3483-3517.
doi: <http://dx.doi.org/10.1175/JCLI3812.1>
- [10] J.B. Weiss, 2009: Nonequilibrium Statistical Mechanics of Tropical Sea Surface Temperature Variability, *Geophysical Research Letters*, 36, L10705, doi:10.1029/2009GL037812.

Lecture 6: Introduction to spatially localized structures

Edgar Knobloch: notes by Srikanth Toppaladoddi and Cédric Beaume
with substantial editing by Edgar Knobloch

December 18, 2012

1 Introduction

Patterns are abundant in Nature. Some, for example, the stripe pattern on a zebra (or zebrafish!) arise for biological reasons, perhaps to serve as camouflage. However, essentially identical patterns are found in a variety of different physical and chemical systems. Figure 1 shows stripe patterns on a sand dune and in the atmosphere while Fig. 2 shows labyrinthine patterns in a ferrofluid system and on a pufferfish. The similarities between these patterns suggest the existence of general principles behind pattern formation that are independent of the detailed physics responsible for their presence. This is so for spatially localized patterns, too. In this lecture we shall look at spatially localized structures in a number of different physical systems in an attempt to illustrate the universal properties of such structures. We also introduce the Swift-Hohenberg equation that turns out to be very useful for studies of such structures, and show, using a multiple-scale analysis, how such an equation may arise in a fluid dynamical context, in this case as a description of gravity-capillary waves on the surface of an inviscid fluid.

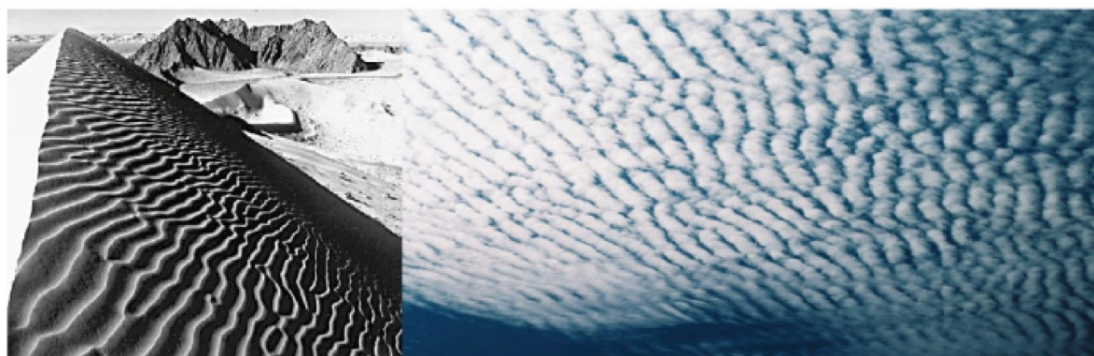


Figure 1: This image shows the stripe patterns on a sand dune (left), and in the cloud layer in the atmosphere (right). The patterns in these disparate systems bear strong resemblance.

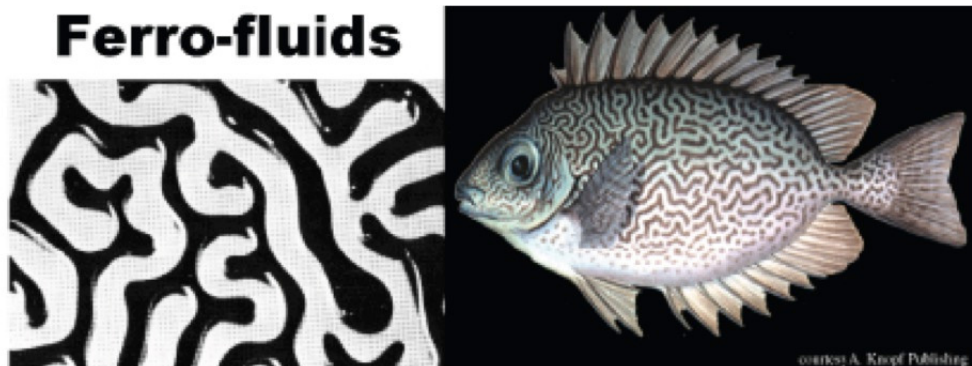


Figure 2: Labyrinthine patterns in a ferrofluid system (left), and on a pufferfish (right).

2 Localized structures in physical systems

There are many physical systems which show the presence of localized structures under appropriate conditions. In these lectures we shall be interested in localized structures in driven dissipative systems. Such structures are frequently referred to as *dissipative solitons* [22]. Structures of this type can be stationary or move. Here, we shall look at a few examples, and then introduce the Swift-Hohenberg equation that is a prototypical equation that exhibits structures of this type.

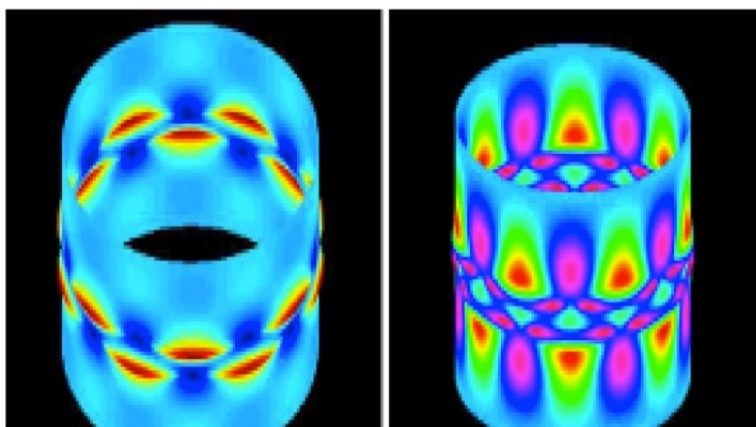


Figure 3: Displacement (left) and stress (right) patterns in a cylinder under axial loading. The displacement is the outward radial displacement measured from an unbuckled state. Both figures show a cellular pattern. From [15].

2.1 Cellular buckling in long structures

Hunt *et al.* [15] showed that when a tall structure, in their case a cylindrical shell, is loaded axially, the buckling of the structure may be confined to mid-section. The internal stress and displacement patterns formed are both cellular, and the number of these structures

increases with the magnitude of the load. Figure 3 shows the resulting cellular pattern, and in particular the localization of the displacement field for loads slightly larger than threshold. These buckled states may be stable, and although they are weaker than the unbuckled state, they are still able to support a load. However, when this load exceeds a critical value the structure collapses further, leading to a progression of buckled states consisting of more and more rows of cells.

The above results are best summarized in terms of a bifurcation diagram that tracks changes in the response of the system as a parameter changes. The variation in the parameter must be quasi-static; in simulations the parameter value is fixed for the duration of the simulation. The final state may then be used as the initial condition for a nearby parameter value. This process is laborious and numerical techniques have been developed to follow different states of the system without resorting to time-stepping. This approach offers considerable advantage in that unstable states can be followed as easily as stable states.

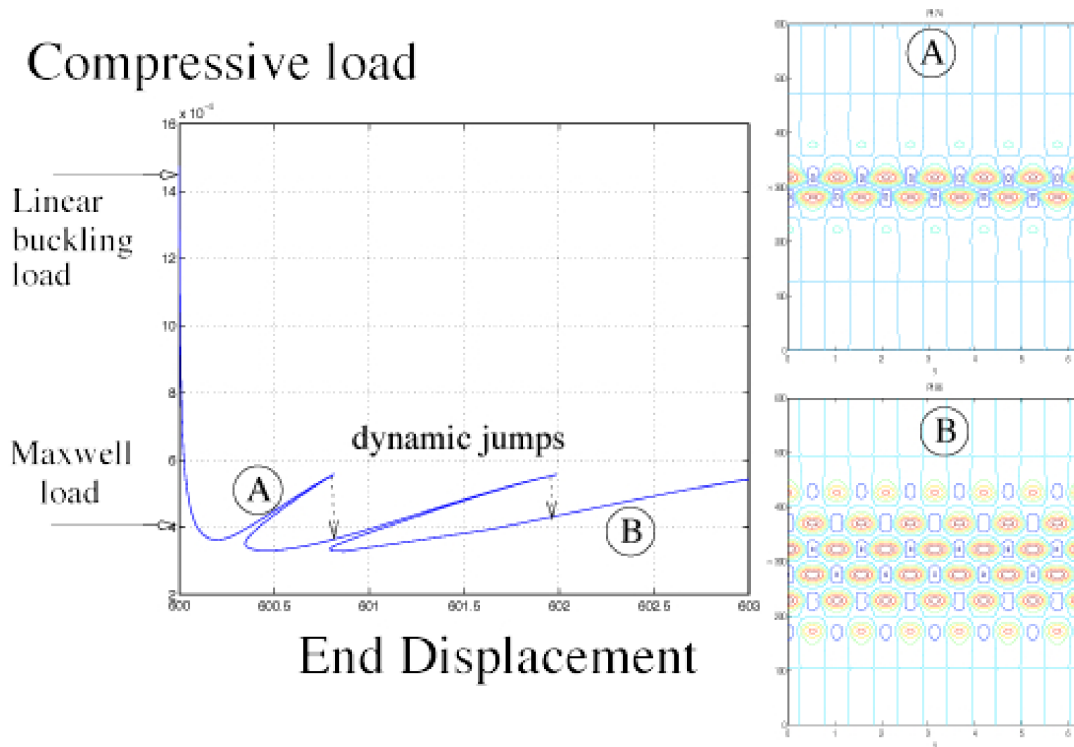


Figure 4: Bifurcation diagram for the buckling of an axially loaded cylinder. From [15].

Figure 4 shows the bifurcation diagram for the buckling problem. The diagram shows steady solutions of the system in terms of the end displacement as a function of the load parameter λ (plotted vertically). The unbuckled state loses stability at the linear buckling load. The bifurcation is strongly subcritical, meaning that for larger loads the buckling is catastrophic. For smaller λ , however, a variety of steady buckled states is present. These differ in the number of rows of cells generated, and these increase by two as the solution branch is followed. The states with positive slope are stable and can support increasing

load despite being buckled. When the load is increased too far a dynamic jump occurs to a state with an additional pair of rows etc. Thus there is a range of λ within which multiple stable solutions exist. The figure shows that these solutions are organized around a special value of the load parameter, called the Maxwell load. The significance of this parameter value will become apparent as the lectures proceed.

2.2 Solitons on the surface of a ferrofluid

A ferrofluid is a suspension of small magnetic dipoles. The free surface of this fluid undergoes a buckling instability, called the Rosensweig instability, when a uniform magnetic field of sufficiently large strength is applied in a direction normal to the surface [23]. This instability results in a hexagonal array of stationary peaks. Like the buckling of the cylindrical shell this instability is also strongly subcritical, leading to a broad region of magnetic field strengths for which the hexagonal pattern coexists with the flat surface. Within this region there is a subregion where multiple localized states can be created [23]. This can be done by bringing a bar magnet towards the surface, pulling out a peak, and removing the bar magnet. Remarkably, in this subregion the peak remains, and the process can therefore be repeated, pulling out more and more peaks. Figure 5 shows an example of a structure created in this way. Thus at every point in this subregion a number of different states, consisting of one, two, three or more peaks coexists with the flat and the hexagonal states, and all are simultaneously stable.



Figure 5: Two-dimensional localized structures on the surface of a ferrofluid. From [23].

Figure 6 shows the resulting bifurcation diagram. The diagram shows the surface energy as a function of the applied vertical magnetic field B . When B is increased from $B = 0$, the solution remains qualitatively unchanged until a threshold is reached at $B \approx 9\text{mT}$. At this value, a subcritical instability generates a hexagonal pattern of peaks. Since this is an experiment the small amplitude but unstable hexagons present for smaller B are not seen and the system jumps instead to a large amplitude hexagonal state. When B is decreased the hexagonal pattern persists until $B \approx 8\text{mT}$, where the peaks collapse and the flat interface is restored. The above process thus describes a hysteresis loop within which two stable states

coexist, the flat interface and the hexagonal pattern. The multi-peak states are present at $B = 8.91\text{mT}$, multi-peak states with $n = 1, 2, \dots$ peaks were created by the process just described, leading to a large number of coexisting stable states at this parameter value.

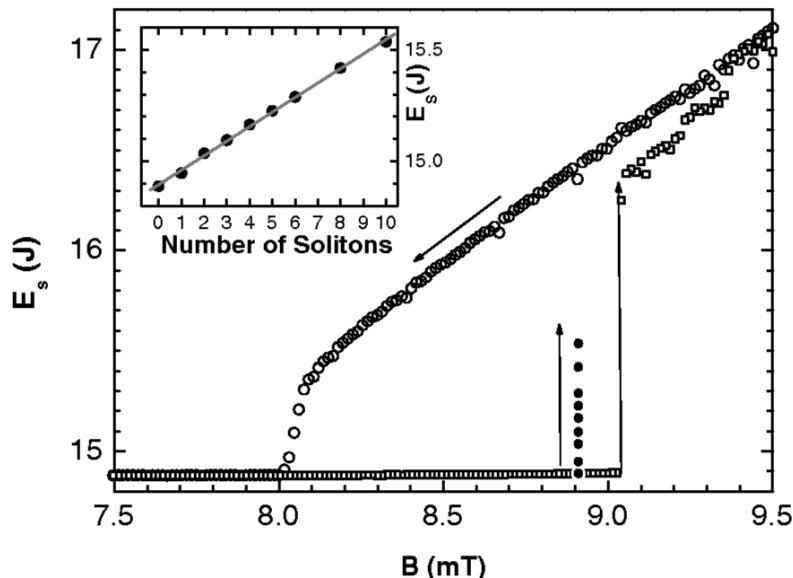


Figure 6: Bifurcation diagram for two-dimensional solitons on the surface of a ferrofluid showing the surface energy as a function of the imposed magnetic field B . Stable steady states with $n = 1, 2, \dots$ peaks are present at $B = 8.9\text{mT}$. From [23].

2.3 Oscillons

Spatially localized oscillations called oscillons were found by Lioubashevski *et al.* [17] in experiments on a clay suspension subjected to vertical vibration. Figure 7 (left panel) shows an oscillon at several different times, while the right panels show different bound states of this type of oscillon. All states oscillate with twice the period of the forcing, i.e., all are subharmonic. Very similar behavior is present in vertically vibrated granular systems [26]. Figure 8 shows the interaction of two or more subharmonic oscillons created in this system.

Similar structures, called cavity solitons, are present in photonic systems [1]. Figure 9 shows how a cavity soliton is written and erased using a localized laser pulse.

2.4 Self-organized patterns in planar DC gas-discharge systems

Strumpel *et al.* [24] found that the discharge current in a DC-driven planar semiconductor gas discharge system is able to self-organize into a variety of nonlinear structures, including in some cases localized current filaments that interact in a manner similar to point vortices in fluid mechanics, i.e., via the Biot-Savart law. Figures 10 and 11 show some of these structures.

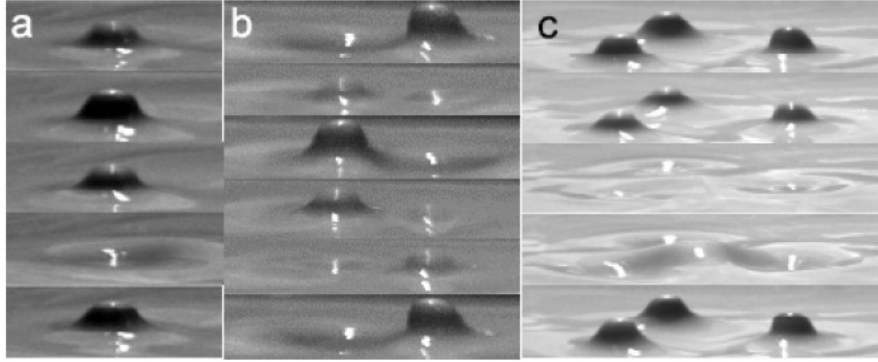


Figure 7: Oscillons on the surface of a clay suspension vibrated harmonically in the vertical direction. Figure (a) shows a single oscillon while (b) and (c) show different bound states of these oscillons. From [17].

2.5 Localized structures in fluid flows

There are many rich fluid dynamical systems where localized structures can be found. Some of them are briefly described here.

2.5.1 Convectons

Convectons, a term coined by Blanchflower [4], are stationary solutions of a convection problem consisting of convection rolls embedded in a background where heat is transported by conduction alone. Good examples of convectons have been observed in doubly diffusive convection. The first computation of convectons is due to Ghorayeb and Mojtabi [14] who studied a vertically extended rectangular cavity heated from one side in the presence of a parallel concentration gradient. When the concentration gradient is chosen appropriately the system possesses a conduction state for all values of a dimensionless number, the Grashof number Gr , that measures the thermal forcing of the system. However, this state loses stability at $Gr = Gr_c$ to a subcritical bifurcation, and for $Gr < Gr_c$ Ghorayeb and Mojtabi found the states shown in Fig. 12. Similar structures have also been found in magnetoconvection [4] and in binary fluid convection [2]. Figures 13 and 14 show examples of structures found in these systems. In all these examples the system forms convectons in response to a finite amplitude perturbation, and does so despite spatially uniform forcing. Each example also exhibits a multiplicity of different localized states under identical conditions.

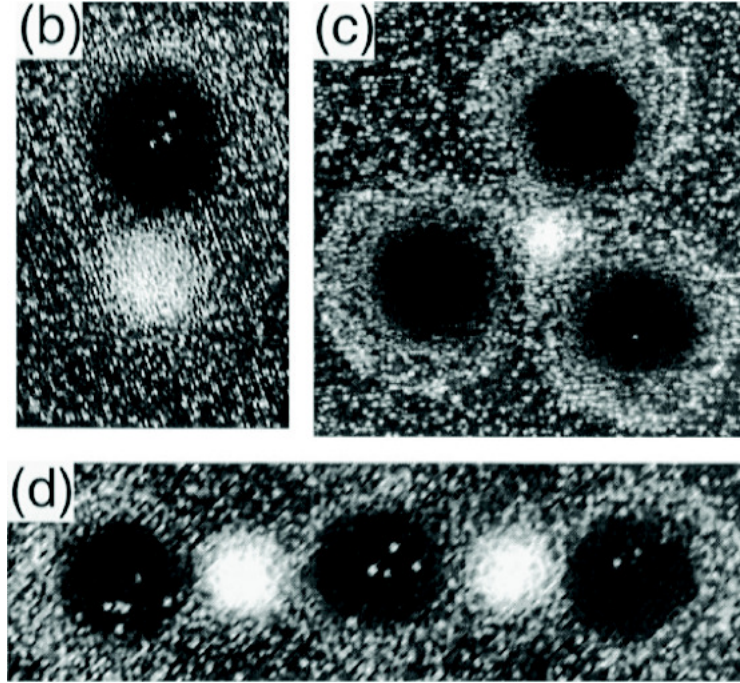


Figure 8: Oscillons in a granular system. From [26].

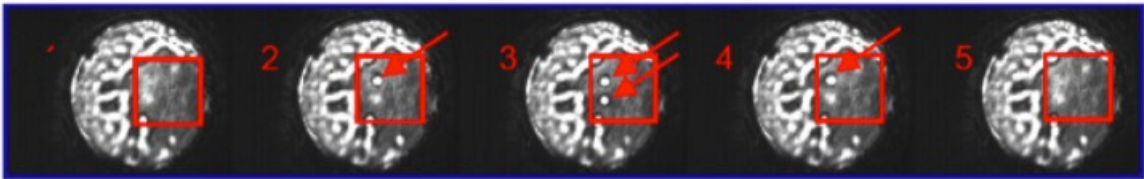


Figure 9: Writing and erasing of cavity solitons. From www.funfacts.org.

2.5.2 Shear flow

Shear flow also exhibits localization phenomena. Figure 15(a) shows a picture from an experiment by Gad-El-Hak *et al.* [12]. These authors studied the response of laminar flow over a stationary plate to a one-time perturbation generated by injecting additional fluid through a minute hole on the plate. The flow was visualized using fluorescent dye techniques. The tiny perturbation develops into a coherent structure whose Λ shape persists in time (Fig. 15(a)). Despite evident localization the structure is spatially and temporally complex.

Plane Couette flow provides perhaps the simplest example of a shear flow and is therefore of particular interest. This flow is generated by the motion of two parallel plates in opposite directions. The resulting linear velocity profile is stable for all plate velocities and a finite amplitude perturbation is needed to trigger persistent turbulence. The boundary in phase space between perturbations that decay to the laminar state and those that evolve into persistent turbulence is populated by unstable *edge states*. As shown in Fig. 15(b) some of these states may be localized. States of this type and the experimentally observed state

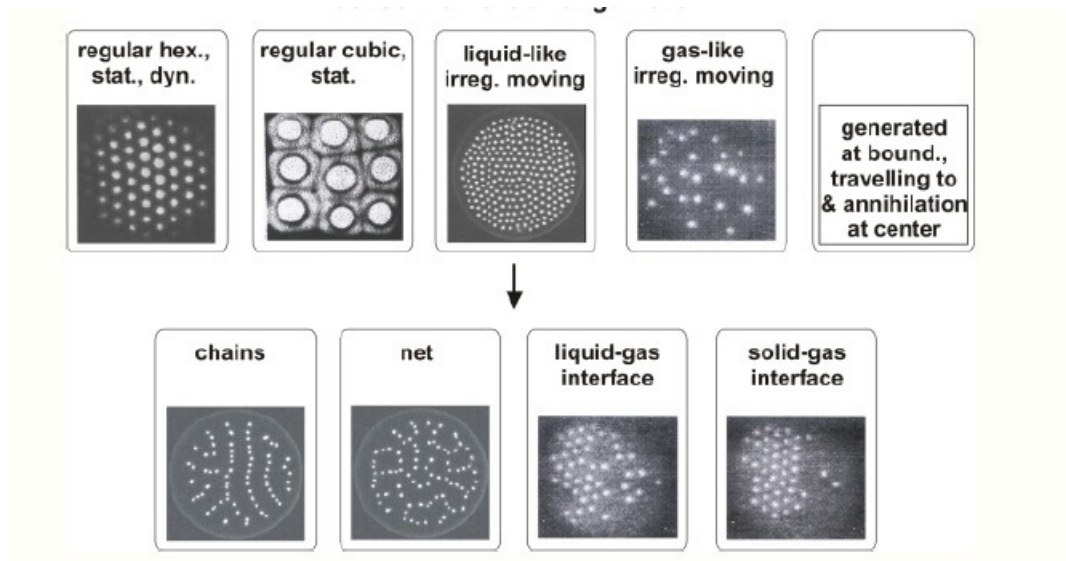


Figure 10: Different spatial patterns formed in a gas discharge system. From [21].

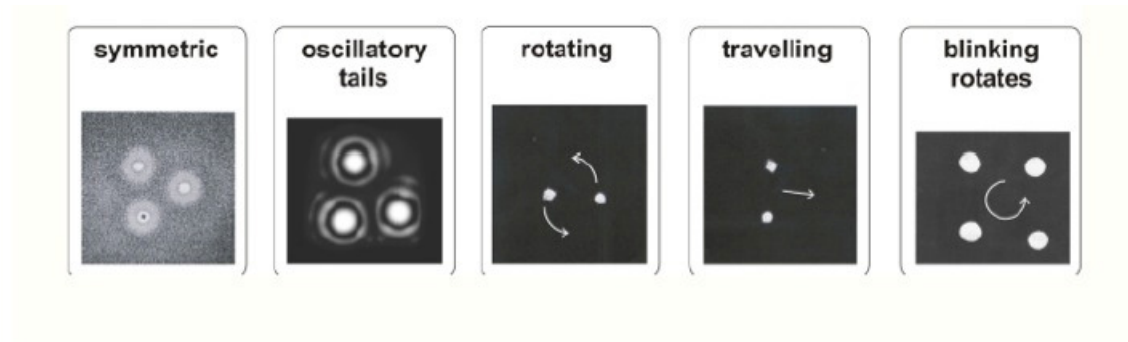


Figure 11: Point vortex-like structures found in a gas discharge system. From [21].

in Fig. 15(a) have some features in common suggesting that they may play a role in the transition to turbulence.

2.5.3 Defects

Defects in an otherwise periodic pattern can and should also be viewed as localized structures. Such defect states are most easily identified using demodulation techniques. Figure 1 shows several examples of defects in an otherwise periodic stripe pattern. Such defects typically move (“climb”) and undergo a variety of interactions. We shall not be discussing defects in these lectures.

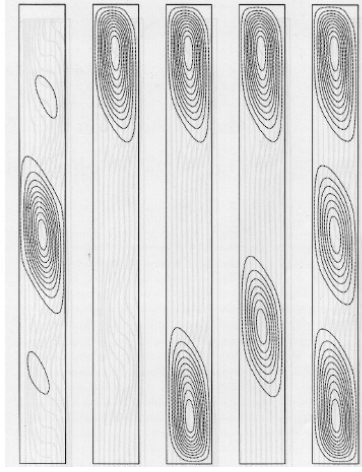


Figure 12: Different stable time-independent spatially localized structures in doubly diffusive convection in a rectangular cavity obtained for identical parameter values. The solutions are visualized using streamlines of the flow. From [14].

3 The Swift–Hohenberg equation

In the preceding section we have established a connection between the presence of spatially localized states and a subcritical bifurcation of a homogeneous state responsible for the coexistence of this state with a spatially periodic state. We have also seen that inside the resulting hysteresis loop one may find a large large multiplicity of coexisting localized states. We now turn to an explanation of this remarkable phenomenon. For this purpose we shall analyze in some detail a model problem, the Swift–Hohenberg equation [7, 8]. This equation was originally suggested as a description of pattern formation in Rayleigh–Bénard convection [19, 25] and it and its variants have led to substantial progress in our understanding of localized structures in driven dissipative systems in both one and two spatial dimensions [3, 18, 20]. However, its simplest realization is in the context of gravity-capillary waves on the surface of a liquid as described next.

3.1 Long gravity-capillary waves

Consider a two-dimensional fluid layer unbounded in x with $-H < y < \zeta(x, t)$, where H is the depth of the fluid and $\zeta(x, t)$ is the elevation of the surface relative to the undisturbed free surface at $y = 0$. The equations describing inviscid water waves read [27]:

$$\phi_{xx} + \phi_{yy} = 0 \quad \text{in} \quad -H < y < \zeta(x, t), \quad (1)$$

$$\phi_y = 0 \quad \text{on} \quad y = -H, \quad (2)$$

$$\zeta_t + \phi_x \zeta_x - \phi_y = 0 \quad \text{on} \quad y = \zeta(x, t), \quad (3)$$

$$\phi_t + \frac{1}{2} (\phi_x^2 + \phi_y^2) + g\zeta - \frac{\kappa \zeta_{xx}}{(1 + \zeta_x^2)^{3/2}} = 0 \quad \text{on} \quad y = \zeta(x, t), \quad (4)$$

where $\phi(x, y, t)$ is the velocity potential, i.e., the velocity $(u, v) = (\phi_x, \phi_y)$. Equation (1) represents the incompressibility of the fluid, while Eq. (2) implies that the bottom boundary

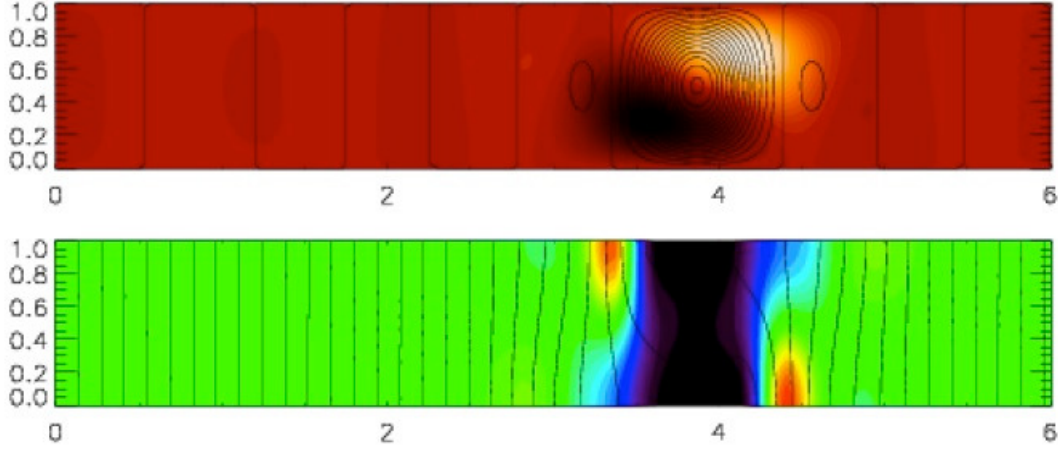


Figure 13: Time-independent spatially localized structure in magnetoconvection. Top panel shows the temperature fluctuation with superposed streamlines; the bottom panel shows contours of magnetic field strength with superposed magnetic field lines. From [5].

is impenetrable. Of the remaining equations Eq. (3) states that the interface moves with the local vertical velocity while Eq. (4) represents the Bernoulli's condition on the free surface. In this equation the last term represents the increase in pressure in the liquid due to surface deformation when the surface tension κ is nonzero.

3.2 Linear theory

The problem (1)–(4) has the trivial solution $\phi \equiv 0$, $\zeta \equiv 0$. We consider infinitesimal perturbations of the free surface of the form $\zeta = \zeta_0 \sin(kx - \omega t)$, where k is the perturbation wavenumber and ω is its frequency. This expression represents a periodic wave traveling to the right with phase speed $c = \omega/k$. Associated with this disturbance is a velocity disturbance given by $\phi = \phi_0(y) \cos(kx - \omega t)$, where the function $\phi_0(y)$ captures the decrease of the velocity with depth. With this Ansatz Eq. (1) yields

$$\phi_{0yy} - k^2 \phi_0 = 0. \quad (5)$$

The boundary condition (2) implies that $\phi_{0y} = 0$ at $y = -H$ and hence that

$$\phi_0 = A \cosh[k(y + H)], \quad (6)$$

where A is an arbitrary constant. The perturbed velocity potential then reads

$$\phi = A \cosh[k(y + H)] \cos(kx - \omega t). \quad (7)$$

Equation (3), linearized about $y = 0$, now yields

$$\zeta_0 \omega = -Ak \sinh(kH), \quad (8)$$

while Eq. (4) yields

$$-\omega A \cosh(kH) + g\zeta_0 + \kappa k^2 \zeta_0 = 0. \quad (9)$$

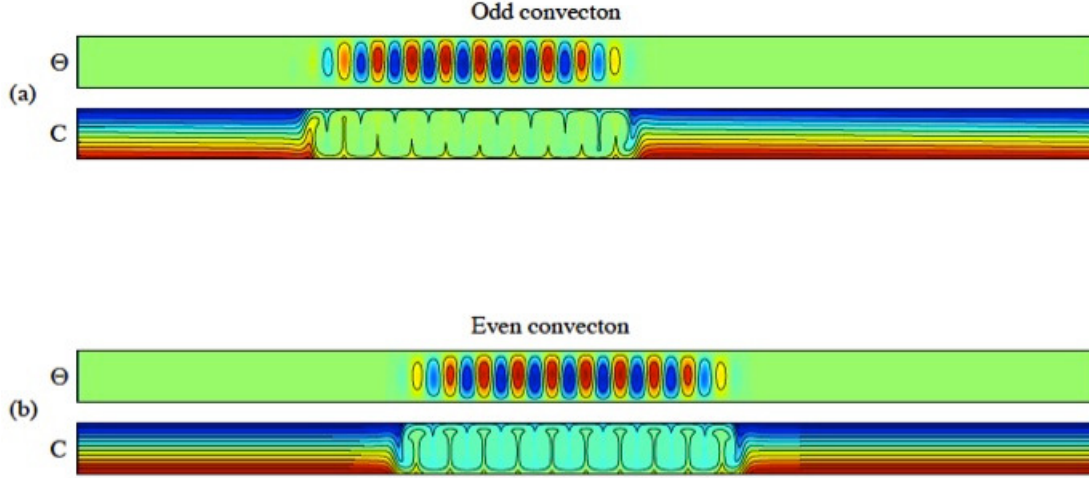


Figure 14: Coexisting stable odd and even convectons in binary fluid convection, shown in terms of the contours of the temperature fluctuation Θ relative to the conduction profile and of the concentration field C . From [2].

Elimination of the arbitrary amplitude A yields finally the dispersion relation for infinitesimal gravity-capillary waves:

$$\omega^2 = (g + \kappa k^2)k \tanh(kH). \quad (10)$$

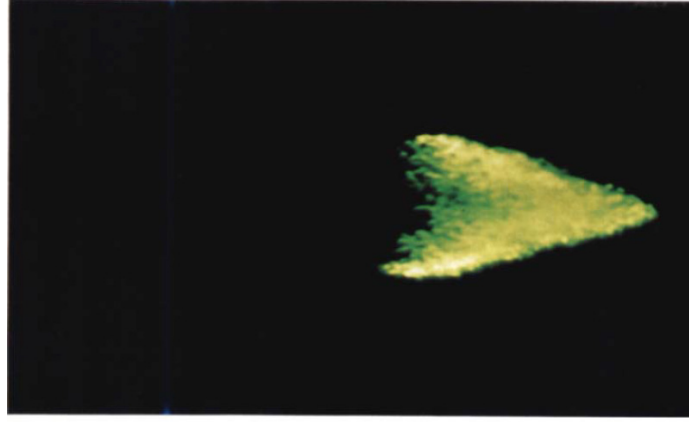
We are interested in long waves, i.e., waves for which $kH \ll 1$. In this limit, the Taylor expansion of the hyperbolic tangent gives $\tanh(kH) = kH(1 - k^2 H^2/3) + \mathcal{O}(k^5 H^5)$ and the dispersion relation (10) becomes

$$\omega^2 = gk^2 H + gk^4 H^3 (\text{Bo} - 1/3) + \mathcal{O}(k^6), \quad (11)$$

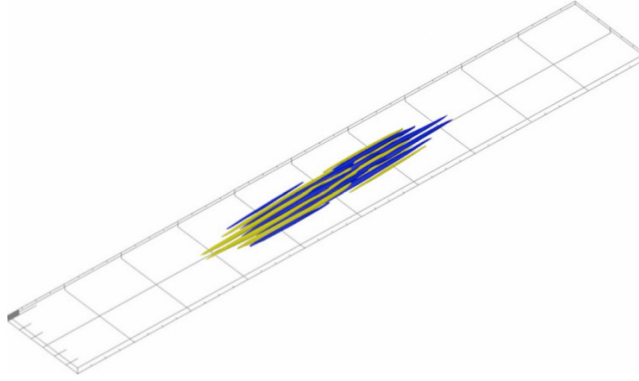
where $\text{Bo} \equiv \kappa/gH^2$ is the Bond number. Thus long waves are nondispersive at leading order but with a dispersive correction at higher order as described by the second term provided $\text{Bo} \neq 1/3$. The special case $\text{Bo} = 1/3$ is thus of particular interest, and in the following we study the weakly nonlinear regime near this special value of Bo .

3.3 Weakly nonlinear regime

Weakly nonlinear traveling waves are most easily found in the frame moving with the speed of the wave since in this reference frame the wave becomes stationary. We therefore set $\xi = x - ct$, and choose for c the long wave phase speed $c = \sqrt{gH}$. This will not in fact be the speed of the traveling wave since nonlinearity will modify its speed but it is a good first guess.



a)



b)

Figure 15: (a) Two-dimensional spatially localized structure in boundary shear flow, viewed from above (from [12]). (b) Edge solution in plane Couette flow at $Re = 375$ in a $2 \times 30 \times 200$ domain. The structure is elongated in the streamwise direction, with yellow (blue) indicating positive (negative) streamwise velocity perturbation (from [10]).

In this frame Eqs. (1)–(4) become

$$\phi_{\xi\xi} + \phi_{yy} = 0 \quad \text{in} \quad -H < y < \zeta(\xi, t), \quad (12)$$

$$\phi_y = 0 \quad \text{on} \quad y = -H, \quad (13)$$

$$\zeta_t + c\zeta_\xi + \phi_\xi\zeta_\xi - \phi_y = 0 \quad \text{on} \quad y = \zeta(\xi, t), \quad (14)$$

$$\phi_t + c\phi_\xi + \frac{1}{2}(\phi_\xi^2 + \phi_y^2) + g\zeta - \frac{\kappa\zeta_{\xi\xi}}{(1 + \zeta_\xi^2)^{3/2}} = 0 \quad \text{on} \quad y = \zeta(\xi, t). \quad (15)$$

Mass conservation requires that we impose the additional condition

$$\int_{-\infty}^{\infty} \zeta \, d\xi = 0 \quad (16)$$

on all our solutions.

We begin by defining a small parameter ϵ in terms of the departure of the Bond number away from its critical value, i.e., we write $\kappa = \kappa_0 + \epsilon^2 \kappa_2$, where $\kappa_0 \equiv gH^2/3$ (corresponding to $\text{Bo} = 1/3$). Next we look for long waves with $\mathcal{O}(\epsilon)$ wavenumber, i.e., waves whose wavelength λ satisfies the relation $H/\lambda = \mathcal{O}(\epsilon)$. To do so, we introduce a large spatial scale $X = \epsilon\xi$ and a slow time scale $T = \epsilon^5 t$ that describes the evolution of the wave in the moving frame. The next step is harder because one needs to identify the scaling of the magnitudes of ϕ and ζ with ϵ that will lead to a balance between nonlinearity and the assumed weak dispersion. The correct choice is $\phi \rightarrow \epsilon^3 \phi$ and $\zeta \rightarrow \epsilon^4 \zeta$, yielding the scaled problem

$$\epsilon^2 \phi_{XX} + \phi_{yy} = 0 \quad \text{in} \quad -H < y < \epsilon^4 \zeta(X, T), \quad (17)$$

$$\phi_y = 0 \quad \text{on} \quad y = -H, \quad (18)$$

$$\epsilon^6 \zeta_T + \epsilon^2 c \zeta_X + \epsilon^6 \phi_X \zeta_X - \phi_y = 0 \quad \text{on} \quad y = \epsilon^4 \zeta(X, T), \quad (19)$$

$$\begin{aligned} \epsilon^4 \phi_T + c \phi_X + \epsilon^2 \frac{1}{2} (\epsilon^2 \phi_X^2 + \phi_y^2) + g \zeta \\ - \epsilon^2 (\kappa_0 + \epsilon^2 \kappa_2) \zeta_{XX} = \mathcal{O}(\epsilon^{12}) \quad \text{on} \quad y = \epsilon^4 \zeta(X, T). \end{aligned} \quad (20)$$

We now expand ϕ and ζ in powers of ϵ^2 : $\phi = \phi_0 + \epsilon^2 \phi_2 + \dots$ and $\zeta = \zeta_0 + \epsilon^2 \zeta_2 + \dots$. The leading order of Eqs. (17)–(18) indicates that $\phi_0 = f_0(X, T)$, where $f_0(X, T)$ is to be determined. At $\mathcal{O}(\epsilon^2)$, we obtain $\phi_{2yy} = -f_{0XX}$ with the boundary condition $\phi_{2y} = 0$ on $y = -H$. Thus

$$\phi_2 = -\frac{1}{2}(y+H)^2 f_{0XX} + f_2(X, T), \quad (21)$$

where $f_2(X, T)$ is unknown. Equations (19)–(20) on the boundary $y = \epsilon^4 \zeta(X, T)$ give at leading order:

$$c \zeta_{0X} = -H f_{0XX}, \quad (22)$$

$$c f_{0X} + g \zeta_0 = 0. \quad (23)$$

In view of the mass conservation condition (16), Eq. (22) can be integrated and gives $c \zeta_0 = -H f_{0X}$ which, when combined with equation (23), gives the dispersion relation for long waves, viz., $c^2 = gH$.

At next order, Eq. (17) yields

$$\phi_{4yy} = -\phi_{2XX} = \frac{1}{2}(y+H)^2 f_{0XXXX} - f_{2XX}, \quad (24)$$

which can be integrated twice with respect to y :

$$\phi_4 = \frac{1}{24}(y+H)^4 f_{0XXXX} - \frac{1}{2}(y+H)^2 f_{2XX} + f_4(X, T), \quad (25)$$

where the boundary condition $\phi_{4y} = 0$ at $y = -H$ has been used to eliminate one constant of integration. The following order gives

$$\phi_{6yy} = -\phi_{4XX} = -\frac{1}{24}(y+H)^2 f_{2XXXX} - f_{4XX}, \quad (26)$$

leading to

$$\phi_{6y} = -\frac{1}{120}(y+H)^5 f_{0XXXXXX} + \frac{1}{6}(y+H)^3 f_{2XXXX} - (y+H)f_{4XX}. \quad (27)$$

These expressions are to be complemented with corresponding boundary conditions from Eqs. (19)–(20). At $\mathcal{O}(\epsilon^4)$, Eq. (19) reads:

$$c\zeta_{2X} = \phi_{4y} = \frac{1}{6}H^3 f_{0XXXX} - Hf_{2XX}, \quad (28)$$

or

$$c\zeta_2 = \frac{1}{6}H^3 f_{0XXX} - Hf_{2X}, \quad (29)$$

where we have again used the mass conservation relation (16) to fix the constant of integration. At $\mathcal{O}(\epsilon^2)$, Eq. (20) reads:

$$c\phi_{2X} + g\zeta_2 - \kappa_0\zeta_{0XX} = 0, \quad (30)$$

or equivalently,

$$c\left(-\frac{1}{2}H^2 f_{0XXX} + f_{2X}\right) + g\zeta_2 + \frac{c\kappa_0}{g}f_{0XXX} = 0. \quad (31)$$

Notice that Eqs. (29) and (31) are identical provided $\kappa_0 = gH^2/3$. This fact confirms that we have scaled the linear terms correctly.

We proceed next to $\mathcal{O}(\epsilon^6)$ in Eq. (19):

$$\zeta_{0T} + c\zeta_{4X} + f_{0X}\zeta_{0X} = -\frac{1}{120}H^5 f_{0XXXXXX} + \frac{1}{6}H^3 f_{2XXXX} - Hf_{4XX} - \zeta_0 f_{0XX}. \quad (32)$$

The last term in this equation arises from the ζ contribution to ϕ_{2y} . Equation (20) at $\mathcal{O}(\epsilon^4)$ yields:

$$\phi_{0T} + c\phi_{4X} + \frac{1}{2}f_{2X}^2 + g\zeta_4 - \kappa_0\zeta_{2XX} - \kappa_2\zeta_{0XX} = 0, \quad (33)$$

where ϕ_4 is to be evaluated at $y = 0$ using Eq. (25). Eliminating f_4 and ζ_4 from the resulting equations we obtain a solvability condition which can in turn be simplified by eliminating f_0 in favor of ζ_0 . We obtain

$$\frac{2c}{H}\zeta_{0T} - \frac{3g}{H}\zeta_0\zeta_{0X} + \kappa_2\zeta_{0XX} + \frac{1}{30}gH^4\zeta_{0XXXX} = -\kappa_0\zeta_{2XX} - \frac{1}{3}cH^2f_{2XXXX}. \quad (34)$$

The right hand side of this equation can be evaluated in terms of ζ_0 with the help of Eq. (31) and the relation $\kappa_0 = gH^2/3$ leading finally to an evolution equation satisfied by ζ_0 :

$$\frac{2c}{H}\zeta_T - \frac{3g}{H}\zeta\zeta_X + \kappa_2\zeta_{XX} - \frac{1}{45}gH^4\zeta_{XXXX} = 0. \quad (35)$$

In writing this equation we have dropped the subscript 0 on ζ_0 . The resulting equation generalizes the Korteweg–de Vries equation by retaining higher order dispersion.

Solitary waves traveling to the right with speed V and without change of shape may now be obtained by writing $z \equiv X - VT$ to boost the reference frame by just the right amount

so that the nonlinear solution remains stationary. In this frame such a wave satisfies the ordinary differential equation

$$\frac{1}{45}gH^4\zeta'''' - \kappa_2\zeta'' + \frac{2cV}{H}\zeta + \frac{3g}{2H}\zeta^2 = 0 \quad (36)$$

obtained after one integration with respect to the variable z . Here the prime denotes a derivative with respect to z . The resulting equation is the simplest case of the Swift–Hohenberg equation, hereafter SH20, because it only includes a single nonlinearity of second order. Despite its simplicity this equation has a remarkably rich solution structure that includes a large number of solutions homoclinic to $\zeta = 0$, i.e., solitary waves [6, 11].

We remark that Eq. (36) is dissipative in *space* although the time-dependent problem from which it was derived is conservative, with an energy that is conserved in time.

4 The Korteweg–de Vries equation

The Korteweg–de Vries equation (named after [16]) can be derived from Eqs. (17)–(20) using a different scaling that is valid for all values of Bo that are not close to the critical value $\text{Bo} = 1/3$. This time we write $X = \epsilon\xi$, $T = \epsilon^3t$, $\phi = \mathcal{O}(\epsilon)$, $\zeta = \mathcal{O}(\epsilon^2)$ and assume that $\kappa - \kappa_0 = \mathcal{O}(1)$. Thus, the small parameter ϵ is now defined by the ratio H/λ instead of being defined in terms of the Bond number. Proceeding as in the preceding section we obtain at second order

$$\zeta_T + \zeta\zeta_X + \zeta_{XXX} = 0, \quad (37)$$

where T and X have been rescaled to eliminate constants.

Waves of constant form can be found by writing $\xi \equiv X - VT$ and integrating the resulting equation twice. The Korteweg–de Vries equation (37) then takes the form of an equation for a particle in a potential,

$$\frac{1}{2}\zeta_\xi^2 + U(\zeta) = E, \quad (38)$$

where E is a constant and

$$U(\zeta) \equiv \zeta^3/6 - V\zeta^2/2. \quad (39)$$

The potential $U(\zeta)$ is represented in Fig. 16. Sinusoidal oscillations are present around the local minimum of the potential provided $E + 2V^2/3 \ll 1$. As E increases the oscillations become more and more nonlinear and their (spatial) period increases.¹ When $E = 0$ the solutions have infinite period, i.e., they are solitary waves. These form a one parameter family,

$$\zeta = a \operatorname{sech}^2 \left[\frac{a}{2\sqrt{3}} \left(X - \sqrt{gH}t - \frac{a}{3}T \right) \right], \quad (40)$$

parametrized by the wave amplitude a . Thus all finite amplitude solitary waves travel faster than \sqrt{gH} and larger solitons travel faster than smaller solitons. These solutions interact in a particle-like manner, i.e., they are in fact *true solitons* [13, 28]. This is a

¹A second constant of integration must be included in $U(\zeta)$ in order to satisfy the mass conservation condition (16).

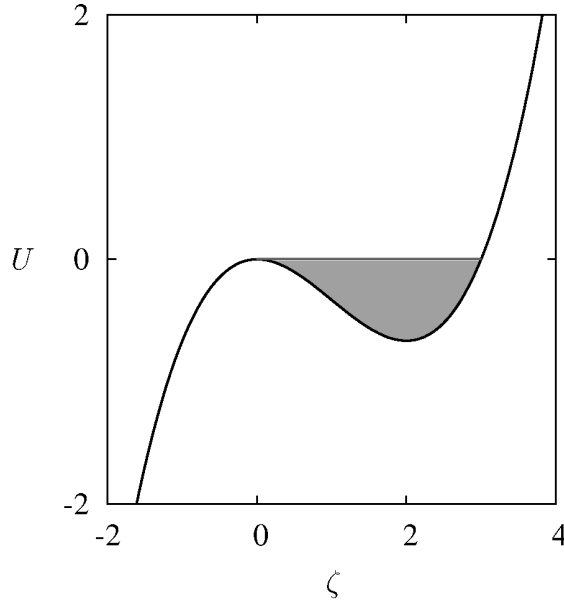


Figure 16: Potential $U(\zeta)$ in Eq. (39) when $V = 1$. The gray region indicates periodic solutions and the horizontal line delimitating this region at the top corresponds to a solitary wave.

consequence of complete integrability of the Korteweg–de Vries equation as an infinite-dimensional Hamiltonian system.

Soliton behavior of the solutions of the Korteweg–de Vries equation is shown in Fig. 17. The left figure shows one soliton drifting to the right without change of shape. The second figure shows the collision between two solitons with different amplitudes and hence different speeds. During their collision, they pass through each other and resume their course at the same speed after a slight delay.

5 Spatial eigenvalues and localization

In the Korteweg–de Vries problem one cannot tell the direction of propagation of the wave from the solution profile or even that the wave is traveling. This is a consequence of the invariance of the water wave problem under Galilean transformation, but this is not the case in driven dissipative systems. In such systems a solitary wave travels whenever it is not reflection symmetric. Generically, only reflection-symmetric states are stationary.

For solitary waves in driven dissipative systems, we therefore need to distinguish between stationary solitary waves and traveling ones. Suppose that $u_t = g(u, u_x, u_{xx}, \dots)$, where g is real-valued and $g(\mathbf{0}) = 0$. Then, $g(u, u_x, u_{xx}, \dots) = 0$ is a dynamical system in space, with phase space (u, u_x, u_{xx}, \dots) , and its solutions represent steady states. Of particular interest is the fixed point $u = 0$ in this phase space. This point represents a spatially homogeneous state and this state must have at least one unstable and one stable direction *in space* in order

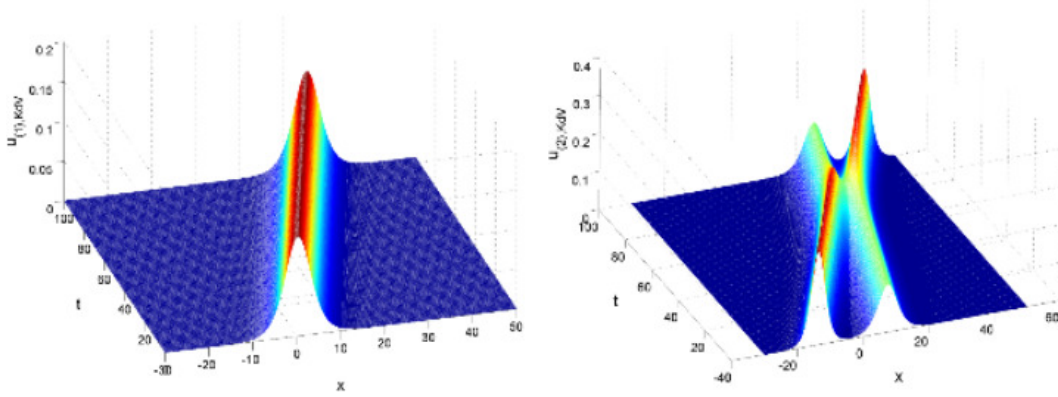


Figure 17: Left: spatio-temporal visualization of a Korteweg–de Vries soliton. Right: same type of visualization but for two different solitons. The soliton with larger amplitude travels faster as indicated by Eq. (40). After the collision the solitons continue their course with the same velocity but with a slight delay due to the collision. Courtesy L. Gelens.

that a solitary wave be present. Thus a necessary condition for the existence of solitary waves biasymptotic to the homogeneous state $u = 0$ is that $u = 0$ is a hyperbolic fixed point. To determine conditions for this to be so we must examine the spatial eigenvalues of $u = 0$. For this purpose we linearize $g(\mathbf{0}) = 0$ around $u = 0$,

$$g_u(\mathbf{0})u + g_{u_x}(\mathbf{0})u_x + g_{u_{xx}}(\mathbf{0})u_{xx} + \dots = 0, \quad (41)$$

and look for solutions with $u = u_0 \exp \lambda x$. The spatial eigenvalues λ are thus given by

$$P(\lambda) = 0, \quad (42)$$

where P is real-valued so that $P(\lambda) = 0 \Rightarrow P(\bar{\lambda}) = 0$. If, in addition, the system is *spatially reversible*, meaning that it is invariant under spatial reflection, $x \rightarrow -x$, $u \rightarrow u$,² then $P(\lambda) = 0 \Rightarrow P(-\lambda) = 0$. Thus, if $u = 0$ has two negative real eigenvalues it also has two positive real eigenvalues. Likewise, if λ is a complex root of $P(\lambda) = 0$ then so are $-\lambda$ and $\pm\bar{\lambda}$ and the eigenvalues form a quartet in the complex plane. Thus, unless an eigenvalue has a zero real part, $u = 0$ has a two-dimensional unstable manifold W^u and a two-dimensional stable manifold W^s . If these manifolds intersect it is possible to find a trajectory that leaves $u = 0$ as x increases from $-\infty$ and returns to $u = 0$ as $x \rightarrow \infty$, i.e., a spatially localized solution. The likelihood of such an intersection is very much less when $u = 0$ has only one negative eigenvalue (and hence one positive eigenvalue), with the remaining eigenvalues on the imaginary axis.

It follows that in spatially reversible systems P is in fact a function of λ^2 and the simplest nontrivial case yields $P(\lambda) \equiv \lambda^4 + b\lambda^2 + a = 0$. Figure 18 depicts the location of the four eigenvalues of the spatial problem in the complex plane as a function of the parameters a and b . Below the curve $C_2 \cup C_3$, the eigenvalues lie on the axes, meaning that either their

²We remark that the Korteweg–de Vries equations (35) and (37) have a different type of spatial reversibility: $x \rightarrow -x$, $\zeta \rightarrow -\zeta$.

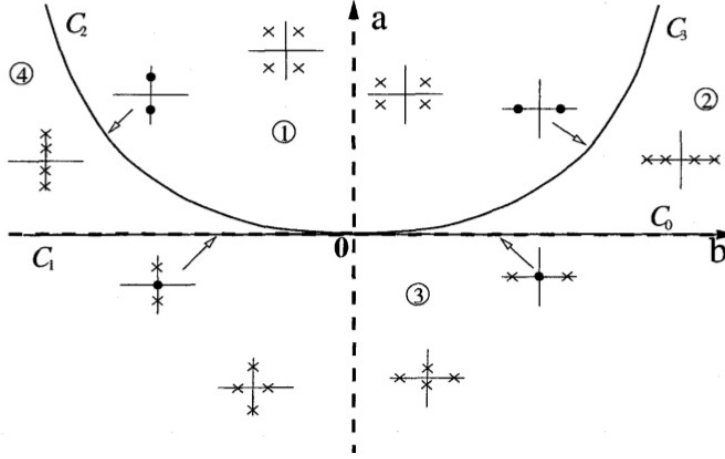


Figure 18: Roots of the equation $\lambda^4 + b\lambda^2 + a = 0$ in the (a, b) plane. From [9].

real part or their imaginary part is zero. Above this curve the eigenvalues form a complex quartet. We focus on the transition occurring at C_2 . In the region labeled 4 in Fig. 18, all the eigenvalues lie on the imaginary axis, meaning the eigenmodes are purely oscillatory in space. As a or b increase the eigenvalues collide on the curve C_2 and move into the complex plane forming a quartet as anticipated above. This transition will provide a key to the appearance of spatially localized states as discussed in the next lecture.

In the Korteweg–de Vries case (37), the phase space of the equivalent particle-in-potential problem is two-dimensional and the fixed point $(u, u_x) = \mathbf{0}$ has a one-dimensional stable manifold W^s and a one-dimensional unstable manifold W^u . Consider the surface Σ representing $u_x(x=0) = 0$ which is intersected by all spatially reversible solutions. Its dimension is $\dim(\Sigma) = 1$. The intersection $W^u \cap \Sigma$ is then a point and by reversibility this point is also on $W^s \cap \Sigma$. Thus the point $W^u \cap \Sigma$ lies on a homoclinic orbit to $(u, u_x) = \mathbf{0}$. This result also follows from “energy conservation” since both manifolds lie in the energy surface $E = 0$. Moreover, if $E \neq 0$ no homoclinic orbit is present implying that the homoclinic orbit is present at a single parameter value only.

The situation is quite different in the generalized Korteweg–de Vries equation such as Eq. (35) because this equation is of fifth order in space. Here the phase space of the equivalent dynamics problem is four-dimensional and in region 4 of Fig. 18 the fixed point $(u, u_x, u_{xx}, u_{xxx}) = \mathbf{0}$ has a two-dimensional stable and a two-dimensional unstable manifold. In four dimensions these manifolds will not intersect in general but we can find a large number of homoclinic orbits to $(u, u_x, u_{xx}, u_{xxx}) = \mathbf{0}$ by examining the vicinity of a *heteroclinic cycle* between this point and a symmetric periodic orbit Γ when such an orbit is present and is hyperbolic. This cycle consists of a heteroclinic connection from $\mathbf{0}$ to Γ followed by a heteroclinic connection from Γ back to $\mathbf{0}$. Note that if one can establish the presence of the first connection then the return connection follows using spatial reversibility. The periodic orbit plays a vitally important role in the generation of spatially localized states. The reason is that Γ has one zero eigenvalue (more correctly a Floquet multiplier equal to one) that is doubled by spatial reversibility. For Γ to be hyperbolic there must in

addition be one stable Floquet multiplier and one unstable Floquet multiplier. Under these conditions Γ has a three-dimensional center-stable manifold W^{cs} and a three-dimensional center-unstable manifold W^{cu} . Since an intersection between the two-dimensional unstable manifold W^u of $\mathbf{0}$ and the three-dimensional center-stable manifold W^{cs} of Γ is generic in four dimensions such an intersection cannot be perturbed away by making small changes to the parameter values (or indeed the equation). We call such intersections *structurally stable* and conclude, invoking spatial reversibility, that under these conditions the dynamical system $g = 0$ possesses a structurally stable heteroclinic cycle. Since such a heteroclinic cycle is associated with nearby homoclinic orbits (such orbits in fact accumulate on the cycle) it follows that near such a cycle one will find a plethora of homoclinics that persist over a finite parameter interval. We call such solitary waves *robust*.

In the next lecture we shall provide a concrete illustration of this abstract geometric argument. However, the argument suggests that the key to finding time-independent spatially localized states in reversible systems is provided by the presence of a heteroclinic connection $\mathbf{0} \rightarrow \Gamma$, i.e., of a *front* connecting a spatially homogeneous state to a spatially periodic state.

We mention that if spatial reversibility is absent then a heteroclinic cycle of the above type becomes of higher codimension and the situation becomes quite different. This is why the properties of traveling solitary waves differ substantially from those of stationary structures in spatially reversible systems.

References

- [1] T. Ackemann, W. J. Firth and G.-L. Oppo. Fundamentals and applications of spatial dissipative solitons in photonic devices. *Adv. Atomic, Molecular, and Optical Physics*, **57**, pp. 323–421, 2009.
- [2] O. Batiste, E. Knobloch, A. Alonso and I. Mercader, Spatially localized binary-fluid convection. *J. Fluid Mech.*, **560**, pp. 149–158, 2006.
- [3] M. Beck, J. Knobloch, D. J. B. Lloyd, B. Sandstede and T. Wagenknecht. Snakes, ladders and isolas of localized patterns. *SIAM J. Math. Anal.* **43**, pp. 936–972, 2009.
- [4] S. Blanchflower. Magnetohydrodynamic convectons. *Phys. Lett. A*, **261**, pp. 74–81, 1999.
- [5] S. M. Blanchflower. *Modelling Photospheric Magnetoconvection*. Ph.D. Thesis, University of Cambridge, 1999.
- [6] B. Buffoni, A. R. Champneys and J. F. Toland. Bifurcation and coalescence of a plethora of homoclinic orbits for a Hamiltonian system. *J. Dyn. Diff. Eq.* **8**, pp. 221–279, 1996.
- [7] J. Burke and E. Knobloch. Localized states in the generalized Swift–Hohenberg equation. *Phys. Rev. E* **73**, 056211, 2006.
- [8] J. Burke and E. Knobloch. Snakes and ladders: Localized states in the Swift–Hohenberg equation. *Phys. Lett. A* **360**, pp. 681–688, 2007.

- [9] A. R. Champneys. Homoclinic orbits in reversible systems and their applications in mechanics, fluids and optics. *Physica D* **112**, pp. 158–186, 1998.
- [10] Y. Duguet, P. Schlatter and D. S. Henningson. Localized edge states in plane Couette flow. *Phys. Fluids* **21**, 111701, 2009.
- [11] A. R. Champneys and J. F. Toland. Bifurcation of a plethora of multi-modal homoclinic orbits for autonomous Hamiltonian systems. *Nonlinearity* **6**, pp. 665–721, 1993.
- [12] M. Gad-El-Hak, R. F. Blackwelder and J. J. Riley. On the growth of turbulent regions in laminar boundary layers. *J. Fluid Mech.* **110**, pp. 73–95, 1981.
- [13] C. S. Gardner, J. M. Greene, M. D. Kruskal and R. M. Miura. Method for solving the Korteweg–de Vries equation. *Phys. Rev. Lett.* **19**, pp. 1095–1097, 1967.
- [14] K. Ghorayeb and A. Mojtabi. Double diffusive convection in a vertical rectangular cavity. *Phys. Fluids* **9**, pp. 2339–2348, 1997.
- [15] G. W. Hunt, M. A. Peletier, A. R. Champneys, P. D. Woods, M. Ahmer Wadee, C. J. Budd and G. J. Lord. Cellular buckling in long structures. *Nonlinear Dynamics* **21**, pp. 3–29, 2000.
- [16] D. J. Korteweg and G. de Vries. On the change of form of long waves advancing in a rectangular canal and on a new type of long stationary waves. *Phil. Mag.* **39**, pp. 422–443, 1895.
- [17] O. Lioubashevski, Y. Hamiel, A. Agnon, Z. Reches and J. Fineberg. Oscillons and propagating solitary waves in a vertically vibrated colloidal suspension. *Phys. Rev. Lett.* **83**, pp. 3190–3193, 1999.
- [18] D. J. B. Lloyd, B. Sandstede, D. Avitabile and A. R. Champneys. Localized hexagon patterns of the planar Swift–Hohenberg equation. *SIAM J. Appl. Dyn. Sys.* **7**, pp. 1049–1100, 2008.
- [19] Y.-P. Ma and E. A. Spiegel. A diagrammatic derivation of (convective) pattern equations. *Physica D* **240**, pp. 150–165, 2011.
- [20] S. McCalla and B. Sandstede. Snaking of radial solutions of the multi-dimensional Swift–Hohenberg equation: a numerical study. *Physica D* **239**, pp. 1581–1592, 2010.
- [21] H.-G. Purwins. Dissipative solitons in physical systems (<http://www.osti.gov/eprints/topicpages/documents/record/112/2448809.html>).
- [22] H.-G. Purwins, H. U. Bödeker and Sh. Amiranashvili. Dissipative solitons. *Adv. Phys.* **59**, pp. 485–701, 2010.
- [23] R. Richter and I. V. Barashenkov. Two-dimensional solitons on the surface of magnetic fluids. *Phys. Rev. Lett.* **94**, 185403, 2005.

- [24] C. Strumpel, Yu. A. Astrov and H.-G. Purwins. Nonlinear interaction of homogeneously oscillating domains in a planar gas discharge system. *Phys. Rev. E* **64**, pp. 4889–4897, 2000.
- [25] J. Swift and P. C. Hohenberg. Hydrodynamic fluctuations at the convective instability. *Phys. Rev. A* **15**, pp. 319–328, 1977.
- [26] P. B. Umbanhowar, F. Melo and H. L. Swinney. Localized excitations in a vertically vibrated granular layer. *Nature* **382**, pp. 793–796, 1996.
- [27] G. B. Whitham. *Linear and Nonlinear Waves*. Wiley, 1974.
- [28] N. J. Zabusky and M. D. Kruskal. Interaction of 'solitons' in a collisionless plasma and the recurrence of initial states. *Phys. Rev. Lett.* **15**, pp. 240–243, 1965.

Lecture 7: The Swift-Hohenberg equation in one spatial dimension

Edgar Knobloch: notes by Vamsi Krishna Chalamalla and Alban Sauret
with substantial editing by Edgar Knobloch

January 10, 2013

1 Introduction

Let us consider the Swift-Hohenberg equation in one spatial dimension:

$$u_t = r u - (q_c^2 + \partial_x^2)^2 u + f(u). \quad (1)$$

Here $f(u)$ represents the nonlinear terms in u and r is the bifurcation parameter. The parameter q_c represents a characteristic wavenumber, i.e., it selects a characteristic lengthscale given by $2\pi/q_c$. In unbounded domains the wavenumber q_c can be set equal to $q_c = 1$ but this is not the case on finite domains.

Despite its simplicity, Eq. (1) has very remarkable properties and we shall use it here as a “normal form” for systems exhibiting spatially localized structures on the real line. The equation is of fourth order in x and reversible in space, i.e., it is equivariant under $x \rightarrow -x$, $u \rightarrow u$. Motivated by the experiments summarized in the previous lecture we select a *bistable* nonlinearity of the form $f(u) = b_2 u^2 - u^3$ (hereafter SH23) and $f(u) = b_3 u^3 - u^5$ (hereafter SH35), with $b_2 > 0$ (resp., $b_3 > 0$); the latter nonlinearity leads to an additional symmetry, $x \rightarrow x$, $u \rightarrow -u$, that plays an important role in the properties of the solutions and is analogous to the so-called Boussinesq symmetry of Rayleigh-Bénard convection with identical boundary conditions at the top and bottom.

Equation (1) has variational structure, i.e., it possesses a Lyapunov functional $F[u(x, t)]$, such that

$$u_t = -\frac{\delta F}{\delta u}, \quad (2)$$

where F is given by

$$F = \int_{-\infty}^{\infty} dx \left[-\frac{1}{2} r u^2 + \frac{1}{2} [(q_c^2 + \partial_x^2) u]^2 - \int_0^u f(v) dv \right]. \quad (3)$$

It follows that

$$\frac{dF}{dt} = -\left(\frac{\partial u}{\partial t}\right)^2 \leq 0, \quad (4)$$

and hence that $dF/dt < 0$ provided $\partial u/\partial t \neq 0$ somewhere in the domain. Thus on a finite domain with null boundary conditions all solutions evolve towards stationary states; on an

unbounded or periodic domain solutions in the form of moving fronts are possible. In the following we will think of the functional $F[u]$ as the (free) energy of the system. Stable (unstable) solutions correspond to local minima (maxima) of this energy. We shall see that in appropriate parameter regimes the energy landscape described by the free energy (3) can be exceedingly complex.

2 Linear stability of the uniform state

2.1 The temporal view

The usual way to examine the stability of the state $u = 0$ is to linearize Eq. (1) about this state and look for solutions of the form $u \propto \exp(\sigma_k t + i k x)$, where σ_k is the growth rate of a perturbation with wavenumber k . The growth rate σ_k is given by the dispersion relation

$$\sigma_k = r - (q_c^2 - k^2)^2. \quad (5)$$

The marginal stability curve is determined by setting $\sigma_k = 0$ and then minimizing the marginal value $r = r_k$ with respect to the wavenumber k . This calculation leads to the prediction $r = 0$ for the onset of instability, and of the associated wavenumber, $k = q_c$.

Observe that if one takes $r < 0$ then the condition for marginal stability, $r = (q_c^2 - k^2)^2$, has no solution for real k but it does have a solution with k complex. In contrast, if $r > 0$ there is a pair of real solutions, $k = k_{\pm}$, with $k_- < q_c < k_+$. As r decreases to zero from above the wavenumbers k_{\pm} approach $k = q_c$ from opposite directions and at $r = 0$ they collide at $k = q_c$. Thus the minimum of the marginal stability curve is in fact associated with the collision of two roots of the marginal dispersion relation.

2.2 The spatial view

We can appreciate what is happening if we focus on steady states from the outset. These satisfy the ordinary differential equation (ODE)

$$r u - \left(q_c^2 + \frac{d^2}{dx^2} \right)^2 u + f(u) = 0. \quad (6)$$

As explained at the end of the preceding lecture we can also study the stability of the trivial flat state $u = 0$ *in space* by linearizing (6) around the $u = 0$ state and looking for solutions of the form $u \propto \exp(\lambda x)$. We obtain

$$(q_c^2 + \lambda^2)^2 - r = 0. \quad (7)$$

For $r < 0$ the spatial eigenvalues of $u = 0$ form a complex quartet (see Fig. 1a). At $r = 0$ these eigenvalues collide pairwise on the imaginary axis (see Fig. 1b) and for $r > 0$ they split but remain on the imaginary axis (see Fig. 1c) [3]. It should be evident that the temporal and spatial points of view are closely related; in particular, the onset of instability in the temporal point of view is equivalent to the presence of a pair of purely imaginary spatial eigenvalues of double multiplicity.

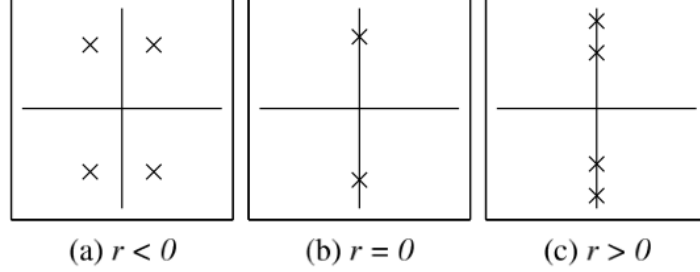


Figure 1: The behavior of the spatial eigenvalues λ of $u = 0$. (a) $r < 0$, (b) $r = 0$, (c) $r > 0$.

It is useful to look at the transition at $r = 0$ in a little more detail. We write $r = \epsilon^2 \mu$, where $\mu = \mathcal{O}(1)$ and $\epsilon \ll 1$. We then find that for $\mu < 0$ the spatial eigenvalues are $\lambda = \pm \epsilon (2q_c)^{-1} \sqrt{-\mu} \pm i(q_c + \mathcal{O}(\epsilon^2))$ while for $\mu > 0$ the eigenvalues are $\lambda = \pm i \epsilon (2q_c)^{-1} \sqrt{\mu} \pm i(q_c + \mathcal{O}(\epsilon^2))$. These considerations suggest that when $r < 0$ the solutions near $u = 0$ will be growing or decaying as $u \sim \exp(\pm \epsilon \sqrt{-\mu} x / 2q_c)$, i.e., that the amplitude of such solutions will vary on a long scale $X \equiv \epsilon x$ while their wavenumber will remain close to q_c . We will take advantage of this insight in the next section.

3 Weakly nonlinear analysis

We now consider the steady states of SH35 with $f(u) = b_3 u^3 - b_5 u^5$ (SH35); the coefficient b_5 can be scaled to unity but is retained here to emphasize the contribution of the fifth order term. The steady states satisfy the ODE

$$r u - \left(q_c^2 + \frac{d^2}{dx^2} \right)^2 u + b_3 u^3 - b_5 u^5 = 0. \quad (8)$$

Because of the symmetry $x \rightarrow x$, $u \rightarrow -u$ the weakly nonlinear theory for this case is simpler than for SH23. Indeed, we can establish the presence of homoclinic orbits near $r = 0$ by setting $r \equiv \epsilon^2 \mu < 0$ with $\mu = \mathcal{O}(1)$. As suggested by the linear theory in the preceding section we use a multiple scale expansion with spatial scales x and $X \equiv \epsilon x$, and introduce the Ansatz:

$$u_\ell(x) = \epsilon u_1(x, X) + \epsilon^2 u_2(x, X) + \dots, \quad (9)$$

where

$$u_1(x, X) = Z(X; \epsilon) e^{iq_c x} + c.c. \quad (10)$$

The following calculation determines $Z(X; \epsilon)$. For reasons that will become apparent the calculation needs to be done to fifth order in the small parameter ϵ . For this reason it is simplest to perform the calculation at $r = 0$ and then figure out what additional terms involving μ have to be added. We begin by writing

$$\frac{d}{dx} = \frac{\partial}{\partial x} + \epsilon \frac{\partial}{\partial X}. \quad (11)$$

Matching terms order by order in ϵ gives:

$$\mathcal{O}(\epsilon) : (\partial_x^2 + q_c^2)^2 u_1 = 0 \quad (12)$$

$$\mathcal{O}(\epsilon^2) : (\partial_x^2 + q_c^2)^2 u_2 = -4\partial_{xX} (\partial_x^2 + q_c^2) u_1 \quad (13)$$

$$\mathcal{O}(\epsilon^3) : (\partial_x^2 + q_c^2)^2 u_3 = -4\partial_{xX} (\partial_x^2 + q_c^2) u_2 - 4\partial_{xxXX} u_1 - 2\partial_{XX} (\partial_x^2 + q_c^2) u_1 + b_3 u_1^3 \quad (14)$$

$$\mathcal{O}(\epsilon^4) : (\partial_x^2 + q_c^2)^2 u_4 = -4\partial_{xX} (\partial_x^2 + q_c^2) u_3 - 4\partial_{xxXX} u_2 - 2\partial_{XX} (\partial_x^2 + q_c^2) u_2 - 4\partial_{xXX} u_1 + 3b_3 u_1^2 u_2 \quad (15)$$

$$\mathcal{O}(\epsilon^5) : (\partial_x^2 + q_c^2)^2 u_5 = -4\partial_{xX} (\partial_x^2 + q_c^2) u_4 - 4\partial_{xxXX} u_3 - 2\partial_{XX} (\partial_x^2 + q_c^2) u_3 - 4\partial_{xXX} u_2 - \partial_X^4 u_1 + 3b_3 (u_1 u_2^2 + u_1^2 u_3) - b_5 u_1^5. \quad (16)$$

We solve these equations order by order. The $\mathcal{O}(\epsilon, \epsilon^2)$ equations are solved by

$$u_1(x, X) = A_1(X)e^{iq_c x} + c.c., \quad u_2(x, X) = A_2(X)e^{iq_c x} + c.c., \quad (17)$$

where $A_{1,2}(X)$ are as yet undetermined and *c.c.* denotes a complex conjugate. The Ansatz

$$u_3(x, X) = A_3(X)e^{iq_c x} + C_3(X)e^{3iq_c x} + c.c. \quad (18)$$

in the $\mathcal{O}(\epsilon^3)$ equation leads to the two results

$$4q_c^2 A_1'' = -3b_3 A_1 |A_1|^2, \quad C_3 = \frac{b_3}{64q_c^4} A_1^3, \quad (19)$$

with A_3 arbitrary. The Ansatz

$$u_4(x, X) = A_4(X)e^{iq_c x} + C_4(X)e^{3iq_c x} + c.c. \quad (20)$$

in the $\mathcal{O}(\epsilon^4)$ equation likewise leads to

$$4q_c^2 A_2'' = 4iq_c A_1''' - 3b_3 (2|A_1|^2 A_2 + A_1^2 \bar{A}_2); \quad (21)$$

the expression for C_4 in terms of $A_{1,2}$ is not needed in what follows. Finally, the $\mathcal{O}(\epsilon^5)$ equation with the Ansatz

$$u_5(x, X) = A_5(X)e^{iq_c x} + C_5(X)e^{3iq_c x} + E_5(X)e^{5iq_c x} + c.c. \quad (22)$$

yields

$$\begin{aligned} 4q_c^2 A_3'' &= 4iq_c A_2''' + A_1'''' - 3b_3 (2A_1 |A_2|^2 + \bar{A}_1 A_2^2 + 2|A_1|^2 A_3 + A_1^2 \bar{A}_3) \\ &\quad + \left(-\frac{3b_3^2}{64q_c^4} + 10b_5 \right) A_1 |A_1|^4 \end{aligned} \quad (23)$$

after elimination of C_3 . Equations (19), (21) and (23) can now be assembled into a single equation for $Z(X, \epsilon) \equiv A_1(X) + \epsilon A_2(X) + \epsilon^2 A_3(X) + \dots$,

$$4q_c^2 Z'' = -3b_3 Z |Z|^2 + 4iq_c \epsilon Z''' + \epsilon^2 \left[Z'''' + \left(-\frac{3b_3^2}{64q_c^2} + 10b_5 \right) Z |Z|^4 \right] + \mathcal{O}(\epsilon^3). \quad (24)$$

The higher derivatives can be eliminated iteratively, resulting in the amplitude equation

$$\begin{aligned}
4 q_c^2 Z'' &= -3 b_3 Z |Z|^2 - \frac{3 i \epsilon b_3}{q_c} (2 Z' |Z|^2 + Z^2 \bar{Z}') + \epsilon^2 \left[\frac{9 b_3}{2 q_c^2} (2 Z |Z'|^2 + (Z')^2 \bar{Z}) \right. \\
&\quad \left. + \left(-\frac{327 b_3^2}{64 q_c^4} + 10 b_5 \right) Z |Z|^4 \right] + \mathcal{O}(\epsilon^3).
\end{aligned} \tag{25}$$

Equation (25) represents the Ginzburg-Landau approximation to the Swift-Hohenberg equation (8) at $r = 0$ [5].

4 Normal form theory

The linear problem at $r = 0$ is degenerate because the purely imaginary eigenvalues $\lambda = \pm i q_c$ have *double multiplicity*. The presence of this degeneracy is a consequence of the spatial reversibility of the equation and this fact allows us to make use of normal form theory developed for a Hopf bifurcation in systems that are reversible in time. For this reason the bifurcation at $r = 0$ is often referred to as the reversible Hopf bifurcation with 1 : 1 resonance or sometimes as the Hamiltonian-Hopf bifurcation.¹ The normal form for this bifurcation is derived and analyzed in [9], and is given by

$$\dot{A} = i q_c A + B + i A P(\mu; y, w), \tag{26}$$

$$\dot{B} = i q_c B + i B P(\mu; y, w) + A Q(\mu; y, w), \tag{27}$$

where $y \equiv |A|^2$, $w \equiv \frac{i}{2}(A \bar{B} - \bar{A} B)$. Here μ is the bifurcation parameter and P and Q are (infinite) polynomials with real coefficients:

$$P(\mu; y, w) = p_1 \mu + p_2 y + p_3 w + p_4 y^2 + p_5 w y + p_6 w^2 + \dots, \tag{28}$$

$$Q(\mu; y, w) = -q_1 \mu + q_2 y + q_3 w + q_4 y^2 + q_5 w y + q_6 w^2 + \dots \tag{29}$$

Although these equations look quite different from the equation obtained through multiple scale analysis the two calculations are in fact one and the same. To see this we set $\mu = 0$ and write $(A, B) = (\epsilon \tilde{A}(X), \epsilon^2 \tilde{B}(X)) e^{i q_c x}$, obtaining

$$\epsilon^2 A' = \epsilon^2 B + i \epsilon A \left[\epsilon^2 p_2 |A|^2 + \epsilon^3 p_3 \frac{i}{2} (A \bar{B} - \bar{A} B) \right] + \mathcal{O}(\epsilon^5), \tag{30}$$

$$\begin{aligned}
\epsilon^3 B' &= i \epsilon^2 B \left[\epsilon^2 p_2 |A|^2 + \epsilon^3 p_3 \frac{i}{2} (A \bar{B} - \bar{A} B) \right] \\
&\quad + \epsilon A \left[\epsilon^2 q_2 |A|^2 + \epsilon^3 q_3 \frac{i}{2} (A \bar{B} - \bar{A} B) + \epsilon^4 q_4 |A|^4 \right] + \mathcal{O}(\epsilon^6).
\end{aligned} \tag{31}$$

Equation (30) now yields a power series expansion for B in terms of A ,

$$B = A' - i \epsilon p_2 A |A|^2 + \epsilon^2 \frac{p_3}{2} A (A \bar{A}' - \bar{A} A') + \mathcal{O}(\epsilon^3), \tag{32}$$

¹Hamiltonian systems are reversible in time; eq. (8) is in fact a Hamiltonian system in space [11]

and this equation can be used to eliminate B from Eq. (31):

$$\begin{aligned} A'' = & q_2 A |A|^2 + i\epsilon \left[\left(3p_2 - \frac{1}{2} q_3 \right) A' |A|^2 + \left(p_2 + \frac{1}{2} q_3 \right) A^2 \bar{A}' \right] \\ & + \epsilon^2 \left[p_3 ((A')^2 \bar{A} - A A' \bar{A}') + (q_4 - q_3 p_2 + p_2^2) A |A|^4 \right] + \mathcal{O}(\epsilon^3). \end{aligned} \quad (33)$$

Finally, writing $Z = A + \epsilon^2 \rho A |A|^2 + \mathcal{O}(\epsilon^4)$ allows one to compare the result with Eq. (25) and thereby deduce the normal coefficients:

$$\rho = \frac{9b_3}{16q_c^4}, \quad p_2 = -\frac{9b_3}{16q_c^3}, \quad q_2 = -\frac{3b_3}{4q_c^2}, \quad p_3 = 0, \quad q_3 = -\frac{3b_3}{8q_c^3}, \quad q_4 = -\frac{177b_3^2}{128q_c^6} + \frac{5b_5}{2q_c^2}. \quad (34)$$

The remaining coefficients p_1 and q_1 are determined as part of the *unfolding*. This term is used to refer to the reintroduction of the bifurcation parameter into the description. As indicated earlier, we write $r = \epsilon^2 \mu < 0$, where $\mu = \mathcal{O}(1)$, and compute the resulting linear terms. The unfolded version of (33) through $\mathcal{O}(\epsilon)$ is

$$\begin{aligned} A'' = & -q_1 \mu A + q_2 A |A|^2 + i\epsilon \left[2p_1 \mu A' + \left(3p_2 - \frac{1}{2} q_3 \right) A' |A|^2 \right. \\ & \left. + \left(p_2 + \frac{1}{2} q_3 \right) A^2 \bar{A}' \right] + \mathcal{O}(\epsilon^2) \end{aligned} \quad (35)$$

and since $Z = A + \mathcal{O}(|A|^2 A)$ this equation corresponds to the amplitude equation [5]

$$4q_c^2 Z'' = -\mu Z - 3b_3 Z |Z|^2 + \frac{i\epsilon}{q_c} [-\mu Z' - 3b_3 (2Z' |Z|^2 + Z^2 \bar{Z}')] + \mathcal{O}(\epsilon^2). \quad (36)$$

Matching terms through linear order gives

$$p_1 = -\frac{1}{8q_c^3}, \quad q_1 = \frac{1}{4q_c^2}. \quad (37)$$

5 Homoclinics and heteroclinics

The normal form (26)–(27) is completely integrable [9], with integrals

$$K \equiv \frac{1}{2} (A \bar{B} - \bar{A} B), \quad H \equiv |B|^2 - \int_0^{|A|^2} Q(\mu, s, K) ds. \quad (38)$$

Note that orbits homoclinic to $(0, 0)$ lie in the surface $H = K = 0$. In this case the equation for $a \equiv |A|^2 > 0$ takes the particle-in-potential form

$$\frac{1}{2} \left(\frac{da}{dX} \right)^2 + V(a) = 0, \quad (39)$$

where

$$V(a) \equiv 2q_1 \mu a^2 - q_2 a^3 - \frac{2}{3} q_4 a^4. \quad (40)$$

The shape of the (truncated) potential $V(a)$ depends on the coefficients q_1 , q_2 and q_4 determined in the previous section. The essential role played by the coefficient q_4 is now evident.

The behavior of solutions of (39)–(40) when $q_4 < 0$ is shown in Fig. 2. The insets show the effective potential $V(a)$ associated with each region in the (μ, q_2) parameter plane. Shading indicates the existence of homoclinic orbits to $a = 0$; elsewhere, $a = 0$ is a local minimum of the potential and no homoclinic orbits are possible. We see that homoclinic orbits exist in the whole half-space $\mu < 0$, i.e., in the subcritical region. The transition from region (d) to region (c) involves a local bifurcation at $\mu = 0$ which creates a small amplitude homoclinic orbit. The transition from region (a) to region (b) involves a global bifurcation at $\mu = 0$ which creates a large amplitude homoclinic orbit at $\mu = 0$; the turning point of the orbit occurs at $a_0 = -3q_2/(2q_4) > 0$.

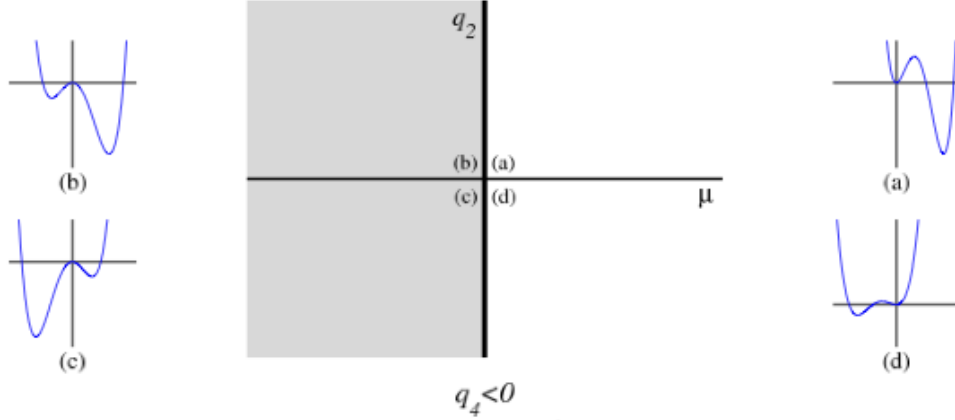


Figure 2: Summary of the behavior of Eqs. (26)–(27) when $q_4 < 0$. Shading indicates the existence of homoclinic orbits to the fixed point at the origin. Insets show $V(a)$ characteristic of the four regions (a)–(d). At $\mu = 0$, there is a local (global) bifurcation in $q_2 < 0$ ($q_2 > 0$). From [9].

The behavior of solutions of Eqs. (39)–(40) when $q_4 > 0$ is summarized in Fig. 3. In this case, homoclinic orbits to $a = 0$ only occur in region (d). In regions (a) and (e), a local minimum of the potential is located at $a = 0$ so a particle that starts at this point remains at rest. In regions (b) and (c), the trajectory of a particle that starts at $a = 0$ is unbounded. The boundary between regions (c) and (d), marked in the figure with a dot-dashed line, is given by

$$\mu^* = -\frac{3q_2^2}{16q_1q_4} \quad (41)$$

and corresponds to the presence of a *heteroclinic cycle* between the origin and the point $a = -3q_2/q_4 > 0$ corresponding to a periodic solution $Z(X)$.

Note that the leading order amplitude equation

$$4q_c^2 Z'' = -\mu Z + 4q_c^2 q_2 Z|Z|^2 + \mathcal{O}(\epsilon) \quad (42)$$

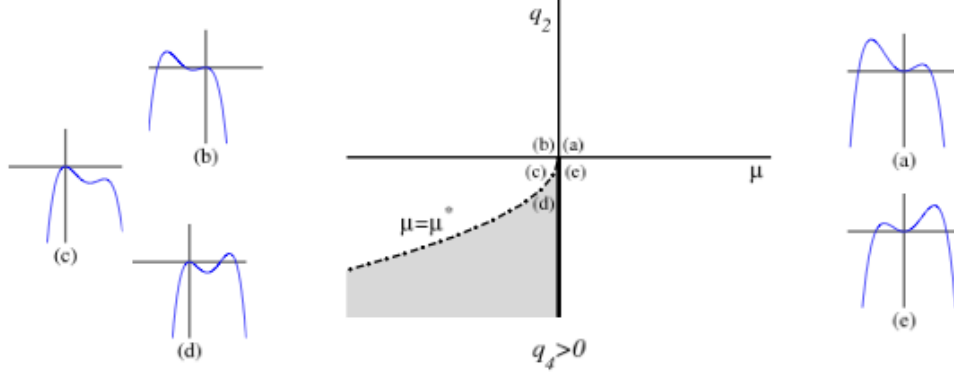


Figure 3: Summary of the behavior of Eqs. (26)–(27) when $q_4 > 0$. Shading indicates the existence of homoclinic orbits to the fixed point at the origin. Insets show $V(a)$ characteristic of the five regions (a)–(e). A heteroclinic cycle is present along the dot-dashed line $\mu = \mu^*$. From [9].

has two types of solutions when $q_2 < 0$, $\mu < 0$. One is constant:

$$Z(X) = \left(\frac{\mu}{4 q_c^2 q_2} \right)^{1/2} e^{i\phi} + \mathcal{O}(\epsilon) \quad (43)$$

and corresponds to

$$u(x) = \left(\frac{r}{4 q_c^2 q_2} \right)^{1/2} \cos(q_c x + \phi) + \mathcal{O}(r), \quad (44)$$

while the other is spatially localized:

$$Z(X) = \left(\frac{\mu}{2 q_c^2 q_2} \right)^{1/2} \operatorname{sech} \left(\frac{X \sqrt{-\mu}}{2 q_c} \right) e^{i\phi} + \mathcal{O}(\epsilon) \quad (45)$$

and corresponds to

$$u(x) = 2 \left(\frac{r}{2 q_c^2 q_2} \right)^{1/2} \operatorname{sech} \left(\frac{x \sqrt{-r}}{2 q_c} \right) \cos(q_c x + \phi) + \mathcal{O}(r). \quad (46)$$

For the periodic states the spatial phase ϕ is arbitrary; this is not so for the localized states for which the spatial phase ϕ is locked to $0, \pi/2, \pi, 3\pi/2$ when terms beyond all orders are kept. Thus in SH35 four branches of localized states bifurcate from $u = 0$ at $r = 0$. Of these the branches with $\phi = 0, \pi$ correspond to solutions that are reflection-symmetric while those with $\phi = \pi/2, 3\pi/2$ are odd under reflection. The $\phi = 0, \pi$ states are related to one another by the symmetry $u \rightarrow -u$ as are the $\phi = \pi/2, 3\pi/2$ states. Thus in a bifurcation diagram that represents the solution amplitude as a function of r one finds two branches, one of even states and the other of odd states. The above calculation shows, in addition, that such localized states are only present when the periodic state bifurcates subcritically and hence are present in the region of coexistence between the periodic state and the trivial state $u = 0$, cf. lecture 6. Analogous results, not discussed here, show that in the case of

SH23 two branches of localized states bifurcate from $u = 0$ at $r = 0$. Both correspond to even states and are characterized by $\phi = 0, \pi$. In this case the $\phi = 0, \pi$ states are no longer related by symmetry and the bifurcation diagram therefore also consists of two distinct branches.

The selection of the spatial phase ϕ is a highly subtle point [7, 8, 10]; however, one can get a good appreciation of the issues involved by substituting the approximate solution (46) into Eq. (1). Note in particular that states of the form (46) have no particular symmetry unless ϕ takes one of the special values just mentioned. Such asymmetric states are in fact present but are only created in *secondary* bifurcations from the primary branches of localized states that bifurcate from $u = 0$. Figure 4 shows schematically the number and connectivity of the resulting localized states in the SH23 and SH35 cases: in the SH35 case four asymmetric branches are created at finite amplitude and connect each of the two even branches with each of the two odd branches (see Sect. 7 below).

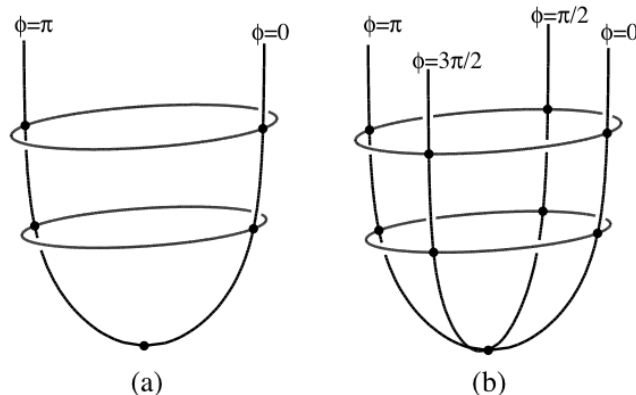


Figure 4: Schematic diagram showing the number and connectivity of the branches of localized states for (a) SH23 and (b) SH35. In (a) each rung consists of two distinct branches connecting the two constant phase branches; in (b) each rung consists of four distinct branches connecting each constant phase branch with its two neighbors. From [3].

6 Example: Natural doubly diffusive convection

Natural convection is a term given to convection driven by horizontal temperature convection. When the fluid is a mixture of two components (eg., water and salt) and the gradients of both temperature and (salt) concentration are horizontal we speak of natural doubly diffusive convection.

Motivated by the results in Sect 2.5.1 of lecture 6, we examine an infinite vertical slot filled with such a mixture. We adopt no-slip boundary conditions on the vertical plates and suppose that these are maintained at fixed but different temperatures and concentrations. These can be arranged such that the buoyancy force due to the temperature field is exactly balanced by the buoyancy force arising from the concentration field. In this case the system possesses a conduction state characterized by linear variation of temperature and

concentration across the system and no flow. This state will be stable for small temperature differences but is expected to lose stability as this temperature difference, traditionally measured by the dimensionless Grashof number $Gr \equiv g\alpha\Delta T\ell^3/\nu^2$, increases. Here α is the coefficient of thermal expansion, ΔT is the imposed temperature difference, and ℓ is the separation between the two plates, assumed to be placed at $x = 0, \ell$.

Linear analysis about the conduction state with respect to two-dimensional spatially growing perturbations looks for solutions of the time-independent linearized equations of the form $(\tilde{u}, \tilde{w}, \tilde{T}, \tilde{C})(x) \exp(\lambda z)$, where $\lambda \equiv q_r + i q_i$ is the spatial growth rate. This formulation leads to the dimensionless equations [2]:

$$\lambda \tilde{u} = -\partial_x \tilde{p} + \nabla^2 \tilde{u} \quad (47)$$

$$\lambda \tilde{w} = -\partial_z \tilde{p} + \nabla^2 \tilde{w} + Gr (\tilde{T} - \tilde{C}) \quad (48)$$

$$0 = \partial_x \tilde{u} + \partial_z \tilde{w} \quad (49)$$

$$\lambda \tilde{T} = \tilde{u} + \frac{1}{Pr} \nabla^2 \tilde{T} \quad (50)$$

$$\lambda \tilde{C} = \tilde{u} + \frac{1}{Sc} \nabla^2 \tilde{C} \quad (51)$$

with the boundary conditions $\tilde{u} = \tilde{w} = \tilde{T} = \tilde{C} = 0$ at $x = 0, 1$. Here $Pr \equiv \nu/\kappa$ is the Prandtl number and $Sc \equiv \nu/D$ is the Schmidt number. In contrast to the Swift-Hohenberg equation, this problem is an eigenvalue problem for λ that has to be solved for each value of Gr and fixed values of the remaining parameters. Such a problem has in general an infinite number of eigenvalues, but we are interested here only in the leading eigenvalues, i.e., the eigenvalues whose real parts are closest to zero.

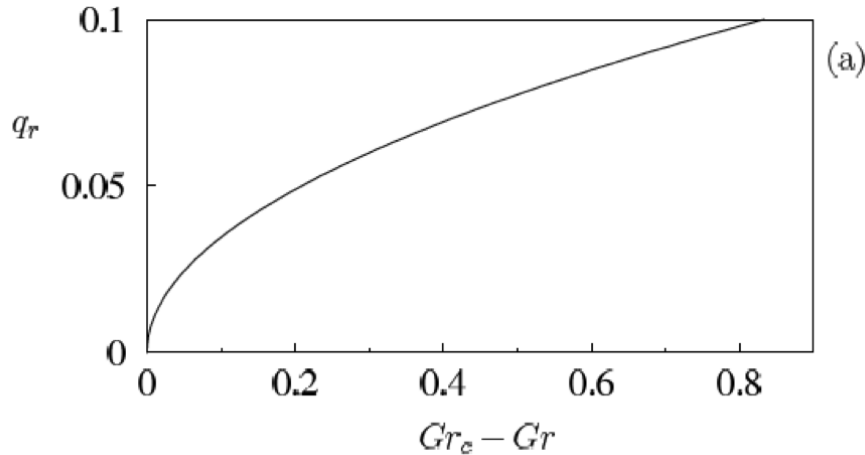


Figure 5: The spatial growth rate q_r as a function of the distance from the critical Grashof number Gr_c in the subcritical regime $Gr < Gr_c$. From [2].

Solution of this problem indicates that the four leading eigenvalues form a pair of purely imaginary eigenvalues $q_r = 0$, $q_i \equiv q_c = \pm 2.5318$ of double multiplicity when $Gr_c = 650.9034$. Thus at this value of Gr the solution takes the form of a spatially periodic wavetrain. Moreover, one also finds that (Fig. 5)

- $Gr < Gr_c$: $\lambda = \pm i q_c \pm O(\sqrt{Gr_c - Gr})$
- $Gr > Gr_c$: $\lambda = \pm i q_c \pm i O(\sqrt{Gr - Gr_c})$,

implying that the leading spatial eigenvalues behave exactly as in the Swift-Hohenberg equation. This is a consequence of the reversibility of the equations with respect to the symmetry Δ : $(x, z) \rightarrow (1 - x, -z)$, $(\tilde{u}, \tilde{w}, \tilde{T}, \tilde{C}) \rightarrow -(\tilde{u}, \tilde{w}, \tilde{T}, \tilde{C})$ which plays exactly the same role as the symmetry $x \rightarrow -x$, $u \rightarrow u$ in SH23. Thus in this case we expect *two* branches of localized states of even parity (with respect to Δ), corresponding to $\phi = 0, \pi$. Theory predicts that these branches will only be present if the coefficient q_2 in the normal form (26)–(29) is negative. This will be so if the branch of periodic states with wavenumber q_c bifurcates *subcritically*. The theory also predicts that if this is the case the branches of localized states also bifurcate subcritically. Thus the prediction of localized states in the present system reduces to the computation of the direction of branching of periodic states. This is a standard calculation that can be done in a periodic domain of period $2\pi/q_c$, i.e., in a small domain, although it may have to be done numerically. For $Pr = 1$, $Sc = 11$ this bifurcation is indeed subcritical [2]; moreover, two branches of even parity localized states are present and these also bifurcate subcritically, exactly as predicted by SH23 [4].

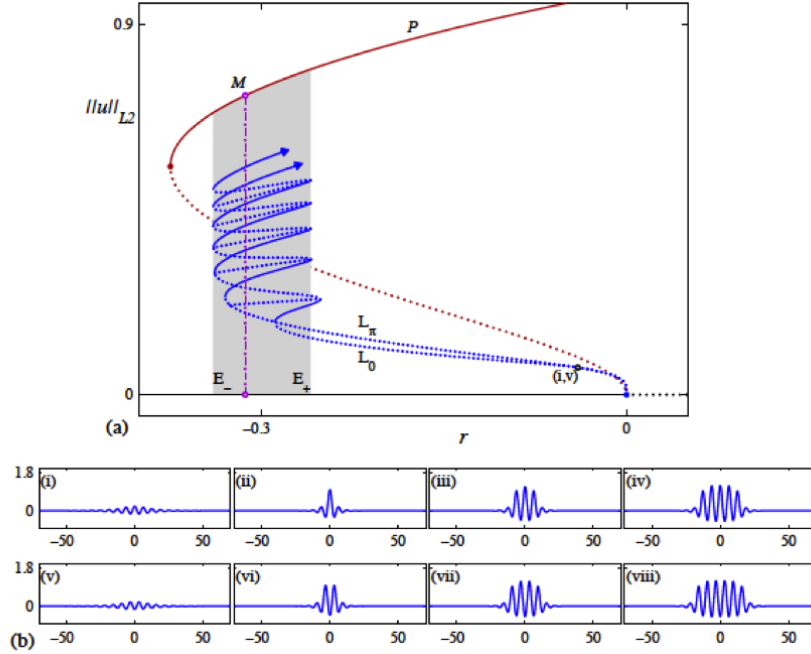


Figure 6: (a) Bifurcation diagram showing the snakes-and-ladders structure of localized states. Away from the origin the snaking branches L_0 and L_π are contained within a snaking region (shaded) between E_- and E_+ , where $r(E_-) \approx -0.3390$ and $r(E_+) \approx -0.2593$. Solid (dotted) lines indicate stable (unstable) states. (b) Sample localized profiles $u(x)$: (i)–(iv) lie on L_0 , near onset and at the 1st, 3rd, and 5th saddle-nodes from the bottom, respectively; (v)–(viii) lie on L_π , near onset and at the 1st, 3rd, and 5th saddle-nodes, respectively. Parameters: $b_2 = 1.8$. From [4].

7 Snakes-and-ladders structure of the pinning region: SH23

In this section we describe what happens when the small amplitude results are extended into the fully nonlinear regime using numerical continuation. We describe the results for SH23,

$$u_t = r u - (q_c^2 + \partial_x^2)^2 u + b_2 u^2 - u^3. \quad (52)$$

Figure 6 shows the L_2 norm, $\|u\| \equiv \int_{-\infty}^{\infty} u^2(x) dx$, of the localized states $L_{0,\pi}$ as a function of the bifurcation parameter r . The L_2 norm (per unit length) of the periodic state, labeled P , is shown for comparison. The figure shows that the two branches of even parity localized states that bifurcate subcritically from $u = 0$ at $r = 0$ enter a shaded region, hereafter the *snaking* or *pinning* region, in which they undergo repeated saddle-node bifurcations as they snake across the region. These saddle-nodes converge exponentially rapidly to a pair of r -values, hereafter $r(E_-)$ and $r(E_+)$, representing the boundaries of the shaded region. The convergence is monotonic and from the right in both cases. The lower panels show a series of profiles of $u(x)$ at successive saddle-nodes and reveal that the states labeled L_0 are characterized by a peak in the center while those labeled L_π have a dip in the center. The panels show that each localized state nucleates a pair of peaks or cells, one on either side, in the vicinity of $r = r(E_-)$. As one proceeds up the branch to the next fold on the right, at $r = r(E_+)$, the peaks or cells grow to the height of the coexisting periodic state P and the branch turns around to repeat the process. Thus as one proceeds up the intertwined $L_{0,\pi}$ branches the localized states repeatedly add cells on either side while preserving their parity, each back-and-forth oscillation increasing the width of the state by two wavelengths $2\pi/q_c$. On the real line this process continues indefinitely as both branches approach the periodic state P .

Figure 7(a) is a close-up view of Fig. 6, focusing on the rung states which connect the $L_{0,\pi}$ snaking branches. These states are asymmetric with respect to the reflection $x \rightarrow -x$ (Fig. 7(b)). In generic translation-invariant systems such states would drift. This is not so here because of the gradient structure of Eq. (52) and the rung states correspond to stationary states. The rungs are created in pitchfork bifurcations which break the $u(x) \rightarrow u(-x)$ symmetry of the $L_{0,\pi}$ states. Consequently each rung in the figure corresponds to two states related by reflection symmetry and hence of identical L_2 norm.

The location of these pitchfork bifurcations is determined by linearizing Eq. (52) about a localized solution $u = u_0(x)$ and solving the eigenvalue problem

$$\mathcal{L}[u_0(x)] \tilde{U} \equiv \{r - (q_c^2 + d_x^2)^2 + 2b_2 u_0 - 3u_0^2\} \tilde{U} = \sigma \tilde{U} \quad (53)$$

for the eigenvalues σ and for the corresponding eigenfunctions \tilde{U} . This problem has to be solved numerically; if the domain used is much larger than the length of the localized structure the resulting eigenvalues will be independent of the boundary conditions imposed at the boundary. The eigenvalues comprise the spectrum of the linear operator $\mathcal{L}[u_0(x)]$ and this spectrum consists of two components depending on the symmetry of the eigenfunctions. Even eigenfunctions share the symmetry of $u_0(x)$ and correspond to *amplitude* modes. These modes are neutrally stable ($\sigma = 0$) at saddle-node bifurcations. Odd eigenfunctions will be called phase modes. There is always one neutrally stable phase mode, the Goldstone mode. To see this we consider two stationary solutions of Eq. (52), $u_0(x+d)$ and $u_0(x)$, i.e., a pair

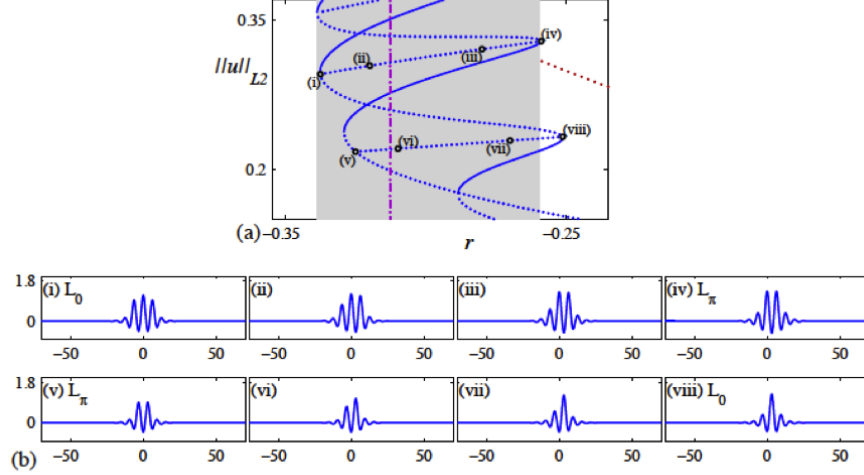


Figure 7: (a) Close-up view of Fig. 6(a) showing two rungs connecting the snaking branches L_0 and L_π . Solid (dotted) lines indicate stable (unstable) states. (b) The profiles (i) and (viii) lie on L_0 while (iv) and (v) lie on L_π . The remaining profiles are asymmetric and lie on the rungs. From [4].

of solutions related by translation. We subtract the equations satisfied by these solutions, divide by d and take the limit $d \rightarrow 0$. The result is

$$\mathcal{L}[u_0(x)] u'_0 = 0, \quad (54)$$

implying that u'_0 is a neutrally stable eigenfunction of $\mathcal{L}[u_0(x)]$ for all parameter values. Evidently the presence of this mode is a consequence of the translation invariance of the system. In addition, there is a discrete set of neutrally stable phase modes associated with symmetry-breaking bifurcations of $u_0(x)$, i.e., the creation of the rung states. Figure 8(b) shows each of these eigenfunctions, computed as described above, for a relatively long localized state high up the snakes-and-ladders structure. We make two important observations: the amplitude and phase modes are localized in the vicinity of the fronts bounding $u_0(x)$; by adding and subtracting these modes we construct eigenfunctions localized at one or other front. This observation implies that both the saddle-nodes and the pitchfork bifurcations are associated with instabilities of individual fronts. This picture becomes better and better as the length of $u_0(x)$ becomes longer, i.e., for long localized structures the fronts at either end can be treated independently, and in this regime the localized structure $u_0(x)$ can be considered to be a bound state of a pair of fronts.

Figure 9 shows the eigenvalues σ along the $L_{0,\pi}$ snaking branches starting from the primary bifurcation at $r = 0$ and moving upward along each branch. The phase and amplitude modes are labeled. We see that close to $r = 0$ both states are amplitude-unstable, as expected of a subcritical bifurcation. In contrast, the phase eigenvalues are almost zero, with L_0 phase-stable and L_π phase-unstable. Each zero of the amplitude eigenvalue generates a saddle-node bifurcation and since σ oscillates about zero each solution

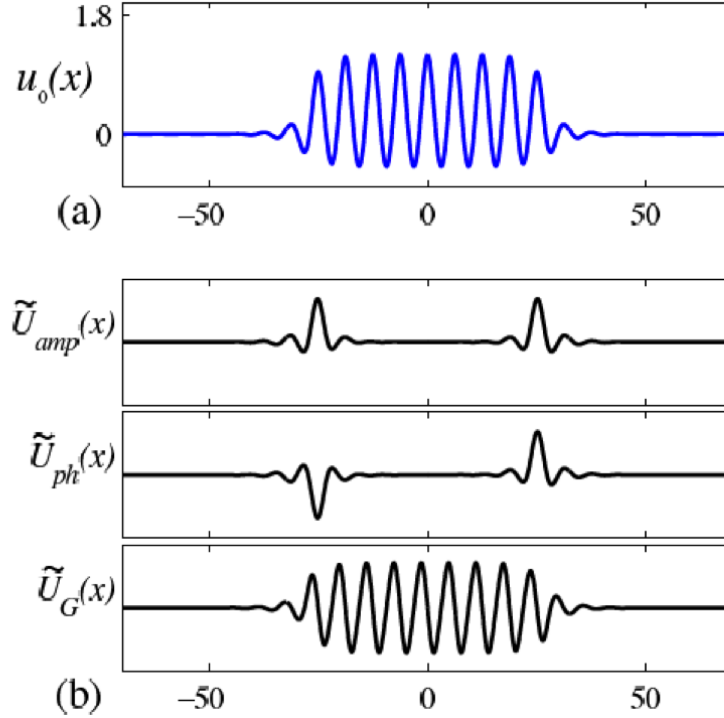


Figure 8: (a) A localized state $u_0(x)$ at E_- high up the L_0 snaking branch. (b) From top to bottom, the corresponding amplitude, phase, and translational modes. Parameters: $b_2 = 1.8$, $r = -0.3390$. From [4].

gains and loses amplitude stability at successive saddle-nodes. The phase eigenvalue also oscillates about zero and tracks ever more closely the amplitude eigenvalue. Thus as one proceeds up the snaking structure the bifurcations to the rung states approach ever closer to the saddle-nodes (in fact exponentially rapidly), although they always remain on the unstable part of the branch. Thus near a saddle-node of a long localized structures one finds three near-marginal modes, the amplitude and phase modes, as well as the Goldstone mode. This fact will be useful in interpreting the dynamical behavior one finds just outside of the snaking region as discussed in lecture 8.

The above results account for the stability changes indicated in Figs. 6 and 7; no other eigenvalues are ever involved. A similar calculation shows that the asymmetric rung states are always unstable. Altogether, the results show that in the snaking region one finds an *infinite* number of coexisting stable symmetric localized structures of different lengths. These come in two types, with maxima or minima in their symmetry plane. Each state can be realized in the time-dependent problem by selecting an appropriate finite amplitude (localized) initial condition. The results for SH35 are essentially identical.

7.1 Multipulse states

In fact things are much more complicated. This is because the snaking region also contains a variety of multipulse states [6]. The term multipulse refers to the fact that the phase space

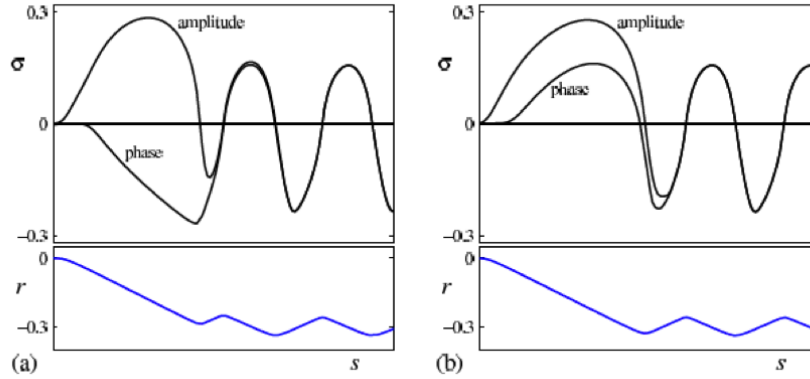


Figure 9: Spectrum of growth rates σ along the (a) L_0 and (b) L_π branches of localized states in SH23 as a function of the arc length s along each branch, measured from the bifurcation at the origin. The lower panels show the location in r of the corresponding branches. Parameters: $b_2 = 1.8$. From [4].

trajectory comes close to the origin after the first localized state (pulse) but only forms a homoclinic orbit to the origin after a second (two-pulse) or more (multipulse) excursions. Multipulse states should be thought of as (weakly) bound states of two or more localized structures of the type we have been discussing.

Multipulse states can be equispaced forming a periodic array of identical localized structures. Such states are not very different from the single pulse states and it will come as no surprise that they also snake (Fig. 10). But one can also find two-pulse states consisting of identical pulses that are separated by a distance that is less than the average interpulse spacing. The locations of such pulses are ‘quantized’ in terms of half wavelengths π/q_c . Specifically, two identical L_0 pulses can have a local maximum or a local minimum at the half way location between them [6]. On a periodic domain of a large but finite period there is thus a finite number of such these states. These do not snake but instead lie on nested isolas. The nested isolas in turn form a vertical stack of like states, each stack consisting of bound states of localized states of ever increasing length (Fig. 11). The break-up of the two-pulse states into isolas as soon as they are not evenly spaced is a consequence of asymmetry in the interaction between the pulses.

In addition, one can also find two-pulse states consisting of different localized states [6]. Thus the snaking region consists of an unimaginable variety of different localized structures a large fraction of which can be stable.

7.2 Finite size effects

Figure 10(a) reveals two additional insights. The figure is computed on a periodic domain of length Γ with periodic boundary conditions. We see that for $\Gamma < \infty$ the multiple bifurcation at $r = 0$ breaks up into a primary bifurcation to a periodic wavetrain, together with a secondary bifurcation from this state to the (two) branches of localized states that takes

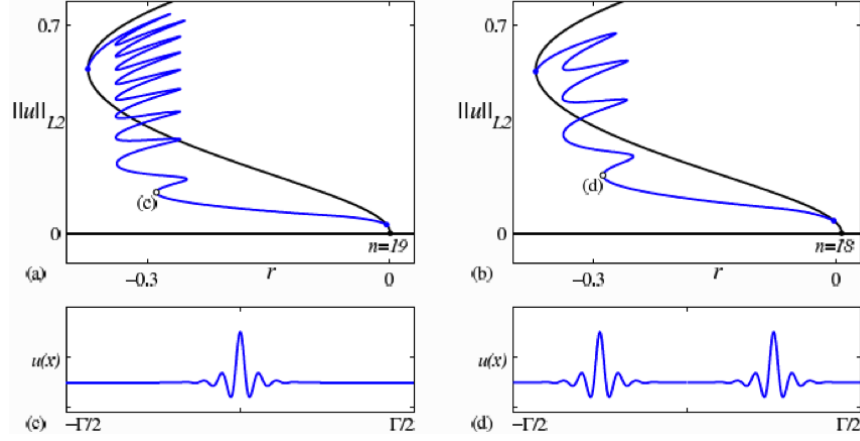


Figure 10: Bifurcation diagrams showing (a) a L_0 single-pulse snaking branch, and (b) a two-pulse snaking branch consisting of two evenly spaced copies of L_0 , both on the same periodic domain of period Γ . (c,d) Sample profiles at the points indicated in the bifurcation diagrams; the states in (d) are separated by $\Gamma/2$. Similar branches consisting of L_π pulses are omitted. Parameters: $b_2 = 1.8$, $\Gamma = 118$. From [6].

place at small but nonzero amplitude. This is almost certainly the reason why spatially localized states have been discovered only recently: almost all textbooks on hydrodynamic instability immediately impose periodic boundary conditions when studying the instability of a homogeneous base state. This innocuous assumption pushes the bifurcation to localized states to finite amplitude where its discovery requires not only knowledge of the finite amplitude periodic state but also a linear stability analysis of a nontrivial periodic state requiring Floquet theory. As we have seen the problem becomes so much easier if posed on the whole real line!

Figure 10(a) also reveals that on a finite periodic domain snaking does not continue for ever. Once the localized structure has grown to fill the domain no additional growth is possible and the branch of localized states exits the snaking region and terminates near the fold on the branch of periodic states. The details of this transition are in general complex since they depend on exactly how much space is left, i.e., on $\Gamma \bmod \lambda_c$, where λ_c is the critical wavelength [1]. Observe, however, that near the fold the localized states resemble holes in an otherwise periodic wavetrain. We shall come across hole states in subsequent lectures. For now the lesson learnt is that holes are related to secondary bifurcations near the fold of the periodic state.

Note, finally, that Fig. 10(b) shows that on a smaller domain, here $\Gamma/2$, a single pulse state bifurcates from the periodic states at a larger amplitude, and that the resulting branch also terminates further from the fold.

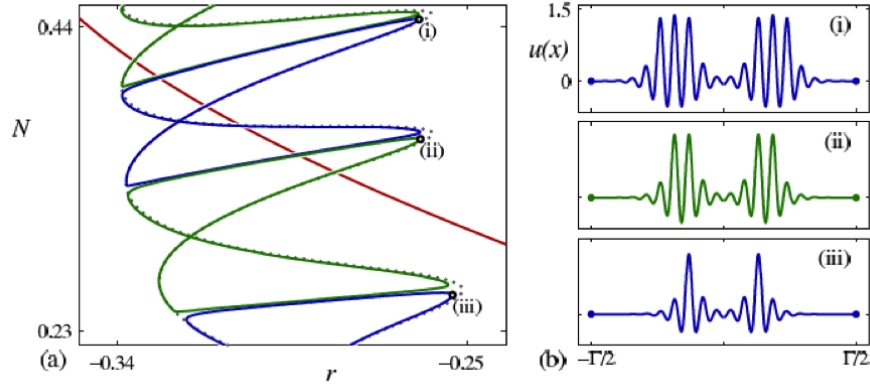


Figure 11: (a) Bifurcation diagram showing isolas of symmetric but unevenly spaced two-pulse states. In the main diagram, only one isola at each level of the isola stack is plotted to avoid clutter. (b) Profiles at the points labeled in the bifurcation diagram; the states are separated by distances less than $\Gamma/2$. Parameters: $b_2 = 1.8$, $\Gamma = 118$. From [6].

References

- [1] A. Bergeon, J. Burke, E. Knobloch and I. Mercader. Eckhaus instability and homoclinic snaking. *Phys. Rev. E* **78**, 046201, 2008.
- [2] A. Bergeon and E. Knobloch. Spatially localized states in natural doubly diffusive convection. *Phys. Fluids* **20**, 034102, 2008.
- [3] J. R. Burke. Localized States in Driven Dissipative Systems, PhD Thesis, University of California at Berkeley, 2008.
- [4] J. Burke and E. Knobloch. Localized states in the generalized Swift-Hohenberg equation. *Phys. Rev. E* **73**, 056211, 2006.
- [5] J. Burke and E. Knobloch. Homoclinic snaking: Structure and stability. *Chaos* **17**, 037102, 2007.
- [6] J. Burke and E. Knobloch. Multipulse states in the Swift-Hohenberg equation. *Discrete and Continuous Dyn. Syst. Suppl.*, pp. 109–117, 2009.
- [7] S. J. Chapman and G. Kozyreff. Exponential asymptotics of localized patterns and snaking bifurcation diagrams. *Physica D* **238**, pp. 319–354, 2009.
- [8] A. D. Dean, P. C. Matthews, S. M. Cox and J. R. King. Exponential asymptotics of homoclinic snaking. *Nonlinearity* **24**, pp. 3323–3352, 2011.
- [9] G. Iooss and M. C. Pérouème. Perturbed homoclinic solutions in reversible 1:1 resonance vector fields. *J. Diff. Eq.* **102**, pp. 62–88, 1993.
- [10] G. Kozyreff and S. J. Chapman. Asymptotics of large bound states of localized structures. *Phys. Rev. Lett.* **97**, 044502, 2006.

- [11] L. Yu. Glebsky and L. M. Lerman. On small stationary localized solutions for the generalized 1-D Swift–Hohenberg equation. *Chaos* **5**, pp. 424–431, 1995.

Lecture 8: Pinning and depinning in one and two dimensions

Edgar Knobloch: notes by Rosalind Oglethorpe and Felicity Graham
with substantial editing by Edgar Knobloch

January 10, 2013

1 Pinning region (SH23)

Recall that the Swift-Hohenberg (SH) equation has multiple steady states in a ‘snakes-and-ladders’ structure, which is contained in a region of r called the snaking or pinning region. The width of this region can be understood on the basis of a geometrical picture of phase space behavior and a physical (“intuitive”) picture in terms of front pinning. The pictures are complementary as well as useful.

1.1 Mathematical explanation of the pinning region

The time-independent SH equation is of fourth order in space,

$$u_{xxxx} + 2q_c^2 u_{xx} + (q_c^4 - r)u = f(u) \quad (1)$$

so the phase space is four-dimensional. This equation conserves the spatial Hamiltonian

$$H = -\frac{1}{2} (r - q_c^4) u^2 + q_c^2 u_x^2 - \frac{1}{2} u_{xx}^2 + u_x u_{xxx} - \int_0^u f(v) dv, \quad (2)$$

i.e., $dH/dx = 0$. Since the homogeneous state $u_{xxx} = u_{xx} = u_x = u = 0$ corresponds to $H = 0$ any homoclinic orbit connecting this state, hereafter O , to itself must lie in the level set $H = 0$, i.e., in a three-dimensional surface in four dimensions. As explained in lecture 6 to find such homoclinics it is advantageous to look for a heteroclinic cycle between O and a periodic orbit γ that also lies in $H = 0$. Near this cycle we expect to find orbits homoclinic to O that start from O and wind a finite number of times around γ before returning to O .

Because of translation invariance periodic orbits of Eq. (1) are not isolated – for each H there is a continuous family of such orbits. In the following we pick $H = 0$ and select one representative from this family, for example by assigning the origin $x = 0$ to the maximum value of u along the orbit. We call the resulting orbit γ . A point on this orbit with phase ϕ relative to $x = 0$, $\gamma(\phi)$, will be a fixed point of a “time- T ” map, where T is the (spatial) period of the orbit, and we may pick ϕ to correspond to a point of symmetry on γ , for example $\phi = 0$ [15]. Note that T depends in general on H . By construction the “time- T ” map is two-dimensional and has two fixed points, O and $\gamma(\phi)$. The result of repeated application of the “time- T ” map can therefore be represented in a plane, as shown in fig. 1. The figure shows the two fixed points as solid black points; these lie on a green line representing solutions with

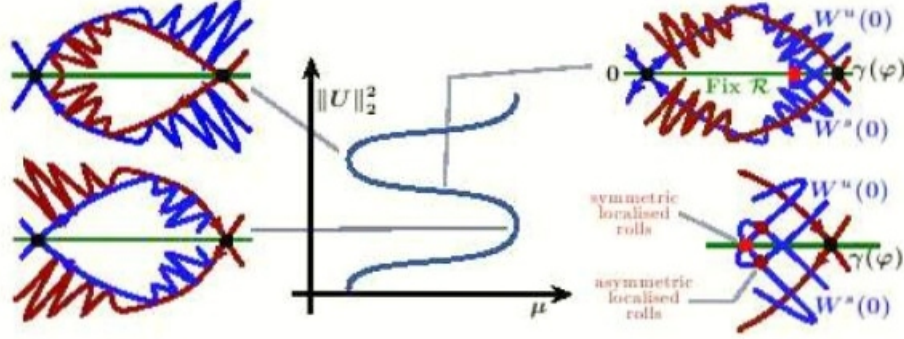


Figure 1: A cartoon of the stable and unstable manifolds for the fixed points O and $\gamma(\phi)$ in the planar representation, at different values of μ in the pinning region. From [15, 2].

the symmetry $u(-x) = u(x)$. The figure shows the intersections of the stable and unstable manifolds of O , labeled $W^{s,u}(O)$, with the surface $H = 0$. Both are one-dimensional and are shown in blue, and consist of points that approach O after an infinite number of backward and forward applications of the map. The intersection of corresponding (three-dimensional) center-stable and center-unstable manifolds of γ with $H = 0$ are shown in brown and are also one-dimensional. Since we are dealing with a discrete map these manifolds consist of discrete sequences of points obtained by applying the map to different points in the stable and unstable manifolds of these fixed points. Because of the discrete nature of the resulting two-dimensional dynamics we expect the unstable manifold $W^u(O)$ to intersect transversally with the center-stable manifold $W^s(\gamma)$ (top right panel in the figure). The point of intersection is simultaneously on both manifolds implying that forward iterations take it to $\gamma(\phi)$ while backward iterations take it to O , i.e., such a point is a heteroclinic point. Each image of this point, forward or backward, will also be a heteroclinic point since it must again lie on an intersection of these manifolds. Since the forward iterates accumulate on γ the unstable manifold $W^u(O)$ must execute increasingly wild gyrations near $\gamma(\phi)$ as indicated in the figure. This is a consequence of the Hamiltonian nature of Eq. (1) which implies that the “time- T ” map is area-preserving. Thus the areas of the (primary) lobes are all the same and since the foot of the lobes shrinks towards $\gamma(\phi)$ their length must grow in proportion. Spatial reversibility implies that $W^s(O)$ undergoes identical behavior and hence that $W^u(O)$ and $W^s(O)$ must intersect. The primary intersections must lie on the green curve and hence correspond to solutions with $u(-x) = u(x)$ that lie simultaneously in $W^u(O)$ and $W^s(O)$ (large red dot). Such solutions represent symmetric homoclinic solutions of Eq. (1). Observe that since the primary intersections accumulate on $\gamma(\phi)$ there will in fact be an infinite number of such homoclinic solutions corresponding to symmetric localized structures of ever larger length. The figure also indicates that associated with each primary intersection there is a pair of secondary intersections (small red dots, bottom right panel in the figure). These do not lie in the green line and hence correspond to asymmetric homoclinic points, i.e., the rung states of lecture 7.

Figure 1 shows that the *heteroclinic tangle* described above is created, as the bifurcation

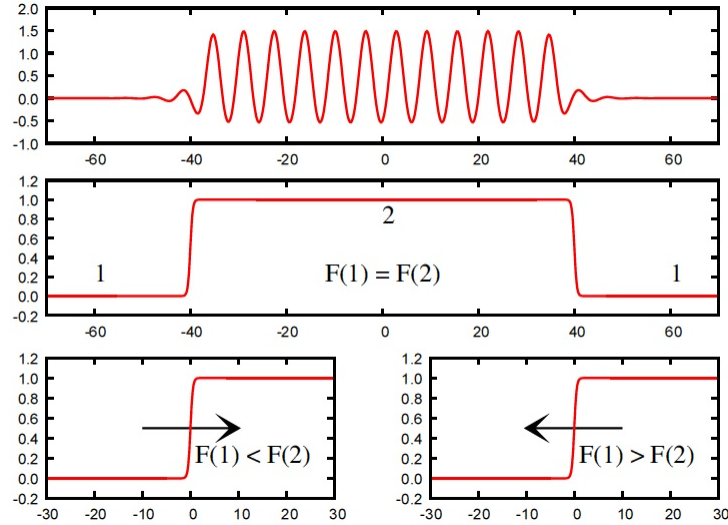


Figure 2: A cartoon of the motion of a front separating phase 1 (liquid) from phase 2 (gas) either side of the Maxwell point $F(1) = F(2)$ (bottom panels). The quantity F represents the free energy. The front is stationary only at the Maxwell point (middle panel). The top panel shows the case when phase 2 is a crystalline solid.

parameter μ (equivalently r) increases, at the point of first tangency between $W^u(O)$ and $W^s(\gamma)$ (top left panel) and destroyed at the point of last tangency (bottom left panel). Thus the snaking region is bounded on either side by the location of tangencies between these manifolds and no (long) localized states are present outside of the parameter interval between these two tangencies [2, 15].

An essentially identical picture applies to reversible but non-Hamiltonian systems since the fundamental properties of the heteroclinic tangle depend only on the presence of a transversal intersection between $W^u(O)$ and $W^s(\gamma)$ together with spatial reversibility. For this reason the geometrical picture sketched here has a far greater applicability than one may imagine at first sight. This is a consequence of the fact that a transversal intersection between manifolds cannot be destroyed by small perturbations in the parameter μ , i.e., it is a consequence of structural stability.

1.2 Physical explanation of the pinning region

Consider now the energetics of the system. The Lyapunov function F (defined in lecture 7) can be thought of as the free energy of the system. This allows us to compare the energy of the zero state and of the periodic state. Equilibria correspond to critical points of F , and without loss of generality we can define $F = 0$ at $u = 0$. We can calculate F for the periodic orbit with onset wavenumber q_c , which is a well-defined integral, and find the point where $F = 0$ for the periodic orbit. This construction defines the “Maxwell point” $r = r_M$ by analogy with standard phase transitions, for example, a transition between a gas and a liquid (fig. 2). At a critical temperature T_c (equivalently r_c) the liquid (phase 1) and gas (phase 2) coexist with equal energy and the insertion of a front separating the

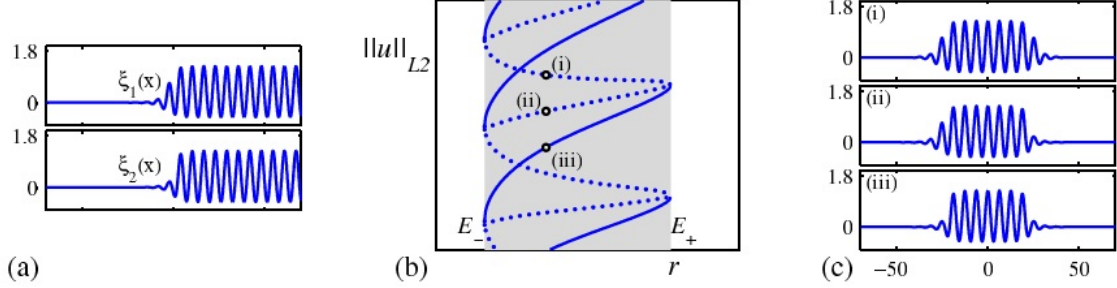


Figure 3: (a) The two types of fronts ξ_1 (unstable) and ξ_2 (stable) in SH23. (b) A section of the bifurcation diagram. (c) Three different localized states constructed from ξ_1 and ξ_2 . From [3].

two states does not cost additional energy (middle panel in fig. 2). If the temperature is lowered (bottom left panel in fig. 2), $T < T_c$, the energy of the liquid phase is less than the energy of the gas phase, and we expect the gas to condense. In this case the front between the two phases moves into the gas phase, effectively replacing the gas with liquid. If the temperature is raised (bottom right panel in fig. 2), $T > T_c$ and the front will propagate to the left turning the liquid into gas. The front is therefore stationary only when $T = T_c$ (that is, the critical temperature can be thought of as the ‘Maxwell temperature’). Now suppose that one of the phases is structured, for example a crystalline solid (top panel in fig. 2). Here, small temperature perturbations will not result in front motion as the front is held back by a “pinning potential” due to the structured state behind it [13]. This pinning allows stationary fronts over a range of T about T_c , and the temperature must be changed by a finite amount to overcome the effective pinning potential and allow the fronts to move. There are many coexisting steady states within the interval of temperatures around T_c , where the fronts are pinned since in this region it costs little to insert fronts between the two competing phases.

At each value of r in the pinning region one can identify two types of front, ξ_1 and ξ_2 , as shown in fig. 3(a). These fronts can be placed back to back to construct localized structures. The three different localized states that can be constructed from these fronts at each parameter value are shown in fig. 3(c), with the location of these states indicated in the bifurcation diagram in fig. 3(b) using solid dots. There are symmetric states with either (i) ξ_1 fronts at either end or (iii) ξ_2 fronts at either end; asymmetric states (ii) consist of one ξ_1 and one ξ_2 front. We can assign stability to these fronts and find that front (i) is unstable while front (ii) is stable. These stability assignments are indicated in fig. 3(b) by solid (stable) and dotted (unstable) lines. The pinning region can thus be thought of as an unfolding of the Maxwell point due to the heterogeneity of one of the states.

1.3 Wavelength selection (SH23)

Consider the wavenumber inside the localized structure. Computations show that the wavenumber (equivalently the wavelength) of the pattern depends on the value of r within the pinning region. This wavenumber is not given by minimizing the free energy F because

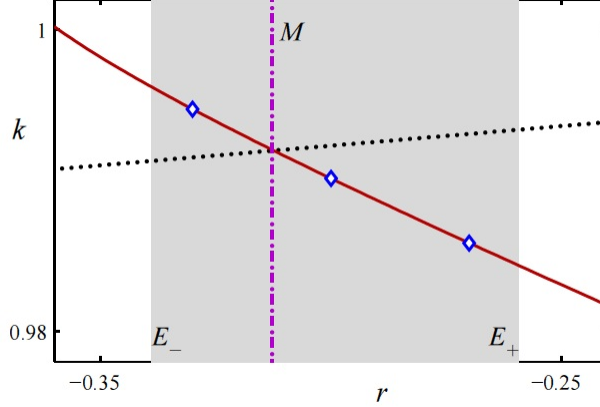


Figure 4: The wavenumber k found by minimizing F (dotted black line), minimizing F with the $H = 0$ constraint (solid red line) and results from numerical simulations (blue diamonds). The pinning region is shaded in grey. From [3].

of the $H = 0$ constraint required of all homoclinic orbits. Figure 4 shows that to the left of the Maxwell point $r = r_M$, k is higher than the Maxwell value, so the wavelength is less than the Maxwell wavelength. For $r < r_M$, the periodic state has a higher energy F than the zero state, so in the absence of pinning the fronts would move inwards eliminating the periodic state. However, in the pinning region they are prevented from moving by the pinning effect. Instead the energy difference between the two states manifests itself in a compression of the resulting steady structure. Conversely, for $r > r_M$ the periodic state has lower energy than the zero state, so in the absence of pinning the fronts would move outwards and the structure would grow. Since the fronts are prevented from moving by the pinning effect the structure instead stretches. The variation of $k(r)$ can be calculated by minimising F subject to the constraint $H = 0$, and the result agrees well with measurements from numerical calculations (fig. 4).

We remark that the presence of the fronts at either end leads to a unique wavenumber between them, however far apart the fronts are. This is in contrast to spatially *periodic* states for which there is an interval of stable wavenumbers within the so-called Eckhaus stability limits. Evidently wavenumber selection is very sensitive to what happens “at infinity” and in particular the boundary conditions applied there. We may say that the fronts collapse the Busse balloon [8].

1.4 The pinning region in parameter space

The extent of the pinning region for SH23 in the (r, b_2) plane is shown in fig. 5. The pinning region is shaded and bounded by two blue lines corresponding to first and last tangencies as explained above. The region is exponentially thin near its tip at $(0, \sqrt{27/38}q_c^2)$ [6]. Near the tip, i.e., when $r = \mathcal{O}(\epsilon^4)$ and $b_2 = \mathcal{O}(\epsilon^2)$, $\epsilon \ll 1$, the width of the snaking region is exponentially thin, of order $\epsilon^{-4} \exp(-\pi/\epsilon^2)$, a result that requires the use of exponential asymptotics [9].

Away from the exponentially thin region near $r = 0$, the snaking region broadens but

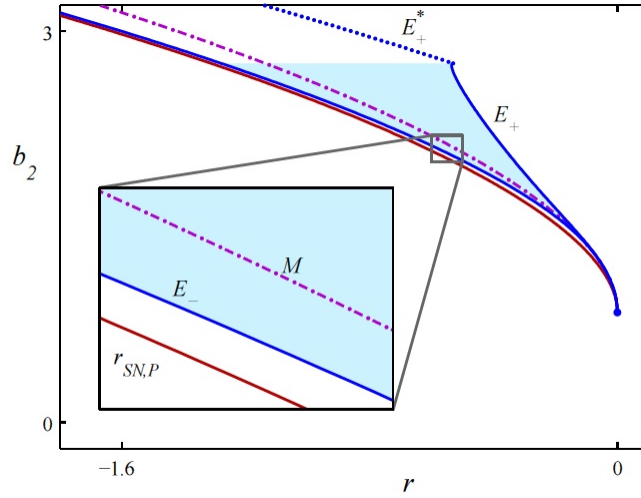


Figure 5: The pinning region (shaded in blue) for SH23 in the (r, b_2) parameter plane. The pinning region for SH35 is similar. From [3].

always straddles the Maxwell line, which is the purple dot-dash line in fig. 5. The red line shows the fold (saddle-node bifurcation) of the periodic orbit γ with wavenumber q_c . The snaking region tracks the fold, but does not reach it. A similar plot can be drawn for the SH35 equation [5].

Additional Maxwell points involving nontrivial homogeneous states are also present and considerably complicate the full picture [6]. These are responsible, for example, for the boundary E_+^* in fig. 5. In fact SH23 is still by no means completely understood.

2 Depinning

If r is moved sufficiently far from r_M the energy difference between the zero state and γ exceeds the pinning potential and the fronts *depin*. The resulting motion can be predicted by projecting SH23 onto the near-marginal eigenfunctions present at either edge of the pinning region.

At the boundary of this region the marginally stable amplitude eigenfunctions are localized near either front of the structure (see lecture 7). Near E_+ , where the state of the system evolves towards the lower energy periodic state, this fact indicates incipient nucleation of new cells just outside the localized state. Direct integration of Eq. (1) reveals time-dependent growth of the structure via sequential nucleation of new cells (fig. 6(a)). The nucleation time depends on the distance from the edge of the pinning region, as indicated in fig. 6(b). The time diverges at the edge of the pinning region (where it takes an infinite amount of time to nucleate a new cell) and decreases as the distance from the pinning region increases. The speed of the front, which is a ‘pushed front’ because it propagates into a stable state [14], can be calculated from the time it takes to nucleate cells at the front. To the left of the pinning region (where the solution moves towards the lower energy zero state) the fronts move inwards via sequential annihilation of cells with the same dependence on

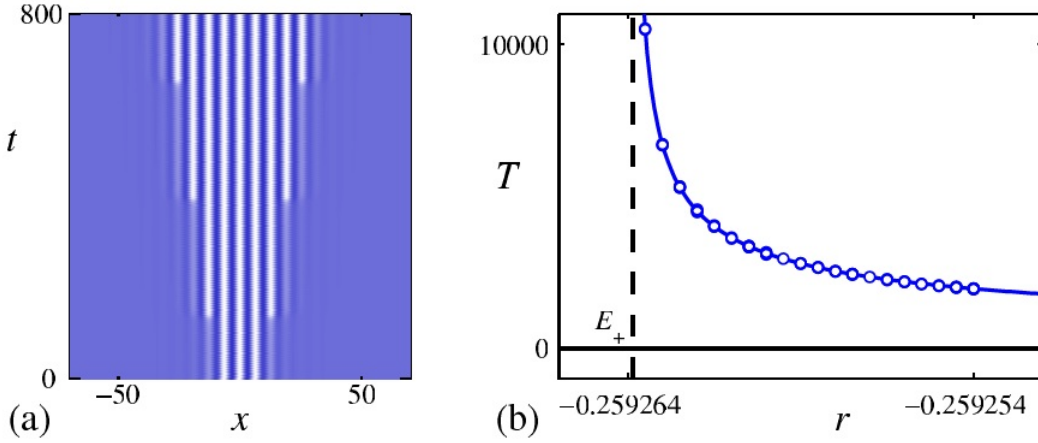


Figure 6: (a) Space-time plot of the evolution of a localized structure in time, and (b) the nucleation time T as a function of r . From [3].

the distance from E_- as in the E_+ case.

2.1 Theory

To calculate the speed of the front we need the time taken to nucleate (or annihilate) a cell [6]. For this purpose we suppose that

$$r = r(E_-) + \delta, \quad (3)$$

where $r(E_-)$ denotes the left edge of the pinning region and $|\delta| \ll 1$. Thus δ determines the distance away from the edge of the pinning region: if $\delta > 0$, then r is inside the pinning region and if $\delta < 0$ then r is outside the pinning region. We anticipate that nucleation takes place on an $\mathcal{O}(|\delta|^{-1/2})$ time scale and therefore introduce the slow time $\tau = |\delta|^{-1/2}t$. Finally we write

$$u(x, t) = u_0(x) + |\delta|^{1/2}u_1(x, \tau) + |\delta|u_2(x, \tau) + \mathcal{O}(|\delta|^{3/2}), \quad (4)$$

where $u_0(x)$ is one of the stationary localized states at the edge of the pinning region, assumed to be of even parity.

Substituting this Ansatz into SH23, we find at $\mathcal{O}(|\delta|^{1/2})$

$$\mathcal{L}[d_x, u_0]u_1(x, \tau) = 0, \quad (5)$$

where \mathcal{L} is the linearised SH operator evaluated at $r = r(E_-)$. The solutions of this problem¹ were found in lecture 7:

$$u_1(x, t) = a(t)\tilde{U}_{amp} + b(t)\tilde{U}_{ph} + c(t)\tilde{U}_G. \quad (6)$$

Of these marginal modes the amplitude mode \tilde{U}_{amp} is even while the remaining two are odd. We may therefore suppose that the ‘centre of mass’ remains fixed and take $b = c = 0$.

¹In the following we treat the exponentially small phase eigenvalue as zero.

Thus it suffices to determine the evolution of $a(t)$, the amplitude of the mode responsible for depinning.

For this purpose we proceed to $\mathcal{O}(|\delta|)$ obtaining

$$\mathcal{L}[\mathrm{d}_x, u_0]u_2(x, \tau) = \partial_\tau u_1 - [\mathrm{sgn}(\delta)u_0 + b_2u_1^2 - 3u_0u_1^2]. \quad (7)$$

For the ordering assumed in the Ansatz (4) to remain valid on the timescale $\tau = \mathcal{O}(1)$ the solution $u_2(x, \tau)$ must remain $\mathcal{O}(1)$ on this timescale. This will only be so if an appropriate solvability condition is imposed on the right hand side of Eq. (7). To find this solvability condition we apply the so-called Fredholm alternative [] and multiply Eq. (7) by \tilde{U}_{amp} and integrate over x from $-\infty$ to ∞ . Since $\mathcal{L}[\mathrm{d}_x, u_0]$ is self-adjoint the left hand side vanishes after integration by parts, leaving the condition

$$\alpha_1 \mathrm{d}_t a = \alpha_2 \mathrm{sgn}(\delta) + \alpha_3 a^2, \quad (8)$$

where

$$\alpha_1 \equiv \int_{-\infty}^{\infty} \tilde{U}_{amp}^2 \mathrm{d}x, \quad \alpha_2 \equiv \int_{-\infty}^{\infty} u_0 \tilde{U}_{amp} \mathrm{d}x, \quad \alpha_3 \equiv \int_{-\infty}^{\infty} (b_2 - 3u_0) \tilde{U}_{amp}^3 \mathrm{d}x. \quad (9)$$

This is the required evolution equation for the amplitude of the nucleation mode. The nucleation time, which is the time T for the solution to move from one fold of the snaking branch to the next one below, is approximately the time taken for $a(\tau)$ to go from $-\infty$ to ∞ . Writing this condition in terms of the original time we obtain

$$T_- = \frac{\pi \alpha_1}{(\alpha_2 \alpha_3 \delta)^{1/2}} \approx 4.388 |\delta|^{-1/2}, \quad \delta < 0. \quad (10)$$

This prediction compares well with the simulation result

$$T_- \approx (4.57 \pm 0.34) |\delta|^{-0.499 \pm 0.006}, \quad \delta < 0. \quad (11)$$

The method can be similarly applied near the right edge of the snaking region, $r = r(E_+) + \delta$, $0 < \delta \ll 1$, with corresponding prediction

$$T_+ = \frac{\pi \alpha_1}{(\alpha_2 \alpha_3 \delta)^{1/2}} \approx 5.944 \delta^{-1/2}, \quad \delta > 0, \quad (12)$$

and simulation result

$$T_+ \approx (6.04 \pm 0.18) \delta^{-0.501 \pm 0.003}, \quad \delta > 0. \quad (13)$$

The nucleation time, T , thus depends on the inverse square root of the distance from the folds in the snaking region. These are very well aligned high up the bifurcation diagram, so here T is independent of which fold is considered and the nucleation front therefore moves with constant speed. This is not so low down the snaking diagram where the folds do not line up with the edge of the pinning region.

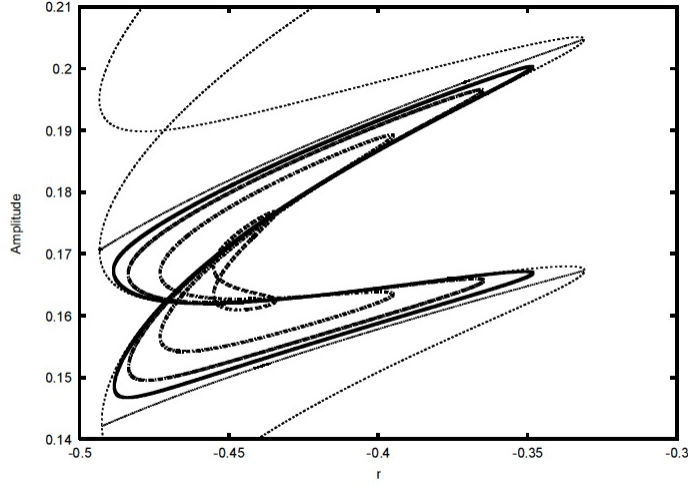


Figure 7: One set of isolas with $b_2 = 2$ and $\gamma = 0.05, 0.10, 0.20, 0.35$. From [4].

3 Broken symmetry and drift

It is interesting to examine the effect of broken spatial reversibility on the nucleation process. For this purpose we may add a dispersive term to SH23 to obtain

$$\partial_t u = (r - (1 + \partial_x^2)^2) u + \gamma \partial_x^3 u + b_2 u^2 - u^3. \quad (14)$$

We anticipate that when $\gamma \neq 0$ the solutions will drift, and therefore look for steady solutions drifting with speed c . Such solutions satisfy the ODE

$$0 = (r - (1 + d_x^2)^2) u + c d_x u + \gamma d_x^3 u + b_2 u^2 - u^3, \quad (15)$$

where x is now the comoving coordinate and c is a nonlinear eigenvalue, i.e., c is determined as part of the solution.

Figure 7 shows the solution to this problem. One finds that the presence of dispersion destroys the snakes-and-ladders structure of the snaking region and that the drifting localized states fall on a stack of figure-eight isolas, one of which is shown in the figure. All the localized states now travel: $c = c(r)$ along each isola (not shown). Note in particular that as γ increases the isolas shrink and eventually disappear. Thus drifting localized structures are absent for large dispersion.

To the immediate right of the pinning region, $r = r(E_+) + \delta$ for $\delta \ll 1$, the nonzero value of γ leads to asymmetry between the nucleation rates associated with the leading and trailing fronts. This is shown in fig. 8, where all the patterns drift slowly to the right. For small enough δ , nucleation only occurs at the leading front but fails at the trailing front (fig. 8(a)). Further from the saddle-node, the rate of nucleation increases (as in the symmetric case) so that nucleation now takes place at both fronts, albeit at different rates. As a result the trailing front overcomes the slow drift of the structure downstream, and propagates upstream (fig. 8(b)). However, increasing γ can prevent nucleation at the trailing front so that the pattern only grows at the leading front (fig. 8(c)). The front speed for the asymmetric problem (15) can be calculated in much the same way as in the symmetric problem (see section 2.1) as discussed next.

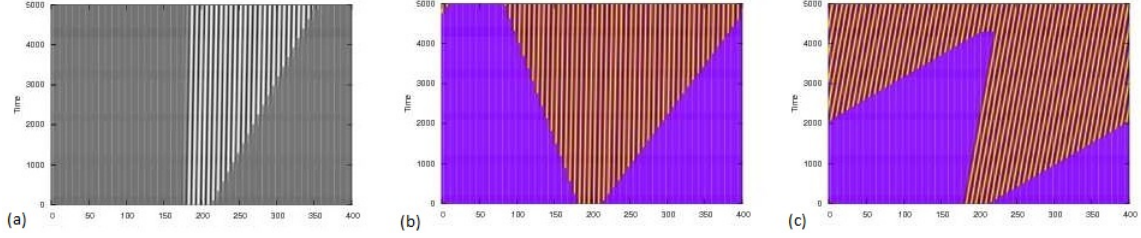


Figure 8: Space-time plots showing asymmetric front propagation when $b_2 = 2$: (a) $\gamma = 0.001, \delta = 0.00015$; (b) $\gamma = 0.001, \delta = 0.00065$; (c) $\gamma = 0.01, \delta = 0.00065$. From [4].

3.1 Theory

For small dispersion the drift speed c is expected to be of order γ . We therefore write $r = r(E_+) + \delta$, take $\gamma = \sigma|\delta|$, $\sigma = \mathcal{O}(1)$, and write []

$$u(x, t) = u_0(x + \theta(T)) + |\delta|^{1/2} u_1(x + \theta(T), \tau) + |\delta| u_2(x + \theta(T), \tau) + \dots, \quad (16)$$

where $\tau = |\delta|^{1/2} t$, $T = |\delta| t$ and $\theta(T)$ captures the drift of the leading order localized structure, i.e., $c = \theta_t = |\delta| \theta_T$. Note that the drift and nucleation occur on disparate timescales: the perturbations u_1 and u_2 drift on the same slow time T as u_0 , but can also grow on a different, and faster, timescale τ . The leading order, $\mathcal{O}(1)$, terms are

$$r(E_+) u_0 - (1 + \partial_x^2)^2 u_0 + b_2 u_0^2 - u_0^3 = 0. \quad (17)$$

This is the equation for steady solutions of the reversible SH23 equation with solutions $u_0 = u_0(x + \theta(T))$. At next order, $\mathcal{O}(|\delta|^{1/2})$,

$$\mathcal{L}[\partial, \square] u_1 \equiv (r(E_+) - (1 + \partial_x^2)^2 + 2b_2 u_0 - 3u_0^2) u_1 = 0, \quad (18)$$

and u_1 , as in section 2.1, is a superposition of three (almost) marginal modes. Since the translation has been included by introducing the phase $\theta(T)$, the \tilde{U}_G mode is already included. Thus

$$u_1 = a(\tau) \tilde{U}_{amp}(x + \theta(T)) + b(\tau) \tilde{U}_{ph}(x + \theta(T)). \quad (19)$$

At $\mathcal{O}(|\delta|)$,

$$u_0' \theta_T + u_{1\tau} = \mathcal{L} u_2 + \text{sgn}(\delta) u_0 + \sigma u_0''' + (b_2 - 3u_0) u_1^2. \quad (20)$$

Since the kernel of \mathcal{L} is spanned by three independent solutions, the three marginal modes, we must impose three different solvability conditions on u_2 . These will in turn determine the evolution of $\theta(T)$, $a(\tau)$ and $b(\tau)$.

To obtain the solvability conditions we multiply Eq. (20) in turn by the three marginal modes, u_0' (i.e., the Goldstone mode), \tilde{U}_{amp} and \tilde{U}_{ph} , and integrate over x from $-\infty$ to ∞ . The first solvability condition predicts the drift speed

$$\theta_t = -0.9663\gamma, \quad (21)$$

which agrees well with the drift speed measured from numerical simulations. The solvability conditions for the phase and amplitude modes give coupled equations for a and b . However,

if the structure described by u_0 is long enough, the two fronts at either end decouple from one another (lecture 6) and the two equations reduce to [4]

$$(a \pm b)_\tau = \alpha_1 \text{sgn} \delta \mp \beta \sigma + \alpha_3 (a \pm b)^2. \quad (22)$$

We define the nucleation time at the leading front as

$$T_{\text{leading}} = \int_{-\infty}^{\infty} \frac{d\tau}{a - b} = \frac{\pi}{\alpha_3^{1/2}} \frac{1}{(\alpha_1 \delta + \beta \gamma)^{1/2}} \quad (23)$$

and at the trailing front as

$$T_{\text{trailing}} = \int_{-\infty}^{\infty} \frac{d\tau}{a + b} = \frac{\pi}{\alpha_3^{1/2}} \frac{1}{(\alpha_1 \delta - \beta \gamma)^{1/2}}. \quad (24)$$

The value of δ for which the nucleation time diverges corresponds to the value at which nucleation ceases, and is given by

$$\delta_c^{\text{leading}} = -\beta \gamma / \alpha_1 = -0.3543 \gamma, \quad \delta_c^{\text{trailing}} = \beta \gamma / \alpha_1 = 0.3543 \gamma. \quad (25)$$

These predictions agree well with numerical simulations [4].

4 Two-dimensional structures

We now consider the two-dimensional (2D) Swift-Hohenberg equations SH23

$$u_t = ru - (\nabla^2 + 1)^2 u + b_2 u^2 - u^3, \quad (x, y) \in \mathbb{R}^2, \quad (26)$$

and SH35

$$u_t = ru - (\nabla^2 + 1)^2 u + b_3 u^3 - u^5, \quad (x, y) \in \mathbb{R}^2. \quad (27)$$

In both these equations $u = u(x, y, t)$ and $\nabla^2 \equiv \partial_x^2 + \partial_y^2$. These equations are reversible in both x and y but steady state solutions still correspond to critical points of the Lyapunov energy function F . In 2D, there is a larger range of different types of localized structures that arise, including stripes, spots, targets, squares and hexagons. For a more extensive treatment of this topic, we refer the reader to [5].

4.1 Wall and body modes

Stripe-like localized structures in 2D (e.g. fig. 9) are only stable inside a subregion of the 1D pinning region (fig. 10). This is a consequence of the presence of distinct 2D instabilities that destabilize localized stripes that are stable in 1D. These instabilities can be divided into “wall” modes which are characterized by a y -dependent eigenfunction that is localized at the fronts, and “body” modes whose eigenfunction extends across the whole localized structure.

Figures 11(a,b) show the evolution of a wall mode in SH23. Depending on the parameters the excitation of the wall mode may lead to depinning (fig. 11(a)) with both inward and

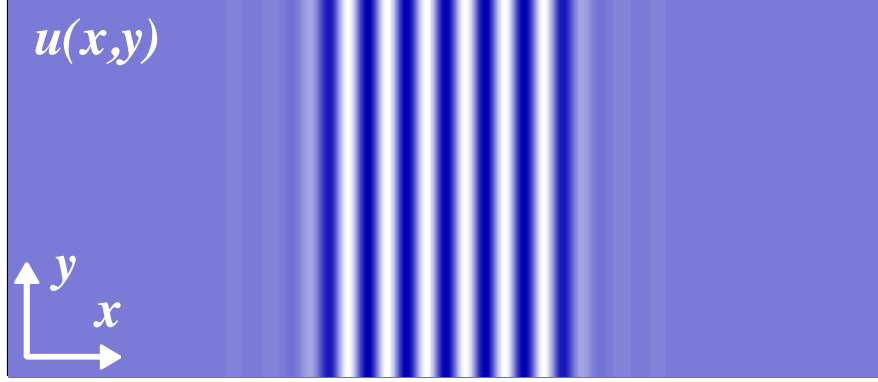


Figure 9: Localized 2D stripe in SH23. From [5].

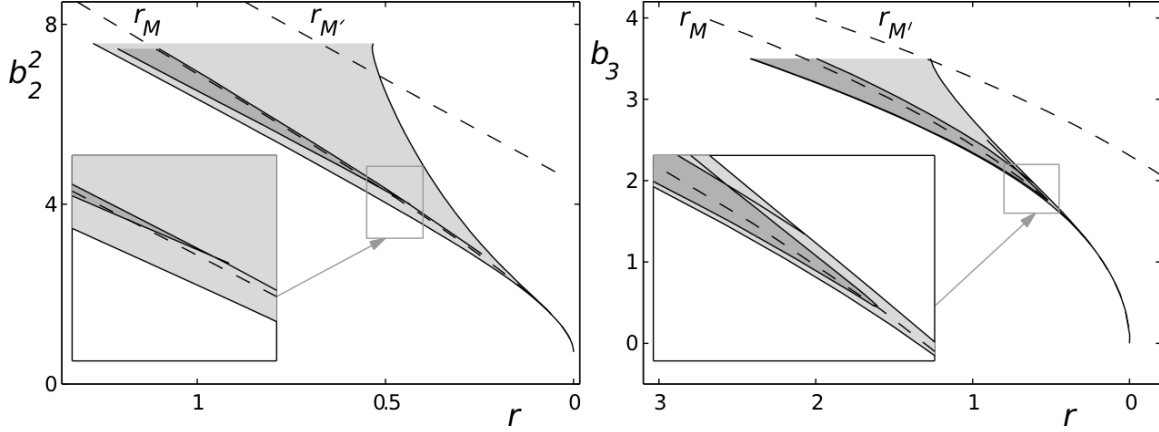


Figure 10: Stability regions for the 1D (light) and 2D (dark) localized structures in (a) SH23 and (b) SH35. From [5].

outward front propagation that converts the stripe state into a hexagonal array of spots that invades the whole domain. It is also possible to choose parameters such that there is not enough energy to depin the front connecting the structure to the background state (fig. 11(b)). In this case the outer fronts remain pinned and the instability propagates only inwards, turning the localized stripes into a localized patch of hexagons.

An example of the body mode is illustrated in fig. 11(c). As the mode evolves the whole structure buckles into a zigzag structure. In the case shown the buckling is strong enough to depin the fronts on either side resulting in the growth of a set of transverse stripes. The wavelength of the stripes is determined dynamically by the motion of the fronts and so is

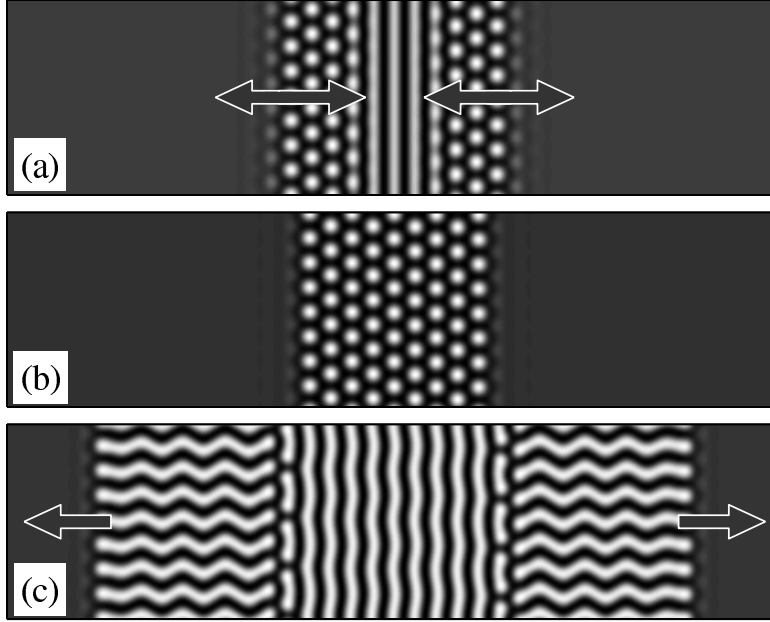


Figure 11: Evolution of (a,b) the wall mode, and (c) the body mode in SH23. From [5].

not the equilibrium wavelength. As a result the perpendicular stripes undergo their own zigzag instability that brings their wavelength closer to their equilibrium wavelength. SH35 undergoes similar instabilities but hexagonal coordination is no longer the preferred case. Instead the instabilities may generate moving fronts that undergo dendrite-like instabilities or lead to a dynamically selected labyrinthine pattern.

4.2 Two-dimensional spatially localized states

In the preceding section we have seen that time evolution can lead to stable localized states with nontrivial 2D structure. It is possible to follow solutions of this type numerically as a function of the parameters. Figure 12(a) from [1] shows one such steady-state solution of SH35 (right panel, corresponding to the red dot in the bifurcation diagram in the left panel). Following the solution numerically towards lower values of r (fig. 12(b)), we find that the amplitude $\|u\|_2^2$ begins to grow as the structure sends out “fingers” that extend farther and farther outwards. Since the front that connects this “finger” state with the background states only sees behind it a translation-invariant state no pinning takes place. In this case the pinning region is absent (we speak of *collapsed snaking*) and a heteroclinic cycle between the background state and the “finger” state is only present at a single parameter value. However, as we follow the solution in the other direction, we observe the formation of a rug-like structure associated with a snaking bifurcation diagram (fig. 12(c)). Here, the snaking is caused by the pinning of each front to stripes parallel to the front. It is remarkable that solutions of the form shown in figs. 12(b,c) in fact lie on the *same* solution branch.

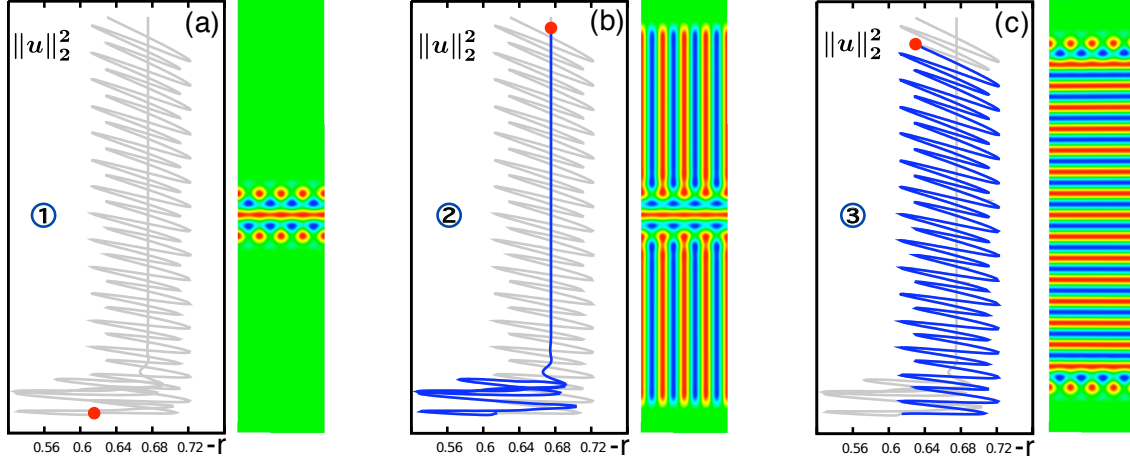


Figure 12: Bifurcation diagram of a localized stripe pattern in SH35. (a) A localized state identified through time integration. (b) Collapsed snaking. (c) Snaking. Each figure shows the appropriate portion of the bifurcation diagram (left panel) and the solution profile $u(x,y)$ (right panel) corresponding to the location indicated by the red dot. The profiles are shown with x vertically and y horizontally. From [1].

It is useful to think of structures such as that shown in fig. 12(b) in terms of a phase space representation, treating x as an unbounded time-like variable while y remains bounded (with Neumann boundary conditions imposed). This description is analogous to that employed in fig. 1: in fig. 13(a) the black dot represents the zero state while the red point represents an extended state of periodic stripes with finite y -wavenumber that fills the whole domain. A connection (1) between these two fixed points in the phase plane represents a front connecting the zero state to the patterned state (a heteroclinic orbit). An excursion (2) from the patterned state back to itself represents a defect in the patterned state. Spatial reversibility implies the existence of a complete heteroclinic cycle. As in 1D, numerical calculations identify homoclinic orbits with exactly this template, such as state (3) in fig. 13(b).

Figure 14 shows a detail of the bifurcation diagram for SH35. The sequence of transitions along the snaking branch produces alternating stable and unstable states, which grow in space. The growth mechanism is slightly different at points 3 and 7 compared with points 1, 5 and 9 owing to the Neumann boundary conditions in y used in the calculation. This leads to the observed misalignment of successive folds.

The rug-like structures in fig. 14 are just one set of localized structures present in this system; however, other structures are present as well. For example, it is possible to produce odd rug-like structures that also snake (dotted grey line in fig. 15). There are also rungs (blue line of fig. 15) of asymmetrical states that connect even states (solid grey line in fig. 15) to odd states. These Z-shaped rungs are unstable throughout as indicated by the eigenvalues shown in fig. 15(a). However, S-shaped rungs connecting even states to even states possess a stable middle segment (fig. 16).

Other structures that arise in 2D are checkerboard rugs (this live on isolas, of which

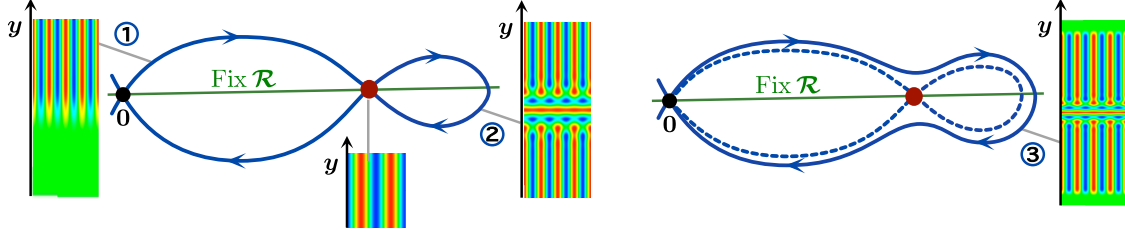


Figure 13: Phase plane description of collapsed snaking. From [1].

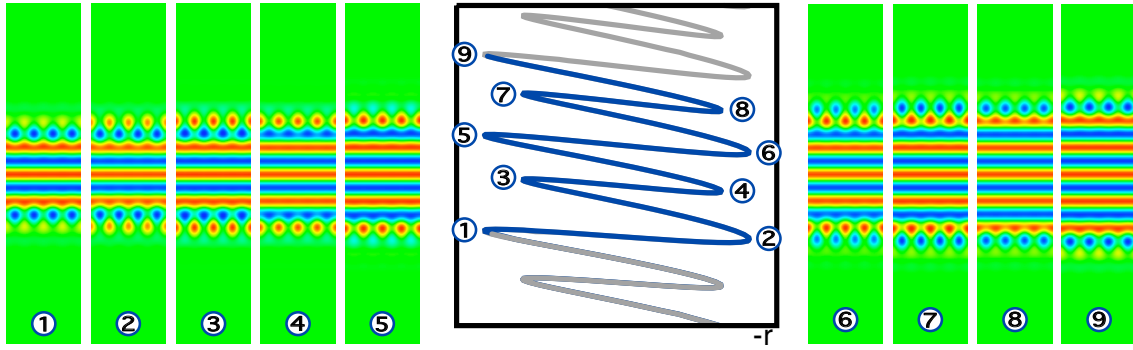


Figure 14: A section of the snaking branch from fig. 12 and the corresponding solution profiles at successive folds. From [1].

there is likely an infinite stack; fig. 17) and barrel-shaped structures (fig. 18). The latter are of particular interest since the fronts on the left and right are clearly pinned to the stripe pattern inbetween, while the curved boundaries likely experience weaker pinning arising from the circumferential wavelength gradient introduced by the curvature of the boundary. Perhaps of greatest interest are the leaf-like structures shown in fig. 19. These structures have a convex boundary that becomes, in some cases, concave near the cusps of the leaf. This fact implies that it is not possible to think of these structure as being produced by an effective surface tension since surface tension cannot produce structures that are concave. An understanding of the sharp, internally-generated cusp-like features of these structures represents a major challenge from the point of view of pde theory.

In SH23 the presence of the quadratic nonlinear term leads to a preference for hexagonal structures instead of stripes [8]. The different localized structures present in SH23 are discussed in [10]. As shown in fig. 20, localized hexagons, targets and spots occur in the different regions in the parameter plane as shown in fig. 20(a). The green line shows the fold of the extended periodic hexagonal pattern. Figure 20(b) shows the region near $r = 0$ and fig. 20(c) shows the bifurcation diagram for two different localized states, namely localized targets and hexagons. Pinning takes place as in 1D, although as the structure grows its effect decreases and snaking may collapse. We mention that target patterns behave quite

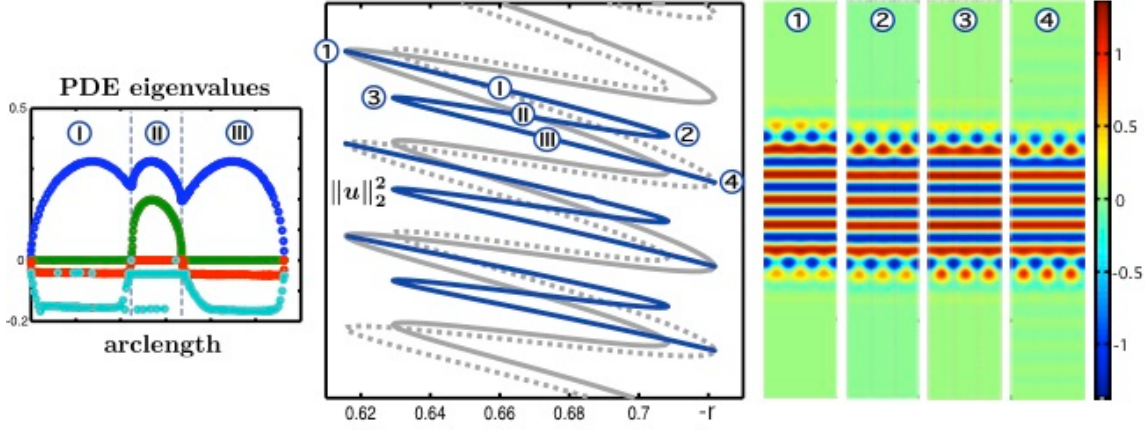


Figure 15: Unstable rung-like Z-shaped branches of asymmetrical states connecting even and odd parity branches (middle panel). The eigenvalues of the solutions as a function of arclength are shown in the left panel. The changes in the solution structure across the Z-shaped branch are shown in the right panel. From [1].

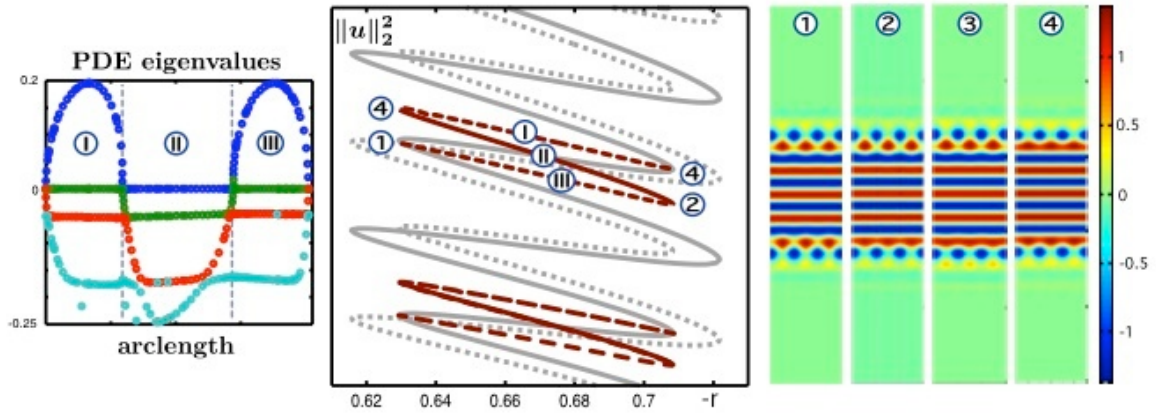


Figure 16: Rung-like S-shaped branches of asymmetrical states connecting even states to even states (middle panel). The eigenvalues of the solutions as a function of arclength (left panel) show that the middle segment is stable. The changes in the solution structure across the S-shaped branch are shown in the right panel. From [1].

differently from spots. The former are present only in the subcritical regime while spots are present even in the supercritical regime [11].² This important point may explain the

²There are in fact two types of spots, spot A which is present regardless of the direction of branching of

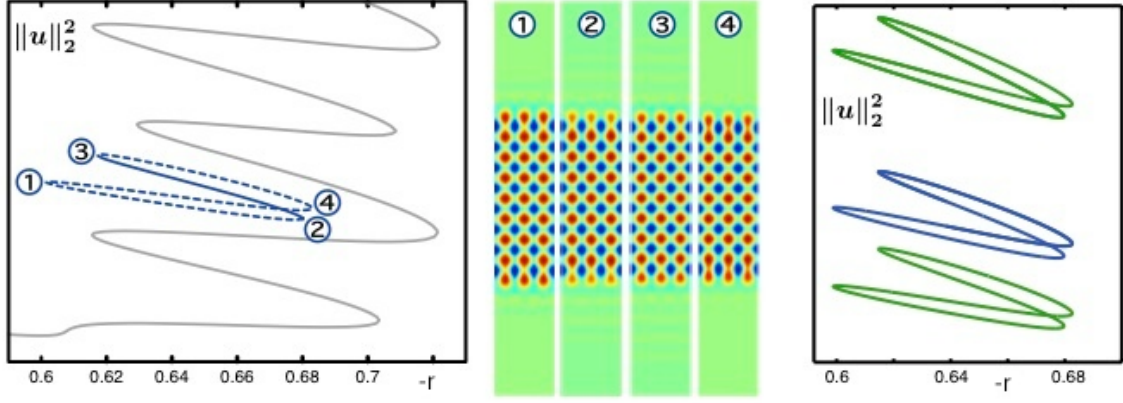


Figure 17: Left panels: localized checkerboard patterns on an isola. Solid line represents stable solutions. Right panel: part of a stack of such isolas with broader structures at the top and narrower structures at the bottom. From [1].

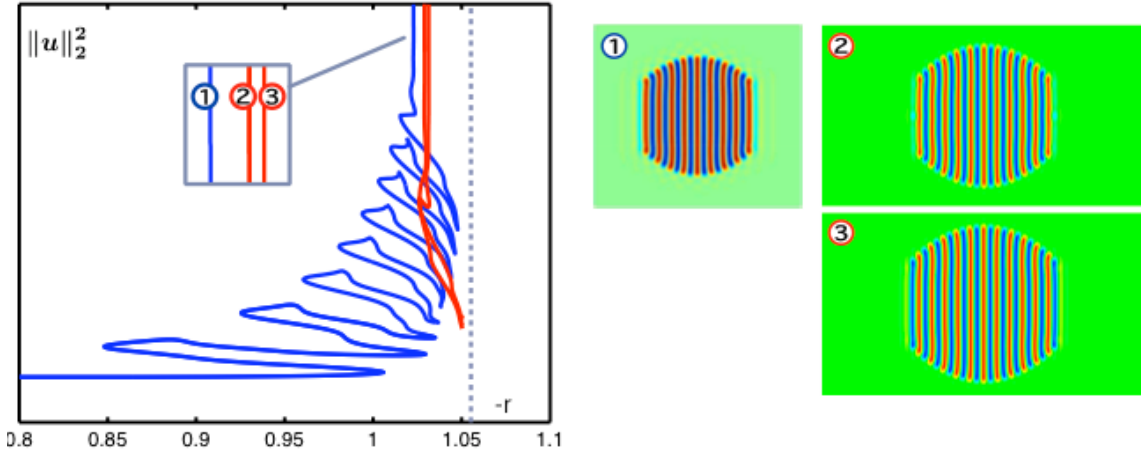


Figure 18: Left panel: barrel-shaped localized structures initially snake but large structures of this type lead to collapsed snaking. Right panel: subsidiary barrel-shaped structures differing by one stripe. From [1].

prevalence of spots in experiments.

Consider the hexagonal patch corresponding to the first fold in parameter space shown in fig. 21. It is possible to follow the solution branch numerically in parameter space [10]. At point 1, a regular hexagonal crystalline solution is present (note the “echoes” along the periphery the structure, which is a consequence of the oscillatory front between the the stripe pattern and spot B which is only found in the subcritical regime [12].

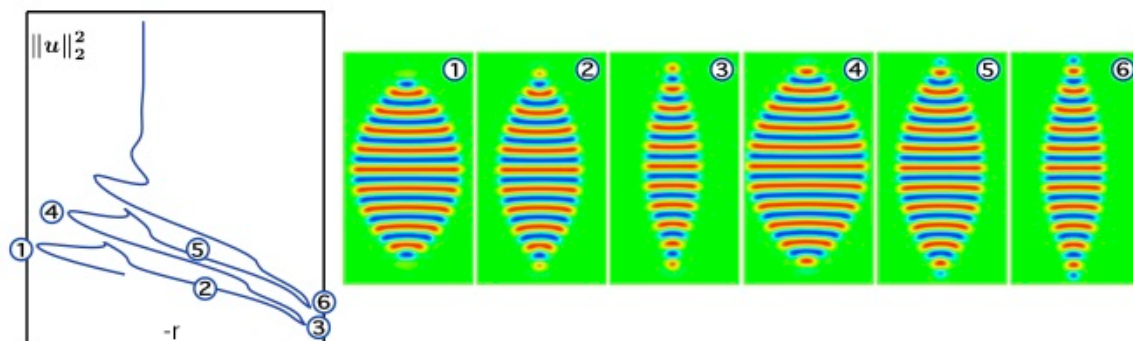


Figure 19: Planar leaf-like solutions of SH35. From [1].

hexagonal structure and the background state). By point 2 the structure has evolved by adding a cell at the mid-point of every edge. Further cells have been added symmetrically along the boundary by point 3, but the resulting structure is not hexagonal. The hexagonal structure reforms near point 4. Since the edges now consist of five cells apiece and the subsequent evolution differs from that just described. One must therefore proceed further up the solution branch in order to form a hexagonal structure with an even number of cells along each edge before the type of growth described in going from point 1 to point 4 recurs. The misalignment of the folds provides an indication of the energy associated with the nucleation of cells in different locations along the edges. Comparison of the energy F for the different states shown in fig. 21 could provide an explanation why the hexagonal structure grows in the manner it does.

5 Oscillons

In lecture 6, we saw the difference between “standard” and “reciprocal” oscillons. Here, we consider steady, localized solutions to the forced complex Ginzburg-Landau (FCGL) equation. Our motivation for looking at this problem is two-fold. Firstly, oscillons have been observed in experiments. Secondly, the FCGL equation is similar to the SH equation when written in terms of the real and imaginary parts as coupled second order equations are equivalent to a problem of fourth order in space. However, the equation does not have a Lyapunov function, so we expect interesting dynamics.

5.1 Forced Ginzburg-Landau equation

Oscillons are typically subharmonic instabilities, and are easily observable in the vicinity of a subharmonic resonance (or 2:1 resonance) when an oscillatory system with natural frequency ω is driven with a driving frequency $\Omega \approx 2\omega$. If the detuning $\nu \equiv \omega - \Omega/2$ is small the system will oscillate with frequency $\Omega/2$ instead of ω . This oscillation is called a phase-locked oscillation since the phase of the driving and response remain in phase. Outside of this region, the response frequency is no longer locked to the forcing frequency and the

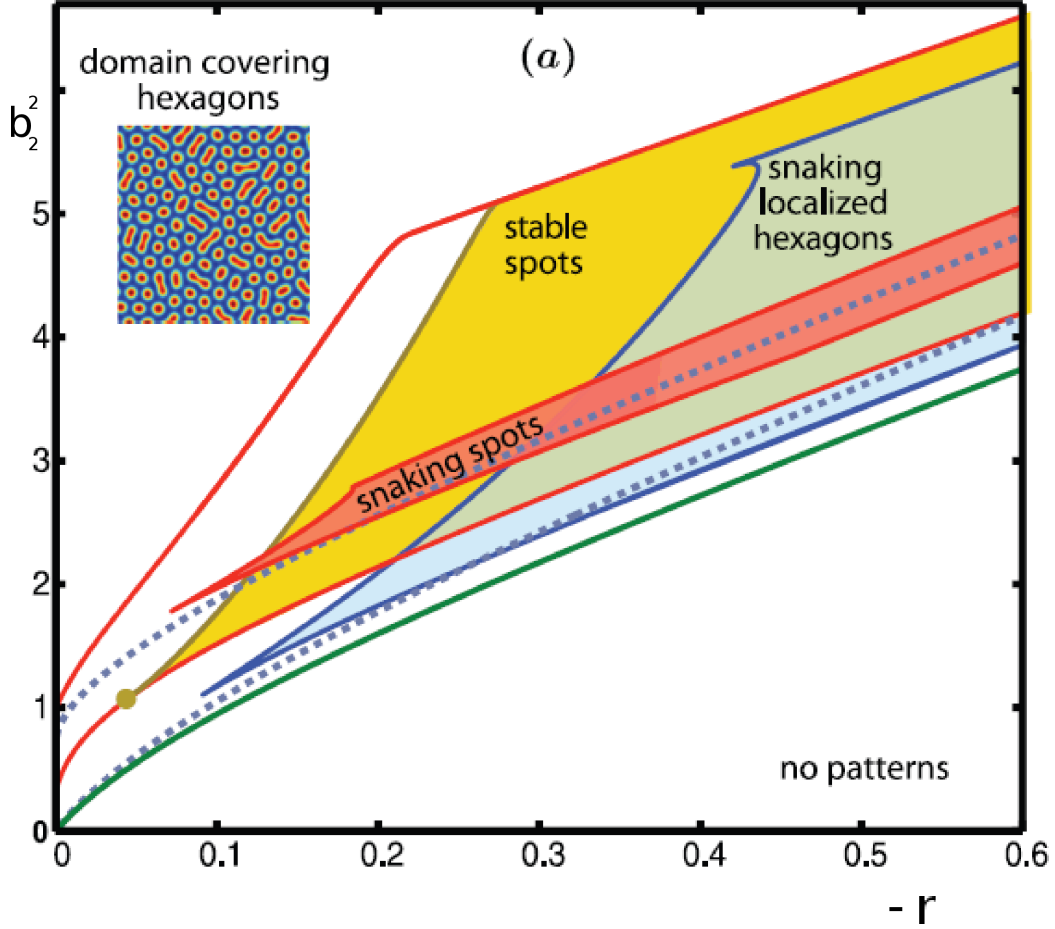


Figure 20: Localized hexagons, targets and spots in SH23. From [10].

phase slips [7]. We can describe the resulting phase-locked oscillations, including standard and reciprocal oscillons by examining the small amplitude

have been observed in the solutions of the FCGL equation for the amplitude of the phase-locked oscillation.

We suppose a dynamic observable $w(x, t)$ can be written in the form

$$w(x, t) = w_0 + A(\tilde{x}, \tilde{t})e^{i\Omega t/2} + \text{c.c.} + \dots, \quad (28)$$

where w_0 is a steady homogeneous state of the system, $A(\tilde{x}, \tilde{t})$ is the (small) complex amplitude of the forced subharmonic response, and \tilde{x} and \tilde{t} are suitable slow spatial and temporal scales. The oscillation amplitude $A(\tilde{x}, \tilde{t})$ obeys the following evolution equation

$$A_{\tilde{t}} = (\mu + i\nu)A - (1 + i\beta)|A|^2A + (1 + i\alpha)A_{\tilde{x}\tilde{x}} + \gamma\bar{A}, \quad (29)$$

where μ represents the (small) distance from onset of a (supercritical) homogeneous oscillatory instability and γ is the (small) amplitude of the forcing. The coefficients α , β

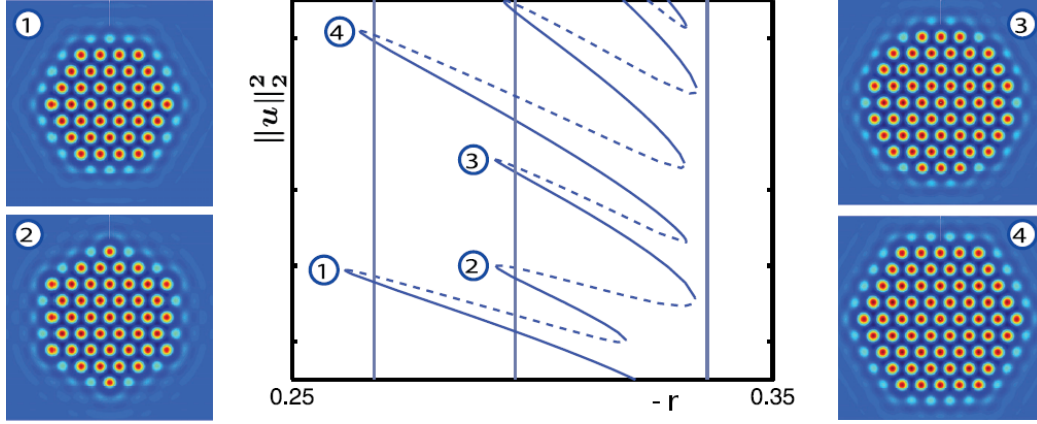


Figure 21: Bifurcation diagram for localized hexagons in SH23 showing the L_2 norm as a function of the bifurcation parameter $-r$. The sidepanels illustrate the solution profiles at the points labeled in the middle panel. Solid (dashed) lines indicate stable (unstable) solutions. From [10].

represent dispersion and nonlinear frequency correction, and are assumed to be $\mathcal{O}(1)$.³ In the following we drop the tildes on \tilde{x} and \tilde{t} .

Given the large number of parameters in equation (29), we expect that the system will display a wide range of behaviors. We restrict our attention to two cases corresponding to the parameter μ , namely when $\mu < 0$ and $\mu > 0$, respectively. In the case $\mu > 0$ the unforced system is self-exciting, but the free oscillations are damped when $\mu < 0$. In both cases, we assume that $\beta > 0$ and allow α to be positive or negative. The key observation is that the subharmonic forcing in the damped case creates a region of bistability between $A = 0$ and a large amplitude phase-locked state A_u^+ with uniform amplitude [7]. Inside this region one expects localized states created by the same mechanism as in the Swift-Hohenberg equation.

We consider the damped case $\mu < 0$ in the (ν, γ) plane and find that a saddle-node bifurcation involving the uniform phase-locked states A_u^+ and A_u^- occurs at $\gamma = \gamma_b \equiv |\nu - \beta\mu|/\rho_\beta$, $\rho_\beta \equiv \sqrt{1 + \beta^2}$, whenever $\nu > \nu_\beta \equiv -\mu/\beta$. At this point, the uniform state has two zero spatial eigenvalues and two real nonzero spatial eigenvalues. Along the larger amplitude A_u^+ branch the zero eigenvalues split along the real axis and A_u^+ has two-dimensional stable and unstable manifolds. Thus localized states may exist in the form of orbits homoclinic to A_u^+ . We calculate these as follows.

To find these states, we expand γ about the fold γ_b : $\gamma = \gamma_b + \epsilon^2\delta$, where $\epsilon^2\delta$ depends on the distance to the fold, $\epsilon \ll 1$ and $\delta > 0$. We solve the time-independent problem as in [7] (their Appendix C)

$$(\mathcal{L} + \mathcal{N}) \begin{bmatrix} U \\ V \end{bmatrix} = 0, \quad (30)$$

where $A = U + iV$, \mathcal{L} is a linear operator and \mathcal{N} is a nonlinear operator. Localized states

³Specifically if $\mu = \mathcal{O}(\epsilon^2)$ the forcing amplitude and frequency must satisfy $\gamma = \mathcal{O}(\epsilon^2)$, $\nu = \mathcal{O}(\epsilon^2)$ and the response satisfies $A = \mathcal{O}(\epsilon)$, $\tilde{x} = \epsilon x$ and $\tilde{t} = \epsilon^2 t$.

biasymptotic to A_u^+ take the form

$$\begin{bmatrix} U \\ V \end{bmatrix} = \begin{bmatrix} U \\ V \end{bmatrix}^+ + \begin{bmatrix} u \\ v \end{bmatrix}, \quad (31)$$

where the first term is the phase-locked state A_u^+ and the second term corresponds to space-dependent terms that decay to zero in the limit $x \rightarrow \pm\infty$. We can approximate A_u^+ by the series

$$\begin{bmatrix} U \\ V \end{bmatrix}^+ = \begin{bmatrix} U_0 \\ V_0 \end{bmatrix} + \epsilon \begin{bmatrix} U_1 \\ V_1 \end{bmatrix} + \epsilon^2 \begin{bmatrix} U_2 \\ V_2 \end{bmatrix} + \dots, \quad (32)$$

where

$$\begin{bmatrix} U_0 \\ V_0 \end{bmatrix} = \begin{bmatrix} \eta_b \\ 1 \end{bmatrix} \Upsilon_0, \quad \begin{bmatrix} U_1 \\ V_1 \end{bmatrix} = \sqrt{\delta} \begin{bmatrix} \xi_b \\ 1 \end{bmatrix} \Upsilon_1. \quad (33)$$

Here

$$\eta_b = \beta + \rho_\beta, \quad \xi_b = \frac{\eta_b \nu + (1 - \beta \eta_b) |A_u(\gamma_b)|^2}{\nu - (\beta + \eta_b) |A_u(\gamma_b)|^2}, \quad (34)$$

$$\Upsilon_0 = \frac{|A_u(\gamma_b)|}{\sqrt{1 + \eta_b^2}}, \quad \Upsilon_1 = \text{sgn}[\xi_b \eta_b + 1] \sqrt{\frac{\eta_b}{(\xi_b \eta_b + 1)(\xi_b - \eta_b)}}. \quad (35)$$

We expand the space-dependent second term in equation (31) as

$$\begin{bmatrix} u \\ v \end{bmatrix} = \epsilon \begin{bmatrix} u_1 \\ v_1 \end{bmatrix} + \epsilon^2 \begin{bmatrix} u_2 \\ v_2 \end{bmatrix} + \dots,$$

noting that all the quantities in this equation depend on x in the slow spatial scale $X \equiv \epsilon^{1/2}x$. The linear operator in equation (30) can be written $\mathcal{L} = \mathcal{L}_0 + \epsilon \mathcal{L}_1 + \epsilon^2 \mathcal{L}_2$, where

$$\mathcal{L}_0 = \begin{bmatrix} \mu + \gamma_b & -\nu \\ \nu & \mu - \gamma_b \end{bmatrix}, \quad \mathcal{L}_1 = \begin{bmatrix} 1 & -\alpha \\ \alpha & 1 \end{bmatrix} \partial_{XX}, \quad \mathcal{L}_2 = \begin{bmatrix} \delta & 0 \\ 0 & -\delta \end{bmatrix}. \quad (36)$$

The nonlinear terms can be written $\mathcal{N} = \mathcal{N}_0 + \epsilon \mathcal{N}_1 + \epsilon^2 \mathcal{N}_2 + \dots$, where

$$\mathcal{N}_0 = - \begin{bmatrix} U_0 & V_0 \end{bmatrix} \begin{bmatrix} U_0 \\ V_0 \end{bmatrix} \begin{bmatrix} 1 & -\beta \\ \beta & 1 \end{bmatrix}, \quad \mathcal{N}_2 = -2 \begin{bmatrix} U_0 & V_0 \end{bmatrix} \begin{bmatrix} U_1 + u_1 \\ V_1 + v_1 \end{bmatrix} \begin{bmatrix} 1 & -\beta \\ \beta & 1 \end{bmatrix}, \quad (37)$$

$$\mathcal{N}_2 = - \left\{ \begin{bmatrix} U_1 + u_1 & V_1 + v_1 \end{bmatrix} \begin{bmatrix} U_1 + u_1 \\ V_1 + v_1 \end{bmatrix} + 2 \begin{bmatrix} U_0 & V_0 \end{bmatrix} \begin{bmatrix} U_2 + u_2 \\ V_2 + v_2 \end{bmatrix} \right\} \begin{bmatrix} 1 & -\beta \\ \beta & 1 \end{bmatrix}. \quad (38)$$

At order ϵ^0 , the stationary solutions to equation (30) satisfy

$$\{\mathcal{L}_0 + \mathcal{N}_0\} \begin{bmatrix} U_0 \\ V_0 \end{bmatrix} = \begin{bmatrix} 0 \\ 0 \end{bmatrix}. \quad (39)$$

This equality can be determined from the definition of U_0 and V_0 . At order ϵ , we have the following expression

$$\{\mathcal{L}_0 + \mathcal{N}_0\} \begin{bmatrix} U_1 + u_1 \\ V_1 + v_1 \end{bmatrix} = -\{\mathcal{L}_1 + \mathcal{N}_1\} \begin{bmatrix} U_0 \\ V_0 \end{bmatrix}. \quad (40)$$

The X -independent terms in this equation cancel (from the definition of U_1 and V_1), and we obtain

$$\left\{ \mathcal{L}_0 + \mathcal{N}_0 - 2 \begin{bmatrix} 1 & -\beta \\ \beta & 1 \end{bmatrix} \begin{bmatrix} U_0^2 & U_0 V_0 \\ U_0 V_0 & V_0^2 \end{bmatrix} \right\} \begin{bmatrix} u_1 \\ v_1 \end{bmatrix} = \begin{bmatrix} 0 \\ 0 \end{bmatrix}. \quad (41)$$

Hence, we write

$$\begin{bmatrix} u_1 \\ v_1 \end{bmatrix} = \begin{bmatrix} \xi_b \\ 1 \end{bmatrix} B(X), \quad (42)$$

where $B(X)$ is an unknown function of X . We proceed to order ϵ^2 , obtaining

$$\{\mathcal{L}_0 + \mathcal{N}_0\} \begin{bmatrix} U_2 + u_2 \\ V_2 + v_2 \end{bmatrix} = -\{\mathcal{L}_1 + \mathcal{N}_1\} \begin{bmatrix} U_1 + u_1 \\ V_1 + v_1 \end{bmatrix} - \{\mathcal{L}_2 + \mathcal{N}_2\} \begin{bmatrix} U_0 \\ V_0 \end{bmatrix}. \quad (43)$$

As previously, the X -independent terms cancel. To obtain the solvability condition for this equation, we take the scalar product with

$$\Xi_b = \begin{bmatrix} -\eta_b & 1 \end{bmatrix}, \quad (44)$$

and eliminate the u_2, v_2 terms, so that

$$a_b B_{XX} = b_b (2V_1 B + B^2). \quad (45)$$

Here,

$$a_b = 1 + \alpha \xi_b + \alpha \eta_b - \eta_b \xi_b, \quad b_b = -\frac{\Upsilon_0(1 + \eta_b^2)}{\Upsilon_1^2}, \quad (46)$$

and we must have $b_b < 0$. Equation (45) yields either spatially homogeneous solutions $B = -2V_1$, or the solution

$$\begin{bmatrix} U \\ V \end{bmatrix} = \begin{bmatrix} U_0 \\ V_0 \end{bmatrix} - \epsilon \begin{bmatrix} U_1 \\ V_1 \end{bmatrix} + \dots, \quad (47)$$

corresponding to the other branch of uniform phase-locked states, A_u^- . Equation (45) also possesses X -dependent solutions of the form

$$B(X) = -3\Upsilon_1 \sqrt{\delta} \operatorname{sech}^2 \left\{ \left(\frac{\Upsilon_1 \sqrt{\delta}}{2a_b/b_b} \right)^{1/2} X \right\}. \quad (48)$$

These correspond to the solution

$$\begin{bmatrix} U \\ V \end{bmatrix} = \begin{bmatrix} U \\ V \end{bmatrix}^+ - 3\Upsilon_1 \sqrt{\gamma - \gamma_b} \begin{bmatrix} \xi_b \\ 1 \end{bmatrix} \operatorname{sech}^2 \left\{ (\gamma - \gamma_b)^{1/4} \left(\frac{\Upsilon_1}{2a_b/b_b} \right)^{1/2} x \right\}, \quad (49)$$

describing reciprocal oscillons, i.e., ‘holes’ in an otherwise uniformly oscillating state. If this state is followed numerically one finds that the holes deepen and fill with the trivial state $A = 0$. Pinning is absent since the spatial eigenvalues of A_u^+ are real.

Other localized states are also present and these are discussed in [7].

References

- [1] D. Avitabile, D. J. B. Lloyd, J. Burke, E. Knobloch and B. Sandstede. To snake or not to snake in the planar Swift-Hohenberg equation. *SIAM J. Appl. Dyn. Sys.*, **9**, pp. 704–733, 2010.
- [2] M. Beck, J. Knobloch, D. J. B. Lloyd, B. Sandstede and T. Wagenknecht. Snakes, ladders and isolas of localized patterns. *SIAM J. Math. Anal.* **41**, pp. 936–972, 2009.
- [3] J. R. Burke. Localized States in Driven Dissipative Systems. PhD Thesis, University of California at Berkeley, 2008.
- [4] J. Burke, S. M. Houghton and E. Knobloch. Swift-Hohenberg equation with broken reflection symmetry. *Phys. Rev. E* **80**, 036202, 2009.
- [5] J. Burke and E. Knobloch. Homoclinic snaking: structure and stability. *Chaos* **17**, 037102, 2007.
- [6] J. Burke and E. Knobloch. Localized states in the generalized Swift–Hohenberg equation. *Phys. Rev. E* **73**, 056211, 2006.
- [7] J. Burke, A. Yochelis and E. Knobloch. Classification of spatially localized oscillations in periodically forced dissipative systems. *SIAM J. Appl. Dyn. Sys.* **7**, pp. 651–711, 2008.
- [8] R. B. Hoyle. *Pattern Formation: An Introduction to Methods*, Cambridge University Press, 2006.
- [9] G. Kozyreff and S. J. Chapman. Asymptotics of large bound states of localized structures. *Phys. Rev. Lett.* **97**, 044502, 2006.
- [10] D. J. B. Lloyd, B. Sandstede, D. Avitabile and A. R. Champneys. Localized hexagon patterns of the planar Swift-Hohenberg equation. *SIAM J. Appl. Dyn. Sys.* **7**, pp. 1049–1100, 2008.
- [11] D. J. B. Lloyd and B. Sandstede. Localized radial solutions of the Swift-Hohenberg equation. *Nonlinearity*, **22**, pp. 485–524, 2009.
- [12] S. McCalla and B. Sandstede. Snaking of radial solutions of the multi-dimensional Swift-Hohenberg equation: A numerical study. *Physica D* **239**, pp. 1581–1592, 2010.
- [13] Y. Pomeau. Front motion, metastability and subcritical bifurcations in hydrodynamics. *Physica D* **23**, pp. 3–11, 1986.
- [14] W. van Saarloos. Front propagation into unstable states. *Phys. Rep.* **386**, pp. 29–222, 2003.
- [15] P. D. Woods and A. R. Champneys. Heteroclinic tangles and homoclinic snaking in the unfolding of a degenerate reversible Hamiltonian-Hopf bifurcation. *Physica D* **129**, pp. 147–170, 1999.

Lecture 9: Spatially localized structures in fluid flows

Edgar Knobloch: notes by Bevin Maultsby and Yuan Guo
with substantial editing by Edgar Knobloch

January 5, 2013

1 Defect-mediated snaking

In lecture 8 we explained the origin of the snaking-pinning region in parameter space containing a large multiplicity of spatially localized single-pulse states of ever greater length as well as a great variety of bound states of such structures called multipulse states. We also discussed the behavior of the system outside this region focusing on different types of depinning. We saw that in one spatial dimension structures in the Swift-Hohenberg equation grow by adding new cells on the outside, and examined some of the ways localized structures in two spatial dimensions grow in size as one follows them through parameter space. Certain aspects of this behavior appear to be universal in the sense that they depend only on the presence of a structurally stable transverse intersection of certain stable and unstable manifolds. However, other mechanisms for growth exist as well and we begin this lecture by describing one such mechanism that arises in the forced complex Ginzburg-Landau equation.

We consider a continuous system in one spatial dimension near a bifurcation to spatially homogeneous oscillations with natural frequency ω in the presence of spatially homogeneous forcing with frequency Ω . We focus on the behavior near strong resonances of the form $\Omega/\omega = n$, where $n = 1, 2$.

1.1 2:1 resonance

Suppose that a dynamical observable $w(x, t)$ takes the form

$$w = w_0 + Ae^{i\Omega t/n} + c.c. + \dots$$

where w_0 represents the homogeneous equilibrium state and $A(x, t)$ is a complex amplitude. Under appropriate conditions the oscillation amplitude $A(x, t)$ obeys the forced complex Ginzburg-Landau equation (FCGL),

$$A_t = (\mu + i\nu)A - (1 + i\beta)|A|^2A + (1 + i\alpha)A_{xx} + \gamma\bar{A}^{n-1}, \quad (1)$$

as obtained in lecture 8. Here μ represents the distance from onset of the oscillatory instability, ν is the detuning from the unforced frequency, and α , β and $\gamma > 0$ represent dispersion, nonlinear frequency correction and the forcing amplitude, respectively, all suitably scaled. Figures 1(a,b) show the (ν, γ) parameter plane for $n = 2$ (subharmonic resonance) and

suitable values of the remaining parameters. The figure shows the curve $\gamma = \gamma_0$ corresponding to a subcritical bifurcation of phased-locked states from the trivial $A = 0$ state. An analysis similar to that performed for the Swift-Hohenberg equation at $r = 0$ shows that this bifurcation is also associated with a bifurcation to spatially localized states. This time these states take a top hat form (the spatial eigenvalues λ at $\gamma = \gamma_0$ are real) and there is only one branch of such states that bifurcates at $\gamma = \gamma_0$. These eigenvalues become complex along $\gamma = \gamma_0^T$, i.e., the bifurcation at $\gamma = \gamma_0^T$ is precisely of the type discussed in lecture 7 in the context of the Swift-Hohenberg equation.¹ The figure also shows the line $\gamma = \gamma^T$ of analogous bifurcations that occur along the upper branch of the spatially uniform phase-locked states A^+ . These states are stable in time in the shaded region where the spatial eigenvalues λ are complex (region 1, lecture 6), and unstable in time outside, where the spatial eigenvalues are purely imaginary (region 4, lecture 6). The bifurcation at $\gamma = \gamma^T$ is supercritical (towards lower γ) between the two open diamonds and subcritical otherwise. The figure also shows the line of heteroclinic connections between $A = 0$ and $A = A^+$, i.e., the curve of collapsed snaking, where the localized states created at $\gamma = \gamma_0$ terminate (Fig. 2(a)). This curve, $\gamma = \gamma^{CS}$, crosses the curve $\gamma = \gamma^T$ at $\nu = \nu^*$. For $\nu > \nu^*$ the state $A = A^+$ is hyperbolic in space and heteroclinic connections involving A^+ are therefore possible. This is no longer so when $\nu < \nu^*$, where A^+ becomes a center. It follows that something new must take place as ν decreases through $\nu = \nu^*$.

Figure 2(a) shows the bifurcation diagram of solutions at $\nu = 1.35$, larger than the critical value $\nu^* \simeq 1.3077$, plotted in terms of the L^2 norm N defined as

$$N = \sqrt{\frac{1}{l} \int_{-l/2}^{l/2} |A(x)|^2 + |A_x(x)|^2 dx},$$

while Fig. 2(b) shows the real and imaginary part of the complex amplitude $A \equiv U + iV$ at a location high up the collapsed snaking branch, labeled L_0 in Fig. 2(a). The oscillations at the fronts at either end are a reflection of the complex spatial eigenvalues of A^+ in the region $\nu > \nu^*$.

The bifurcation diagram for steady solutions at a value of $\nu = 1.26 < \nu^*$ is shown in Fig. 3. Here we can see that the behavior of the spatially homogeneous states $A = 0$ and A^\pm remains similar to the previous case, but the behavior of the localized states is very different: a single snaking branch L_0 of spatially localized states bifurcates from $A = 0$ at $\gamma = \gamma_0$ but this branch must now interact with the spatially periodic solutions created at $\gamma = \gamma^T$ that surround A^+ when $\nu < \nu^*$. In standard homoclinic snaking between $A = 0$ and a periodic orbit (lecture 7) this process makes use of two intertwined branches of localized states in the form of localized wavepackets. Here, on the other hand, one starts with a single branch L_0 of top hat profiles on top of which oscillations gradually develop as one approaches the snaking region shown in Fig. 3(a). The resulting L_0 branch combines elements from the classical picture into a single branch and it does so via a distinct growth mechanism which we call defect-mediated snaking (DMS).

The growth of the localized states along the DMS branch is illustrated in Fig. 4. This branch contains two distinct families of states. One consists of uniform amplitude segments, which resemble the localized states found in regular homoclinic snaking and is represented

¹The superscript T refers to Alan Turing since the famous Turing instability is exactly of this type.

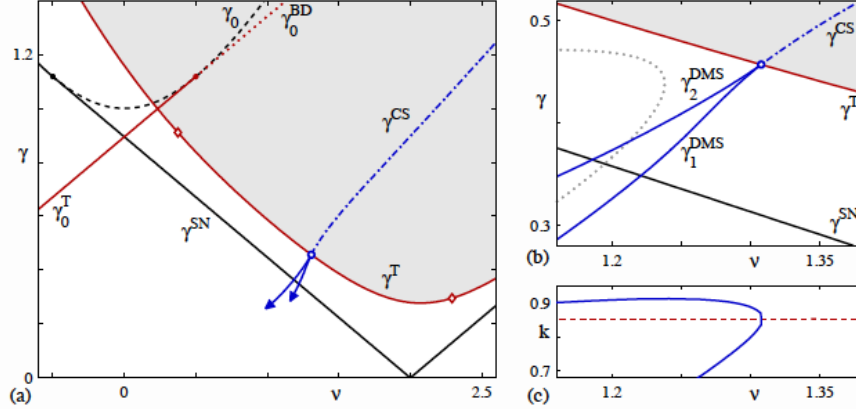


Figure 1: Parameter plane for $\alpha = -2$, $\beta = 2$ and $\mu = 1$ in Eq. (1). The curve γ_0 is plotted as a solid line in $\nu < \nu_\beta$, where the bifurcation to the uniform phase-locked states is supercritical, and dashed in $\nu > \nu_\beta$, where it is subcritical. The (solid) line γ_0^T in $\nu < \nu_\alpha$ represents a Turing bifurcation on $A = 0$. The corresponding bifurcation on the spatially homogeneous state A^+ is denoted by γ^T . The shaded region contains states A^+ that are stable in time. A heteroclinic cycle between $A = 0$ and $A = A^+$ forms along the dot-dashed line γ^{CS} corresponding to collapsed snaking. (b) Detail near the codimension-two point $\nu = \nu^*$ marked with an open circle, where collapsed snaking turns into defect-mediated snaking within $\gamma_1^{DMS} < \gamma < \gamma_1^{DMS}$. The dotted line shows the pinning region $\gamma_2^{HS} < \gamma < \gamma_2^{HS}$ containing regular homoclinic snaking. (c) The solid line shows the wavenumber range included in defect-mediated snaking as a function of ν . The dashed line shows $k_T(\nu)$. The wavenumber range shrinks to $k_T(\nu^*)$ as ν increases towards ν^* . From [10].

by solid lines. The other consists of defect segments, shown by means of dashed lines. Figure 4 shows that the DMS branch alternates between two types of uniform amplitude segments: those where $V(x)$ has a minimum at $x = 0$ (labeled by the spatial phase $\Phi = 0$) or maximum at $x = 0$ (labeled by the spatial phase $\Phi = \pi$); these two segments are separated by a defect segment. Evidently the defect is a steady state analog of a pacemaker: as one proceeds up the DNS branch the defect at $x = 0$ repeatedly splits in two thereby inserting a new wavelength into the localized states and pushing the existing cells apart.

The oscillatory wavetrain high up the DMS branch necessarily resembles the periodic wavetrain created at $\gamma = \gamma^T$ provided this wavetrain is hyperbolic in space. It turns out that this requirement corresponds to a region of the (γ, k) plane called the Eckhaus-stable region [7]. In this region a periodic wavetrain with wavenumber k is stable in time (Fig. 5, region I), while outside this region the wavetrain is unstable with respect to phase slips (Fig. 5, region II), which force the wavenumber into the Eckhaus-stable region. In region II all Floquet multipliers of the wavetrain lie on the unit circle and the wavetrain is nonhyperbolic. Consequently no heteroclinic connections involving such a wavetrain are possible. It follows that in this case the boundary of the snaking or pinning region is determined by the requirement that the wavenumber k at γ_1^{DMS} and γ_2^{DMS} is neutrally

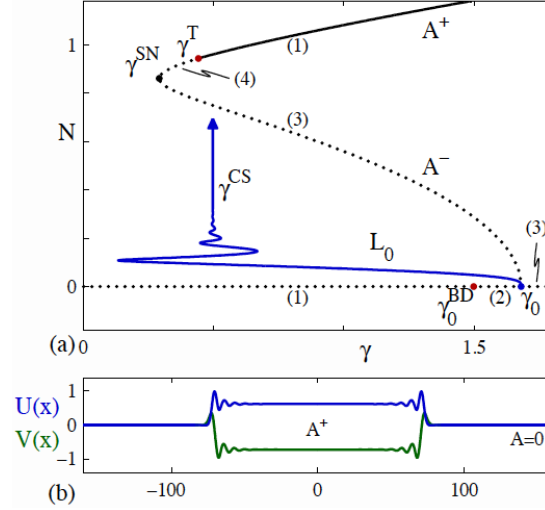


Figure 2: Bifurcation diagram corresponding to the $\nu > \nu^*$, where the branch of localized states undergoes collapsed snaking towards $\gamma = \gamma^{\text{CS}} > \gamma^T$. The localized states are everywhere unstable but are shown as a solid line. The remaining solid (dotted) lines correspond to stable (unstable) homogeneous states. (b) A sample solution far up the collapsed snaking branch, at $\gamma \approx \gamma^{\text{CS}}$. From [10].

stable with respect to the Eckhaus instability (Fig. 5, end points of the curve C). In this case it is therefore the γ -dependence of the wavenumber k selected by the fronts on either side that is ultimately responsible for the boundaries of the snaking region. Although it looks like this mechanism is quite different from that discussed in lecture 8, viewed appropriately, it is in fact the same [4].

1.2 1:1 resonance

Similar behavior to that described above takes place when $n = 1$, i.e., in the 1:1 resonance, even though the $A = 0$ state is now absent and the phase symmetry $(A) \rightarrow (Ae^{2\pi i/n})$ is trivial [10]. Instead of describing this behavior we focus on different types of depinning that arises in systems of this type.

Figure 6 shows type I depinning that is associated with the top hat profiles present for $\nu > \nu^*$: the structure either expands uniformly or shrinks uniformly, unless γ is chosen such that the uniform state becomes unstable (as in Fig. 6(c)).

More interesting is type-II depinning that occurs outside of the DMS pinning region $\nu < \nu^*$. We find that, in contrast to the depinning in the Swift-Hohenberg equation, in the FCGL the fronts move by gradually deleting cells through repeated phase slips. These phase slips eliminate/insert new wavelengths into the structure and hence control the inward/outward speed of the fronts on either side of the structure. These phase slips take place at preferred locations within the structure implying that the structure grows so to speak from within, with a constant front profile at either end. The phase slips occur because the depinned fronts move, thereby compressing/stretching the structure and forcing

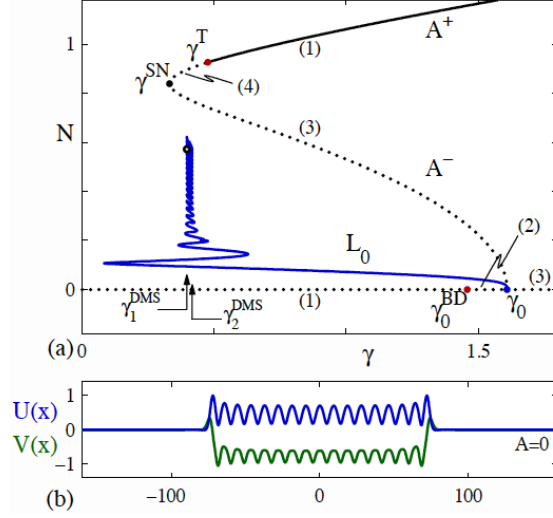


Figure 3: (a) Bifurcation diagram corresponding to the $\nu = 1.26$, where the branch of localized states undergoes defect-mediated snaking. The localized states are present within the pinning interval $\gamma_1^{DMS} \leq \gamma \leq \gamma_2^{DMS}$. The remaining solid (dotted) lines represent stable (unstable) homogeneous solutions. (b) A sample solution high up the snaking branch. From [10].

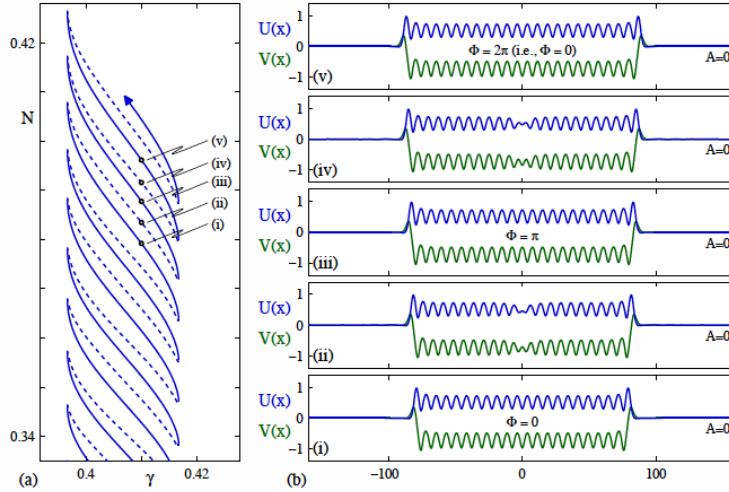


Figure 4: (a) Detail of the L_0 snaking branch. The uniform amplitude segments of the branch are shown as solid lines, while the defect segments are shown as dashed lines. (b) Five sample solutions, all at $\gamma = 0.41$. The spatial phase Φ is indicated for each profile on a uniform amplitude segment. From [10].

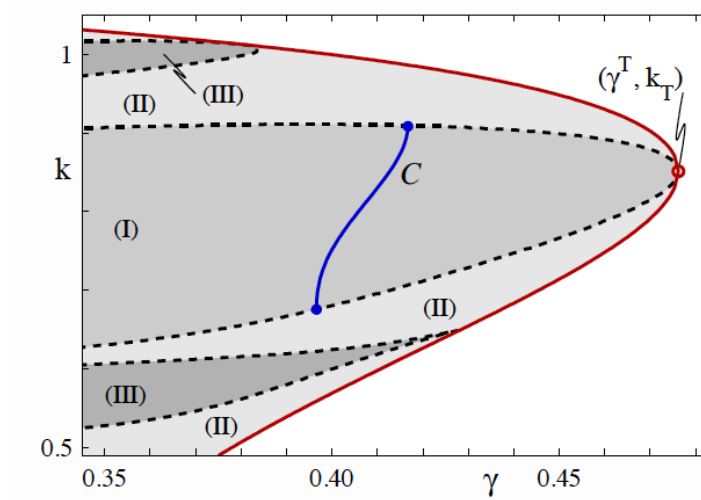


Figure 5: Section of the surface of spatially periodic states for the parameters used. The surface is bounded by the neutral stability curve of the A^+ state. The curve C shows the wavenumber $k(\gamma)$ of the patterns included in defect-mediated snaking; this wavenumber spans the width of the Eckhaus-stable interval. From [10].

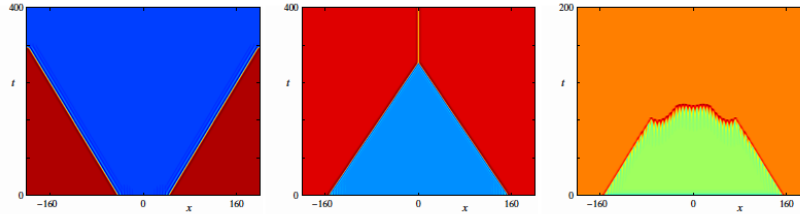


Figure 6: Type-I depinning at $\gamma = \gamma^{CS} + d_\gamma$. (a) $d_\gamma = 0.04$; (b) $d_\gamma = -0.04$; (c) $d_\gamma = -0.24$. From [10].

the wavenumber outside of the Eckhaus-stable region. The phase slip then attempts to return the wavenumber into the stable region until pattern compression/expansion moves it outside again, triggering a further phase slip.

When the structure is short the phase slips occur in the center (Fig. 7); for longer structures phase slips occur simultaneously in a pair of symmetrically located points which move inward and outward with the moving fronts (Fig. 7). We may refer to the former case as slow depinning and the latter as fast depinning. Similar phase slips eliminate phase when a nonlinear wave is incident on a solid boundary [15]. Figure 8 looks at this process in more detail.

Evidently in this type of problem the front speed is determined by the competition between natural front motion and the ability of the phase slips to keep up. This is a subtle process that remains incompletely understood [11].

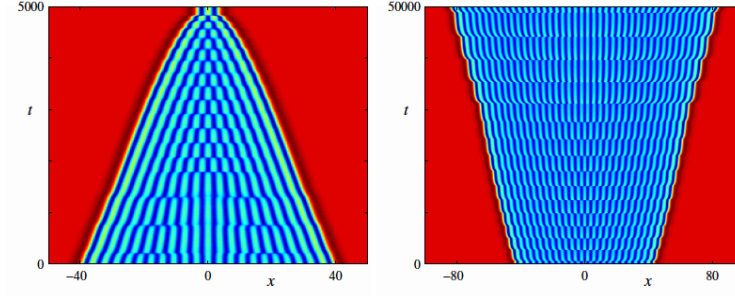


Figure 7: Type-II LS depinning at (a) $\gamma = \gamma_1^{DMS} - 1 \times 10^{-3}$; (a) $\gamma = \gamma_2^{DMS} + 1 \times 10^{-4}$. From [10].

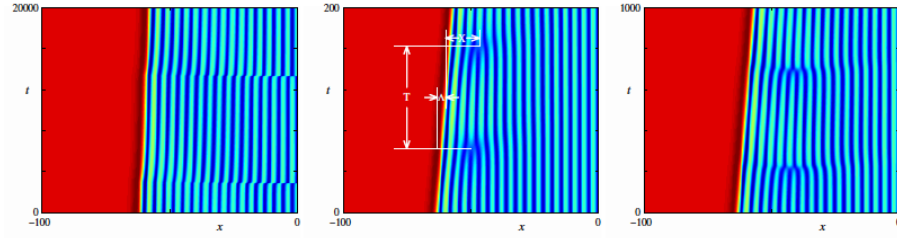


Figure 8: Type-II depinning: (a) Slow depinning ($d - \gamma = -2 \times 10^{-5}$): phase slips take place at the center $x = 0$. (b) Fast depinning ($d_\gamma = -4 \times 10^{-3}$): phase slips take place at a constant distance from the moving front. (c) Intermediate case ($d_\gamma = -1 \times 10^{-3}$): phase slips gradually move towards the front. From [10].

2 Spatially localized binary fluid convection

Convectons are localized convecting structures. Examples of convectons arising in several different systems were described in lecture 6. One of these systems is binary mixture convection. A binary mixture consists of two miscible components, one of which consists of larger molecular weight molecules than the other. Common experimentally studied examples are salt-water and ethanol-water mixtures. Both mixtures are characterized by cross-diffusion quantified by a separation ratio S . When $S > 0$ the lighter component of the mixture migrates towards the hot boundary while the heavier component migrates towards the cold boundary. This is a kinetic effect and indeed $S > 0$ is typical of gas mixtures. Liquid mixtures at appropriate concentrations may have $S < 0$.² When such a mixture is heated from below the heavier component migrates towards the lower hot boundary and this effect increases the local density and hence competes with thermal buoyancy. In the absence of diffusion effects a mixture with density that decreases in the vertical direction would be stable. This is no longer necessarily the case if diffusion effects are included. Since heat diffuses much faster than concentration temperature perturbations equilibrate rapidly while concentration perturbations do not. A fluid element displaced upwards therefore cools but retains its excess concentration which pushes it back down. If the “spring” provided by the concentration is strong enough to overcome viscosity (i.e., if S is sufficiently negative) this mechanism will lead to growing oscillations. This phenomenon, sometimes called overstability, is characteristic of binary mixtures placed in a thermal gradient. There is a second characteristic effect as well: steady convection is subcritical. This is because the concentration reduces thermal buoyancy near the lower boundary and hence delays the onset of steady convection. However, once steady convection is generated, for example, due to a finite amplitude instability, it mixes the concentration thereby reducing its stabilizing effect. Thus finite amplitude steady convection occurs more easily (i.e., for lower imposed temperature difference) than small amplitude convection.

The above physics is independent of the way the stabilizing concentration gradient is set up. In doubly diffusive convection concentration difference is imposed via the concentration boundary conditions at top and bottom. This is not easily done in the laboratory (although it is possible [14]). Here binary mixtures with a negative separation ratio have a great advantage since the required stabilizing concentration gradient is set up in response to the thermal gradient, i.e., the concentration gradient is set up in a closed container, and no contact with a concentration bath via permeable walls is required.

In the Boussinesq approximation binary fluid convection is described by the Boussinesq equation of state,

$$\rho = \rho_0(1 - \alpha(T - T_0) + \beta(C_1 - \bar{C}_1)), \quad \alpha > 0, \beta > 0,$$

where C_1 is the concentration of the heavier component. The mass flux of the latter depends both on the concentration gradient via the usual Fick’s law but also on the temperature

²This case is sometimes referred to as the anomalous Soret effect.

gradient via cross-diffusion, the *Soret effect*:³

$$\mathbf{j}_1 = -\rho_0 D (S_{\text{Soret}} \bar{C}_1 (1 - \bar{C}_1) \nabla T + \nabla C_1).$$

Here D is the molecular diffusivity of the heavier component. The resulting system is described by the dimensionless equations

$$\begin{aligned} \mathbf{u}_t + (\mathbf{u} \cdot \nabla) \mathbf{u} &= -\nabla P + Pr R [(1 + S)\theta - S\eta] \hat{\mathbf{z}} + Pr \nabla^2 \mathbf{u} \\ \theta_t + (\mathbf{u} \cdot \nabla) \theta &= w + \nabla^2 \theta \\ \eta_t + (\mathbf{u} \cdot \nabla) \eta &= \tau \nabla^2 \eta + \nabla^2 \theta \end{aligned}$$

together with the incompressibility condition

$$\nabla \cdot \mathbf{u} = 0.$$

Here $\mathbf{u} = (u, w)$ is the velocity field in (x, z) coordinates (assumed to be two-dimensional), P is the pressure, and θ is the departure of the temperature from the conduction profile, in units of the imposed temperature difference $\Delta T > 0$ across the layer. The variable η is defined such that its gradient represents the dimensionless flux of the heavier component. Thus $\eta = \theta - \Sigma(x, z, t)$, where $T = 1 - z + \theta(x, z, t)$ and $C = 1 - z + \Sigma(x, z, t)$ is the concentration of the heavier component in units of the concentration difference that develops across the layer as a result of cross-diffusion. The system is specified by four dimensionless parameters: the Rayleigh number

$$R = \frac{g \alpha \Delta T l^3}{\nu \kappa}$$

providing a dimensionless measure of the imposed temperature difference ΔT , the separation ratio

$$S = \bar{C}_1 (1 - \bar{C}_1) S_{\text{Soret}} \frac{\beta}{\alpha}$$

that measures the resulting concentration contribution to the buoyancy force due to cross-diffusion, and the Prandtl and Lewis numbers defined as

$$Pr = \frac{\nu}{\kappa}, \quad \tau = \frac{D}{\kappa}.$$

Here ν is the kinematic viscosity of the mixture, κ is the thermal diffusivity and l is the height of the layer. All lengths have been nondimensionalized using l while time has been nondimensionalized using the thermal diffusion time in the vertical, l^2/κ .

As in all problems of this type the boundary conditions are key. Experimentally realistic boundary conditions demand that the velocity vanishes at the top and bottom (no-slip boundary conditions) and that the boundaries are impermeable (the vertical flux of C_1 vanishes on the boundaries). We also assume that the thermal mass of the boundaries is large compared to that of the liquid mixture so that the boundaries remain at fixed temperature even while the fluid convecting. If this is the case (in practice this is rarely

³In this discussion we ignore the *Dufour effect* which is responsible for setting up a temperature gradient in response to a concentration gradient. This effect is small in liquids although it may be important in gas mixtures.

checked) we may suppose that the temperature fluctuation θ vanishes at the top and bottom. We thus have:

$$u = w = \theta = \eta_z = 0 \quad \text{on} \quad z = 0, 1.$$

It remains to specify the boundary conditions in the horizontal. In the following we use either periodic boundary conditions (PBC) with period Γ in x , or Neumann boundary condition (NBC), or insulating closed container boundary conditions (ICCBC) at $x = \pm\Gamma/2$, where

$$\begin{aligned} \text{NBC} \quad & u = w_x = \theta_x = \eta_x = 0 \quad \text{on} \quad x = 0, \Gamma, \\ \text{ICCBC} \quad & u = w = \theta_x = \eta_x = 0 \quad \text{on} \quad x = 0, \Gamma. \end{aligned}$$

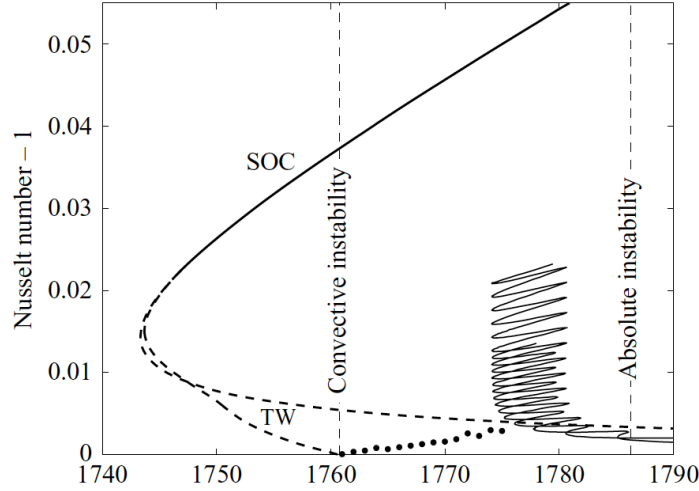


Figure 9: Bifurcation diagram showing the time-averaged Nusselt number \bar{N} as a function of the Rayleigh number R when $\Gamma = 60$. The conduction state loses stability at $R_c = 1760.8$. Steady spatially periodic convection (SOC) acquires stability at a parity-breaking bifurcation marking the destruction of a branch of spatially periodic traveling waves (TW). Above threshold small-amplitude dispersive chaos is present (solid dots), which leads into the pinning region ($1774 < R < 1781$) containing a multiplicity of stable localized states of both even and odd parity. From [1].

2.1 Convectons

The above equations and boundary conditions are invariant under the symmetries $x \rightarrow -x$, $(u, w, \theta, \eta) \rightarrow (-u, w, \theta, \eta)$ and $(x, z) \rightarrow (-x, 1-z)$, $(u, w, \theta, \eta) \rightarrow -(u, w, \theta, \eta)$ analogous to the symmetries $x \rightarrow -x$, $u \rightarrow u$ and $x \rightarrow x$, $u \rightarrow -u$ of SH35. We expect, therefore, the presence of steady solutions satisfying

$$\begin{aligned} (u(x, z), w(x, z), \theta(x, z), \eta(x, z)) &= (-u(-x, z), w(-x, z), \theta(-x, z), \eta(-x, z)), \\ (u(x, z), w(x, z), \theta(x, z), \eta(x, z)) &= -(u(-x, 1-z), w(-x, 1-z), \theta(-x, 1-z), \eta(-x, 1-z)) \end{aligned}$$

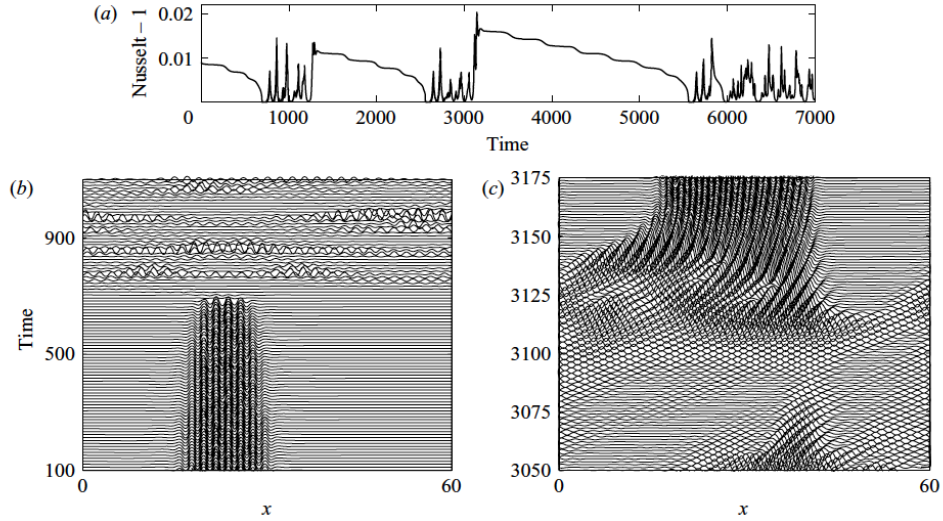


Figure 10: (a) The Nusselt number $N(t)$ at $R = 1774$ showing relaxation oscillations between dispersive chaos and localized steady convection. (b,c) Space-time plots at two different time intervals in the time series (a), showing (b) the destruction of localized steady convection, and (c) the formation of localized steady convection from dispersive chaos. Time is in units of the thermal diffusion time in the vertical. From [1].

relative to a suitable origin in x . The former have even parity and correspond to the states L_0, L_π of SH35 while the latter have odd parity when $z = 1/2$ and correspond to the states $L_{\pi/2}, L_{3\pi/2}$. These are the only steady solutions that can bifurcate from the conduction state $(u, w, \theta, \eta) = \mathbf{0}$.

Spatial stability analysis of the conduction state of the type described in lecture 7 shows that on the real line a branch of periodic states with wavenumber $k = k_c$ bifurcates from the conduction state when $R = R_c$ and that this bifurcation (if it exists and is subcritical) is accompanied by the simultaneous bifurcation of even and odd spatially localized states. As explained on physical grounds we expect the primary bifurcation to periodic states to be subcritical when S is sufficiently negative and this is indeed the case.

The equations describing binary fluid convection are not variational, however, and consequently one finds persistent time-dependent solutions as well. These are typically associated with the presence of a Hopf bifurcation from the conduction state that precedes the onset of steady convection (Fig. 9). This bifurcation generates branches of traveling and standing waves [9]. The former are subcritical (Fig. 9) implying that neither time-dependent state is stable near onset [9]. Instead one finds that the solution takes the form of a spatiotemporally chaotic states called dispersive chaos ([3], solid dots in Fig. 9). Numerical time-integration shows that this state undergoes a rapid focusing instability as R increases, forming transient localized structures (Fig. 10(b,c)) which then gradually erode in the same manner as one finds in SH35 and ultimately collapse back into spatiotemporal chaos. Since this state is unstable to the focusing instability, the process repeats, generating a chaotic relaxation oscillation (Fig. 10(a)). The successive localized states tend to form in the same location because the collapsing structure leaves a footprint in the slowly diffusing concentration field.

A very small increase in R , to $R = 1775$, suffices to stabilize the localized structure against erosion and the localized state that grows out of the chaotic state remains stable for the duration of the simulation [1]. Based on the study of SH35 described in lecture 8 we interpret this transition as passage from outside to inside of the pinning region. Of course the present system yields an eighth order dynamical system for steady states so one needs to be careful with this type of argument but here it appears as if the additional dimensions do not play a role.

It is important to observe that when the localized structure is present the waves in the background disappear, creating a localized state embedded in a quiescent background conduction state. At first sight this is surprising since, as already mentioned, the conduction state is unstable to oscillations. Batiste et al. [1] show that in the regime where waves are absent the conduction state is only convectively unstable. This means that a localized disturbance propagates faster than it grows⁴ and so interacts with the localized structure before it has had a chance to develop. The collision with the localized structure reduces locally the length scales and hence enhances dissipation. In fact, in the convectively unstable regime the presence of nonperiodic boundaries always leads to eventual decay [15] and this is the case here as well. To get sustained waves in the background one must raise the Rayleigh number R past the threshold for absolute instability (Fig. 9); this threshold can be computed by solving a linear boundary value problem [1]. The solution determines the dispersion relation $\omega(k)$ as a function of R . At the absolute instability threshold $R = R^*$ this relation has a double root $\omega(k)$, provided a certain pinching condition holds. However, the double root is usually located in the complex k plane and hence the boundary value problem that has to be solved is in fact complex-valued. This requirement together with the condition of marginal stability (i.e., the requirement that ω is real) yields four conditions which suffice to determine ω , $k = k_r + ik_i$ and R^* . Figure 11 shows k_i and ω as functions of k_r at $R < R^*$ and $R > R^*$, demonstrating the presence of a double root at $R = R^*$.

Figure 9 summarizes the results in the form of a bifurcation diagram showing the (time-averaged) convective heat flux $\bar{N} - 1$ as a function of R for the parameters used. The figure shows the branch of traveling waves (TW) and indicates that steady overturning convection (SOC) remains unstable past the fold on the left and only acquires stability at a higher amplitude, where the TW branch terminates on the SOC branch in a parity-breaking bifurcation. Near this bifurcation the phase speed of the TW decreases to zero as the square root of the distance from the termination point. Stationary convectons are present in a parameter regime where the SOC are stable and it is this fact that is ultimately responsible for their stability. After all, long convectons resemble a long interval of the periodic state and so tend to inherit the stability properties of the coexisting periodic state.

To construct the unstable SOC and TW solutions (dashed lines) we have employed numerical continuation. The ability to perform such computations is key for understanding the behavior of flows of this complexity. Numerical continuation is of course particularly helpful for constructing the convecton branches. Here the fact that some of these states are stable is of great help since they can be found by direct numerical simulation. Once one even and one odd state is found in this way the equilibrated solution can be inserted into the continuation code and the whole snaking diagram constructed (Fig. 9). We mention

⁴Recall that standing waves are unstable to traveling waves.

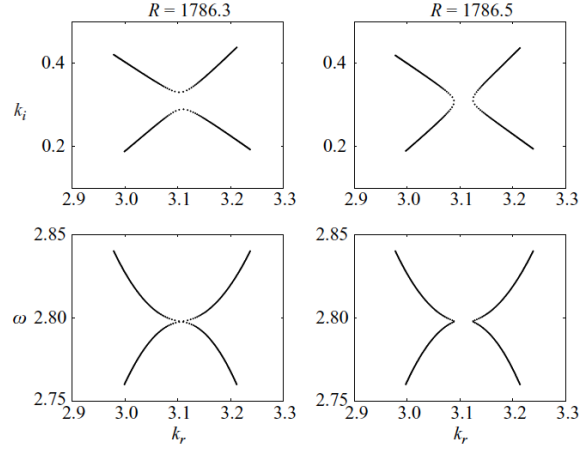


Figure 11: Spatial branches of zero growth rate modes in the complex k plane showing the pinching process that occurs at $R = R^* \approx 1786.4$, when $S = -0.021$, $\sigma = 6.22$, $\tau = 0.009$. From [1].

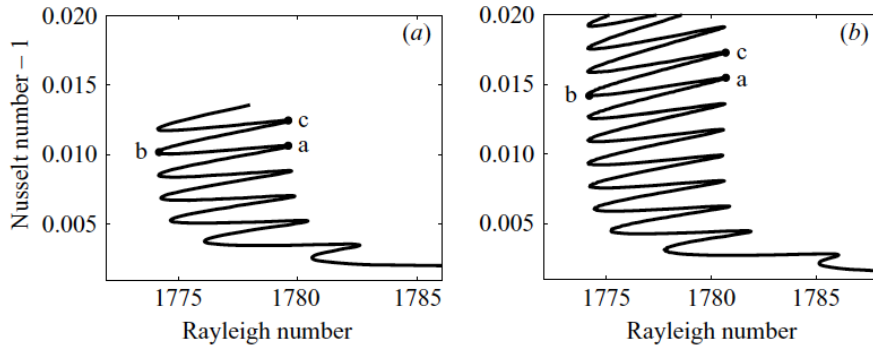


Figure 12: Branches of (a) odd- and (b) even-parity convectons in a $\Gamma = 60$ domain as a function of the Rayleigh number R . Both branches exhibit snaking. From [1].

that in the present problem the asymmetric states on the rungs of the snakes-and-ladders structure generically drift, i.e., they take the form of drifting (and unstable) convectons. Such states can be computed by looking for steady solutions in a moving frame, with the speed c of the frame determined as a nonlinear eigenvalue, much as in lecture 8. These states, like the standing waves SW created in the primary Hopf bifurcation, are not shown in the figure.

Figure 12(a) shows a detail of the snaking branch of odd parity convectons while Fig. 12(b) shows the corresponding even parity convectons. As in SH35 the solutions lying on the segments above the left folds and below the right folds correspond to stable solutions, indicating that the pinning or snaking region is populated by a large number of coexisting stable localized states (as well as periodic convection). Figure 13 shows sample convecton profiles near the folds on each branch in Fig. 12 at the points indicated. These indicate that each convecton acquires a pair of rolls between corresponding folds, one on each side,

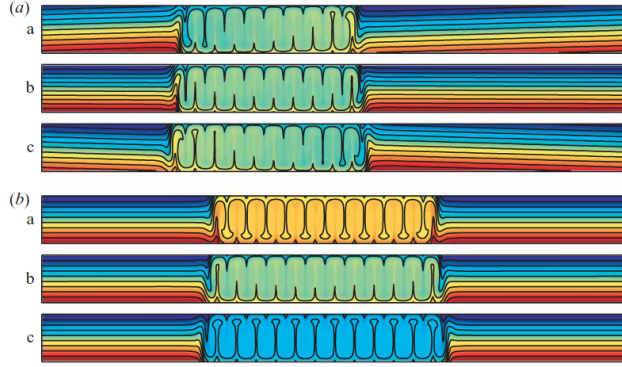


Figure 13: Convecton profiles on (a) the odd-parity branch, and (b) the even-parity branch at the turning points indicated in Fig. 12(a,b) in terms of contours of constant C . Each wavelength contains a pair of rolls. From [1].

as one goes up each snaking branch. Once again, this is exactly as in SH35. However, there is one new effect that is absent from SH35. The structure of even convectons is affected by the rolls at either end: a counter-clockwise rotating roll at the right end entrains fluid of higher concentration into the convecton, while a clockwise roll at the left does the same, thereby enhancing the mean concentration within the structure (point a in Fig. 12(b)). The opposite occurs at point c in Fig. 12(b) since the direction of rotation of outermost rolls is now opposite to that at point a . Thus at point c the structure entrains lower concentration fluid from above at both ends resulting in lower than average concentration within the structure. The effect is yet more interesting for odd parity convectons. For these states both outermost rolls rotate in the same direction, implying that at point a in Fig. 12(a) the structure entrain higher concentration fluid from the right while rejecting it on the left. This results in a pronounced concentration gradient within the structure. The net effect is that an odd parity convecton acts like a *pump*: at point a it pumps concentration from right to left, while at point c it pumps concentration from left to right. This effect is visible in the slight tilt of the constant concentration contours outside of the convecton (Fig. 13(a)).

3 Snaking in periodic and finite domains

We now look at snaking occurring in domains with different boundary conditions. To illustrate what happens when the lateral boundary conditions are changed from PBC to ICCBC we show in Fig. 14(a) the snaking diagram in a periodic domain of length $\Gamma = 14$. This is qualitatively similar to Fig. 9 except that here the whole snaking diagram has been computed. In particular we see that, when the localized structure fills almost the whole domain, snaking ceases and the snaking branches exit the pinning region and terminate on a branch of periodic states, here P_7 , consisting of 7 pairs of rolls. Except for the difference in the widths of the pinning regions for even and odd states (discussed further below) the picture is as expected on the basis of SH35.

Figure 14(b) shows the corresponding result in a $\Gamma = 14$ domain with ICCBC and the same parameter values. The picture is dramatically different. The widths of the snaking

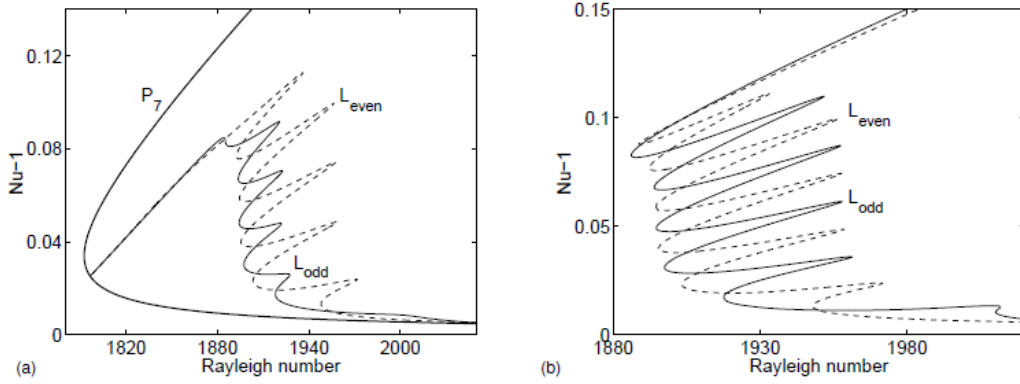


Figure 14: Binary fluid convection with $\Gamma = 14$: $S = -0.1$, $\sigma = 7$, and $\tau = 0.01$. (a) Periodic boundary conditions (PBC). (b) Insulating closed container boundary conditions (ICCBC). From [12].

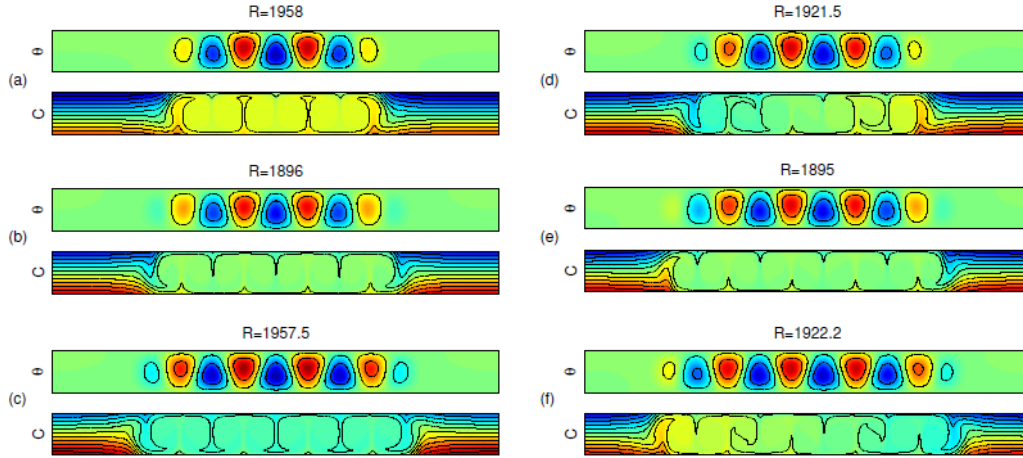


Figure 15: Convectons with PBC, $\Gamma = 14$. Profiles (a)-(c) have even parity while (d)-(f) have odd parity. From [12].

regions for the two convection types are now identical, and the convecton branches no longer terminate on a branch of periodic states. This is, of course, because no periodic states exist with ICCBC. Instead the snaking branches continuously change into large amplitude branches of spatially extended states that fill the domain – except for defects at the lateral boundaries where the vertical velocity is required to vanish.

The fact that the ICCBC have such a large effect on odd parity convectons is a consequence of the interaction between concentration pumping and the lateral boundaries. The presence of a lateral wall in the pumping direction results in concentration build-up. As a result the convecton no longer sits in a homogeneous background, and is instead confined between two different concentrations. Such a convecton is best thought of as half of a bound state of two back-to-back odd parity convectons on a domain $\Gamma = 28$ but with PBC. This construction is in fact exact with NBC instead of ICCBC but the ICCBC results are actually quite close to the NBC results except for the vicinity of the lateral walls. Since such bound

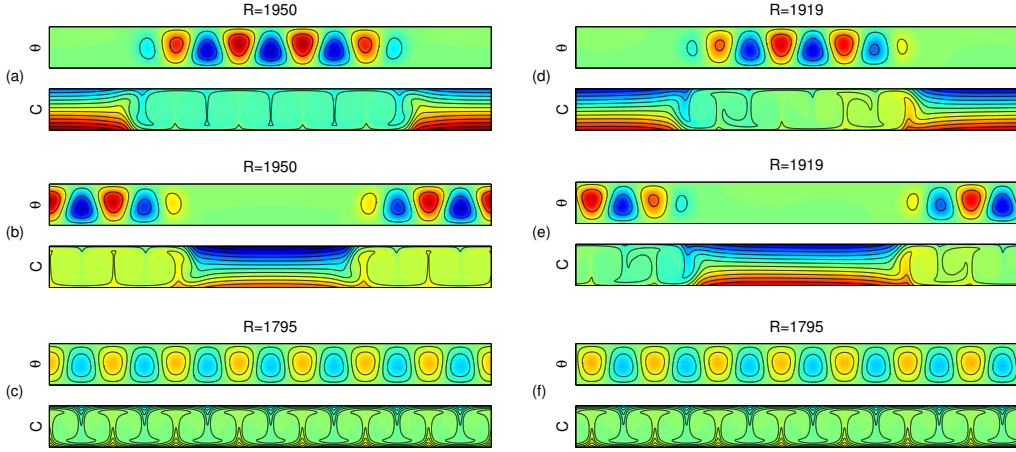


Figure 16: Convectons and holes with PBC, $\Gamma = 14$. Profiles (a)-(c) have even parity while (d)-(f) have odd parity. From [12].

states occupy the same pinning region as the one-pulse even convectons it follows that the width of odd parity states with ICCBC will be the same as the width of even parity states with ICCBC, in contrast to the PBC case.

3.1 Periodic boundary conditions (PBC)

To understand the above argument in more detail we revisit the PBC case and note that we can shift each solution horizontally by half the domain width and/or reflect it in the horizontal midplane. Consider, for example, Fig. 16. In Fig. 16(a), we see an even parity convecton inside the pinning region at $R = 1950$; to get to Fig. 16(b), we shift Fig. 16(a) by half the domain width and reflect the result in the midplane. Although there is now a hole present in the middle of the container, it is the same solution and hence falls on the same solution branch in Fig. 14. Moreover, Figs. 16(a) and (b) are phase-matched with the periodic state shown in Fig. 16(c), and in fact bifurcate from it at $R = 1795$.

We repeat this process for the odd parity states in Figs. 16(d)–(f). In this case, Figs. 16(d) and 16(e) bifurcate from the periodic state in Fig. 16(f) and do so again at $R = 1795$. This is because the periodic states in Figs. 16(c) and (f) are related by translation by half a wavelength, i.e. they are the same solutions. The even and odd parity convectons are of course different solutions. We see therefore that the bifurcation from the branch of periodic states that leads to localized states produces simultaneously two branches of such states, of even and odd parity (Fig. 14(a)). This is a generally property of Eckhaus bifurcations from a period wavetrain and can be demonstrated using Floquet theory together with weakly nonlinear theory.

However, secondary bifurcations of Eckhaus type do not always generate spatially modulated states that snake. Figure 17 shows an example of a secondary bifurcation on the branch P_6 , consisting of 6 pairs of rolls within Γ , that leads to the simultaneous branching of a pair of nonsnaking branches. Close to the bifurcation these states, hereafter mixed mode states M_{even} and M_{odd} , take the form of large scale, small amplitude modulation of a

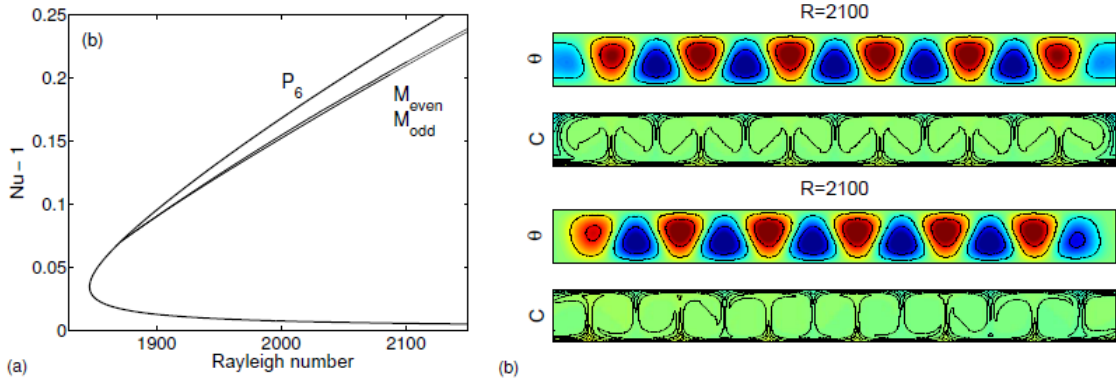


Figure 17: Mixed modes M_{even} and M_{odd} with PBC and $\Gamma = 14$. (a) Bifurcation diagram showing that both modes bifurcate from P_6 but do not snake. (b) Profiles of M_{even} (top panels) and M_{odd} (bottom panels) showing the presence of a defect at either side.

periodic wavetrain and hence resemble the hole states discussed above. However, as one follows the hole branches away from the bifurcation point the hole deepens and broadens, and as this happens, snaking sets in. When Γ is finite the resulting states are nothing by the usual convectons, and the hole states therefore reconnect to the primary branch of periodic states when these are still of very small amplitude. In contrast, the small dip in the states M_{even} and M_{odd} does not broaden as one moves away from the bifurcation, although it deepens forming a defect in an otherwise periodic wavetrain (see Fig. 17). On the real line states of this type describe a periodic array of defects in a periodic wavetrain, with defect period Γ .

3.2 Neumann Boundary Conditions (NBC)

Neumann boundary conditions require that the lateral walls are free-slip and no-flux but translation invariance is now absent. All solutions with NBC on a domain Γ can be constructed from the set of PBC solutions with period 2Γ simply by translating the PBC solutions and keeping those that satisfy NBC on the smaller domain. This construction works because of the presence of “hidden” symmetry [5]. Observe that even solutions with NBC set in via a pitchfork bifurcation from the conduction state but set in via a transcritical bifurcation with other boundary conditions respecting reflection symmetry. Moreover, solutions with NBC have a well-defined mode number that specifies the number of “wavelengths” in the domain; in contrast, with generic boundary conditions the number of cells is not fixed, and will in general change as parameters are varied. All this is a consequence of hidden symmetry inherited from the translation invariance of the PBC problem within which the NBC problem is embedded.

In Fig. 18(a) we show an even solution at $R = 1920$ satisfying NBC with $\Gamma = 14$. The location of this solution is indicated in Fig. 18(b) using a solid dot. The solution satisfies PBC with period 2Γ , and terminates on a branch labeled SOC_{14} consisting of 14 cells within Γ . Of course SOC_{14} is the same as (a segment of) P_7 but we no longer have periodic boundary conditions and cannot therefore refer to SOC_{14} as a periodic state. Figure 18(a)

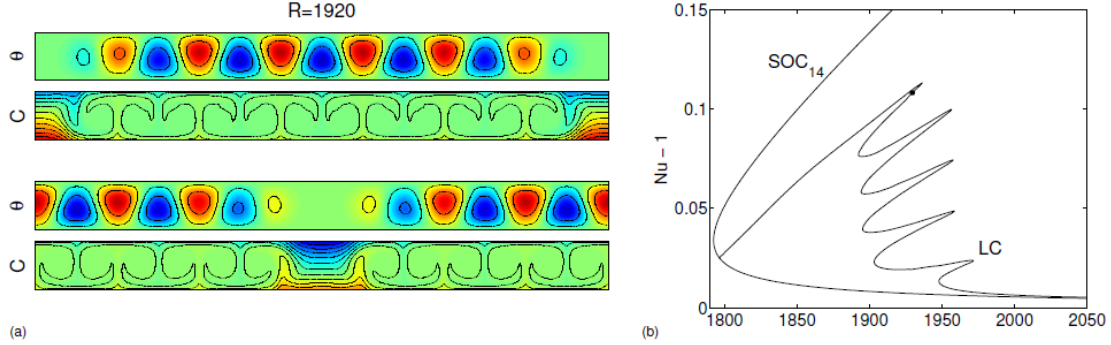


Figure 18: Even parity states with NBC and $\Gamma = 14$. (a) Convecton (top panels) and hole (bottom panel) states at $R = 1920$. These solutions are related by a hidden translation. (b) The corresponding bifurcation diagram showing a single branch of localized states LC (convectons). The dot indicates the location of *both* profiles in (a).

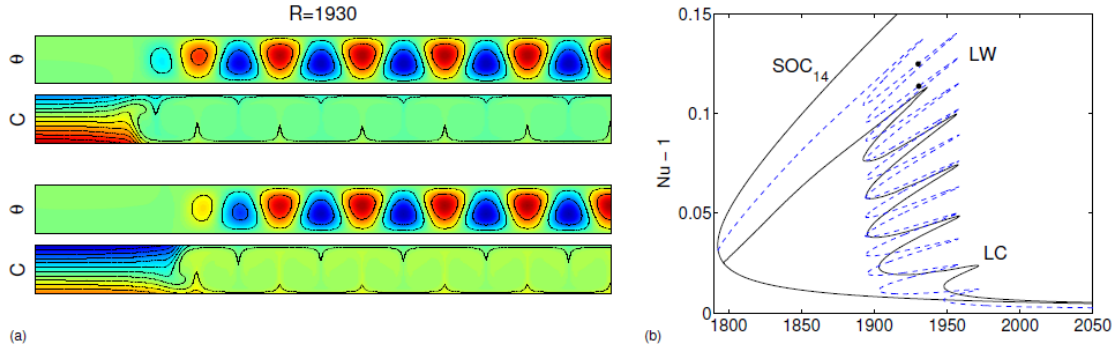


Figure 19: Wall states with NBC and $\Gamma = 14$. (a) Two different wall states LW at points indicated in the bifurcation diagram in (b). The wall states snake with double the frequency of the LC states in Fig. 18, superposed for comparison.

also shows that despite NBC (which destroy translations) we can still construct a hole state from a convecton state by embedding the problem in the PBC problem with 2Γ , performing the translations there, and reimposing NBC. It follows that there should only be one branch of localized solutions in Fig. 18(b) despite the fact that the convecton and hole states in Fig. 18(a) are not related by any of the reflection symmetries respected by NBC! All this is a consequence of the fact that with NBC one can reflect a solution in the lateral wall without introducing discontinuities (“cusps”) in derivatives – a fact that guarantees that the solution with its reflection solves the partial differential equation in the doubled domain.

We can use the above procedure to construct a “wall-attached localized state,” i.e., a nonlinear wall mode, as shown in Fig. 19(a). This solution also satisfies NBC with $\Gamma = 14$ and PBC with $\Gamma = 28$ and resembles the type of state computed by Ghorayeb & Mojtabi [6]. These wall modes also snake, as indicated by blue dashed lines in Fig. 19(b). The figure shows, moreover, that the snaking occurs with twice the frequency of the LC states shown in Fig. 18(a). This is because these states are really states with period 2Γ , because of the hidden symmetry, instead of the period Γ of the LC state. Because of this each back-and-

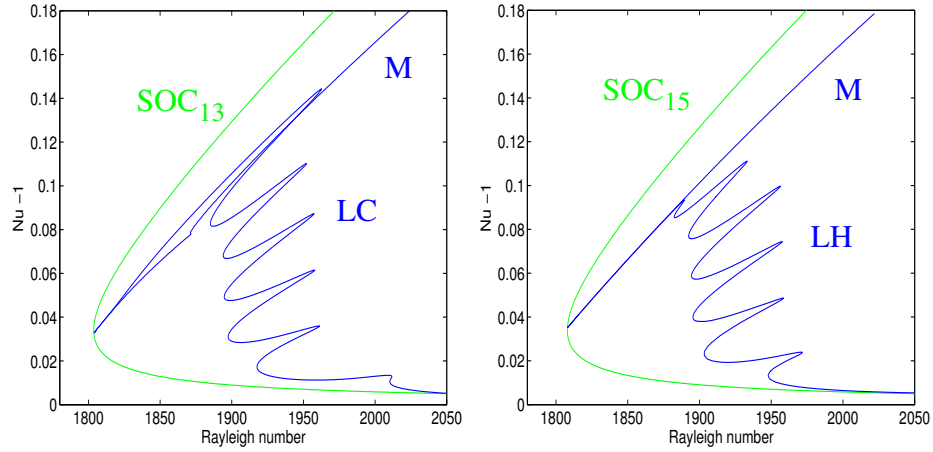


Figure 20: Odd parity states with NBC and $\Gamma = 14$. (a) Localized convectons LC terminate on SOC_{13} . (b) Localized holes LH terminate on SOC_{15} . Each termination point is accompanied by branch of even parity mixed modes labeled M.

forth oscillation on the snaking branch results in the addition of two cells to LC (one on either side) but only one cell to LW. Thus twice as many oscillations are required in order to fill the domain. Note that the larger intrinsic period 2Γ implies that the LW terminate closer to the fold on SOC_{14} than the LC branch as this distance decreases with increasing aspect ratio of the system [2].

We can also apply the above procedure to odd parity states, as shown in Fig. 20. The result is now different because convectons and holes are no longer related by a hidden symmetry. As a result the LC states terminate on the branch SOC_{13} of 13 rolls in the domain while the LH states terminate on the branch SOC_{15} of 15 rolls in the domain. Note that both SOC_{13} and SOC_{15} have odd parity. Since LC and LH now terminate on different branches it follows that each termination point must involve a second branch of modulated states as well. These missing states must have even parity since each Eckhaus bifurcation generates states of either type, and these take the form of the nonsnaking mixed modes already described (Fig. 20).

3.3 Insulating closed container boundary conditions (ICCBC)

The above construction does not work as soon as the boundary conditions differ from NBC. Nonetheless, the procedure suggests the type of states that may be present with the more realistic ICCBC. All such solutions will necessarily have defects at the boundaries owing to the no-slip velocity boundary condition. Figure 21 shows examples of even localized structures at two locations in the bifurcation diagram. As already mentioned the branch undergoes a smooth transition from snaking to a large amplitude domain-filling state with a defect at either lateral wall. This is also the case for odd parity localized structures as shown in Fig. 22. Similar bifurcation diagrams are encountered in the Swift-Hohenberg model with mixed (Robin) boundary conditions where the details of the breakup of the NBC bifurcation diagrams as the boundary conditions are changed and the transition to

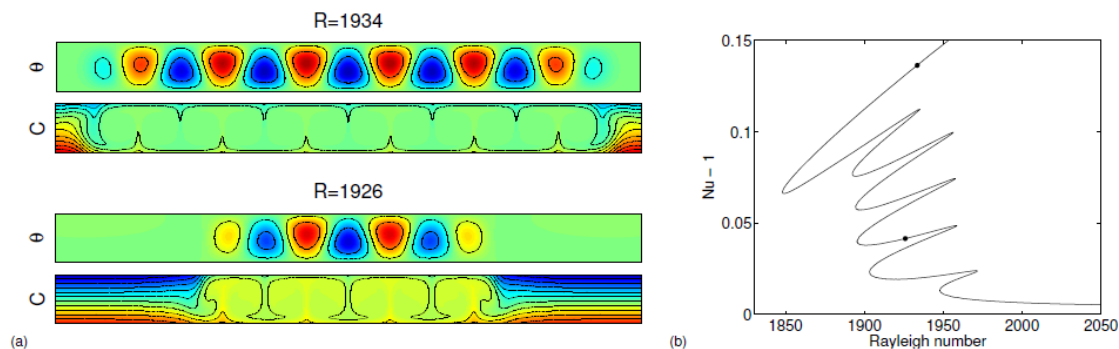


Figure 21: (a) Two different even parity convectons with ICCBC and $\Gamma = 14$. (b) The corresponding solution branch with dots denoting the location of the states in (a).

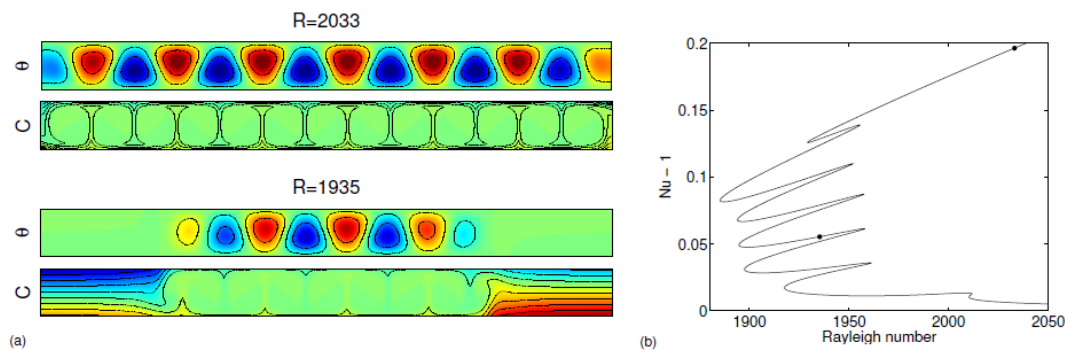


Figure 22: (a) Two different odd parity convectons with ICCBC and $\Gamma = 14$. (b) The corresponding solution branch with dots denoting the location of the states in (a).

“snaking without bistability” can be investigated [8].

Finally, we can also find examples of the wall-attached modes predicted by the NBC construction. Figure 23(a) shows two such states while Fig. 23(b) shows the corresponding solution branch (dashed), with the branch of even parity LC states superposed for comparison. We see that the LW branch oscillates back-and-forth with twice the frequency of the LC branch, exactly as in the NBC case, and for the same reason. However, once the domain is almost full the LW branch terminates on the LC branch – in the ICCBC case this is possible since the defect at the right wall can broaden sufficiently to resemble the partly filled vicinity of the left wall (or vice versa), thereby restoring reflection symmetry to the solution.

It remains to mention that the stability properties of these states have not been investigated in detail.

References

- [1] O. Batiste, E. Knobloch, A. Alonso and I. Mercader, 2006. Spatially localized binary-fluid convection. *J. Fluid Mech.* **560**, pp. 149–158, 2006.

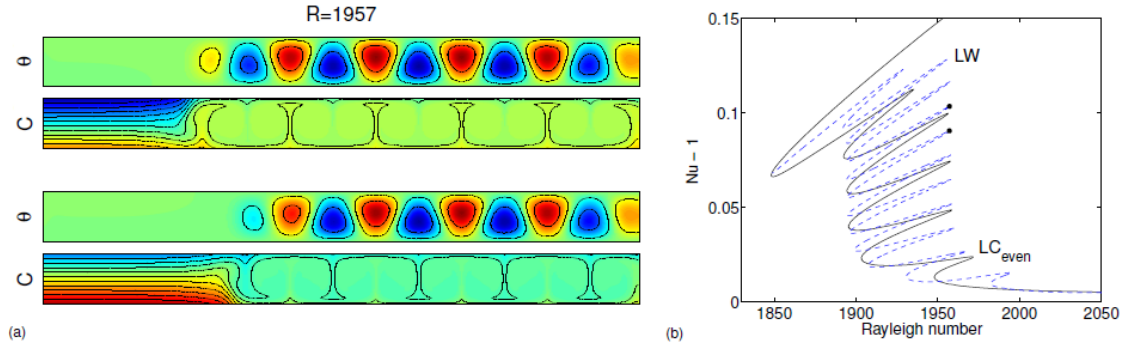


Figure 23: (a) Two wall states with ICCBC and $\Gamma = 14$. (b) The corresponding solution branch labeled LW with the LC branch from Fig. 21 superposed.

- [2] A. Bergeon, J. Burke, E. Knobloch and I. Mercader. Eckhaus instability and homoclinic snaking. *Phys. Rev. E* **78**, 046201, 2008.
- [3] C. S. Bretherton and E. A. Spiegel. Intermittency through modulational instability. *Phys. Lett. A* **96**, pp. 152–156, 1983.
- [4] A. R. Champneys, E. Knobloch, Y.-P. Ma and T. Wagenknecht. Homoclinic snakes bounded by a saddle-center periodic orbit. *SIAM J. Appl. Dyn. Syst.* **11**, pp. 1583–1613, 2012.
- [5] J. D. Crawford, M. Golubitsky, M. G. M. Gomes, E. Knobloch and I. N. Stewart. Boundary conditions as symmetry constraints, in *Singularity Theory and its Applications*, Warwick 1989, Part II, M. Roberts and I. Stewart (eds), Lecture Notes in Mathematics 1463, Springer-Verlag, New York, pp. 63–79, 1991.
- [6] K. Ghorayeb and A. Mojtabi. Double diffusive convection in a vertical rectangular cavity. *Phys. Fluids* **9**, pp. 2339–2348, 1997.
- [7] R. B. Hoyle. *Pattern Formation: An Introduction to Methods*, Cambridge University Press, 2006.
- [8] S. M. Houghton and E. Knobloch. Homoclinic snaking in bounded domains. *Phys. Rev. E* **80**, 026210, 2009.
- [9] E. Knobloch. Oscillatory convection in binary mixtures. *Phys. Rev. A* **34**, pp. 1538–1549, 1986.
- [10] Y.-P. Ma, J. Burke, E. Knobloch. Defect mediated snaking in the forced complex Ginzburg-Landau equation. *Physica D* **239**, pp. 1867–1883, 2010.
- [11] Y.-P. Ma and E. Knobloch. Depinning, front motion, and phase slips. *Chaos* **22**, 033101, 2012.
- [12] I. Mercader, O. Batiste, A. Alonso and E. Knobloch. Convection in periodic and bounded domains. *Fluid Dyn. Res.* **42**, pp. 025505, pp. 1–10, 2010.

- [13] I. Mercader, O. Batiste, A. Alonso and E. Knobloch. Convectons, anticonvectons and multiconvectons in binary fluid convection. *J. Fluid Mech.* **667**, pp 586–606, 2011.
- [14] A. A. Predtechensky, W. D. McCormick, J. B. Swift, A. G. Rossberg and H. L. Swinney. Traveling wave instability in sustained double-diffusive convection. *Phys. Fluids* **6**, pp. 3923–3935, 1994.
- [15] S. Tobias, M. R. E. Proctor, and E. Knobloch. Convective and absolute instabilities of fluid flows in finite geometry. *Physica D* **113**, pp. 43–72, 1998.

Lecture 10: More applications

Edgar Knobloch: notes by Duncan Hewitt and Pedram Hassanzadeh
with substantial editing by Edgar Knobloch

January 9, 2013

1 The Swift-Hohenberg Equation as a Model

The Swift-Hohenberg equation has proved to be a very useful model system for studying the properties of spatially localized structures in physical systems. This is because of the following properties:

- The equation is fourth order in the spatial variables
- The equation has an intrinsic length scale $2\pi/q_c$
- The equation is spatially reversible
- The equation exhibits bistability due to competing nonlinear terms
- The equation is relatively easy to analyze, at least in one dimension.

The main reason the equation can be understood in such detail is a consequence of the spatial reversibility and the fact that it can be written as a variational problem,

$$u_t = -\frac{\delta F}{\delta u} \quad \text{where} \quad F = \int_{-\infty}^{\infty} dx \left[-\frac{1}{2}ru^2 + \frac{1}{2} \left[\left(q_c^2 + \frac{\partial^2}{\partial x^2} \right) u \right]^2 - \int_0^u f(v)dv \right]. \quad (1)$$

In this section we consider the symmetries of the Swift-Hohenberg equation in one spatial dimension, and examine the effects of breaking some of these symmetries. In the following sections we will use these results as a basis for examination of more complex systems, such as those arising in fluid mechanics.

1.1 Two Cases: SH23 and SH35

We first look at two cases of the Swift-Hohenberg equation with different nonlinear terms, and different corresponding symmetries, namely, SH23 and SH35.

SH23 has $f(u) = b_2u^2 - u^3$ and the following reflection and translational symmetries:

- $R_1 : x \longrightarrow -x, \quad u \longrightarrow u$
- $T : x \longrightarrow x + d, \quad u \longrightarrow u.$

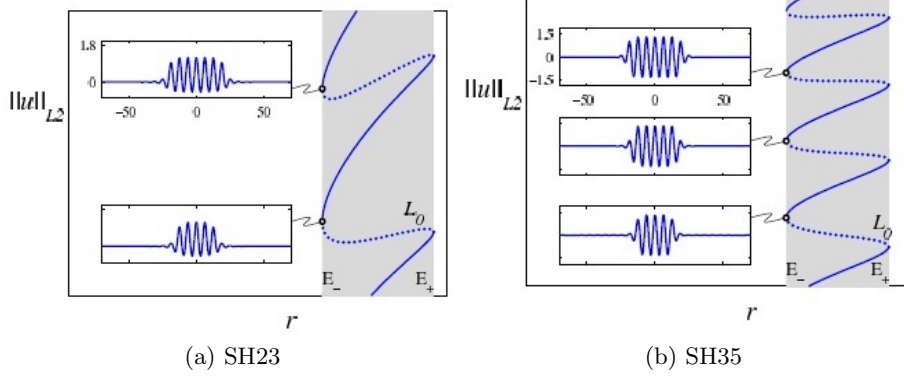


Figure 1: Growth along the L_0 branch of states with even symmetry. The pinning region is shaded. (a) SH23. (b) SH35. From [3].

As a result there are two types of localized solutions, those fixed by R_1 (even states L_0 , L_π), and asymmetric “rung” states with no symmetry, together with their translates.

SH35 has $f(u) = b_3 u^3 - u^5$ and the following reflection and translational symmetries:

- $R_1 : x \longrightarrow -x, \quad u \longrightarrow u$
- $R_2 : x \longrightarrow x, \quad u \longrightarrow -u$
- $T : x \longrightarrow x + d, \quad u \longrightarrow u.$

As a result there are three types of localized solutions: those fixed by R_1 (even states L_0 , L_π) and their translates; those fixed by $R_1 \circ R_2$ (odd states $L_{\pi/2}$, $L_{3\pi/2}$) and their translates, and asymmetric “rung” states. It is important to observe that L_0 and L_π are related by R_2 , and likewise for $L_{\pi/2}$, $L_{3\pi/2}$. Consequently the bifurcation diagram in Fig. 1(b) contains only a single branch of even states and a single branch of odd states.

Figure 1 compares the growth along the L_0 branches in SH23 and SH35 and shows that SH35 has twice as many turns compared to SH23. It is therefore of interest to explore what happens when the symmetry R_2 of SH35 is progressively broken. How does the snaking branch in Fig. 1(b) deform into the snaking branch in Fig. 1(a)? What are the consequences of this process?

1.1.1 Variational case

To study the effect of breaking the R_2 symmetry in SH35, we add a term ϵu^2 to the right-hand side SH35,

$$u_t = ru - (1 + \partial^2/\partial x^2)^2 u + b_3 u^3 - u^5 + \epsilon u^2. \quad (2)$$

When $\epsilon \neq 0$ this equation, like SH23, possesses only R_1 and T symmetries, and hence the only symmetric states are L_0 , L_π . The odd parity states $L_{\pi/2}$, $L_{3\pi/2}$ become states with no symmetry and reconnect with the rung states forming two different types of branches: S branches and Z branches [8]. Figure 2 shows the effect of breaking the R_2 symmetry (for $\epsilon = 0.03$).

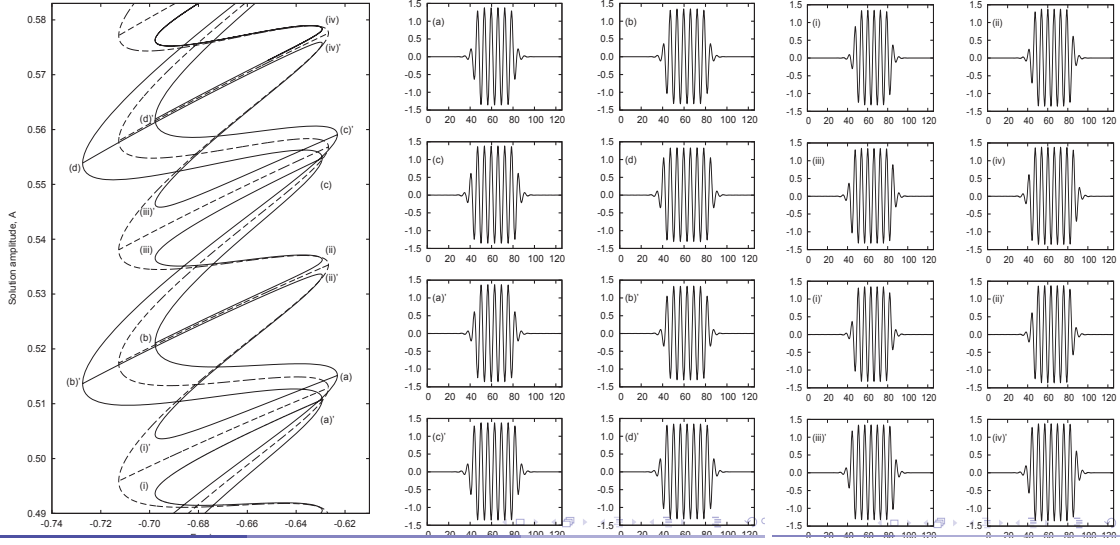


Figure 2: The snakes-and-ladders structure in the variational case with $\epsilon = 0.03$ and $b_3 = 2$. The solution branches for $\epsilon = 0$ are shown dashed. For $\epsilon \neq 0$ the even parity branch splits into two distinct even parity states L_0 and L_π , while the odd parity states reconnect with original “rung” states forming pairs of disconnected branches of asymmetric states referred to as S and Z branches. The solutions $u(x)$ at the saddle nodes: (a)–(d) are from the L_π branch, and (a')–(d') are from the L_0 branch. (i)–(iv) are solutions at the saddle-nodes on the S branches, and (i')–(iv') are from the Z branches. From [8].

Figure 3 shows the effect of increasing ϵ for the variational case (2). Both symmetric and asymmetric states are stationary, and the Z branches are stretched by increasing ϵ .

1.1.2 Nonvariational case

We can also break the R_2 symmetry by adding the term $\epsilon(\partial u/\partial x)^2$ to SH35. The new equation, i.e.,

$$u_t = ru - (1 + \partial^2/\partial x^2)^2 u + b_3 u^3 - u^5 + \epsilon(\partial u/\partial x)^2, \quad (3)$$

is not variational, i.e., it cannot be written in the form (1). The effect of increasing ϵ in this case is qualitatively similar to the variational case. However, here the asymmetric states are no longer stationary, as shown in Fig. 4.

Because (asymmetric) states are now nonstationary, we can consider the effect of collisions between two such states. Figure 5(a) shows a collision between two identical localized states drifting in opposite direction. The result is a symmetric (and, therefore, stationary) state. In contrast, Figs. 5(b)–5(e) show that collisions of nonidentical states can lead to other types of behavior. The collisions result in either stationary (symmetric) states or moving (asymmetric) states. The outcome of the collision is determined in general by the shape of the approaching fronts – whether these are like (in phase) or unlike (out of phase). See Figs. 5(b)–5(e) and [8] for more details.

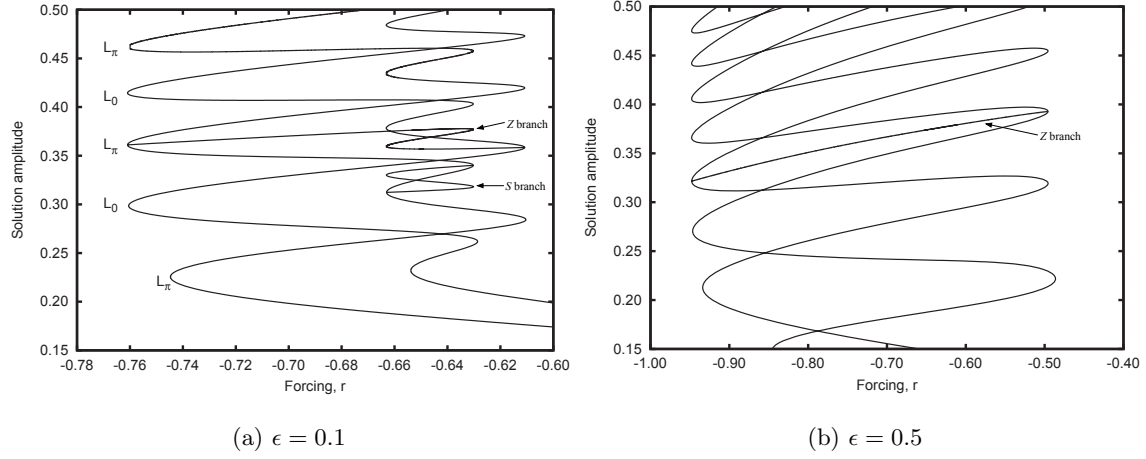


Figure 3: The effect of increasing ϵ in the variational case, with $b_3 = 2$: only one S and one Z branch is shown. In (b) the S branch has vanished and the Z branch has straightened out. From [8].

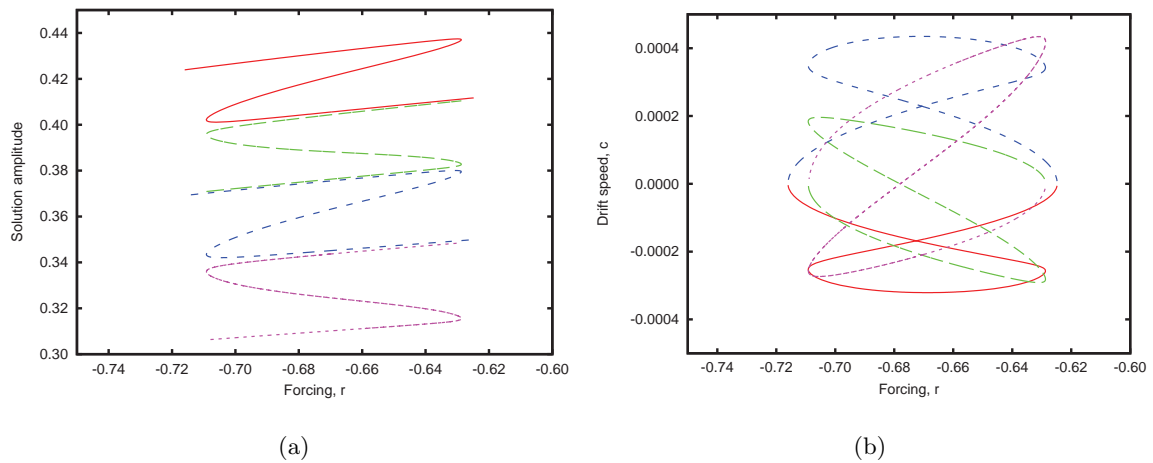


Figure 4: (a) The S and Z branches in the nonvariational case when $\epsilon = 0.01$ and $b_3 = 2$. (b) The corresponding drift speed c ; when $\epsilon \neq 0$ c is generically nonzero although it can vanish at isolated values of the bifurcation parameter r . From [8].

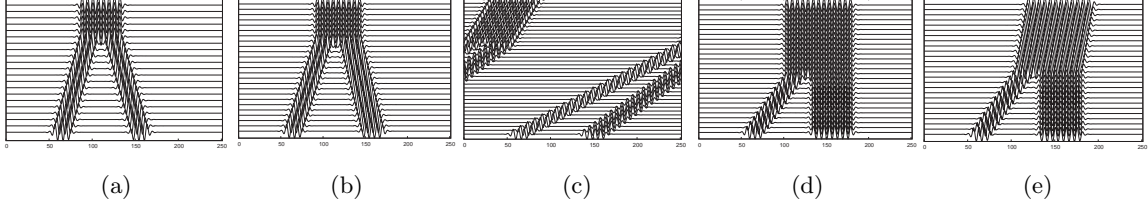


Figure 5: Space-time diagrams showing the collision of different states, for $r = -0.65$, $b_3 = 2$ and $\epsilon = 0.1$: (a) two identical states, resulting in a symmetric state; (b)–(e) nonidentical collisions, resulting in either symmetric (stationary) or asymmetric (moving) localized states. Time increases upward. From [8].

In all cases the collisions are inelastic and the length of the final state exceeds the combined length of the colliding states. This is a consequence of the fact that additional nucleation events take place just before the collision.

2 Applications

We now briefly consider the relevance of the Swift–Hohenberg results to several physical systems. Specifically we consider (1) collisions between convectons, and (2) ‘multipulse’ states (multiple localized states in the domain) in systems which share the symmetry properties of the Swift-Hohenberg equation, but not its variational behavior.

2.1 Binary fluid convection

Two-dimensional binary-fluid convection was discussed in lecture 9. In particular lecture 9 described in some detail the properties of spatially localized solutions termed convectons. We use this same system now to generate moving convectons. To do so we relax the midplane symmetry of the system that was imposed through the use of the Boussinesq approximation and of identical boundary conditions at top and bottom. In the following we retain the Boussinesq approximation and imagine the top and bottom boundaries in contact with appropriate heat baths, of temperature T_U and T_L , respectively, with flux boundary conditions

$$\frac{dT_-}{dz} = -\frac{B_-}{d} (T_L - T_-) \quad \text{at} \quad z = 0, \quad (4)$$

$$\frac{dT_+}{dz} = -\frac{B_+}{d} (T_+ - T_U) \quad \text{at} \quad z = l, \quad (5)$$

where l is the depth of the layer, T_+ and T_- are the temperatures immediately outside the upper and lower heat baths (which vary in time), and B_{\pm} are the Biot numbers of the boundaries: $B = 0$ corresponds to insulating boundaries, while $B = \infty$ corresponds to pure conducting boundaries. The key observation here is that, if $B_+ \neq B_-$, these boundary conditions mark a departure from the symmetric conditions imposed in lecture 9.

The system is characterized by cross-diffusion such that the concentration field is coupled to the temperature field: the effects of this coupling are described by a separation ratio S .

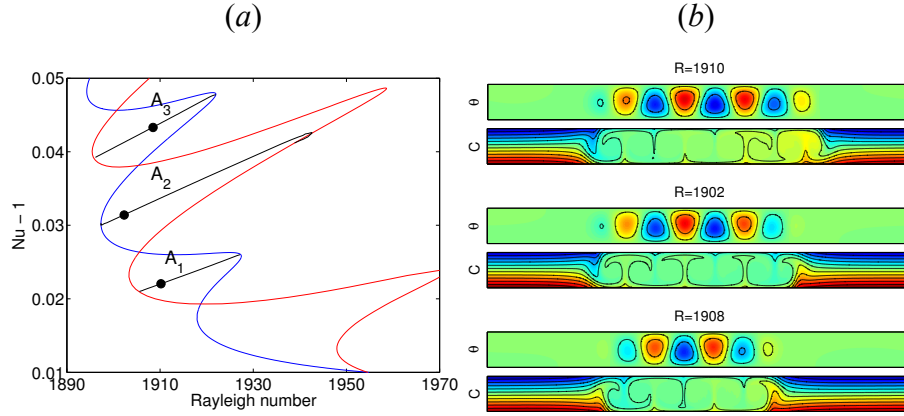


Figure 6: (a) Bifurcation diagram for $\beta = 1$ showing odd (blue curve) and even (red curve) states together with the asymmetric states (black curves). (b) Contours of constant temperature fluctuation (upper panels) and concentration (lower panels) for traveling convections on the rungs of the snakes-and ladders bifurcation diagram. The location of each state is indicated by dots in (a). Parameters: $S = -0.1$, $\sigma = 7$, and $\tau = 0.01$. From [12].

Here (as in lecture 9) we assume that $S < 0$, such that the heavier molecular weight fluid migrates up the temperature gradient, towards the hotter bottom boundary. As a result we have bistability between the background conduction state and the periodic convecting state. The brief overview that follows is based on [12], where further details may be found.

In order to characterize the amplitude of convection and construct a bifurcation diagram we must define a parameter that characterizes the system, i.e., we need a parameter that remains fixed even during time-dependent evolution of the system. The usual Rayleigh number, defined in terms of the temperature drop ΔT across the fluid layer, is inappropriate as soon as the temperature of the boundaries can change in response to the heat deposited by flow, in other words, as soon as the boundaries fail to be perfectly conducting. For this purpose we define the Rayleigh number Ra in terms of the temperature difference $\Delta T'$ across the layer *in the conduction state* [12]. When the boundaries are perfectly thermally conducting this definition reduces to the usual definition. We also define the Prandtl number $\sigma = \nu/\kappa$, the ratio of viscosity to thermal diffusivity, and the Lewis number $\tau = D/\kappa$, the ratio of compositional to thermal diffusivity. In the following we assume that the lower boundary is perfectly conducting ($B_- = \infty$) and suppose that the upper boundary is characterized by a finite Biot number B_+ . Under these conditions the thermal boundary conditions (4) and (5), written in terms of dimensionless variables, become

$$(1 - \beta)\theta_z + \beta\theta = 0 \quad \text{on} \quad z = 1, \quad \theta = 0 \quad \text{on} \quad z = 0, \quad (6)$$

where θ is the dimensionless departure of the temperature from its conduction profile. Here β is the effective Biot number of the upper boundary and is given by $\beta \equiv B_+/(1 + B_+)$. We also impose no-slip impenetrable boundary conditions on the upper and lower boundaries. It follows that $\beta = 1$ implies that the system is symmetric, with a perfectly conducting boundary at $z = 1$ as well as $z = 0$. If instead $\beta = 0$, the upper boundary is perfectly

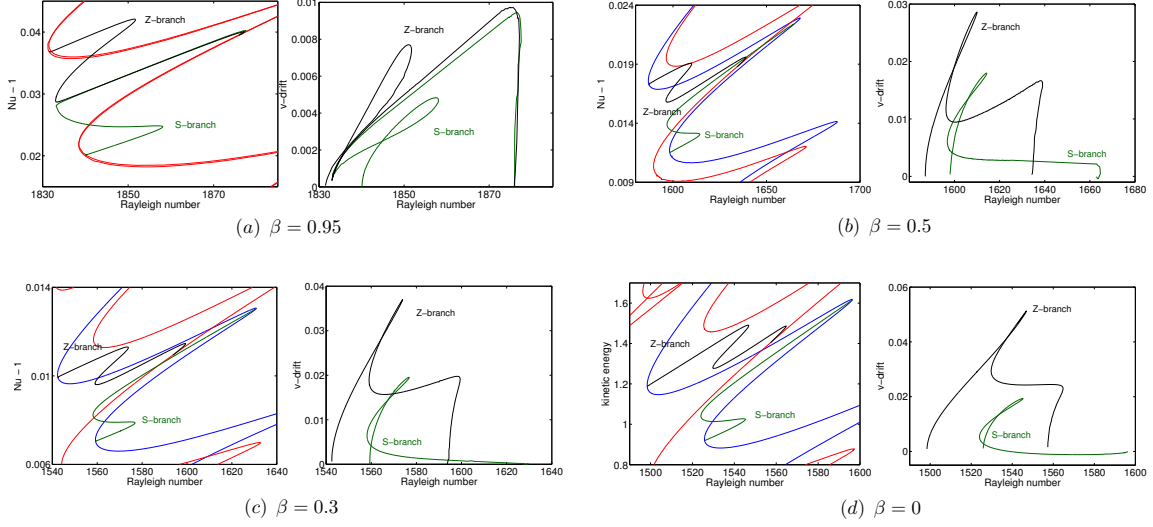


Figure 7: Left panels: bifurcation diagrams showing the even parity states generated by splitting of the $\beta = 1$ even states and the S and Z states resulting from the reconnection between the $\beta = 1$ odd states and the asymmetric rung states, for different values of β . Right panels: velocity c of the S and Z states. The parameter values are given in Fig. 6. From [12].

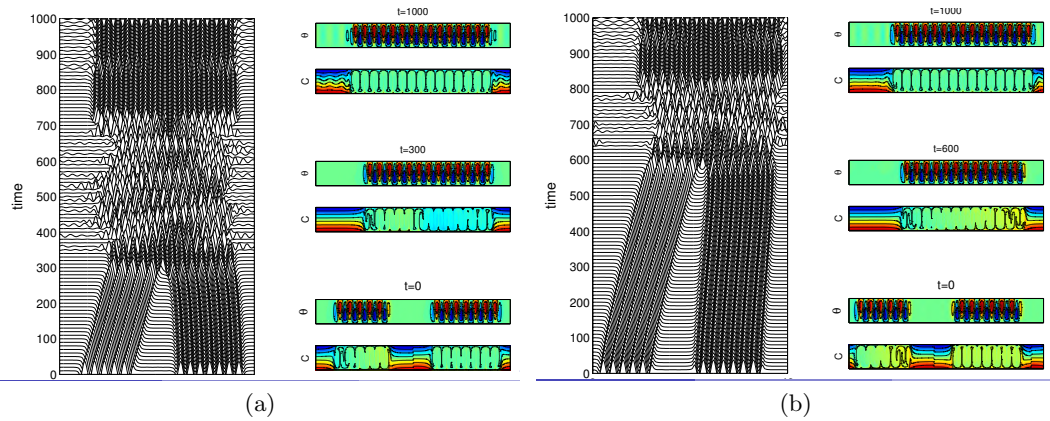


Figure 8: Space-time plots showing two different collisions of two states, with $S = -0.5$, $\beta = 0.9$, $\sigma = 0.6$, $\tau = 0.03$, and $Ra = 2750$. The collisions result in complex dynamics and the generation of waves, and ultimately end up in a symmetric state higher up the snaking branch than either of the initial states. From [12].

insulating. Thus the departure of β from $\beta = 1$ provides a measure of the magnitude of the breaking of the midplane reflection symmetry in this system.

It follows that when $\beta = 1$, the system has a midplane symmetry, and we then expect that both odd and even solutions are present and stationary. Figure 6(a) shows the resulting snakes-and-ladders bifurcation diagram and reveals that the asymmetric rung states now drift (Fig. 6(a)). This is a consequence of the absence of variational structure of the equations. Three of the resulting drifting convectons are shown in Fig. 6(b).

When $\beta < 1$ the midplane symmetry is absent, and the snakes-and-ladders structure of the pinning region breaks up. The odd parity solutions and the rung states become drifting S and Z states, just as in the case of SH35 with a nonvariational R_2 symmetry-breaking term. Figure 7 shows the bifurcation diagrams for a sequence of different values of $\beta < 1$ as specified below each pair of panels. The even parity solutions have split into two, and the new S and Z states now drift. One can check [12] that the Z branch connects the two even parity branches produced by the splitting of the even parity states while the S branch connects an even parity branch to itself. The corresponding speeds of the S and Z states are shown in Fig. 7(b).

Since some of states now move we can study collisions between them by direct numerical integration in time, just as in the Swift-Hohenberg equation. The nice thing about generating moving convection by breaking the midplane symmetry is that in principle one has access to multiple drifting states of different lengths, all of which are simultaneously stable. However, it turns out that for the parameter values used in lecture 9 the drifting convectons are unstable. This is no longer so for the parameter values characteristic of liquid ^3He - ^4He mixtures and in Fig. 8 we show two of the resulting collisions [12]. Unlike the Swift-Hohenberg equation, this system supports waves, and the collisions result in complex dynamics. However, ultimately a new symmetric state is formed with a greater width than either of the incident convectons, just as in the Swift-Hohenberg equation.

The correspondence between the behavior of this complex physical system and the corresponding behavior in the Swift-Hohenberg equation is striking. The reason that the Swift-Hohenberg equation is so successful at describing complex systems of this type is ultimately due to the presence of a tangency between the unstable manifold of a homogeneous state and the stable manifold of a periodic orbit. Once these manifolds intersect transversely as described in lecture 8 the intersections are robust and hence insensitive to (small) changes in parameter values, and indeed in the equations and boundary conditions themselves.

2.2 Binary fluid convection in a porous medium

Next we consider binary fluid convection in a two-dimensional fluid-saturated porous layer, characterized by porosity ϵ and a separation ratio S , which controls the separation between lighter and heavier components. Again, if $S < 0$ the heavier component migrates toward the hotter boundary. As in the bulk binary fluid convection case discussed in lecture 9, the competing effects of composition and temperature on the density lead to bistability between the background conduction state and a periodic convecting state. The discussion of the section is based on [10], to which the reader is referred for more information.

The flow $\mathbf{u} = (u, w)$ in the porous medium is described by Darcy's law and is incompressible, while the temperature T and concentration C satisfy advection-diffusion equations.

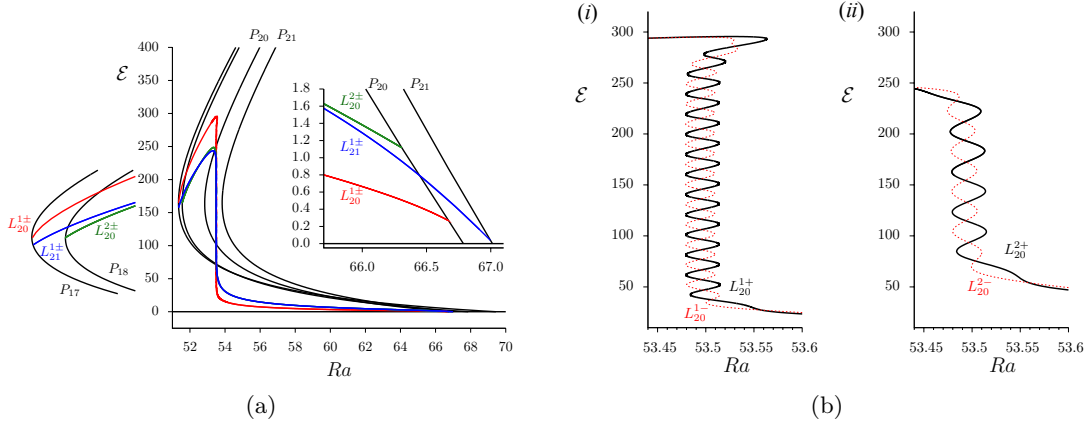


Figure 9: (a) Bifurcation diagram showing secondary branches of localized states connecting different periodic states. The inset shows enlargements of the behavior near the onset and termination of the secondary branches. The snaking region is not resolved on this plot. (b) The snaking region from (a), showing (i) examples of even (solid) and odd (dashed) single-pulse states, and (ii) equally spaced two-pulse states. The parameters are $\tau = 0.5$ and $S = -0.1$. From [10].

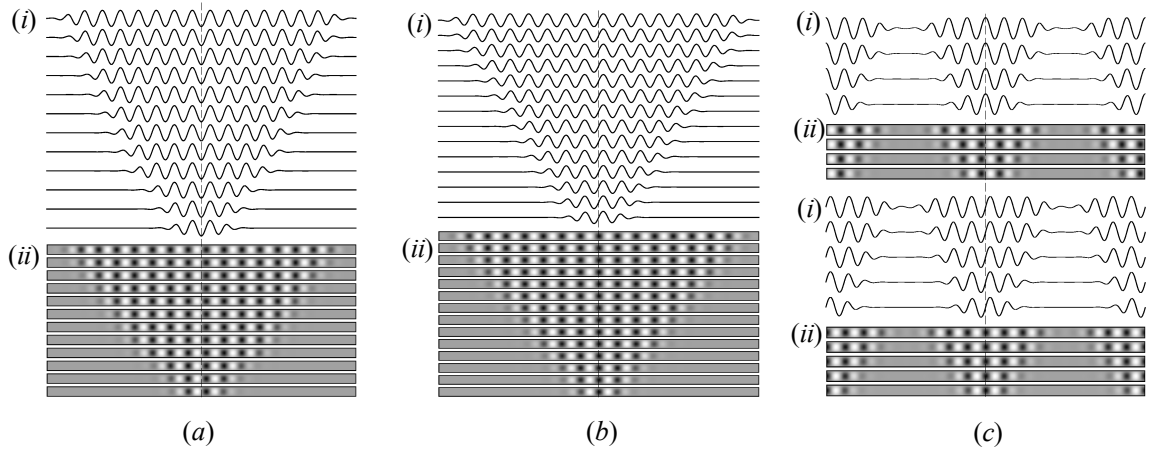


Figure 10: Line plots of the midplane vertical velocity w (i) and the streamfunction (ii) up the snaking region, for $\tau = 0.5$ and $S = -0.1$: (a) even parity state; (b) odd parity state; (c) even and odd states for two convectons. From [10].

These equations are given in dimensionless form by

$$\mathbf{u} = -\nabla p + Ra(T + SC)\mathbf{e}_z, \quad \nabla \cdot \mathbf{u} = 0, \quad (7)$$

$$\partial_t T = -(\mathbf{u} \cdot \nabla)T + \nabla^2 T, \quad (8)$$

$$\epsilon \partial_t C = -(\mathbf{u} \cdot \nabla)C + \tau(\nabla^2 C - \nabla^2 T). \quad (9)$$

To obtain these equations we have used a linear equation of state $\rho = \rho_0(1 - \alpha(T - T_0) + \beta(C - C_0))$, where $\alpha > 0$ and $\beta > 0$ are the constant coefficients of thermal and compositional expansion, respectively. The dimensionless parameters are the Lewis number $\tau = D/\kappa$, the Rayleigh number $Ra = g\alpha\Delta T l/\lambda\kappa$, and the separation ratio $S = S_{\text{soret}}\beta/\alpha < 0$. Here λ is the Darcy friction coefficient and l is the layer depth.

The boundary conditions are given by

$$w = T - 1 = (C - T)_z = 0 \quad \text{at} \quad z = 0, \quad (10)$$

$$w = T = (C - T)_z = 0 \quad \text{at} \quad z = 1, \quad (11)$$

and are periodic in the x direction with period Γ . We consider the departure from the base (conduction) state $T = 1 - z$, $C = 1 - z$, $\mathbf{u} = 0$, given by the variables $(\theta, \Sigma, \mathbf{u})$. The equations for these variables have important symmetry properties:

- Invariance under translations in x ;
- Invariance under reflection with respect to $x = 0$ (R_1);
- Invariance under reflection with respect to $z = 1/2$ (R_2).

With periodic boundary conditions in the horizontal, these operations generate the symmetry group $O(2) \times Z_2$, and as a consequence we expect the equations to exhibit behavior that is qualitatively similar to that already described for SH35. Figure 9(a) demonstrates that this is indeed the case. The figure reveals the presence of several subcritical branches of periodic states of which the branch P_{20} sets in first. This is a consequence of choosing a periodic domain $\Gamma = 20$ for the computations. The figure also shows three pairs of secondary branches of localized states, all of which snake. In particular, the branches labeled $L_{20}^{1\pm}$ bifurcate together from P_{20} at smallest amplitude and terminate together on P_{17} . The reason why on finite periodic domains the snaking branches may terminate on a different periodic state than the one they bifurcate from (or indeed on two different branches) can be traced to the Rayleigh number dependence of the wavelength within the localized structure as discussed in detail in [2]. Figure 10(a) shows the even parity states L_{20}^{1+} at successive left saddle-nodes proceeding up the snaking diagram while Fig. 10(b) shows similar results for the odd parity states L_{20}^{1-} . Both are single-pulse states in the sense that as $\Gamma \rightarrow \infty$ the phase space trajectory returns to the conduction after a single visit to a neighborhood of the limit cycle corresponding to the periodic state. In contrast, the branches $L_{20}^{2\pm}$ bifurcate from P_{20} at larger amplitude (and terminate on P_{18}) because they are branches of equidistant two-pulse states (Fig. 10(c)). The states L_{20}^{2+} consist of a bound state of two identical even parity pulses in the domain Γ , while L_{20}^{2-} consists of a bound state of two identical odd parity pulses in Γ . Since the pulses are equidistant they behave exactly like

single-pulse states in a domain $\Gamma/2$ as seen in Fig. 9(a). As mentioned in lecture 7 this is no longer the case for unequally spaced two-pulse states which are located on isolas within the snaking region. In contrast, the two-pulse states L_{21}^{1+} bifurcating from the second primary branch P_{21} consist of a bound states of *opposite* even parity states, i.e., equidistant bound states of a pulse with a maximum in the middle and a pulse with a minimum in the middle. Similarly, L_{21}^{1-} are equidistant bound states of two opposite odd parity states (with opposite slopes on their centerline).

Lo Jacono et al [10] also study the various tertiary branches analogous to the rung states in standard homoclinic snaking but this time connecting the branches of two-pulse states. Related results based on SH23 are described in [9].

2.3 Rotating convection

For a different application, we look at the classical problem of rotating Rayleigh-Bénard convection in two dimensions [13]. For this problem, the governing equations are

$$Ra \theta_x - Ta v_z + \nabla^4 \psi = \sigma^{-1} [\nabla^2 \psi_t + J(\psi, \nabla^2 \psi)] \quad (12)$$

$$\psi_x + \nabla^2 \theta = \theta_t + J(\psi, \theta) \quad (13)$$

$$Ta \psi_z + \nabla^2 v = \sigma^{-1} [v_t + J(\psi, \theta)], \quad (14)$$

where the three-dimensional velocity field in the rotating frame is $\mathbf{u} = (-\psi_z, v, \psi_x)$ with poloidal streamfunction ψ , and $J(f, g) \equiv f_x g_z - f_z g_x$. Here $v(x, z, t)$ is the zonal velocity, θ is the departure of the temperature from the pure conduction profile $T = 1 - z$, $\sigma \equiv \nu/\kappa$ is the Prandtl number and $Ra \equiv g\alpha\Delta T l^3/\nu\kappa$ is the Rayleigh number, where ΔT is the temperature difference across a fluid layer of height l . The importance of rotation is measured by the Taylor number $Ta = 2\Omega l^2/\nu$ (inverse Ekman number), where Ω is the (constant) rotation rate about the vertical axis. Following [13], we use the stress-free boundary conditions at $z = 0, 1$,

$$\psi = \psi_{zz} = \theta = v_z = 0. \quad (15)$$

With these boundary conditions

$$\frac{d\bar{V}}{dt} = 0, \quad \text{where} \quad \bar{V} \equiv \int_D v(x, z, t) dx dz, \quad (16)$$

where D refers to the domain $[-\Gamma/2, \Gamma/2] \times [0, 1]$. Thus the total zonal momentum \bar{V} is a conserved quantity. See [1] for further details. The vertically averaged zonal momentum, $V(x) \equiv \int_0^1 v(x, z) dz$, satisfies

$$\sigma \frac{dV}{dx} = - \int_0^1 \psi_z v dz, \quad (17)$$

implying that in steady states a horizontal zonal shear is balanced by the Reynolds stress on the right side of the equation. In the following we introduce the quantity $\Delta V \equiv V(x = L/2) - V(x = -L/2)$ that measures the zonal velocity difference across a convection of length L . This is always anticyclonic, i.e., $\Delta V < 0$ (see Fig. 12 and 13).

Figure 11 shows the bifurcation diagrams for the average poloidal kinetic energy $\mathcal{E} \equiv 1/(2\Gamma) \int_D (\psi_x^2 + \psi_y^2) dx dy$ as a function of Ra in the subcritical and supercritical regimes.

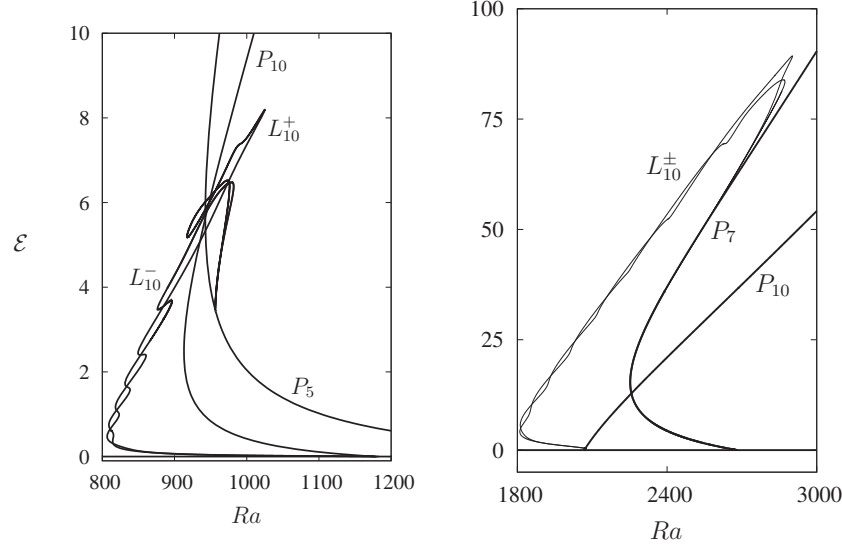


Figure 11: The average poloidal kinetic energy as a function of Ra showing slanted snaking. (a) The subcritical case with $Ta = 20$, $\sigma = 0.1$. (b) The supercritical case with $Ta = 40$, $\sigma = 0.6$. The label P_n refers the periodic solutions with n wavelengths within the domain $\Gamma = 10\lambda_c$; P_{10} bifurcates subcritically in (a) and supercritically in (b). From [1].

The behavior of the snaking region is notably different from that of the Swift–Hohenberg equation that we have seen before: Fig. 11(a) (subcritical) shows that the snaking exists *beyond* the bistability region, and Fig. 11(b) shows that the presence of snaking even in the supercritical case. In both cases, the two intertwined branches form *slanted snaking* [1]. The dramatic change in the snaking scenario is a result of the finite period Γ of the domain together with the conservation of zonal momentum, cf. [5, 11]. In the limit that $\Gamma \rightarrow \infty$ or if the free-slip boundary condition is replaced with no-slip boundary conditions, the flux conservation will be lost and snaking is expected to become vertical as in the standard snaking scenario (cf. the Swift-Hohenberg equation).

Figures 12 and 13 present the solution profiles corresponding to Figs. 11(a,b), respectively. These results show that cyclonic shear in the convection-free zones compensates the anticyclonic shear produced by the convectons and is a consequence of periodic boundary conditions with finite period Γ . The solutions in both cases grow in the same manner as one proceeds up the snaking branches despite the fact that in Fig. 11(b) no distinct nucleation events take place, i.e., no saddle-nodes are present. This type of snaking has been called “smooth snaking” [6].

Slanted snaking is a consequence of the expulsion of shear from the convection – negative shear implies that the structure rotates more slowly than the frame. Conservation of zonal momentum now implies that the flow outside the convection must rotate faster, i.e., that the resulting convection is embedded in a shear layer that it generates for itself. To understand this process in a little more detail we write $Ra = Ra_c + \epsilon^2 r$, where $r = \mathcal{O}(1)$, $\epsilon \ll 1$, and

introduce slow scales $X = \epsilon x$ and $T_2 = \epsilon^2 t$. We look for solutions in the form [4]

$$\psi = \frac{\epsilon}{2} \left(a(X, T_2) e^{ikx} + c.c. \right) \sin(\pi z) + h.o.t., \quad (18)$$

$$\theta = \frac{\epsilon k}{2p} \left(ia(X, T_2) e^{ikx} + c.c. \right) \sin(\pi z) + h.o.t., \quad (19)$$

$$v = \epsilon V(X, T_2) + \frac{\epsilon T \pi}{2p} \left(a(X, T_2) e^{ikx} + c.c. \right) \cos(\pi z) + h.o.t. \quad (20)$$

The large scale zonal velocity V is necessary to capture the shear that builds up across a convection and enters at $\mathcal{O}(\epsilon)$; its inclusion is a consequence of the phase-like quality of the variable v , i.e., the invariance of Eqs. (12)–(14) with the boundary conditions (15) with respect to $v \rightarrow v + c$, where c is a constant. At third order we obtain the equations [4]

$$\frac{p(3k^2\sigma - k^2 + 2\pi^2)}{\sigma k^2} a_{T_2} = ra + 12pa_{XX} - \frac{3pk^2}{8}(1 - \xi^2)|a|^2a - \frac{T\pi^2}{\sigma k^2} aV_X, \quad (21)$$

$$V_{T_2} = \sigma V_{XX} + \frac{T\pi^2}{4p} (|a|^2)_X, \quad (22)$$

where $\xi \equiv \frac{T\pi^2}{\sqrt{3}pk^2\sigma} > 0$. In rescaled form these equations become

$$\eta A_{T_2} = rA + A_{XX} - \frac{1 - \xi^2}{2} |A|^2 A - \xi AV_X, \quad (23)$$

$$V_{T_2} = V_{XX} + \xi (|A|^2)_X, \quad (24)$$

where $\eta \equiv \frac{3k^2\sigma - k^2 + 2\pi^2}{12k^2}$. The quantity η vanishes at the Takens-Bogdanov point $Ra_H = Ra_c$ where Ra_H is the critical Rayleigh number for the onset of a Hopf mode with the same wavenumber k . In the present work we are interested in the case in which the conduction state loses stability at a steady state bifurcation, i.e., a Hopf bifurcation is absent. In this case $\eta > 0$.

In the stationary case with PBC on the large scale X Eq. (24) implies that

$$V_X = \xi (\langle |A|^2 \rangle - |A|^2), \quad (25)$$

where $\langle \cdot \rangle$ represents a spatial average over the domain. Thus $V_X > 0$ if $|A|^2 < \langle |A|^2 \rangle$, i.e., outside the convection, while $V_X < 0$ if $|A|^2 > \langle |A|^2 \rangle$, i.e., inside the convection, exactly as found in Figs. 12 and 13. Moreover, using Eq. (25) to eliminate V_X from Eq. (23) we obtain the *nonlocal* equation [4]

$$rA + A_{XX} - \frac{1}{2}(1 - 3\xi^2)|A|^2 A - \xi^2 \langle |A|^2 \rangle A = 0. \quad (26)$$

It follows that there are four possible scenarios for the primary–secondary bifurcations with PBC: (1) both bifurcations are subcritical ($\xi^2 > 1$), (2) the primary bifurcation is supercritical while the secondary bifurcation is subcritical ($3/7 < \xi^2 < 1$), (3) both bifurcations are supercritical ($1/3 < \xi^2 < 3/7$), and (4) the primary bifurcation is supercritical but no secondary bifurcation is present ($\xi^2 < 1/3$) [1, 7]. When the domain period Γ is sufficiently

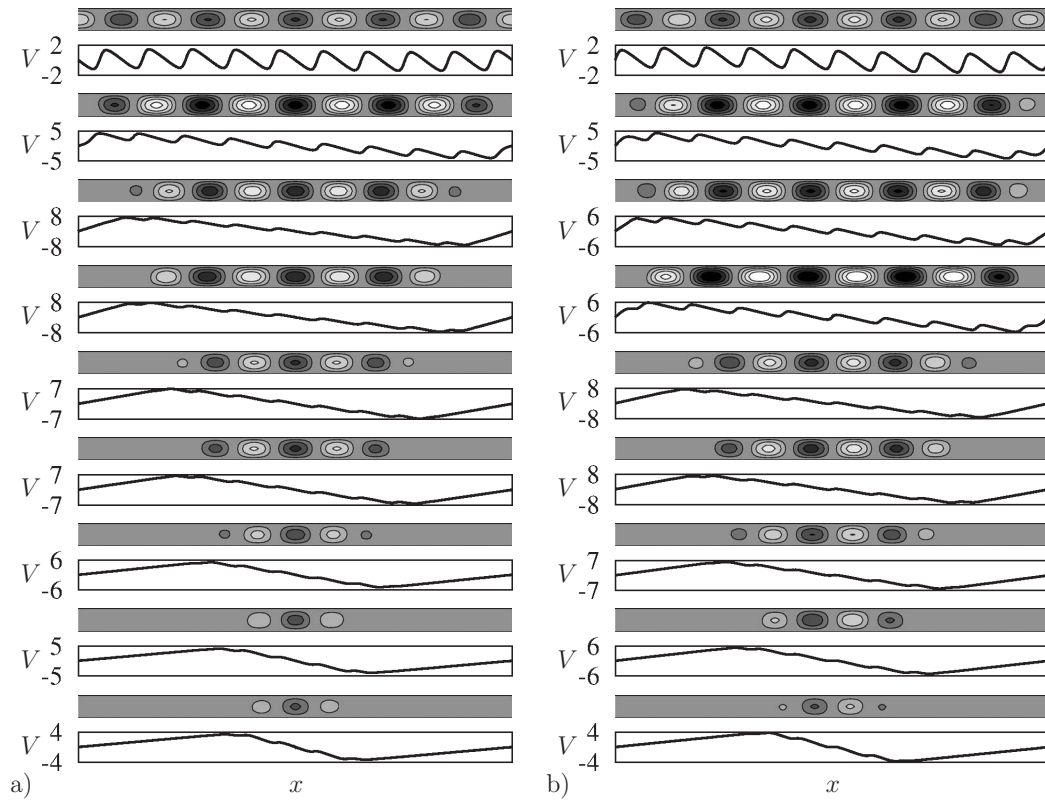


Figure 12: Solution profiles at successive saddle-nodes on (a) L_{10}^- , (b) L_{10}^+ in Fig. 11(a) (subcritical case). Upper panels show the contours of the streamfunction $\psi(x, z)$, and the lower panels show $V(x)$. From [1].

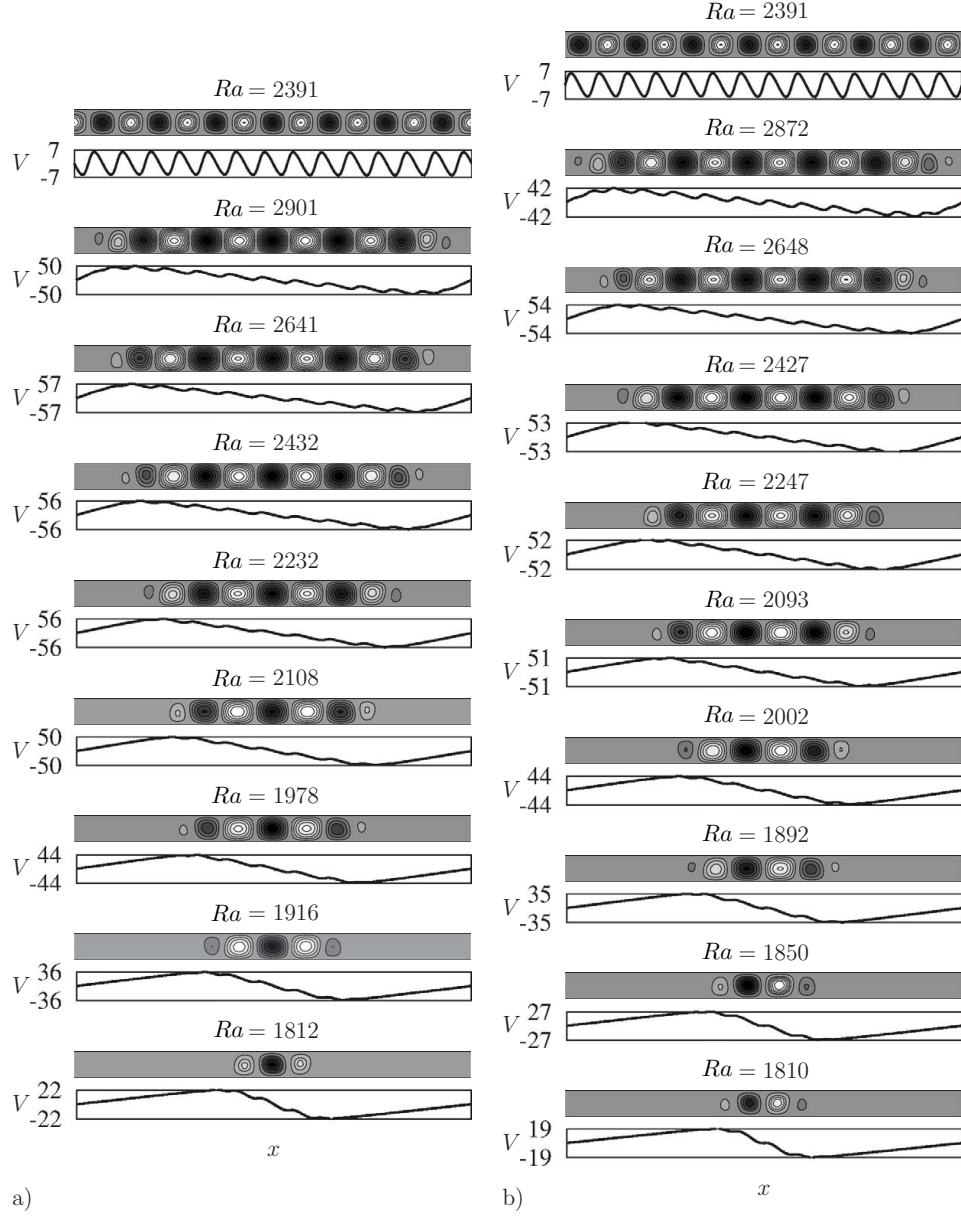


Figure 13: Solution profiles at successive saddle-nodes on (a) L_{10}^- , (b) L_{10}^+ in Fig. 11(b) (supercritical case). Upper panels show the contours of the streamfunction $\psi(x, z)$, and the lower panels show $V(x)$. From [1].

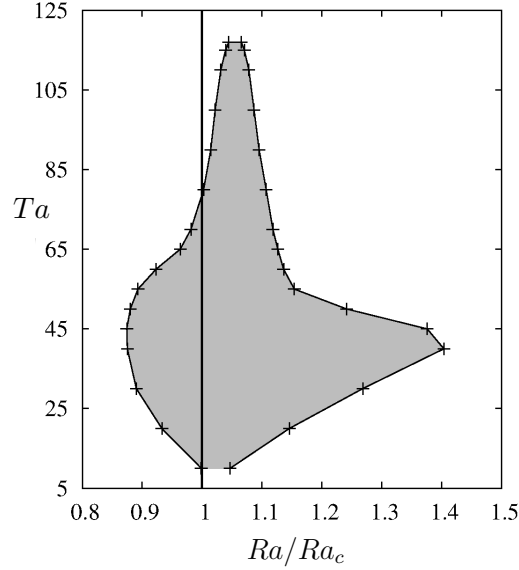


Figure 14: The existence region of convectons in the (Ra, Ta) plane when $\sigma = 0.6$, with the onset of periodic convection marked as a vertical line. From [1].

large the secondary bifurcations that form convectons occur at small enough amplitude that the transitions are captured well by the above asymptotic analysis.

The range of existence of localised states in Ra depends on both the Taylor number Ta and the Prandtl number. For sufficiently large values of Ta , or for values of Ta that are too small, there are no localized states, as shown in Fig. 14. For small values of Ta , there are no localized states because the rotation is too weak for shear expulsion to take place. For $Ta \gtrsim 60$, the wavelength of the localized states decreases significantly, due to the requirements of the Taylor-Proudman theorem and for $Ta \gtrsim 110$ the convectons are sheared out and the average poloidal kinetic energy of the states decreases to zero. Further details and discussion of the effect of changing Ta can be found in [1].

References

- C. Beaume, A. Bergeon, H.-C. Kao and E. Knobloch. Convectons in a rotating fluid layer, *J. Fluid Mech.*, in press.
- A. Bergeon, J. Burke, E. Knobloch and I. Mercader. Eckhaus instability and homoclinic snaking. *Phys. Rev. E* **78**, 046201, 2008.
- J. R. Burke. *Localized States in Driven Dissipative Systems*. PhD thesis, University of California, Berkeley, 2008.
- S. M. Cox and P. C. Matthews. New instabilities in two-dimensional rotating convection and magnetoconvection. *Physica D* **149**, pp. 210–229, 2001.

- J. H. P. Dawes. Localized pattern formation with a large-scale mode: slanted snaking. *SIAM J. Appl. Dyn. Sys.* **7**, pp. 18–206, 2008.
- J. H. P. Dawes and S. Lilley. Localized states in a model of pattern formation in a vertically vibrated layer. *SIAM J. Appl. Dyn. Sys.* **9**, pp. 238–260, 2010.
- F. J. Elmer. Nonlinear and nonlocal dynamics of spatially extended systems: Stationary states, bifurcations and stability. *Physica D* **30**, pp. 321–342, 1988.
- S. Houghton and E. Knobloch. Swift-Hohenberg equation with broken cubic-quintic nonlinearity. *Phys. Rev. E* **84**, 016204, 2011.
- J. Knobloch, D. J. B. Lloyd, B. Sandstede and T. Wagenknecht. Isolates of 2-pulse solutions in homoclinic snaking scenarios. *J. Dyn. Diff. Eq.* **23**, 93–114, 2011.
- D. Lo Jacono, A. Bergeon and E. Knobloch. Spatially localized binary fluid convection in a porous medium. *Phys. Fluids* **22**, 073601, 2010.
- D. Lo Jacono, A. Bergeon and E. Knobloch. Spatially localized magnetoconvection. *J. Fluid Mech.* **687**, pp. 595–605, 2011.
- I. Mercader, O. Batiste, A. Alonso and E. Knobloch. Travelling convectons in binary fluid convection. *J. Fluid Mech.*, under review.
- G. Veronis. Large-amplitude Bénard convection in a rotating fluid, *J. Fluid Mech.* **31**, pp. 113–139, 1968.

Thixotropic gravity currents

Duncan R. Hewitt

September 28, 2012

1 Introduction

Fluids that undergo reversible and time-dependent changes to their internal structure as a result of flow are called thixotropic. Specifically, the internal structure of a thixotropic fluid is broken down by the presence of flow, while in the absence of flow, the structure rebuilds, and the fluid is said to ‘heal’ over time. Typically, the break-down of structure is relatively rapid, while the rebuilding of structure is slow.

Thixotropic behaviour has been reported in a wide range of fluids [6, 18]. Industrial drilling fluids and cements, printing inks and paints, oils and grease, biological fluids (e.g. blood), and food products such as mayonnaise, yoghurt, and ketchup have all been shown to exhibit elements of thixotropy. More complex fluids, such as dry foams and granular media, also exhibit many of the same phenomena as thixotropic fluids [12]. In nature, mineral slurries and certain mud and clay suspensions are thixotropic: part of the motivation for this study comes from mudslides, in which large volumes of mud can suddenly become ‘de-structured’ and catastrophically fail.

Thixotropic fluids are most commonly colloidal suspensions, with a microstructure that exhibits weak attractive forces between particles: this leads to flocculation and ‘structuring’ in the fluid at rest, while flow-induced mechanical stresses can break down this structure. On a macro-scale, this behaviour can be described by variations in the fluid viscosity. Thixotropic fluids are, therefore, typically modelled with a non-Newtonian variable viscosity, which decreases dramatically in the presence of shear, but increases slowly when the fluid is at rest. This rheology gives rise to a variety of phenomena: variable yield-stress behaviour, hysteresis in the constitutive relationship, and ‘jamming’ or ‘avalanching’ in the fluid (see, e.g. [1, 7, 10, 19]). We will examine these features in this report.

There has been a relatively wide range of work presenting rheological measurements and models for thixotropic fluids (see section 2). However, there have been very few studies that incorporate this rheology into a physical scenario. In this report, we consider the flow of a finite shallow layer of thixotropic fluid down an inclined plane under the action of gravity. Such a system has been well studied in the case of a Newtonian fluid [15, 16], and an ideal yield-stress (e.g. Bingham) fluid [4, 14, 17]. A previous study of a ‘dam-break’ of thixotropic fluid [8] has explored the gravity-driven flow of a (non-shallow) thixotropic fluid by tracking characteristics. There are, however, currently no systematic studies of the shallow thixotropic gravity current on a slope. Brief experimental observations of such a system by Coussot *et al.* [10], using bentonite clay, have suggested that this system can exhibit dramatic ‘avalanche’ behaviour: they found that fluid inclined at a certain angle

will not move at all, while fluid inclined at a slightly larger angle will dramatically collapse and flow rapidly down the inclined plate. In the latter case, they observed that a structured ‘horseshoe’ of fluid at the back of the current remained immobile, while the front of the current flowed down the slope. In the present study, we attempt to reproduce and explore such behaviour experimentally, and to describe it theoretically and numerically.

The report is structured as follows. In section 2, we discuss the rheological model of thixotropy that we will employ, including our simplifying ‘rapid-transit’ approximation. In section 3, we outline the governing equations for flow in a shallow layer (directly following [2]). In section 4, we present numerical results of the system, in both two and three dimensions, and discuss the main qualitative features of the flow. In section 5, we examine the stability of the system, and show that the flow is unstable to a form of interfacial instability. In general, this instability is relatively benign, in that it does not significantly destabilise the flow. Finally, in section 6 we present experimental results of the system using two different thixotropic fluids: a bentonite clay solution, and Heinz tomato ketchup. Broadly speaking, the experimental results show good qualitative agreement both with previously published observations [10], and with our numerical simulations.

2 Thixotropic model

2.1 Basic rheological model

A range of rheological models that describe the effects of thixotropy have been proposed (see, e.g. [6, 18]). Many of these models employ a time-dependent *structure parameter* $\lambda(t)$ to describe the amount of internal structure in the fluid [1, 10, 13, 19, 21]. The viscosity $\mu(\lambda)$ is then given as a prescribed function of the structure parameter. The constitutive equation for such a fluid, which relates the deviatoric stress tensor τ_{ij} to the rate of strain tensor $\dot{\gamma}_{ij}$, is given by the generalised Newtonian form,

$$\tau_{ij} = \mu[\lambda(t)] \dot{\gamma}_{ij}. \quad (1)$$

In this report, we use a rheological model of this form, which is outlined and discussed below. Our model is adapted from models presented by Coussot *et al.* [10, 11] and by Moller *et al.* [19, 20]. The main difference in our model is the (implicit) inclusion of an ‘absolute yield stress’, above which the fluid will flow irrespective of its structure: this removes an unphysical feature of the previous models, namely that infinite-viscosity fluid remains so for arbitrarily large stresses.

The structure parameter lies in the range $0 \leq \lambda \leq 1$: $\lambda = 1$ corresponds to fully structured fluid, and $\lambda < 1$ corresponds to fluid that is de-structured to some degree. The structure parameter is assumed to satisfy an evolution equation of the form

$$\frac{D\lambda}{Dt} = \frac{1 - \lambda}{T} - \alpha\lambda\dot{\gamma}, \quad (2)$$

where $\dot{\gamma} = \sqrt{\dot{\gamma}_{ij}\dot{\gamma}_{ij}/2}$ is the second invariant of the rate of strain tensor $\dot{\gamma}_{ij}$, $T > 0$ is the constant ‘healing timescale’ for the fluid, and $\alpha > 0$ is a constant that controls the de-structuring of the fluid by the flow. The two terms on the right-hand side of (2) correspond, respectively, to the rebuilding or ‘healing’ of the fluid structure at rest, and the destruction

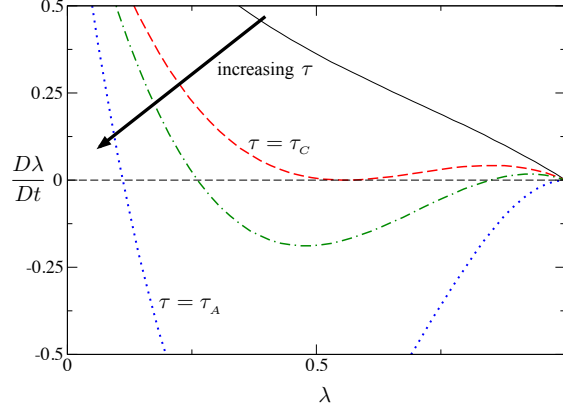


Figure 1: Phase diagram for λ , given by (4), for $\Gamma = 20$, $\beta = 0.9$, and increasing values of the stress τ as marked. There is a bifurcation at the critical value $\tau_c = 4\beta/\Gamma$: below this stress, the only fixed point is at $\lambda = 1$, which is stable, and corresponds to the structured state; above this stress there are two additional fixed points $\lambda_1 < \lambda_2 < 1$, the lower of which is stable. At a higher stress $\tau = \tau_A = 1/\Gamma(1 - \beta)$, the unstable fixed point (λ_2) reaches $\lambda = 1$, and the fixed point at $\lambda = 1$ becomes unstable.

of structure by gradients in the flow. Empirical measurements [1, 7, 11, 20] suggest that both T and α are typically large, such that destruction of structure is fairly rapid, while regeneration of structure is very slow.

The structure parameter is related to the viscosity through an equation of the form

$$\mu = \frac{\mu_0 \dot{\gamma}^{n-1}}{(1 - \lambda)^m (1 - \beta\lambda)}, \quad (3)$$

where μ_0 is a constant reference viscosity, and $m \geq 1$, n , and $0.5 < \beta < 1$ are constant parameters. The viscosity increases with the structure λ , and diverges as the fluid becomes fully structured ($\lambda \rightarrow 1$). Therefore, if the fluid is fully structured, the constitutive equation (1) implies that the strain rate $\dot{\gamma}$ is zero.

Throughout this report, for simplicity, we take the parameters $m = n = 1$, such that the viscosity does not explicitly depend on the rate of strain $\dot{\gamma}$. The model can be generalised to give shear thinning or thickening behaviour (by changing n), or to give a different sensitivity of the viscosity on the structure (by changing m).

The evolution equation for λ (2) can be re-written in terms of the second invariant of the stress $\tau = \sqrt{\tau_{ij}\tau_{ij}/2}$, using the constitutive equation (1) and the viscosity equation (3) (here with $n = m = 1$), which gives

$$T \frac{D\lambda}{Dt} = (1 - \lambda) [1 - \Gamma\lambda(1 - \beta\lambda)\tau], \quad (4)$$

where $\Gamma = \alpha T/\mu_0$.

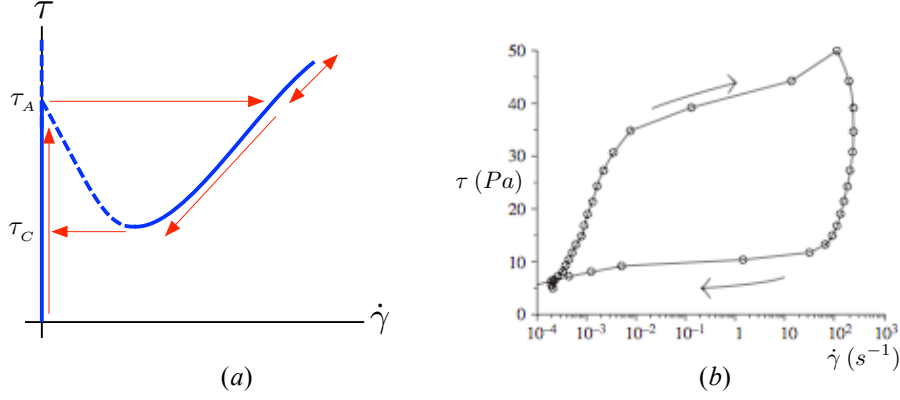


Figure 2: Constitutive relationships (1), showing the stress τ against the rate of strain $\dot{\gamma}$: (a) schematic of the model relationship at the steady-state solutions of (4) (thick blue), where dashed lines correspond to unstable fixed points, and the thin red arrows signify the ‘rapid-transit’ (see section 2.3) hysteresis behaviour that might be expected in a stress-ramp test; (b) measurements of 10 wt% bentonite clay under an increasing and decreasing stress-ramp test, taken from [19].

2.2 Implications of the model

The phase diagram for λ from (4) is shown in figure 1. For sufficiently small values of the stress, there is only one fixed point in the range $0 \leq \lambda \leq 1$, which is stable, and located at $\lambda = 1$. Therefore, if the stress is sufficiently small, the fluid always evolves towards the fully structured state. However, at the *critical stress* $\tau = \tau_C = 4\beta/\Gamma$, there is a bifurcation at $\lambda = \lambda_C = 1/2\beta$, and two additional fixed points $\lambda_{1,2}$ are created:

$$\lambda_{1,2} = \frac{1}{2\beta} \left[1 \mp \left(1 - \frac{4\beta}{\Gamma\tau} \right)^{1/2} \right]. \quad (5)$$

The lower value, λ_1 , is a stable fixed point, which decreases as τ increases, while λ_2 is unstable and increases with τ . As the stress is increased further and reaches the *absolute stress* $\tau = \tau_A = 1/\Gamma(1 - \beta)$, this unstable fixed point λ_2 reaches $\lambda = 1$, and so, for $\tau > \tau_A$, the fixed point at $\lambda = 1$ becomes unstable. Therefore, if the applied stress is very large, the fluid always evolves towards a de-structured state, corresponding to a small value of λ .

For a given value of the structure λ , there is a corresponding viscosity $\mu(\lambda)$, given by (3), which defines a relationship between the stress τ and the rate of strain $\dot{\gamma}$, given by the constitutive equation (1). This relationship is plotted schematically for the fixed points of (4) in figure 2(a). As discussed above, we can see that for small values of the stress $\tau < \tau_C$, the fluid will evolve to the structured state with $\dot{\gamma} = 0$ ($\lambda = 1$). For large stress $\tau > \tau_A$, the fluid will evolve to a de-structured state, with $\dot{\gamma} > 0$ ($\lambda \ll 1$).

For intermediate values of the stress $\tau_C < \tau < \tau_A$, the behaviour of the fluid will depend on the stress history of the sample: in other words, it will depend on which side of the unstable fixed point the structure parameter currently lies. The system therefore exhibits hysteresis, as can be seen by considering a simple stress-ramp experiment. Suppose the

fluid is initially fully structured, and a gradually increasing stress is applied. The shear rate will remain zero until the stress exceeds the absolute stress, $\tau > \tau_A$. At this point, the fluid will ‘de-structure’, λ will decrease towards the small stable fixed point, and $\dot{\gamma}$ will increase towards the stable branch. If the stress is then decreased, the strain rate will remain on the stable (non-zero) branch until the stress falls below τ_C , at which point the structure parameter will evolve back towards $\lambda = 1$, and the shear rate will decay to zero. Experimental results of such a test on bentonite clay are shown in figure 2(b).

It should be noted that if the fluid is not initially fully structured, such that $\lambda < 1$, then the corresponding initial viscosity μ_I has some finite value. Alternatively, the viscosity of a real fluid is unlikely to be unbounded, in which case μ_I represents the upper bound that can be attained. In either case, we would not expect the rate of strain to remain zero as the stress is increased: instead it should follow the linear constitutive relationship $\tau = \mu_I \dot{\gamma}$. The corresponding stress at which the fluid evolves to the ‘de-structured’ small- λ stable branch would then be smaller than τ_A , and the effects of hysteresis would be smaller. This behaviour can be seen in the experimental measurements of figure 2(b), where the initial slope of the curve is not vertical.

The extent of hysteresis in the system is controlled by the parameter β . As the value of β is increased towards 1, the value of τ_A increases towards ∞ , while τ_C remains finite: the size of the hysteresis loop therefore increases. Alternatively, as β is decreased towards $1/2$, $\tau_A \rightarrow \tau_C$, and there is no hysteresis in the system. On setting $\beta = 0$ and ignoring the time derivative in (4), this thixotropic rheology reduces to that for an ideal Bingham yield-stress fluid, with yield stress $1/\Gamma$.

It is worth, at this point, drawing a comparison between this thixotropic model (for non-zero β) and models for ideal yield-stress fluids (i.e. Bingham or Herschel–Buckley models [3]). The thixotropic model does incorporate the idea of a yield stress, as for stresses below τ_C the strain rate always evolves to zero. However, there are some significant differences. Firstly, in the thixotropic model the value of the ‘yield stress’ is dependent on the stress history of the particular fluid element: the system exhibits hysteresis, and the extent of the hysteresis loop in the constitutive relationship is given by the extent to which the fluid is structured at that particular time. In contrast, in an ideal yield-stress fluid the yield stress is constant. Secondly, in the thixotropic model there is a discontinuity in the steady-state rate of strain at the ‘yield stress’, which has been described as a ‘viscosity bifurcation’ [11]: the viscosity, which is infinite for smaller stresses, discontinuously becomes finite and relatively small as the stress is increased past the ‘yield stress’. In an ideal yield-stress fluid, however, the viscosity varies continuously away from infinity as the stress is increased past the yield stress. A more detailed discussion of the differences between thixotropic models of this form and yield-stress models can be found in [20]. In sections 4 and 6, we will compare the behaviour of thixotropic and ideal yield-stress fluids numerically and experimentally, and show that there are significant phenomenological differences between the two types of fluid.

2.3 Rapid-transit

Rheological measurements and observations of a variety of thixotropic fluids [1, 7, 11, 20] have shown that there is a significant separation of timescales between the ‘healing’ time T ,

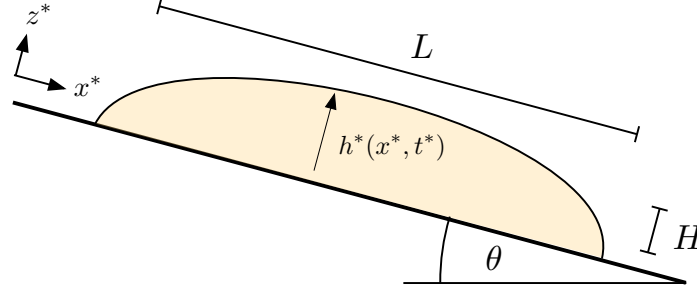


Figure 3: Schematic showing the system under consideration: fluid of aspect ratio $\varepsilon = H/L \ll 1$ on a slope of angle θ , in two dimensions.

which is typically large, and the timescale over which the fluid evolves to the steady state under stress, which is often much smaller. Motivated by these observations, we make a simplifying ‘rapid-transit’ approximation to the evolution equation for λ (4): the evolution to the steady state is assumed to be instantaneous, and the material derivative is replaced by zero. Equation (4) therefore becomes

$$(1 - \lambda) [1 - \Gamma \lambda (1 - \beta \lambda) \tau] = 0. \quad (6)$$

The relevant root λ of (6) for a given stress τ is determined by the stability of the full time-dependent equation (4).

The constitutive relationship (1) is then given exactly by the steady-state curve plotted in figure 2(a). At the bifurcation points $\tau = \tau_C$ and $\tau = \tau_A$, the structure parameter jumps to the structured ($\lambda = 1$, $\dot{\gamma} = 0$) or de-structured ($\lambda \ll 1$, $\dot{\gamma} > 0$) branches, as shown by the arrows in figure 2(a). For intermediate values of the stress $\tau_C < \tau < \tau_A$, the corresponding value of λ depends on the stress history of the fluid.

3 Gravity driven flow in a shallow layer

In this study, we incorporate the rheological ‘rapid-transit’ thixotropic model into the problem of shallow fluid flow on an inclined plane. In order to distinguish between dimensional and dimensionless variables, in this section we denote all dimensional quantities with a *. The problem formulation is independent of the rheology, and exactly follows that given in [2].

3.1 Dimensional formulation

We consider the flow (u^*, w^*) of a finite volume of fluid of density ρ , in two dimensions (x^*, z^*) , where the x^* -axis is aligned along a slope inclined at a constant angle θ to the horizontal. The fluid lies in a shallow layer, such that the typical depth scale H is much smaller than the typical along-slope scale L . We define their ratio to be $\varepsilon = H/L \ll 1$. The fluid has depth $z^* = h^*(x^*, t^*)$, as shown in figure 3.

The flow is incompressible,

$$\frac{\partial u^*}{\partial x^*} + \frac{\partial w^*}{\partial z^*} = 0, \quad (7)$$

and satisfies the Cauchy momentum equations,

$$\rho \left(\frac{\partial u^*}{\partial t^*} + u^* \frac{\partial u^*}{\partial x^*} + w^* \frac{\partial u^*}{\partial z^*} \right) = \rho g \sin \theta - \frac{\partial p^*}{\partial x^*} + \frac{\partial \tau_{xz}^*}{\partial z^*} + \frac{\partial \tau_{xx}^*}{\partial x^*}, \quad (8)$$

$$\rho \left(\frac{\partial w^*}{\partial t^*} + u^* \frac{\partial w^*}{\partial x^*} + w^* \frac{\partial w^*}{\partial z^*} \right) = -\rho g \cos \theta - \frac{\partial p^*}{\partial z^*} + \frac{\partial \tau_{xz}^*}{\partial x^*} + \frac{\partial \tau_{zz}^*}{\partial z^*}. \quad (9)$$

The deviatoric stress tensor τ_{ij}^* is related to the rate of strain tensor $\dot{\gamma}_{ij}^*$ by the constitutive equation (1). The boundary conditions are given by no normal or tangential flow at the base,

$$u^* = w^* = 0 \quad \text{at} \quad z^* = 0, \quad (10)$$

no normal stress at the upper boundary,

$$(\tau_{ij}^* - p^* \delta_{ij}) n_j = 0 \quad \text{at} \quad z^* = h^*(x^*, t^*), \quad (11)$$

and the kinematic condition at the upper boundary,

$$\frac{\partial h^*}{\partial t^*} + u^* \frac{\partial h^*}{\partial x^*} - w^* = 0 \quad \text{at} \quad z^* = h^*(x^*, t^*), \quad (12)$$

where $\mathbf{n} \propto (-h_{x^*}^*, 1)$ is a vector that is normal to the surface $z^* = h^*$. The kinematic condition (12), combined with the continuity equation (7), gives

$$\frac{\partial h^*}{\partial t^*} + \frac{\partial}{\partial x^*} \int_0^{h^*} u^* dz^* = 0. \quad (13)$$

3.2 Dimensionless formulation

We scale x^* with L , z^* with H , and the pressure p^* with $\rho g H \cos \theta$. We take a constant velocity scale U , and scale u^* with U , w^* with HU/L , and time t^* with L/U . The stress τ_{ij}^* is scaled with $\mu_0 U/H$. We assume that the horizontal pressure gradients balance the vertical gradients of the shear stress, and thus identify $U = H^3 g \cos \theta / L \mu_0$.

As discussed above, we define the ratio $H/L = \varepsilon \ll 1$. With respect to dimensionless variables, (8), (9), and (13) are given by

$$\varepsilon^2 Re \left(\frac{\partial u}{\partial t} + u \frac{\partial u}{\partial x} + w \frac{\partial u}{\partial z} \right) = S - \frac{\partial p}{\partial x} + \frac{\partial \tau_{xz}}{\partial z} + \varepsilon \frac{\partial \tau_{xx}}{\partial x}, \quad (14)$$

$$\varepsilon^4 Re \left(\frac{\partial w}{\partial t} + u \frac{\partial w}{\partial x} + w \frac{\partial w}{\partial z} \right) = -1 - \frac{\partial p}{\partial z} + \varepsilon^2 \frac{\partial \tau_{xz}}{\partial x} + \varepsilon \frac{\partial \tau_{zz}}{\partial z}, \quad (15)$$

$$\frac{\partial h}{\partial t} + \frac{\partial}{\partial x} \int_0^h u dz = 0, \quad (16)$$

where $S = \varepsilon^{-1} \tan \theta$, and the Reynolds number Re is given by $Re = \rho U L / \mu_0$. The components of the rate of strain tensor are given by

$$\dot{\gamma}_{xx} = -\dot{\gamma}_{zz} = 2\varepsilon \frac{\partial u}{\partial x}, \quad \dot{\gamma}_{xz} = \frac{\partial u}{\partial z} + \varepsilon^2 \frac{\partial w}{\partial x}. \quad (17)$$

The stress boundary condition (11) becomes

$$\begin{pmatrix} \varepsilon \tau_{xx} - p & \varepsilon \tau_{xz} \\ \varepsilon \tau_{xz} & -\varepsilon \tau_{xx} - p \end{pmatrix} \begin{pmatrix} -\varepsilon \partial h / \partial x \\ 1 \end{pmatrix} = \mathbf{0} \quad \text{at} \quad z = h(x, t); \quad (18)$$

3.3 Leading order equations

Under the assumption that $S \sim O(1)$ and Re is no larger than $O(1/\varepsilon)$, the leading order terms in ε from (14) and (15) give

$$0 = S - \frac{\partial p}{\partial x} + \mu \frac{\partial^2 u}{\partial z^2}, \quad (19)$$

$$0 = -1 - \frac{\partial p}{\partial z}. \quad (20)$$

Together with the leading order boundary conditions from (11), equations (19) and (20) give

$$p = h - z, \quad (21)$$

$$\tau_{xz} = \mu \frac{\partial u}{\partial z} = \left(S - \frac{\partial h}{\partial x} \right) (h - z). \quad (22)$$

If the viscosity μ is a constant, (16) and (22) can be combined, and reduce to the usual governing equation for a Newtonian viscous gravity current on a slope [16]. Here, instead, the viscosity is given as a function of the structure parameter λ (3), and the structure parameter $\lambda(\tau)$ is given by the rapid transit model, discussed in section 2.3. These equations are given here in dimensionless form:

$$\mu(\lambda) = \frac{1}{(1 - \lambda)(1 - \beta\lambda)}, \quad (23)$$

$$(1 - \lambda)[1 - \Gamma\lambda(1 - \beta\lambda)|\tau_{xz}|] = 0, \quad (24)$$

where we have set the parameters $n = m = 1$, rescaled the parameter Γ as $\Gamma = \alpha T/\varepsilon$, and replaced the stress τ by $|\tau_{xz}|$ following (17). Since we expect α and T to be large, we also typically consider Γ to be large.

3.4 Anatomy of the flow

Before we present our numerical results, it will be helpful to examine the anatomy of the flow, which is shown schematically in figure 4. From the rheological model, and the hysteresis behaviour shown in figure 2, we should expect changes in the fluid structure, and thus changes in the flow, at the bifurcation stresses: that is, at the critical and absolute values of the stress, τ_C and τ_A . In the shallow-layer formulation, the stress is dominated by the shear stress τ_{xz} , which is given by (22), and is a linearly decreasing function of z . The contour $\tau = \tau_C$ therefore defines a surface $z(\tau_C) \leq h$. Above this surface, the stress is less than the critical value, and, as such, the fluid is structured: $\lambda = 1$, and $\dot{\gamma} = \partial u/\partial z = 0$.

Similarly, the contour $\tau = \tau_A$ defines a surface $z(\tau_A) \leq z(\tau_C)$. Below this surface, the stress is greater than the absolute value, and the fluid is de-structured: therefore $\lambda \ll 1$, and $\partial u/\partial z > 0$.

Between the two stress surfaces, $z(\tau_C) < z < z(\tau_A)$, the structure of the flow depends on the history of each fluid element. Suppose that the fluid is initially fully structured. Then, when the fluid is inclined, the de-structured fluid will be exactly bounded above by the absolute stress surface $z = z(\tau_A)$. However, as the flow evolves, de-structured fluid

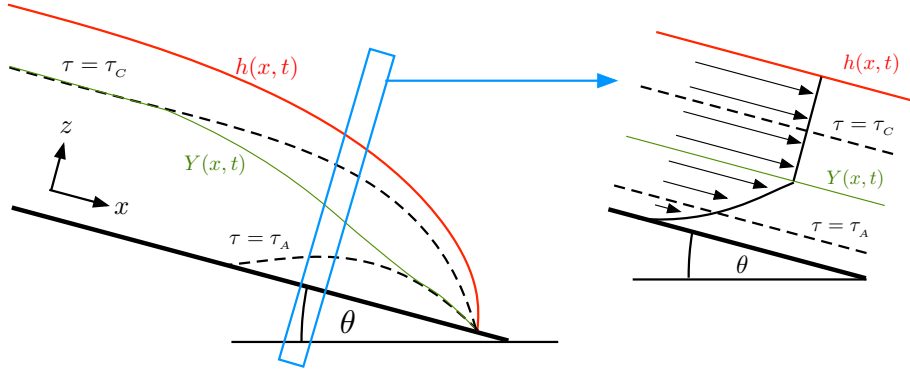


Figure 4: Schematic showing the flow of thixotropic fluid down a slope of angle θ . The height $h(x, t)$ is shown in red. Lines of constant shear stress $\tau = \tau_A$ and $\tau = \tau_C$ are shown dashed. Above the line $\tau = \tau_C$, the fluid is fully structured and $\lambda = 1$, while below the line $\tau = \tau_A$, the fluid is de-structured and $\lambda \ll 1$. The yield surface $z = Y(x, t)$ (green), which separates structured and de-structured flow, is bounded by these stress contours. Between the two contours, the structure of the flow is determined by the local stress history: in this region the yield surface is a material curve which satisfies (26). The inset shows a typical velocity profile $u(z)$ through a slice of the flow as marked: $u(z)$ increases from zero at the base up to the yield surface, at which point there is a discontinuity in $\partial u / \partial z$, and plug flow in the structured region above the yield surface.

elements will remain de-structured until the stress falls below the critical stress τ_C . These fluid elements will also move with the flow, and so there is a material curve which runs between the two stress contours, and separates the structured and de-structured fluid.

We can, therefore, define a yield surface $z = Y(x, t)$ which runs throughout the current and separates the structured fluid above from the de-structured fluid below (figure 4). At points in the flow where the absolute stress surface $z(\tau_A)$ is moving up into structured fluid, the yield surface lies along this stress surface. Similarly, at points in the flow where the critical stress surface is moving down into de-structured fluid, the yield surface lies along this stress surface. Between the two stress surfaces, the yield surface is a material curve, as discussed above. Therefore, in this region $z(\tau_C) < z < z(\tau_A)$ the yield surface satisfies a kinematic condition,

$$\frac{\partial Y}{\partial t} + u \frac{\partial Y}{\partial x} - w = 0 \quad \text{on} \quad z = Y(x, t), \quad (25)$$

which, together with incompressibility (7), reduces to an evolution equation for Y in this region:

$$\frac{\partial Y}{\partial t} + \frac{\partial}{\partial x} \int_0^Y u \, dz = 0. \quad (26)$$

For clarity, a summary of our complete model is given here. The leading-order stress contribution (22) and the rheological model (23), (24), are given by

$$\tau_{xz} = \mu(\lambda) \frac{\partial u}{\partial z} = \left(S - \frac{\partial h}{\partial x} \right) (h - z), \quad (27)$$

$$\mu(\lambda) = \frac{1}{(1-\lambda)(1-\beta\lambda)}, \quad (28)$$

$$(1-\lambda)[1-\Gamma\lambda(1-\beta\lambda)|\tau_{xz}|] = 0. \quad (29)$$

The relevant root $0 \leq \lambda \leq 1$ of (29) is given by the stability of the full time-dependent equation (4). Equations (27)–(29) are solved together with the evolution equation (16) for the height of the current $h(x, t)$,

$$\frac{\partial h}{\partial t} + \frac{\partial}{\partial x} \int_0^h u \, dz = \frac{\partial h}{\partial t} + \frac{\partial}{\partial x} \int_0^Y (h-z) \frac{\partial u}{\partial z} \, dz = 0. \quad (30)$$

The location of the yield surface $Y(x, t)$ depends on the stress history of the fluid. In regions where the absolute stress surface $z(\tau_A)$ is moving up into structured fluid, or where the critical stress surface $z(\tau_C)$ is moving down into de-structured fluid, the yield surface $Y(x, t)$ lies along the respective stress surface (figure 4). Otherwise, the yield surface lies between the two stress surfaces and evolves as a material curve (26):

$$\frac{\partial Y}{\partial t} + \frac{\partial}{\partial x} \int_0^Y u \, dz = \frac{\partial Y}{\partial t} + \frac{\partial}{\partial x} \int_0^Y (Y-z) \frac{\partial u}{\partial z} \, dz = 0. \quad (31)$$

4 Numerical results

4.1 Initial conditions

The initial height profile $h(x, t = 0)$ for our numerical calculations is given by the final rest state of a finite volume of fluid that has slumped under gravity on a horizontal plate. This state corresponds to one in which the stress in the current has fallen below the critical stress τ_C at all points: the fluid then becomes structured and stops flowing.

Applying this stress condition at $z = 0$, (27) (with $S = 0$) gives a simple differential equation for the height of the final state on a horizontal plate,

$$\left| h \frac{\partial h}{\partial x} \right| = \tau_C = \frac{4\beta}{\Gamma}. \quad (32)$$

Equation (32) can be combined with a volume-conservation condition, and solved to give a profile (centred on $x = 0$)

$$h(x) = \left[\left(\frac{6\beta V}{\Gamma} \right)^{2/3} - \frac{8\beta}{\Gamma} |x| \right]^{1/2}, \quad (33)$$

where V is the constant volume of fluid. Equation (33) is identical to the final state obtained for an ideal yield-stress fluid with yield stress τ_C . This final state is then used as an initial condition in the numerical calculations. In addition, in these simulations we assume that the fluid which has attained this initial condition has then been left to rest on the horizontal plane for sufficient time that the initial structure has fully healed throughout the fluid, and is uniformly given by $\lambda = 1$.

4.2 Two-dimensional results

We have solved the governing equations (30)-(31) numerically. The calculations were significantly simplified by analytically integrating over the vertical component z in these equations using (27)-(29), and thus reducing the system to a one-dimensional model (these calculations result in fairly involved analytic expressions, which are not shown here). The resulting one-dimensional equations were solved numerically, using second-order centred finite differences in space, and a second-order midpoint method in time.

Numerical results for $\Gamma = 20$, $\beta = 0.95$, and $S = 1.5$ are shown in figure 5. In addition to the height of the interface $h(x, t)$, this figure shows the two stress surfaces and the yield surface that were discussed in section 3.4.

The initial stress on the fluid is greatest at the base, below the highest point of the current. Therefore, as fluid begins to move, the most significant de-structuring occurs there, and leads to a partial collapse of the fluid column above. This process results in the formation of a ‘nose’ at the front of the current (figures 5*c* and *d*). There is a local minimum in the height profile in the interior of the current, and, most notably, at the back of the current there is a raised remnant of structured fluid that remains immobile. In contrast, figure 5(*e*) also shows the evolution of an ideal Bingham yield-stress fluid, with a yield stress given by τ_A , and the same initial profile. Here, the height of the current has quite a different profile, being highest at the front, not having a height minimum in the middle of the current, and not leaving a raised remnant at the back, at least for the length of the computation shown.

Some notable oscillations can be observed in the results of figure 5. These features appear to take the form of high-wavenumber travelling waves, which are typically first observed on the material part of the yield surface $z = Y$ near to one of the stress contours. The waves are independent of the temporal resolution of the simulations, but do exhibit some dependence on the spatial resolution. However, the macro-scale features of the flow remain almost unaltered, as the waves move with the flow and are rapidly damped when the yield surface joins one of the two stress contours. In section 5, we rationalize these waves in the form of an instability of the material part of the yield surface.

4.2.1 Critical angle

The stress on the fluid increases with the slope S (27). If the slope is not sufficiently high, the stress will be below the absolute value τ_A throughout the fluid. The fluid will therefore remain structured, and there will be no flow. However, if any of the fluid is de-stabilised, then it will remain destabilised until the stress on that fluid parcel falls below the critical value τ_C . We therefore find that there is a critical value of S , corresponding to a critical angle, below which there is no flow, and above which the fluid will de-structure and flow. This behaviour agrees with the ‘avalanching’ above a critical angle, which was reported in [10].

The critical angle can be calculated analytically. The initial condition for the height of the current is given by $|h\partial h/\partial x| = \tau_C$ (see section 4.1). For a given inclination angle, and thus a given value of S , the new stress along the base of the current is given by

$$\tau = \left| S - \frac{\partial h}{\partial x} \right| h = \tau_C + Sh. \quad (34)$$

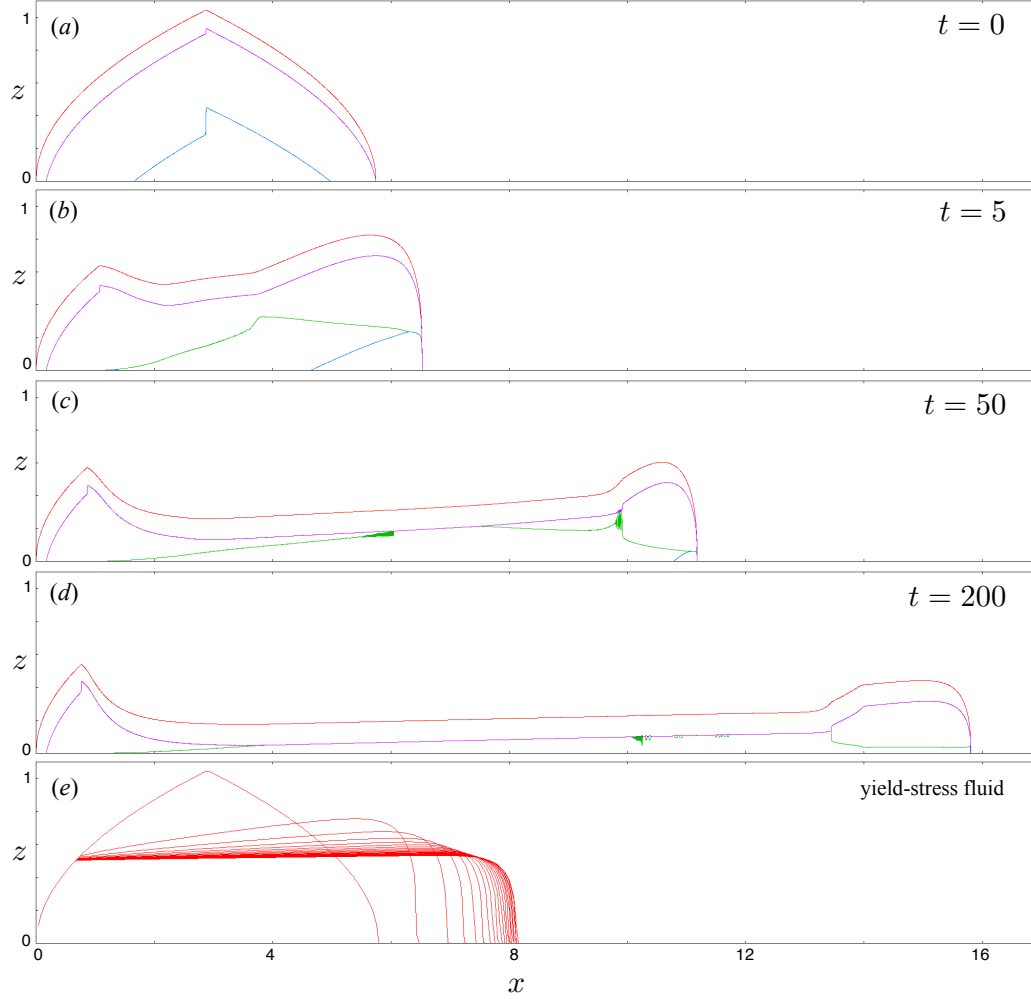


Figure 5: Numerical results of the two-dimensional system, for $\Gamma = 20$, $\beta = 0.95$, $S = 1.5$, and an initial volume of fluid $V = 4$. The lines show the height of the current $h(x, t)$ (red), the yield surface $Y(x, t)$ (green), the critical stress contour (purple), and the absolute stress contour (blue), at times: (a) $t = 0$; (b) $t = 5$; (c) $t = 50$; and (d) $t = 200$. For comparison, (e) shows the height of an ideal Bingham yield-stress fluid, with yield stress (Bingham number) τ_A , slope $S = 2$, and the same initial conditions as (a). The height profile in (e) is printed every 10 time units.

The fluid will de-structure if this stress exceeds the absolute value τ_A . Therefore, for a given initial height profile, the critical angle Θ is given by

$$S = \frac{\tan \Theta}{\varepsilon} = \frac{\tau_A - \tau_C}{\max_x h} = \frac{(1 - 2\beta)^2}{(6\beta\Gamma^2 V)^{1/3} (1 - \beta)}, \quad (35)$$

where $\max_x h$ signifies the maximum value of h over all values of x , which we have substituted from the initial height profile (33), for a given constant volume of fluid V . We have also substituted the expressions for $\tau_A = 1/\Gamma(1 - \beta)$ and $\tau_C = 4\beta/\Gamma$ from section 2.2.

4.2.2 Final rest state

As in the case on a horizontal plate (section 4.1), the final rest state for the current is given by the height profile that corresponds to the stress on the base falling below the critical value everywhere. After this point, the fluid re-structures and there is no further flow. Therefore the final state is identical to that for an ideal yield-stress fluid with a yield stress τ_C [14], and is given by

$$\left| S - \frac{\partial h}{\partial x} \right| h = \tau_C. \quad (36)$$

Equation (36) has a solution $h(x)$ that is given implicitly by

$$\log \left(1 - \frac{S}{\tau_C} h \right) + \frac{S}{\tau_C} h = \frac{S^2}{\tau_C} (x - x_F), \quad (37)$$

where x_F is a constant of integration corresponding to the final position of the nose of the current. If the back of the current has not moved from the initial state, then (37) is matched with the initial condition there, in such a way as to conserve volume. This matching determines x_F . Equation (37) gives profiles for the height that are almost flat, with a localised steep drop at the nose. Therefore, perhaps surprisingly, the theory predicts that the raised structured remnant at the back of the current (figure 5) will eventually collapse to give a roughly flat end state. This end state is not attained until the stress on the fluid is everywhere below the critical stress, and numerical results suggest that the approach to this state is extremely slow compared with the initial rate of spreading of the current.

4.3 Three-dimensional results

We can also perform the analysis of section 3 for three-dimensional flow, which includes the cross-slope co-ordinate y and velocity v . The leading order equations (c.f. (27) and (30) in two dimensions) reduce to

$$\frac{\partial h}{\partial t} + \frac{\partial}{\partial x} \int_0^h u \, dz + \frac{\partial}{\partial y} \int_0^h v \, dz = 0, \quad (38)$$

$$\tau_{xz} = \mu(\lambda) \frac{\partial u}{\partial z} = \left(S - \frac{\partial h}{\partial x} \right) (h - z), \quad \tau_{yz} = \mu(\lambda) \frac{\partial v}{\partial z} = -\frac{\partial h}{\partial y} (h - z), \quad (39)$$

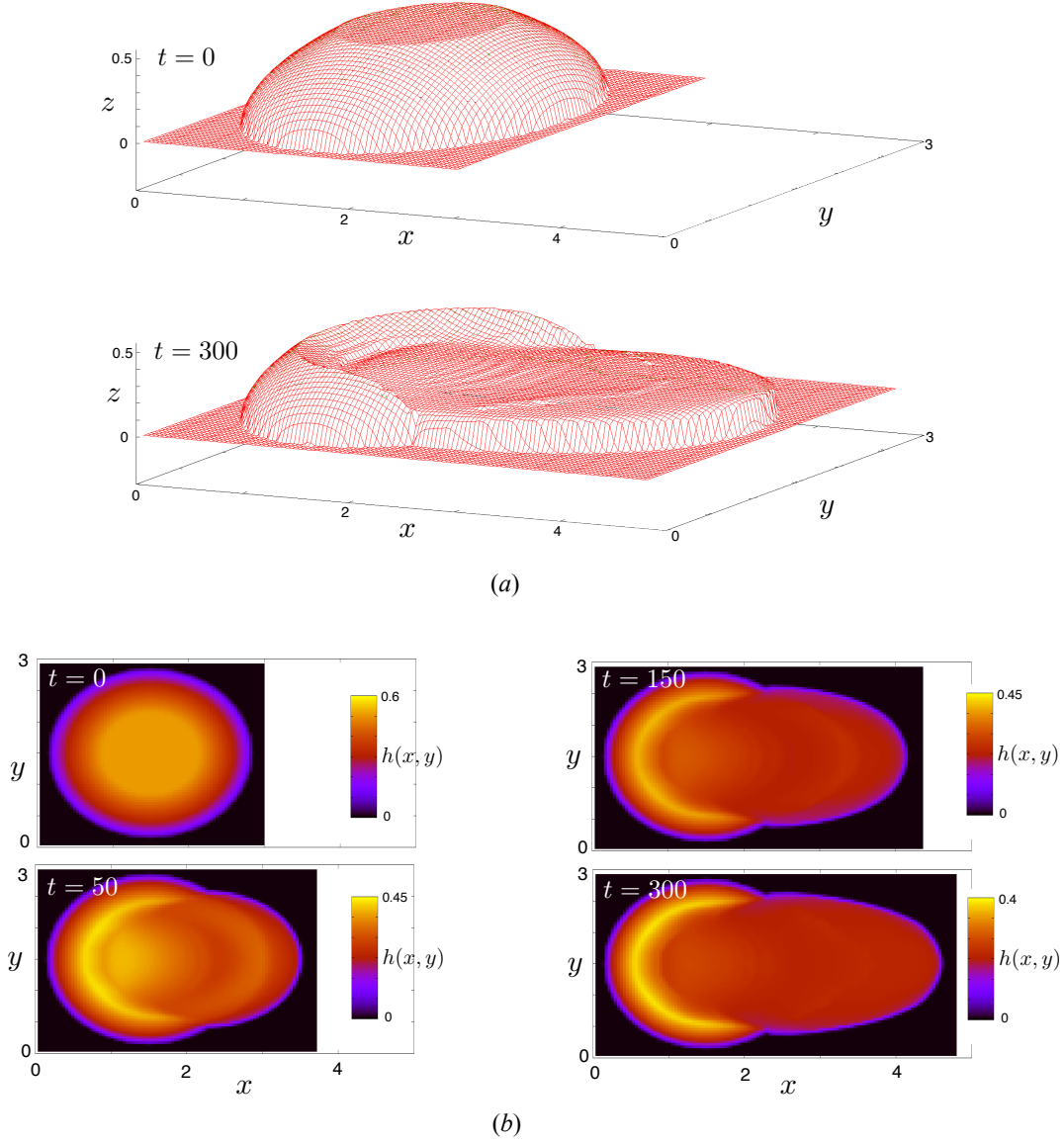


Figure 6: Numerical results of the three-dimensional system, for $\Gamma = 20$, $\beta = 0.9$, $S = 1$, and an initial volume of fluid $V = 2$: (a) the height of the current $h(x, y, t)$ visualised in three dimensions, for $t = 0$ and $t = 300$; (b) colour maps of the height of the current, viewed from above, for $t = 0$, $t = 50$, $t = 150$, and $t = 300$ as marked. A clear ‘horseshoe’ of structured fluid can be seen at the back of the current.

$$\tau = \sqrt{\tau_{xz}^2 + \tau_{yz}^2} = (h - z) \sqrt{\left(S - \frac{\partial h}{\partial x}\right)^2 + \left(\frac{\partial h}{\partial y}\right)^2}, \quad (40)$$

and the rapid-transit rheological model is the same as previously (28), (29).

As mentioned in section 4.2, we can calculate the integrals in the vertical component of (38) analytically (not shown here), and thus reduce the system to a two-dimensional model in x and y . We have solved (38)–(40) numerically, using a modification of the one-dimensional routine discussed in section 4.2.

Figure 6 shows solutions of the height $h(x, y, t)$ at different times, for $\Gamma = 20$, $\beta = 0.9$, and $S = 1$. Similar qualitative features to the two-dimensional model can be seen. Firstly, the fluid appears to collapse most rapidly in the centre. Secondly, a distinct remnant of structured fluid is left behind at the back of the current, which persists as the nose flows away down the slope. This structured remnant appears to be very similar to the observations of a ‘horseshoe’ that were reported in [10]. There is less of a distinct raised nose in these simulations as in the one-dimensional results (figure 5); this appears to be due to the lower value of β used here, which corresponds to a smaller hysteresis loop in the constitutive equation. At values of β closer to 1, the calculations show noticeable high-wavenumber oscillations in the material part of the yield surface $z = Y$, which are also visible as ripples in the free surface $z = h$: these are analogous to the features seen in the two-dimensional results, and are discussed in the following section. Their possible physical relevance is considered in the context of our experimental results with ketchup (section 6.2).

5 Stability

It has been shown that two inclined shallow layers of Newtonian [9] or non-Newtonian power-law [5] fluid with differing viscosities can be unstable to an interfacial instability, even in the absence of inertia, due to the additional degrees of freedom given by the material surface between the layers. We might, therefore, expect to find a similar interfacial instability in the shallow thixotropic layer, when the yield surface is a material curve which separates infinite-viscosity structured fluid above from relatively low-viscosity de-structured fluid below. Indeed, as mentioned in section 4, we can observe instabilities forming on the material yield surface in our numerical simulations.

In this section we consider the linear stability of an idealised two-dimensional system, in which the background height $z = h$ and yield surface $z = Y$ are both constant. The yield surface is a material curve lying between the two stress contours $\tau = \tau_A$ and $\tau = \tau_C$, as shown in figure 7(a). This study is limited to times before the yield surface touches either of these stress contours. We begin this section by performing a theoretical stability analysis, which shows that the system is always weakly unstable to perturbations at any wavenumber. We then present numerical simulations of the system, which reveal that the instability results in the generation of travelling shocks on the yield surface.

5.1 Theoretical stability analysis

The system is governed by continuity below and above the yield surface, and by the kinematic condition at both $z = Y$ and $z = h$. These conditions give governing equations (30)

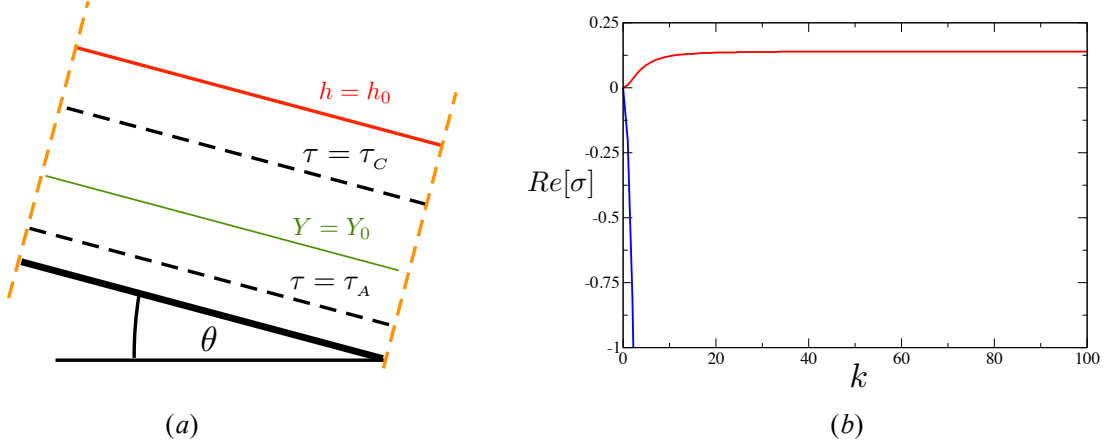


Figure 7: (a) The system under consideration in the linear stability analysis: the background height and yield surface are given by the constants h_0 and Y_0 respectively, and, for the numerical calculations, the boundaries are periodic. (b) The two roots of the growth rate, for $\Gamma = 20$, $\beta = 0.95$, $S = 2$, $h_0 = 1$, $Y_0 = 0.25$. One root (blue) decays like $-k^2$; the other (red) tends to a small positive constant for large values of k .

and (31), which can be written in the form

$$\frac{\partial h}{\partial t} + \frac{\partial}{\partial x} F(h, Y) = 0, \quad \frac{\partial Y}{\partial t} + \frac{\partial}{\partial x} G(h, Y) = 0. \quad (41)$$

The functions F and G are the fluxes of h and Y respectively, given by

$$F = \int_0^h u \, dz = \int_0^Y (h - z) \frac{\partial u}{\partial z} \, dz, \quad (42)$$

$$G = \int_0^Y u \, dz = \int_0^Y (Y - z) \frac{\partial u}{\partial z} \, dz. \quad (43)$$

The rate of strain $\partial u / \partial z$ (27) depends on the structure parameter λ , which itself is a function of the shear stress (29), and thus a function of z . The fluxes (42), (43) can therefore be written as

$$F(h, h_x, Y) = (S - h_x) \int_0^Y (h - z)^2 (1 - \lambda) (1 - \beta \lambda) \, dz, \quad (44)$$

$$G(h, h_x, Y) = (S - h_x) \int_0^Y (h - z) (Y - z) (1 - \lambda) (1 - \beta \lambda) \, dz, \quad (45)$$

where h_x is the partial derivative of h with respect to x , and, from (29), the structure parameter is given by

$$\lambda(z, h, h_x) = \frac{1}{2\beta} \left[1 - \left(1 - \frac{4\beta}{\Gamma (h - z) (S - h_x)} \right)^{1/2} \right]. \quad (46)$$

These integrals (44) and (45) can be calculated analytically (not shown here).

We perform a linear stability analysis of (41) by looking for normal modes, with growth rate σ and wavenumber k :

$$h = h_0 + \tilde{h}e^{\sigma t + ikx}, \quad Y = Y_0 + \tilde{Y}e^{\sigma t + ikx}, \quad (47)$$

where h_0 and Y_0 are the constant background values of the height and the yield surface, and \tilde{h} and \tilde{Y} are small perturbations which satisfy $\tilde{h}, \tilde{Y} \ll h_0, Y_0$. Neglecting terms that are non-linear in the perturbation quantities, we find that the growth rate σ satisfies a dispersion relationship of the form

$$\sigma^2 + \sigma (Ak^2 + Bik) + Cik^3 + Dk^2 = 0 \quad (48)$$

where A, B, C , and D are real functions of the governing parameters of the problem, Γ, β, S, h_0 , and Y_0 , and are given in terms of the fluxes F and G by

$$A = \frac{\partial F}{\partial h_x}, \quad B = \frac{\partial F}{\partial h} + \frac{\partial G}{\partial Y}, \quad C = -\frac{\partial G}{\partial h_x} \frac{\partial F}{\partial Y}, \quad D = \frac{\partial G}{\partial h} \frac{\partial F}{\partial Y} - \frac{\partial G}{\partial Y} \frac{\partial F}{\partial h}, \quad (49)$$

all evaluated at $h = h_0, Y = Y_0$, and $h_x = 0$.

Unstable modes k correspond to a positive real part of the growth rate $Re[\sigma]$, and marginally stable wavenumbers are obtained when $Re[\sigma] = 0$. Equation (48) gives marginal stability only at $k = 0$, which means that any unstable (or stable) solutions will be unstable (or stable) for all wavenumbers k . In the limit of large k , (48) gives two roots $\sigma_{1,2}$ with leading order real parts given by

$$Re[\sigma_1] = -Ak^2 + O(1), \quad Re[\sigma_2] = \frac{C^2 - ABC - A^2B}{A^3} + O(k^{-1}). \quad (50)$$

The algebra for this problem is significantly simplified if we consider the limit of large Γ , and expand the coefficients in powers of $1/\Gamma$. For ease of notation we also define the quantity $\Theta_0 = h_0 - Y_0$. To leading order in $1/\Gamma$, we find that $A = [h_0^3 - \Theta_0^3]/3 > 0$, and

$$\frac{C^2 - ABC - A^2B}{A^3} = \frac{3h_0^3\Theta_0^3(h_0 - \Theta_0)^4(h_0 + 2\Theta_0)^2S^2}{4(h_0^3 - \Theta_0^3)^3} > 0. \quad (51)$$

Therefore, in the limit of large Γ , the first root σ_1 has a negative real part, with a magnitude that grows like k^2 . However, the second root σ_2 has a positive real part, that is a constant to leading order for large values of k . We can also show that for small k the unstable mode grows like k^2 , and then increases monotonically to this constant value for large k . The system is therefore unstable to perturbations of any wavenumber. For parameter settings relevant to the full slump problem, the positive growth rate is typically extremely small in magnitude.

We have also shown numerically that this behaviour is generic for arbitrary values of Γ : that is, there is always one negative root that decays like k^2 , and one positive root that grows monotonically from zero at $k = 0$ to a (typically very small) constant for large k . Therefore all wavenumbers are unstable. An example of the two roots is plotted in figure 7(b).

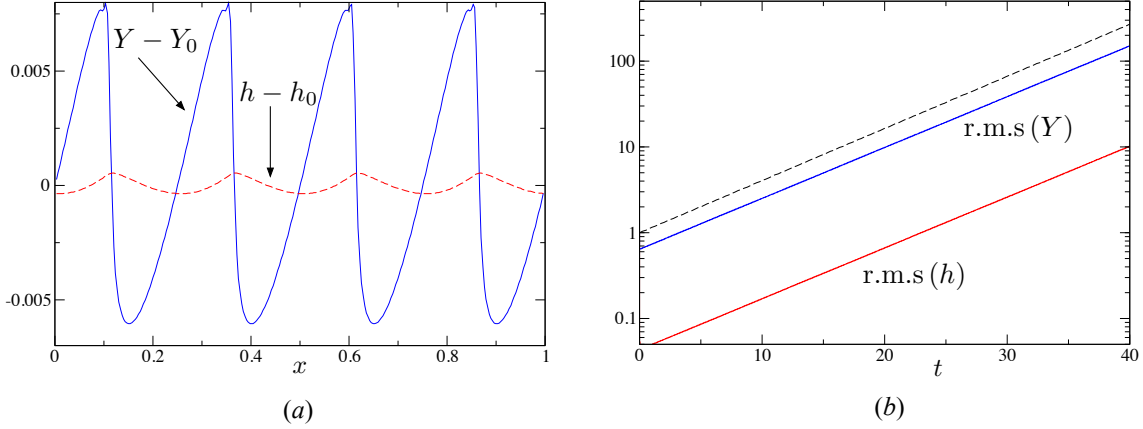


Figure 8: Numerical stability results for an initial perturbation of amplitude 10^{-5} and wavenumber $k = 8\pi$, for $\Gamma = 20$, $\beta = 0.95$, $S = 2$, $h_0 = 1$, and $Y_0 = 0.25$: (a) the perturbations to the yield surface $Y - Y_0$ (blue, solid) and to the height $h - h_0$ (red, dashed), at time $t = 50$, showing the formation of shocks in the yield surface; and (b) the measured root-mean-squared yield surface (blue) and height (red), scaled by the initial perturbation amplitude, and compared to the theoretical unstable growth rate $|e^{\sigma t}|$ (dashed) for large k , calculated from (50).

5.2 Numerical stability analysis

We can simulate the setup shown in figure 7(a) directly, with periodic boundary conditions in the x -direction. The height h and the yield surface Y are both subjected to the same small single-mode perturbation, which then evolves according to (41). Figure 8 shows the results of such a simulation, for an initial perturbation with wavenumber $k = 8\pi$, corresponding to 4 waves. The resulting perturbation to the height and to the yield surface (figure 8a) are observed to grow extremely slowly in comparison with the advection time of the background velocity. The instability is more prominent on the yield surface than on the height of the current. In the non-linear regime, the instability appears to lead to the formation of shocks on the material yield surface, with the same wavenumber as the original perturbation. We find that these shocks drive the initiation of high wavenumber oscillations, and this behaviour is perhaps a feature of our numerical scheme. The corresponding deformation of the height of the current takes the form of travelling waves. The measured amplitude of the perturbations gives the same growth rate as the theoretical prediction (50) for large k (figure 8b).

The analysis of this section shows that the idealised system is unstable to an interfacial instability at all wavenumbers, in the regions where the yield surface is a material curve. This result has important implications for our numerical simulations of the full slump problem, as instabilities with length scales down to the grid scale might be expected to form, and the results will likely vary with the spatial resolution of the computation. However, it should be remembered that the full system is not periodic in x , but rather the material part of the yield surface is bounded at each end by either critical or absolute stress contours, which limit the development and propagation of the instability. Furthermore, because the

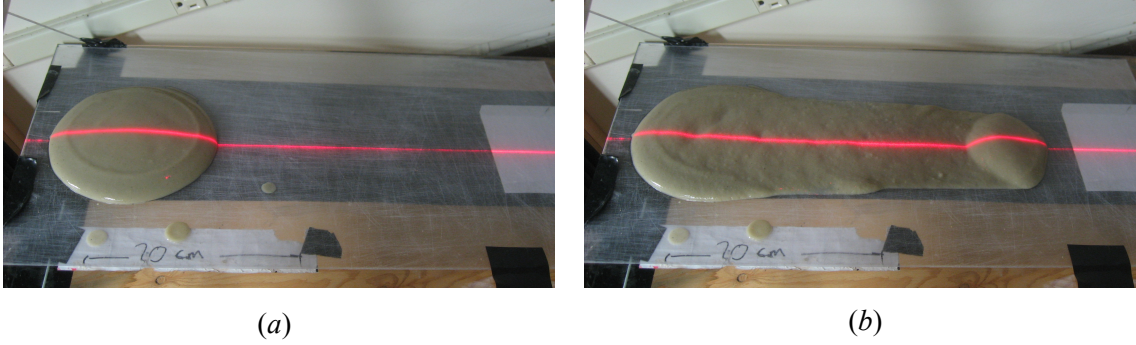


Figure 9: Snapshots of a typical experiment in progress, with 10% by volume bentonite solution, $T_{\text{age}} = 240$ minutes, and an angle of 20° : (a) after $t = 5$ seconds; (b) after $t = 50$ seconds. For scale, the tattered white paper below the sample in each picture is 20 cm long.

growth rate is (typically) extremely small, the background advection of the flow is much faster than the growth of instabilities, and we expect them to be rapidly transported along the yield surface until they reach one of the stress contours. This behaviour is observed in the numerical results of section 4, where the instabilities are typically quashed by the absolute or critical stress contours before they significantly destabilise the flow and cause any noticeable deformation to the height $z = h$ of the current. It should, however, be noted that this is not always the case: particularly at smaller values of Γ and larger values of β , we find that instabilities on the yield surface can result in wave generation and deformation of the height of the current.

6 Experimental results

We have carried out a series of experiments to compare with the numerical simulations of our model. Our experimental setup consisted of a $\approx 1 \text{ m}^2$ glass plate, which was hinged at one end, and could be tilted and held at a desired angle using a pulley system. The plate was joined to a frame, which allowed for a laser pointer and a camera to be held in the same frame of reference as the plate. Samples of fluid were placed on the plate, which was then lifted to a given angle (details of the preparation of the fluid and the initialisation of the experiment are discussed below). A laser line was projected onto the fluid surface from directly above, facing down the slope, which allowed for measurements of the height of the current along the midplane (see figure 9 for typical photographs of the system during an experiment).

We performed experiments with two different thixotropic fluids: bentonite clay solution (10% by volume, *Quik-Gel* sodium bentonite, *Baroid drilling fluids*), and tomato ketchup (*Heinz*). Each of these fluids have been observed to exhibit thixotropy [6, 18]: in particular, there have been a variety of rheological measurements of bentonite [11, 19], which suggest that it exhibits many of the features of our rapid-transit rheological model (section 2). In order to ensure reproducibility in the results, all the fluid samples were initially subjected to vigorous shear for at least 30 minutes. This shear was intended to remove any initial

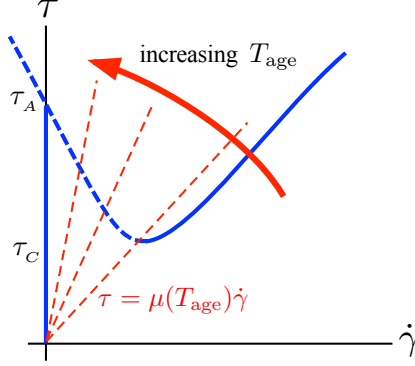


Figure 10: Schematic of the steady-state constitutive relationship (thick blue), as in figure 2, together with the local linear relationship between τ and $\dot{\gamma}$ for increasing ageing times T_{age} as marked (thin red dashed). The time-dependent ‘effective yield stress’, above which the fluid de-structures, is given by the intersection between the curves. For $T_{\text{age}} = 0$, the effective yield stress is equal to the critical stress τ_C , and there is no hysteresis in the system. As $T_{\text{age}} \rightarrow \infty$, the effective yield stress tends towards the absolute stress τ_A , and $\lambda \rightarrow 1$.

structure in the fluid. A fixed volume (150 ml) of the fluid was then slumped on a horizontal plate, by pouring into a hollow cylindrical (5 cm radius) mould, which was then lifted. In this way, the fluid attained its rest state on a flat plate, which corresponds to the initial condition of the numerical simulations (section 4). Samples were then left to age for different periods of time T_{age} . During this time, the samples were kept under airtight covers to limit the effects of evaporation. The substrate for the experiments was made of sanded perspex, in order to avoid any slip at the base of the current. There is an important phenomenological distinction between this ‘genuine’ slip, in which the whole fluid column slides on the substrate, and the apparent slipping of structured fluid which is actually due to lubrication from a de-structured layer at the base of the current. The latter effect, which results in a thin layer of fluid being left behind on the substrate, is consistent with the theoretical ‘no-slip’ boundary condition on the base of the current (10), and was observed in many of our experiments.

Before presenting our experimental results, we briefly consider how we expect the behaviour of the fluid to vary with different ageing times T_{age} , based on the theoretical model that was discussed in section 2. While the fluid sample is at rest, the structure should evolve according to (2), with $\dot{\gamma} = \mathbf{u} = 0$: *i.e.*

$$\frac{\partial \lambda}{\partial t} = \frac{1 - \lambda}{T}. \quad (52)$$

For a given ageing time T_{age} , there is a corresponding value of λ , given by (52). This value of λ corresponds to a viscosity, $\mu(\lambda)$, and thus to a linear constitutive relationship $\tau = \mu(\lambda)\dot{\gamma}$. The local value of the stress at which the fluid becomes de-structured (the ‘effective yield stress’) is then given by the intersection between this linear constitutive relationship and the steady state hysteresis loop (shown schematically in figure 10). If the ageing time T_{age} is small, this effective yield stress will be very close to the critical stress τ_C ,

and we would therefore expect the sample to behave rather like a simple yield-stress fluid. As T_{age} increases, the sample should increasingly exhibit the features that we observed in our numerical simulations (section 4), as the effective yield stress increases towards τ_A , and the extent of hysteresis in the system increases. Moreover, the discontinuity in $\dot{\gamma}$ at the effective yield stress will also increase with T_{age} , and the system should exhibit increasingly dramatic ‘avalanche’ behaviour.

6.1 Bentonite

We examined the behaviour of different bentonite solutions with filtered water: 7.5%, 10%, and 12.5% bentonite by volume. The 12.5% solution was very viscous, and so suffered from slipping on the substrate, while the 7.5% solution had a relatively low viscosity, which appeared to result in some inertial effects, and caused the fluid to flow too rapidly for accurate measurements. Here, therefore, results are presented only for the 10% bentonite solution.

Figure 11 shows measurements of the height profiles over time, for different ageing times T_{age} , at a fixed angle of 20° . Figure 12 shows the height profiles at different ageing times for a slightly larger inclination angle of 24° . As a comparison, we also carried out some experiments with a ‘joint compound’ solution (*Sheetrock* all-purpose joint compound), which, over the timescale of an experiment, appeared very like an ideal yield-stress fluid. Measurements of the height of the joint compound are shown in figure 11(a).

These measurements show that the behaviour of bentonite is strongly dependent upon the ageing time. Consider, for example, the results on a 20° slope (figures 11b-d). For very small ageing times, the behaviour is similar to the joint compound (yield-stress fluid, figure 11a), although the formation of a nose at the front of the downward-moving current is more pronounced: there is no raised ‘horseshoe’ at the back of the current, and the fluid evolves rapidly after the experiment starts. However, as the ageing time T_{age} increases, the samples display behaviour that is more similar to the numerical simulations of section 4: there is an increasingly pronounced residual ‘horseshoe’ of fluid left behind at the back of the current, and the thinnest part of the current for late times is in the middle, between the horseshoe and the nose. These features are even more striking if the slope is increased by 4° (figure 12). Here, the sample thins very dramatically in the interior, which results in an extremely pronounced nose at the head of the current and residual horseshoe at the rear. This behaviour is more dramatic than is predicted by the theoretical model, possibly because of the destructuring effects of extensional stresses in the current, which the model does not take into account. This issue is discussed in section 7. It is important to highlight that, even in the most extreme examples (e.g. figure 12c), the nose did not appear to be slipping on the substrate as it moved down the slope, but rather there was always a thin lubricating layer of de-structured fluid along the base.

Figure 13(a) shows the final position of the nose of the current, x_F , as a function of the inclination angle, for different ageing times T_{age} . As discussed above, we anticipate that for larger ageing times, the stress (and hence the angle) at which the fluid de-structures (and evolves to the small- λ stable branch of the constitutive relationship), should increase, and the corresponding flow after de-structuring should be increasingly dramatic (as the value of $\dot{\gamma}$ on the small- λ stable branch will be larger). Both of these features can be observed in

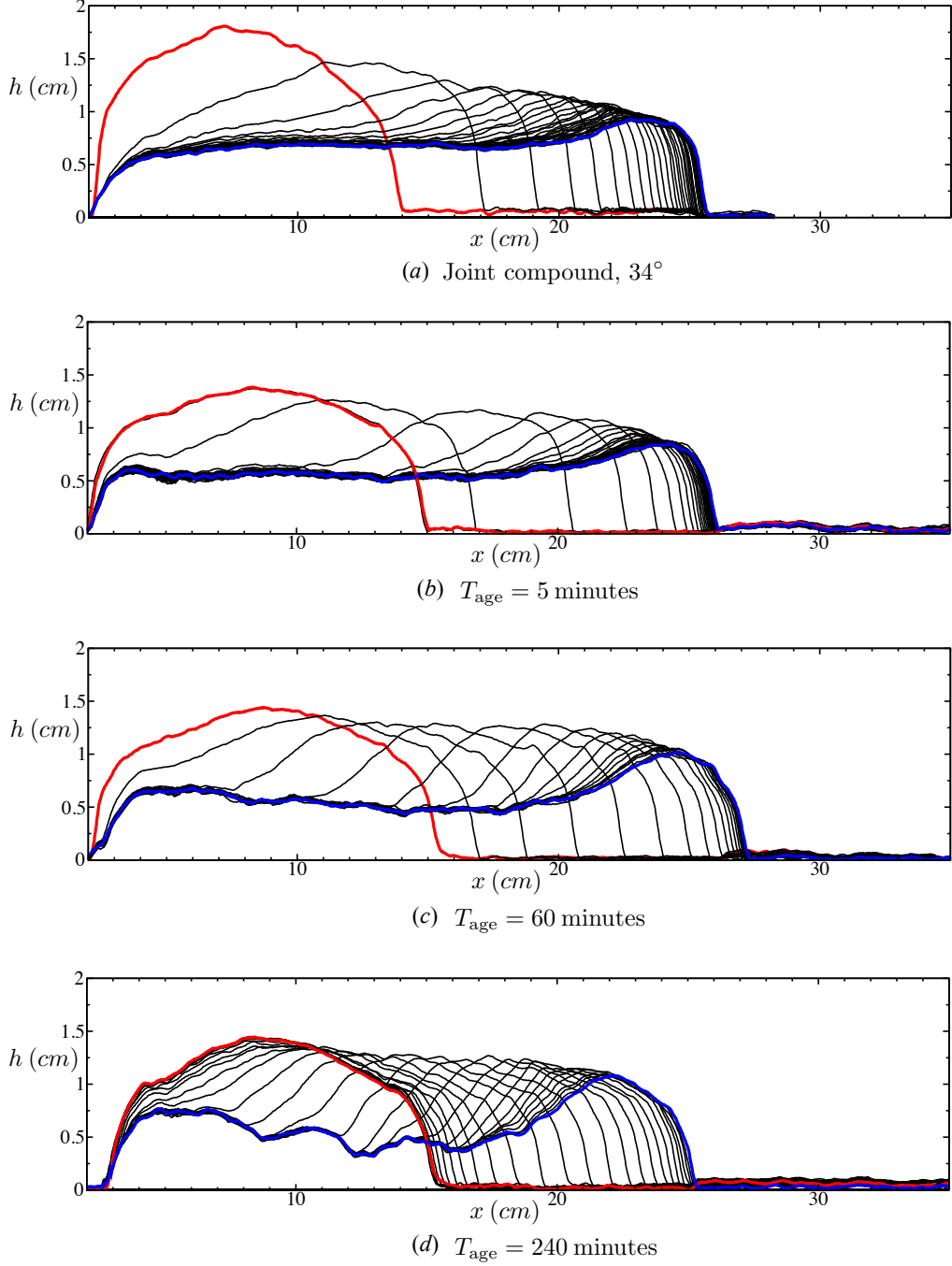


Figure 11: Snapshots of the height of the midplane over time, measured using a laser line, for (a) a joint compound solution on a 34° slope, which behaves very like an ideal yield-stress fluid [14, 17], and for (b) – (d) 10% (by volume) bentonite solution on a 20° slope, for different ageing times T_{age} as marked. The x axis gives the distance from the back of the current. Lines are plotted every ≈ 2 seconds, except in (b), where lines are plotted every ≈ 0.5 seconds. Red and blue lines signify the initial and final profiles, respectively. As T_{age} increases, the response of the bentonite increasingly differs from the ideal yield-stress behaviour in (a), as discussed in the text, and in the caption to figure 12.

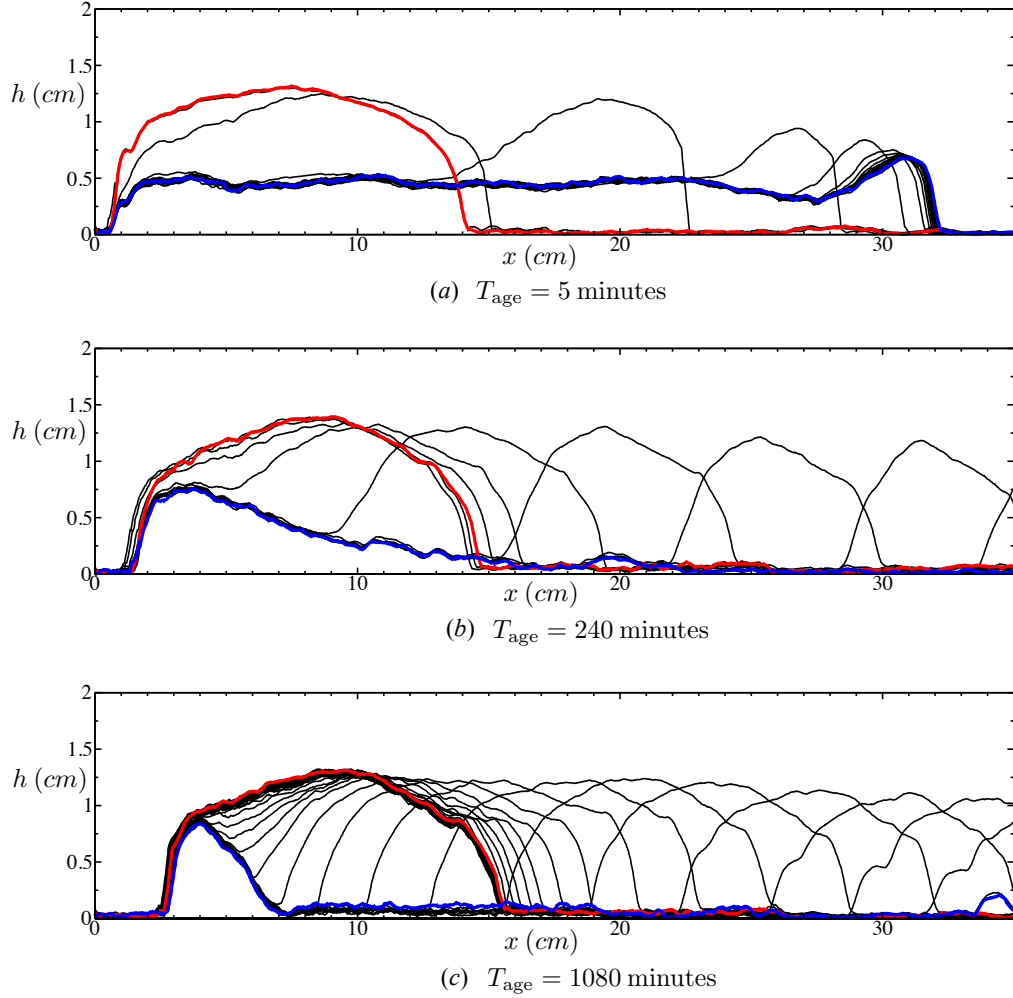


Figure 12: Snapshots of the height of the midplane over time for 10% (by volume) bentonite solution on a 24° slope, for different ageing times T_{age} as marked.. Lines are plotted every ≈ 2 seconds, except in (a), where lines are plotted every ≈ 0.5 seconds. Red and blue lines signify the initial and final profiles, respectively. In (b) and (c), the nose of the current eventually moves off the end of the plate. For the larger values of T_{age} , the same qualitative features that were observed in the numerical results (section 4) can be seen: the back of the current remains fixed (the ‘horseshoe’), and there is a ‘nose’ of fluid which moves rapidly down the slope. The sample in (d), which is aged for 1080 minutes, does not move on a 20° slope, which exemplifies the increasingly dramatic ‘avalanche’ behaviour of the fluid for large T_{age} .

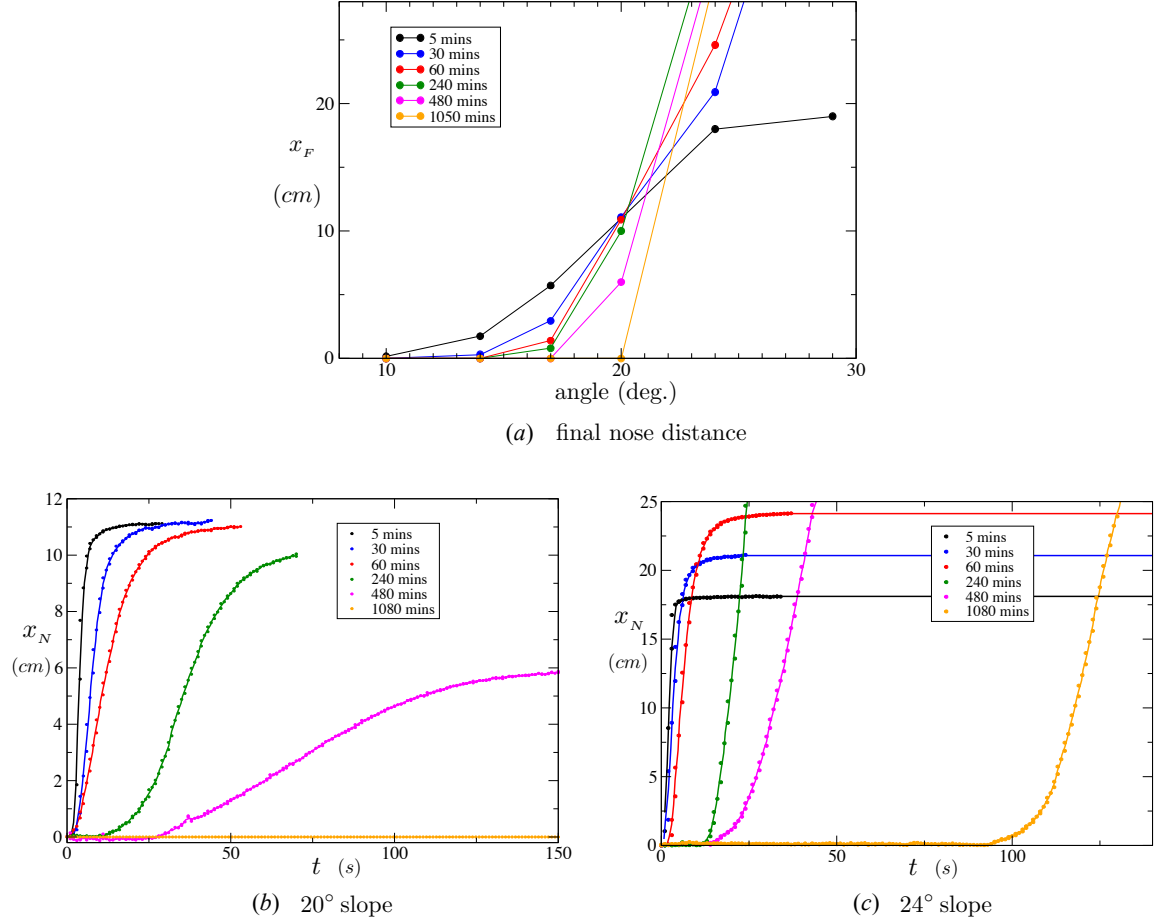


Figure 13: Position of the nose of the current for 10% (by volume) bentonite solution: (a) the final distance travelled by the nose x_F , for different ageing times T_{age} , showing the increasingly narrow band of angles over which the de-structuring of the fluid becomes more dramatic; (b) the distance travelled by the nose $x_N(t)$ on a 20° slope; and (c) the distance travelled by the nose $x_N(t)$ on a 24° slope. Notice the change in curvature of the lines in (b) and (c) for longer ageing times. Measurements which appear above the top of the graph signify that the current reached the end of the plate.

figure 13(a): for small values of T_{age} , the final distance of the nose x_F steadily increases with the angle of inclination, while for larger T_{age} , there is an increasingly thin band of angles over which x_F changes dramatically. This ‘avalanche’ behaviour is most clearly observed in the samples that were left to age for $T_{\text{age}} = 1080$ minutes, where the fluid remains stationary on a 20° slope, but fails dramatically and flows off the bottom of the plate at 24° .

The transient behaviour of the nose of the current $x_N(t)$ is shown for two different angles in figures 13(b) and (c), again for different values of T_{age} . These figures reveal a change in the evolution of the current for larger ageing times. For small values of T_{age} , the nose of the current moves most rapidly at $t = 0$, as in the case of an ideal yield-stress fluid. However, as T_{age} increases the nose of the current takes increasingly long to move, and then gradually accelerates. This behaviour agrees with previous observations made by Coussot *et al.* [10]. We anticipate that this slow acceleration is a result of the gradual breakdown of structure in the fluid, which mathematically corresponds to the slow evolution of the structure parameter λ towards the steady state, as modelled by time derivative in (2). This behaviour is not, therefore, captured by the rapid-transit model, and thus is not observed in our numerical results.

Figures 13(b) and (c) also show that the current comes to an abrupt halt after flowing down the plane. The shape of this final profile is much like the profile during the flow: the immobile current has a clear raised horseshoe at the back and a raised nose at the front. This behaviour is quite unlike that predicted by the numerical simulations (section 4.2.2), which suggest that the flow should slowly evolve towards a final profile that is approximately flat. The reasons for this difference are unclear.

6.2 Ketchup

We have also carried out experiments using Heinz tomato ketchup. Ketchup is an interesting and complex multicomponent fluid, and is difficult to use experimentally due to its tendency to separate over time. In particular, ketchup readily expels vinegar, which gathers around the base of the sample if it is left at rest for more than a few minutes. Despite these difficulties, which suggest caution is needed in analysing these results, it is still possible to observe clear thixotropic behaviour, and to draw qualitative comparisons both with the measurements for bentonite and with our theoretical model. While we gathered a range of measurements using ketchup, we will only briefly discuss the qualitative behaviour here, because of this separation problem.

Figure 14 shows snapshots of the height of the current over time, for different ageing times T_{age} . Although the dependence on T_{age} seems much less dramatic than with bentonite (figure 11), we still observe the development of a structured horseshoe of fluid at the rear of the current for large ageing times, which is absent for smaller ageing times. We found that ketchup does not exhibit the same catastrophic failure at a particular angle that we observed in fully structured bentonite (e.g. figure 12c), except at much larger angles, when the fluid starts to slip on the base (see the discussion of slip above), so that the nature of the experiment changes.

A photograph of the ketchup current (figure 15a) shows the structured horseshoe remnant, and the gravity current extruding down the slope. This picture highlights the complex structure of the surface of the current: the evident surface structure is perhaps the result

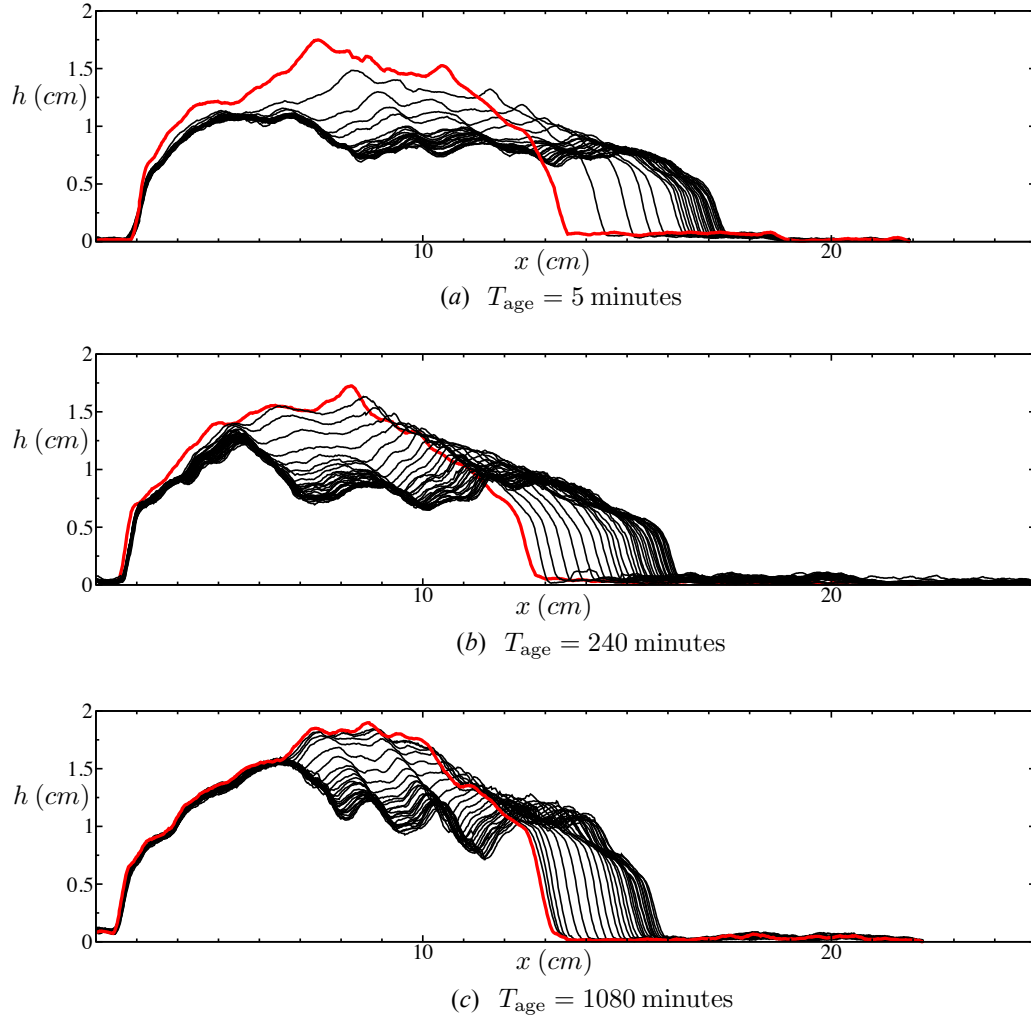


Figure 14: Snapshots of the height of the midplane over time for Heinz tomato ketchup on a 14° slope, for different ageing times T_{age} as marked.. Lines are plotted every ≈ 10 seconds. Red lines signify the initial profiles: in contrast to bentonite, the samples continue to move slowly down the slope for very long times, and thus the final position of the slump is not necessarily attained. For larger values of T_{age} there is a clear structured horseshoe at the rear of the current.

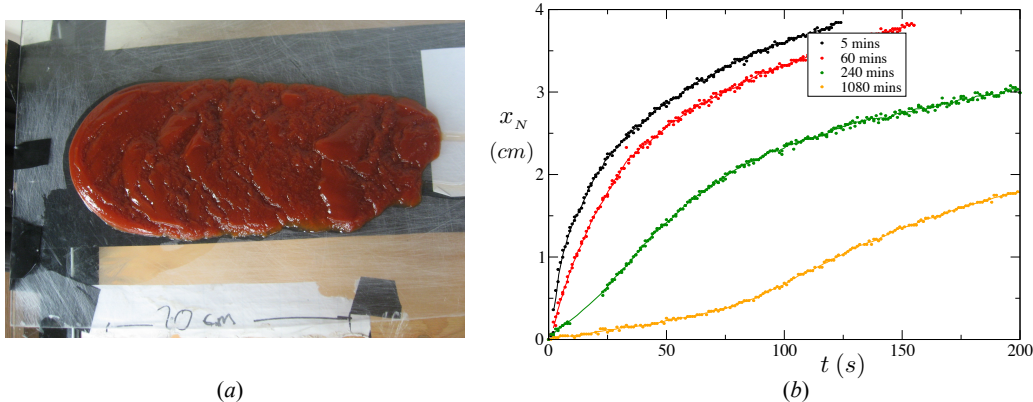


Figure 15: Results with Heinz tomato ketchup: (a) a photograph from above of a ketchup current after an experiment (downslope is to the right), showing a structured horseshoe at the back (left), and significant surface texture on the rest of the current; and (b) the evolution of the nose of the current $x_N(t)$ on a 14° slope, showing the same change in curvature that was observed with bentonite (figure 13b and c). Unlike bentonite, the current continued to flow throughout the experiment, rather than coming to a halt.

of an instability, such as the interfacial instability that was analysed in section 5.

Figure 15(b) shows the evolution of the position of the nose $x_N(t)$ for different values of T_{age} . As in the case of bentonite (figure 13b and c), the current gradually accelerates for longer ageing times, in contrast to the behaviour at small values of T_{age} . Interestingly, the ketchup current continued to flow throughout the experiment, rather than coming to an abrupt halt like the bentonite.

7 Conclusions

As discussed in section 1, despite a range of rheological studies of thixotropy there has been relatively little work that couples the rheology to the flow in a physical system. In this report we have presented and discussed a rheological model for thixotropic fluids, and applied it in the context of gravity-driven flow on a slope. We modelled this system both numerically and experimentally, and, despite some intriguing differences, on the whole we found broad qualitative agreement between the results.

In section 2, we presented a rheological model that we use to describe the effects of thixotropy. This model is based on a selection of previous models (e.g. [11, 19]), but also includes the concept of an *absolute stress* τ_A , above which even fully structured fluid will de-structure and begin to flow. In addition, based on previous empirical observations [1, 7, 11, 20], we introduced the simplifying ‘rapid-transit’ approximation, which assumes that λ evolves instantaneously to its steady-state value.

In sections 3 and 4, we applied our rapid-transit rheological model to the problem of a finite shallow current on a slope, and presented numerical results of the flow in two and three dimensions. For these theoretical results, we assumed that the fluid was initially fully structured. We found that the flow is characterized by a raised ‘horseshoe’ of structured

fluid at the back of the current, in agreement with previous experimental observations [10]. The model also shows that there is a critical angle, above which the current will flow (in some cases, dramatically), and below which the current will not move.

Motivated by the presence of high-wavenumber fluctuations in these numerical results, in section 5 we explored the stability of an idealised shallow-layer system. We found that the internal interface (yield surface) between the structured and de-structured fluid is always weakly unstable to perturbations at any wavelength. Within this idealised system, we numerically followed the instability into the non-linear regime, and found that the instability develops into travelling shocks on the material part of the yield surface. However, the growth rate of the instability is typically extremely small compared to the rate of propagation of the current, and, in the full (non-idealised) system, the material part of the yield surface is always bounded by a constant stress contour at either end, which damp any oscillations. On the whole, therefore, this instability does not appear to have a significant effect on the propagating current.

Finally, in section 6, we presented experimental results of the same shallow-layer inclined system, with two thixotropic fluids: bentonite clay solution, and tomato ketchup. We observed that, as the ageing time T_{age} increased, the bentonite solution evolved in qualitative agreement with the theoretical predictions: from simple yield-stress-fluid behaviour for small T_{age} , to increasingly dramatic ‘avalanche’ behaviour for larger T_{age} . The shape of the current for larger T_{age} is similar to that predicted by the numerical simulations: a notable structured horseshoe of fluid at the back of the current; a thinner region in the interior; and a nose at the front. However, unlike the numerical predictions, which suggest that the current should evolve slowly to a relatively flat final profile, the bentonite always came to an abrupt halt after flowing some way down the plane, leaving a pronounced horseshoe and nose at the back and front of the current respectively. The reasons for this different behaviour are not clear, although perhaps the neglect of extensional stresses in the theoretical model could be relevant (see the discussion below).

The results for ketchup are more difficult to analyse, due to the material separating into its constituent fluid components. However, we again observe that the shape of the current increasingly resembles the numerical solutions for larger ageing times, with a structured horseshoe at the back of the current. The ketchup current also undergoes an instability or deformation of the free surface as it flows down the slope, which may be related to the instability process in the theoretical model (section 5). The evolution of the nose of the current for both ketchup and bentonite solution undergoes a qualitative change for different values of T_{age} (as in [10]), from initial gradual deceleration for small T_{age} , to initial gradual acceleration for larger T_{age} . This behaviour is not captured by the numerical results, presumably because of the rapid-transit approximation.

While many of the main phenomenological features of the experimental results agree well with both the numerical and theoretical models, we find that bentonite can undergo even more dramatic de-structuring than the numerical solutions suggest. This difference is perhaps due to the details of the rheological model, in which, for example, the viscosity may have a more sensitive dependence on the strain rate. However, the difference could also be explained by the neglect of extensional stresses from the theoretical shallow-layer model (section 3). Flow in a de-structured layer may induce significant extensional stresses in the structured (and therefore much more viscous) layer above, which are not included in the

model. If the upper layer is sufficiently viscous, these extensional stresses can contribute to the stress invariant τ at the same order of ε as the shear stress. The inclusion of extensional stresses would lead to more of the current becoming de-structured, which would result in an increased thinning of the interior of the current, as is observed experimentally. It has proved somewhat complicated to develop a consistent model that incorporates extensional and shear stresses throughout the current, and this remains an intriguing avenue for further study.

Acknowledgments

A great many thanks are due to the directors, staff, principal lecturers, and administrators of the 2012 WHOI GFD summer program, and to all who came and went from Walsh cottage during the program. I would particularly like to thank Neil Balmforth, both for suggesting this project, and for countless helpful and stimulating discussions. His interest and input have been invaluable in this work. I would also like to thank Colm Caulfield for his kind encouragement during and prior to this summer, and Anders Jensen for his assistance with the experimental work. Finally, I am extremely grateful to all the other fellows for contributing to such an interesting, inspiring and enjoyable summer.

References

- [1] A. ALEXANDROU, N. CONSTANTINOU, AND G. GEORGIOU, *Shear rejuvenation, aging and shear banding in yield stress fluids*, J. Non-Newtonian Fluid Mech., 158 (2009), pp. 6–17.
- [2] N. BALMFORTH AND R. CRASTER, *A consistent thin-layer theory for Bingham plastics*, J. Non-Newtonian Fluid Mech., 84 (1999), pp. 65–81.
- [3] ———, *Geomorphological Fluid Mechanics*, Springer, 2001, ch. Geophysical aspects of Non-Newtonian fluid mechanics.
- [4] N. BALMFORTH, R. CRASTER, AND R. SASSI, *Shallow viscoplastic flow on an inclined plane*, J. Fluid Mech., 470 (2002), pp. 1–29.
- [5] N. BALMFORTH, R. CRASTER, AND C. TONIOLO, *Interfacial instability in non-Newtonian fluid layers*, Phys. fluids, 15 (2003), pp. 3370–3384.
- [6] H. BARNES, *Thixotropy — a review*, J. Non-Newtonian Fluid Mech., 70 (1997), pp. 1–33.
- [7] D. BONN, H. TANAKA, P. COUSSOT, AND J. MEUNIER, *Ageing, shear rejuvenation and avalanches in soft glassy materials*, J. Phys.: Condens. Matter, 16 (2004), pp. S4987–S4992.
- [8] H. CHANSON, S. JARNY, AND P. COUSSOT, *Dam break wave of thixotropic fluid*, J. Hydr. Eng., 132 (2006), p. 280.

- [9] K. CHEN, *Wave formation in the gravity-driven low Reynolds number flow of two liquid films down an inclined plane*, Phys. Fluids A, 5 (1993), p. 3038.
- [10] P. COUSSOT, Q. NGUYEN, H. HUYNH, AND D. BONN, *Avalanche behaviour in yield stress fluids*, Phys. Rev. Lett., 88 (2002), p. 175501.
- [11] ———, *Viscosity bifurcation in thixotropic, yielding fluids*, J. Rheol., 46 (2002), pp. 573–589.
- [12] F. DA CRUZ, F. CHEVOIR, D. BONN, AND P. COUSSOT, *Viscosity bifurcation in granular materials, foams, and emulsions*, Phys. Rev. E, 66 (2002), p. 051305.
- [13] P. DE SOUZA MENDES, *Modelling the thixotropic behavior of structured fluids*, J. Non-Newtonian Fluid Mech., 164 (2009), pp. 66–75.
- [14] A. HOGG AND G. MATSON, *Slumps of viscoplastic fluids on slopes*, J. Non-Newtonian Fluid Mech., 158 (2009), pp. 101–112.
- [15] H. HUPPERT, *The propagation of two-dimensional and axisymmetric viscous gravity currents over a rigid horizontal surface*, J. Fluid Mech., 121 (1982), pp. 43–58.
- [16] J. LISTER, *Viscous flows down an inclined plane from point and line sources*, J. Fluid Mech., 242 (1992), pp. 631–653.
- [17] K. LIU AND C. MEI, *Slow spreading of a sheet of Bingham fluid on an inclined plane*, J. Fluid Mech., 207 (1989), pp. 505–529.
- [18] J. MEWIS, *Thixotropy*, Adv. Colloid Interface Sci., 147-148 (2009), pp. 214–227.
- [19] P. MOLLER, A. FALL, V. CHIKKADI, D. DERKS, AND D. BONN, *An attempt to categorize yield stress fluid behaviour*, Phil. Trans. R. Soc. A, 367 (2009), pp. 5139–5155.
- [20] P. MOLLER, J. MEWIS, AND D. BONN, *Yield stress and thixotropy: on the difficulty of measuring yield stress in practice*, Soft Matter, 2 (2006), pp. 274–283.
- [21] A. PUTZ AND T. BURGHELEA, *The solid-fluid transition in a yield stress shear thinning physical gel*, Rheol. Acta, 48 (2009), pp. 673–689.

Smoothing out sandpiles: rotational bulldozing of granular material

Alban Sauret

October 3, 2012

1 Introduction

1.1 Dense granular flow

Predicting the dynamics of dense granular flow plays an important role in engineering and geophysical flow which involve the transport of granular materials such as for instance cereals, rocks or sand. In the past decade, most of the studies have focused on the flow of granular material on inclined surface due to the obvious applications in rock avalanches, landslides and pyroclastics flows [14, 7] (for a review, see e.g. [6]). However, the bulldozing of granular materials, i.e. the action to push the granular material with a blade on a flat plane, has not received so much attention. Indeed, it is not straightforward to build an experimental setup which allows the study of the steady dynamics of bulldozing granular material in a reproducible way. Moreover, the theoretical description of such flow remains complicated as the rheology of dense granular flow is difficult to capture and until quite recently there was no acceptable continuum model for a granular material [9].

In this project, we explore a problem of granular flow on a plane layer: the rotating bulldozing of a sandpile. Starting from an initial sandpile, we use a rotating blade to transport this sandpile and characterize the motion of the granular materials and the shape of the dune built against the blade. The use of a rotating blade instead of a straight blade with a rectilinear motion allows the system to be recirculated and thereby observing the dynamics over long times. In addition, the variation of speed along the blade potentially allows for richer dynamics. Therefore, the aim of this work is to provide the first experimental results with a rotating bulldozer and characterize the key features of the dynamics.

1.2 Bulldozer-related problems

Surprisingly, there are relatively few previous experimental modeling studies of problems of bulldozing sands. The earliest study by Bagnold [2] considers a 2D situation of a plate immersed in a layer of sand of given thickness. Then the plate is pulled at a given force and the amount of material in the dune keeps increasing at the same rate (see figure 1.a). During the build-up of the dune, the velocity of the blade pulled at a given force exhibits some oscillations due to the episodic avalanching of the dune. From laboratory experiments Bagnold, [2] provided a qualitative picture of the shape and the flow in the dune during the build-up (figure 1.b). However, none of these experiments consider the steady regime where

the amount of granular material in the dune does not change. In addition, no quantitative measurement of the shape of the dune or the velocity of the sand has been provided. More recently, some studies focused on the “song of dunes” problem [5, 1]. A possible experimental setup to measure the loud sound emitted by the motion of an avalanche is based on a rotating blade pushing a layer of sand. Here, the dynamics is also non-steady and the quantitative shape of the dune built by the motion of the blade has not been characterized. Another relevant situation which has been studied over the past few years is a wheel or an inclined plow blade with a given angle of attack. The wheel or the blade is free to move vertically in response to the granular material and after few passages on the granular bed a pattern develops on the road which are called washboard ripples [15, 13]. Note that this situation is not used to push or drag granular materials contrary to the bulldozer problem and therefore the dynamics of the sand remains different.

However, none of these studies provide quantitative experimental results of the shape of the dune carried by a bulldozer and especially in a rotating bulldozer where the rotation is susceptible to bring an interesting new dynamics because of the difference of normal velocity along the blade. Here, in addition to our experiments and the quantitative description of the shape of the dune, we will consider the “ $\mu(I)$ ” rheology to describe the dense granular flow as an incompressible liquid with no variation of volume fraction during the dense flow [9]. Such a rheology has been used with success to describe the flow of granular layers on inclined surfaces [6]. In this paper, we will also use a shallow water model as it may allow us to describe the dynamics observed.

1.3 Constitutive law for dense granular flow: the $\mu(I)$ -rheology

The description of dense granular flow through the conservation of momentum and mass requires a continuum description of the material. When granular material flows like a liquid, the local tangential stress τ and the local normal stress p are found to satisfy

$$\tau = \mu(I) p \quad \text{with} \quad I = \frac{\dot{\gamma} d}{\sqrt{p/\rho}} \quad (1)$$

where $\mu(I)$ is an analogue to a coefficient of friction, while ρ and d are the particle density and diameter. Note that I is the inertial number and represents the ratio of an inertial time scale $\sqrt{d^2 p/\rho}$ and the shear deformation time scale $\dot{\gamma}^{-1}$ [4, 12]. A constitutive relation, the so-called $\mu(I)$ -rheology, has been suggested based on experimental and numerical results (see e.g. GdR Midi [12]):

$$\mu(I) = \mu_1 + \frac{(\mu_2 - \mu_1) I}{I + I_0}. \quad (2)$$

This coefficient interpolates a friction coefficient between μ_1 at $I = 0$ and $\mu \rightarrow \mu_2$ for $I \rightarrow \infty$. I_0 , μ_1 and μ_2 depend on the material considered (see table 1). Jop et al. have provided a 3D generalization of this constitutive law and successfully compared it to experiments on granular flows on a pile between rough sidewalls [8, 9]. The granular material is still consider as an incompressible fluid with an internal stress tensor σ_{ij} given by:

$$\sigma_{ij} = -p \delta_{ij} + \tau_{ij}. \quad (3)$$

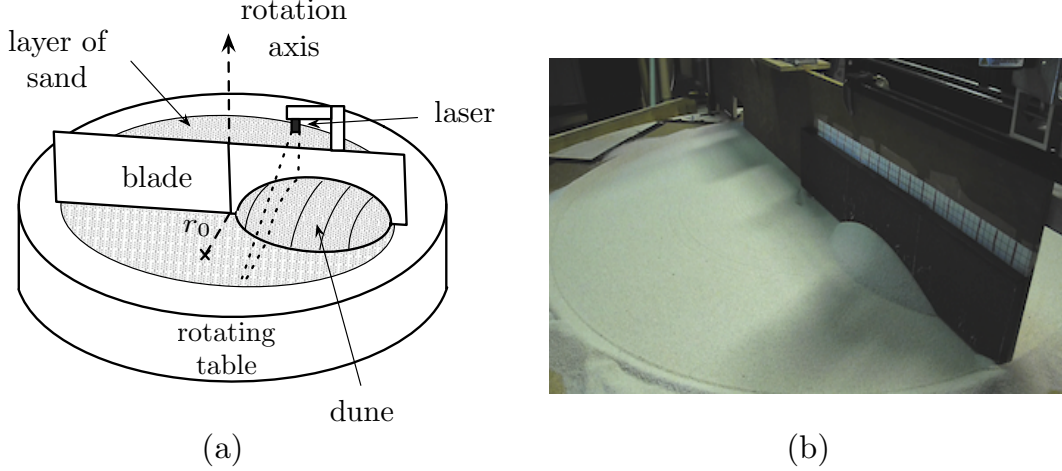


Figure 2: (a) Schematic illustration and (b) photo and of the experimental setup.

2 Experimental setup

2.1 The rotating bulldozer

The experimental apparatus, shown in Fig. 2, consists of a rotating table of 2.2 m diameter which rotates around its axis at an angular velocity Ω . The rotation rate of the table lies in the range 0.05 to 2 rad.s^{-1} .

The surface of the rotating table is coated with sandpaper to suppress slipping of particles on the surface of the table. In the absence of sandpaper, the particles slip on the surface of the table and the structure of the flow is different: the avalanching dune becoming buffered from the upstream static layer by a compressing, sliding layer of grain (see appendix A). In this report, we only focus on the no-slip boundary conditions.

A blade consisting of a flat vertical board, and fixed in the laboratory frame, is secured above the rotating table and acts as a rotating bulldozer (see figure 2(a) & 2(b)). The blade consists of a 1.50 m long and 40 cm height wood plate to which we attach a plywood plate coated with sandpaper to ensure no-slip boundary conditions on the blade. The blade is perpendicular to the surface of the rotating table and is held at a given height around 1 cm. It leads to the presence of an underlying layer of granular materials with a constant thickness. Prior to any experiments, we add granular material on the table which is set in rotation. The granular material build up a bed atop the table. It fills up the gap and its surface is smoothed out by the blade. After a sufficiently long time, we obtain a layer of constant thickness with compaction which does not vary appreciably between two successive experiments. Then, a sandpile is formed by slowly pouring grains onto a selected point on the surface of the existing uniform bed, producing a nearly conical mound with a slope given by the static angle measured previously. We define the initial position of the sandpile as the coordinate of its center, i.e. the radius r_0 from the center of the table where the height of the sandpile is maximum (see figure 2(a)). In the present study, we have used $r_0 = 15, 25$ or 35 cm. Typical parameters used in this study are summarized in table 2.

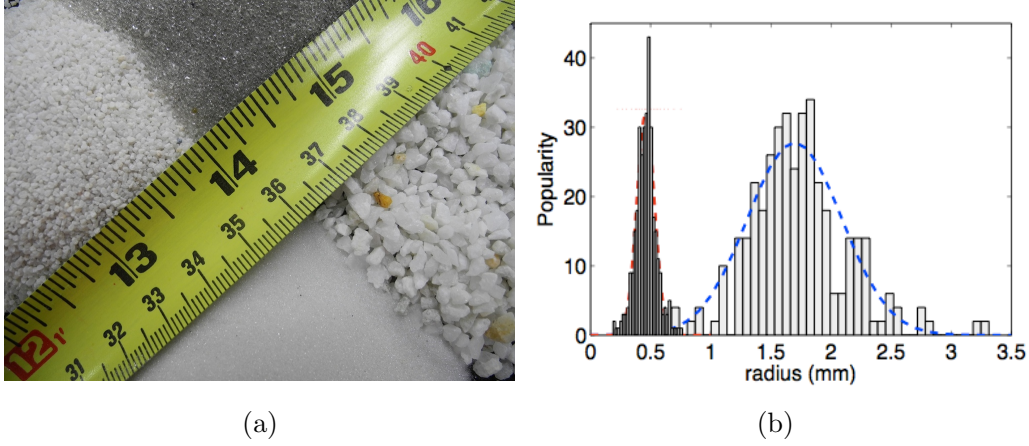


Figure 3: (a) Photograph of the four granular materials. From left clockwise; aquarium sand ($d = 0.9$ mm), fine glass beads ($d = 0.1$ mm), coarse grit ($d = 3$ mm) and spherical glass beads ($d = 1$ mm). Only results for aquarium sand and spherical glass beads are presented in this report. (b) Size distribution of the coarse grit (white) and the aquarium sand (grey).

Note that in the present bulldozer experiment, because the blade is held at a constant height, no washboard instability is observed [3, 13, 15].

Rotation rate	$0.05 - 2 \text{ rad.s}^{-1}$
Radius of the blade	0.7 m
Diameter of the particles	0.1 mm - 3 mm
Mass of the dune	0.1 – 1 kg
Initial position of the dune (radially from the center of the table)	15, 25 & 35 cm

Table 2: Range of parameters used in the experiments.

2.2 Granular materials

In this report we present results of bulldozer experiments for different granular media as shown in figure 3(a):

- (i) Aquarium sand, of irregular shape, but overall mean diameter of approximately 0.9 mm.
- (ii) Spherical fine glass beads (ballotini) of mean diameter 0.1 mm.
- (ii) Spherical glass beads (ballotini) of mean diameter 1 mm.
- (iv) Coarse grit, of irregular shape, but overall mean diameter of approximately 3 mm.

The size of the aquarium sand and coarse grit particles have been estimated by direct visualization and postprocessing of the picture. Their resulting size distribution is given in figure 3(b). Assuming that the distribution of the particle size can be fitted by a gaussian

distribution, we obtain a distribution of the equivalent radius $r = \sqrt{A/\pi}$ given by

$$N = N_0 \exp \left[-\frac{(r - r_{moy})^2}{2\sigma^2} \right]. \quad (5)$$

For example, for the aquarium sand the mean radius of the particle is $r_{moy} \simeq 0.46$ mm and the mean deviation around $\sigma \simeq 0.075$ cm (figure 3(b)). The size distribution of the glass beads were directly obtained from the manufacturer: the size of the fine glass beads¹ ranges in $d = 0.09 - 0.15$ mm and the other glass beads² (ballotini) have a size $d = 0.8 - 1.2$ mm.

Then, we can characterize, for the two granular media used in this report, the angle of repose, θ_r , which measures how layers of the medium slide over one another. To estimate a static angle of friction, we make a sandpile of a granular material and measure the typical slope. Rough estimates give an angle of $\theta_r = 22 \pm 2^\circ$ for the 1 mm glass beads and $\theta_r = 44 \pm 4^\circ$ for the aquarium sand. Note that all the experiments were performed in an air-conditioned laboratory maintained at 21°C with humidity controlled. The granular materials were kept dry as moistening the materials, even by a small amount, may have lead to different results.

3 Initial conditions and phenomenology

The initial sandpile is set on the table as described in section 2.1. For each granular material, different initial mass in the sandpile had been considered which leads to different radius and height of the initial sandpile. In addition, the slope of the sandpile is given by a static angle of friction estimated previously. Thus, knowing r_0 the initial radial position of the center of the sandpile and m the mass of granular material in the sandpile allow us to define entirely the system.

The table is then set in rotation, accelerating to a prescribed rotation rate, Ω , or rotation period, T_{rot} , in typically less than 2 seconds (well before the sandpile hits the blade). Thus, the collision of the sandpile and the subsequent dynamics take place at constant rotation velocity. The collision forces a rearrangement of the sandpile into an avalanching dune that is pushed forwards by the blade (figure 4.b). The rearrangement typically takes place in two phases. First, there is a relatively rapid phase (spanning times of order $0.1 T_{rot}$) in which the dune builds up perpendicular to the blade and adjusts into a quasi-steady shape in that direction (figure 4.c). Thereafter, a slower phase ensues (lasting times of order T_{rot}) in which the dune spreads laterally and shifts radially outwards (figure 4.d).

In the following, we define our system using the coordinate system (x, y, z) (see figure 5.a). The plane (xz) is the plane perpendicular to the blade (see figures 5.a and b). The plane (yz) denotes the plane defined by the blade (see figures 5.a and c). When the table is set in rotation, the center of the sandpile r_0 will hit the blade at the coordinate $r_0 = y_0$. Thus in the following we only refer to y_0 which is the location along the blade where the center of the sandpile hits the blade. In all experiments presented in this report, the height measurement of the dune were done at a distance y which corresponds to the location where the maximum of the dune hits the blade, i.e. $y = y_0$. Experimental observations show that

¹#8 from Kramer Industries

²A-100 from Potters Industries

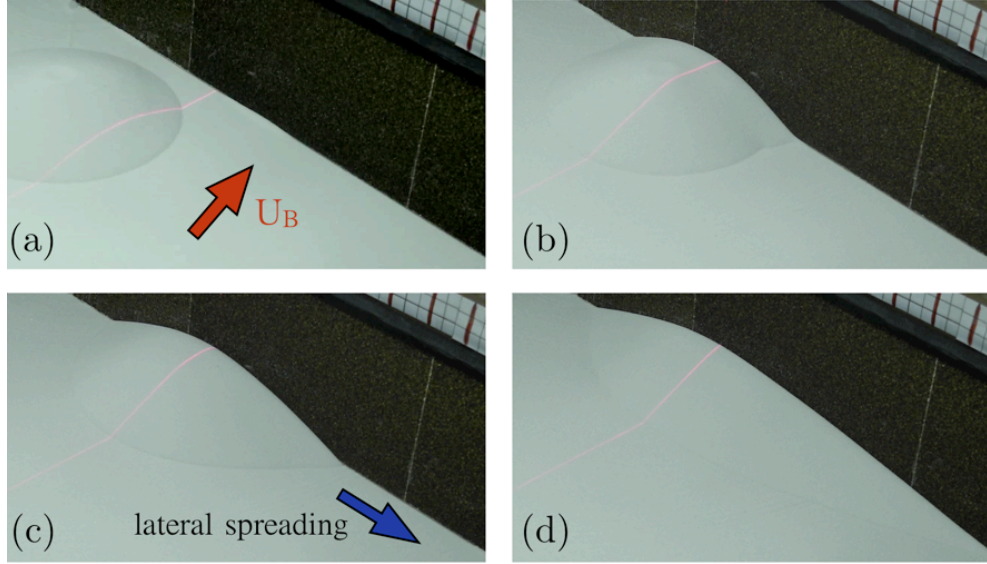


Figure 4: Four successive pictures of the bulldozing sandpile (a) Initial sandpile showing the direction of the underlying layer (red arrow) while the blade is fixed in the laboratory frame. (b) Collision of the sandpile against the blade and quick organization of the dune. (c) Build-up of a quasi-steady structure at a given radius in a short timescale and lateral spreading of the dune (direction indicated by the blue arrow). (d) The slope of the dune at a given radius remains similar but the dune is still subject to lateral spreading. In all pictures, the red laser line is at a constant radius and shows the topography of the dune at this radius.

the time scale $T_x \sim 0.1T_{rot}$ to build-up the dune perpendicularly to the blade, i.e. in the plane (xz) , is shorter than the typical time scale $T_y \sim T_{rot}$ for the lateral spreading of the dune in the (yz) plane. Therefore, we split our discussion of the dynamics into two parts. In the next section, we will consider the build-up of a dune perpendicular to the plane and study the typical profile of the dune in the quasi-steady regime that results. Then, we will consider the lateral spreading of the dune using an approximate model for the slope of the dune.

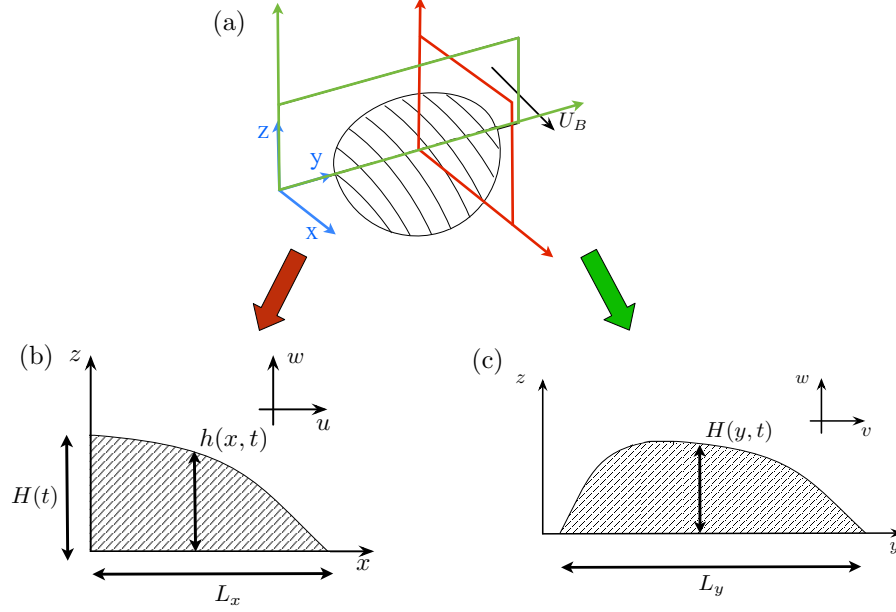


Figure 5: (a) Schematic of the bulldozed dune with the system of coordinates (x, y, z) . (b) 2D perpendicular slice in the (xz) plane at a given y -value defining the height $h(x, y, t)$, which reaches a maximum $H(y, t)$ near the bulldozer blade. (c) Front view of the dune in the plane (yz) , showing a typical profile of the dune height on the bulldozer blade $H(y, t)$.

4 Dynamics of the dune perpendicular to the blade

In this section, we consider the profile of the dune in a (xz) plane perpendicular to the bulldozer blade. The non-intrusive method to measure the profile of the dune as a function of the distance to the blade is described in appendix B.

4.1 Experimental observations

Prior to any systematic study, we verify that our experiments are fairly reproducible. Using the aquarium sand, we run two experiments with the same initial conditions, $y_0 = 25$, $m = 1$ kg and the same rotation rate $\Omega = 0.05$ rad/s. Then, we measure the profile of the dune every 5 seconds at a given radial position. The results for two different experiments are illustrated in figure 6 and confirm that the shape of the dune at a given time is fairly reproducible even if the agreement is not perfect. There are two main sources of

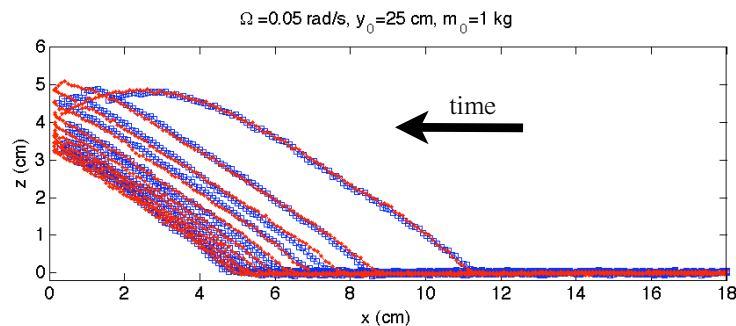


Figure 6: Profile of the dune in a (xz) plane perpendicular to the blade at $y = 25$ cm for $y_0 = 25$, $m = 1$ kg, $\Omega = 0.05$ rad/s. The profiles are taken every 5 seconds (and the direction of time is given by the arrow). The red line and the blue square are two different experiments.

disagreement: the measurement method presented in appendix B has uncertainties around ± 2 mm which already leads to a slight mismatch. In addition to this uncertainties, other disagreement arise because of direct experimental error. For example, the mass of particles to build an initial sandpile is fixed, but the way the particles are packed into the sandpile can be different. Furthermore, the exact position of the initial sandpile can also slightly vary by a few millimeters. Nevertheless, the comparison of two experiments shows that the errors measuring the profile at a given time is much smaller than the profile itself. For a dune against the blade of typical size between 5 and 10 cm, an estimate of the uncertainties would be of the order of a few millimeters. However, we have to notice that the measurement of the profile of the dune for the first few millimeters against the blade is difficult to achieve and therefore the description of the shape of the dune is better along the slope and in the junction with the underlying layer.

Experiments varying the initial mass of aquarium sand in the sandpile for a given initial position $y_0 = 25$ and rotation rate $\Omega = 0.05$ rad/s are shown in figures 7(a), (b), (c) & (d). The size of the initial sandpile depends on the amount of granular material. After a

sufficiently long time to obtain a quasi-steady regime, the dune has a shape similar to a triangle. The size of the dunes are different between all these experiments but their shape seem to remain the same for all mass. It is confirmed by a rescaling of the profile: for all experiments (figure 7(a), (b), (c) & (d)) we rescale the distance by the maximum height $H(y, t)$ (for given y) of the dune at the time considered (which height naturally changes with time). It leads to a nice collapse on a single curve at long time (see figure 7(e)). Therefore, the shape of the dune in the (xz) plane, for low rotation rates seems to be independent of the size of the dune at the scale of our experimental setup.

Note that the results presented in figure 6 and 7 are typical of all the granular material considered in this study. In addition, the gap thicknesses or the low rotation rate does not have a noticeable influence on this shape.

From the rescaled profile, one can consider that the slope will be well fitted by a straight line with an angle equals to the dynamic angle. However figure 7(f) shows that although the shape looks like a dune with a straight slope, there is a slight deviation at the tip (i.e. the furthest distance from the bulldozer blade) of the dune.

4.2 Simple model

4.2.1 Mathematical formulation

We consider granular flow in a slice perpendicular to the bulldozer blade at a given radial position y (see figure 5(b)). Because the time-scale of the motion in the x and in the y directions are different, we assume that in a quasi-steady regime the flow remains two-dimensional in the x direction. We denote $(u(x, z, t), w(x, z, t))$ as the velocity field, $p(x, z, t)$ is the isotropic pressure and τ is the deviatoric stress tensor. The fluid is assumed to be incompressible. The conservation of mass and momentum leads to the governing equations in cartesian coordinates:

$$u_x + w_z = 0, \quad (6)$$

$$\rho(u_t + u u_x + w u_z) = -p_x + \partial_x \tau_{xx} + \partial_z \tau_{xz}, \quad (7)$$

$$\rho(w_t + u w_x + w w_z) = -p_z - \rho g + \partial_x \tau_{xz} + \partial_z \tau_{zz}. \quad (8)$$

We use the $\mu(I)$ rheology [9] as a constitutive law for the granular material. For the present 2D situation it writes:

$$\tau = p \mu(I) \frac{\dot{\gamma}}{|\dot{\gamma}|}, \quad \dot{\gamma} = \begin{pmatrix} 2u_x & u_z + w_x \\ u_z + w_x & 2w_z \end{pmatrix}, \quad |\dot{\gamma}| = \sqrt{4u_x^2 + (u_z + w_x)^2}, \quad (9)$$

with

$$\mu(I) = \mu_1 + \frac{(\mu_2 - \mu_1)I}{I + I_0}, \quad I = \frac{|\dot{\gamma}| d}{\sqrt{p/\rho}} \quad (10)$$

In addition, the granular material has to satisfy a no-slip condition on the bottom, at $z = 0$:

$$u(x, 0, t) = w(x, 0, t) = 0, \quad (11)$$

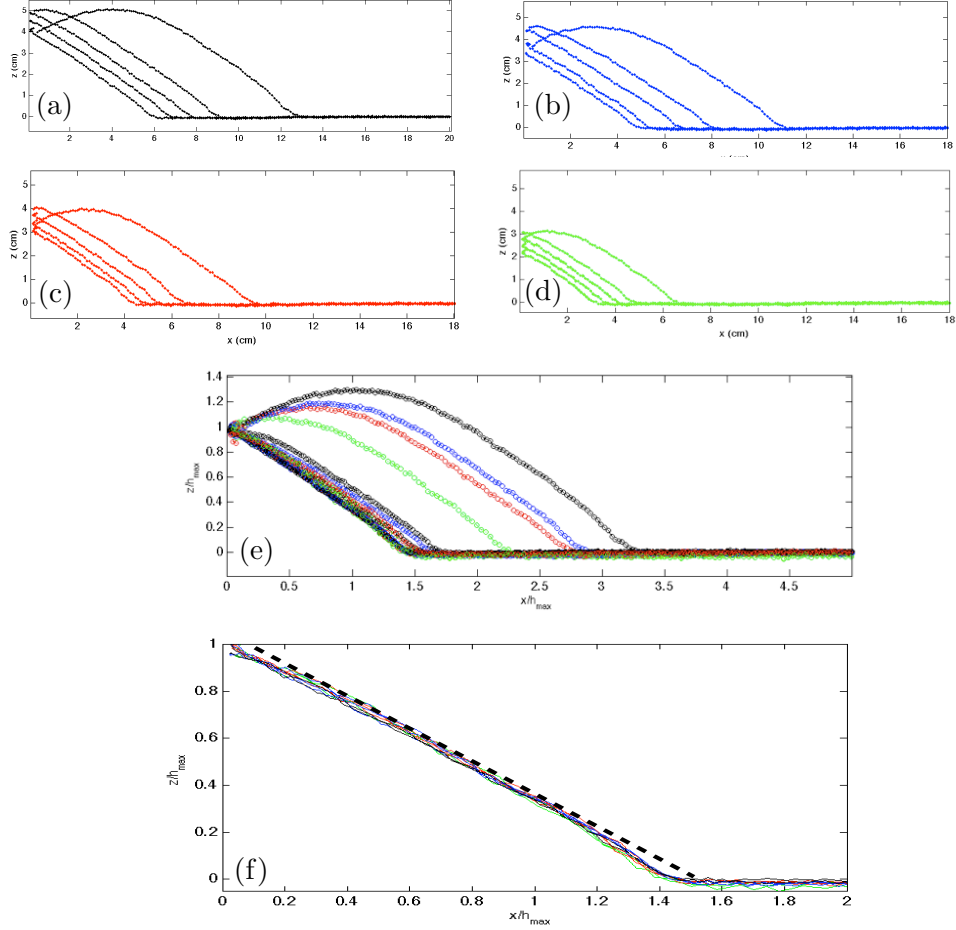


Figure 7: Topography of the bulldozed dune at the radial position $y = 25$ cm for $\Omega = 0.05$ rad/s, $y_0 = 25$ cm and (a) $m = 1000$ g; (b) $m = 750$ g; (c) $m = 500$ g; (d) $m = 250$ g; (e) Rescaled topography of the dune for all the mass considered in (a), (b), (c) and (d). (f) Close-up view of the shape of the dune; the black dotted-line is a straight line. Time go from the right to the left and are taken every 10 seconds.

and is stress-free at its surface, $z = h(x, t)$, leading to:

$$\frac{1}{\sqrt{1+h_x^2}} \begin{pmatrix} \tau_{xx} - p & \tau_{xz} \\ \tau_{xz} & \tau_{zz} - p \end{pmatrix} \begin{pmatrix} -h_x \\ 1 \end{pmatrix} = \begin{pmatrix} 0 \\ 0 \end{pmatrix}. \quad (12)$$

Note that the continuity equation (16) can be averaged over the depth of the dune to obtain

$$h_t + \frac{\partial}{\partial x} \left(\int_0^h u dz \right) = 0. \quad (13)$$

4.2.2 Dimensionless equations

Considering the different variables of the problem, we can make the equations dimensionless by introducing the new variables:

$$x = L \hat{x}, \quad z = H \hat{z}, \quad h = H \hat{h}, \quad u = U \hat{u}, \quad w = \frac{H}{L} U \hat{w}, \quad t = \frac{L}{U} \hat{t}, \quad (14)$$

$$p = \rho g H \hat{p}, \quad \tau_{ij} = \rho g \frac{H^2}{L} \hat{\tau}_{ij} \quad (15)$$

where L and H denote the characteristic fluid extension and depths respectively (see figure 5(b)). U is a velocity scale, typically the speed of the bulldozer. Then, dropping the hat, the previous equations (6)-(8) can be rewritten as

$$u_x + w_z = 0, \quad (16)$$

$$\epsilon F^2 (u_t + u u_x + w u_z) = -\epsilon p_x + \epsilon^2 \partial_x \tau_{xx} + \epsilon \partial_z \tau_{xz}, \quad (17)$$

$$\epsilon^2 F^2 (w_t + u w_x + w w_z) = -p_z - 1 + \epsilon^2 \partial_x \tau_{xz} + \epsilon \partial_z \tau_{zz}, \quad (18)$$

where $\epsilon = H/L$ is the aspect ratio of the dune and $F = U/\sqrt{gH}$ is the Froude number. The constitutive model of the granular material is given by

$$\tau = p \mu(I) \frac{\dot{\gamma}}{|\dot{\gamma}|}, \quad \dot{\gamma} = \begin{pmatrix} 2\epsilon u_x & u_z + \epsilon^2 w_x \\ u_z + \epsilon^2 w_x & 2\epsilon w_z \end{pmatrix}, \quad |\dot{\gamma}| = \sqrt{4\epsilon^2 u_x^2 + (u_z + \epsilon^2 w_x)^2} \quad (19)$$

with

$$\mu(I) = \mu_1 + \frac{(\mu_2 - \mu_1)}{1 + \mathcal{I}}, \quad \mathcal{I} = \frac{|\dot{\gamma}|}{\sqrt{p}} \mathcal{U}, \quad \mathcal{U} = \frac{U d}{I_0 H \sqrt{gH}}. \quad (20)$$

Note also that μ_1 and μ_2 which are directly related to the slope of the dune are also of order ϵ :

$$\hat{\mu}_j = \frac{\mu_j}{\epsilon} \quad j = 1, 2. \quad (21)$$

The boundary conditions now writes:

$$u(x, 0, t) = w(x, 0, t) = 0 \quad (22)$$

and

$$(1 + \epsilon^2 h_x^2) \tau_{xz} - 2\epsilon h_x \tau_{xx} = (1 + \epsilon^2 h_x^2) p - (1 - \epsilon^2 h_x^2) \epsilon \tau_{zz}, \quad (23)$$

4.2.3 Long-wave model

To be able to obtain a simple qualitative shape of the dune, we need to introduce a shallow-slope approximation. In this approximation, the ratio of the vertical and horizontal scale of the dune is $\epsilon = H/L \ll 1$. This assumption is quite strong regarding the experimental shape of the dune where $\epsilon \sim 0.2 - 0.5$, however it constitutes a simple way to provide a qualitative shape from analytical studies.

4.3 Quasi-steady case without inertia

In the experiments shown in figure 7, the Froude number is typically of order $F \sim 0.02$. Thus, a first step is to assume that the deviation from a straight slope can be understood assuming that $F \ll 1$ in the equations (17) and (18). Physically, it means that we neglect the inertia of the granular material. This assumption leads to the governing equations:

$$u_x + w_z = 0, \quad (24)$$

$$-\epsilon p_x + \epsilon^2 \partial_x \tau_{xx} + \epsilon \partial_z \tau_{xz} = 0, \quad (25)$$

$$-p_z - 1 + \epsilon^2 \partial_x \tau_{xz} + \epsilon \partial_z \tau_{zz} = 0. \quad (26)$$

Equations (25-26) at the leading-order give:

$$p = (h - z), \quad (27)$$

$$\tau_{xz} = -h_x (h - z). \quad (28)$$

Then, from the constitutive equation given by the $\mu(I)$ -rheology (20), we can write

$$\tau_{xz} = p\mu(I) \frac{u_z}{|u_z|} \quad (29)$$

which leads to

$$h_x = -\mu(I). \quad (30)$$

Then, using the constitutive relation given by (20), we obtain

$$h_x = -\mu_1 - \frac{(\mu_2 - \mu_1)}{1 + \mathcal{I}} \quad \text{with} \quad I = \frac{|\dot{\gamma}| d}{\sqrt{p/\rho}} \mathcal{U} = \frac{u_z}{\sqrt{(h - z)}} \mathcal{U}. \quad (31)$$

This relation leads to an expression for the z -derivative of u :

$$u_z = \frac{\sqrt{h - z}}{\mathcal{U}} \left(\frac{\mu_1 - h_x}{h_x - \mu_2} \right). \quad (32)$$

Then, integration of the relation (32) with the boundary condition $u(z = 0) = 0$ leads to a Bagnold-like profile (see for instance [11]):

$$u = \frac{2}{3\mathcal{U}} \left(\frac{\mu_1 - h_x}{h_x - \mu_2} \right) [h^{3/2} - (h - z)^{3/2}], \quad (33)$$

We use the continuity equation averaged over the height of the dune (13) for the steady state ($\partial_t = 0$) to evaluate the height of the dune $h(x)$:

$$\frac{\partial}{\partial x} \left(\int_0^h u \, dz \right) = 0. \quad (34)$$

We integrate this relation with respect to x with the boundary condition $u(x = 0) = \hat{U}_B$ where $\hat{U}_B = U_B/U$ is the dimensionless velocity of the blade with respect to the underlying

layer. Because the table is rotating, this velocity at a given radial position y is $U_B = \Omega y$. It leads to

$$\int_0^h u \, dz = h \hat{U}_B. \quad (35)$$

Then with the expression (33) we finally obtain

$$\hat{U}_B = \frac{1}{h} \int_0^h u \, dz = \frac{2}{5\mathcal{U}} \left(\frac{\mu_1 - h_x}{h_x - \mu_2} \right) h^{3/2}, \quad (36)$$

From this relation, we obtain an equation for the height of the dune at a given distance from the blade $h(x)$ in the limit where the inertial effects are neglected, i.e. at $F \ll 1$:

$$h_x = \frac{\mu_1 h^{3/2} + F_2 \mu_2}{h^{3/2} + F_2}, \quad (37)$$

where F_2 is defined by

$$F_2 = \frac{5}{2} \hat{U}_B \mathcal{U}. \quad (38)$$

Coming back to the dimensional expression, the coefficient F_2 writes:

$$F_2 = \frac{5}{2} \frac{U_B d}{I_0 H \sqrt{g H}}. \quad (39)$$

We consider the aquarium sand with typical experimental parameters $\Omega = 0.05$ rad/s, $y = y_0 = 25$ cm, $U_B = \Omega y$, $H = 5$ cm, $d = 1$ mm, and for I_0 , μ_1 and μ_2 the value provided by Jop et al. [9]. The resulting profiles are plotted in figure 8. We can see that the shape of the dune shows some qualitative agreement with the experiments. The profile of the dune is close to a straight slope except when the dune meet the underlying layer where the profile becomes concave as observed in the experiments. However, the analytical theory depends on F_2 which is inversly proportional to $H^{3/2}$. Thus, when the dune becomes smaller, the value of F_2 increases and the profile should change. However, the experiments seem to show the same profile all the time. It may be due that experiments were typically performed with a height of the dune in the range $H \sim 3 - 10$ cm. For smaller height of the dune, the experimental measurements are not sufficiently accurate. Thus, the range of F_2 performed for a given rotation rate does not allow to see a huge variation of F_2 . The only way to increase its value is a larger value of the velocity of the blade which will be the point of the next section.

4.4 Influence of the different parameters

The shape observed for aquarium sand, i.e. a straight slope and a curvature near the tip of the dune should be valid for different granular materials in the limit $F \rightarrow 0$. Indeed, the analytical model presented in the previous section relies on the $\mu(I)$ rheology which is valid for sand as well as for glass beads. Figure 9(a) illustrates the profile of the dune for 1 mm spherical glass beads and the same parameters as shown in figure 6 after the initial build-up of the dune in the (xz) plane (i.e. approximately after $0.1 T_{rot}$). Again we can see that the shape of the dune exhibits a curvature near the tip explained by our simple

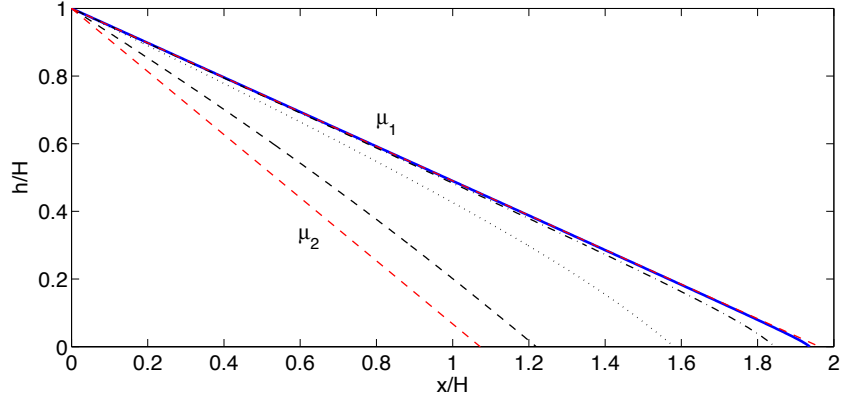


Figure 8: Analytical profile of the dune. The blue continuous line is for the experimental parameters: $H = 6$ cm, $\Omega = 0.05$ rad/s, $y = y_0 = 25$ cm, $U_B = \Omega y$, $d = 1$ mm leading to $F_2 = 8.5 \times 10^{-4}$. The red dashed lines indicate the slope given by μ_1 and μ_2 .

model. We can also study the influence of the different parameters: the mass (figure 9(b)) or various initial position (figure 9(c)) always in the limit of vanishing Froude number. The profile of the dune seems not to change with these different parameters. Note that with the glass beads the profiles look slightly more curved everywhere. It may be due the shape of the particles which are spherical contrary to the aquarium sand. In this case the particle will be likely inclined to roll and the speeds at the surface will increase. This effect is not yet totally understood.

4.5 What about inertia?

We have previously focused on the shape of the dune in the limit where the inertial effects are neglected, i.e. for a Froude number $F \ll 1$. However, experimental observations suggest that the shape of the dune can be modified by inertial effects as illustrated in figure (10) when we increase the rotation rate of the bulldozer. Instead of having an inclined and nearly-flat profile as observed in the previous section, we have a transition to a profile where a significant curvature appears. The profile observed when increasing the Froude number is similar to the “S-shape” observed in rotating drums (see for instance [16]). In figure (10) the Froude number ranges from 0.4 to 1 and its influence has now to be considered to account for the curvature of the profile.

To study the effect of inertia, we consider the leading-order version of (17) with $F = O(1)$. We depth-integrated this equation and use the first order profile (33) obtained previously. It leads to:

$$F^2 \left[\frac{\partial}{\partial t}(hU) + \frac{\partial}{\partial x} \left(\int_0^h u^2 dz \right) \right] = -h_x - \tau_{xz}(x, 0, t) \quad (40)$$

where

$$U = \frac{1}{h} \int_0^h u dz \quad (41)$$

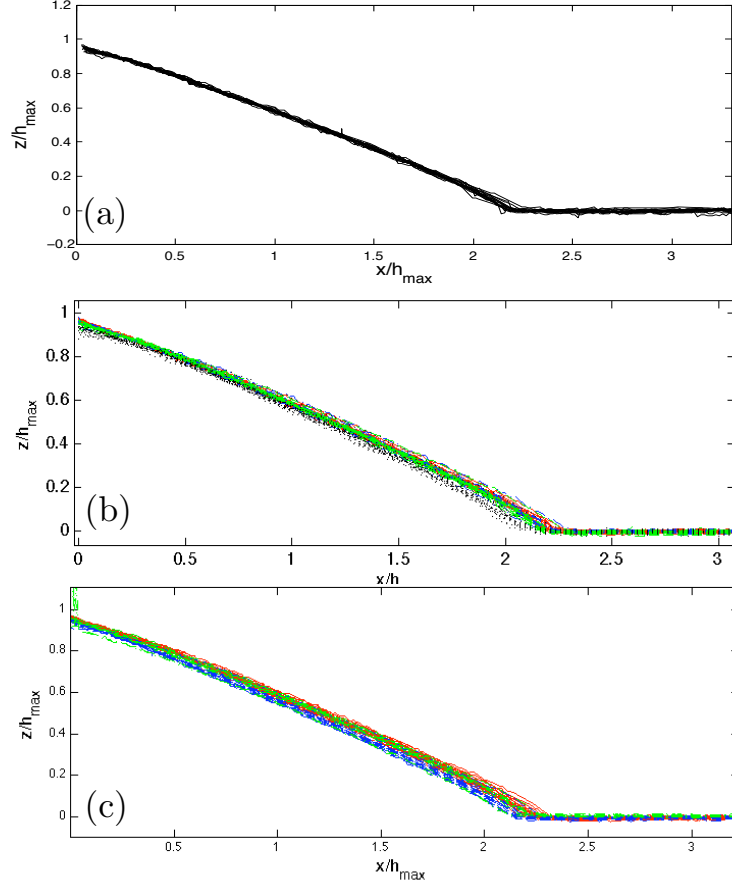


Figure 9: Profile of the dune for the 1 mm spherical glass beads (a) $\Omega = 0.05$ rad/s, $m = 1$ kg, $y = 25$ cm; (b) for the same parameters and various mass: $m=1000$ g (red), $m=750$ g (blue), $m=500$ g (green), $m=250$ g (black); (c) for various initial radial position: $y_0 = 15$ cm (red), $y_0 = 25$ cm (blue), $y_0 = 35$ cm (green). In all these figures, the time is taken every 10 seconds after the build-up of the dune is achieved.

is the vertical average of the velocity u . To evaluate the inertial terms on the left of this equation and the basal drag, we consider the steady state with constant flux, $(hU)_x = 0$, and exploit the velocity profile of the inertia-less problem, namely

$$u = \frac{5U}{3h^{3/2}} [h^{3/2} - (h-z)^{3/2}] \quad (42)$$

After a little algebra, we arrive at

$$h_x \left(1 + \frac{5U^2}{4gh} \right) = -\mu(I_b). \quad (43)$$

where

$$I_b = \frac{5Ud}{2H\sqrt{gH}} \quad (44)$$

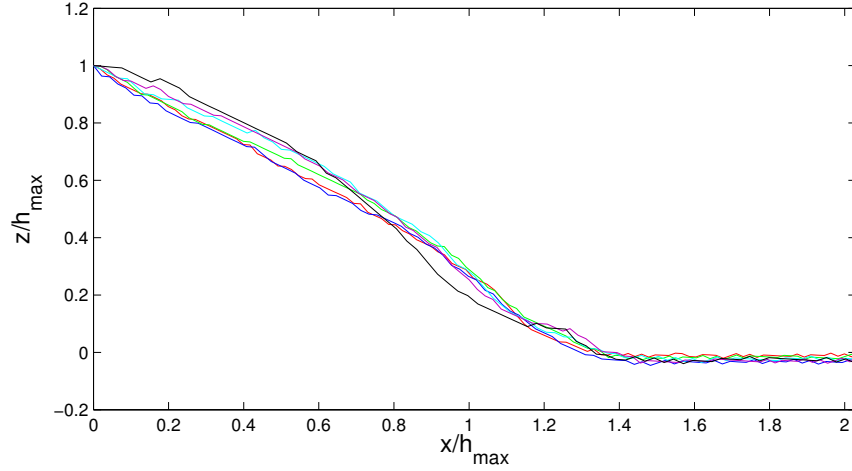


Figure 10: Profile of the dune for different rotation rates $\Omega = 0.8$ rad/s (red), $\Omega = 1$ rad/s (blue), $\Omega = 1.25$ rad/s (green), $\Omega = 1.5$ rad/s (cyan), $\Omega = 1.75$ rad/s (magenta) and $\Omega = 2$ rad/s (black) with $m = 1000$ g, $y_0 = y = 35$ cm and the granular material is the aquarium sand of diameter $d = 0.9$ mm. Profiles are taken at arbitrary times after the build-up of the dune.

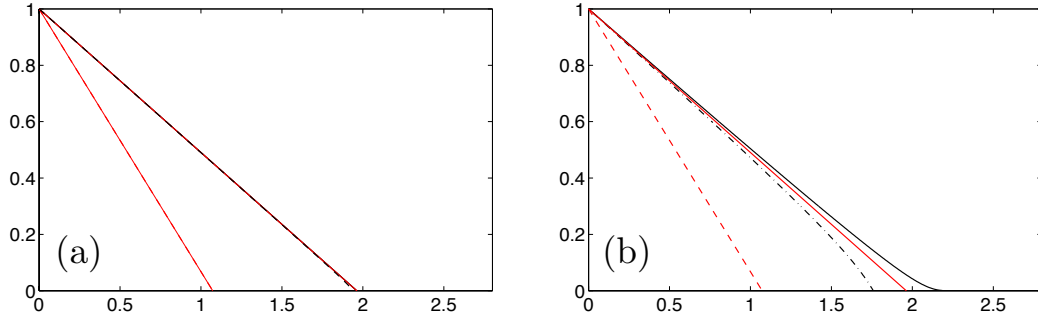


Figure 11: (a) Analytical profile of the dune for the aquarium sand, $y_0 = y = 25$ cm, $d = 1$ mm, $H_0 = 5$ cm and $\Omega = 0.05$ rad/s. (b) Analytical profile of the dune for the aquarium sand, $y_0 = y = 40$ cm, $d = 1$ mm, $H_0 = 5$ cm and $\Omega = 1$ rad/s leading to a larger Froude number. In both figures the black continuous line are obtained with the relation (43) and the black dotted-line are obtained with the relation (37).

Note that this relation is exactly the relation (31) in the limit of vanishing Froude number, i.e. for vanishing velocity U . The term $5U^2/(4gh)$ accounts for the inertial effects. Resulting profiles calculated with this model are shown in figure 11(a) and (b). Figure 11(a) is plotted for a small rotation rate, $\Omega = 0.05$ rad/s. In this case, we see that

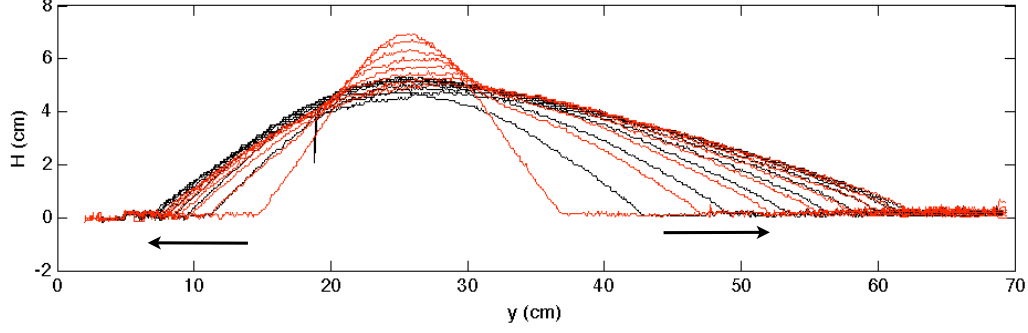


Figure 12: 2D profile of the dune in the plane (yz) for $\Omega = 0.05$ rad/s, $y_0 = 25$ cm, $m = 1000$ g. The granular material used is the 0.9 mm aquarium sand. The red line corresponds to an initial condition where the sand is initially put against the blade whereas the black line indicates the initial condition where a sandpile is set at a distance $y_0 = 25$ cm from the center. The arrows indicate the time-direction.

the profile is similar to the results of the previous section: the Froude number is small. However, for larger velocity, i.e. larger Froude number, the tail of the dune is modified as illustrated by the figure 11(b). The curvature of the profile is more important, as observed experimentally. However, even if the shape of the tail is captured qualitatively, the profile of the dune closer to the blade remains straight in our analytical model whereas in the experiments the curvature is also important in this region.

5 Lateral spreading of the dune

In section 3, we have seen that the motion of the dune can be decomposed into a build-up of the dune perpendicular to the blade and a lateral spreading of the dune along the blade. This lateral spreading effect is present for a rotating blade where the normal velocity to the blade depends on the distance to the center y through the relation $U_{\perp} = y\Omega$. Furthermore, because the front of the blade is position slightly ahead of the centre of the rotating table, there is a tangential velocity along the blade, U_{\parallel} , that advects the dune radially outwards (see below in 5.1.1).

Figure 12 illustrates the two-dimensional dynamics against the blade. Starting from a symmetric sandpile, the dune spreads along the blade and breaks its symmetry: the spreading is faster in this direction where the velocity of the blade is larger.

5.1 Mathematical modelling

5.1.1 Velocity of the bulldozer

First, we calculate the velocity induced by the rotating table at the velocity Ω in the frame of the blade. We use cartesian coordinates where the axis of rotation is at the position $(x = -\delta, y = 0)$ (see figure 13). Introducing r , the distance from the rotating axis, and θ , the angle between the y -axis and $(O_B M)$, one can write the coordinates of a point M as

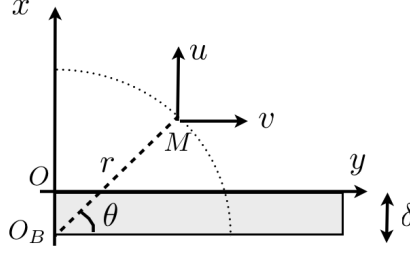


Figure 13: Schematic and coordinates in the (xy) plane. δ is the thickness of the blade. $x = 0$ is taken at the surface of the blade.

$(x_M = r \sin \theta - \delta, y_M = r \cos \theta)$. Thus the velocity field (U, V) is given by

$$U = -\Omega r \cos \theta = -\Omega y, \quad (45a)$$

$$V = \Omega r \sin \theta = \Omega (x + \delta). \quad (45b)$$

5.1.2 Conservation of mass

Let us express the conservation of mass averaged over z :

$$\frac{\partial h}{\partial t} + \frac{\partial}{\partial x} \left(\int_0^h u dz \right) + \frac{\partial}{\partial y} \left(\int_0^h v dz \right) = 0, \quad (46)$$

which can be rewritten as

$$\frac{\partial h}{\partial t} + \frac{\partial}{\partial x} (h U + F_x) + \frac{\partial}{\partial y} (h V + F_y) = 0, \quad (47)$$

where U (resp. V) accounts for the x -velocity (resp. y -velocity) of the underlying layer in the reference frame of the blade and F_x (resp. F_y) is the flux along the x -direction (resp. y -direction).

5.1.3 Modelling the shape of the dune perpendicularly to the blade

We want to build a simple model of evolution of the shape of the bulldozed dune in the (yz) plane (Fig. 14(a)), thus we need an estimation of the shape of the dune in the direction perpendicular to the blade. From the experimental observations, at low rotation rate, we can assume that for all positions y the slope can be approximated as straight line slope μ which is a parameter of the granular material and height $H(y, t)$ (see Fig. 14(b)). Thus, the equation of the dune in the xz plane can be written as

$$h(x, y, t) = H(y, t) - \mu x \quad (48)$$

This is a rough estimation of the shape but largely simplifies the problem from three dimensions to two dimensions.

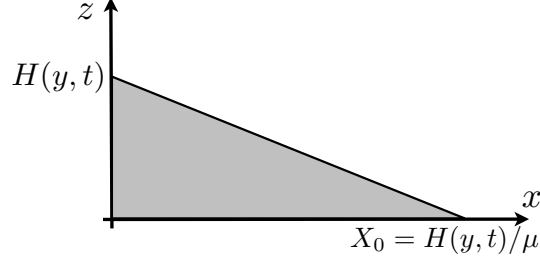


Figure 14: Schematic of the approximated shape of the 2D profile in the plane (xz) .

5.1.4 Advection-diffusion equation

Following the experimental observations, our main idea is that adjustments to the granular flow in the x -direction take place relatively quickly, and so the dune is in a quasi-steady state in this direction. This demands that the net horizontal flux in (47), namely $hU + F_x$, must be small, with any residual matching the slow time variation of h and weak flux along the blade. That is, $F_x \sim -hU$. To explore the slower lateral spreading and time evolution, we integrate (47) over the x -direction to obtain the relation:

$$\frac{\partial}{\partial t} \left(\int_0^X h \, dx \right) + [hU + F_x]_0^X + \frac{\partial}{\partial y} \left(\int_0^X hV + F_y \, dx \right) = 0. \quad (49)$$

We evaluate all the terms of this relation with $X = H(y, t)/\mu$. The first term leads to

$$\frac{\partial}{\partial t} \left(\int_0^X h \, dx \right) = \frac{\partial}{\partial t} \left(\frac{H^2}{2\mu} \right) \quad (50)$$

Then, due to the presence of the blade, there is a no-normal flow condition at $x = 0$ which implies that $H(y, t)U(x=0) + F_x(x=0) = 0$. At the end of the dune, at $X = H(y, t)/\mu$, by definition the flux drops to zero, i.e. $F_x(x=X) = 0$ and the height of the dune $h(x=X)$ also vanishes. This, the second term of the relation (49) vanishes:

$$[hU + F_x]_0^X = 0. \quad (51)$$

We can separate the last term of the relation (49), and we have:

$$\begin{aligned} \frac{\partial}{\partial y} \left(\int_0^X hV \, dx \right) &= \frac{\partial}{\partial y} \left(\int_0^X h\Omega(x+\delta) \, dx \right), \\ &= \frac{\partial}{\partial y} \left(\frac{\Omega\delta H^2}{2\mu^2} + \frac{\Omega H^3}{6\mu^2} \right). \end{aligned}$$

For a free-surface gravity-driven flow, one expects that the flux, $\mathbf{F} = (F_x, F_y)$, is proportional to the surface slope. That is, $\mathbf{F} \approx -\Gamma \nabla h$, where the factor Γ encapsulates the detailed physics of the granular flow. For example, for the shallow, inertia-less flow described by the $\mu(I)$ law in section 4, one can generalize the analysis and find

$$\Gamma = \frac{2I_0\sqrt{g}}{5d} \frac{h^{5/2}}{|\nabla h|} \left(\frac{\mu_2 - \sqrt{h_x^2 + h_y^2}}{\sqrt{h_x^2 + h_y^2} - \mu_1} \right) \quad (52)$$

Hence,

$$F_y \approx F_x \frac{h_y}{h_x} \approx -\frac{h U H_y}{\mu} \quad (53)$$

given our assumptions on the quasi-steady profile in x ($F_x \approx -h U$ and (48)). After integration we obtain

$$\frac{\partial}{\partial y} \left(\int_0^X F_y dx \right) = \frac{\partial}{\partial y} \left(\frac{H^2 H_y}{2 \mu^2} \Omega y \right). \quad (54)$$

In conclusion, the relation (49) leads finally to the evolution equation for $H(y, t)$:

$$\frac{\partial H^2}{\partial t} + \frac{\partial}{\partial y} \left(\Omega \delta H^2 + \frac{\Omega H^3}{3 \mu} \right) + \frac{\partial}{\partial y} \left(\frac{H^2 H_y}{\mu} \Omega y \right) = 0. \quad (55)$$

Note that this equation is an advection-diffusion equation which can be solved using a defined initial condition. The initial height will be chosen to fit with the initial sandpile.

5.2 Time-evolution of the dune

We can solve the partial differential equation (55) numerically. An example of the profile obtained is plotted in figure (15.a). This profile is plotted for the parameter used in the experimental results shown in figure (15.b). First, the thickness of the blade, $\delta = 1$ cm, is directly measure on the experimental setup. The slope of the dune perpendicularly to the blade is obtained from experiments done in section 4: $\mu \simeq \tan(40^\circ)$ for the aquarium sand. In addition, note that the diffusivity in (55) vanishes in the limit $H \rightarrow 0$. To avoid the implied singularity, the computation also includes a pre-wetted layer everywhere, i.e. the initial condition are:

$$H(y, t = 0) = \max(H_0 - \mu |y - y_0|) + \gamma_0, \quad (56)$$

where γ_0 is the thickness of the pre-wetted layer and $\max(H_0 - \mu |y - y_0|)$ is a triangular function centered in y_0 of height H_0 . H_0 is chosen as an adjustment parameter.

We can see that the spreading of the dune is non-symmetric and the maximum height of the dune travels outward with time. Although the agreement is not quantitative, the qualitative feature of the lateral spreading is well captured by our simple toy-model. In addition this maximum height decreases during the spreading in a qualitative good agreement.

6 Conclusion

In this project, we have studied the dynamics of bulldozed sand using experimental characterizations and some qualitative modelling with granular rheology. The experiments were performed with a rotating bulldozer which allows us to demonstrate that the dynamics of the dune built against the blade can be split into two phases. A first adjustment takes place transverse to the blade, with the dune adopting a quasi-steady profile with almost constant slope. The profile can be qualitatively reproduced with a shallow 2D flow model incorporating the so-called $\mu(I)$ -rheology. The transverse adjustment is followed by a second phase of lateral spreading. A crude model of this second phase reproduces the asymmetrical spreading of the dune along the blade and its gradual outward migration.

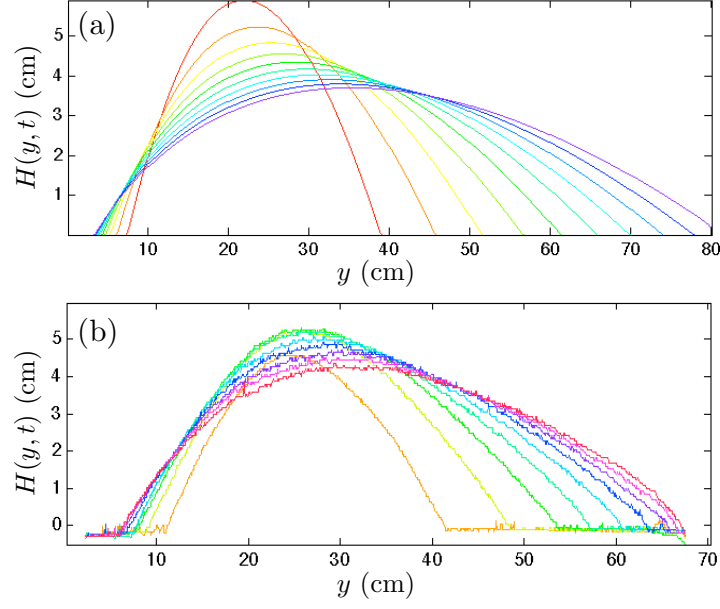


Figure 15: (a) Analytical profile with $\Omega = 0.05$ rad/s, $y_0 = 20$ cm, $\mu = \tan(40\pi/180)$, $\delta = 1$ cm, $H_0 = 9$ cm, $\gamma_0 = 0.01$ cm. (b) Experimental profile obtained with the aquarium sand for $\Omega = 0.05$ rad/s, $y = y_0 = 20$ cm. The profiles are taken every 5 seconds.

We have outlined in this report results based on experiments and suggested analytical modeling of the observed flow. However, one can notice that it exists some discrepancies between the theory and experiments. It may be due to some strong assumptions: the flow perpendicular to the blade was assumed to be shallow which is not totally satisfied. In addition, we used a quasi-steady assumption to split the dynamics into two phases and study them separately, but there may be some interplay between the 2D dynamic and the lateral spreading.

To further understand the dynamic of bulldozed material, extensions of the theory can be done by considering a fully 2D modeling of fluid with a $\mu(I)$ -rheology, i.e. without shallow-water approximations. We will carry 2D particle dynamics with a DEM code to study the flow without lateral spreading. Numerical simulations allow us to have access to various physical quantities such as the velocity inside the dune or the transient shape during the build-up of the dune. Numerical simulation with a $\mu(I)$ rheology [11] can also be compared to DEM simulation to study if the dynamic of the dune can be indeed captured by the $\mu(I)$ rheology.

We will also extend the experiments by performing PIV measurement to obtain the velocity field at the surface of the dune. Some experiments to see if there is any particle exchange between the dune and underlying bed are also needed. We outlined that the sandpaper allow no-slip boundary condition, but examining effects of slip by removing sandpaper would also be interesting as well as studying slower speeds and other materials to look for unsteady avalanching.

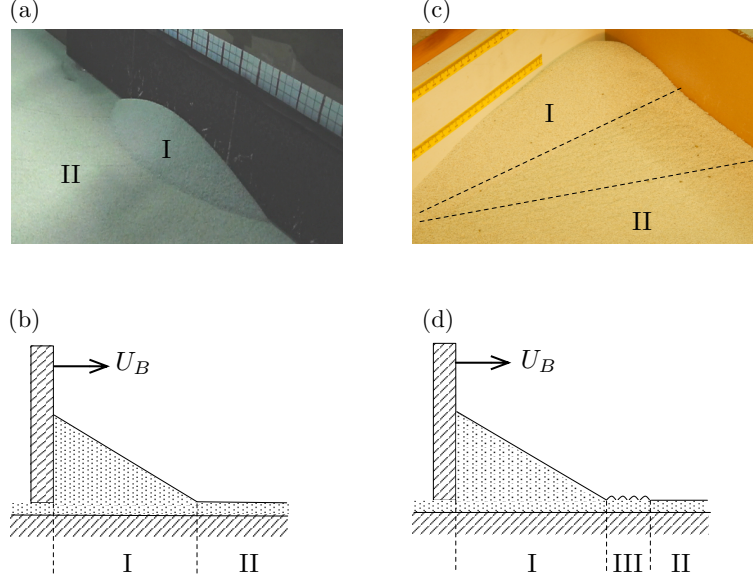


Figure 16: Photo and schematic of bulldozed sand by a blade at velocity U_B for no-slip (a,b) and slip (c,d) boundary conditions at the bottom. I, II and III denotes the three distinct regions which are visible: (I) a dune, (II) a horizontal layer of sand far from the blade, (III) a region where the granular materials is squeezed in a wrinkled layer before being bulldozed.

A Slipping or not slipping?

Depending on the coating of the rotating table, two different regimes can be observed for the bulldozed sand (see figure 16). If the table is coated with sandpaper, the boundary condition at the bottom are no-slip boundary condition. In this case, we observed two different zones: a zone where the sand is bulldozed and a zone far from the blade where the granular material is stationary (see figure 16a.b). This is this situation we study in this report.

However, in the absence of sandpaper on the bottom, the boundary condition on the table is less obvious. There is likely a sliding layer of grain. In this case, the avalanching dune is buffered from the upstream static bed by a compressing, sliding layer of grains. In some exploratory experiments, this layer appeared to lose stability towards a type of buckling instability, rendering the free surface into a wavy pattern (region III on figure 16c.d). This situation is more complicated to describe as the characteristic of the surface becomes really important. This new situation would deserved a proper study in the future but is beyond the scope of this report.

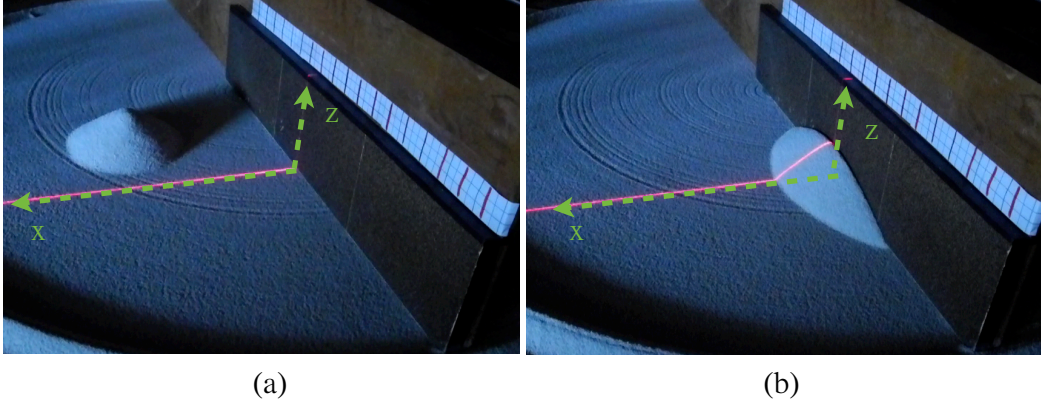


Figure 17: Laser sheet projected on the table (red line). (a) For a flat topography the line remains straight, the height is equal to $h = 0$. (b) When the dune is present, the deviation of the line from a straight line leads to the value of $h(x)$ after initial calibration.

B Diagnostic method: calibration and topography of the dune

In addition to the qualitative visualization of the bulldozing phenomenon, we need to have access to quantitative features. Here, we want to obtain the shape of the dune at an arbitrary radius. However, we need a non intrusive method. We have used a method developed during the summer which relies on the deformation of a laser line projected on a topography. For this method, we project a sheet at a given radius. In the absence of topography, a straight line is observed (see figure 17(a)). However, as soon as a topography is present, the sheet is deformed (see figure 17(b)) and we can measure the distance between the deformed and non-deformed line to have access to the height.

Note that the movie has to be recorded by a camera located in a position such that we can see the whole topography of the dune. Figures 17(a) & 17(b) show a typical example of view to study the entire topography of the dune. However, as can be seen on these two figures, it leads to some problems to describe the topography of the dune as a function of the variables (x, y, z) . Indeed the view is $3D$, thus the axis (Ox) and (Oz) are not perpendicular, in addition the length scales change with the position. Therefore, before postprocessing the movies, we need to calibrate the position of the camera to obtain a direct correspondence between the location of a pixel (x_p, z_p) and the physical values (x, y, z) .

We use a squared board at a given radial position y . One calibration will be valid only for a given value of y which will be the position of our laser sheet (note that in figure 18, y is known from the scale on the top of the blade). Then, we obtain the direction of the axis (Ox) and (Oz) from the edges of the board. Because the axis are not perpendicular, we need to determine the vanishing points which allow us to correct the effects of the perspective. It corresponds to the intersection of the red dashed line in figure 18). Then, we determine the length scales along y and z with the graduation on the grid. In a first approximation, direct measurements show that the correspondence between the measured distance on the

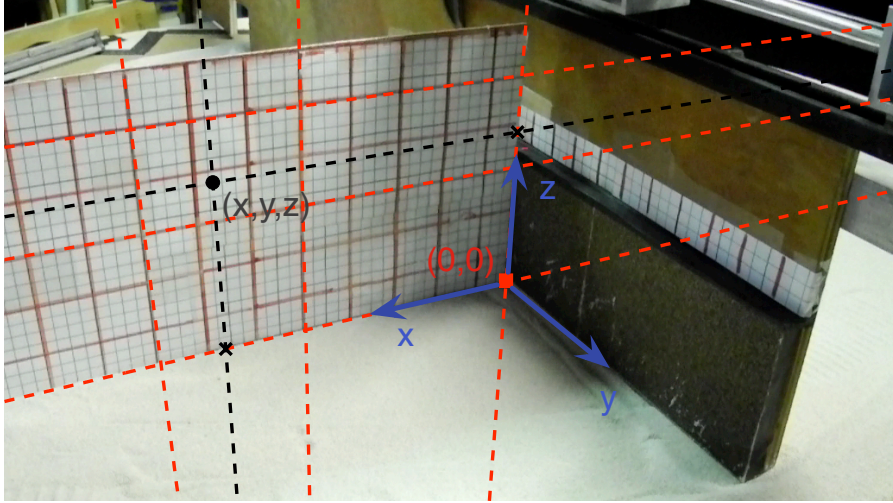


Figure 18: Photo of the calibration process. The board is used to define the direction of the axis, the vanishing points and the lengthscales.

picture and the real distance is linear. After this calibration, we consider a pixel at a known location (x_p, z_p) in our movie, then we project this point on the (Ox) and (Oz) . Using the length scales determine during the calibration process, we obtain the location (x, z) for a given y .

Acknowledgments: Developing an experimental setup from scratch in few weeks has been a difficult but fantastic experience. It would have definitely not be possible without the numerous ideas, the reactivity and the enthusiasm throughout the summer of Neil Balmforth and Colm Caulfield. Thank you for introducing me to the topic of granular material, both experimental and theoretical. We started from a basic idea, what happen if we bulldoze some sand. Then, we encountered some problems during the realization which have been solved one by one and finally our rotating bulldozer was working! These experiments with granular material would not have been possible without Claudia Cenedese's tolerance of so much dust in the lab! I am also grateful to Anders Jensen for many technical innovations on our setup. To conclude, I also would like to thank all the staff and fellows of the GFD Summer Program. Spending the summer at Walsh Cottage provided me an unique educational opportunity and incredible experience.

References

- [1] B. ANDREOTTI, *Sonic sands*, Rep. Prog. Phys., 75 (2012), p. 026602.
- [2] R. BAGNOLD, *The shearing and dilatation of dry sand and the singing mechanism*, Proc. Roy. Soc. A, 295 (1966), pp. 219–232.

- [3] A.-F. BITBOL, N. TABERLET, S. MORRIS, AND J. MCELWAIN, *Scaling and dynamics of washboard roads.*, Phys. Rev. E, 79 (2009), p. 061308.
- [4] F. DA CRUZ, *Écoulements de grains secs: forttement et blocage*, thèse de l'école nationale des ponts et chaussées, Université de Nice Sophia-Antipolis, 2004.
- [5] S. DOUADY, A. MANNING, P. HERSEN, H. ELBELRHITI, S. PROTIERE, A. DAERR, AND B. KABBACHI, *The song of the dunes as a self-synchronized instrument*, Phys. Rev. Lett., 97 (2006), p. 018002.
- [6] Y. FORTERRE AND O. POULIQUEN, *Flows of dense granular media.*, Annu. Rev. Fluid Mech., 40 (2008), pp. 1–24.
- [7] K. HUTTER, T. KOCH, C. PLUSS, AND S. SAVAGE, *The dynamics of avalanches from initiation to runout. part ii: experiments.*, Acta Mechanica, 109 (1995), pp. 127–165.
- [8] P. JOP, Y. FORTERRE, AND O. POULIQUEN, *Crucial role of side walls for granular surface flows: consequences for the rheology.*, J. Fluid Mech., 541 (2005), pp. 167–192.
- [9] ———, *A constitutive law for dense granular flows.*, Nature, 441 (2006), p. 727.
- [10] L. LACAZE AND R. KERSWELL, *Axisymmetric granular collapse: a transient three dimensional flow test of viscoplasticity.*, Phys. Rev. Lett., 102 (2009), p. 108305.
- [11] P.-Y. LAGRÉE, L. STARON, AND S. POPINET, *The granular column collapse as a continuum: validity of a two-dimensional navier-stokes model with a $\mu(i)$ -rheology.*, J. Fluid Mech., 686 (2011), pp. 378–408.
- [12] G. MIDI, *On dense granular flows.*, Eur. Phys. J. E., 14 (2004), pp. 341–365.
- [13] B. PERCIER, S. MANNEVILLE, J. MCELWAIN, S. MORRIS, AND N. TABERLET, *Lift and drag forces on an inclined plow moving over a granular surface*, Phys. Rev. E, 84 (2011), p. 051302.
- [14] S. SAVAGE AND K. HUTTER, *The dynamics of avalanches of granular materials from initiation to runout. part i: analysis.*, Acta Mechanica, 86 (1991), pp. 201–223.
- [15] N. TABERLET, S. MORRIS, AND J. MCELWAIN, *Washboard road: The dynamics of granular ripples formed by rolling wheels*, Phys. Rev. Lett., 99 (2007), p. 068003.

Spin down of a stellar interior

Rosalind Oglethorpe

October 3, 2012

1 Introduction

Helioseismology has revealed a lot of information about the structure and dynamics of the solar interior, and we expect astroseismology from the Kepler probe to soon reveal similar information about other solar-type stars. The Sun and solar-type stars have two regions: a convective outer zone and a radiative inner zone [3, 10]. The radiative zone is stably stratified and energy transport is dominated by photon radiation.

Helioseismology has revealed that the convection zone is differentially rotating, as shown in Figure 1. At the equator, the rotation is fast with a period of about 25 days. The period increases with latitude, reaching about 30 days near the poles. The reason for this differential rotation is not yet completely understood. It is known that the turbulence in rotating convection is strongly anisotropic and causes a net flux of angular momentum towards the equator, but there are also many other processes involved in driving the differential rotation [8].

The radiative zone, by contrast, is in uniform rotation, as shown in Figure 1, with a period of about 27 days (the same as at approximately 30 degrees latitude in the convection zone). The two regions are separated by a rotational shear layer, which is called the tachocline [13]. Observations (for example, see Figure 1) reveal that the tachocline is very thin. This is surprising, because (as shown by [13]) the rotational shear should propagate into the interior on a relatively fast timescale, advected by meridional flows associated with the so-called ‘thermal-spreading’ process.

1.1 Thermal spreading

To understand thermal spreading, let’s consider a thought-experiment in which, at time $t = 0$, the outer convection zone is differentially rotating and the inner radiative zone is uniformly rotating. Isobars in the uniformly rotating radiative zone are approximately spherical at first. As the differential rotation propagates into the top of the radiative zone, the Coriolis force due to the perturbation of the angular velocity must be compensated by a pressure perturbation, \hat{P} (see Figure 2(a)). In hydrostatic equilibrium, the latter must be compensated by a change in the local density, and ultimately induces a temperature perturbation \hat{T} . The sign of the Coriolis force is such that the polar tachocline becomes somewhat hotter than the regions below, while the equatorial tachocline is somewhat cooler.

If the system is also in thermal equilibrium, advective and diffusive heat transport must compensate each other. As the temperature perturbation diffuses outwards, inward flows are

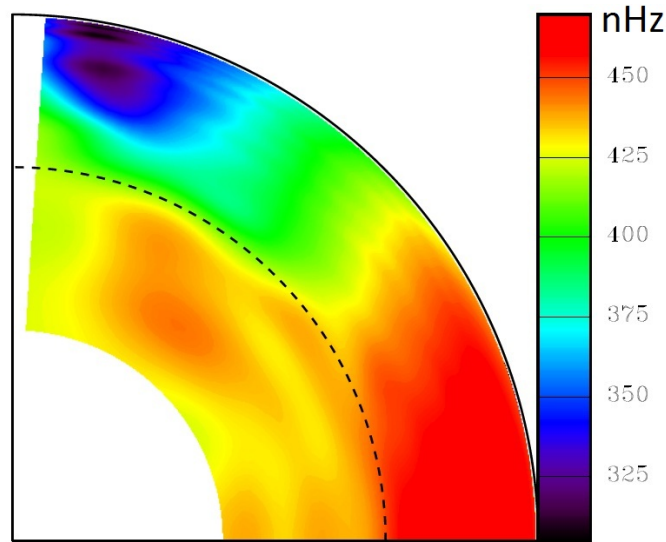


Figure 1: A graph of the angular velocity in the solar interior, from [3]. The outer convective zone is differentially rotating, and the inner radiative zone is uniformly rotating. The dashed line indicates the boundary between the convection zone and the radiative zone.

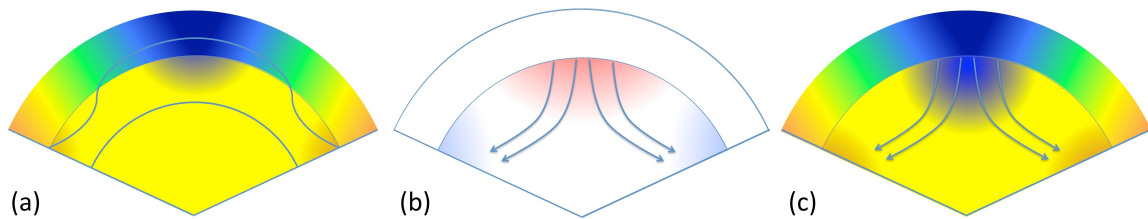


Figure 2: A schematic of the thermal spreading process. (a) Isobars are perturbed by the propagation of the differential rotation into the radiative zone (colour shows angular velocity and grey lines show isobars). (b) This pressure perturbation causes a temperature perturbation, and the diffusion of this temperature perturbation is balanced by inward flows to maintain thermal equilibrium (colour shows temperature perturbation and grey arrows show flows). (c) These inward flows advect the differential rotation further into the interior (third picture).

generated to balance the thermal diffusion (see Figure 2(b)). The latter transport angular momentum, so the differential rotation spreads into the radiative zone (see Figure 2(c)). Spiegel and Zahn [13] studied this process in detail. They found that the depth h of the tachocline grows via thermal spreading as

$$h \approx r_0 \left(\frac{t}{t_{ES}} \right)^{1/4}, \quad (1)$$

where r_0 is the radius of the radiative zone, t is time and

$$t_{ES} = \left(\frac{N}{2\Omega} \right)^2 \frac{r_0^2}{\kappa} \quad (2)$$

is the global Eddington-Sweet timescale. It is important to note here that viscosity plays no role in the process. By thermal spreading alone, Spiegel and Zahn argued that the thickness of the tachocline by now should be about a third of the total depth of the radiative zone. This is clearly at odds with observations from helioseismology (Figure 1). They concluded that there must be some other mechanism to stop the growth of the tachocline and the propagation of meridional flows into the interior.

1.2 The effect of an interior magnetic field: the Gough and McIntyre model

One mechanism that could impose a uniform rotation in the radiative zone is a primordial magnetic field, confined to the radiative zone [7]. The induction equation for a magnetic field is

$$\frac{\partial \mathbf{B}}{\partial t} = \nabla \times (\mathbf{u} \times \mathbf{B} - \eta \nabla \times \mathbf{B}), \quad (3)$$

where \mathbf{u} is the velocity of the flow, \mathbf{B} is the magnetic field and η is the magnetic diffusivity. For a steady axisymmetric magnetic field with negligible meridional flows and magnetic diffusivity, (3) simply becomes

$$\nabla \times (\mathbf{u} \times \mathbf{B}) = (\mathbf{B} \cdot \nabla) \mathbf{u} - (\mathbf{u} \cdot \nabla) \mathbf{B} = 0, \quad (4)$$

using the solenoidal condition $\nabla \cdot \mathbf{B} = 0$. If we rewrite \mathbf{u} as

$$\mathbf{u} = (0, 0, r \sin \theta \Omega), \quad (5)$$

in spherical coordinates (where Ω is the rotation rate), (4) yields Ferraro's law of isorotation [4],

$$\mathbf{B} \cdot \nabla \Omega = 0, \quad (6)$$

which states that angular velocity is constant on magnetic field lines. Hence, as long as the magnetic field is confined to the radiative zone then (6) can enforce a uniform rotation in the interior. If the magnetic field lines are anchored in the convection zone, by contrast, (6) would promote the propagation of the differential rotation into the interior.

Unfortunately, by (3), magnetic fields diffuse over long timescales, so that any initially confined field slowly expands into the convection zone. Thus, differential rotation in the

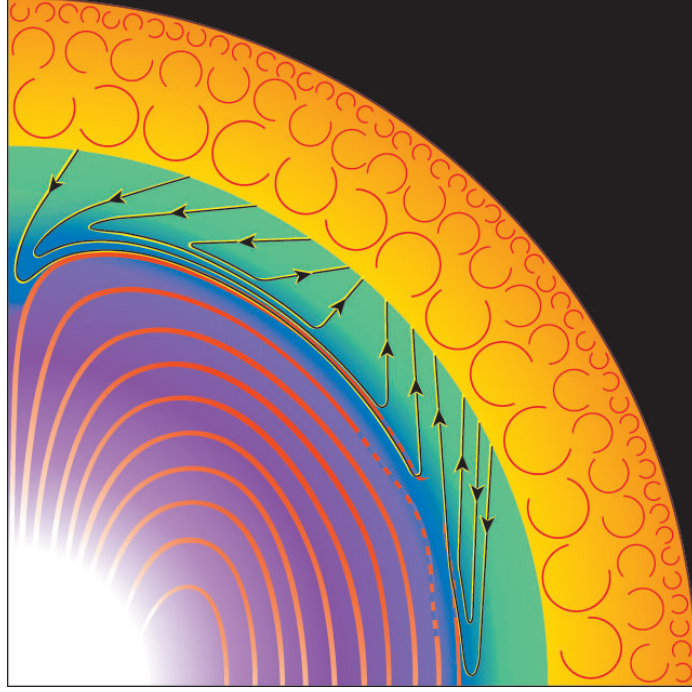


Figure 3: A schematic of the current tachocline paradigm, from [6]. The purple region is the magnetically dominated interior, with magnetic field lines shown in red. The blue region is the tachopause (thickness exaggerated by a factor of 50) and the green region is the tachocline (thickness exaggerated by a factor of 5). The arrows represent meridional flows in the tachocline. The yellow region is the convection zone.

radiative zone is expected unless there is a mechanism to keep the field actively confined against diffusion [2, 14]. Gough and McIntyre [6] showed that one way of keeping the field confined within the radiative zone is for the downwelling flows associated with the tachocline thermal spreading to balance the outward diffusion of the magnetic field.

A schematic of the current tachocline paradigm is shown in Figure 3, from [6]. In this model, the interior is magnetically dominated and in rigid rotation. Between this interior and the outer convection zone, there is a magnetic-free, stably stratified tachocline with thermally driven downwelling flows which confine the magnetic field. A thin magnetic boundary layer, called the tachopause, separates the tachocline from the rest of the interior.

1.3 The effect of spin down

The Gough and McIntyre model assumes that the system is in a steady state. However, there are several different possible sources of time-dependence in the problem, including the very slow (and complicated) timescale of the stellar evolution, the time for the diffusion of the magnetic field, the timescale of the decrease in rotation rate, and many others. We will focus on the effect of the decreasing rotation rate.

In addition to the internal primordial field, solar-type stars also host a distinct ‘dynamo field’ generated in the convection zone by turbulent fluid motions. In the Gough and McIn-

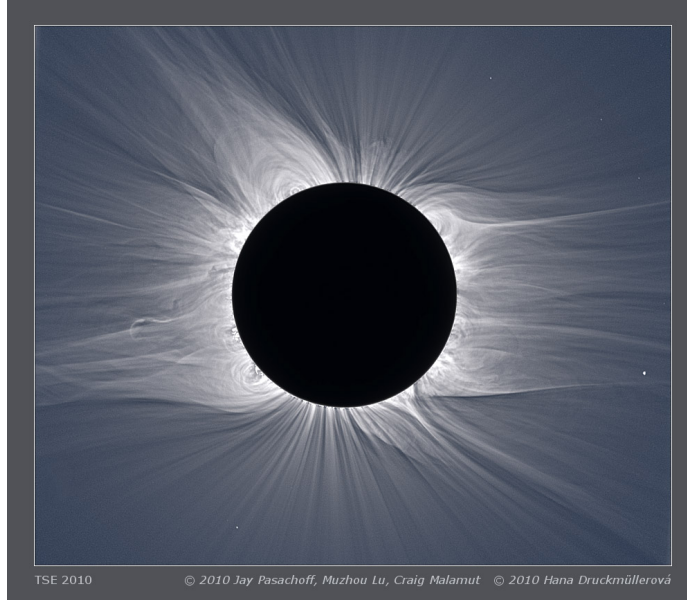


Figure 4: A photograph of the solar wind during the 11 July 2010 Solar eclipse, from [9].

tyre model, this magnetic field is assumed to be spatially separated from the primordial field by the magnetic-free tachocline. This dynamo field emerges at the surface and eventually becomes part of the solar wind. Figure 4 shows a photo of the solar wind during a solar eclipse. Charged particles travel along the field lines out from the star, and their angular velocity slows down by conservation of angular momentum. However, by Ferraro’s law of isorotation, the angular velocity must be constant along field lines. This exerts a magnetic torque on the outer layers of the star, causing them to slow down.

Skumanich [11] looked at the rotation rates of several clusters of solar-type stars, and found that the mean stellar rotation rate decays as a power law with time, as

$$\Omega \sim t^{-1/2}. \quad (7)$$

This project aims to look at the effect of spin down on the model by [6]. In what follows, we first study how spin down propagates into a non-magnetic interior, and then look at what happens if a magnetic field is included in the radiative zone.

2 Stratified, non-magnetic spin down

We first consider the spin down of a stratified, non-magnetic star. We build upon the work of Bretherton and Spiegel [1], which is now discussed for clarity and completeness.

2.1 Spin-down of an unstratified, non-magnetic star

Bretherton and Spiegel [1] were the first to study the spin down of an unstratified star. They consider a star with an outer convection zone and an inner radiative zone, and model it as an unstratified sphere of fluid (which represents the radiative zone) surrounded by a

spherical shell of porous medium (the convection zone). The interior region has radius a , and the total radius of the star is b . Since $Pr \ll 1$, the viscosity is negligible.

The porous medium is rotating with an angular velocity $\Omega(t)$, which slows down over time as

$$\Omega(t) = \Omega_0 \exp(-kt), \quad (8)$$

where Ω_0 is the initial rotation rate and k is the spin down rate. The spin down is assumed to be slow, so that $k \ll \Omega_0$. Bretherton and Spiegel look for a ‘steady state’, where the $D\mathbf{u}/Dt$ term is negligible in the momentum equation expressed in a frame rotating with angular velocity $\Omega(t)$. The ‘steady state’ equations of motion in the porous medium are Darcy’s law and the incompressibility condition:

$$\frac{1}{\tau} \mathbf{u} = -\frac{1}{\rho} \nabla \hat{P}, \quad \nabla \cdot \mathbf{u} = 0, \quad (9)$$

where τ is the Darcy friction timescale and \hat{P} is the pressure perturbation away from hydrostatic equilibrium. The equations of motion in the interior are

$$2\boldsymbol{\Omega} \times \mathbf{u} - k\boldsymbol{\Omega} \times \mathbf{r} = -\frac{1}{\rho} \nabla \hat{P}, \quad \nabla \cdot \mathbf{u} = 0. \quad (10)$$

The first term in (10) is the Coriolis force, and the second is Euler’s force which is due to the deceleration of the frame. Solving these equations, then matching \hat{P} and the normal velocity at the interface between the interior and the porous medium, $r = a$, yields for instance the angular velocity perturbation $\hat{\Omega}(r, \theta, t)$ everywhere in the star. The angular velocity in the interior turns out to be uniform, with value

$$\hat{\Omega}_c = \frac{3a^5 + 2b^5}{b^5 - a^5} \frac{k}{4\Omega\tau}, \quad (11)$$

in the rotating frame. Since $\hat{\Omega}_c > 0$, there is a constant lag in the propagation of the spin down into the interior.

In short, the porous medium and the interior are each uniformly rotating, but the interior is always rotating faster, since $\hat{\Omega}_c$ is always positive. The lag depends on the rate of spin down, k , the rotation rate of the porous medium, Ω , and the Darcy relaxation time scale of the porous medium, τ .

2.2 Spin down of a stratified non-magnetic star (cylindrical model)

2.2.1 The model

We now consider a similar model to [1], but with a stratified interior and with differential rotation in the convection zone. Because of the added complexity, we have to model a cylinder instead of a full sphere, with gravity parallel to the rotation axis. This adds a geometrical error, but on the other hand allows for a fully analytical solution. This cylinder can be viewed as the polar regions of the star. The lower part is filled with stratified fluid, with constant buoyancy frequency N and negligible viscosity ν , from $z = 0$ to $z = z_{cz}$, and with a porous medium from $z = z_{cz}$ to $z = 1$. Figure 5 is a diagram of the model set up.

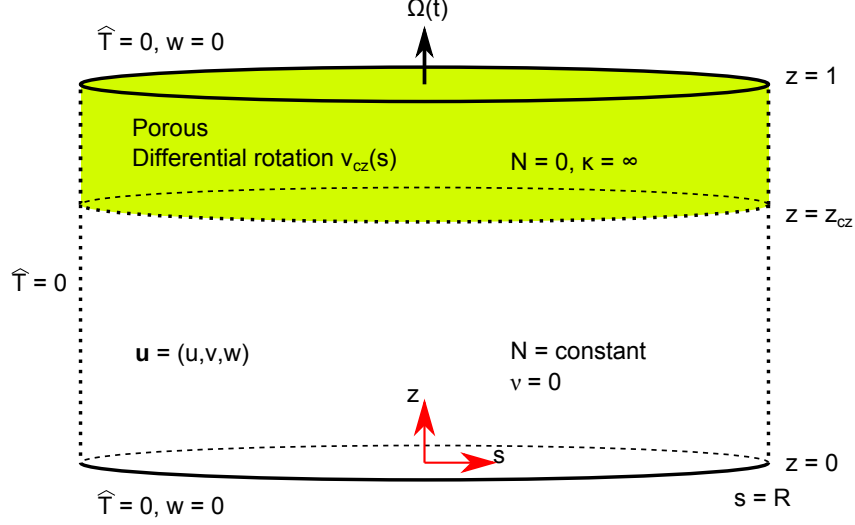


Figure 5: A diagram of the cylindrical model set up. The region from $z = 0$ to $z = z_{cz}$ is filled with a stably stratified fluid, with constant buoyancy frequency N , and the viscosity ν is negligible. The region from $z = z_{cz}$ to $z = 1$ (yellow) is filled with a differentially rotating porous medium.

The porous medium is rotating with angular velocity $\Omega(t)$, and following [1] we work in a frame rotating with angular velocity $\Omega(t)$. The cylinder has radius R and unit height. We use cylindrical coordinates (s, ϕ, z) in the rotating frame, and assume axisymmetry with respect to the axis of rotation (which is in the vertical z direction) so that $\partial/\partial\phi = 0$. In these coordinates, we write the velocity relative to the rotating frame as $\mathbf{u} = (u, v, w)$.

The real dynamics of a stellar convection zone are very complicated. Our main goal here is to model rapid momentum transport from the surface down to the top of the radiative zone. The simplest possible model that has such a property is one with a Darcy friction term, as in [1, 5]. We replace the effect of the Reynolds stresses with a Darcy forcing term in the convection zone ($z > z_{cz}$), so that in this region the velocity of the fluid relaxes to the assumed velocity of the porous medium on a timescale τ . In the rotating frame, we consider that the porous medium may be also differentially rotating, with velocity $v_{cz}(s)\mathbf{e}_\phi$. We require the net angular momentum of the porous medium in the rotating frame to be zero, so the differential rotation does not apply any torque to the system. The porous medium represents the convection zone, where $N \approx 0$, and (for simplicity) we also take its thermal diffusivity to be effectively infinite¹, so that the temperature perturbation $\hat{T} = 0$ for $z > z_{cz}$. The momentum equation for the fluid in the porous medium is then

$$\frac{\partial \mathbf{u}}{\partial t} + 2\mathbf{\Omega} \times \mathbf{u} + \dot{\mathbf{\Omega}} \times \mathbf{r} + \frac{\mathbf{u} - v_{cz}(s)\mathbf{e}_\phi}{\tau} = -\frac{1}{\rho}\nabla\hat{P}. \quad (12)$$

In the ‘bulk’ of the fluid ($z < z_{cz}$) we make several assumptions to simplify the equations (as in, for example, [1], [6] and [13]). We use the Boussinesq approximation (for

¹This assumption gives the solution to lowest order in κ_b/κ_p , where κ_p and κ_b are the thermal diffusivities in the porous medium and the plug, respectively, and $\kappa_p \gg \kappa_b$

example, [12]) and assume that the fluid is incompressible everywhere. We assume that the Rossby number, which is the ratio of the Coriolis acceleration to the advective term, is small. Under this assumption, flows are sufficiently slow that we can neglect the non-linear advective term in the momentum equation. We assume the flow is hydrostatic and geostrophic, so viscous forces are much less important than Coriolis forces. We also assume that the flows are sufficiently steady and slow for the system to be in thermal equilibrium, with heat diffusion being balanced by the advection of the background entropy.

The momentum equation in the bulk is then

$$\frac{\partial \mathbf{u}}{\partial t} + 2\mathbf{\Omega} \times \mathbf{u} + \dot{\mathbf{\Omega}} \times \mathbf{r} = -\frac{1}{\rho} \nabla \hat{P} + \frac{g}{T} \hat{T} \hat{\mathbf{e}}_z, \quad (13)$$

where T is the mean temperature and ρ is the mean density.

We choose the boundary conditions to have zero temperature perturbation, \hat{T} , and vertical velocity, w , at $z = 0$ and $z = 1$. We solve the equations separately for $z > z_{cz}$ and $z < z_{cz}$, and match \hat{T} , w and pressure perturbation \hat{P} at the radiative-convective interface z_{cz} . In short,

$$\hat{T} = 0 \text{ at } z = 0, z = 1, \quad (14)$$

$$w = 0 \text{ at } z = 0, z = 1, \quad (15)$$

$$\hat{T}(z = z_{cz}^-) = \hat{T}(z = z_{cz}^+), \quad (16)$$

$$\hat{P}(z = z_{cz}^-) = \hat{P}(z = z_{cz}^+), \quad (17)$$

$$w(z = z_{cz}^-) = w(z = z_{cz}^+). \quad (18)$$

Boundary conditions at the side wall $s = R$ are more difficult to choose, as we want them to have as little influence as possible on the flow inside the cylinder. We choose

$$\hat{T} = 0 \text{ at } s = R. \quad (19)$$

This boundary condition allows a radial flow across the side wall, which by conservation of mass must be zero overall. We assume that the flow into and out of the cylinder through the side walls has negligible influence on the flow in the cylinder. From (13) the radial and vertical momentum equations in the bulk are

$$\frac{1}{\rho} \frac{\partial \hat{P}}{\partial z} = \frac{g}{T} \hat{T}, \quad (20)$$

$$2\Omega v = \frac{1}{\rho} \frac{\partial \hat{P}}{\partial s}. \quad (21)$$

Using the side wall boundary condition (19) in (20) gives $\hat{P} = 0$ at $s = R$. Combining (20) and (21) yields the thermal wind equation

$$2\Omega \frac{\partial v}{\partial z} = \frac{g}{T} \frac{\partial \hat{T}}{\partial s}. \quad (22)$$

We also have the equations for thermal equilibrium,

$$\frac{N^2 T}{g} w = \kappa \nabla^2 \hat{T}, \quad (23)$$

where κ is the thermal diffusivity in the bulk, and incompressibility

$$\frac{1}{s} \frac{\partial}{\partial s}(su) + \frac{\partial w}{\partial z} = 0. \quad (24)$$

Combining (22), (23) and (24) gives an equation relating u and v

$$-N^2 \frac{\partial}{\partial s} \left(\frac{1}{s} \frac{\partial}{\partial s}(su) \right) = 2\Omega\kappa \left(\frac{\partial^4 v}{\partial z^4} + \frac{\partial}{\partial z} \frac{\partial}{\partial s} \left(\frac{1}{s} \frac{\partial}{\partial s}(sv) \right) \right). \quad (25)$$

The first term on the right hand side is equivalent to the thermal spreading term found in [13], and indicates that there is transport of angular momentum by downwelling meridional flows. A second equation for u and v comes from the ϕ -component of the angular momentum equation (13),

$$\frac{\partial v}{\partial t} + 2\Omega u + \dot{\Omega} s = 0. \quad (26)$$

We then combine (25) and (26) to find v .

2.2.2 ‘Steady state’ solution

Following [1] we first look for a ‘steady state’ solution, where (26) becomes

$$2\Omega u + \dot{\Omega} s = 0. \quad (27)$$

This immediately gives

$$u = -\frac{s}{2} \frac{\dot{\Omega}}{\Omega}, \quad (28)$$

and conservation of mass, with the boundary condition (15), gives

$$w = \frac{\dot{\Omega}}{\Omega} z. \quad (29)$$

Note that the frame is slowing down, so $\dot{\Omega} < 0$. Solving (23) with boundary conditions (19) then gives

$$\hat{T} = \sum_n J_0 \left(\lambda_n \frac{s}{R} \right) \left[\alpha_n \sinh \lambda_n \frac{z}{R} - \frac{C_n z R^2}{\lambda_n^2} \right], \quad (30)$$

with λ_n the zeros of the Bessel function $J_0(x)$ and

$$C_n = \frac{N^2 T}{g\kappa} \frac{\dot{\Omega}}{\Omega} \frac{2}{\lambda_n J_1(\lambda_n)}. \quad (31)$$

The unknown coefficients α_n can be related to C_n using the boundary condition (16). Since $\hat{T} = 0$ in the porous medium:

$$\alpha_n = \frac{C_n z_{cz} R^2}{\lambda_n^2} \frac{1}{\sinh \lambda_n \frac{z_{cz}}{R}}. \quad (32)$$

Equations (20) and (21) then give \hat{P} and v , up to the unknown set of integration constant $\{p_n\}$:

$$\frac{1}{\rho}\hat{P} = \frac{g}{T} \sum_n J_0\left(\lambda_n \frac{s}{R}\right) \left[\frac{\alpha_n R}{\lambda_n} \cosh \lambda_n \frac{z}{R} - \frac{C_n z^2 R^2}{2\lambda_n^2} + p_n \right], \quad (33)$$

$$v = \frac{g}{2\Omega T} \sum_n \frac{dJ_0(\lambda_n \frac{s}{R})}{ds} \left[\frac{\alpha_n R}{\lambda_n} \cosh \lambda_n \frac{z}{R} - \frac{C_n z^2 R^2}{2\lambda_n^2} + p_n \right]. \quad (34)$$

To find v , by finding p_n , we also need to solve the equations in the porous medium.

In the porous medium, $\hat{T} = 0$, and the ϕ -component of the momentum equation (12) in steady state reduces to

$$2\Omega u + \dot{\Omega} s = -\frac{v - v_{cz}(s)}{\tau}, \quad (35)$$

where τ is the time scale of the Darcy force. For ease of algebra, we assume that τ is sufficiently small that, to the lowest order² in τ , and

$$v \cong v_{cz}(s). \quad (36)$$

From (12), the radial and vertical momentum equations are

$$\frac{1}{\rho} \frac{\partial \hat{P}}{\partial z} = -\frac{w}{\tau}, \quad (37)$$

$$\frac{1}{\rho} \frac{\partial \hat{P}}{\partial s} = -\frac{u}{\tau} + 2\Omega v_{cz}(s). \quad (38)$$

Combining these with incompressibility $\nabla \cdot \mathbf{u} = 0$ gives

$$\nabla^2 w = 0. \quad (39)$$

Using the boundary condition (15), we can write w as

$$w = \sum_n B_n \sinh \left[\lambda_n \left(\frac{z}{R} - \frac{1}{R} \right) \right] J_0 \left(\lambda_n \frac{s}{R} \right), \quad (40)$$

for some constants B_n and λ_n . Equation (37) then gives

$$\frac{1}{\rho} \hat{P} = \sum_n J_0 \left(\lambda_n \frac{s}{R} \right) \left[-\frac{B_n}{\tau} \frac{R}{\lambda_n} \cosh \left[\lambda_n \left(\frac{z}{R} - \frac{1}{R} \right) \right] + P_n \right], \quad (41)$$

and using the boundary condition (17) at $s = R$ gives that λ_n are the zeros of $J_0(x)$ as in the bulk solution. Incompressibility also gives

$$u = \sum_n \frac{dJ_0(\lambda_n \frac{s}{R})}{ds} \frac{R}{\lambda_n} B_n \cosh \left[\lambda_n \left(\frac{z}{R} - \frac{1}{R} \right) \right], \quad (42)$$

²This expansion is not necessary, and the calculation can be done without it. However, the solutions are not as simple and lose clarity.

so that (38) becomes

$$\frac{1}{\rho} \frac{\partial \hat{P}}{\partial s} + \frac{u}{\tau} = \sum_n \frac{dJ_0(\lambda_n \frac{s}{R})}{ds} P_n = 2\Omega(t) v_{cz}(s), \quad (43)$$

which uniquely defines P_n ,

$$P_n = -\frac{4\Omega(t)}{\lambda_n J_1^2(\lambda_n)} \int_0^R \frac{s}{R} v_{cz}(s) \lambda_n J_1\left(\lambda_n \frac{s}{R}\right) ds. \quad (44)$$

Matching w and \hat{P} at $z = z_{cz}$ gives

$$B_n = \frac{\dot{\Omega}}{\Omega} \frac{2z_{cz}}{\lambda_n J_1(\lambda_n) \sinh \lambda_n \left(\frac{z_{cz}}{R} - \frac{1}{R}\right)}, \quad (45)$$

and

$$p_n = \frac{T}{g} P_n - \frac{T}{g} \frac{B_n R}{\tau \lambda_n} \cosh \left[\lambda_n \left(\frac{z_{cz}}{R} - \frac{1}{R} \right) \right] - \frac{\alpha_n R}{\lambda_n} \cosh \left(\lambda_n \frac{z_{cz}}{R} \right) + \frac{C_n z^2 R^2}{2\lambda_n^2}, \quad (46)$$

so that the azimuthal velocity (34) becomes

$$v = -\frac{1}{\Omega} \sum_n \frac{J_1(\lambda_n \frac{s}{R})}{\lambda_n J_1(\lambda_n)} \frac{\dot{\Omega}}{\Omega} \left[\frac{N^2}{\kappa} \frac{z_{cz} R^2}{\lambda_n^2} \left(\frac{\cosh \lambda_n \frac{z}{R} - \cosh \lambda_n \frac{z_{cz}}{R}}{\sinh \lambda_n \frac{z_{cz}}{R}} - \frac{\lambda_n}{2z_{cz} R} (z^2 - z_{cz}^2) \right) - \frac{1}{\tau \tanh \lambda_n \left(\frac{z_{cz}}{R} - \frac{1}{R}\right)} \right] + v_{cz}(s). \quad (47)$$

2.2.3 Physical interpretation of the ‘steady-state’ solution

In order to understand this solution more physically, let’s define the different time scales in this problem as

$$t_{sd} = -\frac{\Omega}{\dot{\Omega}}, \quad t_{ES} = \left(\frac{N}{2\Omega} \right)^2 \frac{R^2}{\kappa}, \quad t_{\Omega} = \frac{1}{\Omega}, \quad t_{\tau} = \tau, \quad (48)$$

where t_{sd} is the spin down timescale, t_{ES} is the global Eddington-Sweet timescale, which is the timescale for thermal spreading [13], t_{Ω} is the rotation timescale and t_{τ} is the Darcy friction timescale. We re-write (47) in terms of these timescales,

$$v = \frac{1}{t_{sd}} \sum_n \frac{J_1(\lambda_n \frac{s}{R})}{\lambda_n J_1(\lambda_n)} \left[\frac{t_{ES}}{t_{\Omega}} \frac{4z_{cz}}{\lambda_n^2} \left(\frac{\cosh \lambda_n \frac{z}{R} - \cosh \lambda_n \frac{z_{cz}}{R}}{\sinh \lambda_n \frac{z_{cz}}{R}} - \frac{\lambda_n}{2z_{cz} R} (z^2 - z_{cz}^2) \right) - \frac{t_{\Omega}}{t_{\tau}} \frac{z_{cz}}{\tanh \lambda_n \left(\frac{z_{cz}}{R} - \frac{1}{R}\right)} \right] + v_{cz}(s). \quad (49)$$

This expression shows that v has two separate parts, one which depends on the spin down and one which depends on the differential rotation. We first consider the case with no differential rotation, $v_{cz}(s) = 0$, to isolate the effect of the spin down. Equation (49) shows that v depends on t_{sd} as well as ratios of the other three timescales, t_{ES}/t_{Ω} and t_{Ω}/t_{τ} .

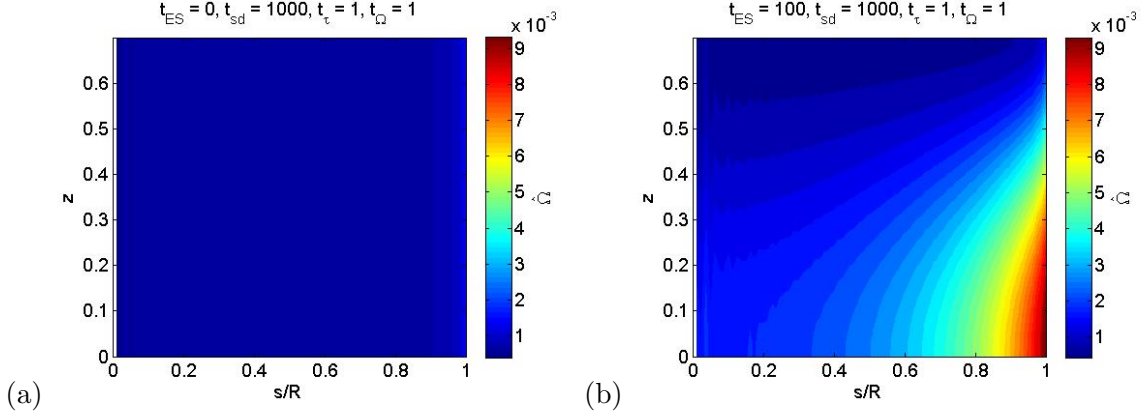


Figure 6: Contour plots of $\hat{\Omega}$ in the ‘steady state’ solution. (a) Unstratified case. $\hat{\Omega}$ is constant with depth and strictly positive everywhere. (b) Stratified case. $\hat{\Omega}$ is strictly positive everywhere, and increases with depth and cylindrical radius.

If there is no stratification in the bulk, $t_{ES} = 0$ and $v(s, z = 0) = v(s, z = z_{cz}) = v(s) > 0$. This implies that the azimuthal velocity is independent of depth, as expected from the Taylor-Proudman constraint, and that there is a lag in the interior with respect to the porous medium. The angular velocity perturbation, $\hat{\Omega} = v/s$, is

$$\hat{\Omega} = \frac{t_{\Omega}}{t_{\tau} t_{sd}} \sum_n \frac{J_1(\lambda_n \frac{s}{R})}{s \lambda_n J_1(\lambda_n)} \frac{z_{cz}}{\tanh \lambda_n (\frac{1}{R} - \frac{z_{cz}}{R})}, \quad (50)$$

which is similar to the result from [1]. Indeed, $\hat{\Omega}$ contains the same ratio of timescales as in [1] but with a different geometrical factor, which is naturally expected since we are using a cylinder rather than a sphere.

If the bulk is stratified, $t_{ES} > 0$, then $v(s, z = 0) > v(s, z = z_{cz}) > 0$, showing that the lag increases with depth. This can be interpreted in two ways. On the one hand, one may view that the spin down is propagated more quickly to the top of the bulk, near the porous medium, than to the bottom which is further away. Alternatively one may also consider that as the stratification increases, the thermal wind (22) can support more vertical shear, so the lag at the bottom increases. Figure 6 shows contour plots of $\hat{\Omega}$ in the bulk for $t_{ES} = 0$ and $t_{ES} > 0$. For $t_{ES} = 0$, Figure 6(a) shows an approximately uniform lag, which is constant with depth. For $t_{ES} > 0$, Figure 6(b) shows that the lag increases with both depth and with s .

2.2.4 Time-dependent solution

Having found the ‘steady state’ solution, we now return to the time-dependent equations to find when this ‘steady state’ is valid. We expand v again on the same basis of Bessel functions, as

$$v = \sum_n \frac{dJ_0(\lambda_n \frac{s}{R})}{ds} \tilde{v}_n(z, t). \quad (51)$$

Combining (25) and (26) with this ansatz gives

$$\frac{\partial \tilde{v}_n}{\partial t} + \left(\frac{2\Omega(t)R}{N\lambda_n} \right)^2 \kappa \frac{\partial^4 \tilde{v}_n}{\partial z^4} - \left(\frac{2\Omega(t)}{N} \right)^2 \kappa \frac{\partial^2 \tilde{v}_n}{\partial z^2} = \frac{\dot{\Omega}R^2}{\lambda_n^2} \frac{4}{\lambda_n J_1(\lambda_n)}. \quad (52)$$

The first and second terms on the left hand side recover the equation found by [13] for the thermal spreading of differential rotation into the interior using a boundary layer approximation, and the third term on the right hand side completes the full expression for thermal spreading in the absence of a boundary layer approximation. The right hand side contains the global forcing term arising from Euler's force. Thus the evolution of the angular momentum in the bulk has two contributions: a transport by meridional flows, which is the thermal spreading found by [13], and a global extraction of angular momentum by the spinning down of the frame.

To solve (52), we need to express all boundary conditions in terms of $v_n(z)$. The boundary conditions at $z = 0$ are

$$\hat{T} = 0 \Rightarrow \frac{\partial \tilde{v}_n}{\partial z} = 0, \quad (53)$$

$$w = 0 \Rightarrow \frac{\partial^3 \tilde{v}_n}{\partial z^3} = 0. \quad (54)$$

In the porous medium, by contrast, we assume that the dynamics always relax to the steady state on a very rapid timescale. Hence (40), (41) and (42) hold. The boundary conditions at $z = z_{cz}$ are then

$$\hat{T} \text{ continuous} \Rightarrow \hat{T} = 0 \Rightarrow \frac{\partial \tilde{v}_n}{\partial z} = 0, \quad (55)$$

$$\hat{P} \text{ continuous} \Rightarrow \frac{\partial \hat{P}}{\partial s} \text{ continuous} \Rightarrow 2\Omega \tilde{v}_n = -\frac{B_n R}{\tau \lambda_n} \cosh \left[\lambda_n \left(\frac{z_{cz}}{R} - \frac{1}{R} \right) \right] + P_n, \quad (56)$$

$$w \text{ continuous} \Rightarrow \frac{2\Omega \kappa}{N^2} \frac{\partial^3 \tilde{v}_n}{\partial z^3} = B_n \sinh \left[\lambda_n \left(\frac{z_{cz}}{R} - \frac{1}{R} \right) \right], \quad (57)$$

using (55). Equations (56) and (57) combine to give

$$\tilde{v}_n + \frac{R}{\tau \lambda_n} \frac{1}{\tanh[\lambda_n(\frac{z_{cz}}{R} - \frac{1}{R})]} \frac{\kappa}{N^2} \frac{\partial^3 \tilde{v}_n}{\partial z^3} = \frac{P_n}{2\Omega(t)}, \quad (58)$$

where the right hand side is independent of time if $v_{cz}(s)$ is independent of time in the spinning down frame, from (41). The true steady state solution with these inhomogeneous boundary conditions is

$$v = v_{cz}(s), \quad (59)$$

so that, if the differential rotation remains constant while the rotation rate of the frame decays, eventually the forcing from the spin down is negligible compared to the forcing from the differential rotation, and the angular velocity in the bulk is the same as in the porous medium. We write

$$v = \sum_n \frac{dJ_0(\lambda_n \frac{s}{R})}{ds} \tilde{v}_n(z, t) = \sum_n \frac{dJ_0(\lambda_n \frac{s}{R})}{ds} \hat{v}_n(z, t) + v_{cz}(s), \quad (60)$$

where \hat{v}_n obeys (52) with homogeneous boundary conditions

$$\frac{\partial \hat{v}_n}{\partial z} = 0 \quad \text{at } z = 0, z = z_{cz}, \quad (61)$$

$$\frac{\partial^3 \hat{v}_n}{\partial z^3} = 0 \quad \text{at } z = 0, \quad (62)$$

$$\frac{\partial^3 \hat{v}_n}{\partial z^3} = -\frac{N^2 \tau \lambda_n}{\kappa R} \tanh \left[\lambda_n \left(\frac{z_{cz}}{R} - \frac{1}{R} \right) \right] \hat{v}_n \quad \text{at } z = z_{cz}, \quad (63)$$

from (53), (54), (55) and (58).

Equation (52) is separable, so we can write

$$\hat{v}_n = \sum_m T_{nm}(t) Z_{nm}(z), \quad (64)$$

where the eigenfunctions $Z_{nm}(z)$ satisfy

$$\frac{\partial^2}{\partial z^2} \left(\left(\frac{\lambda_n}{R} \right)^2 - \frac{\partial^2}{\partial z^2} \right) Z_{nm}(z) = - \left(\frac{\mu_{nm}}{R^2} \right)^2 Z_{nm}(z) \quad (65)$$

for some constants μ_{nm} . The operator on the left hand side is self-adjoint with the boundary conditions (61) - (63). As with the horizontal modes, we can project onto the vertical modes to find an evolution equation for $T_{nm}(t)$. Since (65) is an equation with constant coefficients, we seek solutions of the form

$$Z_{nm}(z) = e^{\sigma_{nm} z}, \quad (66)$$

and find four solutions for σ_{nm} : $\pm \sigma_{1,nm}$ and $\pm i \sigma_{2,nm}$, where

$$\sigma_{1,nm} = \frac{1}{R} \left[\frac{\lambda_n^2}{2} + \sqrt{\mu_{nm}^2 + \frac{\lambda_n^4}{4}} \right]^{1/2}, \quad \sigma_{2,nm} = \frac{1}{R} \left[\sqrt{\mu_{nm}^2 + \frac{\lambda_n^4}{4}} - \frac{\lambda_n^2}{2} \right]^{1/2}, \quad (67)$$

and where μ_{nm} can be determined using (63). Applying the boundary conditions (61) - (63) we finally find

$$Z_{nm}(z) = \left[\frac{\sigma_{2,nm}}{\sigma_{1,nm}} \frac{\sin \sigma_{2,nm} z_{cz}}{\sinh \sigma_{1,nm} z_{cz}} \cosh \sigma_{1,nm} z + \cos \sigma_{2,nm} z \right]. \quad (68)$$

Projecting (52) onto these eigenfunctions $Z_{nm}(z)$ gives

$$\dot{T}_{nm}(t) + \left(\frac{2\Omega(t)\mu_{nm}}{NR\lambda_n} \right)^2 \kappa T_{nm}(t) = \frac{\dot{\Omega} R^2}{\lambda_n^2} \frac{4}{\lambda_n J_n(\lambda_n)} \frac{\int_0^{z_{cz}} Z_{nm}(z) dz}{\int_0^{z_{cz}} Z_{nm}^2(z) dz} \equiv G_{nm}(t), \quad (69)$$

where $G_{nm}(t)$ is the projection of the global forcing term in (52) onto the vertical modes. Equation (69) can be solved using an integrating factor method to give

$$T_{nm}(t) = \exp \left(- \left(\frac{2\mu_{nm}}{NR\lambda_n} \right)^2 \kappa \int^t \Omega^2(t') dt' \right) \times \quad (70)$$

$$\left[\int_{t_0}^t G_{nm}(t') \exp \left(\left(\frac{2\mu_{nm}}{NR\lambda_n} \right)^2 \kappa \int^{t'} \Omega^2(t'') dt'' \right) dt' + T_{0,nm} \right], \quad (71)$$

with

$$T_{0,nm} = \exp \left(\left(\frac{2\mu_{nm}}{NR\lambda_n} \right)^2 \kappa \int^{t_0} \Omega^2(t) dt \right) \frac{\int_0^{z_{cz}} v(t=t_0) Z_n(z) dz}{\int_0^{z_{cz}} Z_n^2(z) dz}. \quad (72)$$

2.2.5 Physical interpretation of the solutions

As discussed in section 1, there is strong observational and theoretical evidence suggesting that $\Omega(t)$ decays as a power law, with $\Omega(t) = \Omega_0(t/t_0)^{-\alpha}$ for some $\alpha > 0$. In this case,

$$\int^t \Omega^2(t') dt' = \begin{cases} \frac{\Omega^2(t)t}{1-2\alpha} & (\alpha \neq \frac{1}{2}), \\ \Omega^2(t)t \log(t) & (\alpha = \frac{1}{2}), \end{cases} \quad (73)$$

so we expect fundamentally different behaviour for $\alpha \neq 1/2$ and $\alpha = 1/2$. As in (48), the spin down timescale and the global Eddington-Sweet timescale are

$$t_{sd}(t) = -\frac{\Omega(t)}{\dot{\Omega}(t)} = \frac{t}{\alpha}, \quad t_{ES}(t) = \left(\frac{NR}{2\Omega(t)} \right)^2 \frac{1}{\kappa} = \left(\frac{NR}{2\Omega_0} \right)^2 \frac{t^{2\alpha}}{\kappa t_0^{2\alpha}}, \quad (74)$$

where each of them now explicitly depends on time. We also define the local Eddington-Sweet time of each mode as

$$t_{ES}^{nm}(t) = \left(\frac{NR}{2\Omega(t)} \right)^2 \frac{\lambda_n^2}{\mu_{nm}^2 \kappa}. \quad (75)$$

Writing $T_{nm}(t)$ in terms of these timescales yields,

$$T_{nm}(t) = \begin{cases} \exp \left(-\frac{\alpha}{1-2\alpha} \frac{t_{sd}}{t_{ES}^{nm}} \right) \left[G_{nm}(t) t^{\alpha+1} \int_{t_0}^t t'^{-\alpha-1} \exp \left(\frac{\alpha}{1-2\alpha} \left(\frac{t_{sd}}{t_{ES}^{nm}} \right)' \right) + T_{0,nm} \right] & (\alpha \neq \frac{1}{2}), \\ t^{-t_{sd}/2t_{ES}^{nm}} \left[G_{nm}(t) t^{3/2} \int_{t_0}^t t'^{(t_{sd}/2t_{ES}^{nm})'-3/2} + T_{0,nm} \right] & (\alpha = \frac{1}{2}). \end{cases} \quad (76)$$

We see that the behaviour of each mode $T_{nm}(t)$ depends on both α and the ratio of timescales

$$\frac{t_{sd}(t)}{t_{ES}^{nm}(t)} = \frac{1}{\alpha} \left(\frac{2\Omega_0}{NR} \right)^2 \frac{\mu_{nm}^2 \kappa}{\lambda_n^2} t_0^{2\alpha} t^{1-2\alpha}, \quad (77)$$

which itself changes over time for $\alpha \neq 1/2$.

If $\alpha > 1/2$, which corresponds to rapid spin down, (76) shows that the effect of the initial conditions exponentially increases on a timescale of t_{sd}/t_{ES}^{nm} . Although the latter decreases over time, it remains strictly positive so the solution always blows up. This suggests that our original assumptions, for example that $\mathbf{u} \cdot \nabla \mathbf{u}$ is negligible, must break down in the case of rapid spin down, and our solution is not valid. If $\alpha < 1/2$, which corresponds to slow spin down, the initial conditions always decay exponentially and the system relaxes to a ‘steady’ state, where only the global forcing term and the differential rotation influence the system.

Finally, if $\alpha = 1/2$, as suggested by Skumanich’s law [11], we can write

$$T_{nm}(t) = \frac{g_{nm}\Omega(t)}{t_{sd}/2t_{ES}^{nm} - 1/2} + t^{-t_{sd}/2t_{ES}^{nm}} \left[T_{0,nm} - \frac{g_{nm}\Omega_0}{t_{sd}/2t_{ES}^{nm} - 1/2} t_0^{t_{sd}/2t_{ES}^{nm}} \right], \quad (78)$$

with g_{nm} defined as

$$g_{nm} \equiv \frac{G_{nm}(t)t}{\Omega(t)}, \quad (79)$$

which is independent of time. In this case, t_{sd}/t_{ES}^{nm} is also independent of time as seen from (77), so the initial ratio of these two timescales determines the behaviour. The initial conditions decay on a timescale of $t_{sd}/2t_{ES}^{nm}$ for each mode. Since

$$t_{ES}^{nm} < t_{ES} \forall n, m, \quad (80)$$

then if

$$\frac{t_{sd}}{t_{ES}} \gg 1, \quad (81)$$

we also have

$$\frac{t_{sd}}{t_{ES}^{nm}} \gg 1 \forall \mu_{nm}, \lambda_n. \quad (82)$$

In other words, if $t_{sd} \gg t_{ES}$ then the time dependent solution decays to our previous ‘steady state’ solution, which is equivalent to

$$T_{nm}(t) = \frac{g_{nm}\Omega(t)}{t_{sd}/2t_{ES}^{nm}}. \quad (83)$$

If, on the other hand, $t_{sd}/t_{ES} \ll 1$ then there are two classes of modes: small-scale modes for which $t_{sd}/t_{ES}^{nm} > 1$ and large-scale modes for which $t_{sd}/t_{ES}^{nm} < 1$. When $t_{sd}/t_{ES}^{nm} > 1$, (78) shows that the initial conditions decay faster than the global forcing term, so that after some time these small-scale modes are governed only by the global forcing and the differential rotation. However, when $t_{sd}/t_{ES}^{nm} < 1$, the global forcing term in (78) decays faster than the initial conditions, so the initial conditions continue to influence the system even after a long time and the ‘steady state’ solution found in 2.2.2 is not as relevant.

Up to this point in our model, the radiative interior has played no role in the angular momentum transport, and shear propagates to the centre of the star. However, in the magnetized model of a stellar interior by [6] (see Figure 3), the shear only propagates through the tachocline as far as the tachopause, and there interacts with the magnetic field which keeps the interior in solid body rotation. We now want to incorporate the angular momentum transport between the tachocline and the interior into our model, to find out how spin down affects the rotation of the interior below the tachocline. We return to our cylindrical model of a stellar interior, where the porous medium at the top of the cylinder still corresponds to the convection zone, where the ‘bulk of the fluid’ corresponds to the stably stratified, non-magnetic tachocline only, and where we now add an additional ‘ingredient’ to model the interior.

3 Unstratified Ekman layer spin down

In the model by [6], angular momentum transport between the tachocline and the interior is caused by magnetic stresses within a thin boundary layer (the tachopause). There, the primordial magnetic field interacts with the flows in the tachocline, and helps transmit the spin-down information from the outer layers downward. Since magnetic torques are

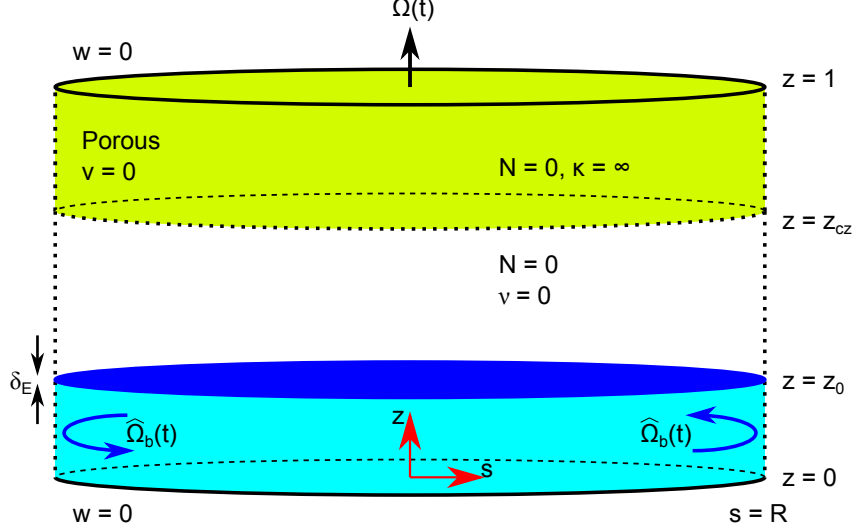


Figure 7: A diagram of the adjusted cylindrical model set up. The region from $z = 0$ to $z = z_0$ (light blue) is a solid base which is free to rotate at angular velocity $\hat{\Omega}_b(t)$ in the rotating frame. The region from $z = z_0$ to $z = z_{cz}$ is filled with unstratified fluid, and the viscosity ν is negligible except for near the base. There is a thin boundary layer above the base, with thickness δ_E , where the viscous forces become dominant. The region from $z = z_{cz}$ to $z = 1$ (yellow) is filled with a porous medium which has zero angular velocity in the rotating frame.

intrinsically nonlinear, to aid our conceptual understanding, we first consider the case of viscous torques.

Our model set up is very similar to the model investigated in the previous section. The bottom of the cylinder now hosts a solid inner cylinder of radius R and thickness z_0 , see Figure 7, shaped like a hockey-puck. The density of the ‘hockey-puck’ is same as the density of the fluid, and it is free to rotate at an angular velocity $\hat{\Omega}_b(t)$ in the rotating frame. Our goal is to find $\hat{\Omega}_b(t)$.

We consider as a first simplified system the unstratified case, where the bulk (from $z = z_0$ to $z = z_{cz}$) is filled with unstratified fluid. For simplicity we assume that there is no differential rotation of the porous medium, although the differential rotation can be included without altering the steps of the calculation significantly. The torque between the fluid and the hockey-puck is communicated through a thin (Ekman) boundary layer of thickness δ_E at $z = z_0$. In this layer viscosity becomes important, and we can no longer neglect the viscous terms in the momentum equation.

In the bulk ($z_0 < z < z_{cz}$), we look for a ‘steady state’ solution as in section 2.2.2, which is now known to be a valid approximate solution as long as the spin down rate is slow enough. For $z > z_0 + \delta_E$, the equations of motion are the same as in section 2.2.2, setting $\hat{T} = 0$ since the bulk is unstratified. Equation (20) becomes

$$\frac{\partial \hat{P}}{\partial z} = 0 \Rightarrow \hat{P} = \hat{P}_0(s) \Rightarrow v = v_0(s), \quad (84)$$

and, as in the previous ‘steady state’ solution,

$$u = -\frac{\dot{\Omega}}{2\Omega}s \Rightarrow w = w_0(s) + \frac{\dot{\Omega}}{\Omega}(z - (z_0 + \delta_E)), \quad (85)$$

where $w_0(s)$ is the vertical velocity at the top of the viscous boundary layer (at $z = z_0 + \delta_E$).

To find an evolution equation for $\hat{\Omega}_b(t)$, we begin by writing the complete angular momentum conservation equation as

$$\frac{\partial}{\partial t}(sv + s^2\Omega) + \nabla \cdot (\mathbf{u}\Omega s^2 + \text{viscous terms}) = 0. \quad (86)$$

Assuming that the tachocline (i.e. the bulk) is in ‘steady’ state while retaining the time dependence of the interior implies that the thermal spreading across the bulk is faster than angular momentum transport across the interior, which we will check a posteriori.

We then integrate (86) over the volume of the hockey-puck and the boundary layer. The viscous terms are negligible at the top of the boundary layer, and we assume that they are also negligible at the side wall in the boundary layer:

$$\int_0^{2\pi} \int_0^{z_0+\delta_E} \int_0^R \frac{\partial}{\partial t}(sv + s^2\Omega) + \nabla \cdot (\mathbf{u}\Omega s^2 + \text{viscous terms}) dV = 0, \quad (87)$$

$$\Rightarrow z_0 \frac{R^4}{4} \left(\frac{d\hat{\Omega}_b}{dt} + \dot{\Omega} \right) + \int_0^R w_0(s) \Omega s^3 ds + R \int_{z_0}^{z_0+\delta_E} u(s=R) \Omega R^2 dz = 0, \quad (88)$$

using the fact that $\delta_E \ll z_0$ (see section 3.1).

There is no flow into the hockey-puck, so the amount of fluid going into the boundary layer through the surface $z = z_0 + \delta_E$ must be the same as the amount of fluid coming out through the side, by conservation of mass

$$2\pi \int_0^R w_0(s) s ds = -2\pi R \int_{z_0}^{z_0+\delta_E} u(s=R) dz. \quad (89)$$

Combining this with (88) gives

$$\frac{d\hat{\Omega}_b}{dt} = -\dot{\Omega} + \frac{4\Omega}{R^4 z_0} \left(R^2 \int_0^R w_0(s) s ds - \int_0^R w_0(s) s^3 ds \right). \quad (90)$$

In order to proceed, we need to determine $w_0(s)$. In order to do this, we now investigate the dynamics of the boundary layer in more detail.

3.1 Boundary layer thickness

In the boundary layer, the viscous term cannot be neglected and becomes an integral part of the momentum balance. Assuming that the boundary layer is thin, so that $\partial/\partial z \gg \partial/\partial s$, and assuming a ‘steady state’, we have

$$2\Omega \times \mathbf{u} + \dot{\Omega} \times \mathbf{r} = -\frac{1}{\rho} \nabla \hat{P} + \nu \frac{\partial^2 \mathbf{u}}{\partial z^2}. \quad (91)$$

The three components of the momentum equation (91) are

$$-2\Omega v = -\frac{1}{\rho} \frac{\partial \hat{P}}{\partial s} + \nu \frac{\partial^2 u}{\partial z^2}, \quad (92)$$

$$2\Omega u + \dot{\Omega} s = \nu \frac{\partial^2 v}{\partial z^2}, \quad (93)$$

$$0 = -\frac{1}{\rho} \frac{\partial \hat{P}}{\partial z} + \nu \frac{\partial^2 w}{\partial z^2}. \quad (94)$$

Combining these three equations with conservation of mass gives

$$-\frac{\partial v}{\partial z} = \frac{\nu^2}{4\Omega^2} \frac{\partial^5 v}{\partial z^5}. \quad (95)$$

Let $\delta_E = \sqrt{\nu/2\Omega}$ and $Z = (z - z_0)/\delta_E = O(1)$ in the boundary layer. Then

$$\frac{\partial v}{\partial Z} + \frac{\partial^5 v}{\partial Z^5} = 0 \quad (96)$$

$$\Rightarrow v = v_0(s) + \sum_{n=0}^3 b_n(s) e^{\lambda_n Z}, \quad \lambda_n = e^{(2n+1)i\pi/4}. \quad (97)$$

$v \rightarrow v_0(s)$ as $Z \rightarrow \infty$, where $v_0(s)$ is the azimuthal velocity in the bulk, so $b_3 = b_4 = 0$, and $v \in \mathbb{R}$, so $b_1 = b_2$. Finally, at $Z = 0$, which is the top of the hockey-puck, $v = s\hat{\Omega}_b(t)$. Using all this information uniquely specifies the boundary layer solution to be:

$$v(s, Z) = v_0(s) + (\hat{\Omega}_b s - v_0(s)) e^{-Z/\sqrt{2}} \cos\left(\frac{Z}{\sqrt{2}}\right). \quad (98)$$

3.2 Jump condition

The hockey-puck rotates with angular velocity $\hat{\Omega}_b(t)$ in the rotating frame, which is as yet unknown. Integrating the angular momentum equation (93) across the viscous boundary layer gives

$$\int_{z_0}^{z_0+\delta_E} s u dz + \frac{\dot{\Omega}}{2\Omega} s^2 \delta_E = \frac{\nu}{2\Omega} \left[\frac{\partial v}{\partial z} \right]_{z_0}^{z_0+\delta_E} = \frac{\nu}{2\Omega} \frac{1}{\delta_E} \left[\frac{\partial v}{\partial Z} \right]_{Z=0}^{Z \rightarrow \infty} = \frac{\delta_E}{\sqrt{2}} (\Omega_b s - v_0(s)). \quad (99)$$

Using conservation of mass and the boundary condition $w = 0$ at $z = z_0$, we find

$$\frac{1}{s} \frac{\partial}{\partial s} \int_{z_0}^{z_0+\delta_E} s u dz = - \int_{z_0}^{z_0+\delta_E} \frac{\partial w}{\partial z} dz = -w(z_0 + \delta_E) \equiv -w_0(s), \quad (100)$$

so that, combining (99) and (100),

$$w_0(s) = \frac{\dot{\Omega}}{\Omega} \delta_E - \frac{\delta_E}{\sqrt{2}} \frac{1}{s} \frac{\partial}{\partial s} (\Omega_b s^2 - s v_0(s)). \quad (101)$$

We now know the vertical velocity profile $w_0(s)$ in terms of the differential rotation $v_0(s)$ in the bulk of the fluid. The latter still remains to be determined, by matching the bulk solution to the porous medium.

The solutions in the porous medium are found exactly as in section 2, and we consider the case where $v_{cz}(s) = 0$,

$$w = \sum_n J_0\left(\lambda_n \frac{s}{R}\right) B_n \sinh\left[\lambda_n \left(\frac{z}{R} - \frac{1}{R}\right)\right], \quad (102)$$

$$u = \sum_n \frac{dJ_0(\lambda_n \frac{s}{R})}{ds} \frac{B_n R}{\lambda_n} \cosh\left[\lambda_n \left(\frac{z}{R} - \frac{1}{R}\right)\right], \quad (103)$$

$$\frac{1}{\rho} \hat{P} = \sum_n J_0\left(\lambda_n \frac{s}{R}\right) \left[-\frac{B_n R}{\tau \lambda_n} \cosh\left[\lambda_n \left(\frac{z}{R} - \frac{1}{R}\right)\right] \right]. \quad (104)$$

We can then match w and \hat{P} at $z = z_{cz}$ to find the solutions for $w_0(s)$, $\hat{P}_0(s)$ and $v_0(s)$ in the bulk:

$$\frac{1}{\rho} \hat{P}_0(s) = \sum_n J_0\left(\lambda_n \frac{s}{R}\right) \left[-\frac{B_n R}{\tau \lambda_n} \cosh\left[\lambda_n \left(\frac{z_{cz}}{R} - \frac{1}{R}\right)\right] \right] \quad (105)$$

$$\Rightarrow v_0(s) = \frac{1}{2\Omega} \sum_n \frac{dJ_0(\lambda_n \frac{s}{R})}{ds} \left[-\frac{B_n R}{\tau \lambda_n} \cosh\left[\lambda_n \left(\frac{z_{cz}}{R} - \frac{1}{R}\right)\right] \right], \quad (106)$$

$$\sum_n J_0\left(\lambda_n \frac{s}{R}\right) B_n \sinh\left[\lambda_n \left(\frac{z_{cz}}{R} - \frac{1}{R}\right)\right] = w_0(s) + \frac{\dot{\Omega}}{\Omega} (z_{cz} - (z_0 + \delta_E)), \quad (107)$$

from (85). Combining these equations with the jump condition (101) gives an equation for $v_0(s)$,

$$v_0(s) = \sum_n \frac{2J_1(\lambda_n \frac{s}{R})}{\lambda_n J_1(\lambda_n)} \left[\frac{2\delta_E \hat{\Omega}_b - \sqrt{2} \frac{\dot{\Omega}}{\Omega} (z_{cz} - z_0)}{2\sqrt{2}\Omega\tau \tanh \lambda_n (\frac{1}{R} - \frac{z_{cz}}{R}) + \frac{\delta_E}{R} \lambda_n} \right], \quad (108)$$

which is similar to (47) in section 2, with no stratification ($N = 0$), but now with two extra terms which depend on δ_E and $\hat{\Omega}_b$. Using (108) in (101) to find $w_0(s)$, (90) finally yields the desired evolution equation for $\hat{\Omega}_b(t)$:

$$\frac{d\hat{\Omega}_b}{dt} = -\dot{\Omega} \frac{z_{cz}}{z_0} - 32 \sum_n \frac{1}{\lambda_n^4} \left[\frac{-\dot{\Omega} \left(\frac{z_{cz}}{z_0} - 1\right) + \sqrt{2} \delta_E \frac{\hat{\Omega}_b \Omega}{z_0}}{1 + \frac{\delta_E \lambda_n}{2\sqrt{2}R\Omega\tau \tanh \lambda_n (\frac{1}{R} - \frac{z_{cz}}{R})}} \right], \quad (109)$$

Note that if there is no viscous boundary layer, so $\delta_E = 0$, it can be shown using the identity $32 \sum_n 1/\lambda_n^4 = 1$ that $d\hat{\Omega}_b/dt = -\dot{\Omega}$. In other words, the hockey-puck continues to rotate at its initial angular velocity as the frame slows down, since the fluid cannot exert any torque on it. However, if $\delta_E > 0$ then the evolution of $\hat{\Omega}_b$ is affected by the boundary layer. Figure 8 shows a plot of $\hat{\Omega}_b/\Omega$ with time for arbitrary parameters, starting with initial condition $\hat{\Omega}_b(t_0) = 0$ and assuming that the frame is spinning down as $\Omega(t) = \Omega_0 \sqrt{t_0/t}$. The ‘steady’ solution, where $d\hat{\Omega}_b/dt$ is neglected, is also plotted. We see that $\hat{\Omega}_b$ relaxes to the ‘steady’ solution on the Ekman timescale across the thickness of the hockey-puck,

$$t_\nu = \frac{z_0}{\sqrt{\nu\Omega}}. \quad (110)$$

This is consistent with assuming a ‘steady’ state for both the hockey-puck and the bulk, so in fact we did not need to consider the time-dependence of the interior in (86)-(88). The

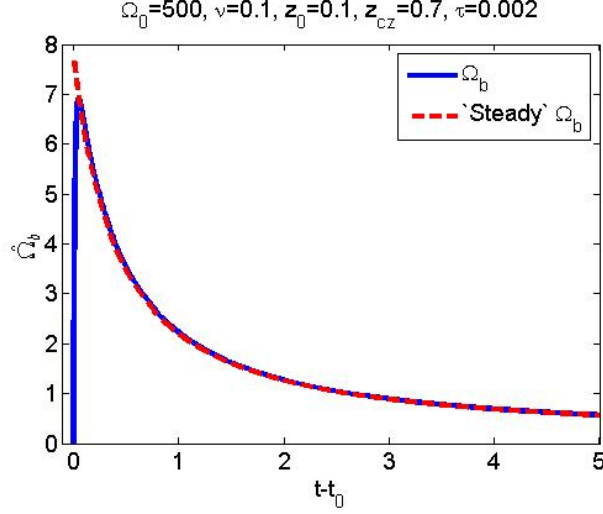


Figure 8: A plot of $\hat{\Omega}_b$ with time (blue solid line) and the corresponding ‘steady’ solution (red dashed line), for arbitrary parameters, with initial condition $\hat{\Omega}_b(t_0) = 0$ and with a spin-down rate of the frame $\Omega(t) = \Omega_0 \sqrt{t_0/t}$. $\hat{\Omega}_b$ relaxes to the ‘steady’ state on the Ekman timescale.

‘steady’ solution decays with time so that the rotation rate of the base (relative to that of the frame) decreases with time as $\Omega(t)$ decreases. In other words, the lag between the two, given by $\hat{\Omega}_b$, also decreases over time.

4 Unstratified magnetic spin down

4.1 Solution in the tachocline and tachopause

In a solar-type star, we expect that the torque acting on the interior is due to magnetic stresses rather than viscous friction. We now consider a similar set up to that of section 3 where the hockey-puck is replaced by a fluid held in rigid rotation by a confined large-scale magnetic field, in the region from $z = 0$ to $z = z_0$, and where the Ekman boundary layer is replaced by a magnetic ‘tachopause’ at $z = z_0$. Assuming that the magnetic field does not exert a torque at the side wall of the cylinder in the boundary layer and that the thickness of the magnetic boundary layer δ is small compared with $z_{cz} - z_0$ or z_0 , the evolution equation for $\hat{\Omega}_b$ is the same as with the viscous boundary layer (90). The difference between the magnetic and the viscous cases comes from the angular momentum transport across the boundary layer, which we now discuss.

Wood *et al.* [15] studied a system very similar to the Gough and McIntyre model [6], but in Cartesian coordinates. They found that the thickness of the magnetic boundary layer is given by

$$\delta = \sqrt{\frac{2\pi\rho\eta\Omega R^2}{B_0^2}}, \quad (111)$$

assuming a horizontal magnetic field with strength B_0 at the bottom of the magnetic bound-

ary layer. They also found a jump condition relating the vertical and ‘azimuthal’ velocities in the tachocline. This jump condition takes exactly the same form as the Ekman jump condition in Cartesian coordinates, namely:

$$w_0(x) = \frac{1}{\sqrt{2}} \delta_E \frac{\partial v_0(x)}{\partial x} \text{ (Ekman)} \quad \text{and} \quad w_0(x) = \frac{\pi}{4} \delta \frac{\partial v_0(x)}{\partial x} \text{ (magnetic)}, \quad (112)$$

where x is the latitudinal direction and v_0 is the azimuthal velocity, and where $\dot{\Omega} = \hat{\Omega}_b = 0$ in the Wood *et al.* model. Hence, by analogy with the way the Cartesian Ekman jump condition can be transformed into cylindrical coordinates, it can be shown that, in cylindrical coordinates, the tachopause jump conditions including the effect of spin-down are:

$$w_0(s) = \frac{\dot{\Omega}}{\Omega} \delta + \frac{\pi}{4} \delta \frac{1}{s} \frac{\partial}{\partial s} \left(s v_0(s) - \hat{\Omega}_b s^2 \right). \quad (113)$$

From section 3, we have the solutions in the bulk and in the porous medium, and using this jump condition, we now find

$$v_0(s) = \sum_n \frac{2J_1(\lambda_n \frac{s}{R})}{\lambda_n J_1(\lambda_n)} \left[\frac{2\pi\delta\hat{\Omega}_b - 4\frac{\dot{\Omega}}{\Omega}(z_{cz} - z_0)}{8\Omega\tau \tanh \lambda_n (\frac{1}{R} - \frac{z_{cz}}{R}) + \pi \frac{\delta}{R} \lambda_n} \right], \quad (114)$$

which, as in the case with a viscous boundary layer, is similar to (47) with $N = 0$, but now with two extra terms which depend on δ and $\hat{\Omega}_b$. Equation (90) becomes

$$\frac{d\hat{\Omega}_b}{dt} = -\dot{\Omega} \frac{z_{cz}}{z_0} - 32 \sum_n \frac{1}{\lambda_n^4} \left[\frac{-\dot{\Omega} \left(\frac{z_{cz}}{z_0} - 1 \right) + \frac{\pi}{2} \delta \frac{\hat{\Omega}_b \Omega}{z_0}}{1 + \frac{\pi \delta \lambda_n}{8R\Omega\tau \tanh \lambda_n (\frac{1}{R} - \frac{z_{cz}}{R})}} \right]. \quad (115)$$

This evolution equation for $\hat{\Omega}_b$ depends on δ , z_0 and B_0 . If we assume that z_0 and B_0 are known, we get δ from (111) and can then evolve $\hat{\Omega}_b(t)$ as in section 3.

4.2 Where is the tachopause?

Unfortunately, by contrast with section 3, z_0 is not actually known a priori - it results from the nonlinear interaction of the field and the downwelling flows. However, while the full solution needs fully nonlinear calculations, we can make an order of magnitude estimate using the magnetic induction equation as in [6] and [15].

The steady magnetic induction equation is, from (3),

$$0 = \nabla \times (\mathbf{u} \times \mathbf{B} - \eta \nabla \times \mathbf{B}), \quad (116)$$

where \mathbf{B} is the magnetic field and η is the magnetic diffusivity. We need the vertical velocity at the top of the magnetic boundary layer to balance the magnetic field diffusion for the magnetic field to remain confined. This implies $w \approx \eta/\delta$. We cannot choose $w_0(s) = \eta/\delta \forall s$, as the s -dependence of $w_0(s)$ is determined by the solutions above the boundary layer. Instead, we set the average of w to be η/δ , so that

$$\int_0^R s w_0(s) ds = \frac{R^2}{2} \frac{\eta}{\delta}. \quad (117)$$

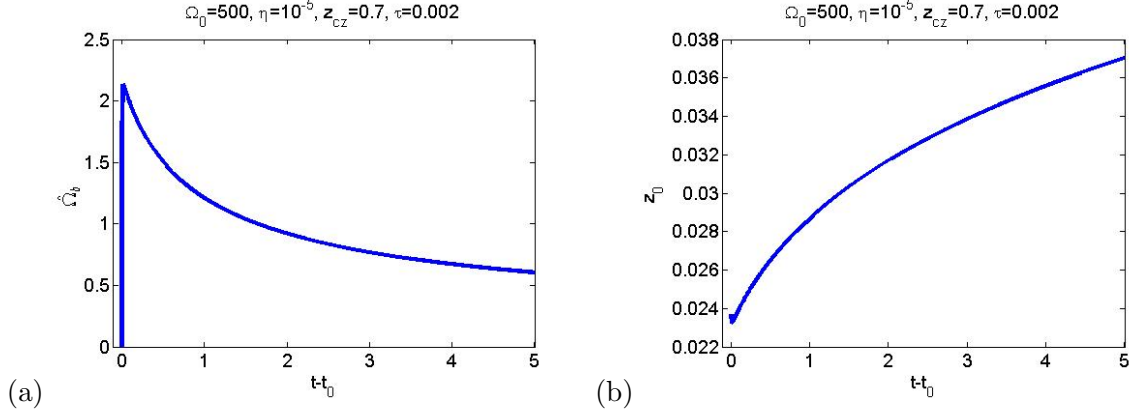


Figure 9: (a) A plot of $\hat{\Omega}_b$ with time and (b) a plot of z_0 with time, with $\rho = 1$ and $B_0^2 = 100\pi$.

Equation (113) becomes

$$\frac{\eta}{\delta} = -\frac{\dot{\Omega}}{\Omega}(z_{cz} - (z_0 + \delta)) + \sum_n \frac{32}{\lambda_n^2} \left[\frac{\dot{\Omega}(z_{cz} - z_0) - \frac{\pi}{2}\delta\hat{\Omega}_b\Omega}{8\Omega + \frac{\pi\delta\lambda_n}{R\tau \tanh \lambda_n(\frac{1}{R} - \frac{z_{cz}}{R})}} \right]. \quad (118)$$

Equations (115) and (118) are two equations for the two unknowns, $\hat{\Omega}_b$ and z_0 , so the system is now fully determined in terms of the internal field strength B_0 . Figure 9(a) shows a plot of $\hat{\Omega}_b$ with time, assuming a constant B_0 . As in Figure 8, $\hat{\Omega}_b$ initially increases rapidly from zero, as in section 3, then starts to decrease with time, so that the lag in the angular velocity between the magnetically dominated region ($z < z_0$) and the porous medium decreases over time. The corresponding depth of the magnetically dominated region, z_0 (shown in Figure 9(b)), increases with time as $\hat{\Omega}_b$ and Ω decrease. However, to find the long-time behaviour of $\hat{\Omega}_b$ and z_0 , we would also need to consider how B_0 changes with time, as this will also affect how z_0 and δ , and therefore also $\hat{\Omega}_b$, change with time.

5 Summary and future work

We have proposed a solution for the spin down of a stratified star. Although we have modelled it as a cylinder with a porous medium at the top, we now discuss our results in the context of real stellar interiors. We first looked at non-magnetic stellar radiative zones. We found that there exists a ‘steady state’ solution. As in Bretherton and Spiegel, these solutions exhibit a lag in the angular velocity between the convection zone and radiative zone below, with the latter always rotating faster than the former. If stratification is very weak, this lag is uniform with depth and agrees with the result from the spherical model found by [1], up to a geometrical factor. When the radiative zone is strongly stratified, the lag increases with depth because the thermal wind can maintain a larger vertical shear.

We have also found time-dependent solutions. The evolution of the angular momentum in the radiative zone has contributions from both transport by meridional flows, through the thermal spreading found by [13] for the propagation of differential rotation into the interior

of a star, and global angular momentum extraction by the spin down of the frame. We have found that $\Omega(t) \sim t^{-1/2}$, which is the case for solar-type stars (see [11]), is a special case for the time-dependent solution. A more rapid spin-down rate cannot be accommodated by a laminar solution, while a slower spin-down rate implies that the system can rapidly converge to the ‘steady state’ solution described above. For $\Omega \sim t^{-1/2}$, the initial conditions decay with time as a power law, rather than the exponential decay found for $\Omega(t) \sim t^{-\alpha}$ with $\alpha < 1/2$.

We then studied the spin down of an unstratified magnetic star. We assume that the radiative interior is held in rigid rotation by a large-scale magnetic field, separated by a non-magnetic tachocline. We found that the spin-down of the frame is transmitted to the magnetically dominated region due to magnetic friction in a magnetic boundary layer separating the tachocline from the interior. The lag between the convection zone and the interior decreases with time, and our solutions are consistent with a ‘steady’ state in both the bulk of the fluid and the interior.

The next step is to combine the stratified and magnetic solutions to find a solution, in our cylindrical model, for the spin down of a stratified, magnetic star. In addition, we need to model the interior magnetic field in more detail and to look at how the magnetic field decays with time, and how this affects and is affected by the depths of the tachocline and magnetic boundary layer. It would also be interesting to solve an equivalent spherical model (as in [1] but with a stratified interior) numerically, which would represent the whole star, and compare this solution to our solution for a cylinder which represents the polar regions of the star.

6 Acknowledgements

I would like to thank Pascale Garaud for her supervision on this project, and all the staff and fellows for such an inspiring and enjoyable summer.

References

- [1] F. P. BRETHERTON AND E. A. SPIEGEL, *The effect of the convection zone on solar spin-down*, The Astrophysical Journal, 153 (1968), pp. 77–80.
- [2] A. S. BRUN AND J.-P. ZAHN, *Magnetic confinement of the solar tachocline*, Astronomy and Astrophysics, 457 (2006), pp. 665–674.
- [3] J. CHRISTENSEN-DALSGAARD ET AL., *The current state of solar modeling*, Science, 272 (1996), pp. 1286–1292.
- [4] V. C. A. FERRARO, *The non-uniform rotation of the sun and its magnetic field*, Monthly Notices of the Royal Astronomical Society, 97 (1937), pp. 458–472.
- [5] P. GARAUD AND L. A. ARREGUIN, *On the penetration of meridional circulation below the solar convection zone. ii. models with convection zone, the taylor-proudman constraint, and applications to other stars*, The Astrophysical Journal, 704 (2009), pp. 1–16.

- [6] D. O. GOUGH AND M. E. MCINTYRE, *Inevitability of a magnetic field in the sun's radiative interior*, *Nature*, 394 (1998), pp. 755–757.
- [7] L. MESTEL AND N. O. WEISS, *Magnetic fields and non-uniform rotation in stellar radiative zones*, *Monthly Notices of the Royal Astronomical Society*, 226 (1987), pp. 123–135.
- [8] M. S. MIESCH, *Large-scale dynamics of the convection zone and tachocline*, *Living Reviews in Solar Physics*, 2 (2005).
- [9] J. M. PASACHOFF, V. RUSIN, H. DRUCKMULLEROVA, M. SANIGA, M. LU, C. MALAMUT, D. B. SEATON, L. GOLUB, A. J. ENGELL, S. W. HILL, AND R. LUCAS, *Structure and dynamics of the 2010 July 11 eclipse white-light corona*, *The Astrophysical Journal*, 734 (2011).
- [10] J. SCHOU ET AL., *Helioseismic studies of differential rotation in the solar envelope by the solar oscillations investigation using the Michelson Doppler imager*, *The Astrophysical Journal*, 505 (1998), pp. 390–417.
- [11] A. SKUMANICH, *Time scales for Ca II emission decay, rotational braking, and lithium depletion*, *The Astrophysical Journal*, 171 (1972), pp. 565–567.
- [12] E. A. SPIEGEL AND G. VERONIS, *On the Boussinesq approximation for a compressible fluid*, *The Astrophysical Journal*, 131 (1960), pp. 442–447.
- [13] E. A. SPIEGEL AND J.-P. ZAHN, *The solar tachocline*, *Astronomy and Astrophysics*, 265 (1992), pp. 106–114.
- [14] A. STRUGAREK, A. S. BRUN, AND J.-P. ZAHN, *Magnetic confinement of the solar tachocline: II. coupling to a convection zone*, *Astronomy and Astrophysics*, 532 (2011), p. A34.
- [15] T. S. WOOD, J. O. MCCASLIN, AND P. GARAUD, *The sun's meridional circulation and interior magnetic field*, *The Astrophysical Journal*, 738 (2011).

SLENDER SWIMMERS IN STOKES FLOW

Srikanth Toppaladoddi
Advisor: Neil J. Balmforth

October 2, 2012

Abstract

In this study, motion of slender swimmers, which propel themselves by generating travelling surface waves, is investigated. In the first approach, slender-body theory (SBT) is used to calculate the propulsion speed. The mathematical machinery used is based on the SBT by Keller & Rubinow [1]. The object considered is of arbitrary cross-section, and the surface waves considered are axisymmetric. The object is modelled using Stokeslet and source distributions along its axis. The propulsion speed is obtained by imposing the condition that the net force on the swimmer, as inertia is absent, is zero.

In the second approach, the object is assumed to be filled with a viscous incompressible fluid and its surface is assumed elastic, and the propulsion speed due to the peristaltic motion of fluid inside is calculated. Also, an improved definition of swimmer efficiency, which takes internal dissipation into account, is introduced.

1 Introduction

A swimmer is defined as “a creature or an object that moves by deforming its body in a periodic way” [2]. The way macroscopic organisms propel themselves is by using inertia of the surrounding fluid. Propulsion in the forward direction is generated due to the intermittent forces acting on the object by the surrounding fluid as a reaction to its pushing the fluid backwards [3]. The typical Reynolds number (Re), which is defined as:

$$Re \equiv \frac{F_i}{F_v} = \frac{UL}{\nu}, \quad (1)$$

where F_i and F_v are inertial and viscous forces, U is the velocity scale, L is the length scale and ν is the kinematic viscosity of the fluid, in the inertial (or Eulerian) regime is $10^2 - 10^6$ for different organisms. Swimming in the Eulerian regime can be broken into components of propulsion and drag; the former is due to some specialized organs which push the fluid backwards, thereby generating a thrust force in the opposite direction, and the latter is because of the forces encountered due to the moving object in a viscous fluid [4]. However, in the Stokes regime ($Re \approx 0$) there is no inertia, and the organisms at those small length scales have to exploit viscous stresses to generate propulsion. Typical range of Re for swimmers in this regime is $10^{-4} - 10^{-1}$.

The study of swimming microorganisms began with Taylor's study of propulsion speed induced on a transversely oscillating two-dimensional sheet in the Stokes regime [4]. Taylor showed that propulsion in a highly viscous environment is possible when an object deforms itself in a way that would generate propulsive forces in the surrounding fluid. He pointed out that separation of swimming into propulsive and drag components in the Stokes regime would lead to Stokes paradox, and that the propulsion is due to exploiting the viscous stresses due to surface deformation. Taylor's analysis has been extended by Lighthill [5] and Blake [6] to study the motion of spheres and cylinders with travelling surface waves respectively.

Stokesian swimmers (swimmers in the Stokes regime) are broadly classified into ciliates and flagellates [3]. The former set have small cilia on their surfaces, which are used for propulsion. Some of the microorganisms which fall into this category are: Paramecium (figure 1) and Opalina. The latter have flagella at the ends which rotate in a helical fashion, or oscillate in the transverse direction to generate propulsion. Spermatozoa (figure 2) and E. Coli are examples of microorganisms in this category.



Figure 1: Pictures showing paramecium. The fine cilia around the surfaces can be clearly seen. Paramecium uses these cilia to propel itself at a top speed of $500\mu m/s$.



Figure 2: Picture showing spermatozoa. Each cell has a flagellum down which the cell sends bending waves to propel itself.

2 Creeping Flow Limit ($Re \approx 0$)

The equation of motion for a viscous fluid are the Navier-Stokes equation:

$$\frac{\partial \mathbf{u}'}{\partial t'} + \mathbf{u}' \cdot \nabla' \mathbf{u}' = -\frac{1}{\rho} \nabla' P' + \nu \nabla'^2 \mathbf{u}', \quad (2)$$

$$\nabla \cdot \mathbf{u}' = 0. \quad (3)$$

Here, $\mathbf{u}' \equiv \mathbf{u}'(\mathbf{x}', t)$ is the velocity field, $P' \equiv P'(\mathbf{x}', t)$ is the pressure field, ρ is the density of the fluid, and ν is the kinematic viscosity of the fluid. Equation 3 results when the flow is assumed incompressible.

In the Stokes regime, the pressure has to be scaled with viscosity, so that the viscous term is balanced by it. To non-dimensionalize equation 2, the following scales are used: $\mathbf{u} = \mathbf{u}'/U$, $\mathbf{x} = \mathbf{x}'/L$, and $P = P'/(μU/L)$, where U and L are some velocity and length scales. Once equation 2 is scaled this way, the resulting equation is:

$$Re \left(\frac{\partial \mathbf{u}}{\partial t} + \mathbf{u} \cdot \nabla \mathbf{u} \right) = -\nabla P + \nabla^2 \mathbf{u}. \quad (4)$$

Substituting $Re = 0$ gives the Stokes equations:

$$\nabla P = \nabla^2 \mathbf{u}; \quad \nabla \cdot \mathbf{u} = 0. \quad (5)$$

Equations 5 are linear, and remain unchanged if the following transformations are effected: $\mathbf{u} \rightarrow -\mathbf{u}$ and $\mathbf{x} \rightarrow -\mathbf{x}$. This implies that the equations are reversible if the velocity and displacement vectors are reversed. One more implication of the linearity is that flow depends instantaneously on the boundary conditions. If the boundary ceases to move then there would be no fluid motion at all. This is a consequence of inertia being absent from the system. This places a strong constraint on the Stokesian swimmers as to how they can deform their bodies to generate propulsive forces.

Purcell summed these effects in his famous scallop theorem, which states that an object in the $Re \approx 0$ regime cannot swim by executing strokes that are “reciprocal” in time [7]. A good example of such a creature is a scallop, which is a swimmer in the Eulerian regime, but has only one degree of freedom. It generates propulsion by quickly closing its shell, thereby pushing the fluid out through its hinge at a high speed, resulting in thrust. Re for this motion is $O(10^5)$ [3]. It then opens its shell very slowly, thereby transferring negligible momentum to the fluid. In the Stokes regime this mechanism would not work, as there is no time in the equations. The scallop’s net displacement would be zero [3].

3 Motivation

As mentioned in the previous section, the propulsion mechanisms of ciliates and flagellates have been well studied for the past 62 years; but there are certain organisms like *Synechococcus* (a type of Cyanobacteria) which neither possess cilia nor flagella on their surface, yet they manage to move at around $25\mu m/s$ [8]. Ehlers *et al.* [8] studied the motion of this bacterium and suspected that the motion might be due to travelling surface waves. However, the bacterium was modelled as a sphere, though it has an aspect ratio, $\epsilon = a/L$, where a is

the diameter and L is the length of the bacterium, $\epsilon < 1$. These bacteria are abundant in the oceans and are a primary source of nutrients to the organisms lying above them in the food chain [9]. Using slender-body theory to find the propulsion speed, so as to take the small aspect ratio into account, is one of the aims of this study.



Figure 3: Synechococcus, a type of Cyanobacteria. It neither has cilia nor flagella to propel itself, and is suspected to use travelling surface waves [8].

Collective motion of microorganisms has been studied in various contexts, and recently it has been speculated that these organisms might be involved in the large scale mixing of oceans – called biogenic mixing of ocean [10]. Hence, a study of the motion of individual cells, which can be used to construct a continuum model for this species, becomes important.

4 Slender-Body Theory

Slender-body theory was developed to exploit the small aspect ratio of objects in calculating the disturbance flow field set up by them in the Stokes regime ($Re \approx 0$). SBT has been able to resolve the Stokes paradox for the case of cylinder, where the governing equations in the two-dimensional form have a logarithmic singularity at infinity. The scale dependence of drag on the cylinder on the aspect ratio can be found using SBT.

In the following analysis, velocities have been scaled by the travelling surface wave speed (c), distances have been scaled with the length of the slender body (L), and time by L/c .

The following are the different regions around the slender object, where different equations are solved:

- **Inner region:** This is the region where the distance from the cylinder, ρ , is such that $\rho \ll L$. One would sense the object to be two-dimensional in this limit, so the governing equation for the fluid flow would be the two-dimensional Stokes equations. The object is assumed to move only along its axis, which is taken to be the z -axis. The velocity field set up due to this can be written down as:

$$\mathbf{u}_{inner}(\mathbf{x}) \sim \mathbf{k}\beta(z) \log\left(\frac{\rho}{a}\right) + \mathbf{e}_r \frac{1}{2\rho} \frac{\partial a^2}{\partial t}, \quad (6)$$

where $\beta(z)$ is some function of z and $a(z, t)$ is the radius of the object. $\beta(z)$ is unknown, and has to be found by matching this solution to the outer solution.

- **Outer region:** In this limit, $|\mathbf{r}| \gg a$. The flow senses the three-dimensional body. However, owing to the small aspect ratio, the object appears to be a singular line from far, and hence can be modelled using singular distributions of force and source densities. The velocity field in this region can be written as:

$$\mathbf{u}_{outer}(\mathbf{x}) = \mathbf{W} + \int_0^1 \left(\frac{\alpha \mathbf{k}}{R} + \frac{\mathbf{R} \mathbf{R} \cdot \mathbf{k} \alpha}{R^3} + \frac{\delta \mathbf{R}}{R^3} \right), \quad (7)$$

where $\alpha(z)\mathbf{k}$ is the Stokeslet distribution, and $\delta(z)$ is the source distribution along the slender body, \mathbf{W} is the far-field velocity of the fluid, and $\mathbf{R} = \mathbf{R}_0 + (z - z')\mathbf{k}$ is the position vector of the point under consideration from the point z' on the centre-line of the object. $\alpha(z)$ is the singular force distribution and $\delta(z)$ is the singular source distribution. The velocity field due to these distributions automatically satisfies the far-field boundary condition of $\mathbf{u}(\mathbf{x}) \rightarrow \mathbf{W}$ as $|\mathbf{x}| \rightarrow \infty$. Both $\alpha(z)$ and $\delta(z)$ are unknown, and have to be found by matching this solution to the inner solution.

- **Matching region** In this region, both the inner and outer solutions are valid. The unknown terms in both these velocity fields are obtained by equating the two velocity fields in the following limits:

$$\lim_{\rho \rightarrow \infty} \mathbf{u}_{inner}(\mathbf{x}) = \lim_{R_0 \rightarrow 0} \mathbf{u}_{outer}(\mathbf{x}). \quad (8)$$

Both sides of equation 8 have singularities (logarithmic and algebraic), which balance each other.

4.1 Evaluation of the Outer Velocity Field

The outer velocity field is partially evaluated to separate out the singularities and to explicitly find their forms. Guided by our knowledge of the inner velocity field we should have $\log(R_0)$ and $1/R_0$ singularities hidden in the $\mathbf{u}_{outer}(\mathbf{x})$ term too. To do this we separate the right hand side (RHS) of equation 7 as in the following:

$$\begin{aligned} u_{z,outer}(\mathbf{x}) = & W + \int_0^1 \frac{\alpha(z') - \alpha(z)}{R} dz' + \int_0^1 \frac{\alpha(z') - \alpha(z)}{R^3} (z - z')^2 dz' \\ & + \int_0^1 \frac{\delta(z') - \delta(z) - \delta_z(z)(z' - z)}{R^3} (z - z') dz' + \int_0^1 \frac{\alpha(z)}{R} dz' \\ & + \int_0^1 \frac{\alpha(z)}{R^3} (z - z')^2 dz + \int_0^1 \frac{\delta(z) + \delta_z(z)(z' - z)}{R^3} (z - z') dz'. \end{aligned} \quad (9)$$

Except for the last three integrals in equation 9 the remaining integrals are well behaved. One can take the limit of $R_0 \rightarrow 0$ in the regular integrals, which on simplification give

$$\begin{aligned}
u_{z,outer}(\mathbf{x}) = & W + 2 \int_0^1 \frac{\alpha(z') - \alpha(z)}{|z - z'|} dz' + \int_0^1 \frac{\delta(z') - \delta(z) - \delta_z(z)(z' - z)}{|z - z'|(z - z')} dz' \\
& + 2 \int_0^1 \frac{\alpha(z)}{R} dz' + \int_0^1 \frac{\delta(z) + \delta_z(z)(z' - z)}{R^3} dz'.
\end{aligned} \tag{10}$$

The singular integrals can be further evaluated by substituting $(z' - z) = R_0 \tan \theta$, and these, after some algebra and further simplification, give the following:

$$\int_0^1 \frac{\alpha(z)}{R} dz' = \alpha(z) \{-2 \log(R_0) + \alpha(z) \log[4z(1 - z)]\}; \tag{11}$$

$$\int_0^1 \frac{\alpha(z)}{R} (z - z')^2 dz' = \alpha(z) \{-2 \log(R_0) + \alpha(z) \log[4z(1 - z)] - 2\}; \tag{12}$$

and,

$$\int_0^1 \frac{\delta(z) + \delta_z(z)(z' - z)}{R^3} (z - z') dz' = \delta(z) \frac{2z - 1}{z(1 - z)} + \delta_z(z) \{2 \log(R_0) - \log[4z(1 - z)] + 2\}. \tag{13}$$

Combining equations 10, 11, 12 and 13 and equating it to the z-component of the inner velocity field, we get

$$\begin{aligned}
\beta(z) \log\left(\frac{\rho}{a}\right) = & W + 2 \int_0^1 \frac{\alpha(z') - \alpha(z)}{|z - z'|} dz' + \int_0^1 \frac{\delta(z') - \delta(z) - \delta_z(z)(z' - z)}{|z - z'|(z - z')} dz' \\
& - 4\alpha(z) \log(R_0) + 2\alpha(z) \log[4z(1 - z)] + \delta(z) \frac{1 - 2z}{z(1 - z)} - 2\alpha(z) \\
& + 2\delta_z(z) \log(R_0) - \delta_z(z) \log[4z(1 - z)] + 2\delta_z(z).
\end{aligned}$$

Equating the terms having the logarithmic singularity gives:

$$\beta(z) = -4\alpha(z) + 2\delta_z(z);$$

and the remaining terms give an integral equation for $\alpha(z)$:

$$\begin{aligned}
\alpha(z) = & \frac{\delta_z(z)}{2} + \frac{1}{4 \log a} \left\{ W + 2 \int_0^1 \frac{\alpha(z') - \alpha(z)}{|z - z'|} dz' + \right. \\
& \int_0^1 \frac{\delta(z') - \delta(z) - \delta_z(z)(z' - z)}{|z - z'|(z - z')} dz' + 2\alpha(z) \log[4z(1 - z)] \\
& \left. + \delta(z) \frac{2z - 1}{z(1 - z)} + \delta_z(z) \{2 - \log[4z(1 - z)]\} \right\}.
\end{aligned} \tag{14}$$

Carrying out a similar analysis for the integral in the radial direction gives:

$$\delta = \frac{1}{4} \frac{\partial a(z, t)^2}{\partial t}. \tag{15}$$

The integral equation for $\alpha(z)$ can be solved iteratively, as done by Keller & Rubinow or by using asymptotic series for α and W in powers of $1/\log(\epsilon)$, where $\epsilon = A/L$ is the aspect ratio, which according to the slender body approximation is $\epsilon \ll 1$. We choose to solve the integral equation using the latter method. From 15, $\delta \sim \epsilon^2$. So, the leading order terms for α and W are $\sim \epsilon^2$. Canceling this common factor from equation 14, and using the following asymptotic series:

$$\alpha = \alpha_0 + \frac{\alpha_1}{\log \epsilon} + \frac{\alpha_2}{(\log \epsilon)^2} + O\left[\frac{1}{(\log \epsilon)^3}\right]$$

$$W = W_0 + \frac{W_1}{\log \epsilon} + \frac{W_2}{(\log \epsilon)^2} + O\left[\frac{1}{(\log \epsilon)^3}\right]$$

in the integral equation 14, and equating terms of the same order we get:

- $O(1)$

$$\alpha_0 = \frac{\Delta_z}{2},$$

where $\Delta_z = \delta_z/\epsilon^2$. Provided $a(z, t)$ vanishes at the ends, the requirement that the force on the object at this order vanishes is automatically satisfied, i.e., $\int_0^1 \alpha_0 dz = 0$.

- $O(1/\log \epsilon)$

$$\alpha_1 = \frac{W_0}{4} + \frac{\alpha_0}{2} + \frac{1}{2} \int_0^1 \frac{\alpha(z') - \alpha(z)}{|z - z'|} dz' + \frac{1}{4} \int_0^1 \frac{\Delta(z') - \Delta(z) - \Delta_z(z)(z' - z)}{|z - z'|(z - z')} dz' + \Delta(z) \frac{2z - 1}{z(1 - z)}.$$

Imposing the same condition, i.e., $\int_0^1 \alpha_1 dz = 0$, we find the swimming velocity at the leading order to be:

$$W_0 = -2 \int_0^1 \alpha_0 dz - 2 \int_0^1 \int_0^1 \frac{\alpha(z') - \alpha(z)}{|z - z'|} dz' dz$$

$$- \int_0^1 \int_0^1 \frac{\Delta(z') - \Delta(z) - \Delta_z(z)(z' - z)}{|z - z'|(z - z')} dz' dz - \int_0^1 \Delta(z) \frac{2z - 1}{z(1 - z)} dz$$

However, after some calculation, it turns out the speed at this order is zero. So, the speed at the next order has to be considered.

- $O(1/(\log \epsilon)^2)$

$$\alpha_2 = -\frac{W_0}{8} \log A^2 - \frac{1}{4} \int_0^1 \frac{\alpha(z') - \alpha(z)}{|z - z'|} \log A^2 dz'$$

$$- \frac{1}{8} \int_0^1 \frac{(\Delta(z') - \Delta(z) - \Delta_z(z)(z' - z))}{|z - z'|(z - z')} \log A^2 dz' - \frac{1}{4} \alpha_0 \log A^2$$

After imposing the condition $\int_0^1 \alpha_2 = 0$, and some algebra, we obtain the general form of the propulsion speed to be:

$$W_1 = -\frac{1}{8} \int_0^1 \frac{\partial^2 A^2}{\partial t \partial z} \log A^2 dz. \quad (16)$$

Equation 16 is the general form of the propulsion speed for a slender body with an arbitrary cross-section. Taking the time average of this equation gives:

$$W_1 = \frac{1}{8} \frac{k}{2\pi} \int_0^1 \int_0^{2\pi/k} \frac{\partial A^2}{\partial z} \frac{1}{A^2} \frac{\partial A^2}{\partial t} dt dz. \quad (17)$$

The general form of the time-averaged propulsion speed of a slender swimmer at the leading order is 17. One needs the information about the way the swimmer is deforming its surface to determine its speed, i.e., the form of the travelling surface waves. Two models are considered in the next section, which lead to propulsion speeds specific to the models of surface deformation considered.

5 Models for Surface Deformation

5.1 Model - 1

Assuming the surface deforms as: $A^2 = f(z)^2 [1 + \theta \sin(kz - kt)]$, and using this in equation 16 gives the propulsion speed as:

$$W = \frac{\epsilon^2}{\log 1/\epsilon} \frac{k^2}{8} S(\theta) \int_0^1 f(z)^2 dz, \quad (18)$$

where $S(\theta) = [1 - (1 - \theta^2)^{1/2}] \approx \theta^2 \left(\frac{1}{2} + \frac{\theta^2}{8} + \dots \right)$, and $f(z)$ represents the undeformed radius of the object. A schematic of the model for $f(z)^2 = 4z(1 - z)$ is shown in figure 4.

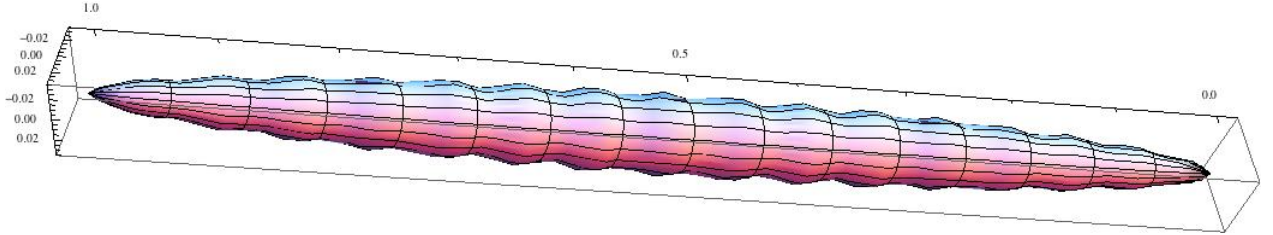


Figure 4: A schematic for model-1, which is $A^2 = f(z)^2 [1 + \theta \sin(kz - kt)]$, where $f(z)^2 = 4z(1 - z)$.

At the leading order, the solution obtained resembles one obtained by Taylor [4]. To test the correctness of the solution, we consider the solution obtained by Setter *et al.* [12] for the case of an infinite cylinder moving due to travelling surface waves. Propulsion speed in that case is:

$$W_{Setter} = -\frac{k^2 \epsilon^2 (\theta/2)^2}{2} \frac{\beta [K_0(\beta)^2 - K_1(\beta)^2]}{\beta K_1(\beta)^2 - 2K_1(\beta)K_0(\beta) - \beta K_0(\beta)^2},$$

where $\beta = ka$ is their non-dimensional radius, $K_0(\beta)$ and $K_1(\beta)$ are modified Bessel functions of second kind of order zero and one respectively. In the limit $\beta \rightarrow 0$, the above solution reduces to:

$$W_{Setter} = \frac{k^2 \epsilon^2 \theta^2}{16 \log(\beta)},$$

which is exactly what we get at the leading order when we substitute $f(z) = 1$ in equation 18.

5.2 Model-2

If one considers the peristaltic motion of fluid inside the organism, assuming that it is completely filled with a viscous incompressible fluid, then model-1 would not be suitable as it does not conserve volume. Hence, a second model for surface area, which conserves volume and vanishes at the ends, is introduced. It is given by:

$$A^2 = \frac{\partial}{\partial z} \left[2z^2 \left(1 - \frac{2z}{3} \right) + 4\theta z^2(1-z)^2 \cos(kz - kt) \right]. \quad (19)$$

The undeformed object is a prolate spheroid, which is $f(z)^2 = 4z(1-z)$ in this case. A schematic of the model is shown in 5.

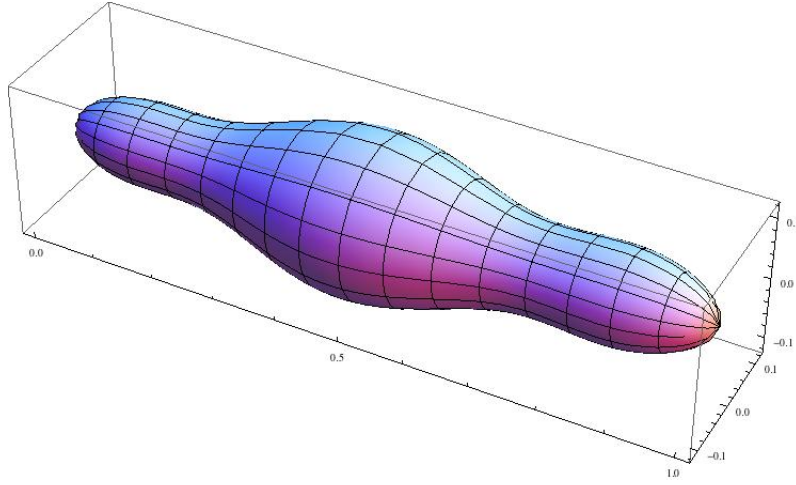


Figure 5: A schematic for model-2, which is $A^2 = \frac{\partial}{\partial z} \left[2z^2 \left(1 - \frac{2z}{3} \right) + 4\theta z^2(1-z)^2 \cos(kz - kt) \right]$.

Using equation 19 in expression 17, we get the propulsion speed as:

$$W = \frac{16k^2\theta^2\epsilon^2}{\log 1/\epsilon} \frac{1}{2\pi} \int_0^1 \int_0^{2\pi} \frac{2G'^2 \sin^2 \phi - G \cos^2 \phi (G'' - k^2 G)}{F + 4\theta (G' \cos \phi - Gk \sin \phi)} d\phi dz, \quad (20)$$

where $F = 4z(1-z)$, $G = z^2(1-z)^2$ and the primes denote the derivatives. Solving equation 20 for $\epsilon = 0.2$ and $\theta = 0.1$ for $1 \leq k \leq 20$, we get the propulsion speed as shown in figure 6. It can be shown by curve fitting that for this model $W \sim k^3$.

This model will be used when we re-define efficiency based on internal dissipation.

6 Efficiency

Efficiency of swimmers can be calculated based on the power input to the swimmer by the surrounding fluid, and energy lost due to drag forces during its motion [13]. The calculations

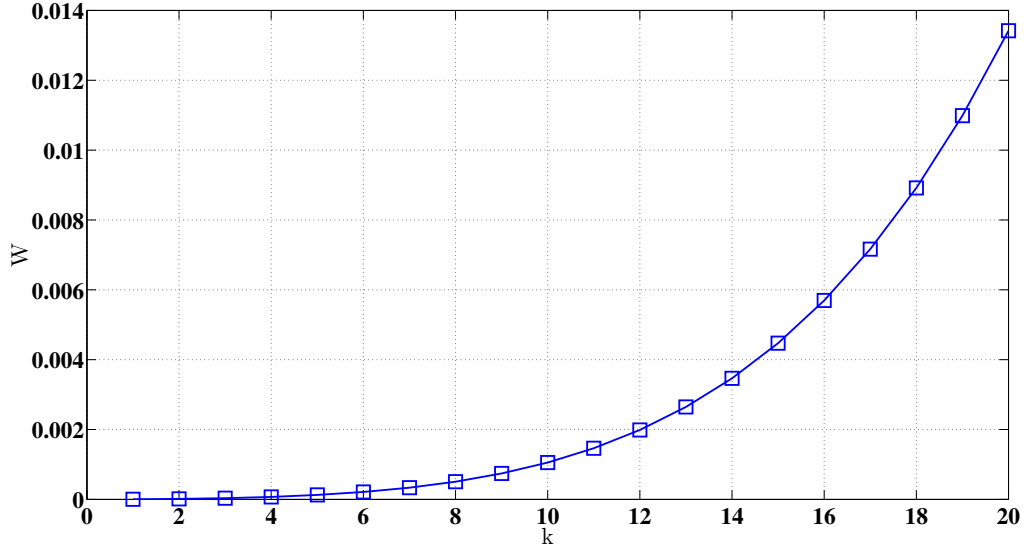


Figure 6: W vs. k for $\epsilon = 0.2$ and $\theta = 0.1$. From this model, $W \sim k^3$.

in this section are for model-1 only, and it will be shown in the next section that when one considers the flow inside the organism, the energy spent in moving the fluid inside is far greater than the energy input outside, and hence it should be taken into account – at least when considering slender swimmers.

From SBT, the velocity field in the inner region can be written as:

$$\mathbf{u} = \beta(z) \log\left(\frac{\rho}{a}\right) \mathbf{k} + \frac{1}{2\rho} \frac{\partial a^2}{\partial t} \mathbf{e}_r.$$

The deviatoric stress tensor is given by:

$$\sigma' = \begin{pmatrix} \sigma_{\rho\rho} & 0 & \sigma_{\rho z} \\ 0 & \sigma_{\theta\theta} & 0 \\ \sigma_{z\rho} & 0 & \sigma_{zz} \end{pmatrix}$$

The unit vector at any point on the deformed surface of the object is given by:

$$\mathbf{n} = \frac{1}{\sqrt{1 + \left(\frac{\partial a}{\partial z}\right)^2}} \begin{pmatrix} 1 \\ 0 \\ \frac{\partial a}{\partial z} \end{pmatrix}$$

The power input to the object is given by: $P = -\int_S (\sigma \cdot \mathbf{n}) \cdot \mathbf{u} dS$, where σ ($= -p\mathbf{I} + \sigma'$) is the stress acting on the body, p is the pressure field, and \mathbf{I} is the identity tensor. p can be calculated from the momentum equation, and it turns out to be $O(\epsilon^2)$. For the calculation of the term $(\sigma \cdot \mathbf{n}) \cdot \mathbf{u}$, we have:

$$(\sigma \cdot \mathbf{n}) \cdot \mathbf{u} \approx \left(\sigma_{\rho\rho} + \frac{\partial a}{\partial z} \sigma_{\rho z} \right) u_\rho + \left(\sigma_{z\rho} + \frac{\partial a}{\partial z} \sigma_{zz} \right) u_z.$$

u_z vanishes on the surface of the object, hence the second term in the above equation does not contribute to the power input. On calculating the stresses, we get:

$$\begin{aligned}\sigma_{\rho\rho} &= -\frac{\mu}{\rho^2} \frac{\partial a^2}{\partial t} = O(1); \\ \sigma_{\rho z} &= \mu \left(\frac{\partial u_\rho}{\partial z} + \frac{\partial u_z}{\partial \rho} \right).\end{aligned}$$

The first term in $\sigma_{\rho z}$ is $O(\epsilon)$ and the second term is $O(1/\log \epsilon)$, hence $\sigma_{\rho z}$ and p can be neglected in comparison to $\sigma_{\rho\rho}$. A little algebra gives the time-averaged power to be:

$$P = -\pi\mu k^2 \epsilon^2 S(\theta) \int_0^1 f(z)^2 dz.$$

Considering the body is moving with a constant speed W , the drag force exerted on it by the viscous fluid in the slender-body limit is [1]:

$$F_d = \frac{2\pi\mu}{\log 1/\epsilon} W;$$

and the dissipation due to this is:

$$D = -\frac{2\pi\mu}{\log 1/\epsilon} W^2;$$

So, the efficiency, $\eta = D/P$, is:

$$\eta = \frac{k^2 \epsilon^2}{32 (\log 1/\epsilon)^3} S(\theta) \int_0^1 f(z)^2 dz. \quad (21)$$

As can be seen from expression 21, the efficiency of the slender swimmer is $O[\epsilon^2/(\log 1/\epsilon)^3]$. This shows that the efficiency of these swimmers, like others, is not large.

7 Tube Dynamics

In this section, we consider the Stokes flow inside of the object. The object is supposed to be made of a viscous incompressible fluid, with its wall (cell wall) being elastic. The aim of doing this is to see if the definition of efficiency could be improved by including terms which are more dominant in the denominator.

Exploiting the small aspect ratio, one could write the equations of motion for the inside fluid to be (lubrication theory):

$$\begin{aligned}\frac{1}{r} \frac{\partial(ur)}{\partial r} + \frac{\partial w}{\partial z} &= 0; \\ \frac{\partial p}{\partial r} &= 0, \\ \frac{\partial p}{\partial z} &= \frac{1}{r} \frac{\partial}{\partial r} \left(r \frac{\partial w}{\partial r} \right)\end{aligned} \quad (22)$$

[11] & [14]. It can be seen that pressure is only a function of the axial co-ordinate. The last equation can be integrated to give:

$$w(r) = \frac{1}{4} \frac{\partial p}{\partial z} (r^2 - a^2).$$

Now, the flux of mass across a cross-section is given by: $F = \int_0^a w 2\pi r dr$, which turns out to be

$$F = -\frac{\pi}{8} \frac{\partial p}{\partial z} a^4. \quad (23)$$

Assuming $a(z, t)$ is known, one can solve for the pressure by integrating the continuity equation, giving

$$\frac{\partial p}{\partial z} = \frac{8}{a^4} \int \frac{\partial a^2}{\partial t} dz = O\left(\frac{1}{\epsilon^2}\right). \quad (24)$$

The above result tells us that the pressure inside the body is far higher than the stresses outside. As has been seen earlier, the viscous normal stress and the pressure outside are $O(1)$ and $O(\epsilon)$ respectively, which are much smaller than the internal pressure which is $O(1/\epsilon^2)$. Calculating the power input from the inside, we get

$$P_{inside} = \int_0^1 \int_0^a r \left(\frac{\partial w}{\partial r} \right)^2 dr dz = \frac{1}{16} \int_0^1 \left(\frac{\partial p}{\partial z} \right)^2 a^4 dz = O(1). \quad (25)$$

The above expression shows that the power spent in moving the inside fluid is far greater than the power being imparted by the outside fluid for a small ϵ . Hence, the efficiency is re-defined as $\eta = D/P_{inside}$, and the input from the outside fluid is neglected.

To include the dissipation term from the inside of the organism, model-1 for the radius cannot be used as it does not conserve volume. A naive substitution of model-1 in to 24 leads to blowing up of pressure at the ends. For this reason model-2 is suitable as it both conserves volume and vanishes at the ends. As has been calculated previously, the propulsion speed generated using model-2 is given by expression 20. Hence, carrying out a similar calculation as has been done for model-1, one finds that the efficiency for model-2 would be $O\left[(\epsilon^2/\log 1/\epsilon)^2\right]$, which is much smaller than the model-1 efficiency.

From this, it can be concluded that if one considers the internal flow, the dissipation is much higher than the dissipation outside, and that the internal dissipation would have to be taken into account in the expression for the efficiency, which would lead to a much smaller value than obtained from just considering the outside dissipation.

8 Solving for the propulsion speed by considering peristaltic motion of the inside fluid

The analysis considered in this section is done by taking a completely different approach from what has been done in the previous sections. The organism is considered to be made up of a viscous incompressible fluid, and its surface is assumed elastic. One could think of the organism using some kind of actuators to exert a force in the radial direction in a particular sequence along its body. This would be responsible for the movement of fluid, as it would generate additional pressure inside. There would be two sources of resistance to this force:

pressure of the fluid and hoop stress. This is schematically shown in figure 7. The resistance due to the wall is modelled as a spring force, and the ‘actuator’ force is modelled as sinusoidal travelling wave down the body. As the pressure inside is $O(1/\epsilon^2)$ times larger than the viscous normal stress from the outside fluid, one can neglect the outside stresses and write the force balance on the surface as:

$$\underbrace{P}_{\text{Pressure}} = \underbrace{D[A(z,t) - f(z)]}_{\text{Spring-like}} + \underbrace{\Theta f(z) \sin(kz - kt)}_{\text{Muscles}}, \quad (26)$$

where D is the ‘spring constant’, Θ is the amplitude of actuator force, $A(z,t)$ is the deformed radius and $f(z)$ is the undeformed radius.

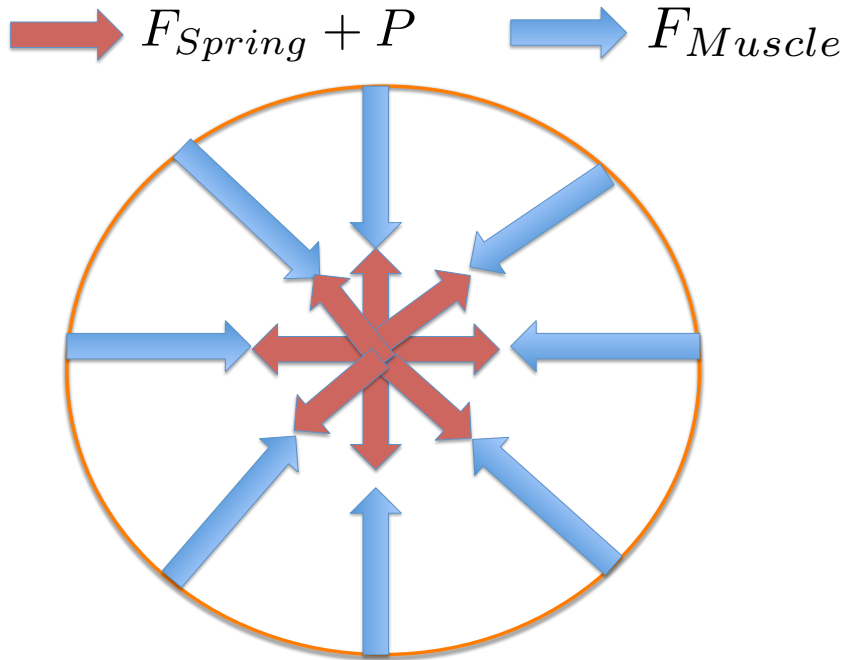


Figure 7: Force balance in the radial direction at a cross-section.

One can solve equation 26 for P , use this to determine $A(z,t)$ and use it in expression 17 to calculate the propulsion speed. The important point to note is that the flow inside is de-coupled from the flow outside, as the pressure is much larger in the inside, and outside stresses do not appreciably affect the flow inside. For this reason, one can make use of the result (equation 17) from slender-body analysis.

The integral form of equation 22 can be shown to be:

$$\frac{\partial (\pi a^2)}{\partial t} + \frac{\partial F}{\partial z} = 0, \quad (27)$$

where F is given by the expression 23. Equations 26 and 27 have to be solved in a time loop. To solve for $a(z,t)$, the initial condition chosen is the undeformed surface, which is $f(z)$. The following steps will lead to the mean propulsion speed:

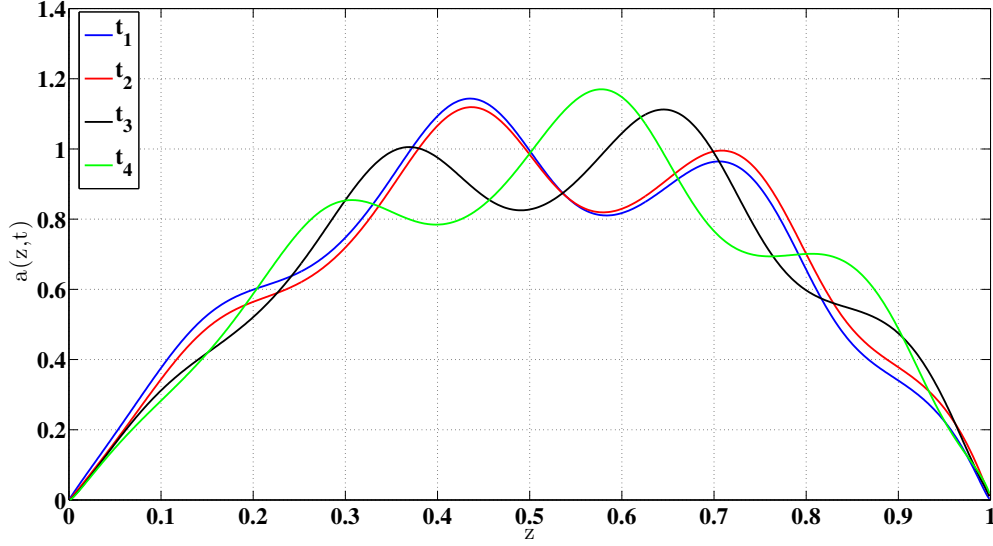


Figure 8: The radius of the organism at different time instances. The vertical axis has been magnified. Here, $t_1 < t_2 < t_3 < t_4$.

1. Solve for P using equation 26, and then calculate $\frac{\partial P}{\partial z}$.
2. Solve equation 27 numerically to obtain $a(z, t)$.
3. Compute $\frac{\partial^2 a(z, t)}{\partial t \partial z}$ and use it in expression 17 to calculate the propulsion speed.

The time evolution of the radius is shown in figure 8. This solution can now be used to compute the propulsion velocity and its mean. The solution for $D = 0.5$, $\Theta = 0.05$, $k = 20$ and $\epsilon = 0.05$ is shown in figure 9. It can be seen that W quickly settles into a periodic state due to the travelling surface waves shown in figure 8. From this the mean propulsion speed can be calculated. The same procedure can be used to compute for different ϵ , with the remaining parameters fixed to the values used in the plot 9. This is shown in figure 10. By curve fitting it can be shown that $W \sim \epsilon^2 / \log(1/\epsilon)$.

Carrying out a similar set of calculations with ϵ , D and Θ fixed to 0.02, 0.5 and 0.05 respectively, and varying k from 5 – 25, we find a quadratic trend in the propulsion speed, viz., $W \sim k^2$. This is shown in figure 11.

From the above results it is seen that the propulsion speed scales as $W \sim k^2 \epsilon^2 / \log(1/\epsilon)$, as was found for model-1. Hence, model-1 and force-balance approach differ from model-2, which was constructed to re-define the efficiency of the swimmer.

9 Summary and conclusions

In this study we have found the propulsion speed for a slender body with arbitrary cross-section, with the only condition that its radius vanishes at both ends. This study was partly motivated by the possible propulsion mechanism of cyanobacterium *Synechococcus* and by

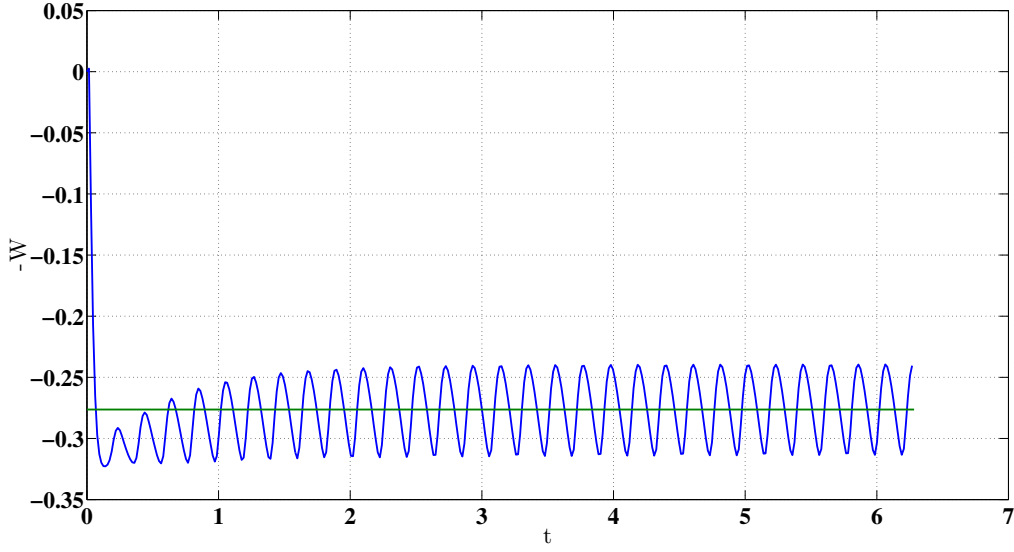


Figure 9: Time evolution of propulsion velocity for $D = 0.5$, $\Theta = 0.05$, $\epsilon = 0.05$ and $k = 20$. The green line indicates the mean value.

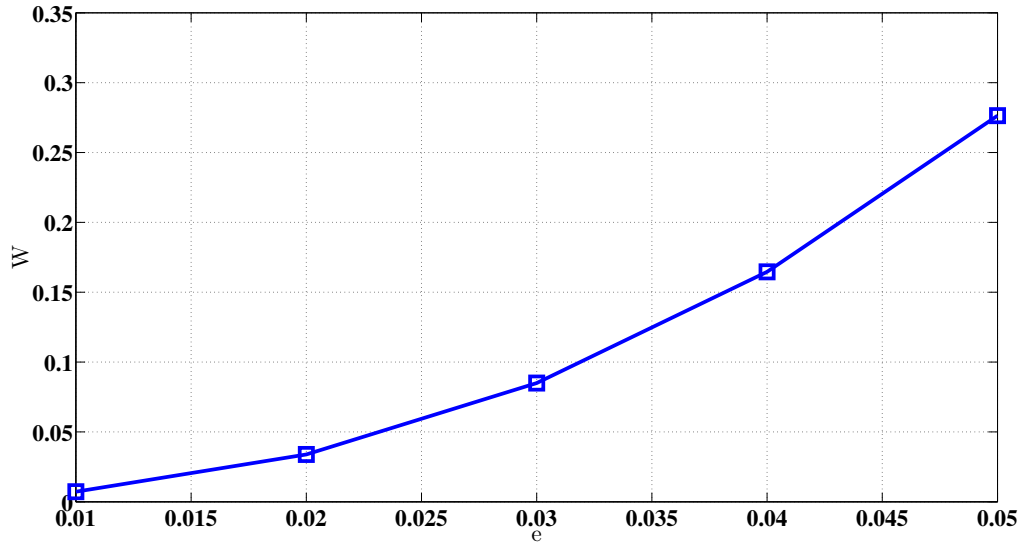


Figure 10: W vs. ϵ for $D = 0.5$, $\Theta = 0.05$ and $k = 20$. It can be shown that $W \sim \epsilon^2 / \log(1/\epsilon)$. Here, C is the speed of the travelling surface wave.

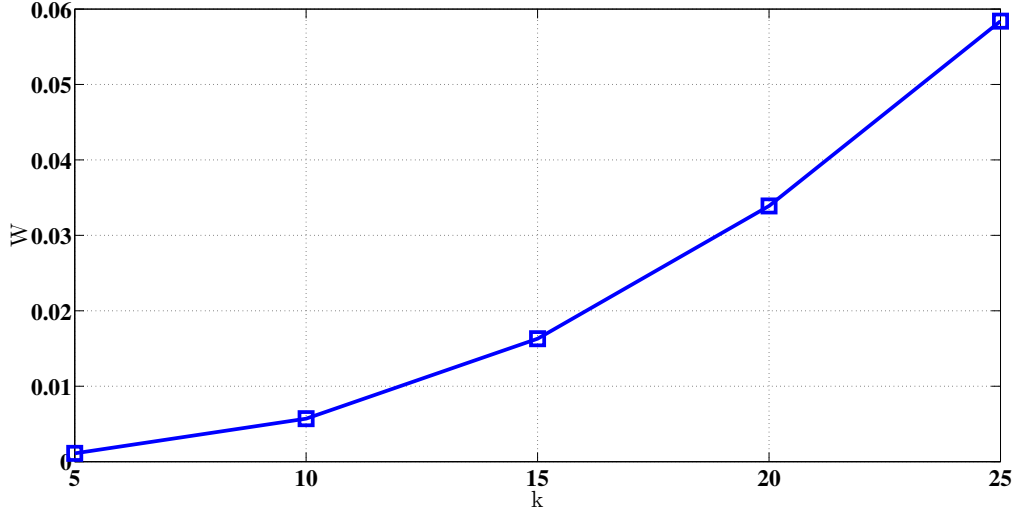


Figure 11: W vs. k for $D = 0.5$, $\Theta = 0.05$, $\epsilon = 0.02$. It is easily seen that $W \sim k^2$.

the study of propulsion of an infinite cylinder using travelling surface waves by Setter *et al.* [12]. The present study is a generalization of their problem, but restricted to slender geometries. This model can also be used to study the motion of other microorganisms like Paramecium, which moves by using the cilia on its surface, which again can be modelled as axisymmetric travelling surface waves.

From this study, it was found that the swimming speed of a slender object scales as $W \sim k^2 \epsilon^2 \theta^2 / \log(1/\epsilon)$ at the leading order. In the vanishing limit of the cylinder radius, the propulsion speed of Setter *et al.* [12] was shown to be the same as obtained by us using the SBT. When one considered the internal flow, the internal dissipation was shown to be much larger than the external dissipation, and was used to re-define the efficiency of the swimmer using an improved model (model-2) for the deformation of surface area. The resulting efficiency was found to be much smaller than the efficiency found for a previous model (model-1). Considering the pressure in the internal and external flows, it was shown that the former is much higher than the latter, and as a result the two flows could be considered to be de-coupled.

Finally, we studied the problem by considering the forces acting at a cross-section, to determine the pressure which is responsible for the fluid motion along the organism's axis, which in turn leads to the generation of travelling surface waves. The fact that the fluid motions are decoupled was used to calculate the propulsion speed using the expression from SBT once the surface deformation was determined. The resulting propulsion speed was found to scale like the propulsion speed from model-1.

10 Future work

An immediate extension of the present slender-body analysis will be to study the interaction of two slender swimmers, and to look for possibilities for generalization to more than

two swimmers. This would help in the construction of models, which would require the disturbance velocity fields as input, to study the large scale motion of these organisms.

In this study the internal fluid was considered to be Newtonian, which is generally not true, as the internal fluid in cells, the cytoplasm, is a suspension, and the stress-strain-rate relationship is not linear. An extension of this study would be to consider a non-Newtonian model for cytoplasm and solve for the resulting flow-field and then integrate it with the SBT.

The mathematical machinery used in this problem will be applied to the study of erosion from a cylindrical body placed in Stokes flow. Geometry of the body corresponding to times $t = 0$ and $t \rightarrow \infty$ serves as two limits of the SBT, however these two limits are separated in time, not space. To investigate this problem, one would have to consider the temporal evolution of the SBT analysis.

Acknowledgements

I would like to express my gratitude to my supervisor, *Neil Balmforth*, for readily agreeing to advise me. This project would not have been possible without *Neil's* constant help, support and patience, especially during the period when I had made numerous errors in my calculations and the time when I had blind faith in *Mathematica's* abilities, which led to a slowdown in my pace and the subsequent breakup with *Mathematica*. Working with *Neil* has been a great learning experience.

I would like to thank *Joe Keller* and *Bill Young* for the helpful discussions, and *John Wettlaufer* for his interest in the project and constant encouragement.

George Veronis and *Charlie Doering* deserve special mention for coaching us and for their patience with the GFD team, especially with the cricketers, on the softball field.

Finally, my thanks to all the fellow Fellows and the participants who made this summer an unforgettable experience!

References

- [1] J. Keller & S. I. Rubinow, Slender-body theory for slow viscous flow, *J. Fluid Mech.*, **75**, pp. 705-714, 1976.
- [2] E. Lauga & T. Powers, The hydrodynamics of swimming microorganisms, *Rep. Prog. Phys.*, **72**, pp. 1-36, 2009.
- [3] G. Subramanian & P. R. Nott, The fluid dynamics of swimming microorganisms and cells, *J. HSc.*, **91:3**, pp. 383-413, 2011.
- [4] G. I. Taylor, Analysis of the swimming of microorganisms, *Proc. Roy. Soc. Lond. Series A*, **209**, pp. 447-461, 1951.
- [5] M. J. Lighthill, On the squirming motion of nearly spherical deformable bodies through liquids at very small Reynolds numbers, *Comm. Pure Appl. Math.*, **109**, pp. 109-118, 1952.
- [6] J. R. Blake, Self propulsion due to oscillations on the surface of a cylinder at low Reynolds numbers, *Bull. Austral. Math. Soc.*, **5**, pp. 255-264, 1971.
- [7] E. M. Purcell, Life at low Reynolds number, *Am. J. Phys.*, **45**, pp. 3-11, 1977.
- [8] K. M. Ehlers, A. D. T. Samuel, H. C. Berg & R. Montgomery, Do cyanobacteria swim using travelling surface waves? *Proc. Natl. Acad. Sci. USA*, **93**, pp. 8340-8343, 1996.
- [9] <http://www.whoi.edu/science/B/people/ewebb/Syne.html>
- [10] K. Katija & J. O. Dabiri, A viscosity-enhanced mechanism for biogenic mixing, *Nature*, **460**, pp. 624-626, 2009.
- [11] L. G. Leal, Advanced transport phenomena: fluid mechanics and convective transport processes, *Cambridge University Press*, New York, 2007.
- [12] E. Setter, I. Bucher & S. Haber, Low-Reynolds-number swimmer utilizing surface traveling waves: analytical and experimental study, *Phys. Rev. B*, **85**, 066304, pp. 1 - 13, 2012.
- [13] S. Childress, Mechanics of swimming and flying, *Cambridge studies in mathematical biology:2*, 1981.
- [14] D. Takagi & N. J. Balmforth, Peristaltic pumping of viscous fluid in an elastic tube, *J. Fluid Mech.*, **672**, pp. 196-218, 2011.

Scattering of internal waves over random topography

Yuan Guo

September 30, 2012

1 Introduction

Internal waves are initially generated as the barotropic tides (described by $\mathbf{U}(t) = \hat{\mathbf{x}}U_0 \cos \omega t$) flow over undulating sea-floor topography. They are an important component in ocean dynamics such as small-scale mixing and dissipation. Internal waves generated by barotropic tides are usually of low mode number so they are of large-scale. Where are those small-scale waves come from? One possible way of generating these small-scale waves is scattering (See Figure 1). Scattering is a linear interaction between the propagating waves and the sea-floor

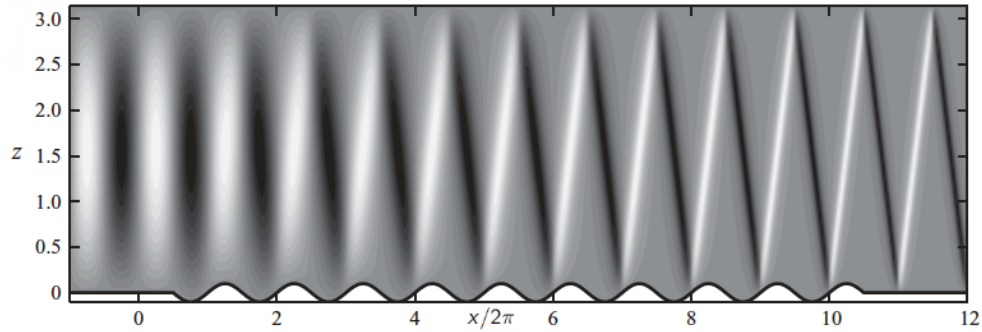


Figure 1: Snapshot at $t = 0$ of $\text{Re}\Psi(x, z)e^{-it}$ for topography $h(x) = 0.1 \sin x$. It is clear from the graph that the width of white or black region (represent the scale of the waves) changes from large to small. This Figure is taken from Bühler & Holmes-Cerfon, 2011

topography. The rugged bottom topography scatters the incoming waves into other spectral modes and redistributes energy flux in the waves number space. Figure 2 is an example of scattering. The incoming waves we use is of mode-one and we can see that by scattering we obtain waves with high-wave number. Details of this redistribution process depend on the shape of the topography, i.e. whether it is subcritical or supercritical (see definition below Equation (7)).

Scattering problem is studied for determined topography by Mülcer & Liu (1999) and subcritical random topography (Section 2.2) by Bühler & Holmes-Cerfon (2011). Here we want to know what will happen when we allow random topography to have supercritical part.

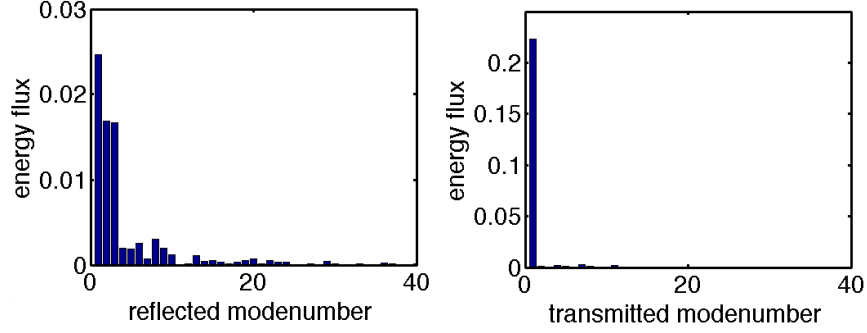


Figure 2: An example of scattering of internal waves. The incoming waves are of mode-one and with energy flux rescaled to unity. We only plot energy flux of the first 40 modes.

In this paper, we study two-dimensional (2D) scattering problem for ocean with finite depth by using linearized two-dimensional (2D) rotating Boussinesq system. Linearization is justified if the tidal excursion is much less than the scale of the topography. For simplicity, the Coriolis frequency f and the buoyancy frequency N are taken to be constants, though N is a function of depth z in real ocean. However, previous experience with variable N indicated that usually allowing for variable N slightly modifies but does not change in a fundamental way the results for constant N . Moreover, a recent study by Grimshaw, Pelinovsky & Talipova (2010) shows that for some profiles of $N(z)$, WKB theory gives exactly the right answer. But, of course our results will be more useful if we can extend them to realistic profile of N . Also we limit our problem to finite topography. The topography may have arbitrary shape but it must be localized, i.e. we assume the bottom is flat in the far field.

The paper is organized as follows. In Section 2, we give the governing equations of our problem and specified what we mean by random topography. In Section 3, we derive a formal solution to the scattering problem. An special geometric structure—wave attractor is studied in details in Section 4. And in Section 5 we present our numerical results of the decay of the expected energy flux and compare them with some know results. Conclusions and some discussions are in Section 6.

2 Mathematical formulation

2.1 Governing equations

Our model is two-dimensional (2D) rotating linear Boussinesq system, in which all fields depend on x (horizontal) and z (vertical) only. This does not prevent a non-zero velocity in y -direction due to the Coriolis force. The equations for velocity field $\mathbf{v} = (u, v, w)$, buoyancy b and pressure P are

$$u_t - fv + P_x = 0, \quad v_t + fu = 0, \quad w_t + P_z = b, \quad b_t + N^2w = 0, \quad (1)$$

and we also need incompressible constraint $u_x + w_z = 0$. For simplicity, assume the Coriolis frequency f and the buoyancy frequency N are constants.

Introducing the stream function $\psi(x, z, t)$ such that $u = \partial_z \psi$, $w = -\partial_x \psi$, we can write Equation (1) as

$$(N^2 + \partial_{tt})\partial_{xx}\psi + (\partial_{tt} + f^2)\partial_{zz}\psi = 0 \quad (2)$$

For boundary conditions, we use rigid top and bottom boundaries at the ocean surface $z = H$ and the bottom $z = h(x)$

$$\psi(x, H, t) = \psi(x, h(x), t) = 0, \quad (3)$$

It is worth mentioning here that the rigid boundary condition on the bottom is not trial and is essential in solving the scattering problem. We focus our attention to the compact region $x \in [-L_x/2, L_x/2]$, and assume the ocean bottom is flat in the far field, i.e. bottom topography $z = h(x)$ is taken to be zero outside the compact region $x \in [-L_x/2, L_x/2]$. For left and right boundaries, we use group velocity to describe the direction of waves, the transmitted waves on the right and reflected waves on the left must obey horizontal radiation condition: energy flux is directed away from the topography. And the incoming waves that enter the region on the left are specified in advance. The geometry of the problem together with the boundary conditions are summarized in Figure 3.

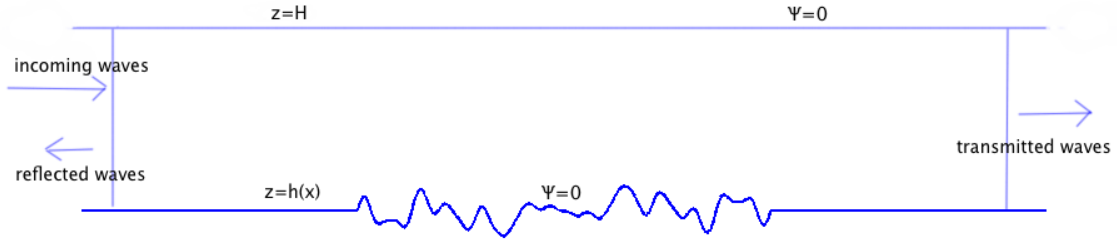


Figure 3: Geometry of the problem and the boundary conditions.

We are interested in time-periodic solutions with given frequency such as the semi-diurnal M_2 tides. And in real ocean $N/f \approx 10$ and $\omega/f \approx 2$ for M_2 tides, hence we assume $f < \omega < N$ and look for solutions of the form

$$\psi(x, z, t) = \text{Re}\Psi(x, z)e^{-i\omega t} \quad (4)$$

where the complex-valued function $\Psi(x, z)$ is to be solved. Then the system is

$$(N^2 - \omega^2)\partial_{xx}\Psi - (\omega^2 - f^2)\partial_{zz}\Psi = 0, \quad \Psi(x, H) = \Psi(x, h(x)) = 0 \quad (5)$$

This is one-dimension (1D) wave equation without time-like variable. But we can still solve it by the method of characteristics.

The slope of the characteristics of all internal waves with the same value of frequency ω is at some fixed angle with the vertical, which we rescale to 45° . In addition, we rescale the ocean depth over the flat bottom to be π and write the non-dimensional variables with a prime as

$$z = \frac{H}{\pi}z', \quad h = \frac{H}{\pi}h', \quad x = \frac{1}{\mu} \frac{H}{\pi}x', \quad \mu = \sqrt{\frac{\omega^2 - f^2}{N^2 - \omega^2}} \quad (6)$$

After dropping the prime the non-dimensional equation for Ψ becomes,

$$\Psi_{xx} - \Psi_{zz} = 0, \quad \Psi(x, \pi) = \Psi(x, h(x)) = 0. \quad (7)$$

The bottom topography is called *subcritical*, *critical* or *supercritical* if the non-dimensional topography slope satisfies $|dh(x)/dx| < 1$, $|dh(x)/dx| = 1$ or $|dh(x)/dx| > 1$.

2.2 Random topography

We consider the simplest case of random topography by choosing $h(x)$ for our considered region $x \in [-L_x/2, L_x/2]$ a section of zero-mean stationary Gaussian process defined on the real line by stationary covariance function $C(x)$ such that

$$\mathbb{E}h(x) = 0 \quad \text{and} \quad \mathbb{E}h(y)h(x+y) = C(x), \quad (8)$$

where \mathbb{E} is the probabilistic expectation. It is easy to generate a complex-valued stationary scalar Gaussian random field $H(x)$ with covariance function $C(x)$ in Fourier space by

$$\hat{H}(k) = \sqrt{\frac{L_x \hat{C}(k)}{2}} (A_k + iB_k) \quad (9)$$

where A_k and B_k are independent Gaussian random variables with mean 0 and variance 1. Then $H = FT^{-1}(\hat{H})$ is a *complex* Gaussian random field satisfying (Yaglom 1962)

$$\mathbb{E}H(y)H(x+y) = C(x). \quad (10)$$

Real-valued field can be generated from complex-valued one by taking real or imaginary part. From our definition, we know if $H = h_1 + ih_2$ is a *complex* Gaussian random field with covariance function $C(x)$, then h_1 and h_2 are independent, *real-valued* Gaussian random fields with covariance function $C(x)/2$ (Hida & Hitsuda 1993). This leads to a nice way of obtaining samples of *real-valued* fields with covariance function $C(x)$, since we only need to generate complex-valued samples with covariance function $2C(x)$ and take their real or imaginary parts.

In Fourier space, we can also compute the covariance function of $h'(x)$ by

$$\mathbb{E}h(y)h(x+y) = C(x) \iff \mathbb{E}h'(y)h'(x+y) = -C''(x). \quad (11)$$

The covariance function $C(x)$ we use for our numerical experiments and its corresponding Fourier transform $\hat{C}(k)$ are

$$C(x) = \sigma^2 \exp\left(-\frac{x^2}{2\alpha^2}\right) \quad \text{and} \quad \hat{C}(k) = \sqrt{2\pi}\sigma^2\alpha \exp\left(-\frac{k^2\alpha^2}{2}\right) \quad (12)$$

hence we have

$$\mathbb{E}h^2 = C(0) = \sigma^2 \quad \text{and} \quad \mathbb{E}h'^2 = -C''(0) = \sigma^2/\alpha^2 \quad (13)$$

3 Solving the wave equation

3.1 The method of characteristics and spectrum scheme

In order to solve the wave equation for Ψ ,

$$\Psi_{xx} - \Psi_{zz} = 0, \quad \Psi(x, \pi) = \Psi(x, h(x)) = 0, \quad (14)$$

one approach is to follow Muller & Liu (2000a) that use the method of characteristics plus a spectral scheme to satisfy the horizontal radiation condition for scattering waves. This method will fail when characteristic paths converge onto some localized geometric structures that are called wave attractors (see Section 4). Another attractive numerical scheme is using a Green's function approach in which we distribute suitable sources with certain density $\gamma(x)$ along the bottom topography (Echeverri *et al* 2010). Though the method of characteristics has some limitations, we still choose it since it is easy to understand and has a clear physical meaning. And we come out of situations that have wave attractors by discarding such samples in our numerical experiment.

The characteristics of Equation (14) are lines with slope ± 1 , i.e. lines along which $x \pm (\pi - z)$ are constants. Use the homogeneous boundary condition on the surface $z = \pi$, the general solution is

$$\Psi(x, z) = f(x + z - \pi) - f(x - z + \pi), \quad (15)$$

and the solution is determined if we can solve for the complex-valued function $f(x)$ for all $x \in \mathbb{R}$. It is helpful to think $f(x)$ is defined at every point along the surface and the value of $\Psi(x, z)$ at any interior point can be easily found by tracing both characteristics back to the ocean surface. The non-trivial boundary condition $\Psi = 0$ at the bottom $z = h(x)$ implies that for all $x \in \mathbb{R}$, f should satisfy

$$f(x + h(x) - \pi) = f(x - h(x) + \pi). \quad (16)$$

Physically, this means $f(x)$ have the same value at any two points on the surface that can be connected by the characteristics (Figure 4). And $f(x)$ is a periodic function of period 2π in the far field where $h(x) = 0$.

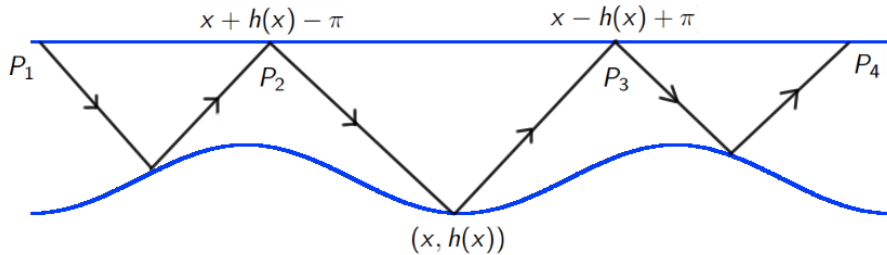


Figure 4: P_1 , P_2 , P_3 and P_4 are connected by characteristics so the function f have the same value at these four surface points.

According to the definition from Muller & Liu (2000a), $T(\xi)$ is the surface distance between two characteristics emanating from the same bottom point ξ . The function $T(\xi)$ is called T -period and reflects the shape of the bottom topography. For flat bottom, T is 2π . Consider two T -periods T_+ and T_- on each side of the topography in the far field. If we trace a characteristic from one T -period, say T_+ , we will end up in either T_+ or T_- in the far field. Hence we can construct a map between T_+ and T_- by tracing a number of characteristics from each period. Since we allow our topography to have supercritical part, T_+ contains a part T'_+ which is mapped to T_- and the other part T''_+ that is mapped to itself. The same happens to T_- . Therefore $T_+ = T'_+ \cup T''_+$, and $T_- = T'_- \cup T''_-$ such that T'_+ is mapped onto T'_- , T''_+ onto itself, T'_- onto T'_+ and T''_- onto itself. And we denote the map from T_+ by \mathcal{M} and the map from T_- by \mathcal{M}^{-1} . To be more explanatory, we depict the situation in Figure 5.

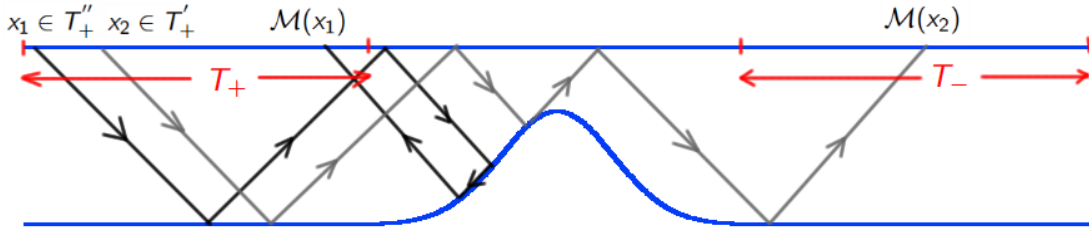


Figure 5: This graph shows how we define T_+ , T_- , T'_+ and T''_+ . Similar definition applies to \mathcal{M}^{-1} except that characteristics start from T_- . Characteristic can be reflected back by supercritical part of the bottom (compare with Figure 4). Bottom topography is $2e^{-x^2/2}$.

The top and bottom boundary conditions imply that

$$f(\mathcal{M}(x)) = f(x) \text{ if } x \in T_+, \quad f(\mathcal{M}^{-1}(x)) = f(x) \text{ if } x \in T_-. \quad (17)$$

And to be more physical, we decompose the complete wave fields in the far field by

$$f(x) = f^0(x) + f^r(x), \quad x \in T_+, \quad f(x) = f^t(x), \quad x \in T_- \quad (18)$$

where $f^0(x)$ for incoming waves, $f^r(x)$ for backward reflected waves and $f^t(x)$ for forward transmitted waves. More specifically, with the periodic condition (17) we have

$$f^0(x) + f^r(x) = \begin{cases} f^t(\mathcal{M}(x)) & x \in T'_+, \quad \mathcal{M}(x) \in T'_- \\ f^0(\mathcal{M}(x)) + f^r(\mathcal{M}(x)) & x \in T''_+, \quad \mathcal{M}(x) \in T''_- \end{cases} \quad (19)$$

$$f^t(x) = \begin{cases} f^0(\mathcal{M}^{-1}(x)) + f^r(\mathcal{M}^{-1}(x)) & x \in T'_-, \quad \mathcal{M}^{-1}(x) \in T'_+ \\ f^t(\mathcal{M}^{-1}(x)) & x \in T''_-, \quad \mathcal{M}^{-1}(x) \in T''_+ \end{cases} \quad (20)$$

As mentioned earlier, in the far field over zero bottom topography, f^0 , f^r and f^t are periodic functions with period 2π . Hence we can expand them as Fourier series and because of the radiation condition they have the form

$$f^0(x) = \sum_{k=1}^{\infty} a_k^0 e^{ikx}, \quad f^r(x) = \sum_{k=0}^{\infty} a_k^r e^{-ikx}, \quad f^t(x) = \sum_{k=1}^{\infty} a_k^t e^{ikx}. \quad (21)$$

Without loss of generality, we can set $a_0^t = 0$, since the two constant terms a_0^r and a_0^t enter our problem in the form $a_0^r - a_0^t$. If we substitute the Fourier representation (21) into the periodic condition and project onto the m th Fourier mode, we obtain a linear system

$$\mathbf{a}^r = B\mathbf{a}^t + T\mathbf{a}^0 + A\mathbf{a}^r, \quad (22)$$

$$\mathbf{a}^t = S\mathbf{a}^0 + D\mathbf{a}^r + C\mathbf{a}^t. \quad (23)$$

where the coefficient matrices are given by

$$\begin{aligned} B_{mk} &= \frac{1}{2\pi} \int_{T'_+} e^{ik\mathcal{M}(x)} e^{imx} dx & m = 0, 1, 2, \dots & \quad k = 1, 2, 3, \dots \\ T_{mk} &= \frac{1}{2\pi} \int_{T''_+} e^{ik\mathcal{M}(x)} e^{imx} dx & m = 0, 1, 2, \dots & \quad k = 1, 2, 3, \dots \\ A_{mk} &= \frac{1}{2\pi} \int_{T'_+} e^{-ik\mathcal{M}(x)} e^{imx} dx & m = 0, 1, 2, \dots & \quad k = 1, 2, 3, \dots \\ S_{mk} &= \frac{1}{2\pi} \int_{T'_-} e^{ik\mathcal{M}^{-1}(x)} e^{-imx} dx & m = 1, 2, 3, \dots & \quad k = 1, 2, 3, \dots \\ D_{mk} &= \frac{1}{2\pi} \int_{T'_-} e^{-ik\mathcal{M}^{-1}(x)} e^{-imx} dx & m = 1, 2, 3, \dots & \quad k = 1, 2, 3, \dots \\ C_{mk} &= \frac{1}{2\pi} \int_{T''_-} e^{ik\mathcal{M}^{-1}(x)} e^{-imx} dx & m = 1, 2, 3, \dots & \quad k = 1, 2, 3, \dots \end{aligned}$$

We can solve this linear system by truncating at a certain number of modes, and find the solution once the mapping functions \mathcal{M} and \mathcal{M}^{-1} are known.

3.2 Checkerboard map

In order to construct the mapping function \mathcal{M} and \mathcal{M}^{-1} , we only need to know how to decide the 'next' point x_{k+1} if given a point x_k on the surface. We can do this by tracing characteristics. However, there are two characteristics start from every surface point. This leads us to an ambiguous situation that we have two candidates for x_{k+1} . Figure 6 illustrates the double-valued situation for a chosen bottom topography $h(x) = 2e^{-x^2/2}$. We need a way to get rid of the double-valued mapping.

Manually we can distinguish these two candidates once we know the starting direction of the characteristic we need to follow. On a computer, we adopt the checkerboard construction by Balmforth *et al.* (1995) to track the direction of the characteristic. To be specific, we focus our attention on the bottom region $-L < x < L$ containing the random topography ($L > L_x/2$). For right-going and left-going characteristics define the new mapping variable as $x' = x + L$ and $x' = x - L$, respectively. Therefore, the new mapping variable for reflection points of right-going characteristics are positive while negative for left-going characteristics. So we have a way that automatically keep track of the characteristics' directions. Figure 7 shows the checkerboard map for Gaussian bump $h(x) = 2e^{-x^2/2}$. Comparing with Figure 6, we can see that by introducing the new shifted variable we get the desired 1 : 1 map.

We can see from Figure 7, the checkerboard map for topography with supercritical part is discontinuous. The discontinuities come from critical points where the absolute value

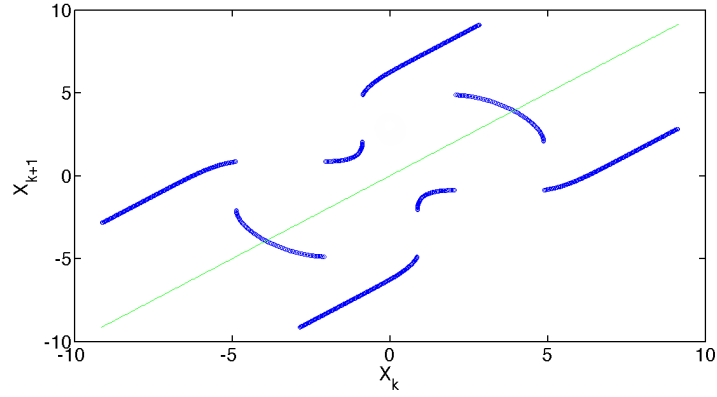


Figure 6: Double-valued map for bottom $h(x) = 2e^{-x^2/2}$.

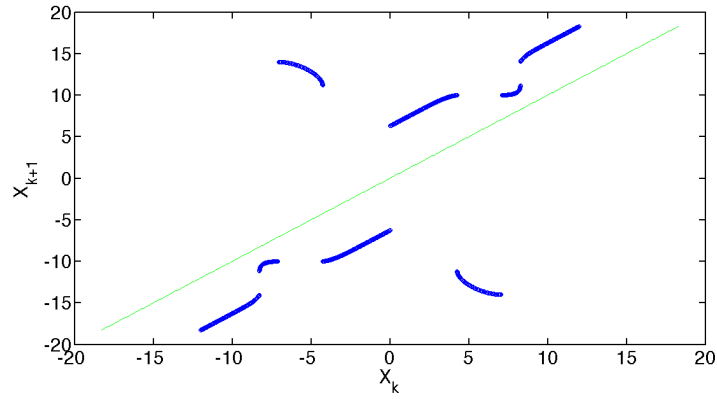


Figure 7: Checkerboard map for bottom $h(x) = 2e^{-x^2/2}$.

of topography slope change from bigger than 1 to smaller than 1. Figure 8 shows how discontinuities occur when characteristics hit critical points.

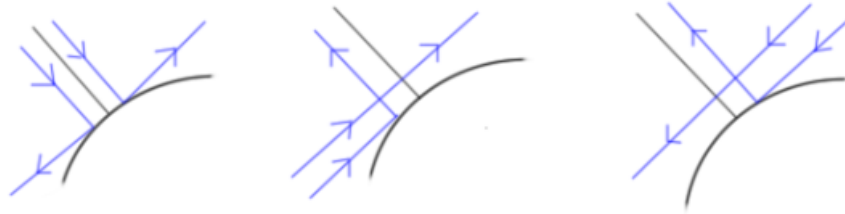


Figure 8: Three cases that can lead to discontinuities for critical points with positive derivatives. Similar cases for critical points with negative derivatives.

It is much more difficult to build the checkerboard map with supercritical topography. Unlike the purely subcritical situation in which characteristic can only go forward and only hits the bottom once between neighboring surface points, characteristic can be reflected back by the supercritical part of the bottom topography and hits several bottom points before it reaches the surface again. Hence we are in a rather complicated situation in letting the computer know which characteristic to follow while also need to solve for the intersections of characteristics and the bottom (this is the most time-consuming part in numerical experiments). We need to switch to another characteristic at these intersection points. Figure 9 shows all the eight cases that could happen when characteristics intersect with the bottom and indicates the characteristic we should choose.

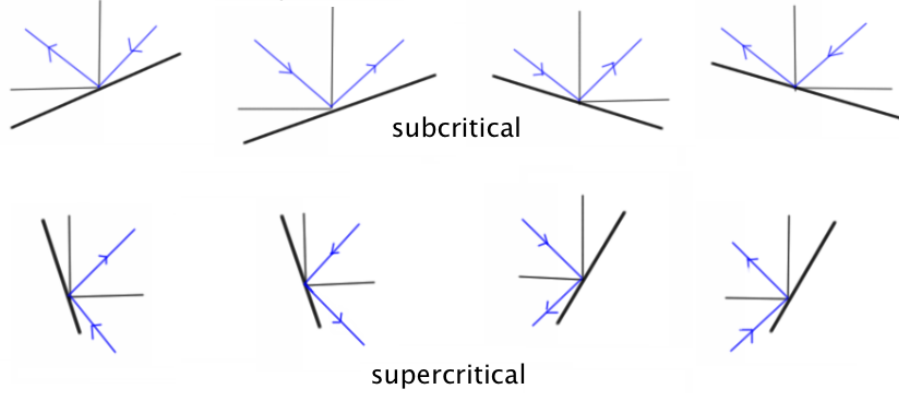


Figure 9: Eight Cases that could happen when characteristics intersect with the bottom.

Allowing the bottom topography to have supercritical part makes the problem more complicated. Can we only consider subcritical case? Some models have been built to describe the shape of the bottom topography. One of them is the analytic spectrum created by Bell (1975). This is an estimate of the power spectrum based primarily on topographic data from the abyssal hill region of the ocean basin in the eastern central North Pacific. And the bottom topography is modeled as a random distribution of statistically independent hills. The spectrum is defined such that the variance of the dimensional height $\tilde{h}(x, y)$ is

$$\mathbb{E}\tilde{h}^2 = \frac{\pi}{2} \int_0^{k_c} \frac{F_0 k}{(k^2 + k_0^2)^{3/2}} dk \approx (125m)^2 \quad (24)$$

where $F_0 = 250m^2$ cycles km^{-1} , $k_0 = 0.025$ cycles km^{-1} and the effective cut-off wave number $k_c = 2.5$ cycle km^{-1} . The variance of the slope is

$$\mathbb{E}|\nabla\tilde{h}|^2 \approx (125m)^2 k_0 k_c \approx 0.2^2. \quad (25)$$

This is the spectrum for 2D topography. In order to apply it to our 1D topography, we need to assume the topography is isotropic, i.e. assuming each of the two parts of the derivative $|\nabla\tilde{h}|^2 = \tilde{h}_x^2 + \tilde{h}_y^2$ has the same expected value. Therefore, the 1D model topography has

$$\mathbb{E}|\tilde{h}'|^2 \approx (125m)^2 k_0 k_c / 2 \approx 0.14^2. \quad (26)$$

The typical value of the slope of characteristics before non-dimensionalization is $\mu = 0.17$. So if we assume the bottom is modeled as a zero-mean stationary Gaussian process, the supercritical part takes up about 22.5% of the ocean bottom, which implies that the supercritical part shouldn't be neglected.

Although there is evidence that the ocean topography is not strictly isotropic, measurements of eastern central North Pacific may not be able to represent the whole sea topography and more recent models are proposed by Goff & Jordan (1988) and Nikurashin & Ferrari (2010), our consideration of supercritical part is still reasonable. As we mentioned earlier, the supercritical part of the topography makes the checkerboard map discontinuous. The discontinuities could probably lead to significant differences. And we will see in Section 4 that even when the topography contains only a small part of supercritical bottom, say about 5%, there can be wave attractors especially for long topography, which can never happen for purely subcritical bottom.

4 Wave Attractors

In this section, we look at a special geometric structure of the characteristics. As the characteristic can be reflected back by the supercritical part of the bottom, it is possible that the characteristic forms some closed orbits, what is called *wave attractors*. One reason we want to look at wave attractors is that if there are attractors, our method of tracing characteristics to get the map \mathcal{M} and \mathcal{M}^{-1} will fail. Since our path following the characteristics will probably converge onto the closed orbit and can never reach either T-period in this case. We certainly can use other numerical methods such as the Green's function to solve our 1D wave equation. But the wave attractors are still of great interest since their existence can lead to significant different behavior of internal waves. Figure 10 (from Echeverri *et al.* 2011) describes such a situation. The horizontal axis is a parameter value that describes the bottom topography and the vertical axis is the conversion rate that measures how much energy in the barotropic tides is converted to the energy of internal waves. This is related to our problem because this conversion of energy provides a way of realizing the incoming waves. And we can see that the existence of attractors even leads to an ill-posed problem because the numerical results do not converge when increasing the resolution.

4.1 Example of wave attractors

We can have different kinds of wave attractors. And we classify them by the number of reflection points of the closed orbit on the surface. The simplest case is 1-point attractor as shown in Figure 11. The bottom topography is given by $h(x) = B \left(1 - \cos\left(\frac{2\pi x}{A}\right)\right)$, $|x| \leq A$ and 0 elsewhere. The parameter values are $B = 1.15$ and $A = 1.6\pi$. We can also consider the stability of these closed orbits, i.e. whether the characteristic paths converge onto them. Since our problem involves mapping from both directions and the characteristic path is reversible, these closed orbits must be stable from one direction and unstable from the other. For 1-point attractor, the stability can be easily determined by examine whether the fixed point of the map $X_{k+1} = F(X_k)$ is stable or not. As shown in Figure 11, the stable orbit for clockwise characteristic path is indicated by arrows, whereas the other is unstable.

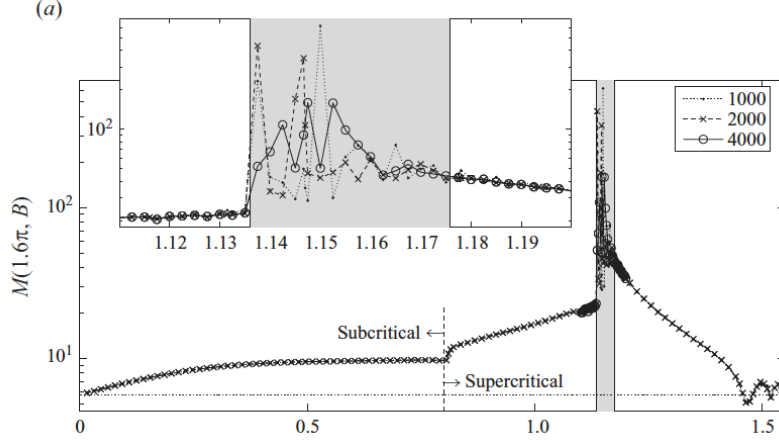


Figure 10: Conversion rates for $h(x) = B \left(1 - \cos\left(\frac{2\pi x}{A}\right)\right)$, $|X| \leq A$ and 0 elsewhere. The parameter values are $B = 1.15$ and $A = 1.6\pi$. And three truncations are shown: $K = N = 1000, 2000$ and 4000 . This Figure is taken from P. Echeverri *et al*, 2011.

Because of the symmetry of the topography, there are two corresponding closed orbits for counterclockwise characteristic path, and the stability of the two orbits is interchanged.

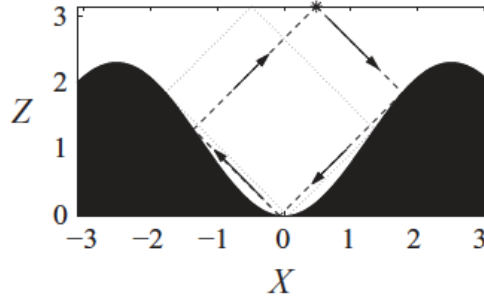


Figure 11: The bottom topography is given by $h(x) = B \left(1 - \cos\left(\frac{2\pi x}{A}\right)\right)$, $|X| \leq A$ and 0 elsewhere, where $B = 1.15$ and $A = 1.6\pi$. Stable orbit for clockwise characteristic path is indicated by arrows. This Figure is taken from P. Echeverri *et al*, 2011.

We can also have 2-point wave attractor, actually this is the most common kind of attractors we find in our numerical simulations (see Section 4.3). Figure 12 is a 2-point wave attractor. Red dots on the surface indicate the location of reflection points of the characteristic path while the black line is the corresponding closed orbit. The stability of multi-point wave attractors is geometrically more complicated since we need to consider all surface points. So we do not go into details here. We can have more than two reflection points on the surface, Figure 13 is an example of 4-point wave attractor founded in our numerical simulations.

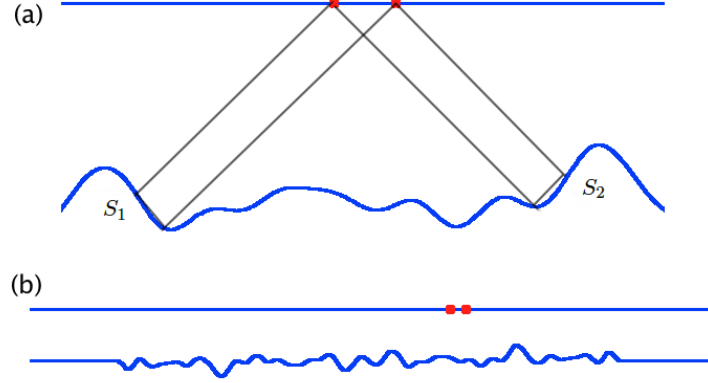


Figure 12: (a) A sample that has 2-point wave attractor in numerical simulations with parameter value $\sigma = 0.25$, $\alpha = 0.5$ for zero-mean stationary Gaussian random field generated by covariance function in Equation (12). S_1 and S_2 are two supercritical points, while other points are subcritical. The whole plot of the random bottom topography is shown in (b). The length of random bottom is 10π .

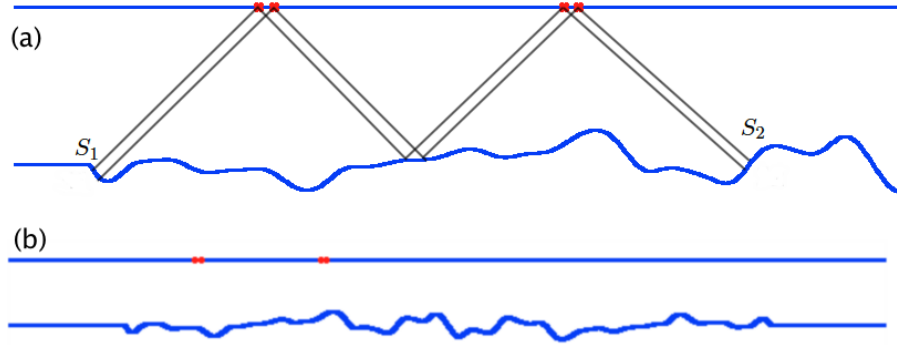


Figure 13: A sample that has 4-point wave attractor in numerical simulations with parameter value $\sigma = 0.25$, $\alpha = 0.5$ for zero-mean stationary Gaussian random field generated by covariance function in Equation (12). S_1 and S_2 are two supercritical points, while other points are subcritical. The whole plot of the random bottom topography is shown in (b). The length of random bottom is 10π .

4.2 Method to detect attractors

Finding 1-point wave attractor is just finding the fixed point for the checkerboard map. To find the fixed point, we only need to check whether the checkerboard map and the straight line $x_k = x_{k+1}$ have any intersection. In Figure 14, we find 4 intersections, and they correspond to the two closed orbits (in Figure 11) in both directions.

To find 2-point attractor, a natural way is to apply the checkerboard map forward two

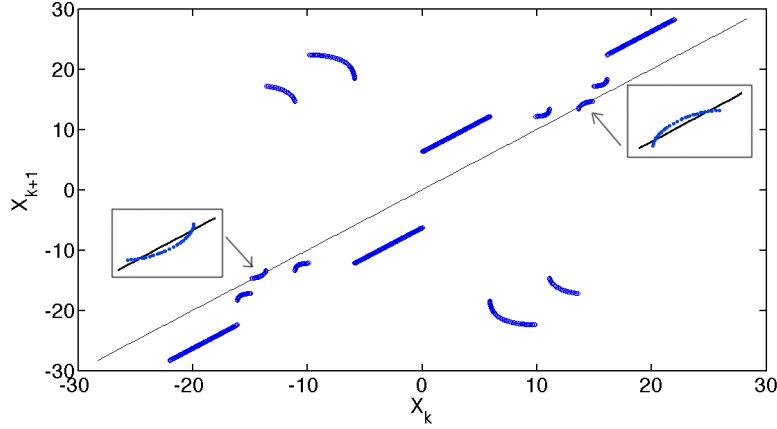


Figure 14: Checkerboard map for topography $h(x) = B(1 - \cos(\frac{2\pi x}{A}))$, $|X| \leq A$, with parameter value $B = 1.15$ and $A = 1.6\pi$. Two magnifications show the structure near the two fixed points

times and then find the fixed points of the map $X_{k+2} = F(X_k)$. However, this method has some shortcomings. Since it is impossible to build checkerboard map for every single point on the surface, we actually build the checkerboard map by discretizing the bottom and then tracing characteristics emanating from every discretized point until they reach the surface. For arbitrary surface point we find its checkerboard map by linear interpolation while keeping an eye on the discontinuities. This process unavoidably leads to some numerical error. Since attractors are delicate structures that are sensitive to errors, this is not the best idea. An alternative way is to find the intersection points of the checkerboard map with the backward checkerboard map $X_{k-1} = G(X_k)$. This method is better because we do not need to find the discontinuities of the map $X_{k+2} = F(X_k)$ and apply linear interpolation, both time saving and with less numerical error. Backward checkerboard map can be easily obtained by just reversing the order of the two coordinates. We use this method to find 2-point wave attractors in our numerical experiments and Figure 15 is the checkerboard map for one particular sample.

Similar ways can be used to find wave attractors involving more reflection points on the surface. Just as the situation for 2-point wave attractor, we don't apply the checkerboard map four times to find the fixed points of the map $X_{k+4} = F(X_k)$ due to potential numerical errors. Instead, we apply the checkerboard map twice and seek the intersection points of the map $X_{k+2} = F_1(X_k)$ with $X_{k-2} = F_2(X_k)$. Again, the map $X_{k-2} = F_2(X_k)$ can be easily found by interchanging the two coordinates of the map $X_{k+2} = F_1(X_k)$. Figure 16 shows the checkerboard map for a sample that have 4-point wave attractor in our numerical simulations.

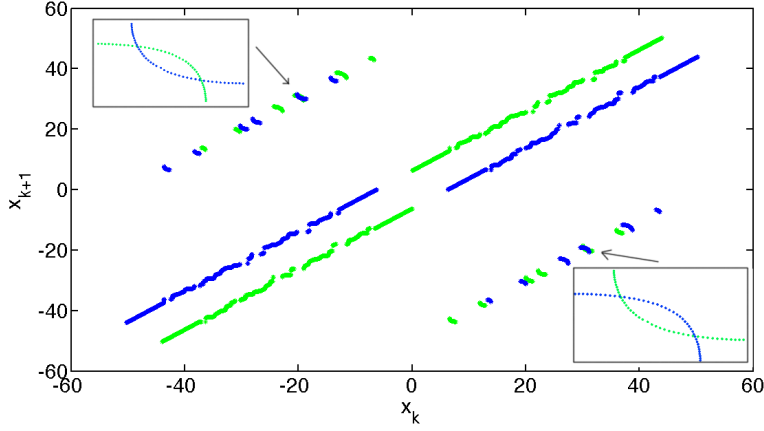


Figure 15: One sample that has 2-point wave attractor with parameter value $\sigma = 0.25$ and $\alpha = 0.5$ for zero-mean stationary Gaussian random field generated by covariance function in Equation (12). The length of random topography is 10π . Magnifications are used to show the structure near the intersection points.

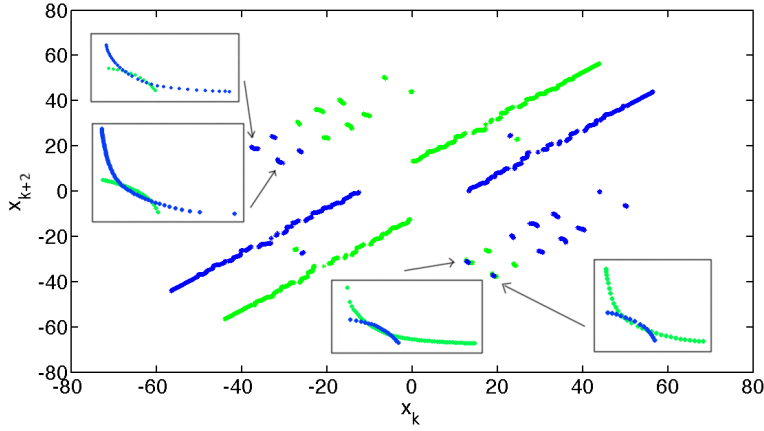


Figure 16: One sample that has 4-point attractor with parameter value $\sigma = 0.25$ and $\alpha = 0.5$ for zero-mean stationary Gaussian random field generated by covariance function in Equation (12). The length of random topography is 10π . Magnifications show the structure near the intersection points.

4.3 Probability of having attractors

In order to get an idea of the probability of having wave attractors, we do several numerical experiments. Here we only look at wave attractors that involving 1 \sim 4 reflection points. More complicated attractors are possible but because of the finite length of the random topography we use (10π in our numerical simulations) and their more complicate structures,

these attractors are of very low probability.

We choose the parameter $\sigma = 0.06, 0.10, 0.13, 0.17, 0.21$ and 0.25 while keeping $\sigma/\alpha = 1/2$ fixed. For this fixed value we can easily estimate the probability of supercritical bottom. Since we model the bottom topography as a section of zero mean stationary Gaussian process, the absolute value of the slope of the bottom is bigger than 1 if and only if it is larger than two standard deviations of the slope, which is σ/α by Equation (13). Therefore about 4.55% of the bottom is supercritical. We plot the results in Figure 17(a), and the probability is calculated for 1000 simulations.

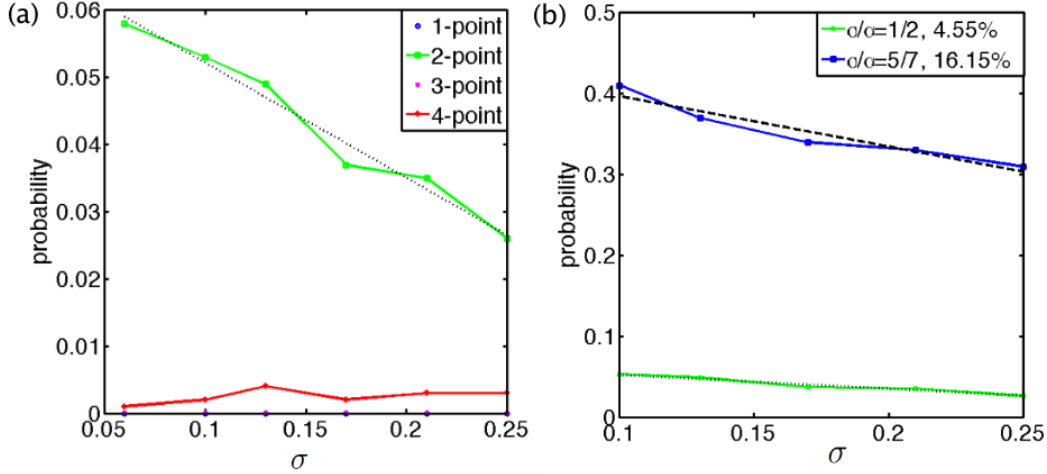


Figure 17: (a) Probability of having attractors for parameter $\sigma = 0.06, 0.10, 0.13, 0.17, 0.21$ and 0.25 with fixed $\sigma/\alpha = 0.5$ in 1000 simulations. (b) Probability of having 2-point attractors for $\sigma/\alpha = 1/2$ (1000 simulations) and $\sigma/\alpha = 5/7$ (100 simulations). The supercritical part is about 4.55% and 16.15% of the random topography, which is of length 10π .

From the graph, we can see there is no 1-point or 3-point attractor. Here is a simple explanation for this. Let $\Delta = \max |h(x)|$ the largest deviation of height, then the distance from P_1 , P_2 and B to the surface are given by $H_{P_1} = \pi + \alpha\Delta$, $H_{P_2} = \pi + \beta\Delta$ and $H_B = \pi + \gamma\Delta$ while α, β and γ are parameters that varying between -1 and 1 . From Figure 18, these three distances have a very nice relation,

$$H_{P_1} + H_{P_2} = H_B.$$

By simple algebra, we have $3\Delta > (\gamma - \alpha - \beta)\Delta = \pi$, which leads to

$$\Delta > \pi/3 \text{ or correspondingly } \sigma > \pi/9 \approx 0.35$$

since we model the topography by Gaussian process. Similar argument suggests we need $\Delta > \pi/5$ or $\sigma > \pi/15 \approx 0.21$ to have 3-point attractor. Hence for small-amplitude topography we are interested in, there is no 1-point or 3-point attractor.

The probability of having 2-point attractors increases as the value of σ decreases. This is because when we reduce the value of σ , the width of each bump also decreases. So we

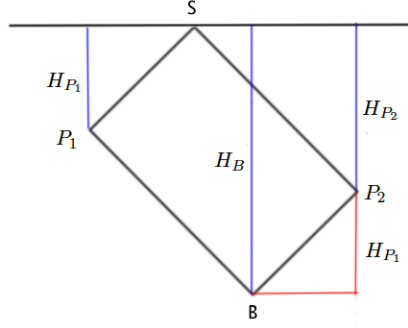


Figure 18: Showing the relation between H_{P_1} , H_{P_2} and H_B . P_1 and P_2 are two supercritical points, B is usually but not necessarily a point on the bottom while S is the surface reflection point.

tend to have more intervals and therefore more supercritical intervals. By examining the structure of 2-point attractor as in Figure 12(a), we can see that we need two supercritical points S_1 and S_2 to form the closed orbit. And they must belong to different supercritical intervals. The length of each supercritical interval may be an issue, but since what we need is only supercritical points S_1 and S_2 , we can assume the length do not have a significant effect on the probability. So if we have more supercritical intervals we tend to have a higher probability of finding 2-point attractors.

Similar arguments can also apply to 4-point attractor, because in order to form 4-point attractor, we also need two supercritical points S_1 and S_2 in different supercritical intervals. This implies the probability should increase when we reduce σ . However, from Figure 18, the probability of 4-point attractors does not show the expected increase. Two reason might account for this. One is the statistical error. From the graph, the existence of 4-point attractors is a rare event, we only get roughly 2 or 3 4-point attractors in 1000 simulations. So the probability of 4-point attractors in these 1000 samples is not convincing. We need more simulations to know how the probability changes with σ . Numerical errors may also have an effect on the total number of 4-point attractors. Although we only apply the checkerboard map twice, there is still some numerical error due to linear interpolation. And attractors are delicate structures and sensitive to numerical errors.

By Figure 17(a), the probability of having 4-point attractors is much less than that of 2-point attractors. Finite length of the topography is one reason, since if considered small amplitude topography the distance between the two supercritical points S_1 and S_2 is roughly 2π for 2-point attractor and 4π for 4-point attractor. And also to form 4-point attractor, we need 6 points in the right place while we only need 4 for 2-point attractor.

We fix $\sigma/\alpha = 5/7$ which will increase the probability of supercritical part to about 16.15%, and only look at the probability of 2-point attractors for parameter value $\sigma = 0.10, 0.13, 0.17, 0.21$ and 0.25 within 100 simulations. According to our arguments that more supercritical intervals leads to higher probability of having 2-point attractors, we expect higher probability of 2-point attractors than the case for $\sigma/\alpha = 1/2$, about 4.55% supercritical part of the topography. This is confirmed in Figure 17(b). Also from the

graph, the relation between the value of σ and the probability is roughly linear. But we do not have an explanation for this so far.

5 Energy Decay

The problem we are aiming for in this project is the energy decay of internal waves caused by scattering over rugged sea-floor topography, i.e. if given mode-one incoming waves, we want to know how much energy is left in the first mode of the transmitted waves. Due to the existence of wave attractors, we only study samples without attractors by throwing away samples that contain attractors.

For random subcritical topography, there is clear evidence that the expected energy flux has exponential decay (Bühler & Holmes-Cerfon 2011) and the decay rate is defined as

$$E_1(n) = \mathbb{E}|a_1^t|^2 = e^{-\lambda_1 n}. \quad (27)$$

where n is the number of bounces on the bottom. Though not being able to derive a rigorous formula for the decay rate λ_1 , they suggest an expression for λ_1 of the form

$$\lambda_1 = \sum_{k=1}^{+\infty} k \hat{C}(k), \quad (28)$$

where $\hat{C}(k)$ is the Fourier transform of the covariance function $C(x)$. And a simpler form is valid for uncorrelated ($|C(x)| \ll C(0)$ for $x \geq 2\pi$) topography

$$\lambda_1 = \Gamma_0 \sqrt{\mathbb{E}|h|^2 \mathbb{E}|h'|^2} = \Gamma_0 \sigma^2 / \alpha, \quad (29)$$

with $\Gamma_0 = 2.5$ for Gaussian covariance function.

Our guess is that we still have exponential decay of energy flux for topography with supercritical part. To test our guess, we fix $\sqrt{\mathbb{E}|h|^2 \mathbb{E}|h'|^2} = \sigma^2 / \alpha$ since for small α , the correlation length, which is proportional to α , is small so our topography remains roughly uncorrelated. And we use $n = L_x / 2\pi$ as our variable, where L_x is the length of the random bottom topography. The parameter value we use is summarized in Table 1 and the results is given in Figure 19. The logarithmic plot clearly indicates decay of expect energy flux. (a) gives a better result than (b) mainly because the parameter α is smaller, which mean smaller correlation length and better approximation of formula (29).

σ^2/α	σ	α	supercritical part
1/22	0.10	0.22	2.79%
1/22	0.09	0.1782	4.77%
5/48	0.25	0.60	1.64%
5/48	0.20	0.384	5.49%
5/48	0.17	0.27744	10.27%

Table 1: The parameter value we use for numerical simulations.

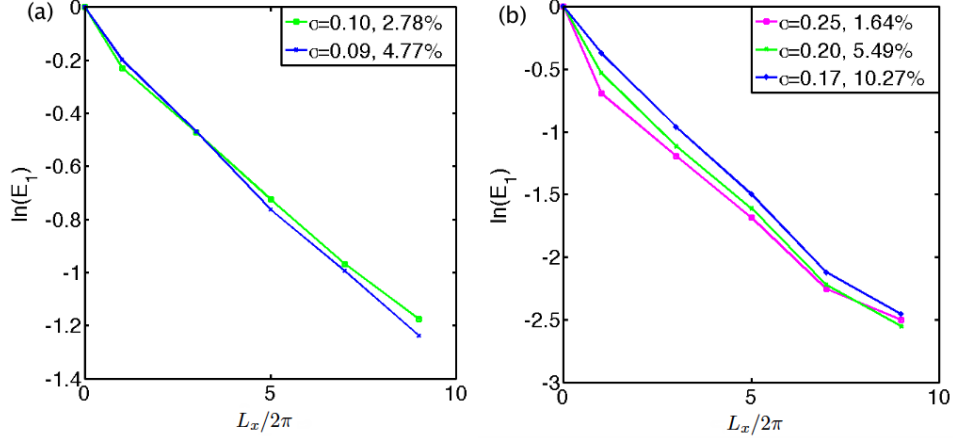


Figure 19: $\sigma^2/\alpha = 1/22$ and $5/48$, respectively. $\sigma = 0.10, 0.09, 0.25, 0.20$ and 0.17 . The expectation at each point is taken to be the average over $N = 50$ topography samples without attractors.

We can use least square method to linearly fit (Figure 20) our data points, for $\sqrt{\mathbb{E}[h]^2 \mathbb{E}[h']^2} = \sigma^2/\alpha = 1/22$ and $5/48$, we get $\lambda_1 \approx 0.132$ and 0.275 , respectively. And we can compare the decay rate we get from numerical simulations with theoretical prediction given by formula (29). The results are collected in Table 2.

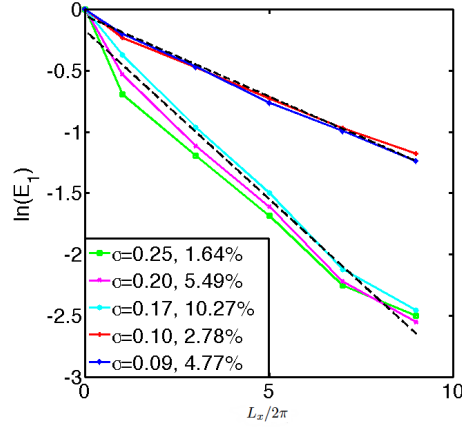


Figure 20: Linearly fit the data points by least square method.

6 Conclusion and discussions

In this project, we find a way to build checkerboard map for arbitrary smooth topography. After being able to obtain the checkerboard map we look at a spacial geometric structure—

σ^2/α	λ_1	$\lambda_1^* = \Gamma_0 \sigma^2/\alpha$	$(\lambda_1 - \lambda_1^*)/\lambda_1 \times 100\%$
1/22	0.132	5/44	13.9%
5/48	0.275	25/96	5.30%

Table 2: λ_1 is the decay rate we get from numerical simulations. λ_1^* is the predicted decay rate taken from formula (29). The last column is the relative error.

wave attractor. We find some factors that can influence the probability of having attractors and give qualitative explanation of them. But rigorous explanation is still missing. The geometric structure of the closed orbits, especially those involving more than one surface reflection points is complicated. So coming up with exact formula for the probability of multi-point attractor is difficult when the topography is generated randomly.

Also our method of finding attractors relies heavily on the checkerboard map. As mentioned in Section 3.2, obtaining the checkerboard map for supercritical topography is not easy and time consuming, so we are limited to rather short topography length (10π in our numerical simulations). Can we find a way to detect wave attractor without using the checkerboard map? After all, the topography is totally determined by its Fourier coefficients $\hat{h}(k)$. So $\hat{h}(k)$ should have some special properties to put several points in the exactly right place to form closed orbit.

We also look at decay of energy flux by using the simplest formula (29) because we can clearly see how our parameter σ and α relate to the decay rate λ_1 . Also due to the difficulties in building checkerboard map, we only look at rather short topography length, say $L_x < 9 \cdot 2\pi$. Numerical error is still an issue, since for finding the maps \mathcal{M} and \mathcal{M}^{-1} , we need to interpolate the checkerboard map several times. The existence of wave attractors forces us to discard samples that have attractors, since our current method can not deal with cases that have attractors. We need other numerical schemes, such as the Green's function to include sample with attractors. And we also need to add a little viscosity to put forward a well-posed problem. Another reason that we do not consider sample with attractors is that the existence of attractors might lead to significant different energy decay mechanism, just like what happens in Figure 10. And we can't explain the exponential decay rigorously.

7 Acknowledgments

This project is done in the Geophysical Fluid Dynamics Program at Woods Hole Oceanographic Institution. I want to thank directors of this year Charles Doering, Oliver Bühler and Colm Caulfield for organizing such a wonderful program. I would also like to thank my summer supervisor Miranda Holmes-Cerfon for her great patience, valuable advice and indispensable help during the whole summer. And of course, special thanks to Prof. Oliver Bühler for recommending me such a nice summer program.

References

- [1] BALMFORTH, N. J., SPIEGEL, E. A. & TRESSER, C. 1995 Checkerboard maps. *Chaos* **5**(1), 216-226
- [2] BELL, T. H. 1975 Statistical features of sea-floor topography. *Deep-Sea Res.* **22**(12), 883-892.
- [3] BÜHLER, O. & HOLMES-CERFON, M. 2011 Decay of an internal tide due to random topography in the ocean. *J. Fluid Mech.* **678**, 271-293.
- [4] ECHEVERRI, P., YOKOSHI, T., BALMFORTH, N. J., & PEACOCK, T. 2011 Tidally generated internal-wave attractors between double ridges. *J. Fluid Mech.* **669**, 354-374.
- [5] GOFF, J. & JORDAN, T. 1988 Stochastic modeling of seafloor morphology: inversion of sea beam data for second-order statistics. *J. Geophys. Res.* **93** (B11), 13589-13608.
- [6] GRIMSHAW, R., PELINOVSKY, E. & TALIPOVA, Y. 2010 Nonreflecting internal wave beam propagation in the deep ocean. *J. Phys. Oceanogr.* **40**(4), 802-813.
- [7] HIDA, T. & HITSUDA, M. 1993 Gaussian processes, representation and applications. *Amer. Math. Soc.*
- [8] HOLMES-CERFON, M. personal notes on generating stationary Gaussian random fields.
- [9] MASS, L. R. & LAM, F. P. 1995 Geometric focusing of internal waves. *J. Fluid Mech.* **300**, 1-41.
- [10] MÜLLER, P. & LIU, X. B. 2000a Scattering of internal waves at finite topography in two dimensions. Part I. Theory and case studies. *J. Phys. Oceanogr.* **30**(3), 532-549.
- [11] NIKURASHIN, M., & FERRARI, R. 2010 Radiation and dissipation of internal waves generated by geotropic motions impinging on small-scale topography: application to the southern ocean. *J. Phys. Oceanogr.* **40**, 2025-2042.
- [12] YAGLOM, A. M. 1962 An introduction to the theory of stationary random functions. *Dover*.

The effect of upwelling and downwelling on turbulent entrainment in a surface stress-driven flow

Vamsi K Chalamalla

September 30, 2012

1 Introduction

Turbulent entrainment and mixing is an important phenomenon in many geophysical flows. The study that we consider here is relevant to the deepening of the oceanic mixed layer due to the turbulent motions created and sustained by various external processes such as wind, convection due to surface cooling and heating, breaking waves and tides. Ekman transport is a phenomenon observed in the ocean [1], where the balance between the drag due to the surface winds and the coriolis force results in a net transport 90° to the direction of wind. The direction of transport i.e towards the coast or away from the coast depends on the direction of wind and the direction of coriolis force. Coastal upwelling occurs when Ekman transport moves surface waters away from the coast. Surface waters are replaced by cooler and denser water from below. Similarly when Ekman transport moves surface waters towards the coast, water piles up near the coast and sinks resulting in downwelling.

The primary objective of this experimental study is to understand the effect of upwelling and downwelling on the shear driven turbulent entrainment. We consider an idealized study, with a two-layer fluid of different initial densities forced by a rotating disc . There has been many studies in the past exploring the turbulent entrainment and mixing process due to some external forcing in the absence of upwelling/downwelling. The most relevant to the present study are Shravat *et al.*[2], Boyer *et al.*[3] and Davies *et al.* [4]. [3] studied the evolution of a mixed layer in a two-layered fluid forced by a rotating disc at the bottom of a cylindrical tank. The basic assumption made in this study is that the rate of work done at the interface is proportional to the rate of increase of potential energy of the system. Another core assumption made in [3] is that the characteristic velocity in the mixed layer remains constant, leading to a conclusion that the depth of the mixed layer increases with time. A primarily experimental study of evolution of two-layer stratified fluid in a cylindrical tank forced at the surface by a horizontal rotating disc has been considered in [2]. They proposed two-theoretical models

1. Constant-velocity ‘V’ model, based on the assumption made by [3]
2. Constant power ‘P’ model , based on the energetics of the system.

The experimental observations from this study are compared with both the theoretical models and concluded that the rate of increase of mixed layer depth decrease with time, which

is in variance with the assumptions made in [3] .

The theoretical models proposed in [2] are taken as reference to compare our experimental results in the present study. A detailed discussion of these theoretical models will be taken up in subsequent sections below. The experimental setup is discussed in section 2 followed by observations in section 3 and finally the concluding remarks in section 4.

2 Experimental setup

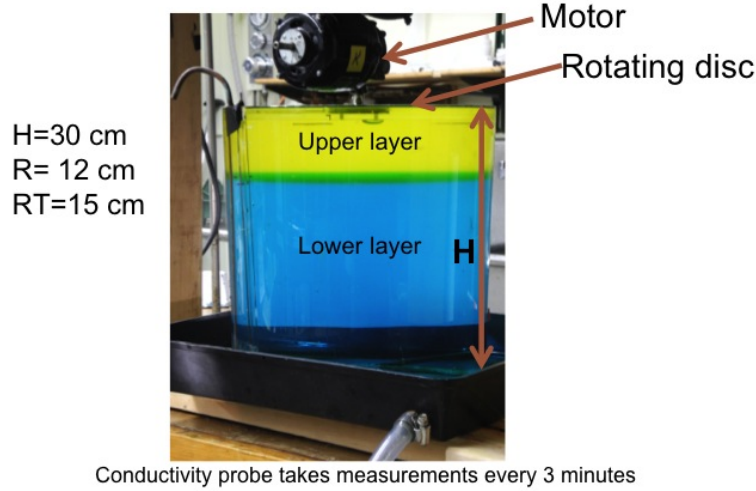


Figure 1: Experimental setup: Cylindrical tank with radius $R_T = 15$ cm and rotating disc of radius $R = 12$ cm.

Figure 1 shows the experimental setup. It has a cylindrical tank of radius 15 cm and a circular disc of radius 12 cm. The total height of the tank H is 30 cm. The tank is filled with two layers of fluid with densities ρ_{U0} (upper layer) and ρ_L (lower layer) with $\rho_L > \rho_{U0}$. The initial density difference between the two layers $\rho_L - \rho_{U0} = \Delta\rho_0 \ll \rho_L$ so that the Boussinesq approximation is valid. The initial depth of the upper layer is denoted by h_0 . The conductivity probe moves up and down within the thin gap between the rotating disc and the edge of the cylinder. The probe moves down by 33 cm from its initial position stopping at 1 cm above the bottom of the tank. The conductivity probe takes a total of 3300 measurements with 100 measurements per each cm, moving vertically with a speed of 5 mm/s. Conductivity measurements are taken only during the downward movement of the probe to avoid contamination of the data by the wake created due to the motion of the probe. The probe takes approximately 1 minute for the downward pass and 1 minute for the upward return pass to the initial position and the wait time between each pass is slightly less than 1 minute. So, the conductivity profiles are available with an interval of 3 minutes at every point in the path of the probe. Density is computed based on these conductivity measurements. The rotating disk is controlled by a motor, shown in figure 1. The vertical position of the disc is adjusted before the experiment such that it is just below the surface of upper layer. The lower and upper layer fluids are dyed with different colors to visualize

the interface between the two layers. All the fluids used in the experiment were stored for couple of days before the experiment to ensure that there is no temperature difference between the fluids, which may result in unnecessary convective motions. To calibrate the probe, the conductivity of upper layer, the lower layer and an equal mixture of lower and upper layer fluids has been measured before and after the experiment. There is little drift in the probe measurements for the experiments which lasted for shorter duration (2 hours). For experiments which lasted more than 3 hours, there is some considerable drift in the probe measurements and the profiles has been corrected keeping the lower layer density constant (i.e ρ_L measured at a later time has been corrected to match with the ρ_L measured at $t=0$). The disc starts rotating as soon as the conductivity probe starts its second profile. Since it takes some time for the rotating disc to spin up the upper layer, we define the zero time for our experiments as 3 minutes after the disc starts rotating. Three different scenarios have been considered in our experiments. Firstly, a standard no-flux experiment with no upwelling or downwelling is considered i.e $Q_B = 0$. The second scenario is the upwelling experiment. Denser fluid is pumped into the tank using a micropump at a volumetric rate $Q_B > 0$ from bottom of the tank. As fluid starts filling up from below, it pushes up the entire fluid in the tank with an average upward velocity given by Q_B/A , where A is the cross-section of the tank given by πR_T^2 . The excess water in the tank overflows from above, which is collected into a tray in which the cylindrical tank is placed as shown in the schematic of the experiment. The third scenario is the downwelling experiment, where the lower layer (denser) fluid is sucked out the tank at a rate $Q_B < 0$ by reversing the direction of the micropump. Simultaneously, fluid of density ρ_{U0} is pumped into the upper layer at the same rate, resulting in a downward velocity (Q_B/A) for the entire volume of the fluid.

3 Experimental results

Table 1 shows the list of different experiments done in our present study. The parameters which are varied in this study are initial density difference between two layers $\Delta\rho_0$, rotation rate of the disc Ω and the initial upper layer depth h_0 . A positive value of Q_B represents an upwelling experiment and negative values of Q_B represents downwelling experiments. When $Q_B = 0$, there is no upwelling or downwelling, we refer to this experiment as no-flux experiment in the following sections.

We observe that the rotating disc at the surface sets the upper layer into turbulent motion, since the Reynolds number in the flow defined by $Re = UR/\nu \equiv \Omega R^2/\nu$ is of the order of 20,000. We do not measure fluid velocities in our experiments, so we do not have quantitative details of the velocity field in the upper layer. But, from previous studies and also the direct observation by looking at the experiment, there is an evidence of large scale circulation in the upper layer as shown schematically in figure 2. There is a mean flow in the upper layer with velocities in the azimuthal and radial directions apart from the turbulent velocities. Fluid particles near the surface are pushed away towards the walls, due to the rotation of the disc. Also, shadowgraph images (which we discuss in more detail below) shows that there is a dome-like structure near the center of the tank at the interface, showing the upward motion of denser fluid as discussed in [3] and [2]. So the fluid particles which are pushed towards the walls at the center come down along the wall, setting up a

<i>Experiment</i>	$Q_B(cc/s)$	$\Delta\rho_0(g/cc)$	$\Omega rad/s$	$h_0(cm)$	$H(cm)$	Symbol
$DL\Delta\rho_{01}\Omega 2h_{01}$	-0.59	0.01782	2	10	30	\triangle
$DH\Delta\rho_{02}\Omega 2h_{01}$	-1.18	0.02382	2	10	30	+
$DL\Delta\rho_{02}\Omega 2h_{01}$	-0.59	0.02382	2	10	30	+
$DL\Delta\rho_{02}\Omega 3h_{01}$	-0.59	0.02382	3	10	30	+
$N\Delta\rho_{02}\Omega 2h_{01}$	0	0.02382	2	10	30	+
$N\Delta\rho_{03}\Omega 2h_{01}$	0	0.03782	2	10	30	\circ
$N\Delta\rho_{04}\Omega 2h_{01}$	0	0.05082	2	10	30	\square
$N\Delta\rho_{03}\Omega 3h_{01}$	0	0.03782	3	10	30	\circ
$N\Delta\rho_{02}\Omega 2h_{02}$	0	0.02382	2	13.5	27	+
$UL\Delta\rho_{01}\Omega 2h_{01}$	0.59	0.01782	2	10	30	\triangle
$UL\Delta\rho_{02}\Omega 2h_{01}$	0.59	0.02382	2	10	30	+
$UL\Delta\rho_{04}\Omega 2h_{01}$	0.59	0.05082	2	10	30	\square
$UL\Delta\rho_{03}\Omega 2h_{01}$	0.59	0.03782	2	10	30	\circ
$UL\Delta\rho_{04}\Omega 3h_{01}$	0.59	0.05082	3	10	30	\square
$UL\Delta\rho_{02}\Omega 2h_{03}$	0.59	0.02382	2	15	30	+
$UH\Delta\rho_{02}\Omega 2h_{01}$	1.18	0.02382	2	10	30	+
$UH\Delta\rho_{04}\Omega 2h_{01}$	1.18	0.05082	2	10	30	\square
$UH\Delta\rho_{03}\Omega 2h_{01}$	1.18	0.03782	2	10	30	\circ

Table 1: Dimensional parameters of the experiments.

return circulation.

The turbulent motions in the upper layer ensure that the fluid in the upper layer is well mixed. As time progresses, the density difference between the two layers decreases as the denser fluid in the lower layer is lifted up against gravity and mixed into the upper layer. Meanwhile, the upper mixed layer grows deeper with time, with a sharp interface between the two layers. All these turbulent motions and the circulation are confined to the upper layer, while the lower layer remains quiescent during the experiment, since the density jump across the interface suppresses the fluid motion to be penetrated into the lower layer. We show the characteristic thickness of the interface d_I in figure 2. The variation in the interfacial thickness is observed to be very little between different experiments, so it is assumed to be a constant in our calculations. An important non-dimensional parameter in this study is the bulk Richardson number given by

$$Ri_B = \frac{g'_U h_U}{\Omega^2 R^2}, \quad (1)$$

where h_U is the depth of the upper layer, $g'_U = g(1 - \bar{\rho}_U/\rho_L)$ is the reduced gravity of the upper layer. Another non-dimensional parameter which is relevant to this study is the interfacial Richardson number defined as,

$$Ri_I = \frac{g'_U d_I}{u_U^2} \equiv \frac{g'_U h_U}{u_U^2 h_U} d_I, \quad (2)$$

where u_U is the characteristic velocity of the upper layer.

The bulk Richardson number Ri_B is a measure of balance between the strength of overall stratification and the external forcing. While the interfacial Richardson number Ri_I represents the balance between a local measure of stratification and shear across the interface. We are particularly interested in how the entrainment depends on the local and bulk parameters of the flow. We define layer richardson number for the mixed layer Ri_L as

$$Ri_L = \frac{g'_U h_U}{u_U^2}, \quad (3)$$

which is based on the mixed (upper) layer depth and the characteristic velocity of the upper layer.

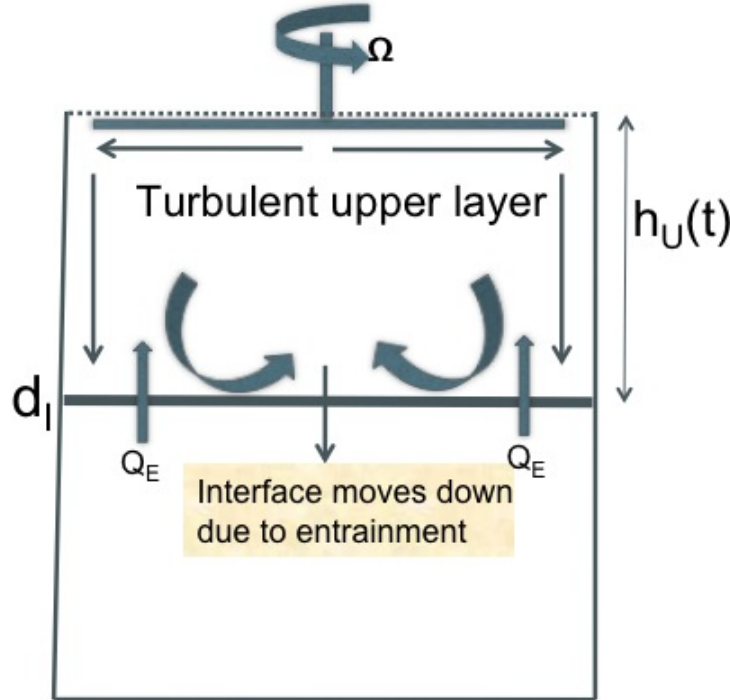


Figure 2: Schematic showing the flow in the upper mixed layer

The blue solid line in the figure 3 shows a typical density profile from the experiment. Normalized density $\hat{\rho}$ is plotted against depth,

$$\hat{\rho} = \frac{\rho - \rho_{U0}}{\rho_L - \rho_{U0}}, \quad (4)$$

Where ρ_{U0} is the initial upper layer density and ρ_L is the density of lower layer, which doesn't change during the experiment. The average of the upper layer and lower layer

densities is calculated and the depth corresponding to the averaged density is considered as the upper(mixed) layer measured from the surface. The red dot shown in the figure represents this interface location. An important assumption made to calculate the interface depth is that the density in the lower layer, i.e below the interface is ρ_L . Actually, it is not exactly true as evident from the density profile (solid line). Due to the secondary mixed layer (as discussed in more detail by [6]) formed just below the interface the average density of the lower layer is slightly below ρ_L , which results in some error which can be quantified from the experimental and the theoretical density profiles.

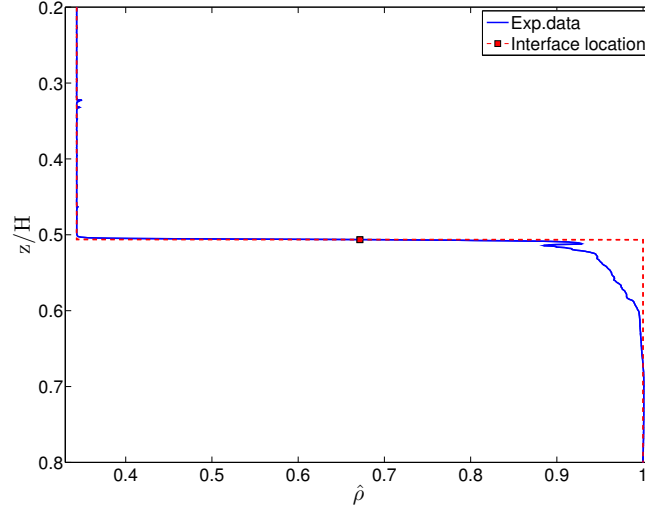


Figure 3: Figure showing the typical density profile from the experimental data. The red dot represents the interface density which is obtained by averaging the density of the upper layer ρ_U and lower layer ρ_L

3.1 Previous theoretical models

As discussed in the introduction of this report, two models were proposed by [2] to study the evolution of mixed layer in a initial two-layered fluid forced by a rotating disc at the surface of mixed layer. The power supplied at the interface in terms of the interfacial stress is given by

$$\mathcal{P} = \pi R^2 c_D \rho_L u_U^3, \quad (5)$$

where c_D is an empirically determined drag coefficient, u_U is the characteristic-velocity of the upper mixed layer and R is the radius of the disc.

The potential energy of the system defined in [2] is given by,

$$\mathbb{PE} = \pi R^2 \left(-g \int_0^{h_U} \rho_U z dz - g \int_{h_U}^H \rho_L z dz + \frac{g \rho_L H^2}{2} \right) \equiv \pi R^2 \rho_L \frac{g'_{UH} h_U^2}{2} \quad (6)$$

According to the assumption that, $\frac{d}{dt}\mathbb{P}\mathbb{E} \propto \mathcal{P}$, we obtain

$$\frac{d}{dt}h_U \propto \frac{u_U^3}{g'_U h_U}, \quad (7)$$

Defining $\frac{d}{dt}h_U$ as the entrainment velocity u_E as discussed in [2]. It is important to remember that [2] discussed no-flux experiments i.e when $Q_B = 0$. More generalized formula for the entrainment velocity will be defined in the later section.

$$u_E \propto \frac{u_U^3}{g'_U h_U}. \quad (8)$$

Now defining the entrainment parameter as u_E/u_U , the entrainment parameter scales with richardson number as

$$\frac{u_E}{u_U} \propto \frac{1}{Ri_L}. \quad (9)$$

From the above equation, the entrainment parameter scales with the inverse of Richardson number for no-flux experiments. In the subsequent sections, we will try to fit our experimental data with this scaling, to check if the data for upwelling and downwelling experiments agrees with it.

To compare the experimental data with the theoretical models, a rescaled time variable was defined in [2] as

$$\tau_* = \frac{R}{h_0} \frac{c_V}{Ri_B} \tau, \quad (10)$$

where τ is the non-dimensional time given by $\tau = \Omega t$, c_V is an empirically determined constant.

V-model is based on the assumption made by [3], that the characteristic velocity in the upper layer remains constant and it scales with the velocity induced by the rotating disc which $R\Omega$. Based on these arguments, the non-dimensional mixed layer depth $\hat{h}_U = h_U/h_0$ varies with τ_* as

$$\hat{h}_U = 1 + \tau_* \quad (11)$$

However, P-model proposed by [2] argue that the constant power input from the rotating disc cannot maintain a constant velocity in the upper layer considering the energetics of the system. They propose that, as the mixed layer deepens more volume of fluid needs to be energized continuously by the rotating disc. The power input from the disc should be balanced by a rate of increase of kinetic energy, the viscous dissipation and the power required to mix the fluid. If a constant velocity in the mixed layer is assumed, then the kinetic energy of the upper layer (discussed in more detail by [2]) given by

$$\mathbb{KE} = \frac{1}{2} \rho_L \pi R^2 h_U u_U^2, \quad (12)$$

increases continuously, so the dissipation of kinetic energy also increases. This is not possible to maintain with a constant power input from the disc, leading to an assumption that the kinetic energy of the upper layer remains constant. Using this assumption, the time evolution of the mixed layer depth \hat{h}_U is given by,

$$\hat{h}_U = (1 + 5\tau_*/2)^{2/5} \quad (13)$$

Figure 4 shows the evolution of interface depth for one of the no-flux experiments with $\Delta\rho = 0.03782g/cc$ and $\Omega = 2s^{-1}$, $h_0 = 10$ cm. The non-dimensional depth $\hat{h}_U = h_U/h_0$ is plotted against τ_* . The black line represents the *P model*, the red line represents the experimental data and the blue line represents the *V model*. Initially, the non-dimensional mixed layer depth increases linearly with time. Since for small τ_* , the P-model reduces to V-model (by neglecting the higher order terms in the expansion), it is difficult to distinguish between P-model and V-model during the initial times. But as time progresses the rate of increase of mixed layer depth is not constant but clearly decreases following the *P model*.

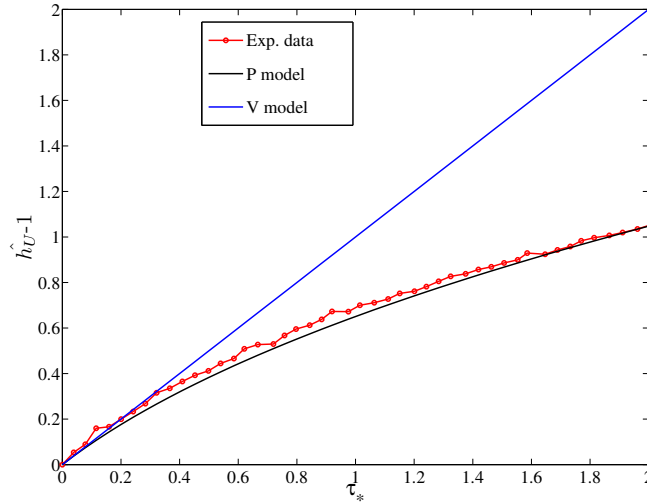


Figure 4: Time evolution of upper layer depth: \hat{h}_U plotted against τ_* . Comparison of experimental data with the theoretical models.

3.2 Equations for upwelling experiment ($Q_B > 0$)

In general, the equation for the rate of mass change in the cylinder is given by,

$$\pi R_T^2 \frac{d}{dt} \left(\bar{\rho}_U h_U + \rho_L (H - h_U) \right) = \rho_L Q_B - \bar{\rho}_U Q_B \quad (14)$$

$$\implies \pi R_T^2 \frac{d}{dt} \left(g \left(\frac{\rho_L - \bar{\rho}_U}{\rho_L} \right) h_U \right) = -g \left(\frac{\rho_L - \bar{\rho}_U}{\rho_L} \right) Q_B \quad (15)$$

$$\implies \pi R_T^2 \frac{d(g'_U h_U)}{dt} = -g'_U Q_B. \quad (16)$$

The equation for the rate of volume change of the upper layer is given by,

$$\pi R_T^2 \frac{dh_U}{dt} = Q_E - Q_B \quad (17)$$

where Q_E is the volumetric entrainment rate across the interface.

Substituting (17) into (16), we obtain an expression for volumetric entrainment rate across the interface Q_E , given by

$$Q_E = -\pi R_T^2 h_U \frac{1}{g'_U} \frac{dg'_U}{dt} \equiv \pi R_T^2 \frac{dh_U}{dt} + Q_B \quad (18)$$

Now, generalizing the definition of entrainment velocity u_E as the volumetric entrainment flux Q_E divided by the cross-section area of the tank,

$$u_E = \frac{dh_U}{dt} + Q_B/(\pi R_T^2). \quad (19)$$

It is important to note that this definition of the entrainment velocity is valid for no-flux ($Q_B = 0$), upwelling ($Q_B > 0$) and downwelling ($Q_B < 0$) experiments.

3.3 Equations for downwelling experiment ($Q_B < 0$)

The equation for the rate of mass change in the cylinder is given as,

$$\pi R_T^2 \frac{d}{dt} \left(\bar{\rho}_U h_U + \rho_L (H - h_U) \right) = \rho_L Q_B - \bar{\rho}_{U0} Q_B \quad (20)$$

$$\implies \pi R_T^2 \frac{d}{dt} \left(g \left(\frac{\rho_L - \bar{\rho}_U}{\rho_L} \right) h_U \right) = -g \left(\frac{\rho_L - \bar{\rho}_{U0}}{\rho_L} \right) Q_B \quad (21)$$

$$\implies \pi R_T^2 \frac{d(g'_U h_U)}{dt} = -g'_U Q_B. \quad (22)$$

As already noted by [2], for no-flux experiments where $Q_B = 0$, $g'_U h_U$ remains constant (mass conservation) i.e the bulk richardson number defined in (1) remains constant. However for upwelling and downwelling experiments mass is not conserved since we are adding external fluid into the tank, and so the bulk Richardson number Ri_B changes during the experiment thus giving us a scope to study the entrainment process over a range of Richardson numbers by performing a single experiment. Specifically, for upwelling experiments since $Q_B > 0$, $g'_U h_U$ decreases and so the bulk Richardson number Ri_B decreases whereas for downwelling experiments, Ri_B increases during the experiment.

It is important to note that for downwelling experiments, fresh water of density ρ_{U0} is added continuously from the top. Mathematical representation of this addition is given by the second term on the R.H.S of (20). Whereas in upwelling experiments the volume of fluid flowing out of the tank has density ρ_U (density of the mixed upper layer), as evident from the second term in R.H.S of (14).

Substituting (17) into (22), we obtain the expression for volumetric entrainment rate across the interface Q_E , given by

$$Q_E = Q_B \left(1 - \frac{g'_{U0}}{g'_U} \right) - \pi R_T^2 h_U \frac{1}{g'_U} \frac{dg'_U}{dt} \equiv \pi R_T^2 \frac{dh_U}{dt} + Q_B \quad (23)$$

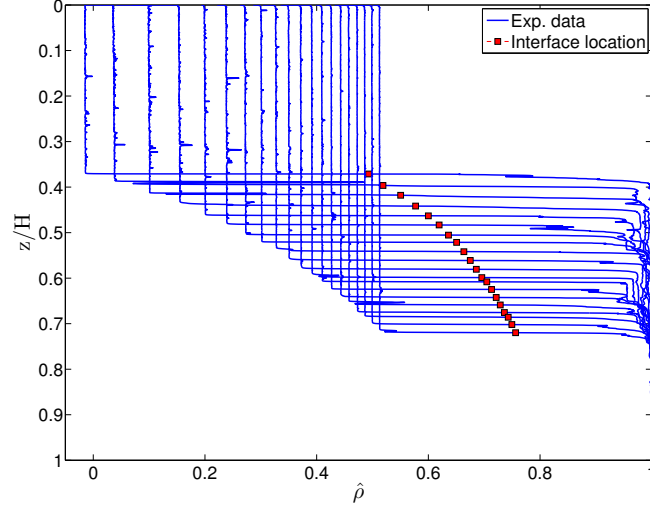


Figure 5: Plots of $\hat{\rho}$ against z/H for an experiment with $\Omega = 2 \text{ rad s}^{-1}$, $\Delta\rho = 0.02382\text{g/cc}$, $Q_B = 0$ Starting with $t=0$, profiles are shown with a time interval of 9 minutes. Experiment $N\Delta\rho_0\Omega 2h_{01}$ shown in table 1

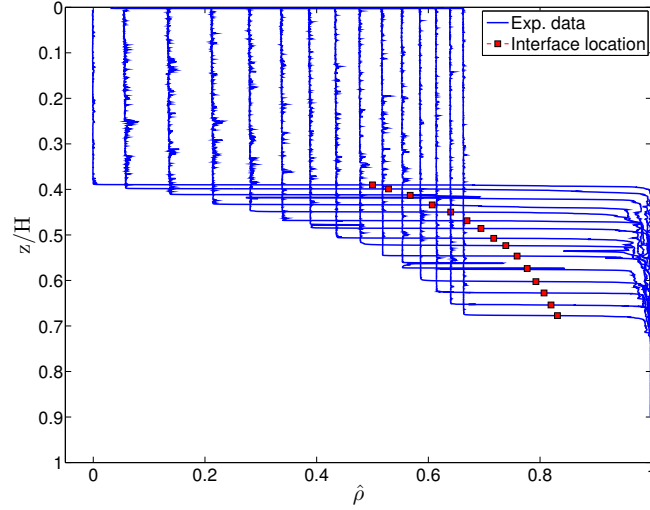


Figure 6: Plots of $\hat{\rho}$ against z/H for an experiment with $\Omega = 2 \text{ rad s}^{-1}$, $\Delta\rho = 0.02382\text{g/cc}$, $Q_B = 0.59 \text{ cc/s}$. Starting with $t=0$, profiles are shown with a time interval of 9 minutes. Experiment $UL\Delta\rho_0\Omega 2h_{01}$ shown in table 1

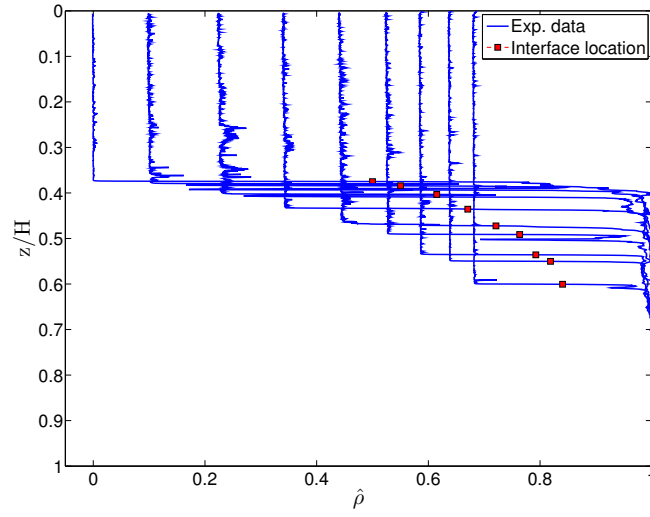


Figure 7: Plots of $\hat{\rho}$ against z/H for an experiment with $\Omega = 2 \text{ rad s}^{-1}$, $\Delta\rho = 0.02382\text{g/cc}$, $Q=1.18 \text{ cc/s}$. Starting with $t=0$, profiles are shown with a time interval of 9 minutes. Experiment $UH\Delta\rho_{02}\Omega 2h_{01}$ shown in table 1

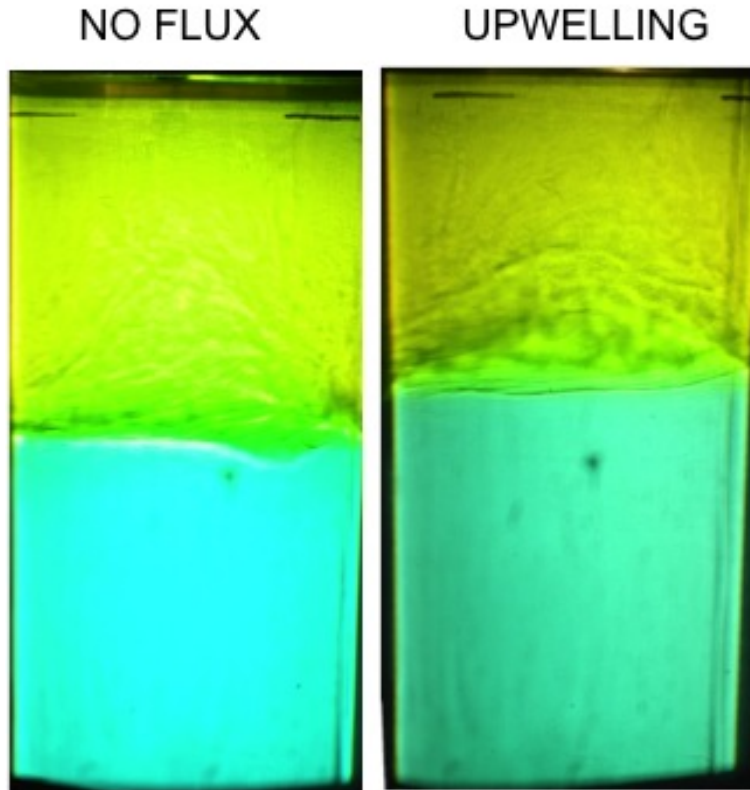


Figure 8: Shadowgraph images of the upwelling and no-flux experiments at a particular time.

Figure 5 shows plots of normalized density profiles of a no-flux experiment with $\Omega = 2 \text{ rad s}^{-1}$, $\Delta\rho = 0.02382\text{g/cc}$, $Q_B = 0$. Density profiles are shown at different time instances starting with $t=0$ (3 minutes from the time disc started rotating). Time goes from left to right in this figure i.e the left most profile is time $t=0$. The time interval between each profile is 9 minutes (every 3 profiles). Red square shaped dots shown in the figure represent the location of interface. As time progresses, the interface moves down, and the density difference between the two layers decreases.

There are four important things to note here,

1. The interface between the two layers is sharp, similar to ‘scouring’ observed by Woods *et al.* (2000) [5],
2. the upper layer is well homogenized (mixed),
3. The interface depth is clearly not varying linearly with time,
4. A secondary relatively thin mixed layer is observed just below the interface, with the density closer to the lower layer density.

Overturning is observed near the interface at certain times indicating a possibility of Kelvin-Helmholtz instability at the interface. Figure 6 shows density profiles for an upwelling experiment with $Q_B = 0.59\text{cc/s}$. The important qualitative difference between the no-flux and upwelling experiment profiles is that the magnitude of density fluctuations in the mixed layer seems to be higher in the upwelling experiment and also the density overturnings at the interface seems to be more frequent in the upwelling experiment. Similarly, figure 7 shows density profiles for an upwelling experiment with $Q_B = 1.18\text{cc/s}$. The density fluctuations seems to be even higher and also the density overturnings are more frequent and intense. Also, the density difference between the two layers is dropping quickly in the case of upwelling experiments compared to the no-flux experiment. Quantitative discussion of these differences will be discussed in the sections below. Figure 8 show the shadowgraph images of the upwelling and no-flux experiments at a particular time instant. Though the images are not very clear, it is apparent that there is more turbulent activity in the upper layer of upwelling experiment, confirming the qualitative differences observed in the density profiles.

Similar comparison between the no-flux and upwelling experiments for different density differences ($\Delta\rho = 0.03782, 0.05082\text{g/cc}$) show the identical qualitative differences observed above, suggesting that this phenomenon is a feature of any upwelling flow irrespective of the range of Richardson numbers. However, there will be quantitative differences in the entrainment rate and the rate of increase of mixed layer depth as the density difference get higher, due to the fact that the entrainment becomes difficult as the stratification grows stronger. A detailed quantitative analysis is required to determine whether this phenomenon is observed independent of the Richardson number. Quantitative comparison of density variance and the entrainment rate is discussed in detail in the following sections.

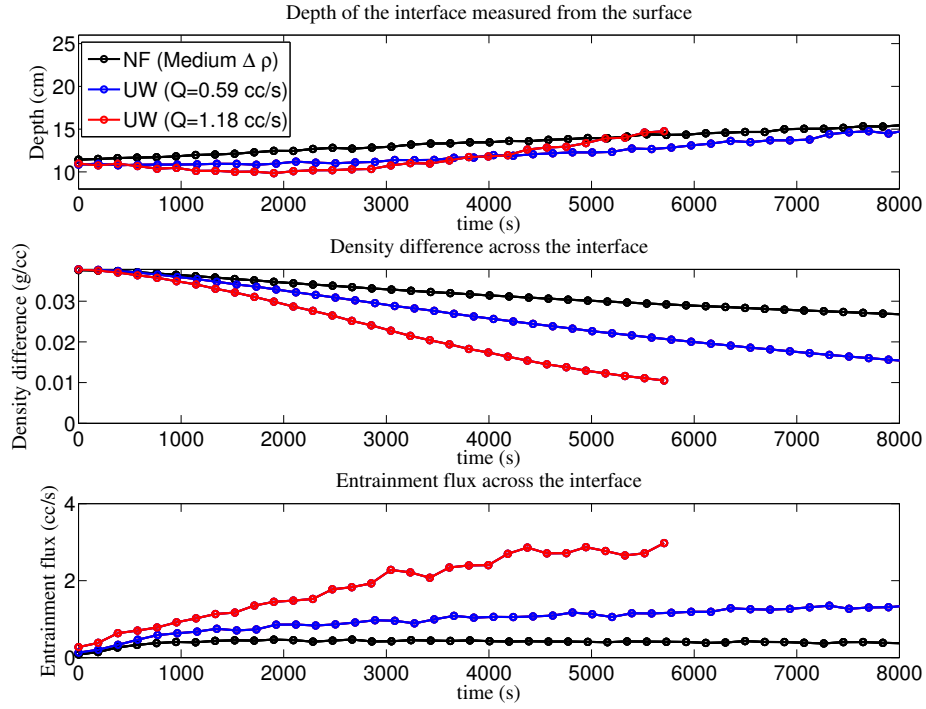


Figure 9: Plots showing the quantitative comparison of no-flux and upwelling experiments $\Omega = 2 \text{ rad s}^{-1}$, $\Delta\rho = 0.03782\text{g/cc}$, $Q_B = (0, 0, 59, 1.18) \text{ cc/s}$. (a) Time evolution of upper layer depth (b) Time evolution of density difference between the upper and lower layer. (c) Time evolution of volumetric entrainment flux Q_E across the interface as defined in (18).

Figure 9 is shown here to explain the quantitative differences between the no-flux and upwelling experiments. Figure 9(a) shows the interface depth plotted against time. Figure 9(b) shows the density difference between the two layers plotted against time and finally figure 9(c) shows the volumetric entrainment rate (defined in (18)) plotted against time. The black line represents the no-flux experiment. Red and blue lines represent upwelling experiments with different upwelling rates Q_B . Initially, the rate at which the depth of the mixed layer increases is slower for upwelling experiments when compared with the no-flux experiment. This is due to the fact that $Q_B > 0$ for upwelling experiments and from equation (17), since Q_B appears with a negative sign on the R.H.S of the evolution equation for mixed layer depth, it decreases the growth rate of mixed layer depth. When $Q_B = 1.18 \text{ cc/s}$, i.e when the upwelling rate is higher, the initial evolution of mixed layer depth shows that $\frac{dh_U}{dt} < 0$ because the upwelling rate Q_B dominates the volumetric entrainment flux Q_E across the interface. But, at a later time, the entrainment flux increases and is higher in upwelling experiments when compared with the no-flux experiment as shown in figure 9(c). As a result, the rate of increase of mixed layer depth is higher for upwelling experiments when compared with the no-flux experiment, as evident from the later time evolution shown in figure 9(a).

Another important quantitative difference to note between the upwelling and no-flux experiment is the rate at which the density difference between two layers drops. For upwelling experiments, the rate of decrease of density difference is higher and it increases with Q_B . This can be attributed to the higher entrainment rate in the upwelling experiments, because more entrainment occurs when the density difference across the interface is relatively weak.

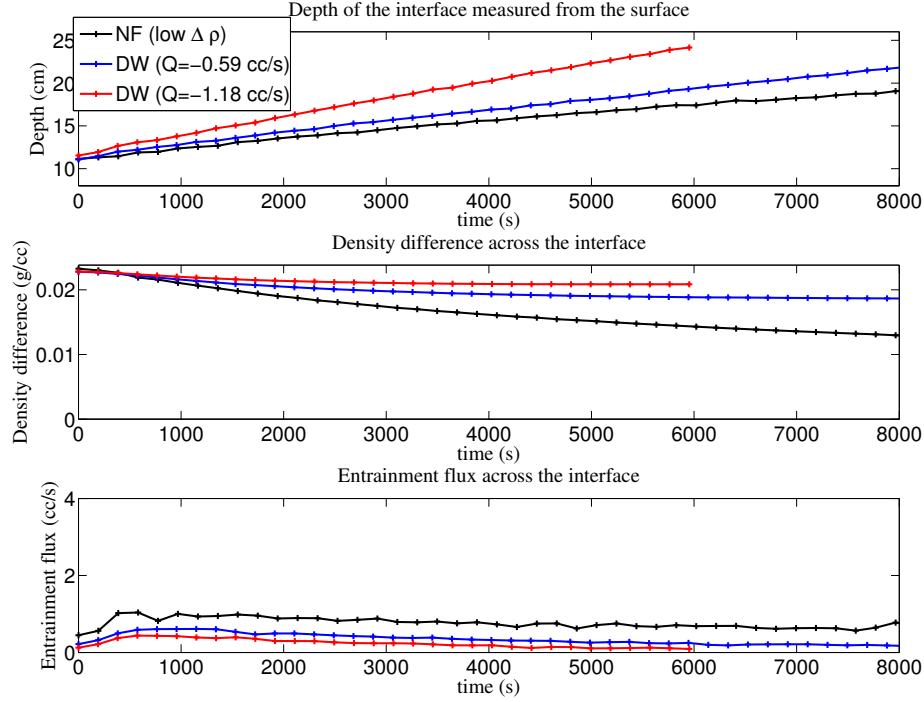


Figure 10: Plots showing the quantitative comparison of no-flux and downwelling experiments $\Omega = 2 \text{ rad s}^{-1}$, $\Delta \rho = 0.02382 \text{ g/cc}$, $Q_B = (0, -0.59, -1.18) \text{ cc/s}$. (a) Time evolution of upper layer depth (b) Time evolution of density difference between the upper and lower layer. (c) Time evolution of volumetric entrainment flux Q_E across the interface as defined in (23).

Figure 10 is shown here to explain the quantitative differences between the no-flux and downwelling experiments. Figure 10(a) shows the interface depth plotted against time, figure 10(b) shows the density difference between the two layers plotted against time and finally figure 10(c) shows the volumetric entrainment rate (defined in equation 11) plotted against time. The black line represents the no-flux experiment. Red and blue lines represent downwelling experiments with different Q_B . Here, the time evolution of mixed layer depth shows that the higher the value of Q_B , higher the rate of increase of mixed layer depth as evident from figure 10(a). Since $Q_B < 0$ for downwelling experiments, from equation (17), it is evident that this term increases the rate of increase of mixed layer depth. Figure 10(b) shows that the rate at which the density difference between two layers drops is slower compared to the upwelling experiments shown in figure 9(b). Also, the volumetric entrainment rate shown in figure 10(c), suggest a reverse trend as compared to the upwelling experi-

ments i.e higher the downwelling rate, lower the volumetric entrainment flux Q_E . However, difference between volumetric entrainment rates of no-flux and downwelling experiments is not as significant as observed in the upwelling experiments. The quantitative analysis of upwelling and downwelling entrainment rates will be discussed in detail in the subsequent sections.

Figure 11 shows the time averaged density variance in a semi log plot plotted against Q_B . Time averaged density variance is given by,

$$\text{Time averaged density variance } \langle \langle \rho'^2 \rangle_z \rangle_t = \frac{1}{T} \frac{1}{(h_U - 2)} \int_{t=0}^T \int_1^{h_U-1} [\rho'(z, t)]^2 \quad (24)$$

where $\rho'(z, t) = \rho(z, t) - \bar{\rho}_U(z)$ is the fluctuating component of the density field, $\bar{\rho}_U(z)$ represents the time average density of the upper (mixed) layer. T is the duration of the experiment. Spatial averaging is done in the upper layer, starting at a depth 1 cm below the surface and stopping at 1 cm above the interface. 'Δ' symbol represents the lowest $\Delta\rho$ considered in our experiments which is 0.01782 g/cc, '+' symbol represents $\Delta\rho = 0.02382$ g/cc, 'o' represents $\Delta\rho = 0.03782$ g/cc and '□' represents the highest density difference which is 0.05082 g/cc. Black and grey color represents no-flux experiments, red and magenta represents downwelling experiments, blue and cyan represent upwelling experiments. As discussed in the previous sections, turbulent fluctuations appear to be higher in the upwelling experiments. The density variance plot shown here quantify the turbulent fluctuations. Clearly, there seems to be a trend in the density variance when plotted against Q_B . It is important to remember that $Q_B > 0$ represents upwelling experiments, $Q_B < 0$ represents downwelling experiments and $Q_B = 0$ represents no-flux experiments. As Q_B goes from negative to positive values, in general the density variance increases significantly. Clearly, the density variance is highest for upwelling experiments with higher Q_B , which suggests that the turbulent fluctuations increase with increasing upwelling rate. However there are two exceptions in the figure with red colored 'Δ' and magenta colored '+'. High density variance is observed in these experiments because of the fact the initial density difference is low in these experiments (see table 1) and also the rotation rate is higher in one of these experiments (magenta colored '+').

The reason for higher turbulent fluctuations in upwelling experiments can be explained using the reynolds stress terms. For example, considering a fluid particle in an upwelling experiment. The fluid particle which is below the interface, due to the vertical velocity induced by the upwelling is moving from static flow field into a turbulent (mixed layer) flow field. As a result, the fluid particle tends to resist the motion resulting in negative u' (fluctuating horizontal velocity), which makes the product $-u'w' > 0$, increasing the reynolds stresses. Evolution equation for turbulent kinetic energy is given by

$$\frac{d(TKE)}{dt} = P - \epsilon + B - \frac{\partial T'_i}{\partial x_j} \quad (25)$$

where P is the turbulent production term given by $-\langle u'w' \rangle \frac{d\bar{U}}{dz}$. Since the mean flow gradi-

ent $\frac{d\bar{U}}{dz} > 0$ the turbulent production term is positive, thus increasing the turbulent kinetic energy.

Now considering the evolution equation for density variance

$$\frac{d(\langle \rho'^2 \rangle)}{dt} = P_\rho - \epsilon_\rho - \frac{\partial T'_{\rho i}}{\partial x_j} \quad (26)$$

where P_ρ is the scalar production term given by $-\langle \rho' w' \rangle \frac{d\bar{\rho}}{dz}$. Since the mean density gradient across the interface $\frac{d\bar{\rho}}{dz} < 0$, fluctuating vertical velocity $w' > 0$ (discussed above) and the density fluctuation ρ' is observed to be positive, the scalar production term is positive, contributing to the increase in density variance.

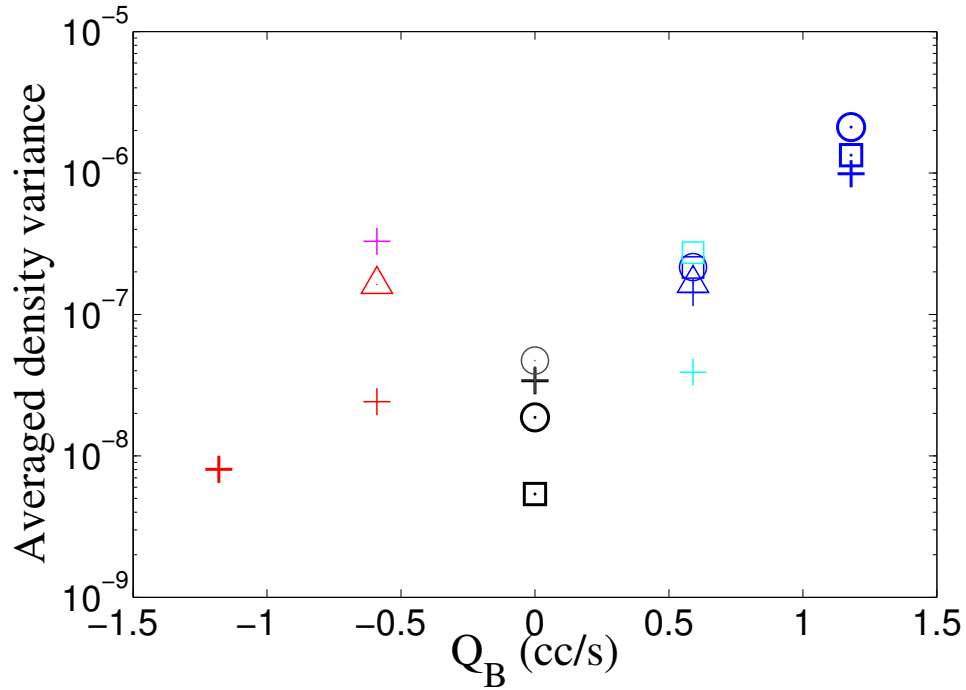


Figure 11: Plot showing the time-averaged density variance for all the experiments.

Figure 12 shows the entrainment parameter defined in (9) plotted against τ_* . Thick solid blue colored lines represent upwelling experiments with $Q_B = 1.18$ cc/s, thin blue/cyan colored lines represent upwelling experiments with $Q_B = 0.59$ cc/s. Red/magenta colored lines represent downwelling experiments. Black/grey colored lines represent no-flux experiments. For all the downwelling and no-flux experiments, the entrainment parameter increases and reaches almost a steady value at a later time. For upwelling experiments with $Q_B = 0.59$ cc/s, the entrainment parameter increases initially and appears to reach a steady value at a later time which is greater than the time taken for no-flux experiments. However at $Q_B = 1.18$ cc/s, the time span for which we have the experimental data, the entrainment hasn't reached a steady value. Another important thing to notice in this figure is that,

for all the downwelling and no-flux experiments, the entrainment parameter appears to be reaching an approximately same steady value irrespective of the initial density difference. Similarly, for upwelling experiments with $Q_B = 0.59$ cc/s, the entrainment parameter seems to be reaching a steady value of approximately 1. For all upwelling experiments with $Q_B = 1.18$ cc/s, the entrainment parameter seems to be reaching a steady value of approximately 2×10^{-4} , which is double the steady value for $Q_B = 0.59$ cc/s. This suggests that, the entrainment parameter may scale with the upwelling rate Q_B , irrespective of the initial density difference. However, due to the large scatter in the data presented in this figure, it is difficult to come to a conclusion regarding the scaling of entrainment parameter with Q_B .

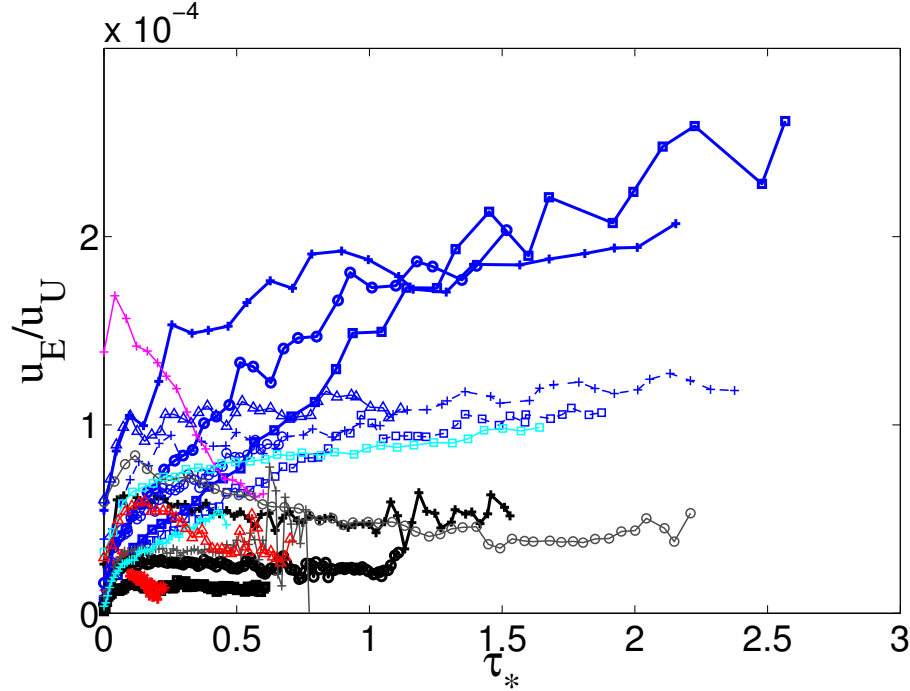


Figure 12: Plots of entrainment parameter plotted against τ^* for all the experiments.

Figure 13 shows the entrainment parameter for all the downwelling and no-flux experiments plotted against $1/Ri_L$ which is defined as

$$1/Ri_L = \frac{u_U^2}{g'_U h_U} \equiv \frac{u_U^2 h_U}{g'_U h_U^2} \propto \frac{\text{KE}}{\text{PE}}, \quad (27)$$

For no-flux experiments, since the denser fluid is continuously lifted up and mixed, the potential energy is expected to increase. Also for downwelling experiments, lighter fluid is added at a greater height and heavier fluid which is at lower height is taken out and also there is entrainment process where the work is done to lift the heavy parcel up. The net change in potential energy of the system during this process is observed to be positive resulting in an increase of potential energy of the system for downwelling and no-flux

experiments. So from figure 13, since x-axis represent the ratio of kinetic energy to the potential energy, time goes from right to left. The experimental data shown in figure 13 seems to fit well with the black solid straight line shown in the same figure, suggesting that the scaling law derived above is valid i.e entrainment parameter is proportional to $1/Ri_L$. So, the entrainment dynamics is dependent on the bulk parameters of flow rather than the local flow dynamics.

In upwelling experiments, the heavier fluid is added into the tank at a lower height (which increases potential energy), whereas the mixed layer fluid overflows out of the tank at a greater height (which reduces potential energy), and also there is an increase in potential energy due to the turbulent entrainment. The net change in potential energy observed in upwelling experiments is negative, thus reducing the potential energy of the system. Figure 14 shows the data from upwelling experiments plotted along with the no-flux and downwelling experiments. For upwelling experiments, since the potential energy of the system is observed to decrease, time goes from left to right in figure 14, whereas the time goes from right to left for all downwelling and no-flux experiments. It is evident from the figure that the entrainment parameter for the upwelling experiments does not obey the same scaling as the downwelling and no-flux experiments, since there is clear deviation as the time progresses. The reason for this deviation from the standard scaling is probably due to the fact the turbulent fluctuations in the upwelling experiments are higher, resulting in different entrainment and interfacial dynamics.

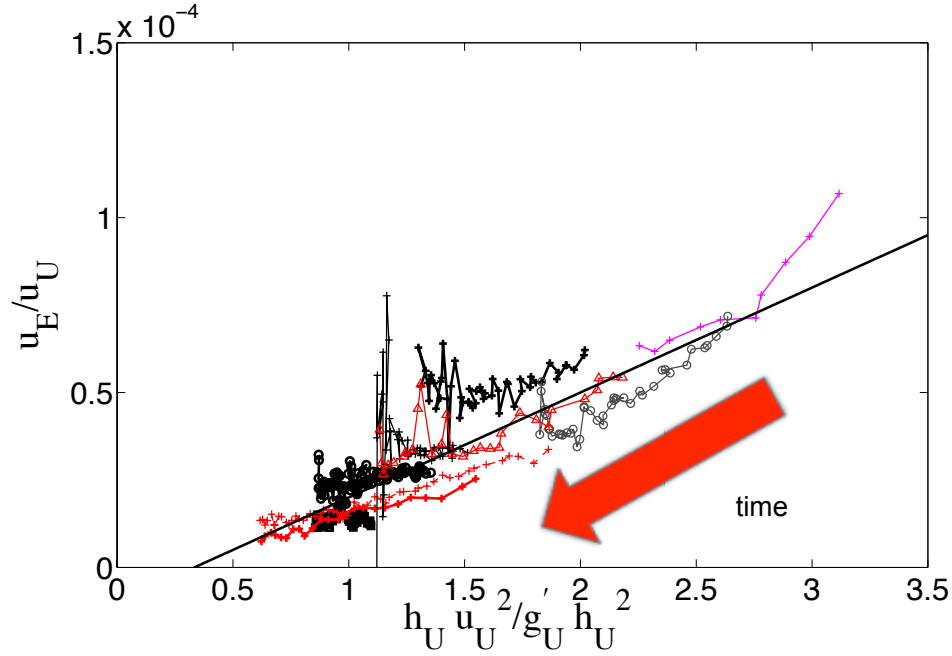


Figure 13: Plots of entrainment parameter plotted against $1/Ri_L$ for all the downwelling and no-flux experiments.

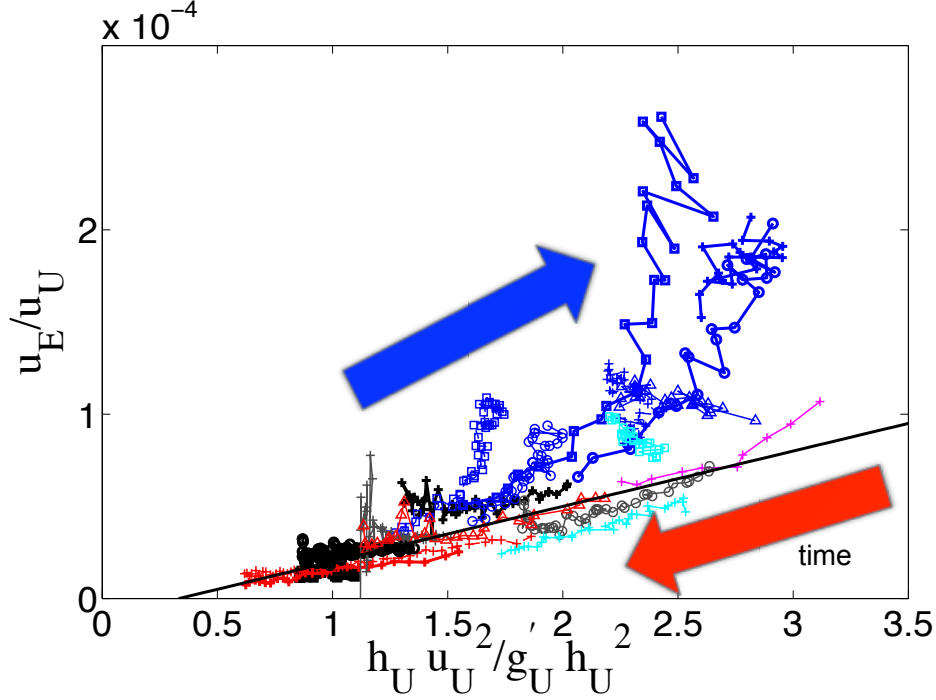


Figure 14: Plots of entrainment parameter plotted against $1/Ri_L$ for all the experiments.

4 Conclusions

We have conducted an experimental study to consider the effect of upwelling and downwelling on the shear-driven turbulent entrainment. Different controlling parameters involved in this study are disc rotation rate Ω , initial upper layer depth h_0 , initial density difference $\Delta\rho_0$. Upwelling and downwelling experiments were performed considering two different flow rates $Q_B = 0.59, 1.18$ cc/s. The layer Richardson number Ri_L as defined in (3) varies from 0.3 to 2. The density profiles for standard no-flux experiments shows that the mixed layer depth does not vary linearly with time, rather its rate of increase drops at later time following the P-model. Qualitative and quantitative analysis of our experimental results show that the upwelling experiments are observed to be qualitatively different with measurably enhanced turbulent fluctuations leading to new and increased entrainment rate. This increase in entrainment rate is probably due to the higher turbulent fluctuations and density variance. A clear trend is observed for time averaged density variance when plotted against Q_B , i.e density variance increases monotonically as Q_B increases. The increase in turbulent fluctuations in upwelling experiments is due to the enhanced reynolds stresses induced by the upwelling. As explained in section 3 above, the upwelling results in the increased scalar and turbulent production terms thus increasing the turbulence and net transport across the interface. Monotonic increase in density variance with Q_B is because the vertical velocity w' increases with Q_B resulting in higher scalar production term.

The entrainment parameter u_E/u_U as defined in (9) for upwelling experiments does not

obey the standard scaling law, which states that the entrainment parameter u_E/u_U is proportional to $1/Ri_L$. Standard scaling suggests that the entrainment rate across the interface is dependent solely on the bulk parameters of the upper layer, rather than the interfacial Richardson number which is the measure of ratio of the local stratification strength and the velocity drop across the interface. Since, for upwelling experiments the entrainment rate is not a function of the layer Richardson number and also the density variance is dependent on the upwelling rate Q_B , more detailed analysis is needed consider the upwelling rate Q_B along with the Richardson number to come up with a scaling law.

Downwelling does not seem to influence the entrainment dynamics significantly. It is evident from the fact that the density variance is low, when compared with the no-flux experiments and also the entrainment parameter obeys the standard scaling law. Since the experiments are performed in lab (small) scale, the relevance of these experimental results in oceanic scales is not clear and needs better understanding through numerical simulations and observational studies in the ocean.

Acknowledgements

This study was part of the Geophysical Fluid Dynamics Program at Woods Hole Oceanographic Institution. I would like to thank Colm Caulfield and Claudia Cenedese for advising me on this project . Also, I would like to thank all the GFD staff and fellows for making this program a memorable experience.

References

- [1] Knauss, J.A., Introduction to Physical Oceanography, Waveland Press. Second Edition. 2005, c1997
- [2] Shravat, A., Cenedese, C. & Caulfield, C. P. 2012. Entrainment and mixing dynamics of surface-stress-driven stratified flow in a cylinder. *J. Fluid Mech.*, 691, 498-517.
- [3] Boyer, D. L., Davies, P. A. & Guo, Y. 1997. Mixing of a two-layer stratified fluid by a rotating disc. *Fluid Dyn. Res.*, 21, 381-401.
- [4] Davies, P. A., Guo, Y., Boyer, D. L. & Folkard, A. M. 1995. The flow generated by the rotation of a horizontal disk in a stratified fluid. *Fluid Dyn. Res.*, 17, 27-47.
- [5] Woods, A. W., Caulfield, C. P., Landel, J. R. & Kuesters, A. 2010. Non-invasive turbulent mixing across a density interface in a turbulent Taylor-Couette flow. *J. Fluid Mech.*, 663, 347-357.
- [6] Georgy Manucharyan , Dynamics of the mixed layers in stratified shear flows, GFD summer program 2010.

Equatorial Quasi-Geostrophy

Felicity S. Graham

November 1, 2012

1 Introduction

The changing sign of the Coriolis force across the equator causes the dynamics of equatorial waves to be quite different from that of the mid- to high-latitudes. The waves that are found in this region play an important role in the El Niño - Southern Oscillation (ENSO) [23; 24; 29], the Madden-Julian Oscillation [17; 30], and in the exchange of energy from the equatorial region to the midlatitudes. Hence, it is important that their dynamics and evolution are well understood. The inviscid, linearized shallow water equations on an equatorial β -plane have been used to study equatorially trapped Kelvin, inertio-gravity and Rossby waves [1; 8; 19; 21]. Furthermore, the effect of nonlinearity on equatorial waves in the context of the shallow water equations has been described by Boyd, in a series of papers in the 1980s [2; 3; 4; 5]. Boyd found solitary wave solutions for the weakly dispersive long Rossby modes as well as for the strongly dispersive Rossby, inertio-gravity and mixed Rossby-gravity modes and also characterized the effect of nonlinearity on the weakly-dispersive (where the effects of nonlinearity dominate over dispersion) Kelvin mode.

While the shallow water equations have been quite successful in understanding the dynamics of the equatorial region, they are nonetheless an approximation to the full nonlinear primitive equations and neglect some physics that are potentially important in the equatorial region. In the present work, we investigate a nonlinear, equatorial quasi-geostrophic model that includes the vertical component of momentum as well as the non-hydrostatic effect, with the aim of extending the work of Boyd in understanding the dynamics and evolution of nonlinear equatorial waves.

The quasi-geostrophic approximation [6; 7] is useful for studying flows with characteristic timescales of a day or more, thus filtering out high-frequency motions. One underlying assumption of the quasi-geostrophic approximation is that the Rossby number, which measures the relative importance of inertial to rotational motion in the momentum equations, is small. The Rossby number is defined as $Ro = U/2\Omega L$, where U and L are characteristic velocities and lengths, respectively. In the “traditional approximation”, the rotation vector Ω is assumed to depend only on the local vertical component, namely the Coriolis parameter $f = 2\Omega \sin \theta$, where θ is the latitude. However, in the “traditional approximation”, the Rossby number is infinite at the equator due to the vanishing of the Coriolis parameter there, rendering the quasi-geostrophic approximation invalid. While the “traditional approximation” is justifiable for problems based in the mid-latitudes [8; 28], the contribution of the local horizontal component of rotation, $2\Omega \cos \theta$, is important in applications in the

tropics [26; 28] and may be necessary for the simulation of some equatorial phenomena [10] (e.g. the Madden-Julian Oscillation).

[13] derived a nonlinear quasi-geostrophic model of the equatorial region, which takes into account the local horizontal component of rotation. Their model, denoted SNH-QGE III (Sideways Non-Hydrostatic Quasi-Geostrophic Equations type III), differs from the classical quasi-geostrophic model of fluid that is thin in the vertical, by assuming the meridional (y -direction) length scale is large compared to the zonal (x -direction) and vertical (z -direction) length scales. It follows that the leading balance in this model is between the zonal and vertical components of momentum, rather than the zonal and meridional components in the thin layer approach.

In the following section, we examine the linearized primitive equations on an equatorial β -plane and the equatorial waves they describe. Section 3 outlines the derivation of the quasi-geostrophic model SNH-QGE III from [13]. Section 4 treats the linearized version of this model, comparing to the results of the linearized primitive equations. Finally, in section 5, the nonlinear version of this quasi-geostrophic model is analyzed, following a similar procedure to that of [3]. In the case when the Brunt-Väisälä frequency is constant the waves are found to behave according to a generalized Swift-Hohenberg equation. By contrast, when the Brunt-Väisälä frequency varies with height, the waves behave according to a generalized Kadomtsev-Petviashvili equation.

2 Primitive equations

2.1 Equatorial waves

Consider the linearized, primitive equations in the following form:

$$\partial_t u' - \beta y v' + 2\Omega w' = -\partial_x p', \quad (1)$$

$$\partial_t v' + \beta y u' = -\partial_y p', \quad (2)$$

$$\partial_t w' - 2\Omega u' = -\partial_z p' - \frac{\rho' g}{\rho_r}, \quad (3)$$

$$\partial_x u' + \partial_y v' + \partial_z w' = 0, \quad (4)$$

$$\partial_t \rho' + \partial_z \bar{\rho} w' = 0, \quad (5)$$

where x is in the zonal direction, y is in the latitudinal direction, z is in the vertical direction, ρ_r is the reference density, $\bar{\rho}$ is the mean density field and ρ' is the perturbation of the density about the mean field. The zonal, latitudinal (or meridional) and vertical components of the 3-dimensional velocity field \mathbf{u} are u' , v' , and w' , respectively and p' is pressure. Apostrophes denote variables that are a function of x , y , z and t , and subscripts denote partial derivatives. The earth's rotation vector $\boldsymbol{\Omega}$ is assumed to depend on both the vertical and horizontal components, namely the Coriolis parameter $f = 2\Omega \sin \theta$ and $f_h = 2\Omega \cos \theta$, respectively. In Eqs. (1) - (5), we have assumed that the horizontal component is constant, $f_h = 2\Omega$, and f varies with latitude, $f \approx \beta y$, for constant β (this is known as the rational β -plane approximation [9]). Eqs. (3) and (5) can be combined by differentiating the former with respect to t . Taking the square of the Brunt-Väisälä frequency, $N^2 = -g\partial_z \bar{\rho}/\rho_r$, to be

constant and assuming solutions of the form $u' = u(y)e^{ikx+ilz-i\omega t}$, and similarly for v' , w' and p' , Eqs. (1) - (5) can be simplified to

$$-i\omega u - \beta y v + 2\Omega w = -ikp, \quad (6)$$

$$-i\omega v + \beta y u = -\partial_y p, \quad (7)$$

$$-i\omega w - 2\Omega u = -ilp + \frac{N^2 w}{i\omega}, \quad (8)$$

$$iku + \partial_y v + ilw = 0. \quad (9)$$

In this section we are interested in waves with frequencies less than the Brunt-Väisälä frequency, $|\omega| < N$. We proceed by eliminating u , w and p in Eqs. (6) - (9), to derive the following equation for v

$$(\omega^2 - N^2 - 4\Omega^2) \frac{d^2 v}{dy^2} - 4\Omega i \ell \beta y \frac{dv}{dy} - k^2 \left(\omega^2 \left[1 + \frac{\ell^2}{k^2} \right] - N^2 \right) v + \ell^2 \beta^2 y^2 v - \frac{k\beta}{\omega} \left(\omega^2 - N^2 + \frac{2\Omega \omega i \ell}{k} \right) v = 0. \quad (10)$$

The standard transformation $v(y) = V(y)e^{-\lambda y^2/2}$ is employed, with $\lambda = -\frac{2\Omega i \ell \beta}{\omega^2 - N^2 - 4\Omega^2}$, to eliminate the first-order derivative, and by rescaling y with $\hat{y} = y\sqrt{N^2 - \omega^2 + 4\Omega^2}$, the following simplified expression for the y -dependent component of the meridional velocity is obtained, namely

$$\frac{d^2 V}{d\hat{y}^2} - \ell^2 \beta^2 (N^2 - \omega^2) \hat{y}^2 V + \sigma V = 0, \quad (11)$$

where $\sigma = \ell^2 \omega^2 - (N^2 - \omega^2) \left(k^2 + \frac{k\beta}{\omega} \right)$. If σ is defined as

$$\sigma = \sigma_n = (2n+1)\ell\beta\sqrt{N^2 - \omega^2}, \quad \text{for } n = 0, 1, 2, \dots, \quad (12)$$

then the solutions to Eq. (11) are given by parabolic cylinder functions of order n that decay exponentially as $|y| \rightarrow \infty$, namely

$$V_n((\beta/\alpha)^{1/2}\hat{y}) = 2^{-n/2} e^{-\beta\hat{y}^2/2\alpha} H_n((\beta/\alpha)^{1/2}\hat{y}), \quad (13)$$

where H_n is the n th physicist's Hermite polynomial and $\alpha^2 = \frac{1}{\ell^2(N^2 - \omega^2)}$. It is worth noting that the local horizontal component of the earth's rotation vector has no effect on the dispersion relation Eq. (12). Once $V_n(y)$ is known, the solutions for u , w and p are easily found

$$u(y) = \frac{i}{k} \left[\left(\frac{N^2 - \omega^2 + \frac{2\Omega i \omega \ell}{k}}{N^2 - \omega^2(1 + \frac{\ell^2}{k^2})} \right) \frac{dV_n}{dy} - \frac{\beta \omega \ell^2 y}{k(N^2 - \omega^2(1 + \frac{\ell^2}{k^2}))} V_n \right], \quad (14)$$

$$w(y) = \frac{\omega}{k} \left[\frac{2\Omega - \frac{i\omega\ell}{k}}{(N^2 - \omega^2(1 + \frac{\ell^2}{k^2}))} \frac{dV_n}{dy} + \frac{i\ell\beta y}{(N^2 - \omega^2(1 + \frac{\ell^2}{k^2}))} V_n \right], \quad (15)$$

$$p(y) = \frac{i}{k} \left[\frac{\omega}{k} \left(\frac{N^2 - \omega^2 + 4\Omega^2}{N^2 - \omega^2(1 + \frac{\ell^2}{k^2})} \right) \frac{dV_n}{dy} - \left(\frac{N^2 - \omega^2 - \frac{2\Omega i \omega \ell}{k}}{N^2 - \omega^2(1 + \frac{\ell^2}{k^2})} \right) \beta y V_n \right]. \quad (16)$$

The surface height is contoured in figure 1 for the $n = 1$ mode and is overlaid with the horizontal velocity field (the u' , v' field). The zonal velocities for the modes $n = 1, 2, 3, 4$ are compared in figure 2. The direction of propagation of waves is consistent with [8] and [19]. Surfaces of constant phase for this system are given by

$$kx + \ell z + \frac{2\Omega\ell\beta\hat{y}^2/2}{\omega^2 - N^2 - 4\Omega^2} = \text{constant}. \quad (17)$$

It is clear that these constant phase surfaces are curved in the y, z plane, which differs from the planar phase surfaces in the x, y plane of the shallow water equations. This is due to the introduction of an imaginary component in the solutions from the local horizontal component of the Coriolis force, a result consistent with that of [22].

2.2 Kelvin waves

We consider the unique case in which the meridional component of the velocity vanishes - the analog of the equatorial Kelvin wave in the shallow water model. First, setting $v = 0$ in Eqs. (6) - (9), we proceed to eliminate u, w and p from these equations and solve for ω algebraically, obtaining

$$\omega^2 = \frac{N^2 k^2}{k^2 + \ell^2}, \quad (18)$$

which yields a non-trivial solution provided $\omega \neq 2\Omega ik/\ell$. The solutions $u(y)$ and $w(y)$ expressed as functions of $p(y)$ are

$$u(y) = \frac{i\ell \left(2\Omega - \frac{i\omega\ell}{k}\right)}{4\Omega^2 + \frac{N^2\ell^2}{k^2 + \ell^2}} p(y), \quad w(y) = -\frac{ik \left(2\Omega - \frac{i\omega\ell}{k}\right)}{4\Omega^2 + \frac{N^2\ell^2}{k^2 + \ell^2}} p(y). \quad (19)$$

Finally, $p(y)$ is found by solving the following equation

$$\frac{dp(y)}{dy} + b p(y) = 0, \quad \text{where} \quad b = i\ell\beta \frac{\left(2\Omega - \frac{i\omega\ell}{k}\right)}{4\Omega^2 + \frac{N^2\ell^2}{k^2 + \ell^2}}. \quad (20)$$

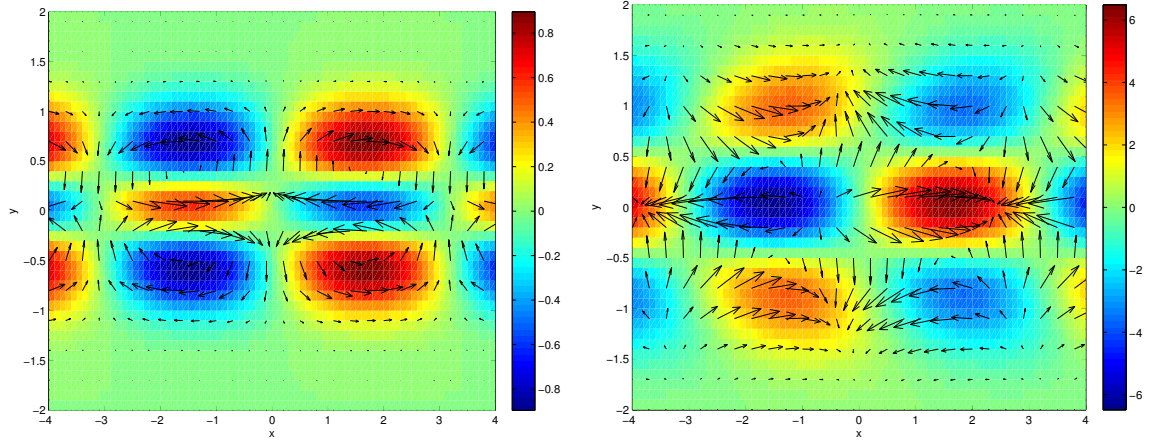
It is then clear that $p(y) = ae^{-by^2/2}$, where a is a complex constant amplitude. The p' is contoured in figure 3, with overlay of a purely zonal velocity field in arrows. Note that the meridional velocity is zero. Since we require that the waves decay meridionally north and south of the equator, the real part of b must be positive. That is,

$$\text{Re}\{b\} = \frac{\omega\ell^2\beta}{k(4\Omega^2 + \frac{N^2\ell^2}{k^2 + \ell^2})} > 0. \quad (21)$$

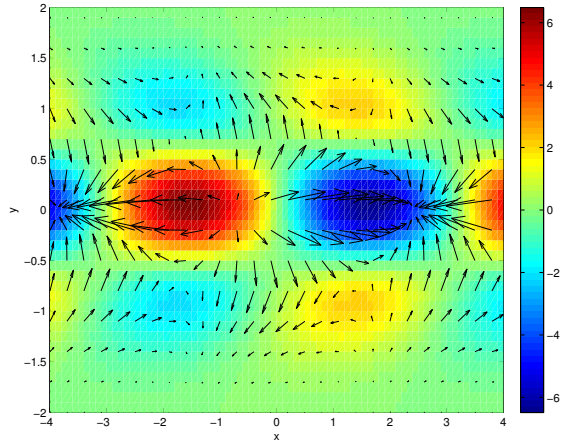
A consequence of this restriction is that ω is positive, namely

$$\omega = \frac{Nk}{\sqrt{k^2 + \ell^2}}. \quad (22)$$

Defining the phase speed as $c_{p_x} = \omega/k$ and the group velocity as $\mathbf{c}_{g_x} = \partial\omega/\partial k$, we find that this Kelvin wave has a positive zonal phase speed and a positive group velocity, and



(a) A westwards propagating Rossby wave with small positive ω , $k = -1$. (b) An eastwards propagating inertio-gravity wave with large positive ω , $k = 1$.



(c) A westwards propagating inertio-gravity wave with large positive ω , $k = -1$.

Figure 1: Pressure (surface height) in contours with overlay of the horizontal (u and v) velocity field in arrows, for $n = 1$ modes (Rossby and inertio-gravity modes) and $|\omega| < N$. The values for the constants are $\ell = 1$, $\beta = 1$, $N = 3$ and $2\Omega = 1$.

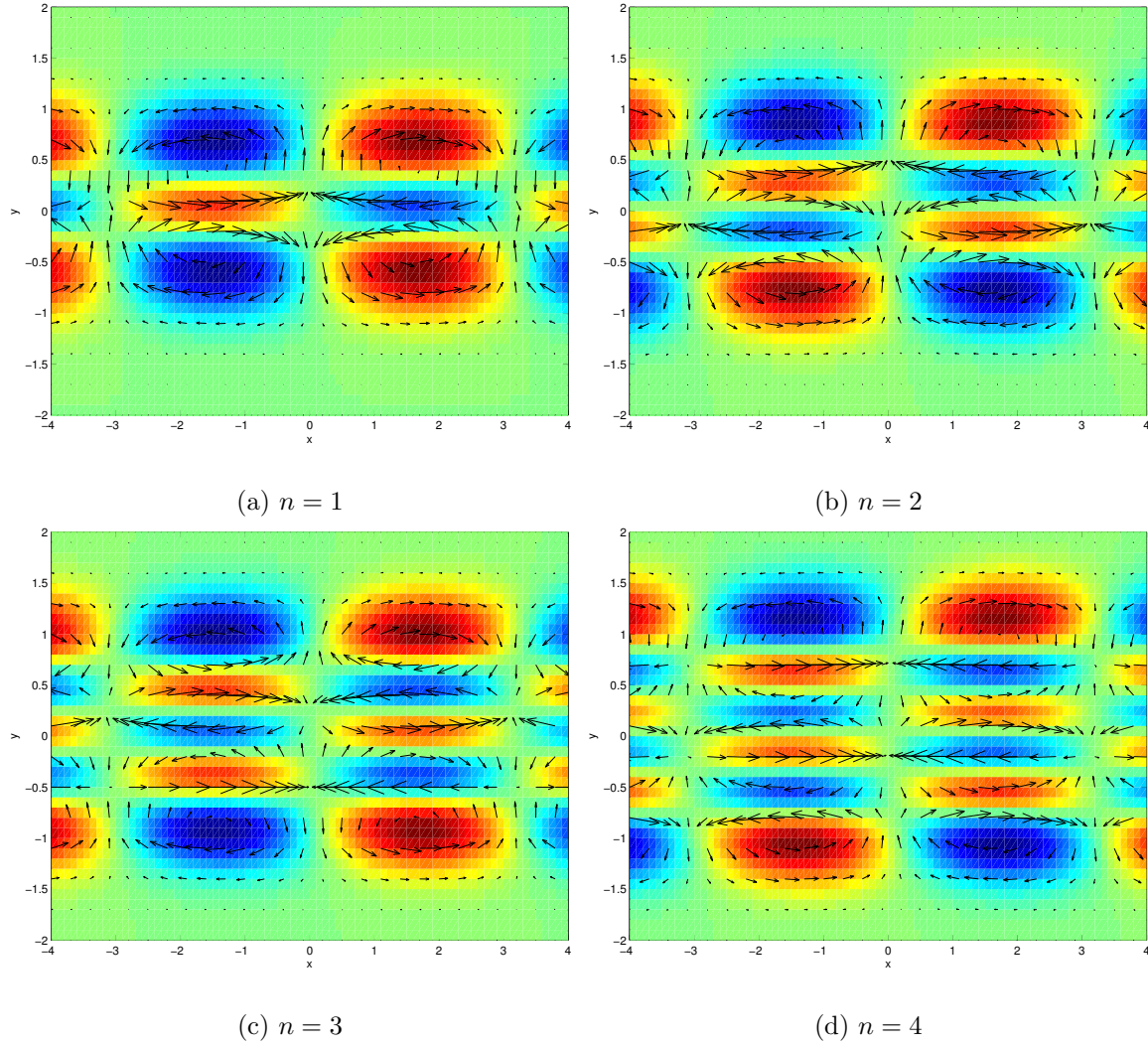


Figure 2: Pressure (surface height) in contours with overlay of the horizontal (u and v) velocity field in arrows, for a westwards propagating Rossby wave with increasing values of n , $|\omega| < N$ and $k = -1$. The values for the constants are $\ell = 1$, $\beta = 1$, $N = 3$ and $2\Omega = 1$.

hence propagates eastwards. However, the phase speed and group velocity are not equal, which means that the wave is dispersive; its shape is not conserved as the wave travels. By contrast, in the shallow water case, Kelvin waves of equivalent height H are non-dispersive; they all travel eastward with the phase speed $c = \sqrt{gH}$, which is equal to the group velocity. We deduce that the additional effects of vertical propagation and stratification, which are not present in the shallow water case, cause the Kelvin wave described by the dispersion relation in Eq. (22) to be dispersive. This result was also found by [12]. As in section 2.1, the local horizontal component of the Coriolis force has no effect on the dispersion relation for the Kelvin wave.

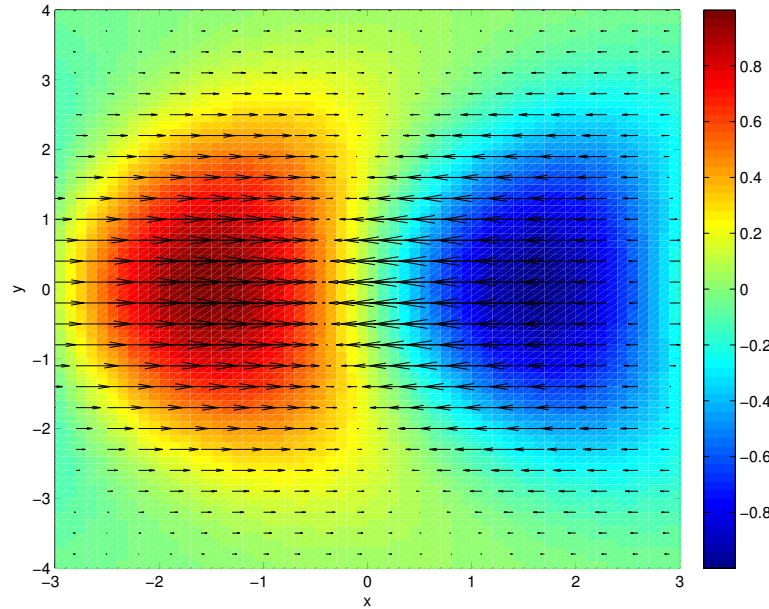


Figure 3: Pressure (surface height) in contours with overlay of the zonal velocity u field in arrows, for the “Kelvin”-like solution, for which $|\omega| < N$. The values for the constants are $k = 1$, $\ell = 1$, $\beta = 1$, $N = 3$ and $2\Omega = 1$.

2.3 Dispersion relation

The dispersion curves from Eqs. (12) and (22) are plotted in figure 4(a). The Kelvin wave is often denoted the $n = -1$ mode, although its dispersion relation comes from Eq. (22) rather than Eq. (12), as it corresponds to the unique case in which the meridional velocity is equal to zero. For the case when $n = 0$ in Eq. (12), known as the mixed Rossby-gravity mode or “Yanai” mode, two of the four solutions to the dispersion relation in Eq. (12) are $\omega = \pm \frac{Nk}{\sqrt{k^2 + \ell^2}}$. In fact, these solutions are not permitted as in deriving the solution we assumed that $\omega^2(1 + \ell^2/k^2) - N^2 \neq 0$. There are two other roots of the dispersion relation when $n = 0$: one is positive and corresponds to an eastwards propagating equatorial inertio-gravity wave, which resembles a Kelvin mode for large zonal scales; the other is negative

and corresponds to a westwards propagating wave, which resembles a Rossby wave for small zonal scales (see figure 4). The key differences between the Kelvin $n = -1$ and the eastwards propagating inertio-gravity wave $n = 0$ is that the Kelvin wave is centered on the equator and has no westwards-propagating component. In the shallow water case, an atmospheric Kelvin wave has an eastwards phase speed of $10\text{-}20 \text{ m s}^{-1}$, whereas an atmospheric inertio-gravity wave has a typical eastwards phase speed of $25\text{-}50 \text{ m s}^{-1}$ [27].

An analog to each of the waves found in figure 4(a) exists in the hydrostatic shallow water equations [8; 19]. For the Kelvin mode, the shallow water dispersion relation is

$$\omega = ck, \quad (23)$$

where $c = \sqrt{gH}$ is the gravity phase speed. When the primitive system in Eqs. (6) - (9) is strongly stratified (i.e. $|\omega| \ll N$), the dispersion relation in Eq. (12) reduces to the shallow water dispersion relation for the higher order modes, namely,

$$\frac{\omega^2}{c^2} - k^2 - \frac{\beta k}{\omega} = (2n + 1) \frac{\beta}{c}, \quad (24)$$

where $c^2 = N^2/\ell^2$ is the analog of the shallow water phase speed. It is well known (e.g. [8; 11]) that for the $n = 0$ mode the dispersion relation in Eq. (24) produces a root, $\omega = -ck$, which is spurious (this relation is assumed not to be true in the derivation of the solution). This root corresponds to a westwards propagating gravity wave; if it were valid, the solution for the meridional component of the velocity would no longer be equatorially-constrained. The key difference between the shallow water dispersion relations and those of Eqs. (12) and (22) is the presence of N^2 in the latter, which is the upper limit of the inertio-gravity, gravity and mixed Rossby-gravity mode frequencies. This is clearly illustrated in figures 4(a) and (b).

2.4 Evanescent waves

The results in the previous sections were obtained by assuming a traveling wave in the vertical direction, $e^{i\ell z}$. If we instead assume that waves decay exponentially from the height $z = 0$ so that the vertical component of u' , v' , w' and p' is given by $e^{-\ell z}$, and this time assume that $|\omega| > N$, we obtain the following solution also in terms of parabolic cylinder functions

$$u(y) = \frac{i}{k} \left[\left(\frac{\omega^2 - N^2 + \frac{2\Omega\omega\ell}{k}}{\omega^2 \left(1 - \frac{\ell^2}{k^2}\right) - N^2} \right) \frac{dV_n}{dy} - \frac{\beta\omega\ell^2 y}{k \left(\omega^2 \left(1 - \frac{\ell^2}{k^2}\right) - N^2 \right)} V_n \right], \quad (25)$$

$$w(y) = \frac{\omega}{k} \left[-\frac{2\Omega + \frac{\omega\ell}{k}}{\left(\omega^2 \left(1 - \frac{\ell^2}{k^2}\right) - N^2 \right)} \frac{dV_n}{dy} + \frac{\beta\ell y}{\left(\omega^2 \left(1 - \frac{\ell^2}{k^2}\right) - N^2 \right)} V_n \right], \quad (26)$$

$$p(y) = \frac{i}{k} \left[\frac{\omega}{k} \left(\frac{\omega^2 - N^2 - 4\Omega^2}{\omega^2 \left(1 - \frac{\ell^2}{k^2}\right) - N^2} \right) \frac{dV_n}{dy} - \left(\frac{\omega^2 - N^2 - \frac{2\Omega\omega\ell}{k}}{\omega^2 \left(1 - \frac{\ell^2}{k^2}\right) - N^2} \right) \beta y V_n \right], \quad (27)$$

where

$$V_n(\hat{y}) = \frac{2^{-n/2}}{\sqrt{\omega^2 - N^2 - 4\Omega^2}} e^{-\beta\hat{y}^2/2\alpha} H_n((\beta/\alpha)^{1/2}\hat{y}) e^{-\lambda\hat{y}^2/2}.$$

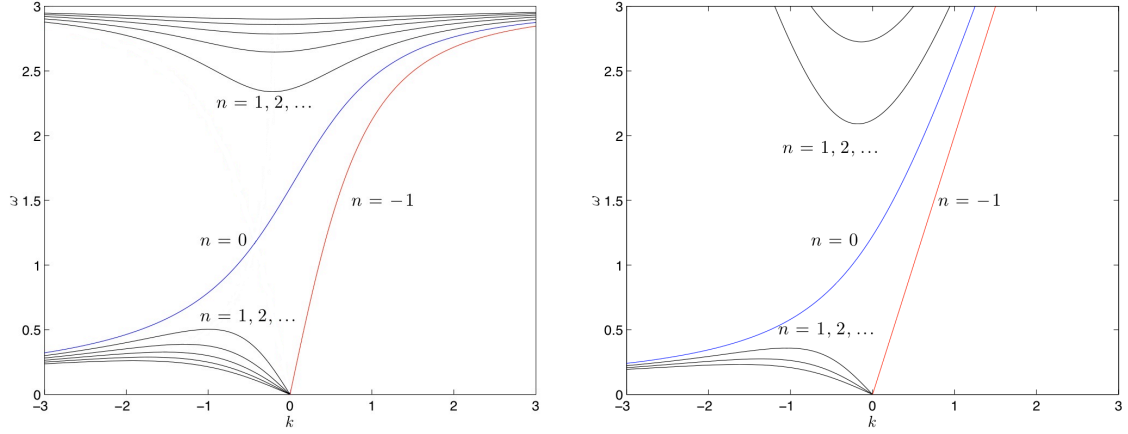


Figure 4: Dispersion curves for: (a) the non-hydrostatic primitive system; and (b) for the shallow water equations. In each figure, the red line is the Kelvin ($n = -1$) mode, refer to Eqs. (22) and (23), respectively, the blue lines are the mixed Rossby-gravity ($n = 0$) mode, refer to Eqs. (12) and (24), respectively, and the black lines are the Rossby (low-frequency) and inertio-gravity (higher-frequency) ($n = 1, 2, \dots$) modes, refer to Eqs. (12) and (24), respectively. Values for the constants are $N = 3$, $\beta = 1$ and $c = 2$.

Here, y has been scaled such that $\hat{y} = y\sqrt{\omega^2 - N^2 + 4\Omega^2}$ and the constants λ and α are defined by

$$\lambda = \frac{\ell\beta}{\omega^2 - N^2 - 4\Omega^2}, \quad \alpha^2 = \frac{1}{\ell^2(\omega^2 - N^2)}.$$

The dispersion curve for this system is

$$\omega^2 \ell^2 - (\omega^2 - N^2)(k^2 - \frac{k\beta}{\omega}) - (2n+1)\beta\ell\sqrt{\omega^2 - N^2} = 0, \quad (28)$$

which is plotted in figure 5.

2.5 Evanescent Kelvin waves

Proceeding as in section 2.4 for the case in which the meridional component of the velocity vanishes, we find that

$$\omega^2 = \frac{N^2 k^2}{k^2 - \ell^2}, \quad (29)$$

which is true provided $\omega \neq 2\Omega k/\ell$ (otherwise, as previously, we obtain the trivial solution for each of u' , w' and p'). The solution for $p(y)$ is

$$p(y) = \mu e^{-\gamma y^2/2}, \quad \text{where,} \quad \gamma = -\frac{\beta\ell(2\Omega + \frac{\omega\ell}{k})}{4\Omega^2 - \frac{N^2\ell^2}{k^2 - \ell^2}}, \quad (30)$$

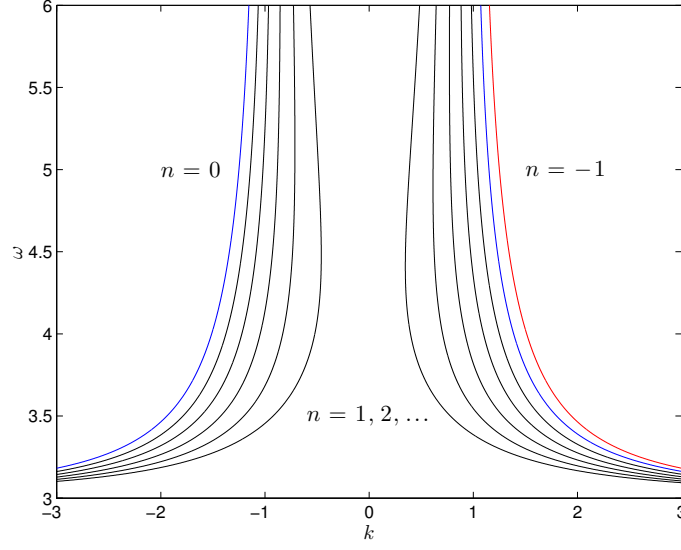


Figure 5: Dispersion curve for evanescent waves ($|\omega| > N$). The red line is the Kelvin mode, the blue lines are the $n = 0$ modes, and the black lines are the $n = 1, 2, \dots$ modes.

and μ is a complex constant. Since we require that the waves decay meridionally north and south of the equator, we must have $\gamma < 0$. Then,

$$\omega = \frac{Nk}{\sqrt{k^2 - \ell^2}}, \quad (31)$$

which is plotted in figure 5, and we assume that $k > \ell > 0$, in which case the waves propagate eastwards and vertically upwards. The solutions u and w are

$$u(y) = -\frac{\ell \left(2\Omega + \frac{\omega\ell}{k}\right)}{4\Omega^2 - \frac{N^2\ell^2}{k^2 - \ell^2}} p(y), \quad w(y) = -\frac{ik \left(2\Omega + \frac{\omega\ell}{k}\right)}{4\Omega^2 - \frac{N^2\ell^2}{k^2 - \ell^2}} p(y). \quad (32)$$

2.6 Remarks on the primitive equations

There are some clear distinctions between our results and those obtained from the hydrostatic shallow water equations on an equatorial β -plane: (i) the addition of the local horizontal component of the Coriolis force introduces an imaginary component in the solutions to the primitive equations, adds curvature to the y, z phase planes in the case when $v' \neq 0$, and adds a phase shift to the wave structure in the case when $v' = 0$; (ii) when a traveling wave is assumed in the vertical, non-hydrostatic effects modify the behavior of the inertio-gravity, gravity and mixed Rossby-gravity modes such that their frequencies are necessarily less than the Brunt-Väisälä frequency and the converse is true for evanescent waves in the vertical; and, (iii) the Kelvin mode no longer obeys the gravity phase speed $c = \sqrt{gH}$, but becomes dispersive under non-hydrostatic effects. This concludes investigation of the

linearized primitive equations; we now turn to the SNH-QGE III model, comparing the linearized version of the model with the results from this section.

3 Quasi-geostrophic Model

We briefly outline the procedure used to derive the SNH-QGE III model analyzed in the following sections. Readers are directed to [13] for a more comprehensive derivation. First, consider the Boussinesq form of the dimensional Navier-Stokes equations in the following form:

$$D_t \mathbf{u}^* + 2\Omega \hat{\boldsymbol{\eta}} \times \mathbf{u}^* = -\frac{1}{\rho_r} \nabla p^* + b^* \hat{\mathbf{z}}, \quad (33)$$

$$D_t b^* - \frac{g}{\rho_r} w^* \partial_z \bar{\rho} = 0, \quad (34)$$

$$\nabla \cdot \mathbf{u}^* = 0. \quad (35)$$

Here, $D_t = \partial_t + \mathbf{u} \cdot \nabla$ is the material derivative, \mathbf{u} is the 3-dimensional velocity vector $\mathbf{u} = (u, v, w)$, and $b = -g\rho'/\rho_r$ is the buoyancy anomaly field of density perturbations, ρ' , about the mean density field $\bar{\rho}$, where ρ_r is the reference density. The total planetary rotation vector is $2\Omega \hat{\boldsymbol{\eta}}$. We consider only motions at the equator and invoke the β -plane approximation with $\hat{\boldsymbol{\eta}} = \hat{\boldsymbol{\eta}}_0 - (y/R)\hat{\boldsymbol{\eta}}_1$, for planetary radius R , where $\hat{\boldsymbol{\eta}}_0 = (0, 1, 0)$ and $\hat{\boldsymbol{\eta}}_1 = (0, 0, -1)$. The asterisk notation in the equations above denotes a dimensional quantity. Let L be a characteristic length scale, and U a characteristic velocity and suppose that $T = L/U$ (we are interested in synoptic scale disturbances where typical values for L and U are 50–100km and 0.4–1m s⁻¹, respectively). We introduce the following non-dimensional numbers

$$\text{Rossby number: } Ro = \frac{U}{2\Omega L}, \quad \text{Reynolds number: } Re = \frac{UL}{\nu},$$

$$\text{Euler number: } P = \frac{\delta p}{U^2 \rho_r}, \quad \text{Peclet number: } Pe = \frac{LU}{\kappa},$$

$$\text{Froude number: } Fr = \frac{U}{N_0 L}, \quad \text{Buoyancy number: } \Gamma = \frac{BL}{U^2} = g \left| \frac{\delta \rho}{\rho_r} \right| \frac{L}{U^2},$$

$$\text{Buoyancy anomaly: } B = g \left| \frac{\delta \rho}{\rho_r} \right|, \quad \text{Reference stratification: } N_0 = \sqrt{\frac{g}{H_\rho}},$$

$$\text{Reference density height: } H_\rho^{-1} = \frac{|(\partial_z \bar{\rho})_r|}{\rho_r},$$

where δp is a dynamic pressure scale, N_0 is a reference stratification, $\delta \rho$ is a density scale, $(\partial_z \bar{\rho})_r$ is a reference density gradient, ν is viscosity and κ is thermal diffusivity.

The system is non-dimensionalized and then scaled in the y -direction by introducing the modulation scale $y = A_Y Y$. The β -effect also operates on this scale, so $A_\beta y \sim A_\beta A_Y Y$ and $A_\beta A_Y = \mathcal{O}(Ro)$. We define $\nabla \rightarrow \nabla_\perp + A_Y^{-1} y \partial_Y$, where $\nabla_\perp = \hat{\mathbf{x}} \partial_x + \hat{\mathbf{z}} \partial_z$. We are interested in flows with characteristic time scales greater than a day, and as such, consider small Rossby numbers ($Ro \sim 1/10$). Write $Ro \equiv \epsilon \ll 1$ and choose the spatial scales

$$A_Y = \epsilon^{-1}, \quad A_\beta = \beta \epsilon^2, \quad P = \epsilon^{-1}, \quad \Gamma = 1,$$

assuming that $\beta \sim \mathcal{O}(1)$. Introducing asymptotic expansions of the form

$$u = u_0 + \epsilon u_1 + \epsilon^2 u_2 + \dots, \quad (36)$$

$$v = v_0 + \epsilon v_1 + \epsilon^2 v_2 + \dots, \quad (37)$$

$$w = w_0 + \epsilon w_1 + \epsilon^2 w_2 + \dots, \quad (38)$$

$$p = p_0 + \epsilon p_1 + \epsilon^2 p_2 + \dots, \quad (39)$$

$$b = b_0 + \epsilon b_1 + \epsilon^2 b_2 + \dots, \quad (40)$$

the leading order set yields geostrophic balance and continuity on the x, z plane, given by

$$\hat{\boldsymbol{\eta}} \times \mathbf{u}_0 = -\nabla_{\perp} p_0, \quad \text{and}, \quad \nabla_{\perp} \mathbf{u} = 0, \quad (41)$$

respectively. The next order set is

$$D_t^0 \mathbf{u}_0 - \beta Y \hat{\boldsymbol{\eta}}_1 \times \mathbf{u}_0 + \hat{\boldsymbol{\eta}}_0 \times \mathbf{u}_1 = -\nabla_{\perp} p_1 - \partial_Y p_0 \hat{\mathbf{y}} + b_0 \hat{\mathbf{z}}, \quad (42)$$

$$D_t^0 \left(b_0 - \frac{1}{\mathcal{F}^2} \bar{\rho}(z) \right) = 0, \quad (43)$$

$$\nabla_{\perp} \cdot \mathbf{u}_1 + \partial_Y v_0 = 0. \quad (44)$$

Note that $D_t^0 = \partial_t + \mathbf{u} \cdot \nabla_{\perp}$ and $\mathcal{F}^2 = \Gamma F r^2$. For a closed system, we require that $\mathcal{F} = \mathcal{O}(1)$. Applying $\hat{\boldsymbol{\eta}}_0 \cdot$ and $\nabla \times$ to Eq. (42), we find that

$$\hat{\boldsymbol{\eta}}_0 \cdot \nabla p_1 = \hat{\boldsymbol{\eta}}_0 \cdot (-D_t^0 \mathbf{u}_0 + \beta Y \hat{\boldsymbol{\eta}}_1 \times \mathbf{u}_0 - \partial_Y p_0 \hat{\mathbf{y}} + b_0 \hat{\mathbf{z}}), \quad (45)$$

$$\hat{\boldsymbol{\eta}}_0 \cdot \nabla \mathbf{u}_1 = D_t^0 \boldsymbol{\omega}_0 - \boldsymbol{\omega}_0 \cdot \nabla_{\perp} \mathbf{u}_0 - \hat{\boldsymbol{\eta}}_0 \partial_Y v_0 - \nabla \times (\beta Y \hat{\boldsymbol{\eta}}_1 \times \mathbf{u}_0 - \partial_Y p_0 \hat{\mathbf{y}} + b_0 \hat{\mathbf{z}}), \quad (46)$$

the latter being the equation for the vorticity $\boldsymbol{\omega}$. We have introduced the large spatial variable Y , which means that Eqs. (45) and (46) contain secular terms that grow with the small variable y . Hence, we require a solvability condition that ensures the terms in Eqs. (45) and (46) balance. In this case, the solvability conditions are obtained by averaging the equations over η and forcing the right-hand sides to equal 0. Then, projecting Eq. (46) onto $\hat{\boldsymbol{\eta}}_0$, we obtain the following closed system that can be written in terms of the geostrophic and ageostrophic streamfunctions, Ψ and Φ , respectively,

$$\mathbf{u}_0 = -\nabla \times (\Psi_0 \hat{\mathbf{y}} + \nabla \times \Phi_0 \hat{\mathbf{y}}), \quad p_0 = \Psi_0, \quad (47)$$

$$D_t^0 \nabla_{\perp}^2 \Psi_0 - (\partial_y + \beta y \partial_z) \nabla_{\perp}^2 \Phi_0 = -\partial_x b_0, \quad (48)$$

$$D_t^0 \nabla_{\perp}^2 \Phi_0 + (\partial_y + \beta y \partial_z) \Psi_0 = 0, \quad (49)$$

$$D_t^0 \left(b_0 - \frac{\bar{\rho}(z)}{\mathcal{F}^2} \right) = 0. \quad (50)$$

This is the SNH-QGE III model. The linearized version of this system is analyzed in the following section and compared to the linearized primitive equations of section 2. In particular, we are interested in whether the system describes the same equatorially constrained waves as the linearized primitive equations (the Kelvin, Rossby, mixed Rossby-gravity and inertio-gravity modes).

4 Investigation of the linearized quasi-geostrophic equations

The linearized reduced quasi-geostrophic model from Eqs. (48) - (50) can be written

$$\partial_t^0 \nabla_{\perp}^2 \Psi - (\partial_y + \beta y \partial_z) \nabla_{\perp}^2 \Phi = -\partial_x b, \quad (51)$$

$$\partial_t^0 \nabla_{\perp}^2 \Phi + (\partial_y + \beta y \partial_z) \Psi = 0, \quad (52)$$

$$\partial_t^0 b - w \frac{\bar{\rho}_z(z)}{\mathcal{F}^2} = 0. \quad (53)$$

Eqs. (51) and (53) are combined by differentiating the former with respect to t . We write the Brunt-Väisälä frequency as $N^2 = -\bar{\rho}_z(z)/\mathcal{F}^2$ and assume that it is constant. Consider first the case when $v = \nabla_{\perp}^2 \Phi = 0$ (from Eq. (47)). Ψ is found by solving $\partial_y \Psi + \beta y \partial_z \Psi = 0$. Assuming a solution of the form

$$\Psi(x, y, z, t) = \tilde{\Psi}(y) e^{ikx + i\ell z - i\omega t}, \quad (54)$$

the y -dependent part of the solution is given by $\tilde{\Psi} = a e^{-i\ell\beta y^2/2}$, where a is a complex constant. Note that this wave is not equatorially constrained; the solution Ψ does not decay to 0 as $y \rightarrow \infty$. The dispersion relation for this wave is similar to that in the primitive equations for the case when $|\omega| < N$, namely,

$$\omega = \pm \frac{Nk}{\sqrt{k^2 + \ell^2}}, \quad (55)$$

except that now there are two roots to the equation, representing eastwards and westwards traveling waves.

We next consider the higher order mode waves, where the meridional velocity is no longer zero. From Eq. (47), the zonal and vertical components of the velocity are $u = \partial_z \Psi$ and $w = -\partial_x \Psi$, so that Eqs. (51) - (53) can be written as one equation in terms of the variable Ψ , namely

$$\partial_{tt} \nabla_{\perp}^2 \Psi + N^2 \partial_{xx} \Psi + \partial_{yy} \Psi + \beta^2 y^2 \partial_{zz} \Psi + \beta \partial_z \Psi + 2\beta y \partial_{yz} \Psi = 0. \quad (56)$$

We again assume a solution of the form given in Eq. (54), which yields the following equation for $\tilde{\Psi}$

$$\frac{d^2 \tilde{\Psi}}{dy^2} + 2i\ell\beta y \frac{d\tilde{\Psi}}{dy} - \beta^2 \ell^2 y^2 \tilde{\Psi} + i\ell\beta \tilde{\Psi} + k^2 \left(\omega^2 \left[1 + \frac{\ell^2}{k^2} \right] - N^2 \right) \tilde{\Psi} = 0. \quad (57)$$

Using the standard transformation $\tilde{\Psi}(y) = \psi(y) e^{-\lambda y^2/2}$, where $\lambda = i\ell\beta$, we obtain the simplified equation

$$\frac{d^2 \psi}{dy^2} + k^2 \left(\omega^2 \left[1 + \frac{\ell^2}{k^2} \right] - N^2 \right) \psi = 0. \quad (58)$$

The waveguide solution that existed in the primitive equations using an equivalent ansatz - traveling wave structures in the zonal and vertical directions - is not apparent in the reduced quasi-geostrophic model. That is, the solution to Eq. (56), for both the Kelvin mode and

the higher order modes, is no longer given in terms of a parabolic cylinder function that decays exponentially north and south of the equator. What happens if we choose a different ansatz? In particular, how does the solution change if we assume a standing wave form in the vertical, rather than a traveling wave? We will run into difficulties if we simply use this ansatz in form of the system given in Eq. (56), hence to proceed, we rescale Eq. (56) in y and perform an asymptotic expansion about the small parameter β .

Recall that the y coordinate in Eq. (56) was scaled in section 3 such that $y = A_y^{-1}y^*$, where y^* was the unscaled meridional variable, and with $A_y = 1/Ro$. In what follows, we introduce a new scaling $y = \beta^{-1/2}Y$, where β is assumed to be small enough such that the distinguished limits in the asymptotic expansion of section 3 are unchanged. This yields the following rescaled equation for Ψ

$$(\partial_{tt}\nabla_{\perp}^2 + N^2\partial_{xx})\Psi + \beta(\partial_{YY} + Y^2\partial_{zz})\Psi + \beta(\partial_z + 2Y\partial_{Yz})\Psi = 0. \quad (59)$$

The slow time $\tau = \beta t$ is introduced along with the expansion

$$\Psi(x, Y, z, t, \tau) = \Psi_0 + \beta\Psi_1 + \dots \quad (60)$$

Note that because we have both a fast and a slow time in the system now, we expect the dispersion relation to involve both a fast and a slow frequency, denoted ω_f and ω_s , respectively. This time we assume a standing wave form in the vertical

$$\Psi_0(x, Y, z, t, \tau) \propto \psi_0(Y, \tau)e^{ikx - i\omega_f t} \sin(\ell z), \quad (61)$$

with the boundary conditions $w = 0$ at $z = 0, H$. At leading order, $\mathcal{O}(\beta^0)$, this expansion yields

$$[\partial_{tt}\nabla_{\perp}^2 + N^2\partial_{xx}]\Psi_0 = 0, \quad (62)$$

from which we derive an expression for the fast frequency,

$$\omega_f = \pm \frac{Nk}{\sqrt{k^2 + \ell^2}}. \quad (63)$$

This is the leading order frequency of the linearized system. At next order, $\mathcal{O}(\beta)$, we obtain

$$[\partial_{tt}\nabla_{\perp}^2 + N^2\partial_{xx}]\Psi_1 = -2\partial_{t\tau}\nabla_{\perp}^2\Psi_0 - (\partial_{YY} + Y^2\partial_{zz})\Psi_0 - (\partial_z + 2Y\partial_{Yz})\Psi_0. \quad (64)$$

The linear operator $\mathcal{L} = \partial_{tt}\nabla_{\perp}^2 + N^2\partial_{xx}$ is self-adjoint, and, by orthogonality of $\sin \ell z$ and $\cos \ell z$, the last two terms involving first derivatives with respect to z vanish from the solvability condition, leaving

$$\langle \Psi_0, [-2\partial_{t\tau}\nabla_{\perp}^2 - (\partial_{YY} + Y^2\partial_{zz})]\Psi_0 \rangle = 0. \quad (65)$$

Taking into account the ansatz from Eq. (61), and assuming that ψ_0 is separable in τ and Y such that $\psi_0(Y, \tau) = \tilde{\psi}_0(Y)e^{i\omega_s\tau}$, we obtain the following expression for $\tilde{\psi}_0$

$$\frac{d^2\tilde{\psi}_0(Y)}{dY^2} - \ell^2 Y^2 \tilde{\psi}_0(Y) + 2\omega_f\omega_s(k^2 + \ell^2)\tilde{\psi}_0(Y) = 0. \quad (66)$$

Eq. (66) can be solved with parabolic cylinder functions, and is equatorially constrained when

$$2\omega_f\omega_s(k^2 + \ell^2) = (2n + 1)\ell, \quad \text{for } n = 0, 1, 2, \dots, \quad (67)$$

where ω_f is the fast frequency defined in Eq. (63). The dispersion relation for the reduced system can be written as $\omega = \omega_f + \beta\omega_s$, leading to the following expression for ω in terms of the horizontal and vertical wavelengths

$$\omega = \frac{Nk}{\sqrt{k^2 + \ell^2}} + \frac{\beta(2n + 1)\ell}{2Nk\sqrt{k^2 + \ell^2}}. \quad (68)$$

How does Eq. (68) compare to the dispersion relations of the primitive equations, namely Eqs. (12) and (22)? Substituting $\omega = \omega_f + \beta\omega_s$ into Eq. (12), we expand in terms of the small parameter β . Then, the leading order expression is identical to Eq. (63) and at next order in β we obtain

$$2\omega_f\omega_s(k^2 + \ell^2) = (2n + 1 \pm 1) \frac{N\ell^2}{\sqrt{k^2 + \ell^2}}. \quad (69)$$

The main differences between Eq. (67) from the exact system and Eq. (69) from the reduced system are the presence of N , $\ell/\sqrt{k^2 + \ell^2}$ and the \pm term on the right-hand side of Eq. (69). The \pm term indicates that the reduced system has filtered out modes that are even with respect to the equator ($n = 1, 3, 5, \dots$). It is likely that the former two terms are a result of the scalings used to derive the quasi-geostrophic system from [13] (for example, that N is a result of the time scaling employed and that k is scaled such that $k = \mathcal{O}(1)$ in the reduced system corresponds to $k \ll 1$ in the primitive equations so that $\ell^2/\sqrt{k^2 + \ell^2} \approx \ell$). In this case, and taking into account the limits of the reduced model, the dispersion relations in Eq. (12) and (68), and indeed the primitive and reduced systems, are then equivalent. We now turn to the fully nonlinear quasi-geostrophic model.

5 Investigation of the nonlinear quasi-geostrophic model

This section introduces two methods of analyzing the nonlinear quasi-geostrophic system in Eqs. (48) - (50): one method involves a similar scaling argument to that presented in section 4 for a constant Brunt-Väisälä frequency, while the other method is not restricted to small values of β and assumes a non-constant vertical stratification.

5.1 Constant Brunt-Väisälä frequency

Consider the nonlinear reduced equatorial system in Eqs. (48) - (50) from section 3. Following [2], we transform Eqs. (48) - (50) to a frame traveling with the wave speed c eastwards, by defining $\xi = x - ct$. We are interested in longwave solutions in the zonal direction that do not change the distinguished limits in the scaling arguments of section 3, namely $X = \epsilon\xi$, where ϵ is a small number. We also introduce the following scalings:

$$\Psi = \epsilon\Psi, \quad \Phi = \epsilon^2\Phi, \quad b = \epsilon b.$$

Proceeding as in section 4, y is rescaled by $y = \beta^{-1/2}Y$ and β by $\beta = \epsilon^4\hat{\beta}$. Eqs. (48) - (50) simplify to

$$-\partial_X b = -c(\epsilon^2\partial_X^2 + \partial_z^2)\partial_X \Psi - \epsilon^2(\partial_Y + \hat{\beta}Y\partial_z)(\epsilon^2\partial_X^2 + \partial_z^2)\Phi + \epsilon[\partial_z\Psi(\epsilon^2\partial_X^2 + \partial_z^2)\partial_X \Psi - \partial_X \Psi(\epsilon^2\partial_X^2 + \partial_z^2)\partial_z \Psi], \quad (70)$$

$$0 = -c(\epsilon^2\partial_X^2 + \partial_z^2)\partial_X \Phi + (\partial_Y + \hat{\beta}Y\partial_z)\Psi + \epsilon[\partial_z\Psi(\epsilon^2\partial_X^2 + \partial_z^2)\partial_X \Phi - \partial_X \Psi(\epsilon^2\partial_X^2 + \partial_z^2)\partial_z \Phi], \quad (71)$$

$$0 = -c\partial_X b + \epsilon\partial_z\Psi\partial_X b - \epsilon\partial_X \Psi\partial_z b - \partial_X \Psi N^2. \quad (72)$$

We make the assumption that the meridional velocity is of the same order as the zonal and vertical velocities and expand the variables Ψ , Φ , b and the phase speed c as follows

$$\Psi = \Psi_0 + \epsilon\Psi_1 + \dots, \quad (73)$$

$$\Phi = \Phi_0 + \epsilon\Phi_1 + \dots, \quad (74)$$

$$b = b_0 + \epsilon b_1 + \dots, \quad (75)$$

$$c = c_0 + \epsilon c_1 + \dots \quad (76)$$

The expansions in Eqs. (73) - (76) are substituted into Eqs. (70) - (72), yielding the leading order set, written as a system in terms of Ψ and Φ only

$$\frac{N^2}{c_0^2}\Psi_{0X} + \Psi_{0Xzz} = 0, \quad (77)$$

$$-c_0\Phi_{0Xzz} + (\partial_Y + \hat{\beta}Y\partial_z)\Psi_0 = 0, \quad (78)$$

which, when the boundary conditions $w = -\Psi_{0X} = 0$ on $z = 0, H$ are satisfied, yields

$$\Psi_0 = A_0(X, Y) \sin\left(\frac{\pi}{H}z\right). \quad (79)$$

This wave is a standing wave in the vertical, which results from the ansatz we have assumed here, which is analogous to that of the linear case in Eq. (61). Suppose that

$$\Phi_0 = B(X, Y) \sin\left(\frac{\pi}{H}z\right) + C(X, Y) \cos\left(\frac{\pi}{H}z\right). \quad (80)$$

Substituting this into Eq. (78), the amplitudes B and C can be expressed in terms of A_0 , namely

$$C_X = -\frac{\hat{\beta}HY}{c_0\pi}A_0, \quad B_X = -\frac{H^2}{c_0\pi^2}A_{0Y}. \quad (81)$$

We are interested in the meridional and zonal structure of the amplitude of Ψ , and particularly how it is modified by nonlinearities. To this end, we proceed to next order.

The first order equations written in terms of Ψ and Φ are

$$\begin{aligned} c_0^2\Psi_{1Xzz} + N^2\Psi_{1X} &= c_0c_1\frac{\pi^2}{H^2}A_{0X}\sin\left(\frac{\pi}{H}z\right) + c_1\frac{N^2}{c_0}A_{0X}\sin\left(\frac{\pi}{H}z\right) \\ &\quad - A_{0X}D_z\sin\left(\frac{\pi}{H}z\right), \end{aligned} \quad (82)$$

$$\Rightarrow (N^2 + c_0^2\partial_z^2)\Psi_{1X} = 2c_0c_1\frac{\pi^2}{H^2}A_{0X}\sin\left(\frac{\pi}{H}z\right). \quad (83)$$

The linear operator ($N^2 + c_0^2 \partial_z^2$) is self-adjoint, which leads to the solvability condition

$$\left\langle \Psi_0, 2c_0 c_1 \frac{\pi^2}{H^2} A_{0X} \sin\left(\frac{\pi}{H} z\right) \right\rangle = 0. \quad (84)$$

We deduce that $c_1 = 0$ and the first order equations are simplified to

$$\frac{N^2}{c_0^2} \Psi_{1X} + c_0 \Psi_{1Xzz} = 0, \quad (85)$$

$$c_0 \Phi_{1Xzz} - (\partial_Y + \hat{\beta} Y \partial_z) \Psi_1 = \Psi_{0z} \Phi_{0Xzz} - \Psi_{0X} \Phi_{0zzz}. \quad (86)$$

The former equation is solved by imposing the boundary conditions $w = -\Psi_{0X} = 0$ on $z = 0, H$, yielding $\Psi_1 = A_1(X, Y) \sin\left(\frac{\pi}{H} z\right)$. Finally, Eq. (86) is solved for Φ_1 , and integrating twice with respect to z , we find

$$\begin{aligned} \Phi_{1X} = & -\frac{\pi}{8c_0 H} \left[(A_{0X} B - A_0 B_X) \sin\left(\frac{2\pi}{H} z\right) + (A_{0X} C - A_0 C_X) \cos\left(\frac{2\pi}{H} z\right) \right] \\ & - \frac{H^2}{c_0 \pi^2} A_{1Y} \sin\left(\frac{\pi}{H} z\right) - \frac{H}{c_0 \pi} A_1 \beta Y \cos\left(\frac{\pi}{H} z\right) - \frac{\pi^3}{2c_0 H^3} (A_{0X} C + A_0 C_X) \left(\frac{z^2}{2} + Dz + E\right), \end{aligned}$$

where

$$-\frac{\pi^3}{2c_0 H^3} (A_{0X} C + A_0 C_X) E = \frac{\pi}{8c_0 H} (A_{0X} C - A_0 C_X) + \frac{H}{c_0 \pi} A_1 \beta Y, \quad (87)$$

$$\frac{\pi^3}{2c_0 H^3} (A_{0X} C + A_0 C_X) D = \frac{2}{c_0 \pi} A_1 \beta Y - \frac{\pi^3}{4c_0 H^2} (A_{0X} C + A_0 C_X). \quad (88)$$

We expect nonlinearities to appear at second order, so proceed with our expansions. At second order, there is cancellation of the nonlinear terms such that Ψ_2 can be written

$$\begin{aligned} c_0 \Psi_{2Xzz} + \frac{N^2}{c_0} \Psi_{2X} = & \left(2c_2 \frac{\pi^2}{H^2} A_{0X} - c_0 A_{0XXX} \right) \sin\left(\frac{\pi}{H} z\right) + \frac{\pi^2}{H^2} \left(B_Y \sin\left(\frac{\pi}{H} z\right) + C_Y \cos\left(\frac{\pi}{H} z\right) \right) \\ & - \frac{\pi^3}{H^3} \left(-\hat{\beta} Y B \cos\left(\frac{\pi}{H} z\right) + \hat{\beta} Y C \sin\left(\frac{\pi}{H} z\right) \right). \end{aligned} \quad (89)$$

On applying the solvability condition $\langle \Psi_{0X}, RHS \rangle$ to Eq. (89) we find that

$$2c_2 \frac{\pi^2}{H^2} A_{0X} - c_0 A_{0XXX} + \frac{\pi^2}{H^2} B_Y - \frac{\pi^3}{H^3} \hat{\beta} Y C = 0. \quad (90)$$

Eq. (81) defines C_X and B_X in terms of A_0 . This is substituted into the above equation, and, after differentiating with respect to X , the following *linear* equation for the amplitude A_0 is obtained

$$2c_2 \frac{\pi^2}{H^2} A_{0XX} - c_0 A_{0XXXX} - \frac{1}{c_0} A_{0YY} + \frac{\pi^2}{c_0 H^2} \hat{\beta}^2 Y^2 A_0 = 0. \quad (91)$$

By assuming A_0 is separable, i.e. $A_0(X, Y) = F(X)G(Y)$, we derive equations for $F(X)$ and $G(Y)$ that involve a separation constant μ . In a similar manner to that presented in

preceding sections, the equation for $G(Y)$ can be solved in terms of equatorially-constrained parabolic cylinder functions only when the separation constant is defined as $\mu = \mu_n = \frac{\pi}{H}\hat{\beta}(2n+1)$, for the positive integer n . The equation for $F(X)$ is the linear Swift-Hohenberg equation. We assume that the solution $F(X)$ is periodic in X , such that

$$2c_2 \frac{\pi^2}{H^2} \hat{k}^2 + c_0 \hat{k}^4 + \frac{\mu_n}{c_0} = 0, \quad (92)$$

which is the analog of the linear dispersion relation from the preceding section 4, this time solving for the phase speed c_2 in terms of the zonal wavenumber k . This result matches that of the linear reduced theory, Eq. (67), when $\mu_n = \frac{\pi}{H}\hat{\beta}(2n+1)$. We proceed to solve Eq. (89) for Ψ_2 . From the solvability condition $\langle \Psi_{0X}, RHS \rangle$ applied to Eq. (89), terms involving $\sin(\frac{\pi}{H}z)$ disappear due to orthogonality, and we obtain the following equation for Ψ_2

$$\Psi_{2Xzz} + \frac{N^2}{c_0^2} \Psi_{2X} = \frac{\pi^2}{c_0 H^2} \left(C_Y + \hat{\beta} Y B \frac{\pi}{H} \right) \cos\left(\frac{\pi}{H}z\right). \quad (93)$$

Once again taking into account the boundary conditions for Ψ on $z = 0, H$, the solution to Eq. (93) is $\Psi_2 = Wz \sin(\frac{\pi}{H}z)$, provided that on substitution into Eq. (93) the following relation between W and A holds

$$W_{XX} = -\frac{\hat{\beta}}{2c_0^2} (A_0 + 2Y A_{0Y}). \quad (94)$$

Here we have also made use of Eq. (81). We were expecting that the second order solvability condition would introduce nonlinearity in our expression for the amplitude A_0 . Instead, due to the scalings chosen, the nonlinearities at this order cancelled leaving the linear Swift-Hohenberg equation once the Y -dependent part had been accounted for by the appropriate parabolic cylinder function. It is therefore necessary to proceed to third order in ϵ to retrieve the nonlinear adjustment to the amplitude equation.

At third order, we find the following equation for Ψ

$$\begin{aligned} \frac{N^2}{c_0} \Psi_{3X} + c_0 \Psi_{3Xzz} = & \left(2c_3 \frac{\pi^2}{H^2} A_{0X} - c_0 A_{1X} X X + 2c_2 \frac{\pi^2}{H^2} A_{1X} \right) \sin\left(\frac{\pi}{H}z\right) \\ & - (\partial_Y + \hat{\beta} Y \partial_z) \Phi_{1zz} + \frac{\pi}{2H} (A_0 A_{0X} X X - A_{0X} A_{0X} X) \sin\left(\frac{2\pi}{H}z\right) \\ & + \frac{\pi^2}{H^2} \left[A_0 W_X \left(1 + \cos\left(\frac{2\pi}{H}z\right) \right) + A_{0X} W \left(1 - \cos\left(\frac{2\pi}{H}z\right) \right) \right]. \end{aligned}$$

The solvability condition yields

$$\begin{aligned} 0 = & 2c_3 \frac{\pi^2}{H^2} A_{0X} - c_0 A_{1X} X X + 2c_2 \frac{\pi^2}{H^2} A_{1X} \\ & + \frac{2\pi^2}{c_0 H^3} (A_{0X} C + A_0 C_X)_Y + \frac{2\pi^2}{3c_0 H^3} (A_{0X} C - A_0 C_X)_Y - \frac{1}{c_0} A_{1YY} \\ & + \hat{\beta} Y \frac{4\pi^3}{3c_0 H^4} (A_{0X} B - A_0 B_X) + \frac{\pi^2}{c_0 H^2} \hat{\beta}^2 Y^2 A_1 \\ & + \frac{8\epsilon\pi}{3H^2} (A_0 W_X + 2A_{0X} W)_X. \end{aligned} \quad (95)$$

Writing A_0 and A_1 by $\tilde{A} = A_0 + \epsilon A_1 + \dots$, and hence B and C from Eq. (81) in terms of \tilde{A} , we employ the transformation $\tilde{A} = \Theta_{XX}$ and combine Eqs. (91) and (95) to obtain the following equation for Θ

$$\begin{aligned}
0 = & 2(c_2 + \epsilon c_3) \frac{\pi^2}{H^2} \Theta_{XXXX} - c_0 \Theta_{XXXXXX} - \frac{1}{c_0} \Theta_{XXYY} + \frac{\pi^2}{c_0 H^2} \hat{\beta}^2 Y^2 \Theta_{XX} \\
& - \frac{4\epsilon\pi\hat{\beta}}{3c_0^2 H^2} (2Y \Theta_{XX} \Theta_X + Y \Theta_{XX}^2)_Y \\
& - \frac{4\epsilon\pi\hat{\beta}}{3c_0^2 H^2} (Y \Theta_{XX} \Theta_{XY} - Y \Theta_{XX} \Theta_{XYY}) \\
& - \frac{4\epsilon\pi\hat{\beta}}{3c_0^2 H^2} (\Theta_{XX} [\Theta_X + 2Y \Theta_{XY}] + 2\Theta_{XX} [\Theta + 2Y \Theta_Y])_X. \tag{96}
\end{aligned}$$

Here the constant c_3 is the nonlinear correction to the phase speed. The constants c_0 and c_2 are defined as

$$c_0 = \frac{NH}{\pi}, \quad c_2 = -\frac{NH^3}{2\pi^3} \hat{k}^2 - \frac{\hat{\beta}(2n+1)}{2N\hat{k}^2}.$$

Note the appearance of the small parameter ϵ in Eq. (96), which implies that the nonlinear terms are small compared to the linear terms from the leading order expansion.

Suppose Θ is separable in X and Y , namely $\Theta(X, Y) = F(X)G(Y)$. Then, from the homogeneous part of Eq. (96) (the first line), we find equations for $F(X)$ and $G(Y)$ that involve a separation constant γ . As previously, provided that $\gamma = \gamma_n = (2n+1)\pi\beta/H$, an equatorially-constrained solution for $G(Y)$ in terms of parabolic cylinder functions exists, and is given by

$$G(Y) = G_n(Y) = 2^{-n/2} e^{-\pi\hat{\beta}Y^2/2H} H_n \left(\sqrt{\frac{\pi\hat{\beta}}{H}} Y \right), \quad \text{for } n = 0, 1, 2, \dots, \tag{97}$$

where H_n is the Hermite polynomial. We wish to remove the Y -dependence of Eq. (96) to investigate the effect of nonlinearities on the zonal wave structure. Consider the simplest choice of function for G_n , that is, $G_n = G_0 = e^{-\pi\hat{\beta}y^2/2H}$. Multiplying each term in Eq. (96) by G_0 and integrating with respect to Y from $-\infty$ to ∞ yields

$$\theta_{\eta\eta\eta\eta\eta} + b\theta_{\eta\eta\eta} - \theta_{\eta\eta} + 4\theta_{\eta}\theta_{\eta\eta} + 3\theta_{\eta\eta}^2 + 2\theta_{\eta\eta\eta}\theta = 0, \tag{98}$$

which is a new equation that is similar to the conserved Swift-Hohenberg (SH) equation [16; 25]. Here, $\theta(\eta)$ and η are the rescaled $F(X)$ and X and $b = -2(c_2 + \epsilon c_3) \frac{\pi^{3/2}\alpha}{H^2}$ is a positive constant. Eq. (98) has the symmetry $\eta \rightarrow -\eta$, $\theta \rightarrow \theta$. We are particularly interested in finding localized solutions to Eq. (98), which have been found in the conserved SH equation (e.g. [20]). Some solutions to Eq. (98) obtained using Neumann boundary conditions are illustrated in figure 6. It is important to note that these are not localized solutions as they depend on the boundary conditions even when the domain becomes large. A future work will investigate possible localized solutions to Eq. (98).

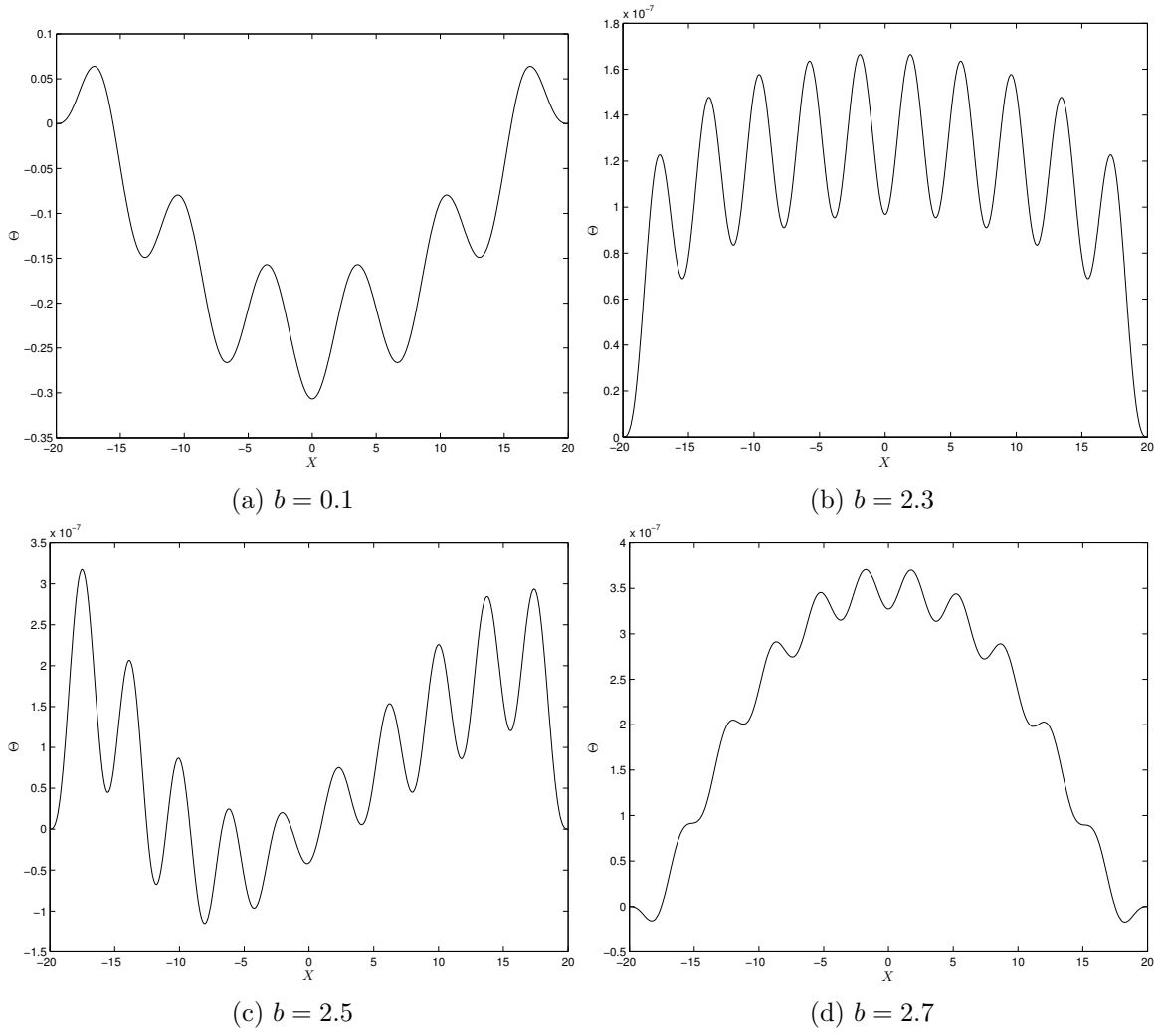


Figure 6: Some solutions to the amplitude equation, Eq. (98), for different values of b .

If we were to choose a parabolic cylinder function that was even with respect to the equator, i.e G_n for $n = 1, 3, 5, \dots$, rather than an odd mode, such as the G_0 chosen above, the nonlinearities would cancel. As in [2], this does not mean that the nonlinear terms are identically zero; rather, choosing a parabolic cylinder function that is even with respect to the equator forces a symmetry that leads to cancellation of the nonlinear terms. It is likely that an alternative scaling for the reduced system exists in which the even modes are retained.

So far we have assumed that the Brunt-Väisälä frequency N is constant and have introduced the scalings such that Eq. (98) applies only in the small β limit. In the following section we return to Eqs. (48) - (50), this time assuming that the Brunt-Väisälä frequency varies with height, which allows us to derive a nonlinear equation for the amplitude of the streamfunction that does not require the imposition of a small β limit.

5.2 Non-constant Brunt-Väisälä frequency

Consider Eqs. (48) - (50) once more, again transforming to the moving frame $\xi = x - ct$ and assuming long waves in the zonal direction $X = \epsilon\xi$. This time we introduce the following scalings

$$\Psi = \epsilon^2 \Psi, \quad \Phi = \epsilon^3 \Phi, \quad b = \epsilon^2 b, \quad (99)$$

where $y = \beta^{-1/2} Y$ and $\beta^{1/2} = \hat{\beta}^{1/2} \epsilon^2$. The physical interpretation of these scalings is that the meridional current is small compared with the zonal and vertical equatorial currents. Eqs. (48) - (50) become

$$\begin{aligned} -\partial_X b &= -c(\epsilon^2 \partial_X^2 + \partial_z^2) \partial_X \Psi - \epsilon^2 \hat{\beta}^{1/2} (\partial_Y + Y \partial_z) (\epsilon^2 \partial_X^2 + \partial_z^2) \Phi \\ &\quad + \epsilon^2 \partial_z \Psi (\epsilon^2 \partial_X^2 + \partial_z^2) \partial_X \Psi - \epsilon^2 \partial_X \Psi (\epsilon^2 \partial_X^2 + \partial_z^2) \partial_z \Psi, \end{aligned} \quad (100)$$

$$\begin{aligned} 0 &= -c(\epsilon^2 \partial_X^2 + \partial_z^2) \partial_X \Phi + \hat{\beta}^{1/2} (\partial_Y + Y \partial_z) \Psi \\ &\quad + \epsilon^2 \partial_z \Psi (\epsilon^2 \partial_X^2 + \partial_z^2) \partial_X \Phi - \epsilon^2 \partial_X \Psi (\epsilon^2 \partial_X^2 + \partial_z^2) \partial_z \Phi, \end{aligned} \quad (101)$$

$$0 = -c \partial_X b + \epsilon^2 \partial_z \Psi \partial_X b - \epsilon^2 \partial_X \Psi \partial_z b - \partial_X \Psi N^2. \quad (102)$$

We assume the following expansions about the small parameter ϵ

$$\Psi = \Psi_0 + \epsilon \Psi_1 + \dots, \quad (103)$$

$$\Phi = \Phi_0 + \epsilon \Phi_1 + \dots, \quad (104)$$

$$b = b_0 + \epsilon b_1 + \dots, \quad (105)$$

$$c = c_0 + \epsilon c_1 + \dots, \quad (106)$$

and obtain the leading order set in terms of Ψ and Φ

$$\frac{N^2}{c_0} \Psi_{0X} + c_0 \Psi_{0Xzz} = 0, \quad (107)$$

$$-c_0 \Phi_{0Xzz} + \hat{\beta}^{1/2} (\partial_Y + Y \partial_z) \Psi_0 = 0. \quad (108)$$

Suppose that N is a function of z , which takes the form $N(z) = N_0 e^{-z}$, for some constant N_0 . Assume also that $\Psi_0(X, Y, z)$ is separable, writing $\Psi_0 = A_0(X, Y) J(z)$, and let $z = -\ln t$.

Then, the solution to J is simply the zeroth mode Bessel function of the first kind, J_0 , defined by the equation

$$\frac{1}{t} \frac{d}{dt} \left(t \frac{dJ_0}{dt} \right) = -\frac{N_0^2}{c_0^2} J_0. \quad (109)$$

We proceed to second order in ϵ and obtain the following set of equations

$$\begin{aligned} -b_{2X} + c_0 \Psi_{2Xzz} &= -c_0 \Psi_{0XXX} - c_2 \Psi_{0Xzz} - \hat{\beta}^{1/2} (\partial_Y + Y \partial_z) \Phi_{0zz} \\ &\quad + \Psi_{0z} \Psi_{0Xzz} - \Psi_{0X} \Psi_{0zzz}, \end{aligned} \quad (110)$$

$$c_0 \Phi_{2Xzz} - \hat{\beta}^{1/2} (\partial_Y + Y \partial_z) \Psi_2 = -c_0 \Phi_{0XXX} - c_2 \Phi_{0Xzz} + \Psi_{0z} \Phi_{0Xzz} - \Psi_{0X} \Phi_{0zzz}, \quad (111)$$

$$-b_{2X} = \frac{N^2}{c_0} \Psi_{2X} + \frac{c_2}{c_0} b_{0X} - \frac{1}{c_0} \Psi_{0z} b_{0X} + \frac{1}{c_0} \Psi_{0X} b_{0z}. \quad (112)$$

Substituting Eq. (112) into Eq. (110) and using Eq. (108) we obtain the solvability condition

$$\begin{aligned} 0 &= -c_0^2 B_{0XXX} \int_0^\infty J_0^2(z) dz + \frac{2c_2 N_0^2}{c_0} B_{0XX} \int_0^\infty e^{-2z} J_0^2(z) dz - \frac{4N_0^2}{c_0} B_{0XX} B_{0X} \int_0^\infty e^{-2z} J_0^3(z) dz \\ &\quad - \hat{\beta} Y^2 B_0 \int_0^\infty \frac{d^2 J_0(z)}{dz^2} J_0(z) dz - \hat{\beta} (1 + 2Y \partial_Y) B_0 \int_0^\infty \frac{dJ_0(z)}{dz} J_0(z) dz \\ &\quad - \hat{\beta} B_{0YY} \int_0^\infty J_0^2(z) dz, \end{aligned} \quad (113)$$

where $B_0 = \int A_0 dX$ (note that the operator $[N^2 + c_0^2 \partial_z^2]$ is self-adjoint and we assume that $B_{0X} \neq 0$). Again using the transformation $z = -\ln t$, this becomes

$$\begin{aligned} 0 &= -c_0^2 B_{0XXX} \int_0^1 \frac{1}{t} J_0^2(\ln t) dt + \frac{2c_2 N_0^2}{c_0} B_{0XX} \int_0^1 t J_0^2(\ln t) dt - \frac{4N_0^2}{c_0} B_{0XX} B_{0X} \int_0^1 t J_0^4(\ln t) dt \\ &\quad - \frac{\hat{\beta}}{2} Y^2 B_0 \int_0^1 \frac{1}{t} [J_0(\ln t) J_2(\ln t) - J_0(\ln t)^2] dt - \hat{\beta} (1 + 2Y \partial_Y) B_0 \int_0^1 \frac{1}{t} J_0(\ln t) J_1(\ln t) dt \\ &\quad - \hat{\beta} B_{0YY} \int_0^1 \frac{1}{t} J_0^2(\ln t) dt. \end{aligned} \quad (114)$$

In this form the integrals involving the factor $1/t$ are infinite in the interval $t = [0, 1]$. Hence, we restrict the interval of integration further such that we integrate from $t = b$ to $t = 1$, where $b = e^{-j_{0,1}}$ and $j_{0,1}$ is the first root of the Bessel function of the first kind $J_0(z)$. This is equivalent to integrating from $z = 0$ to $z = j_{0,1}$. Proceeding in this manner, we obtain

$$\begin{aligned} 0 &= -c_0^2 B_{0XXX} {}_2F_3 \left(\frac{1}{2}, \frac{1}{2}; 1, 1, \frac{3}{2}; -(j_{0,1})^2 \right) j_{0,1} + \frac{2c_2 N_0^2 r}{c_0} B_{0XX} - \frac{4N_0^2 s}{c_0} B_{0XX} B_{0X} \\ &\quad + \frac{\hat{\beta}}{2} Y^2 B_0 \left[{}_2F_3 \left(\frac{1}{2}, \frac{1}{2}; 1, 1, \frac{3}{2}; -(j_{0,1})^2 \right) j_{0,1} - \frac{1}{6} {}_2F_3 \left(\frac{3}{2}, \frac{3}{2}; 1, \frac{5}{2}, 3; -(j_{0,1})^2 \right) (j_{0,1})^3 \right] \\ &\quad - \hat{\beta} B_{0YY} {}_2F_3 \left(\frac{1}{2}, \frac{1}{2}; 1, 1, \frac{3}{2}; -(j_{0,1})^2 \right) j_{0,1} + \frac{\hat{\beta}}{2} (1 + 2Y \partial_Y) B_0. \end{aligned} \quad (115)$$

Here, ${}_2F_3$ is the generalized hypergeometric function and $r \approx 0.4171$, $s \approx 0.3756$. We write Eq. (115) more compactly as

$$-a_1 B_{0XXX} + a_2 B_{0XX} - a_3 B_{0XX} B_{0X} + a_4 Y^2 B_0 - a_5 B_{0YY} + a_6 (1 + 2Y \partial_Y) B_0 = 0, \quad (116)$$

where the constants a_1 to a_6 are positive. Then, by introducing the scalings $S = f_1 B_0$, $\xi = f_2 X$ and $\eta = f_3 Y$, we obtain the simpler equation

$$S_{\xi\xi\xi\xi} - S_{\xi\xi} + S_{\xi\xi}S_{\xi} + \alpha_1 S_{\eta\eta} - (\eta^2 + \alpha_2 + 2\alpha_2\eta\partial_\eta)S = 0. \quad (117)$$

The constants $\alpha_1 = a_5 f_2^4 / a_1 f_3^2$ and $\alpha_2 = a_6 f_2^4 / a_1$ are functions of $\hat{\beta}$, N_0 and the phase speeds c_0 and c_2 . Eq. (117) is a generalization of the Kadomtsev-Petviashvili (KP) equation [14], with the additional terms $2\eta S_\eta$, $\eta^2 S$ and $S_{\eta\eta}$. As with the SH equation, the KP equation permits localized solutions (e.g. [15; 18]). It is possible to remove the η dependence in Eq. (117) such that it is an ODE in ξ only. We assume that S is separable, e.g. $S(\xi, \eta) = E(\xi)D(\eta)$, where $E(\xi)$ and $D(\eta)$ are related by a separation constant γ , and find that the solution to $D(\eta)$ from the homogeneous part of Eq. (117) (i.e. ignoring the nonlinear term) can be expressed in terms of parabolic cylinder functions. When $\gamma = \gamma_n = (2n + 1)\alpha_2$ for the nonnegative integer n , then D is equatorially constrained. Choosing the lowest order mode, D_0 , we multiply Eq. (117) by D_0 and integrate from $-\infty$ to ∞ to remove the η dependence. Finally we rescale $E(\xi)$ to obtain the following equation

$$E_{\xi\xi\xi\xi} - E_{\xi\xi} + E_{\xi\xi}E_{\xi} + \kappa E = 0. \quad (118)$$

Like Eq. (98), Eq. (118) contains only the one parameter $\kappa = \alpha_2(2 - \sqrt{2}) + \alpha_1\alpha_2(\sqrt{2} - 1) - \sqrt{2}\alpha_1/\alpha_2(\alpha_1 - 1)$. Some solutions to Eq. (118) using Neumann boundary conditions are illustrated in figure 7. As with Eq. (98), these are not true localized solutions as they depend on the boundary conditions even for a large domain.

In this section we have undertaken a preliminary investigation of the nonlinear quasi-geostrophic model. Two alternative scalings have been presented that result in two different amplitude equations when the stratification is assumed to be constant and a function of height, respectively. The benefit of the latter scaling is that it does not restrict the resulting equation to the small β limit. As for Eq. (98), a future work will further investigate localized solutions to Eq. (118).

6 Conclusion

The aim of this work was to further that of Boyd in understanding the dynamics and evolution of nonlinear equatorial waves in the context of a reduced, quasi-geostrophic model. The model was derived based on the assumption that the Rossby number is small at the equator, which is perfectly valid when both the vertical and horizontal components of the Earth's rotation are taken into account. Non-hydrostatic effects and the vertical component of momentum were also included in the model. The derivation assumed that the meridional length scale is large compared to the zonal and vertical length scales, such that the quasi-geostrophic balance in this model was between the u and w components of the momentum.

In the first section, the results from the non-hydrostatic, linearized primitive equations were contrasted with those of the shallow water equations. The horizontal component of the Earth's rotation added curvature to the y, z phase planes and introduced an imaginary component into the solutions. Furthermore, non-hydrostatic effects modified the dispersion relation for the inertio-gravity, Kelvin and mixed Rossby-gravity modes, such that their

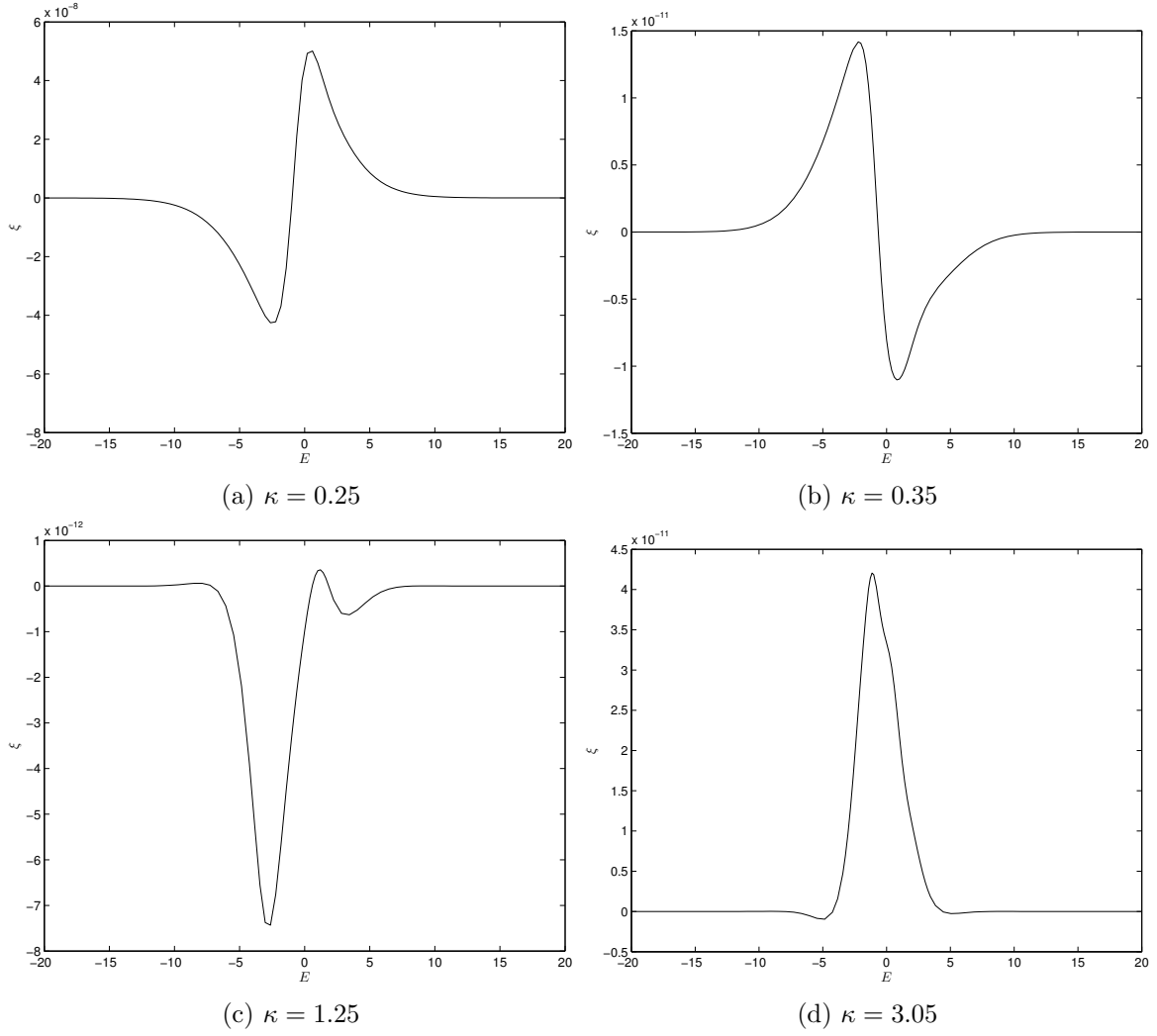


Figure 7: Some solutions to the amplitude equation, Eq. (118), for different values of κ .

frequencies were necessarily less than or greater than the Brunt-Väisälä frequency in the case of vertical traveling and standing waves, respectively.

In contrast with the linearized primitive equations, when a vertical traveling wave solution was assumed in the linearized quasi-geostrophic model, the system was not equatorially-constrained. Rather, a vertical standing wave with rigid lid boundary conditions was required to produce an equatorially-constrained wave. This result held in the small β limit, under which the even modes with respect to the equator were filtered out. It is likely that an alternative scaling of the linearized quasi-geostrophic model that includes the even modes can be found.

Multiple scalings of the nonlinear quasi-geostrophic model were undertaken. The first involved a small β limit, and under the assumption of constant stratification, equatorial waves behaved according to a generalized Swift-Hohenberg equation. Under an alternative scaling that did not require β to be small, and with the assumption that the stratification depended on height, equatorial waves behaved according to a generalized Kadomtsev-Petviashvili equation. Solitary wave solutions to the conserved Swift-Hohenberg equation and the Kadomtsev-Petviashvili equation have been found in previous studies and are a motivation for further work on the equations presented here.

This work is a first step in describing the effects of nonlinearity on equatorial waves in a context apart from the shallow water equations. It is acknowledged that many questions remain to be addressed with respect to the quasi-geostrophic model: for example, what rescaling will yield the even modes, and what effect does changing the vertical dependence of the Brunt-Väisälä frequency have? One clear benefit of this work on the quasi-geostrophic model is that it hints at appropriate methods for analyzing the nonlinear primitive equations, which will be investigated in a subsequent work.

7 Acknowledgments

A very special thanks goes to Edgar Knobloch, who was always patient in putting up with my endless questions and who taught me so much in such a short period of time. Thanks also goes to Keith Julien and Jeffrey Weiss for their thoughts and advice over the summer. I feel very fortunate to have spent time with such an inspiring bunch of scientists and great thinkers. Finally a huge thank you to all the fellows - what a magical summer we had!

References

- [1] R. BLANDFORD, *Mixed gravity-rossby waves in the ocean*, Deep-Sea Research, 13 (1966), pp. 941–961.
- [2] J. P. BOYD, *Equatorial solitary waves. Part I: Rossby solitons*, Journal of Physical Oceanography, 10 (1980), pp. 1699–1717.
- [3] —, *The nonlinear equatorial Kelvin wave*, Journal of Physical Oceanography, 10 (1980), pp. 1–11.
- [4] —, *Equatorial solitary waves. part 2: envelope solitons*, Journal of Physical Oceanography, 13 (1983), pp. 428–449.

- [5] ———, *Equatorial solitary waves. part 3: westward-traveling modons*, Journal of Physical Oceanography, 15 (1985), pp. 46–54.
- [6] J. G. CHARNEY, *On the scale of atmospheric motions*, Geofys. Publ., 17 (1948), pp. 3–17.
- [7] ———, *Geostrophic turbulence*, Journal of the Atmospheric Sciences, 28 (1971), pp. 1087–1095.
- [8] A. E. GILL, *Atmosphere-Ocean Dynamics*, Academic Press, 1982.
- [9] R. H. J. GRIMSHAW, *A note on the β -plane approximation*, Tellus, 27 (1975), pp. 351–356.
- [10] M. HAYASHI AND H. ITOH, *The importance of the nontraditional Coriolis terms in large-scale motions in the tropics forced by prescribed cumulus heating*, Journal of the Atmospheric Sciences, 69 (2012), pp. 2699–2716.
- [11] J. R. HOLTON, *An Introduction to Dynamic Meteorology*, Academic Press, New York, 1979.
- [12] J. R. HOLTON, J. H. BERES, AND X. ZHOU, *On the vertical scale of gravity waves excited by localized thermal forcing*, Journal of the Atmospheric Sciences, 59 (2002).
- [13] K. JULIEN, E. KNOBLOCH, R. MILLIFF, AND J. WERNE, *Generalized quasi-geostrophy for spatially anisotropic rotationally constrained flows*, Journal of Fluid Mechanics, 555 (2006), pp. 233–274.
- [14] B. B. KADOMTSEV AND V. I. PETVIASHVILI, *On the stability of solitary waves in weakly dispersing media*, Soviet Physics - Doklady, 15 (1970), pp. 539–541.
- [15] Y. LIU AND X.-P. WANG, *Nonlinear stability of solitary waves of a generalized Kadomtsev-Petviashvili equation*, Communications in Mathematical Physics, 183 (1997), pp. 253–266.
- [16] D. J. B. LLOYD, B. SANDSTED, D. AVITABILE, AND A. R. CHAMPNEYS, *Localized hexagon patterns of the planar Swift-Hohenberg equation*, SIAM Journal of Applied Dynamical Systems, 7 (2008), pp. 1049–1100.
- [17] R. A. MADDEN AND P. R. JULIAN, *Detection of a 40-50 day oscillation in the zonal wind in the tropical Pacific*, Journal of the Atmospheric Sciences, 28 (1971), pp. 702–708.
- [18] S. V. MANAKOV, V. E. ZAKHAROV, L. A. BORDAG, A. R. ITS, AND V. B. MATVEEV, *Two-dimensional solitons of the Kadomtsev-Petviashvili equation and their interaction*, Physics Letters, 63A (1977), pp. 205–206.
- [19] J. MATSUNO, *Quasi-geostrophic motions in the equatorial area*, Journal of the Meteorological Society of Japan, 44 (1966), pp. 25–43.

- [20] P. C. MATTHEWS AND S. M. COX, *Pattern formation with a conservation law*, Non-linearity, 13 (2000), pp. 1293–1320.
- [21] D. W. MOORE, *Planetary-gravity waves in an equatorial ocean*, PhD thesis, Harvard University, 1968.
- [22] ———, *Equatorial waves and the effect of the horizontal component of the earth's rotation*. June 1993.
- [23] D. W. MOORE AND S. G. H. PHILANDER, *Modeling of the tropical oceanic circulation*, in *The Sea*, E. Goldberg, ed., vol. 6, Wiley, 1977, ch. 8, pp. 319–347, 359–361.
- [24] J. D. NEELIN, D. S. BATTISTI, A. C. HIRST, F.-F. JIN, Y. WAKATA, T. YAMAGATA, AND S. E. ZEBIAK, *ENSO theory*, Journal of Geophysical Research, 103 (1998), pp. 14,261–14,290.
- [25] J. B. SWIFT AND P. C. HOHENBERG, *Hydrodynamic fluctuations at the convective instability*, Physical Review A, 15 (1977), pp. 319–328.
- [26] G. VERONIS, *Comments on Phillips' proposed simplification of the equations of motion for a shallow rotating atmosphere*, Journal of the Atmospheric Sciences, 25 (1968), pp. 1154–1155.
- [27] M. WHEELER AND G. N. KILADIS, *Convectively coupled equatorial waves: analysis of clouds and temperature in the wavenumber-frequency domain*, Journal of the Atmospheric Sciences, 56 (1999), pp. 374–399.
- [28] A. A. WHITE AND R. A. BROMLEY, *Dynamically consistent, quasi-hydrostatic equations for global models with a complete representation of the coriolis force*, Quarterly Journal of the Royal Meteorological Society, 121 (1995), pp. 399–418.
- [29] C. WUNSCH AND A. E. GILL, *Observations of equatorially trapped waves in Pacific sea level variations*, Deep-Sea Research, 23 (1975), pp. 371–390.
- [30] C. ZHANG, *Madden-Julian oscillation*, in *Reviews of Geophysics*, vol. 43, American Geophysical Union, 2005, pp. 1–36.

2:1 Spatial Resonance in Langmuir Circulation

Bevin Maultsby

University of North Carolina

Langmuir circulation in the upper layer of the ocean is studied as 2 : 1 spatial resonance problem with steady state-steady state modal interaction and $O(2)$ symmetry. A center manifold reduction using asymptotic analysis results in a dynamical system with a structurally stable and attracting heteroclinic orbit in an invariant subspace of the center manifold. This heteroclinic orbit is used to illustrate the persistent switching between a two-roll state and a four-roll state in the crosswind plane. Lastly, a set of coupled PDEs are derived to study the Y junctions which mark transitions between these two states.

1 Introduction

Langmuir circulation is a wind- and surface wave-driven convective process in the upper layer of bodies of water. When the speed of the wind over the surface of the water exceeds approximately 3.5 meters per second, it can create pairs of counter rotating vortices with axis parallel to the wind and the direction of wave propagation, see Figure 1. The rotation of these vortices creates a mixing layer, which in the ocean typically ranges from 50 meters to 100 meters deep.

The counter rotation cause regions of upwelling and strong downwelling in the mixing layer. The downwelling, caused when water converges on the surface and is forced downward, may trap dirt and debris, resulting in a visible pattern of “windrows” on the surface of the water. The windrows are not perfectly parallel, however, and often display “Y junctions” where two windrows appear to merge into one windrow, as seen in Figure 1. These Y junctions can point in either direction, but most often the stem of the Y is observed pointing in the direction of the wind.

Suppose there is a box in the cross-wind plane of width W with periodic sidewalls. When there is a single pair of counter-rotating vortices within this box, this will be referred to as a 2-roll state; when there are two pairs of vortices, it is a 4-roll state. A direct numerical simulation in such a box of the governing equations carried about by Zhexuan Zhang at the University of New Hampshire showed a persistent switching between a 4-roll state, to a 2-roll state, and then back to the 4-roll state with a shift by $W/4$. In this project, we are interested in finding a dynamical systems explanation for this switching behavior between two rolls and four rolls using a pair of coupled ODEs. Then we derive a pair of coupled PDEs to study the Lagrangian pattern of Y junctions on the surface.

The rest of this paper is organized as follows. The equations for the fluid motion are given in Section 2. In Section 3, evolution equations describing how the amplitudes of the

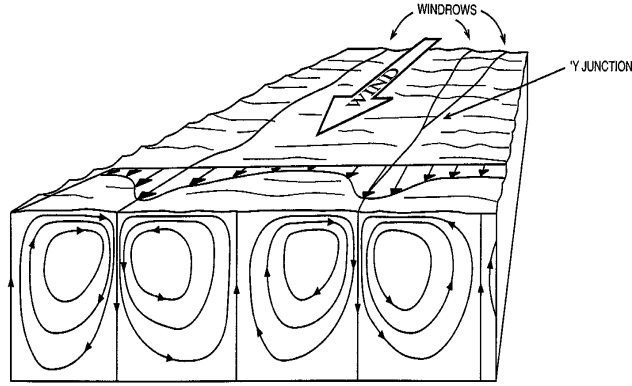


Figure 1: Two pairs of counter-rotating rolls in Langmuir circulation. Note the axes of the rolls is parallel to the direction of the wind. The downwelling between the rolls creates windrows seen on the surface. Where two windrows appear to merge, they form a Y junction. From [15].

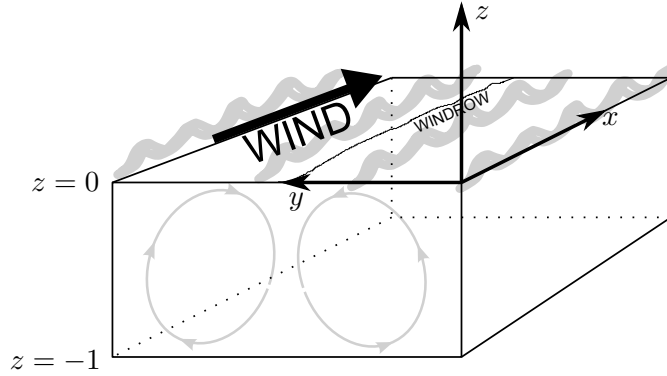


Figure 2: This figure illustrates the spatial coordinate system: x is in the direction of the wind, y is the lateral coordinate in the crosswind plane, and z is the vertical depth (after rescaling, the depth of the water is 1). Note the velocity u is in the x -direction, v is in the y -direction, and w is in the z -direction. Under the coordinate change $(u, v, w) \rightarrow (u, \Omega, \psi)$, u remains the velocity in the x -direction, ψ is the streamfunction in the (y, z) -plane, and Ω is the vorticity.

2-roll state and the 4-roll state vary with time are derived using asymptotic analysis. The dynamics of the resulting ODEs are explored. Lastly, in Section 4, slow advection in the downstream direction is added to the system, yielding a set of reduced 3D equations. These equations add terms to the derived ODEs to convert them into PDEs.

2 The governing equations

Let u be the velocity in the direction of the wind, which we will consider the x -direction. Let v be the velocity in the direction perpendicular to the wind, the y -direction, and let w be the velocity in the vertical z -direction (i.e. z measures the depth of the water). See Figure 2.

The basic flow in the x -direction is a linear Couette flow denoted $U_B(z)$; this state carries the wind stress, so the perturbation to the basic state is zero. Thus the overall velocity in this direction is the sum of $U_B(z)$ and a perturbation term u_p . There is no assumed basic flow in the y - or z -directions, hence the only velocity components in the plane perpendicular to the wind arise from the perturbation. Therefore the terms v and w denote the perturbation terms in the y - and z -directions.

Restricting attention to the (y, z) -plane, there are two symmetries; both can be observed in Figure 1. Once a z -axis is chosen so that it passes between a pair of rolls as in Figure 2, there is a reflection action ζ that changes the (v, w) -velocity components via

$$v(y, z) \rightarrow -v(-y, z), \quad (1)$$

$$w(y, z) \rightarrow w(-y, z), \quad (2)$$

which is an action of $\mathbb{Z}/2\mathbb{Z}$ on (v, w) . The second symmetry stems from translation, $y \rightarrow y + d \bmod W$, where W is the spatial period of y . This is an action of $SO(2)$ on the system. Hence there is overall a group action of $O(2) = SO(2) \rtimes \mathbb{Z}/2\mathbb{Z}$ in the (y, z) -plane.

Let $U = (u, v, w)$. The governing PDE is Navier-Stokes with a Craik-Leibovich forcing term. Craik-Leibovich equations are a surface-wave filtered version of Navier-Stokes in which the average effects of the surface waves show up in a vortex force term, see [8]. The PDE, whose terms will be defined below, is

$$\partial_t U + U \cdot \nabla U = -\nabla p + \frac{1}{La_t^2} [U_s(z) \hat{e}_x \times \omega] + \frac{1}{Re_*} \nabla^2 U. \quad (3)$$

In (3) U is incompressible, so $\nabla \cdot U = 0$, and $\omega = \nabla \times U$ is vorticity. The nondimensional friction Reynolds number Re_* is defined as

$$Re_* := \frac{u_* H}{\nu_e}, \quad (4)$$

where u_* is a given surface friction velocity, often about $0.01 \frac{m}{s}$, H is the depth of the mixed layer, and ν_e is a given eddy viscosity that arises as a result of the time averaging. The Craik-Leibovich term in (3) is

$$\frac{1}{La_t^2} [U_s(z) \hat{e}_x \times \omega]. \quad (5)$$

The function $U_s(z)$ is the Stokes drift. This is a Lagrangian time-averaged velocity following a particle in the surface wave field; it measures the horizontal displacement in the direction of the wind (the \hat{e}_x -direction) as a function of depth z in the water. To simplify the analysis, it can be taken to be linear; to be more realistic, however, we use an exponential profile:

$$U_s(z) = U_{s_0} e^{2\beta z}, \quad (6)$$

where U_{s_0} is the horizontal displacement in the direction of wave propagation at the surface. The number $\beta > 0$ is an inverse scale height of the Stokes drift and will be treated as a parameter. The Craik-Leibovich computation includes a wind stress term given by

$$\tau_w \equiv \rho_w u_*^2, \quad (7)$$

where ρ_w is the density of the water.

In (5), La_t is the “turbulent Langmuir number,”

$$La_t = \sqrt{\frac{u_*}{U_{s_0}}}, \quad (8)$$

which is a measure of the strength of the wind driving compared to the wave driving. As a typical value of U_{s_0} is $0.1 \frac{\text{m}}{\text{s}}$, a typical value for La_t is around 0.3.

Craik and Leibovich derived this theory using multiple time scale asymptotics with a fast time scale for the waves and a slower time scale for the Langmuir currents. Although (3) is already nondimensional, in section 2.1 we rescale the system. Note that we assume there is no Coriolis force, nor any stratification in the fluid.

2.1 Rescaled Equations

For the remainder of Section 1 up to Section 4, we will work in a “2-dimensional, 3 component” (2D/3C) setting. In other words, there are three velocity components (u, v, w) which depend solely on the two spatial coordinates y and z . The 2D/3C assumption is a reasonable one as Langmuir circulation is highly anisotropic; long parallel windrows in the x -direction can be observed on a long scale compared to the scale of the rolls in the crosswind (y, z)-plane.

One of the important consequences of this assumption is that we can rescale the terms in (3) to replace the two parameters La_t and Re_* by the “laminar Langmuir number,”

$$La = \frac{\nu_e}{\sqrt{(u_* Re_*) u_{s_0} H}}, \quad (9)$$

which is a single parameter for the analysis in Section 3. The laminar Langmuir number includes forcing from both the wind and the waves and is typically about ten times smaller than the turbulent Langmuir number. The term $u_* Re_*$ in the denominator is used to scale the flow in the x -direction to make it non-dimensional. The basic flow from the wind in this direction is given by

$$U_B(z) = u_* Re_* \frac{z}{H} + u_0. \quad (10)$$

Here u_* and u_0 have dimensions of speed, Re_* and $\frac{z}{H}$ are dimensionless, thus U_B has units of speed. We scale z so that the depth H of the mixed layer is 1; then after nondimensionalization, the wind stress conditions ends up being

$$\partial_z U_B(z) = 1; \quad (11)$$

we also scale $U_B(z)$ so that $u_0 = 1$. The directional velocities in the y - and z -directions are rescaled differently, using

$$\sqrt{(u_* Re_*) u_{s_0}}. \quad (12)$$

Notice that as Re_* is dimensionless and u_* and u_{s_0} are speeds, the above has a unit of $\frac{m}{s}$.

2.2 Coordinate equations

The assumption that U is incompressible together with the 2D/3C requirement that $\frac{\partial}{\partial x}(\cdot) = 0$ yields a natural definition of a streamfunction ψ , defined up to a constant by

$$\partial_z \psi := v, \quad -\partial_y \psi := w. \quad (13)$$

The vorticity Ω is defined by

$$\Omega = -\nabla^2 \psi. \quad (14)$$

We can rewrite the nondimensionalized version of (3) in component form using the fields u, Ω, ψ rather than the directional velocities u, v, w . This form of the equations is obtained by computing the curl of Craik-Leibovich and then taking the inner product of the result with x ; this computation removes the pressure term from the resulting equations. More simply, as there is no x -dependence, it suffices to cross-differentiate the v and w component equations to get an equation for Ω .

Setting $J(\cdot, \cdot)$ be the Jacobian

$$J(f, g) = \frac{\partial f}{\partial y} \frac{\partial g}{\partial z} - \frac{\partial f}{\partial z} \frac{\partial g}{\partial y},$$

the resulting system of equations can be written in component form as

$$\partial_t u + J(u_p, \psi) - \partial_y \psi \frac{dU_B}{dz} = La \nabla^2 u, \quad (15)$$

$$\partial_t \Omega + J(\Omega, \psi) = -\frac{dU_s}{dz} \partial_y u + La \nabla^2 \Omega, \quad (16)$$

$$\nabla^2 \psi = -\Omega. \quad (17)$$

Notice that with the nondimensionalization, $U_B(z) = z + 1$; (15) therefore simplifies to

$$\partial_t u + J(u_p, \psi) - \partial_y \psi = La \nabla^2 u.$$

2.3 Boundary Conditions

At this point there has been no mention of the boundary conditions for u , Ω and ψ . As the sidewalls of our box are periodic, the fields are correspondingly periodic in y . As is common in air-wind interface, we use shear stress-free conditions, thus $\partial_z v = 0$. Furthermore, $w = 0$ at $z = 0$ due to the Craik-Leibovich filtered term: the surface waves have been averaged out so that there is no vertical displacement at the top. As $w = 0$ and $w = -\partial_y \psi$, the streamfunction does not change with y . As ψ is defined up to a constant, we set

$$\psi = 0 \quad (18)$$

at the top. Moreover, notice

$$\Omega = \partial_y w - \partial_z v = 0. \quad (19)$$

Similarly, at $z = -1$, there is no normal flow, and we assume the same conditions for ψ and Ω at the bottom of the mixed layer $z = -1$.

The conditions on the downstream velocity u are chosen with several points in mind. In particular, the bottom boundary is not a true physical boundary; this is especially true for the deep ocean, where beneath the mixing layer is water whose depth may be considered virtually infinite. At the surface, it is natural to impose a fixed stress condition between the air and water; after rescaling, the boundary condition for u at the top is

$$\partial_z u = 1, \quad (20)$$

implying that $\partial_z u_p = 0$.

The bottom boundary condition on u is chosen not only to reflect the physics of the circulation, but also in way that allows for 2 : 1 spatial resonance theory to be used in our analysis. As the parameter La is inversely proportional to the Reynolds number, then for a fixed wavenumber k , decreasing La (equivalently increasing La^{-1}) has the effect of increased forcing on the system. At some critical value of La , a mode with wavenumber k bifurcates from a stable state to an unstable state. In numerical simulations of (3) with fixed-stress boundary conditions, as the forcing on the system is increased, the first mode to go unstable is $k = 0$. Physically this mode represents one long flat convection cell with an infinitely long wavelength. The preference for these long scales at onset is a consequence of taking the same stress at the bottom of the layer as at the top.

If the first mode to change stability is the physically unrealistic $k = 0$ mode, then no 2 : 1 spatial resonance can be observed from weakly nonlinear theory. Thus in the following calculations, we will use a mixed boundary condition, also known as a Robin boundary condition, at $z = -1$. This condition is physically realistic because though the wind stress is assumed to be fixed, the water in the mixed layer may move at a faster speed than the water below; at the very least, there will be some viscous stress at the bottom layer. The mixed boundary conditions are beneficial as they indicate that the stress is proportional to a difference in speeds in the downstream direction.

The resulting condition

$$\partial_z u - \gamma u = 0 \quad (21)$$

applies to the perturbation u_p , as $U_B(-1) \equiv 0$. The parameter γ is a small, positive constant often referred to as a Biot number. It is discussed in greater detail by Cox and Leibovich

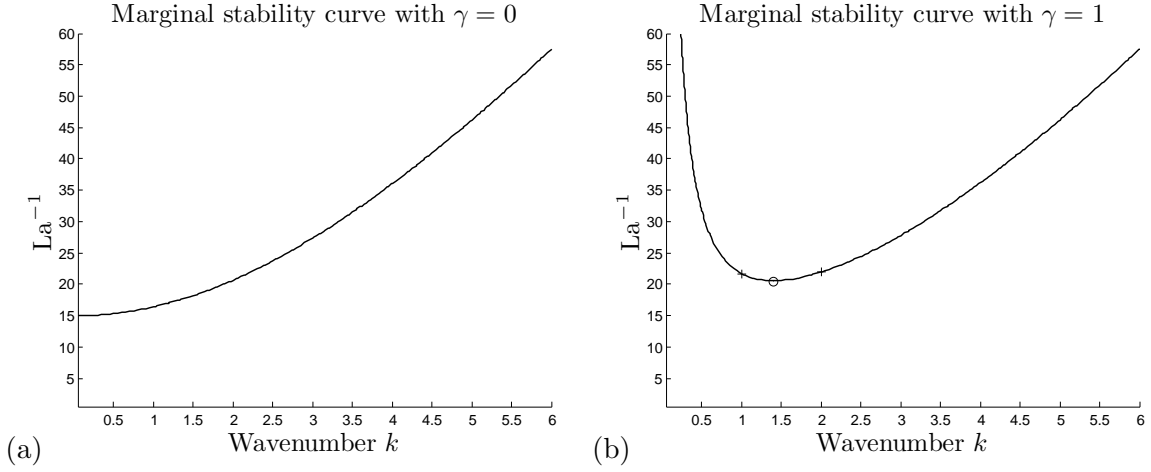


Figure 3: Marginal stability curves for two different sets of boundary conditions. Below each curve the real parts of all eigenvalues are negative, and the system is stable; above the curve there is at least one eigenvalue with positive real part, and the system is unstable. The boundary conditions are identical to those described in Section 2.3 with the exception of the boundary condition on u at $z = -1$. For (a), the bottom boundary condition is $\partial_z u = 0$, while for (b) the bottom boundary condition is $\partial_z u - \gamma u = 0$. As a result of the mixed conditions in (b), the first mode to change stability is no longer at $k = 0$. The two +’s indicate the wavenumbers k_0 and $2k_0$ which change stability at the same La_0 . The \circ marks the wavenumber where the initial onset of instability occurs. The Stokes drift is $U_s(z) = e^{2(4)z}$, and 30 Chebyshev grid points were used.

(c.f. [5], [6], [7]). This stipulation has the added benefit of altering which modes undergo an initial change in stability as La is decreased; in particular $k = 0$ is no longer the first mode to go unstable. See Figure 3 for a comparison between the marginal stability curve with fixed-stress boundary conditions and with mixed boundary conditions.

3 Evolution Equations

It is possible that for some value of La , two modes undergo simultaneous bifurcation; as this arises from varying not only La but also k , this is a codimension-2 bifurcation. The terminology “ $m : n$ spatial resonance” refers to a situation in which two separate modes with spatial ratio is $m : n$ experience such a bifurcation. Of interest here is the case $m = 2, n = 1$, which corresponds to wavenumbers k_0 and $2k_0$ changing stability at the same Langmuir number, which we will denote La_0 .

In this section, we construct equations for the fields u, ψ and Ω in terms of the modes k_0 and $2k_0$. Each mode will contain an amplitude term: $A(t)$ for the k_0 mode, also referred to as the “single mode,” and $B(t)$ for the $2k_0$ mode, the “double mode,” where t is time. These equations describe how the two modes are activated at a particular instant; for example, if $A(T) = 0$ for some time T , then only the $2k_0$ mode is activated, and a 4-roll state is observed at time T .

To illustrate the persistent switching between 4 rolls and 2 rolls in a box of width $2\pi/k_0$, we derive evolution equations $\dot{A} = f_1(A, B)$ and $\dot{B} = f_2(A, B)$. These equations must commute with the representation of $O(2)$ given by

$$\vartheta \cdot (A, B) = (e^{i\vartheta} A, e^{2i\vartheta} B), \quad (22)$$

$$\zeta \cdot (A, B) = (\bar{A}, \bar{B}), \quad (23)$$

where the reflection ζ is defined with respect to a chosen origin in y . A dynamical system that commutes with a group action is referred to as an equivariant dynamical system.

A fixed point (A_0, B_0) of a dynamical system occurs when \dot{A} and \dot{B} evaluated at (A_0, B_0) are both zero. A heteroclinic orbit is a trajectory $\varphi(t)$ in phase space that “connects” two such fixed points (A_0, B_0) and (A_1, B_1) in the sense that

$$\varphi(t) \rightarrow (A_0, B_0) \text{ and } \varphi(-t) \rightarrow (A_1, B_1) \text{ as } t \rightarrow \infty.$$

In other words, the heteroclinic orbit lies in the stable manifold of (A_0, B_0) and the unstable manifold of (A_1, B_1) .

In general, heteroclinic orbits are not structurally stable: a heteroclinic orbit is likely to break into two trajectories as parameters in a system are varied. Dynamical systems exhibiting symmetry properties such as the system under consideration here, however, may yield structurally stable heteroclinic orbits. These cycles, found on the center manifold tangent to the center eigenspace, are robust and persist under a range of parameter values.

There are three codimension-2 mode interactions depending on the type of bifurcation occurring at the two points, see [10] for an overview. As the eigenvalues at the bifurcation points are both zero (with zero imaginary part), of interest here is the steady state/state case, for which the center manifold is 4-dimensional. Thus $(A, B) \in \mathbb{C}^2$.

Using center manifold reduction we derive the amplitude equations for A and B . As shown in [1] and [13], the normal form for such evolution equations up to cubic order is

$$\dot{A} = \mu_1 A + c_{12} \bar{A} B + d_{11} |A|^2 A + d_{12} |B|^2 A, \quad (24)$$

$$\dot{B} = \mu_2 B + c_{11} A^2 + d_{21} |A|^2 B + d_{22} |B|^2 B. \quad (25)$$

where $\cdot = \frac{d}{dt}$. With numerically computed coefficients for these equations, we analyze the resulting dynamics, with particular attention given to the existence of structurally stable heteroclinic orbits.

In addition to the A and B modes in the crosswind plane, the nonlinear terms in (15)-(17) generate an additional mode C for the downstream direction. This is the horizontal mean term with wavenumber zero and will produce a third evolution equation. While A and B have no dependence on C , the evolution equation for C is of the form

$$\dot{C} = \gamma_0 C + \gamma_1 |A(\tau_1)|^2 + \gamma_2 |B(\tau_1)|^2, \quad (26)$$

where $\cdot = \frac{d}{dt}$ and $\tau_1 = \varepsilon t$; the small parameter $\varepsilon > 0$ is described in Section 3.2. In general, if we suppose the Langmuir cells are very strong, then the horizontally averaged downwind velocity is homogeneous except at the top and bottom of the box. The C mode equation (26) computes the tendency to homogenize the horizontal mean velocity.

3.1 Linear Stability Analysis

We first linearize (15)-(17) about the basic flow $U = (U_B(z), 0, 0)$ with $U_B(z) = z + 1$ and obtain

$$\partial_t u - \partial_y \psi = La \nabla^2 u, \quad (27)$$

$$\partial_t \Omega = -\frac{dU_s}{dz} \partial_y u + La \nabla^2 \Omega, \quad (28)$$

$$\nabla^2 \psi = -\Omega. \quad (29)$$

In the above, La is a parameter and not the fixed quantity La_0 . The boundary conditions do not change with the linearization, as they are already linear (and in fact homogeneous). Using the periodicity of y , we make a normal mode ansatz

$$\begin{pmatrix} u(y, z, t) \\ \Omega(y, z, t) \\ \psi(y, z, t) \end{pmatrix} = \begin{pmatrix} \hat{u}(z) \\ \hat{\Omega}(z) \\ \hat{\psi}(z) \end{pmatrix} e^{iky} e^{\sigma t} + \text{c.c.} \quad (30)$$

where σ is the growth rate, k is an unspecified wavenumber in the lateral direction, and the functions $\hat{u}(z), \hat{\Omega}(z), \hat{\psi}(z)$ are the coordinates of the unknown vertical structure of the flow. With this ansatz, (27)-(29) becomes an ordinary differential eigenvalue problem for σ :

$$\begin{pmatrix} La(D^2 - k^2) & 0 & ik \\ -\frac{dU_s}{dz} ik & La(D^2 - k^2) & 0 \\ 0 & 1 & D^2 - k^2 \end{pmatrix} \begin{pmatrix} \hat{u} \\ \hat{\Omega} \\ \hat{\psi} \end{pmatrix} = \sigma \begin{pmatrix} 1 & 0 & 0 \\ 0 & 1 & 0 \\ 0 & 0 & 0 \end{pmatrix} \begin{pmatrix} \hat{u} \\ \hat{\Omega} \\ \hat{\psi} \end{pmatrix}, \quad (31)$$

where $D = \frac{\partial}{\partial z}$. We discretize the z -direction with 30 Chebyshev points and use Chebyshev spectral methods in Matlab¹ to solve this eigenvalue problem as a two-point boundary value problem in z . For each k in a chosen interval, we find the Langmuir number at which point the stability of the system changes. The result is a marginal stability curve, an example of which can be seen in Figure 3(b).

We locate on this curve the wavenumbers k_0 and $2k_0$ which change stability at essentially the same La_0 , and correspondingly set the width of the box in the (y, z) -plane to be $W = \frac{2\pi}{k_0}$. Henceforth, the terms k_0 , $2k_0$ and La_0 refer to the quantities found by this eigenvalue calculation.

For the zero-mode equation with amplitude C , we repeat (31) with $k = 0$ and solve

$$\begin{pmatrix} La_0 D^2 & 0 & 0 \\ 0 & La_0 D^2 & 0 \\ 0 & 1 & D^2 \end{pmatrix} \begin{pmatrix} \hat{u}_0 \\ \hat{\Omega}_0 \\ \hat{\psi}_0 \end{pmatrix} = \sigma \begin{pmatrix} 1 & 0 & 0 \\ 0 & 1 & 0 \\ 0 & 0 & 0 \end{pmatrix} \begin{pmatrix} \hat{u}_0 \\ \hat{\Omega}_0 \\ \hat{\psi}_0 \end{pmatrix}. \quad (32)$$

With the chosen boundary conditions, $\hat{\Omega}_0 = \hat{\psi}_0 = 0$. Then (32) reduces to

$$\frac{\partial}{\partial t} \hat{u}_0(z, t) = La_0 \frac{\partial^2}{\partial z^2} \hat{u}_0(z, t). \quad (33)$$

Writing $\hat{u}_0(z, t)$ as

$$\hat{u}_0(z, t) = C(t) \tilde{u}(z), \quad (34)$$

then C satisfies

$$\frac{dC}{dt} = \sigma C(t). \quad (35)$$

Thus γ_0 in (26) is the eigenvalue σ , which is determined numerically. As $k = 0$ is in the stable regime, $\gamma_0 < 0$.

3.2 Weakly nonlinear analysis

Let $\varepsilon > 0$ be a small parameter. As the shape of the marginal stability curve seen in Figure 3(b) is parabolic near the onset of instability, varying the wavenumber k by ε corresponds to a change in La^{-1} by ε^2 . In particular, since we want small amplitude perturbations just above the onset of instability, a small parameter $\mu > 0$ is used to vary the height of the parameter La^{-1} over the marginal stability curve in Figure 3(b). Then La^{-1} can be written

$$La^{-1} = La_0^{-1} + \mu \varepsilon^2. \quad (36)$$

The role of the small parameter μ will be made more precise in Section 3.4. As we are interested in a weakly nonlinear regime, the small perturbation terms added to each field are $O(\varepsilon)$, and each field can be expanded in powers of ε in the following way:

$$u = U_B + \varepsilon u_1 + \varepsilon^2 u_2 + \dots, \quad (37)$$

$$\Omega = \varepsilon \Omega_1 + \varepsilon^2 \Omega_2 + \dots, \quad (38)$$

$$\psi = \varepsilon \psi_1 + \varepsilon^2 \psi_2 + \dots. \quad (39)$$

¹Based on methods and code in [16].

Lastly, we introduce slow times $\tau_1 = \varepsilon t$ and $\tau_2 = \varepsilon^2 t$ so that

$$\frac{\partial}{\partial t} = \varepsilon \frac{\partial}{\partial \tau_1} + \varepsilon^2 \frac{\partial}{\partial \tau_2}. \quad (40)$$

This separation of time scales will cause the quadratic terms $\bar{A}B$ and A^2 of the evolution equation in (24)-(25) to emerge in the analysis at $O(\varepsilon^2)$, while the rest of the terms will emerge at $O(\varepsilon^3)$. Substituting the terms obtained at each step into (40) yields evolution equations of the form

$$\dot{A} = \varepsilon^2 \mu_1 A + \varepsilon c_{12} \bar{A}B + \varepsilon^2 e_{11} |A|^2 A + \varepsilon^2 e_{12} |B|^2 A, \quad (41)$$

$$\dot{B} = \varepsilon^2 \mu_2 B + \varepsilon c_{11} A^2 + \varepsilon^2 e_{21} |A|^2 B + \varepsilon^2 e_{22} |B|^2 B, \quad (42)$$

where $\dot{\cdot} = \frac{\partial}{\partial t}$. After multiplying both sides of the above by ε and rescaling via

$$\varepsilon A \rightarrow A, \quad \varepsilon B \rightarrow B, \quad \varepsilon^2 \mu_i \rightarrow \mu_i,$$

the equations have the expected form

$$\dot{A} = \mu_1 A + c_{12} \bar{A}B + e_{11} |A|^2 A + e_{12} |B|^2 A, \quad (43)$$

$$\dot{B} = \mu_2 B + c_{11} A^2 + e_{21} |A|^2 B + e_{22} |B|^2 B \quad (44)$$

where μ_i is $O(\varepsilon^2)$, A and B are $O(\varepsilon)$, while c_{1i} and e_{ij} are $O(1)$. For amplitude C of the zero-mode equation, the coefficient γ_0 emerges from the linear stability analysis, while γ_1 and γ_2 are found at $O(\varepsilon^2)$ with the slow time scale τ_1 . Hence C is $O(\varepsilon^2)$.

The leading $O(\varepsilon)$ terms are written

$$u_1(y, z, \tau_1) = A(\tau_1) e^{ik_0 y} u_{11}(z) + B(\tau_1) e^{2ik_0 y} u_{12}(z) + \text{c.c.}, \quad (45)$$

$$\Omega_1(y, z, \tau_1) = A(\tau_1) e^{ik_0 y} \Omega_{11}(z) + B(\tau_1) e^{2ik_0 y} \Omega_{12}(z) + \text{c.c.}, \quad (46)$$

$$\psi_1(y, z, \tau_1) = A(\tau_1) e^{ik_0 y} \psi_{11}(z) + B(\tau_1) e^{2ik_0 y} \psi_{12}(z) + \text{c.c.}, \quad (47)$$

where c.c. denotes the complex conjugate, as each field must be real. We solve the $O(\varepsilon)$ system numerically for the functions u_{ij} , Ω_{ij} and ψ_{ij} , $i, j \in \{1, 2\}$ by solving for the eigenvectors of the system (31) with $\sigma = 0$.

The $O(\varepsilon^2)$ terms u_2, Ω_2, ψ_2 are written similarly but inevitably have more wavenumbers due to the mode-mode interaction in the nonlinear terms of (15)-(17). For example, the $e^{ik_0 y}$ and $e^{2ik_0 y}$ modes interact to generate a mode of wavenumber 3; overall, at $O(\varepsilon^2)$ there are 9 total terms corresponding to each of

$$e^0, e^{\pm ik_0 y}, e^{\pm 2ik_0 y}, e^{\pm 3ik_0 y}, e^{\pm 4ik_0 y}.$$

Notice that the wavenumbers 0, 3 and 4 are all in the stable regime as they lie under the marginal stability curve for the fixed value of La .

We remark further that the mode-mode interaction can reinforce the single mode $e^{ik_0 y}$ and the double mode $e^{2ik_0 y}$. The former occurs when $e^{2ik_0 y}$ interacts with $e^{-ik_0 y}$, while the latter occurs when $e^{ik_0 y}$ interacts with itself. Therefore, when the evolution equations for the amplitudes A and B are written in such a way that these modes are only weakly

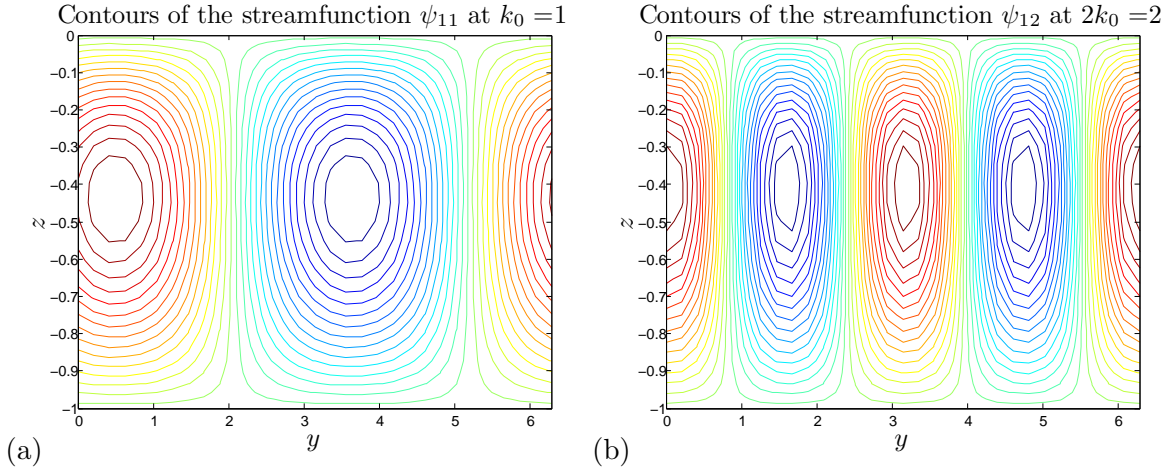


Figure 4: These plots illustrate the Langmuir cells for the (a) 2 roll case and (b) 4 roll case. (a) is obtained by computing $\psi_{11}(z)$ from (47), and then plotting $e^{ik_0 y} \psi_{11}(z)$ in the (y, z) -plane with periodic sidewalls. (b) is obtained the same way for $\psi_{12}(z)$ and $e^{2ik_0 y}$. Thirty Chebyshev grid points were used.

growing, the interaction of \bar{A} and B will produce a source term for A , while A and A will produce a source term for B . These evolution equations are thus modified by the 2 : 1 resonance. Notice that this observation agrees with the normal form equations (24) and (25).

Lastly, we note that the appearance of wavenumber zero terms at $O(\varepsilon^2)$ yields an equation for the C mode; the mean flow averaged over y can be written

$$\bar{u}(z, \tau_1) = U_B(z) + O(\varepsilon^2) = U_B(z) + \varepsilon^2 \hat{u}_1(z) C(\tau_1), \quad (48)$$

where $\hat{u}_1(z)$ is the vertical structure of the $O(\varepsilon^2)$ term. This equation is consistent with (45) as C is $O(\varepsilon)$ in (45). While the horizontal mean at $O(\varepsilon)$ stage in equations (45)-(47) is zero, the mode-mode interactions $e^{ik_0 y}$ with $e^{-ik_0 y}$ and $e^{2ik_0 y}$ with $e^{-2ik_0 y}$ give a nontrivial projection to the horizontal mean. Notice this mode-mode interaction justifies the form of equation (26).

3.2.1 The Fredholm Alternative

Let $\langle \cdot, \cdot \rangle$ be the Hermitian L^2 inner product

$$\langle v_1, v_2 \rangle = \iint_D v_1 \cdot \bar{v}_2 dy dz,$$

where the domain D is the box $[0, 2\pi/k_0] \times [-1, 0]$ in the cross-wind plane, and \cdot denotes the standard Euclidean inner product. Let L be the linear operator

$$L = \begin{pmatrix} La\nabla^2 & 0 & \partial_y \\ 0 & 1 & \nabla^2 \\ -\frac{dU_s}{dz} \partial_y & La\nabla^2 & 0 \end{pmatrix}, \quad (49)$$

and let L^\dagger be its adjoint. By the Fredholm alternative, $L(u, \Omega, \psi)^t = (f, g, h)^t$ has a solution if and only if

$$\left\langle (u^\dagger, \Omega^\dagger, \psi^\dagger)^t, (f, g, h)^t \right\rangle = 0, \quad (50)$$

where $(u^\dagger, \Omega^\dagger, \psi^\dagger)^t$ is in the null space of L^\dagger .

L is an operator acting on the space of triples of functions $(u, \Omega, \psi)^t$ with u , Ω and ψ satisfying the boundary conditions in Section 2.3. Suppose (u^*, Ω^*, ψ^*) satisfies identical boundary conditions to (u, Ω, ψ) . Let M be the diagonal matrix

$$M = \begin{pmatrix} \frac{dU_s}{dz} & 0 & 0 \\ 0 & La & 0 \\ 0 & 0 & 1 \end{pmatrix}, \quad (51)$$

and set $L_M = ML$. Using integration by parts with the definition of the adjoint,

$$\iint_D (u^*, \Omega^*, \psi^*) \cdot \overline{(L_M(u, \Omega, \psi)^t)^t} dy dz = \iint_D \left(L_M^\dagger(u^*, \Omega^*, \psi^*)^t \right) \cdot \overline{(u, \Omega, \psi)} dy dz, \quad (52)$$

we determine that L_M is self-adjoint. A simpler calculation also shows that $M^\dagger = M$. Thus

$$ML = (ML)^\dagger = L^\dagger M^\dagger = L^\dagger M,$$

which implies that

$$L^\dagger = MLM^{-1} = \begin{pmatrix} La\nabla^2 & 0 & \frac{dU_s}{dz}\partial_y \\ 0 & 1 & La\nabla^2 \\ -\partial_y & \nabla^2 & 0 \end{pmatrix}. \quad (53)$$

3.2.2 Order ε

Equations (37)-(39) are substituted into (15)-(17). The $O(\varepsilon)$ equations are

$$-La\nabla^2 u_1 - \partial_y \psi_1 = 0, \quad (54)$$

$$-\frac{dU_s}{dz} \partial_y u_1 + La\nabla^2 \Omega_1 = 0, \quad (55)$$

$$\Omega_1 + \nabla^2 \psi_1 = 0, \quad (56)$$

where u_1, Ω_1, ψ_1 are the functions from (45)-(47). The form of these equations is identical to the linear stability analysis in (27)-(29) with $\frac{\partial}{\partial t} = 0$ as the onset of instability occurs along the marginal stability curve.

There are two separate calculations performed, as ∂_y becomes multiplication by ik_0 when it acts on the single mode and by $2ik_0$ when it acts on the double mode. Solving for eigenvectors $(u_1, \Omega_1, \psi_1)^t$ satisfying

$$L \begin{pmatrix} u_1 \\ \Omega_1 \\ \psi_1 \end{pmatrix} = 0 \quad (57)$$

yields two vectors: $E_1 = (u_{11}, \Omega_{11}, \psi_{11})^t$ for the single mode structure and $E_2 = (u_{12}, \Omega_{12}, \psi_{12})^t$ for the double mode. Plots of ψ_{11} and ψ_{12} are seen in Figure 4.

Set $E_{11} = E_1$, $E_{12} = \overline{E_1}$, $E_{21} = E_2$ and $E_{22} = \overline{E_2}$. Then

$$\begin{pmatrix} u_1 \\ \Omega_1 \\ \psi_1 \end{pmatrix} = Ae^{ik_0y} E_{11} + Be^{2ik_0y} E_{21} + \overline{A}e^{-ik_0y} E_{12} + \overline{B}e^{-2ik_0y} E_{22}.$$

With the same process, we also compute four vectors E_{ij}^\dagger in the kernel of L^\dagger to use in the calculations for the Fredholm alternative in the next two sections.

3.2.3 Order ε^2

After substituting (37)-(39) into (15)-(17), the $O(\varepsilon^2)$ system is

$$La_0 \nabla^2 u_2 + \partial_y \psi_2 = \partial_{\tau_1} u_1 + J(u_1, \psi_1), \quad (58)$$

$$\Omega_2 + \nabla^2 \psi_2 = 0, \quad (59)$$

$$-\frac{dU_s}{dz} \partial_y u_2 + La_0 \nabla^2 \Omega_2 = \partial_{\tau_1} \Omega_1 + J(\Omega_1, \psi_1), \quad (60)$$

Notice that we already have expressions for u_1, ψ_1, Ω_1 from the $O(\varepsilon)$ case. This can be written in terms of the linear operator L and including the slow time τ_1 as

$$L \begin{pmatrix} u_2 \\ \Omega_2 \\ \psi_2 \end{pmatrix} = \begin{pmatrix} \partial_{\tau_1} u_1 + J(u_1, \psi_1) \\ 0 \\ \partial_{\tau_1} \Omega_1 + J(\Omega_1, \psi_1) \end{pmatrix}. \quad (61)$$

The right-hand side can be explicitly computed with the eigenvectors u_1, ψ_1, Ω_1 found in Section 3.2.2. For the solvability criterion (50), we set

$$\left\langle E_{ij}^\dagger, \begin{pmatrix} \partial_{\tau_1} u_1 + J(u_1, \psi_1) \\ 0 \\ \partial_{\tau_1} \Omega_1 + J(\Omega_1, \psi_1) \end{pmatrix} \right\rangle = 0, \quad (62)$$

$i, j = 1, 2$. We compute this inner product numerically using quadrature and obtain the coefficients of the quadratic terms $\overline{A}B$ and A^2 in the evolutions equations for A and B , respectively; below is an example calculation for the $\overline{A}B$ coefficient. For the vectors in the nullspace of L^\dagger computed in Section 3.2.2, let $E_{ij}^\dagger(z) = (E_{ij,1}^\dagger(z), E_{ij,2}^\dagger(z), E_{ij,3}^\dagger(z))^t$. Then the solvability criterion yields a condition on the derivatives of A and B , found by computing

$$\begin{aligned} 0 &= \left\langle E_{11}^\dagger(z) e^{-ik_0y}, \begin{pmatrix} \partial_{\tau_1} u_1(y, z, \tau_1) + J(u_1(y, z, \tau_1), \psi_1(y, z, \tau_1)) \\ 0 \\ \partial_{\tau_1} \Omega_1(y, z, \tau_1) + J(\Omega_1(y, z, \tau_1), \psi_1(y, z, \tau_1)) \end{pmatrix} \right\rangle \\ &= \iint_D \left(E_{11,1}^\dagger(z) e^{-ik_0y} \overline{(\partial_{\tau_1} u_1(y, z, \tau_1) + J(u_1(y, z, \tau_1), \psi_1(y, z, \tau_1)))} \right) dy dz \\ &\quad + \iint_D \left(E_{11,3}^\dagger(z) e^{-ik_0y} \overline{\partial_{\tau_1} \Omega_1(y, z, \tau_1) + J(\Omega_1(y, z, \tau_1), \psi_1(y, z, \tau_1))} \right) dy dz \end{aligned}$$

After simplification, each term in the above integrand contains an expression of the form e^{mik_0y} . If $m \neq 0$, then

$$\int_0^{2\pi/k_0} e^{mik_0y} dy = 0.$$

Hence the only terms from the $\overline{\partial_{\tau_1}(\cdot) + J(\cdot, \psi_1)}$ expressions which contribute nontrivially to the solvability criterion are those whose y -structure after complex conjugation is $e^{ik_0 y}$. Therefore, the solvability criterion can be explicitly written as

$$\begin{aligned}
0 = & \int_{-1}^0 \left(E_{11,1}^\dagger(z) \cdot \left(A_{\tau_1} u_{11}(z) + 2ik_0 \bar{A} B u_{12}(z) \frac{d\bar{\psi}_{11}}{dz} - ik_0 \bar{A} B \bar{u}_{11}(z) \frac{d\psi_{12}}{dz} \right) \right) dz \\
& - \int_{-1}^0 \left(E_{11,1}^\dagger(z) \cdot \left(2ik_0 \bar{A} B \psi_{12}(z) \frac{d\bar{u}_{11}}{dz} - ik_0 \bar{A} B \bar{\psi}_{11}(z) \frac{du_{12}}{dz} \right) \right) dz \\
& + \int_{-1}^0 \left(E_{11,3}^\dagger(z) \cdot \left(A_{\tau_1} \Omega_{11}(z) + 2ik_0 \bar{A} B \Omega_{12}(z) \frac{d\bar{\psi}_{11}}{dz} - ik_0 \bar{A} B \bar{\Omega}_{11}(z) \frac{d\psi_{12}}{dz} \right) \right) dz \\
& - \int_{-1}^0 \left(E_{11,3}^\dagger(z) \cdot \left(2ik_0 \bar{A} B \psi_{12}(z) \frac{d\bar{\Omega}_{11}}{dz} - ik_0 \bar{A} B \bar{\psi}_{11}(z) \frac{d\Omega_{12}}{dz} \right) \right) dz.
\end{aligned}$$

Thus

$$\begin{aligned}
A_{\tau_1} \int_{-1}^0 \left(E_{11,1}^\dagger u_{11} + E_{11,3}^\dagger \Omega_{11} \right) dz = & -ik_0 \bar{A} B \left[\int_{-1}^0 \left(E_{11,1}^\dagger \left(2u_{12} \frac{d\bar{\psi}_{11}}{dz} - \bar{u}_{11} \frac{d\psi_{12}}{dz} \right) \right) dz \right. \\
& + \int_{-1}^0 \left(E_{11,1}^\dagger \cdot \left(2\psi_{12} \frac{d\bar{u}_{11}}{dz} - \bar{\psi}_{11} \frac{du_{12}}{dz} \right) \right) dz \\
& - \int_{-1}^0 \left(E_{11,3}^\dagger \cdot \left(2\Omega_{12} \frac{d\bar{\psi}_{11}}{dz} - \bar{\Omega}_{11} \frac{d\psi_{12}}{dz} \right) \right) dz \\
& \left. + \int_{-1}^0 \left(E_{11,3}^\dagger \cdot \left(2\psi_{12} \frac{d\bar{\Omega}_{11}}{dz} - \bar{\psi}_{11} \frac{d\Omega_{12}}{dz} \right) \right) dz \right]
\end{aligned}$$

The left and right sides of the above can be computed numerically using quadrature methods from [16], chapter 12. Then each integral results in a scalar value, yielding a simple calculation for the coefficient c_{12} in

$$A_{\tau_1} = c_{12} \bar{A} B.$$

In addition, the particular solution $(u_2, \Omega_2, \psi_2)^t$ to (61) is also found numerically in Matlab using the pseudoinverse of the matrix L .

Lastly, due to the presence of wavenumber zero at $O(\varepsilon^2)$, we compute the equation for the amplitude $C(\tau_1)$ of the mean velocity at this order. As a result of horizontal averaging, no Langmuir cells remain; however, there is a correction term in the streamwise flow that reflects the fact that there were cells present. For the solvability criterion to compute the $O(\varepsilon^2)$ contribution to \dot{C} , the zero mode version of (61) is written

$$(LaD^2 - \sigma) \hat{u}_2 = (\varepsilon \partial_{\tau_1} C) \hat{u}_1(z) + J(u_1, \psi_1)_0, \quad (63)$$

where $J(u_1, \psi_1)_0$ refers to the terms in $J(u_1, \psi_1)$ which have no y -dependence. These are the terms that arise from nonlinear interaction between $e^{ik_0 y}$ and $e^{-ik_0 y}$, and $e^{2ik_0 y}$ and $e^{-2ik_0 y}$. Then (63) has a solution if and only if

$$\langle \hat{u}_1, (\varepsilon \partial_{\tau_1} C) \hat{u}_1 + J(u_1, \psi_1)_0 \rangle = 0, \quad (64)$$

which results in

$$\begin{aligned}
(\varepsilon \partial_{\tau_1} C) \int_{-1}^0 |\hat{u}_1(z)|^2 dz &= -|A|^2 \int_{-1}^0 \hat{u}_1(z) (u_{11}(z) \overline{\psi_{11}}(z) + \overline{u_{11}}(z) \psi_{11}(z)) dz \\
&\quad - |B|^2 \int_{-1}^0 \hat{u}_1(z) (u_{12}(z) \overline{\psi_{12}}(z) + \overline{u_{12}}(z) \psi_{12}(z)) dz.
\end{aligned}$$

These integrals are also computed using quadrature methods and yield the coefficients γ_1 and γ_2 from (26). Then

$$\begin{aligned}
\dot{C} &= \sigma C + \varepsilon \partial_{\tau_1} C \\
&= \gamma_0 C + \gamma_1 |A|^2 + \gamma_2 |B|^2.
\end{aligned}$$

3.2.4 Order ε^3

The remaining coefficients up to cubic order emerge from the $O(\varepsilon^3)$ system:

$$\begin{aligned}
\partial_{\tau_1} u_2 + \partial_{\tau_2} u_1 + J(u_1, \psi_2) + J(u_2, \psi_1) - \partial_y \psi_3 &= La_0 \nabla^2 u_3 - La_0^2 \mu \nabla^2 u_1, \\
-\Omega_3 &= \nabla^2 \psi_3, \\
\partial_{\tau_1} \Omega_2 + \partial_{\tau_2} \Omega_1 + J(\Omega_1, \psi_2) + J(\Omega_2, \psi_1) &= -\frac{dU_s}{dz} u_3 + La_0 \nabla^2 \Omega_3 - La_0^2 \mu \nabla^2 \Omega_1.
\end{aligned}$$

Written as matrices with the same linear operator L , the system is

$$L \begin{pmatrix} u_3 \\ \Omega_3 \\ \Psi_3 \end{pmatrix} = \begin{pmatrix} \partial_{\tau_1} u_2 + \partial_{\tau_2} u_1 + J(u_1, \psi_2) + J(u_2, \psi_1) + La_0^2 \mu \nabla^2 u_1 \\ 0 \\ \partial_{\tau_1} \Omega_2 + \partial_{\tau_2} \Omega_1 + J(\Omega_1, \psi_2) + J(\Omega_2, \psi_1) + La_0^2 \mu \nabla^2 \Omega_1 \end{pmatrix}. \quad (65)$$

The right-hand side of (65) is calculated using the results from the previous two sections. As before, we compute the inner product of the right-hand side with the vectors E_{ij}^\dagger numerically using quadrature. The result gives us the coefficients μ_i, e_{ij} , $i, j \in \{1, 2\}$ from (24) and (25). These equations are described in more detail in Section 3.3.

3.3 The evolution equations

Once the vectors u_i , Ω_i and ψ_i have been computed for $i = \{1, 2\}$, we use quadrature methods to solve for the coefficients of the evolution equations. As derived in [1] and [13], the normal form of the equations for A and B up to cubic terms is

$$\dot{A} = \mu_1 A + c_{12} \bar{A} B + d_{11} |A|^2 A + d_{12} |B|^2 A, \quad (66)$$

$$\dot{B} = \mu_2 B + c_{11} A^2 + d_{21} |A|^2 B + d_{22} |B|^2 B. \quad (67)$$

The reflection symmetry $(A, B) \rightarrow (\bar{A}, \bar{B})$ forces the coefficients μ_i, c_{ij}, d_{ij} , $i, j \in \{1, 2\}$, to be real. There are, however, no automatic requirements for the signs of these coefficients. As discussed in the literature on such equivariant dynamical systems, see Armbruster, *et al.* [1] and Porter and Knobloch [12], different dynamical behavior emerges with different combinations of signs.

For the general setting of 2 : 1 spatial resonance, it is possible that c_{12} and c_{11} have the same sign. This situation is referred to as the “+ case” in [1], and it does not yield particularly interesting dynamics. In particular, there is no heteroclinic orbit present in the $\text{Im}(A) = \text{Im}(B) = 0$ plane. The other possibility, that c_{12} and c_{11} have different signs, is referred to in [1] as the “− case” and is more fruitful. For the extensive range of parameter values tested thus far, the evolution equations derived in this work have fallen under this “−” category.

Near the onset of instability, the growth rates μ_1 and μ_2 should be positive. The last sign requirement we make is that e_{11} and e_{22} be negative. This requirement will yield a circle of pure modes discussed in Section 3.4 and seen in Figure 5 and, like the requirement on the quadratic terms, has been satisfied for each set of parameters.

As explored by Chossat in [4], hydrodynamical systems with symmetries often produce evolution equations that fulfill such requirements necessary to exhibit interesting dynamical behavior, such as the class of “−” equations under consideration here. These symmetric systems then yield robust heteroclinic connections in the invariant subspaces of the amplitude equations. Thus hydrodynamics can be rewarding to study from the dynamical systems viewpoint, and it is unsurprising that we find the right type of dynamics in our evolution equations for Langmuir circulation.

As an example of amplitude equations found from the calculations of the previous sections, we derive the following with 30 Chebyshev grid points, $\gamma = 1.5$, and $U_s(z) = e^{2(4z)}$:

$$\dot{A} = 0.0070A - 0.0801\bar{A}B - 0.0758|A|^2A - 0.3867|B|^2A, \quad (68)$$

$$\dot{B} = 0.0152B + 0.0987A^2 - 0.7563|A|^2B - 0.3334|B|^2B, \quad (69)$$

$\cdot = \frac{\partial}{\partial t}$. Additionally, the evolution equation for the horizontal mean term is

$$\dot{C} = -0.0477C + 0.0188|A|^2 + 0.0252|B|^2.$$

As discussed above, (68) and (69) display the desired signs for the coefficients and can be rescaled from the form (66)-(67) to the form (24)-(25), yielding

$$\dot{A} = \mu_1 A + \bar{A}B - 0.9583|A|^2A - 6.0219|B|^2A, \quad (70)$$

$$\dot{B} = \mu_2 B - A^2 - 9.5573|A|^2B - 5.1909|B|^2B. \quad (71)$$

As $A, B \in \mathbb{C}$, they can be written in terms of their real and imaginary parts as

$$\begin{aligned} A &= x_1 + iy_1 = r_1 e^{i\alpha_1}, \\ B &= x_2 + iy_2 = r_2 e^{i\alpha_2}, \end{aligned}$$

from which (66) and (67) can be written in Cartesian coordinates as

$$\dot{x}_1 = x_1(\mu_1 + e_{11}(x_1^2 + y_1^2) + e_{12}(x_2^2 + y_2^2)) + x_1x_2 + y_1y_2, \quad (72)$$

$$\dot{y}_1 = y_1(\mu_1 + e_{11}(x_1^2 + y_1^2) + e_{12}(x_2^2 + y_2^2)) + x_1y_2 - y_1x_2, \quad (73)$$

$$\dot{x}_2 = x_2(\mu_2 + e_{21}(x_1^2 + y_1^2) + e_{22}(x_2^2 + y_2^2)) - (x_1^2 - y_1^2), \quad (74)$$

$$\dot{y}_2 = y_2(\mu_2 + e_{21}(x_1^2 + y_1^2) + e_{22}(x_2^2 + y_2^2)) - 2x_1y_1. \quad (75)$$

Following the terminology of [1], we will call any fixed point $\dot{A} = \dot{B} = 0$ with $r_1 = 0$ but $r_2 \neq 0$ a *pure mode*, and a fixed point $\dot{A} = \dot{B} = 0$ with $r_1 \neq 0$, $r_2 \neq 0$ a *mixed mode*.

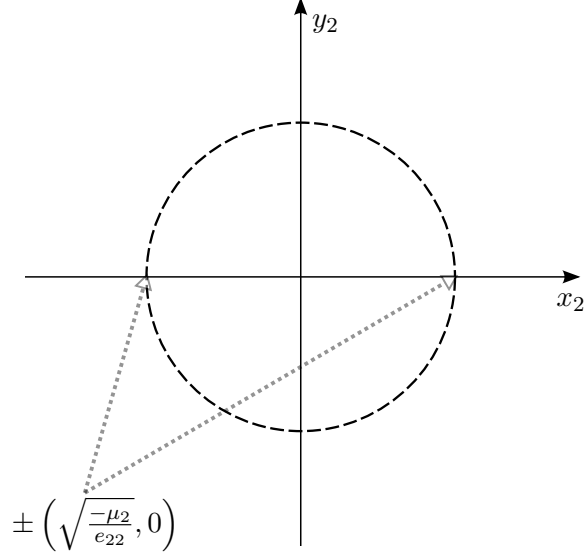


Figure 5: The invariant subspace Σ_1 . There is a circle of pure modes given by $|B|^2 = -\frac{\mu_2}{e_{22}}$. The two points where this circle intersects the x_2 -axis lie in all three invariant subspaces, as seen in Figure 6.

3.4 Dynamics of the Evolution Equations

As simultaneous bifurcation of modes k_0 and $2k_0$ is a codimension-2 bifurcation problem, two parameters are varied to explore the dynamics. Holding the coefficients μ_1 and μ_2 small and varying them does not effect the other coefficients e_{ij} , $i, j \in \{1, 2\}$. These linear term coefficients can be rewritten as

$$(\mu_1, \mu_2) = \mu(\cos \theta, \sin \theta). \quad (76)$$

Thus μ_1 and μ_2 , or equivalently μ and θ , are unfolding parameters; varying μ is equivalent to varying La close to La_0 , while varying θ is equivalent to varying the wavenumbers close to k_0 and $2k_0$.

There are three invariant subspaces for (\dot{A}, \dot{B}) : two 2-dimensional subspaces and their 1-dimensional intersection. The union of the three subspaces can be seen in Figure 6.

1. $\Sigma_1 = \{|A| = 0\}$. On this plane, the flow is given by

$$\dot{A} = 0, \quad \dot{B} = \mu_2 B + e_{22}|B|^2 B, \quad (77)$$

or equivalently, $\dot{x}_1 = \dot{y}_1 = 0$ and

$$\dot{x}_2 = \mu_2 x_2 + e_{22}(x_2^2 + y_2^2)x_2, \quad (78)$$

$$\dot{y}_2 = \mu_2 y_2 + e_{22}(x_2^2 + y_2^2)y_2. \quad (79)$$

There is a fixed point at the origin; moreover, as $e_{22} < 0$ while $\mu_2 > 0$, every point on the circle $x_2^2 + y_2^2 = -\frac{\mu_2}{e_{22}}$ is a pure mode. Of particular interest are the two pure modes on the x_2 axis,

$$\pm \left(0, 0, \sqrt{\frac{-\mu_2}{e_{22}}}, 0 \right), \quad (80)$$

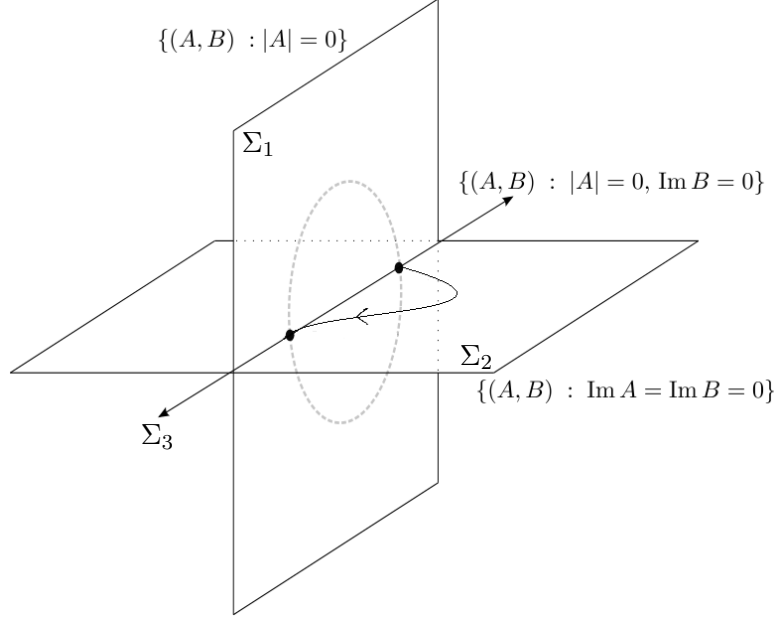


Figure 6: The three invariant subspaces Σ_1 - Σ_3 . A heteroclinic orbit connecting the two pure modes of (80) is pictured in Σ_2 .

seen in Figure 5. These two fixed points appear in Σ_2 below.

2. $\Sigma_2 = \{\text{Im } A = \text{Im } B = 0\}$. The equations for (72)-(75) become

$$\dot{x}_1 = \mu_1 x_1 + x_1 x_2 + e_{11} x_1^3 + e_{12} x_1 x_2^2, \quad (81)$$

$$\dot{x}_2 = \mu_2 x_2 - x_1^2 + e_{21} x_1^2 x_2 + e_{22} x_2^3, \quad (82)$$

with $\dot{y}_1 = \dot{y}_2 = 0$. The flow in this plane is more complicated than for the previous invariant subspace; however, for any choice of coefficients, the pure modes in (80) are also fixed points of (81) and (82). For certain choices of the coefficients, mixed modes may be present, and there may be a heteroclinic connection between the pure modes (80). This possible heteroclinic orbit will be discussed further below.

3. The third invariant subspace is the intersection of the previous two: $\Sigma_3 = \{|A| = 0, \text{Im } B = 0\}$. In other words, this third subspace is the real part of B .

Figure 6 ties together the three invariant subspaces; we see the two pure modes from (80) which lie on the intersection of Σ_3 and the circle of pure modes in $\{|A| = 0\}$ in Σ_1 . The heteroclinic connection found with the equations (68) and (69) is sketched in Σ_2 .

To employ the analysis and results in [1] and [12], we check that the coefficients of (70) and (71) satisfy

$$e_{12} + e_{21} < 2(e_{11}e_{22})^{1/2}, \text{ and} \quad (83)$$

$$\mu_1 - \mu_2 e_{12} e_{22} - (-\mu_2 / e_{22})^{1/2} < 0 < \mu_1 - \mu_2 e_{12} e_{22} + (-\mu_2 / e_{22})^{1/2}, \quad (84)$$

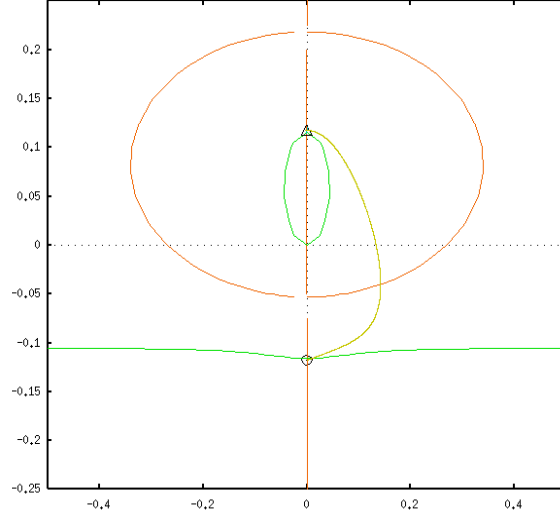


Figure 7: Phase space for Σ_2 with the parameter values of (68)-(69). The curves appearing in all four quadrants are nullclines. The \triangle and \circ mark the pure modes from (80), and there is a heteroclinic orbit pictured between these fixed points. This image was generated using XPPAUT.

in addition to our previous requirements of the signs. These inequalities come from Theorem 3.2 in [1]; in addition, the authors assume further that no mixed modes exist. This assumption is not strictly necessary, but for the equations derived in this project, mixed modes do not appear for a large range of parameter values. With the assumptions (83)-(84), a heteroclinic orbit connecting the points in (80), such as the orbit seen in Figure 7, exists and is structurally stable.

Additionally, we ensure the coefficients satisfy Proposition 5.1 of [1]: if

$$\min \left\{ 2\mu_2, - \left(\mu_1 - \mu_2 e_{12}/e_{22} - (-\mu_2/e_{22})^{1/2} \right) \right\} > \mu_1 - \mu_2 e_{12}/e_{22} + (-\mu_2/e_{22})^{1/2}, \quad (85)$$

then the heteroclinic orbit is locally asymptotically stable and attracts trajectories in a small enough neighborhood. These trajectories spend long amounts of time near the two pure modes where the dynamics are dominated by the linear terms before passing between the two pure modes in a shorter amount of time. This behavior is illustrated in Figure 8(b): the times in which $|A|$ and $|B|$ are flat are the time periods when the trajectory is close to the two pure modes or transitioning rapidly between them, while the spikes correspond to the times when the trajectory is following closely to the heteroclinic orbit.

Here enters the role of μ and θ from (76): we vary these two parameters as necessary in the first quadrant of the (μ_1, μ_2) plane to find a desirable heteroclinic connection. In general, it is not difficult to satisfy (83)-(85), and there is usually a large neighborhood of μ and θ which yield such a heteroclinic orbit.

Once the heteroclinic orbit is located, it is possible to follow a nearby trajectory using the software package XPPAUT [9]. In addition to plotting the trajectory, this package can simultaneously compute the sizes of $|A|$ and $|B|$ for each time step in the integration. The result of such a computation is seen in Figure 8. When the integration begins near the

pure mode $(0, 0, \sqrt{-\mu_2/e_{22}}, 0)$, the A mode is hardly activated. As t grows, the trajectory moves away from this pure mode, and the A mode is activated. At $t = 114$, $\text{Re } B \rightarrow 0$; at this t , the size of $|B|$ reaches a minimum that is very small, as the imaginary part of B near the heteroclinic orbit is close to zero. At this point, the size of $|A|$ nearly reaches its maximum. Then as the trajectory nears the second pure mode, $-(0, 0, \sqrt{-\mu_2/e_{22}}, 0)$, the A mode returns to a nearly inactive state while the B mode becomes the driving mode.

This mode switching behavior is expressed physically in terms of the Langmuir cells in Figure 9. At the start and finish of one pass near the heteroclinic orbit, a four-roll state is observed, whereas when the B mode nearly vanishes, a two-roll state is observed. Moreover, after passing along the heteroclinic orbit, the four-roll state is shifted by $W/4$; this shift resembles the behavior observed in the direct numerical simulation of the PDE.

As seen in Figure 8, this process repeats itself as the trajectory loops around and follows near the heteroclinic orbit again. The connection from $-(0, 0, \sqrt{-\mu_2/e_{22}}, 0)$ to $(0, 0, \sqrt{-\mu_2/e_{22}}, 0)$ is related to the translational invariance of the equations, $(A, B) \rightarrow (e^{i\vartheta} A, e^{2i\vartheta} B)$ from (22), and thus there is no lateral shifting of the rolls during this phase of the trajectory. Instead, the connection between the pure modes appears in Figure 8 to amount to taking a path in the $\{(x_2, y_1)\}$ -plane rotating from the second pure mode to the first one. To calculate this more rigorously, notice that shifting by a fourth of the width of the box, $L = \frac{2\pi}{k_0}$, means a shift of $\frac{\pi}{2k_0}$. Hence

$$A \rightarrow e^{\frac{\pi}{2k_0}ik_0} A = e^{\frac{\pi}{2}i} B = iA, \quad (86)$$

$$B \rightarrow e^{\frac{\pi}{2k_0}2ik_0} B = e^{\pi i} B = -B. \quad (87)$$

The $B \rightarrow -B$ conversion is simply the switch from the second pure mode to the first one. But after the completion of one pass around the heteroclinic orbit, the real and imaginary parts of A switch via

$$(x_1, y_1) \rightarrow i \cdot (x_1, y_1) = (-y_1, x_1). \quad (88)$$

This switch in the real and imaginary parts is illustrated in Figure 10.

Hence the return phase is essentially a reorientation of the manifolds after which the trajectory returns near $(0, 0, \sqrt{-\mu_2/e_{22}}, 0)$ and again follows the heteroclinic orbit in Σ_2 . The second trip following the heteroclinic orbit leads to another brief transition to two rolls, followed by a return to a four-roll state with a half-shift (not pictured, but similar to Figure 9).

4 Reduced 3D equations

Up to this point we have restricted attention to the 2D/3C model to examine the rolls in the (y, z) -plane. To visualize the Y junctions, a 3D Lagrangian pattern on the surface, we reintroduce the x -direction into the PDE.

The equations below are not fully 3D; rather, we are performing asymptotic analysis within the framework of the asymptotic analysis of the previous sections, assuming an even longer scale in the downstream direction. We refer to this slow downstream direction as χ . The incompressibility condition on $U = (u, v, w)$ becomes incompressibility in the transverse plane, which we denote by

$$\nabla_{\perp} U = \partial_y v + \partial_z w = 0.$$

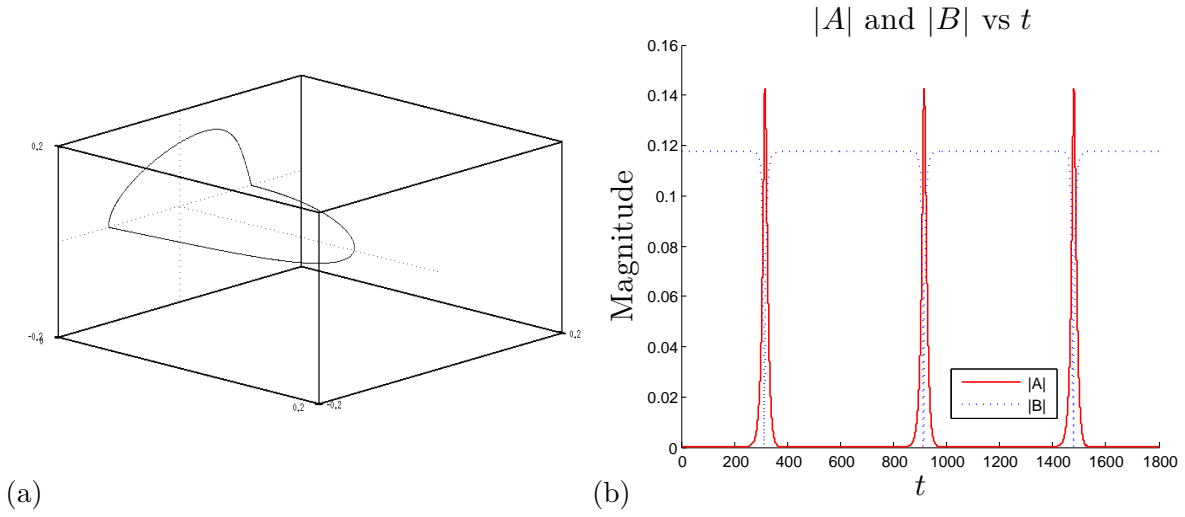


Figure 8: The subspace shown in (a) is $\{\text{Im } B = 0\}$, compare with Figure 5. A trajectory chosen to start near the pure mode $(0, 0, \sqrt{-\mu_2/e_{22}}, 0)$ is pictured. It follows near the heteroclinic orbit of Figure 7 in Σ_2 , transitioning between passes along this heteroclinic orbit via the connection that appears vertical. It passes along the heteroclinic orbit approximately three times during the time of integration. This image was created with XPPAUT. The magnitude of the amplitude A for the single mode k_0 compared to the amplitude B for the double mode $2k_0$ for the trajectory in (a) is plotted in (b). At $t = 313$, the magnitude of B reaches its first minimum. The streamfunction at $t = 0$, $t = 313$ and $t = 500$ is plotted in Figure 9.

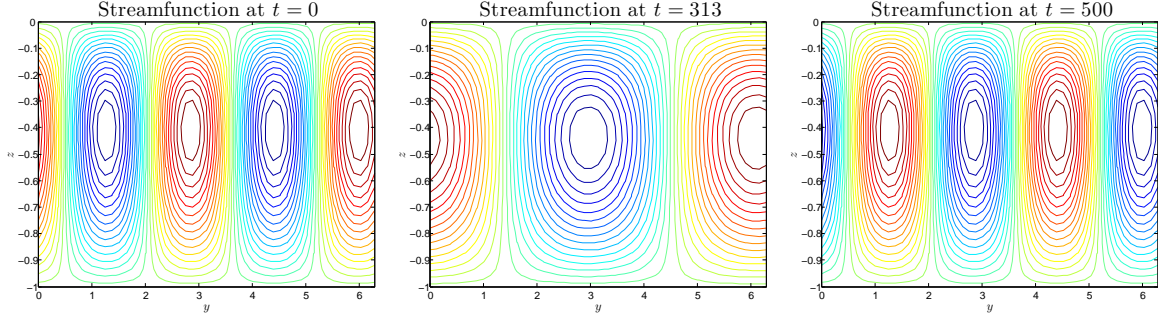


Figure 9: The streamfunction $\psi_1(y, z, t)$ for the trajectory in Figure 8. At the start of the integration ($t = 0$), the orbit is close to the pure mode $(0, 0, \sqrt{-\mu_2/e_{22}}, 0)$, and four rolls are observed. At $t = 313$, when the first minimum of $|B|$ occurs in Figure 8, a two-roll state is observed. At the end of the first loop (around $t = 500$), the orbit has passed near the pure mode $(0, 0, -\sqrt{-\mu_2/e_{22}}, 0)$, and four rolls are again observed, with the predicted shift of half of a period in the y -direction. Repeating this process for all three loops of the orbit continues this pattern.

Hence the streamfunction ψ is still defined in this 3D context.

Following the derivation in Chini *et al.* [3] with their downstream variable X , the coordinate version of the PDE with slow advection in the downstream direction is

$$\partial_t U + J(U, \psi) - \partial_y \psi = -\partial_X \Pi + La \nabla_\perp^2 U, \quad (89)$$

$$\partial_t \Omega + J(\Omega, \psi) + U_s(z) \partial_X \Omega = U'_s(z) (\partial_X \partial_z \psi - \partial_y U) + La \nabla_\perp^2 \Omega, \quad (90)$$

$$\nabla_\perp^2 \Pi = 2J(\partial_y \psi, \partial_z \psi) + \nabla_\perp \cdot (U_s(z) \nabla_\perp u), \quad (91)$$

$$+ U'_s(z) \partial_X \partial_y \psi, \quad (92)$$

$$\nabla_\perp^2 \psi = -\Omega. \quad (93)$$

Unlike in [3], we will assume mixed boundary conditions on u and exponential Stokes drift, as well as different boundary conditions on the pressure as a result of these adjustments.

4.1 Linear analysis

In Section 2, taking the curl of the equations caused the pressure terms to vanish. In this reduced 3D setting, it does not. Hence in addition to the base state $U_B(z)$ in the x -direction from before, we will also linearize about the pressure base state $\Pi_B(z)$. The perturbation terms are $u_p(X, y, z, t)$, $\psi(X, y, z, t)$, $p(X, y, z, t)$ and $\Omega(X, y, z, t)$, and the total fields are written

$$u(X, y, z, t) = U_B(z) + u_p(X, y, z, t), \quad (94)$$

$$\psi(X, y, z, t) = \psi(X, y, z, t), \quad (95)$$

$$\Pi(X, y, z, t) = \Pi_B(z) + p(X, y, z, t), \quad (96)$$

$$\Omega(X, y, z, t) = \Omega(X, y, z, t). \quad (97)$$

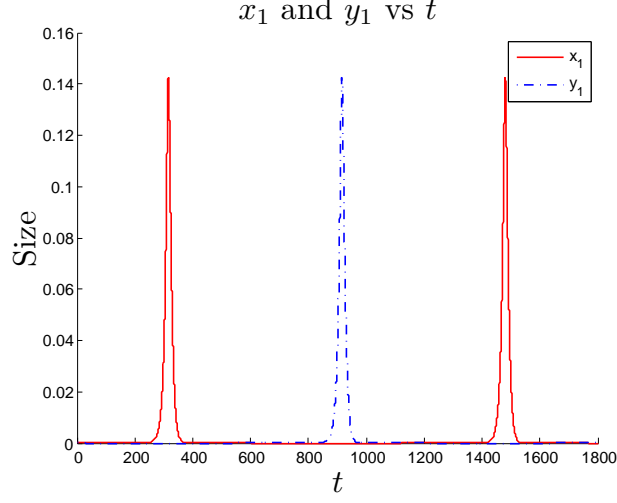


Figure 10: The three trips of the orbit from Figure 8(a) are pictured in terms of the real and imaginary parts of $A(\tau)$, see equation (88).

In addition to the previous boundary conditions on u , Ω and ψ , we note that the boundary condition on the pressure is $\partial_z p = 0$ along $z = 0$ and $\partial_z p = U_s(-1) \cdot \gamma u_p$ along $z = -1$. Linearizing about the base state yields

$$\partial_t u - \partial_y \psi = -\partial_X p + La \nabla_\perp^2 u, \quad (98)$$

$$\partial_t \Omega + U_s(z) \partial_X \Omega = U'_s(z) (\partial_X \partial_z \psi - \partial_y u) + La \nabla_\perp^2 \Omega, \quad (99)$$

$$\nabla_\perp^2 p = \nabla_\perp \cdot (U_s(z) \nabla_\perp u) + U'_s(z) \partial_X \partial_y \psi, \quad (100)$$

$$\nabla_\perp^2 \psi = -\Omega. \quad (101)$$

To reduce from four equations to three, we use the definition of the vorticity Ω in (101) to write

$$\partial_t u - \partial_y \psi = -\partial_X p + La \nabla_\perp^2 u, \quad (102)$$

$$-\partial_t \nabla_\perp^2 \psi - U_s(z) \partial_X \nabla_\perp^2 \psi = U'_s(z) (\partial_X \partial_z \psi - \partial_y u) - La \nabla_\perp^4 \psi, \quad (103)$$

$$\nabla_\perp^2 p = \nabla_\perp \cdot (U_s(z) \nabla_\perp u) + U'_s(z) \partial_X \partial_y \psi. \quad (104)$$

We again make a normal mode ansatz. In this case, there is an additional term for the downstream direction with wavenumber ℓ , resulting in

$$\begin{pmatrix} u \\ \psi \\ p \end{pmatrix} = \begin{pmatrix} \hat{u}(z) \\ \hat{\psi}(z) \\ \hat{p}(z) \end{pmatrix} e^{iky} e^{\sigma t} e^{i\ell X}, \quad (105)$$

where $\hat{u}(z)$, $\hat{\psi}(z)$ and $\hat{p}(z)$ are the structures in the vertical direction. Let $D = \frac{\partial}{\partial z}$ as before, then with the ansatz, (102)-(103) can be written as an eigenvalue problem

$$\sigma u = La(D^2 - k^2)u + ik\psi - i\ell p, \quad (106)$$

$$0 = -[U_s(z)(D^2 - k^2) + U'_s(z)D]u + U'_s(z)k\ell\psi + (D^2 - k^2)p, \quad (107)$$

$$\sigma(D^2 - k^2)\psi = ikU'_s(z)u + [La(D^2 - k^2)^2 - i\ell U_s(z)(D^2 - k^2) - i\ell U'_s(z)D]\psi, \quad (108)$$

with eigenvalue σ . Repeating the steps of Section 3.1, in matrix form this is

$$A \begin{pmatrix} u \\ \psi \\ p \end{pmatrix} = \sigma B \begin{pmatrix} u \\ \psi \\ p \end{pmatrix},$$

where

$$A = \begin{pmatrix} La(D^2 - k^2) & ik & -i\ell \\ ikU'_s(z) & La(D^2 - k^2)^2 - i\ell U'_s(z)(D^2 - k^2) - i\ell U'_s(z)D & 0 \\ -[U_s(z)(D^2 - k^2) + U'_s(z)D] & U'_s(z)k\ell & (D^2 - k^2) \end{pmatrix}$$

and

$$B = \begin{pmatrix} 1 & 0 & 0 \\ 0 & D^2 - k^2 & 0 \\ 0 & 0 & 0 \end{pmatrix}.$$

We set $\det(A - \sigma B) = 0$ to find the dispersion relation numerically, as in the 2D/3C case. In this setting, the horizontal wavenumber k for the single mode is fixed at the value of k_0 computed for the same parameters in the 2D/3C setting. Similarly, the wavenumber is $2k_0$ for the double mode, and the forcing term La is fixed at La_0 .

Once these assignments are made, the growth rate σ becomes of function of ℓ . Computing σ using the same pseudospectral approach as before, we can individually find the real and imaginary parts of σ as functions of ℓ , see Figure 11. The real part of the growth rate is quadratic while the imaginary part is linear; this can be verified by plotting the first and second derivatives of the curves.

Setting the slow variable χ to be $\chi = \varepsilon X$ with ε as before, the equation for the growth rate σ_1 for A becomes

$$\sigma_1 = \mu_1 - i\ell v_{g1} - \nu_1 \ell^2, \quad (109)$$

while for B it is

$$\sigma_2 = \mu_2 - i\ell v_{g2} - \nu_2 \ell^2, \quad (110)$$

where v_{gj} , $j = 1, 2$, denotes the group velocity for the wavepacket. The coefficients are computed numerically; for the parameter set used for (68)-(69), the growth rates are

$$\sigma_1 = \mu_1 - 0.1548i\ell - 0.0521\ell^2, \quad (111)$$

and

$$\sigma_2 = \mu_2 - 0.1666i\ell - 0.0397\ell^2. \quad (112)$$

In Fourier space, we interpret these equations in terms of the ansatz. In physical space, we set $i\ell = \partial_\chi$ and $-\ell^2 = \partial_{\chi\chi}$. Hence to the ODEs we append the slow χ derivatives to obtain a set of reduced PDEs for $A(t, \chi)$ and $B(t, \chi)$:

$$A_t = \mu_1 A - 0.0801 \bar{A}B - 0.0758 |A|^2 A - 0.3867 |B|^2 A - 0.1548 A_\chi + 0.0521 A_{\chi\chi}, \quad (113)$$

$$B_t = \mu_2 B + 0.0987 A^2 - 0.7563 |A|^2 B - 0.3334 |B|^2 B - 0.0833 B_\chi + 0.0099 B_{\chi\chi}. \quad (114)$$

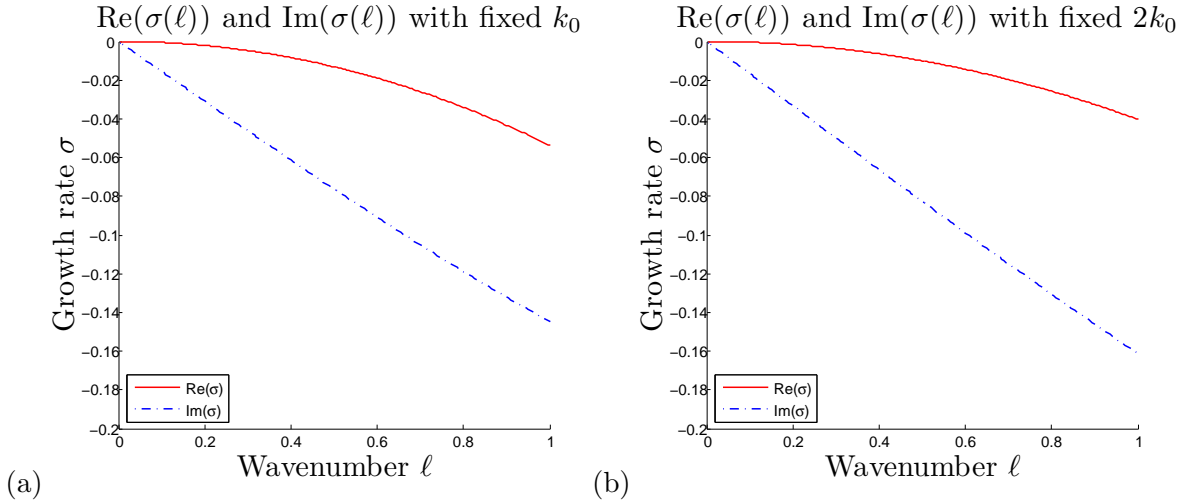


Figure 11: Each plot shows the real and imaginary parts of σ as a function of the downstream wavenumber ℓ , as computed in Section 4.1; (a) is for the k_0 mode, and (b) is for the $2k_0$ mode. The real part of each is quadratic, while the imaginary part is linear.

5 Conclusion

With a 2D/3C model, we performed a center manifold reduction to derive evolution equations for the amplitudes A for the mode $e^{ik_0 y}$ and B for the mode $e^{2ik_0 y}$. Using Matlab, for an extensive range of parameters values we were able to numerically compute coefficients that satisfy certain inequalities guaranteeing the existence of a robust and attracting heteroclinic orbit in an invariant subspace of the center manifold. Numerical simulations of trajectories close to this orbit reveal a switching behavior between a 2-roll state and a 4-roll state consistent with the behavior observed in direct numerical simulations of the governing PDE. The dynamics explored in this paper assumed an idealized state; for analysis of structurally stable heteroclinic cycles in a system with $O(2)$ symmetry with additive noise, we refer to work by Stone and Holmes. In [14], they find that such white noise does not drastically affect the solutions in the phase space of the evolution equations, but rather leads to a particular selection of timescales.

Lastly, we used a set of reduced 3D equations to introduce slow advection in the downstream direction to convert the ODEs to PDEs. A future goal is to derive the PDE for the zero mode to get the drift effect and show how simulating these PDEs will exhibit the Lagrangian Y junction patterns observed on the surface of the ocean. We will also derive a set of equations for A , B and C which couple A and B to C . This coupling will be used to examine how the dynamics of the A and B modes are affected by downstream advection.

6 Acknowledgements

I am very grateful to the Woods Hole Oceanographic Institution and to many individuals for this summer. In addition to thanking my three advisors Edgar Knobloch, Greg Chini and Keith Julien, I would also like to thank Geoffrey Vasil of the University of Toronto for several meaningful conversations in July. I enjoyed sharing this experience with all of the other fellows; in particular, I would like to thank Rosie Oglethorpe, Felicity Graham, Alban Sauret, and Cédric Beaume for useful discussions on my project. Lastly, I appreciated the atmosphere created by all the visitors and faculty and would like to acknowledge Colm-cille Caulfield and Charlie Doering for their direction this summer.

References

- [1] Armbruster, Dieter, John Guckenheimer, and Philip Holmes. Heteroclinic cycles and modulated travelling waves in systems with $O(2)$ symmetry. *Physica 29D*, 257-282 (1988).
- [2] Bhaskaran, Rajesh and Sidney Leibovich. Eulerian and Lagrangian Langmuir circulation patterns. *Physics of Fluids*, 14, 2557 (2002).
- [3] Chini, Gregory P., Keith Julien and Edgar Knobloch. An asymptotically reduced model of turbulent Langmuir circulation. *Geophysical & Astrophysical Fluid Dynamics*, 103: 2,179-197 (2009).
- [4] Chossat, P. The bifurcation of heteroclinic cycles in systems of hydrodynamical type. *Dynam. Cont. Discr. Impuls. Syst.* 8, 575 (2001).
- [5] Cox, Stephen M. and Sidney Leibovich. Langmuir circulations in a surface layer bounded by a strong thermocline. *Journal of Physical Oceanography* Vol. 23, pp. 1300-1345 (1992).
- [6] ———. Large-scale Langmuir circulation and double-diffusive convection: evolution equations and flow transitions. *J. Fluid Mech.* Vol. 276, pp. 189-210 (1994).
- [7] ———. Large-scale three-dimensional Langmuir circulation. *Physics of Fluids* 9, 2851 (1997).
- [8] Craik, A.D.D. and S. Leibovich. A rational model for Langmuir circulations. *J. Fluid Mech.*, Vol. 73, pp. 401-426 (1976).
- [9] Ermentrout, B. Dynamical systems software with continuation and bifurcation capabilities (1999), available via FTP from directory/pub/bardware at ftp.math.pit.edu.
- [10] Krupa, Martin and Ian Melbourne. Nonasymptotically stable attractors in $O(2)$ mode interactions. From *Normal Forms and Homoclinic Chaos*, editors William F. Langford and Wayne Nagata. AMS (1995).
- [11] Mercader, I., J. Prat and E. Knobloch. The 1:2 mode interaction in Rayleigh-Benard convection with weakly broken midplane symmetry. *Int. J. Bif. Chaos.* 11: 27-41 (2001).
- [12] Porter, J. and E. Knobloch. New type of complex dynamics in the 1 : 2 spatial resonance. *Physica D*, 159, 125-154 (2001).
- [13] Proctor, M.R.E. and C.A. Jones. The interaction of two spatially resonant patterns in thermal convection. Part 1. Exact 2:1 resonance. *J. Fluid Mech.* Vol. 188, pp. 301-335 (1988).
- [14] Stone, Emily and Philip Holmes. Random Perturbations of Heteroclinic Attractors. *SIAM J. Appl. Math.* 50(3), 726-743.
- [15] Thorpe, S.A.. Langmuir circulation. *Annu. Rev. Fluid Mech.* 36: 55-79 (2004).
- [16] Trefethen, Lloyd N. *Spectral Methods in Matlab*. SIAM (2000).

Optimal Transport from Wall to Wall

Pedram Hassanzadeh

October 3, 2012

1 Introduction

Transport of heat and mass is of fundamental importance in science and engineering. In some environmental and industrial applications, the aim is to maximize (e.g. in cooling or heating) or minimize (e.g. for pollution and hazards) the transport. In some other problems, such as oil spills, the amount and the path of the transported material must be determined. For problems arising in nature, the focus is on understanding the transport processes and estimating their magnitude. In some problems with extreme parameters, such as mantle convection, the interest is mainly on finding scaling laws relating the magnitude of the transport to some physical parameters.

The focus of this investigation is a generic question: what is the maximum amount of a passive scalar tracer that can be transported by unknown velocity fields satisfying certain constraints. The constraints studied here are that the velocity field is divergence-free and has a fixed (given) amount of (kinetic) energy or a fixed amount of enstrophy. Subsequently, we shall discuss the motivation inspiring these constraints. Furthermore, we restrict our attention to two-dimensional (2D) steady flows.

In the remainder of the Introduction, we will present details of the problem and its mathematical formulation. In sections 2 and 3, we study the problems with fixed energy and fixed enstrophy, respectively. For each problem, we employ the calculus of variations to maximize a functional subjected to the constraints of the problem. The resulting Euler-Lagrange equations are solved numerically and analytically to obtain the optimal velocity field. Upper bounds on the transport are calculated from the optimal velocity fields. At the end of each section, the calculated upper bound is compared with the available results for relevant problems. Section 4 presents the concluding remarks and future work.

1.1 Mathematical Formulation

Here we present the mathematical formulation of the problem described above. For convenience, we only consider heat transport (i.e. with temperature treated as scalar tracer) hereafter. The 2D heat transport is described by the advection-diffusion equation:

$$\dot{T} + \mathbf{v} \cdot \nabla T = \kappa \Delta T, \quad (1)$$

where $T(x, z, t)$ is temperature, $\dot{T} = \partial T / \partial t$, $\Delta = \partial^2 / \partial x^2 + \partial^2 / \partial z^2$, κ is the thermal diffusivity of the fluid (assumed to be constant), and $\mathbf{v}(x, z, t) = (u, w)$ is the divergence-free

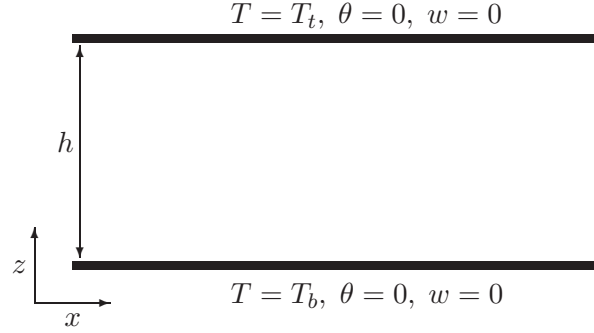


Figure 1: Schematic of the configuration. The top and bottom walls are impermeable and are kept at fixed temperatures.

velocity field, i.e.

$$\nabla \cdot \mathbf{v} = 0. \quad (2)$$

In the absence of advection (i.e. $\mathbf{v} = 0$), the transport is purely by conduction and the temperature field of this case is denoted by Θ . $\theta \equiv T - \Theta$ is the deviation of the temperature field from the purely conducting profile Θ when $\mathbf{v} \neq 0$. The geometry of the problem, shown in Figure 1, consists of two infinite parallel impermeable walls with fixed temperature. Note that the parallel walls can be horizontal or vertical or inclined; we do not use the dynamics of the velocity field (i.e. momentum equations) in our analysis and therefore gravity is irrelevant. We set the walls to be horizontal. The flow is assumed to be periodic in the x direction with characteristic horizontal length scale L , which will be specified later.

In the next two sections, we study velocity fields that either have fixed energy U^2 ,

$$U^2 = \frac{1}{hL} \int_D (\mathbf{v} \cdot \mathbf{v}) \, dx dz, \quad (3)$$

or fixed enstrophy Ω^2 ,

$$\Omega^2 = \frac{1}{hL} \int_D (\boldsymbol{\omega} \cdot \boldsymbol{\omega}) \, dx dz = \frac{1}{hL} \int_D (\nabla \mathbf{v} : \nabla \mathbf{v}) \, dx, \quad (4)$$

where $\boldsymbol{\omega} = \nabla \times \mathbf{v}$ is the vorticity, and D is the $[0, L] \times [0, h]$ domain. The second equality in (4) is true for many boundary conditions including no-slip, free-slip, and periodic. The significance of the second integral is that, multiplied by viscosity, it gives the viscous dissipation rate in Newtonian fluids. As the integrals are equal for the boundary conditions of interest, we use the second representation in this report because it is more convenient.

We non-dimensionalize length with the spacing between the walls h , time with diffusion time scale h^2/κ , and velocity with κ/h . The dimensionless temperature is $(T - T_t)/(T_b - T_t)$. We define the (dimensionless) Peclet number Pe as the ratio of the diffusive time scale to the advective time scale (i.e. a measure of the strength of advection relative to diffusion). For the problem with fixed energy,

$$\text{Pe} \equiv Uh/\kappa, \quad (5)$$

and for the problem with fixed enstrophy,

$$\text{Pe} \equiv \Omega h^2 / \kappa. \quad (6)$$

We also define the aspect ratio Γ as

$$\Gamma \equiv L/h. \quad (7)$$

Notice that hereafter all variables (i.e. \mathbf{v} , T , Θ , θ , x , z , t) are dimensionless, but the notation is not changed for simplicity.

Non-dimensionalizing equations (1)–(2) and the boundary conditions yields

$$\dot{\theta} + \mathbf{v} \cdot \nabla \theta = \Delta \theta + w, \quad (8)$$

$$\nabla \cdot \mathbf{v} = 0, \quad (9)$$

$$\theta(x, 0, t) = \theta(x, 1, t) = 0, \quad (10)$$

$$w(x, 0, t) = w(x, 1, t) = 0, \quad (11)$$

where $\theta(x, z, t) \equiv T(x, z, t) - \Theta(z)$ has been used (note that $\Theta(z) = 1 - z$).

We further define angle brackets $\langle \cdot \rangle$ as the long time-space average:

$$\langle \mathbf{a}(x, z, t) \rangle \equiv \lim_{t \rightarrow \infty} \frac{1}{t} \int_0^t \left\{ \frac{1}{\Gamma} \int_D \mathbf{a}(x, z, s) \, dx dz \right\} ds, \quad D = [0, 1] \times [0, \Gamma]. \quad (12)$$

Therefore, using (5), the fixed energy constraint (3) becomes

$$\text{Pe} = \langle |\mathbf{v}|^2 \rangle. \quad (13)$$

The fixed enstrophy constraint (4) is

$$\text{Pe} = \langle |\nabla \mathbf{v}|^2 \rangle, \quad (14)$$

where (6) has been used.

The Nusselt number Nu measures the heat transport by advection and is defined as the ratio of the heat flux in the *presence* of advection \mathbf{q}_a to the heat flux by pure conduction \mathbf{q}_c . We are interested in the vertical transport between horizontal walls, therefore

$$\text{Nu} \equiv \frac{\langle \mathbf{q}_a \cdot \mathbf{z} \rangle}{\langle \mathbf{q}_c \cdot \mathbf{z} \rangle}, \quad (15)$$

where $\mathbf{q}_c = -\nabla \Theta$ (Fourier's law) and $\mathbf{q}_a = -\nabla T + T \mathbf{v}$. Hence, after a little algebra, the above equation reduces to

$$\text{Nu} = 1 + \langle wT \rangle = 1 + \langle w\theta \rangle. \quad (16)$$

Note that $\langle w\Theta(z) \rangle = 0$ as a result of incompressibility.

1.2 Objective

With the strength of advection (Pe), geometry of the flow (Γ), and strength of transport (Nu) defined, we can now rigorously present the goal of this work.

1. We search over all divergence-free velocity fields \mathbf{v} that have a given (Pe, Γ) (and satisfy (11)), and find the maximum possible Nu (16) (notice that knowing \mathbf{v} , (10) and (8) uniquely determine θ). This Nu is called Nu_{\max} :

$$\text{Nu}_{\max}(\text{Pe}, \Gamma) \equiv \sup_{\mathbf{v}} \{\text{Nu}(\mathbf{v})\}. \quad (17)$$

2. For the same Pe, step 1 is repeated for various values of Γ . For this Pe, the largest value of $\text{Nu}_{\max}(\text{Pe}, \Gamma)$ is called Nu_{MAX} :

$$\text{Nu}_{\text{MAX}}(\text{Pe}) \equiv \sup_{\Gamma} \{\text{Nu}_{\max}(\text{Pe}, \Gamma)\}. \quad (18)$$

3. For this Pe, the Γ in step 2 which gives Nu_{MAX} is dubbed the optimal aspect ratio and noted as $\Gamma_{\text{opt}}(\text{Pe})$

The goal is to find $\text{Nu}_{\max}(\text{Pe}, \Gamma)$, $\text{Nu}_{\text{MAX}}(\text{Pe})$, and $\Gamma_{\text{opt}}(\text{Pe})$ for any Pe, especially in the limit of $\text{Pe} \rightarrow \infty$. In sections 2.5 and 3.4 we show how to interpret the results based on the Rayleigh number Ra commonly arising in buoyancy-driven convection problems.

The time-dependence of the advecting flow merits further discussion. The effect of unsteadiness on transport is not fully understood and whether a time-dependent flow transports more or less than a steady flow (with the same amount of energy or enstrophy) remains an open question. Of course the question can be answered by performing the optimization in step 1 over both space and time, i.e. for $\mathbf{v} = \mathbf{v}(x, z, t)$. Such an analysis is very complicated and is a problem of optimal control theory. Here we focus on steady flows (i.e. $\mathbf{v} = \mathbf{v}(x, z)$) and use calculus of variations in step 1. The steady analysis gives useful insight into the optimal transport problem that can be used to guide future unsteady analyses.

2 Optimal Transport with Fixed Energy

In the first problem, we look into the optimal steady transport with fixed energy. Therefore, equations (8)–(11) and (13) become

$$\mathbf{v} \cdot \nabla \theta = \Delta \theta + w, \quad (19)$$

$$\nabla \cdot \mathbf{v} = 0, \quad (20)$$

$$\text{Pe} = \langle |\mathbf{v}|^2 \rangle, \quad (21)$$

$$\theta(x, 0) = \theta(x, 1) = 0, \quad (22)$$

$$w(x, 0) = w(x, 1) = 0. \quad (23)$$

A simple analysis gives a relatively crude upper bound on Nu as $1 + \text{Pe}/2$. Starting from (16),

$$\begin{aligned} \text{Nu} &= 1 + \langle wT \rangle = 1 + \langle w(T - 1/2) \rangle \leq 1 + \langle |w|^2 \rangle^{1/2} \langle |T - 1/2|^2 \rangle^{1/2} \leq 1 + \frac{\langle |\mathbf{v}|^2 \rangle^{1/2}}{2} \\ &= 1 + \frac{\text{Pe}}{2}, \end{aligned} \quad (24)$$

where the second equality is due to incompressibility and the boundary conditions. The Cauchy–Schwarz inequality has been used in the first inequality. The maximum principle assures $|T| \leq 1$ and consequently $|T - 1/2| \leq 1/2$. The latter has been used in the second inequality. Equation (21) gives the final result. This upper bound, as shown later, is too high, and a full analysis of (19)–(23), as given below, is required to obtain a better estimate, and to find the optimal velocity field.

2.1 Variational Formulation for Steady Flows

Here the variational formulation is presented to maximize $\text{Nu} = 1 + \langle \theta w \rangle$ given constraints (19)–(21) and boundary conditions (22)–(23). Therefore, we aim to maximize the functional \mathcal{F} constructed as

$$\mathcal{F} = \left\langle w\theta - \phi(x, z) (\mathbf{v} \cdot \nabla \theta - \Delta \theta - w) + p(x, z) (\nabla \cdot \mathbf{v}) - \frac{\mu}{2} (|\mathbf{v}|^2 - \text{Pe}^2) \right\rangle \quad (25)$$

where $\phi(x, z)$, $p(x, z)$, and μ are Lagrange multipliers (ϕ and p are functions of x and z to enforce the constraints (19) and (20) point-wise). The Euler-Lagrange equations can be expressed as [2]:

$$0 = \frac{\delta \mathcal{F}}{\delta \mathbf{v}} = (\theta + \phi) \hat{\mathbf{z}} + \theta \nabla \phi - \nabla p - \mu \mathbf{v}, \quad (26)$$

$$0 = \frac{\delta \mathcal{F}}{\delta \theta} = \mathbf{v} \cdot \nabla \phi + \Delta \phi + w, \quad (27)$$

$$0 = \frac{\delta \mathcal{F}}{\delta \phi} = \mathbf{v} \cdot \nabla \theta - \Delta \theta - w, \quad (28)$$

$$0 = \frac{\delta \mathcal{F}}{\delta p} = \nabla \cdot \mathbf{v}, \quad (29)$$

$$0 = \frac{\partial \mathcal{F}}{\partial \mu} = \langle |\mathbf{v}|^2 \rangle - \text{Pe}^2, \quad (30)$$

where $\nabla \cdot \mathbf{v} = 0$ and integration by parts along with boundary conditions (22)–(23) and periodicity in the x direction have been repeatedly employed to derive (26) and (27). Additionally, in deriving (27), it has been assumed that ϕ vanishes at $z = [0, 1]$ (to eliminate a surface term arising from the integration by parts of $\phi \Delta \theta$, i.e. natural boundary conditions). Therefore the boundary conditions are

$$w(x, 0) = w(x, 1) = 0, \quad (31)$$

$$\theta(x, 0) = \theta(x, 1) = 0, \quad (32)$$

$$\phi(x, 0) = \phi(x, 1) = 0. \quad (33)$$

Also notice that using integration by parts, the $+\theta \nabla \phi$ term in (26) can be replaced by $-\phi \nabla \theta$ (since $\nabla(\theta \phi)$ is a perfect gradient and can be absorbed into the ∇p term). As expected for an incompressible flow, the Lagrange multiplier enforcing $\nabla \cdot \mathbf{v} = 0$ in equation (25) (i.e. p), plays a role similar to *pressure* in the resulting equations.

Inspection of equations (26) and (28)–(29) reveals some similarities between these equations and the equations of convection in porous media in the limit of infinite Prandtl–Darcy number (see e.g. [6]), although here, an extra field ϕ exists. This resemblance, which will also be observed in the linear analysis in the next section, will be discussed in section 2.5.

2.2 The Limit of Small Pe: Asymptotic Solution

In the limit of small Pe, $|\mathbf{v}| \ll 1$ (from (30)), which along with (27)-(28) and the maximum principle imply that $|\theta| \ll 1$ and $|\phi| \ll 1$. Therefore in this limit we can linearize equations (26)-(28):

$$\mu \mathbf{v} + \nabla p = (\theta + \phi) \hat{\mathbf{z}}, \quad (34)$$

$$\Delta \phi + w = 0, \quad (35)$$

$$\Delta \theta + w = 0, \quad (36)$$

$$\nabla \cdot \mathbf{v} = 0. \quad (37)$$

Subtracting (36) from (35) and using (32)-(33) gives $\theta = \phi$ in the small Pe regime. Taking the divergence of equation (34) gives

$$\Delta p = 2 \theta_z, \quad (38)$$

where the subscript z means $\partial/\partial z$. Taking Δ of the $\hat{\mathbf{z}}$ -component of (34) results in

$$\mu \Delta w + \Delta p_z = 2 \Delta \theta. \quad (39)$$

Subtracting $\partial/\partial z$ of (38) from (39) gives

$$\mu \Delta w = 2 \theta_{xx}, \quad (40)$$

which along with equation (36) and boundary conditions (31)-(32) can be analytically solved to find (\mathbf{v}, θ) in the small-Pe limit. A Fourier transform in the x direction, these equations become

$$(D_z^2 - k^2) \hat{\theta}_k(z) + \hat{w}_k(z) = 0, \quad (41)$$

$$\mu(D_z^2 - k^2) \hat{w}_k(z) + 2k^2 \hat{\theta}_k(z) = 0, \quad (42)$$

where $D_z = \partial/\partial z$. $\hat{w}_k(z)$ and $\hat{\theta}_k(z)$ are the Fourier coefficients of w and θ with horizontal wavenumber k . Defining L as half of the (dimensionless) wavelength, we see that $\Gamma = \pi/k$. Given the form of these equations and the boundary conditions, the solution is

$$\hat{w}_k(z) = A_k \sin(m\pi z), \quad (43)$$

$$\hat{\theta}_k(z) = B_k \sin(m\pi z), \quad (44)$$

where m is the vertical wavenumber, and A_k and B_k are still undetermined. Substituting into (41) and (42) gives

$$\mu = (2k^2)/(m^2\pi^2 + k^2)^2, \quad (45)$$

$$A_k = (m^2\pi^2 + k^2) B_k. \quad (46)$$

Using equation (37), $\hat{u}_k(z)$ is obtained as

$$\hat{u}_k(z) = i \frac{m\pi}{k} A_k \cos(m\pi z). \quad (47)$$

Substituting (47) and (43) into (30) yields

$$\langle |\mathbf{v}|^2 \rangle = \left(A_k^2 + \frac{m^2 \pi^2}{k^2} A_k^2 \right) = \text{Pe}^2 \Rightarrow A_k = \frac{k}{(m^2 \pi^2 + k^2)^{1/2}} \text{Pe}, \quad (48)$$

which along with (46) gives

$$B_k = \frac{k}{(m^2 \pi^2 + k^2)^{3/2}} \text{Pe}. \quad (49)$$

Knowing A_k and B_k , Nu is obtained from (16):

$$\text{Nu} = 1 + A_k B_k = 1 + \frac{k^2}{(m^2 \pi^2 + k^2)^2} \text{Pe}^2, \quad (50)$$

which for a given $(\text{Pe}, \Gamma = \pi/k)$, is maximized at $m = 1$. As a result, using the notation defined in section 1.2:

$$\text{Nu}_{\max}(\text{Pe}, \Gamma) = 1 + \frac{\Gamma^2}{\pi^2(\Gamma^2 + 1)^2} \text{Pe}^2. \quad (51)$$

The largest value of $\text{Nu}_{\max}(\text{Pe}, \Gamma)$, i.e. Nu_{MAX} , is achieved at $\Gamma_{\text{opt}} = 1$:

$$\text{Nu}_{\text{MAX}}(\text{Pe}) = 1 + \frac{\text{Pe}^2}{4\pi^2} \quad (52)$$

Notice that $(k, m) = (\pi, 1)$ corresponds to the maximum value of $\mu = 1/(2\pi)^2$ (see (45)). Therefore, in the limit of small Pe (i.e. large μ), the maximum transport is achieved via an array of square *convection* cells (rolls) with optimal aspect ratio $\Gamma_{\text{opt}} = 1$. Figure 2 shows this flow field where the square convection cells are clearly seen. The computed flow field (equations (43)-(44) and (47)), and the square cells closely resemble those of the flow in porous media at the onset of linear instability (see e.g. [6]). Additionally, the factor $4\pi^2$ arising in (52) is the critical Ra for instability.

2.3 Small to Large Pe : Numerical Solution

The solution in the limit of small Pe was obtained analytically from the linearized equations in the last section. To find the solution for any Pe , especially for large Pe , the full nonlinear equations (26)-(29) must be solved. Taking the curl of (26) and defining the stream function ψ as $(u = \partial\psi/\partial z, w = -\partial\psi/\partial x)$, (26)-(29) reduce to

$$\text{J}(\theta, \phi) + \mu \Delta\psi + (\theta + \phi)_x = 0, \quad (53)$$

$$-\text{J}(\psi, \phi) + \Delta\phi - \psi_x = 0, \quad (54)$$

$$-\text{J}(\psi, \theta) - \Delta\theta + \psi_x = 0, \quad (55)$$

where $\text{J}(a, b) = \frac{\partial a}{\partial x} \frac{\partial b}{\partial z} - \frac{\partial a}{\partial z} \frac{\partial b}{\partial x}$ is the Jacobian. Boundary conditions (31)-(33) become

$$\psi(x, 0) = \psi(x, 1) = 0, \quad (56)$$

$$\theta(x, 0) = \theta(x, 1) = 0, \quad (57)$$

$$\phi(x, 0) = \phi(x, 1) = 0. \quad (58)$$

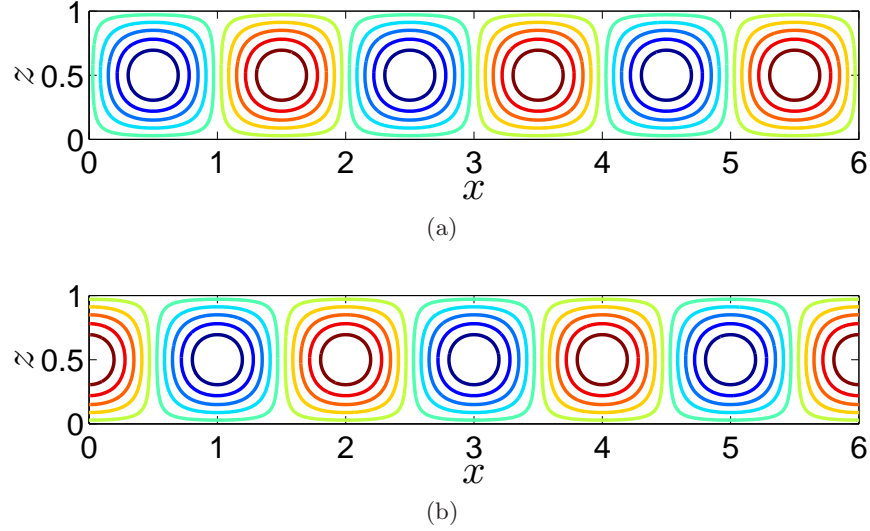


Figure 2: Optimal flow field in the small Pe limit for the fixed energy problem: (a) streamlines ψ , (b) temperature θ .

The above equations and boundary conditions imply an interesting symmetry between θ and ϕ which will be exposed in the numerical results and exploited later to obtain asymptotic solutions.

Rewritten for ψ , equations (30) and (16) are

$$\text{Pe}^2 = \langle \psi_x^2 + \psi_z^2 \rangle, \quad (59)$$

$$\text{Nu}_{\max} = 1 - \langle \psi_x \theta \rangle. \quad (60)$$

Below we present the numerical solution of these equations, obtained using continuation.

2.3.1 Numerical Continuation

Numerical continuation is a strategy to systematically trace a branch of solutions starting from a first guess [3]. In our problem, for a given Γ , we know the solution (analytically) in the limit of small Pe (i.e. large μ), and we want to find the solutions numerically for larger values of Pe (i.e. smaller μ). The continuation algorithm is:

1. We start from the analytical solution for large μ for a given value of Γ .
2. At iteration $N + 1$, μ^{N+1} is set to be 0.1% – 5% smaller than μ^N . We use the solution at iteration N (with μ^N) as a first guess and iteratively find the solution at iteration $N + 1$ (with μ^{N+1}).
3. Using the converged solution of step 2, we calculate $\text{Pe}(\mu^{N+1}, \Gamma)$ and $\text{Nu}_{\max}(\mu^{N+1}, \Gamma)$ from (59) and (60), respectively.
4. Steps 2 and 3 are repeated to reduce μ (i.e. increase Pe) by several orders of magnitude.
5. Steps 1–4 are repeated for several values of Γ .

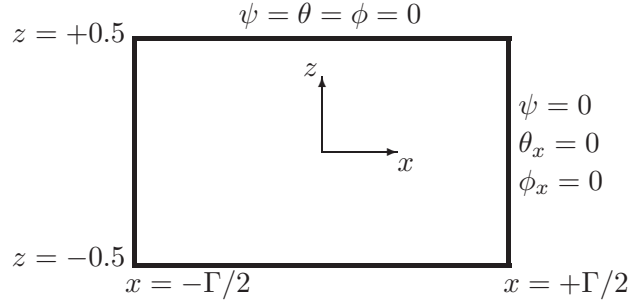


Figure 3: The fixed energy problem: the geometry and boundary conditions of the computational domain corresponding to a single 2D cell. Boundary conditions on the bottom (left) boundary are the same as top (right) boundary.

The result of steps 1–5 is to obtain $\text{Nu}_{\max}(\text{Pe}, \Gamma)$ for a wide range of Pe and Γ . In step 1, the vertical wavenumber m should also be chosen for the linear solution. As discussed later, Nu_{\max} is always obtained with solutions continued from a linear solution with $m = 1$; therefore, for most of the cases we used $m = 1$, although cases with $m = 2$ and linearly superposed solutions with different values of m also have been studied (see section 2.3.3). The percentage reduction of μ in step 2 depends on the degree of nonlinearity of the problem (μ should be varied more slowly as Pe increases). The next section presents details of the iterative method and the numerical scheme used in step 2.

2.3.2 Numerical Method

We use the Newton–Kantorovich iteration scheme [3] with the pseudo-spectral Chebyshev collocation method [18, 3] to solve (53)–(55). Instead of solving these equations in a large horizontally periodic domain including multiple cells (such as the one shown in Figure 2a), we choose the computational domain to be a single cell. Therefore, the computational domain is between the horizontal walls and has a width Γ (Figure 3). This unicellular approach has been used before with great success to study the Rayleigh–Bénard convection [4] and porous media convection [5]. Symmetry boundary conditions have been used on the vertical sides of the domain (at $x = \pm\Gamma/2$). Note that in the computational domain the horizontal walls are located at $z = \pm 0.5$ (instead of $z = 0, 1$ we used before), for convenience when Chebyshev polynomials are employed.

In the following, we describe the Newton–Kantorovich method [3] used in step 2 of the continuation algorithm (section 2.3.1). We use the known solution of the N th iteration $(\psi^N, \theta^N, \phi^N)$ as a first guess to iteratively find a good approximation of the true solution at the $N + 1$ th iteration $(\psi^{N+1}, \theta^{N+1}, \phi^{N+1})$. Rewriting equations (53)–(55) as

$$\Delta\psi = F(\theta_x, \theta_z, \phi_x, \phi_z) \quad (61)$$

$$\Delta\theta = G(\psi_x, \psi_z, \theta_x, \theta_z) \quad (62)$$

$$\Delta\phi = Q(\psi_x, \psi_z, \phi_x, \phi_z) \quad (63)$$

and Taylor expanding the nonlinear terms F , G , and Q about the solution of the N th iteration gives

$$\Delta\psi^{N+1} = F^N + \delta\theta_x F_{\theta_x}^N + \delta\theta_z F_{\theta_z}^N + \delta\phi_x F_{\phi_x}^N + \delta\phi_z F_{\phi_z}^N + \text{H.O.T.}, \quad (64)$$

$$\Delta\theta^{N+1} = G^N + \delta\psi_x G_{\psi_x}^N + \delta\psi_z G_{\psi_z}^N + \delta\theta_x G_{\theta_x}^N + \delta\theta_z G_{\theta_z}^N + \text{H.O.T.}, \quad (65)$$

$$\Delta\phi^{N+1} = Q^N + \delta\psi_x Q_{\psi_x}^N + \delta\psi_z Q_{\psi_z}^N + \delta\phi_x Q_{\phi_x}^N + \delta\phi_z Q_{\phi_z}^N + \text{H.O.T.}, \quad (66)$$

where the subscripts in F , G , and Q denote the Frechet derivatives (e.g. $F_{\psi_x} \equiv \partial F / \partial \psi_x$) (the superscript N means evaluated at iteration N). δ of any quantity is defined as the difference between its value at iterations $N+1$ and N (e.g. $\delta\psi \equiv \psi^{N+1} - \psi^N$). The neglected higher order terms (H.O.T) are $O((\delta\theta_x)^2, (\delta\theta_z)^2, (\delta\phi_x)^2, (\delta\phi_z)^2)$ or smaller. Following the detailed procedure presented in Appendix A, we obtain a system of three linear differential equations (199)–(201). Applying a pseudo-spectral Chebyshev collocation method in both x and z directions results in the following linear matrix equation:

$$\begin{bmatrix} \mu\Delta & (I + \phi_z^N)D_x - \phi_x^N D_z & (I - \theta_z^N)D_x + \theta_x^N D_z \\ -(I - \theta_z^N)D_x - \theta_x^N D_z & \Delta - \psi_z^N D_x + \psi_x^N D_z & O \\ -(I + \phi_z^N)D_x + \phi_x^N D_z & O & \Delta + \psi_z^N D_x - \psi_x^N D_z \end{bmatrix} \begin{bmatrix} \delta\psi \\ \delta\theta \\ \delta\phi \end{bmatrix} = \begin{bmatrix} -\mu\Delta\psi^N - (I + \phi_z^N)\theta_x^N - (I - \theta_z^N)\phi_x^N \\ -\Delta\theta^N + (I - \theta_z^N)\psi_x^N + \psi_z^N\theta_x^N \\ -\Delta\phi^N + (I + \phi_z^N)\psi_x^N - \psi_z^N\phi_x^N \end{bmatrix} \quad (67)$$

where I and O are $M^2 \times M^2$ identity and zero matrices, respectively (M is the number of collocation grid points.) D_x and D_z are the x and z differentiation matrices, respectively; $\Delta = D_{xx} + D_{zz}$. These matrices (with size $M^2 \times M^2$) are constructed using tensor products (also known as Kronecker products) as described in detail in [18]. Boundary conditions are implemented by modifying the rows corresponding to the boundary grid points in the coefficient matrix and the right-hand side matrix in (67). A MATLAB code was developed to construct the elements of (67) and solve it by direct matrix inversion. Once $\delta\psi$, $\delta\theta$, and $\delta\phi$ are calculated, the solution is updated as $\psi^{N+1} = \psi^N + \delta\psi$, $\theta^{N+1} = \theta^N + \delta\theta$, and $\phi^{N+1} = \phi^N + \delta\phi$. The iterations stop when $\delta(\cdot)/\|(\cdot)\|_\infty \leq 10^{-10}$ for all three variables ψ , θ , and ϕ . The Clenshaw-Curtis quadrature [18] is used for all spatial integrations, for example to calculate (59) and (60).

2.3.3 Numerical Results

All the results presented here are obtained using $M = 61$ or 91 . The iterative solution always converged in less than 6 iterations, and the converged solution satisfies (53)–(55) with a relative error of 10^{-10} or smaller, except at the boundaries. Note that we did not solve these equations for the boundary grid points, and instead we used the freed rows in (67) to enforce the Dirichlet and Neumann boundary conditions. The converged solution satisfies the vertical and horizontal boundary conditions with an absolute error of 10^{-10} or smaller.

Figure 4 shows ψ and θ for the case with $\Gamma = 1$ for low to high values of Pe . As Pe increases, Nu_{\max} increases as well. The flow shown in Figures 4a and 4b is still in the linear regime. As Pe (and hence the nonlinearity) increases, the bulk flow structure

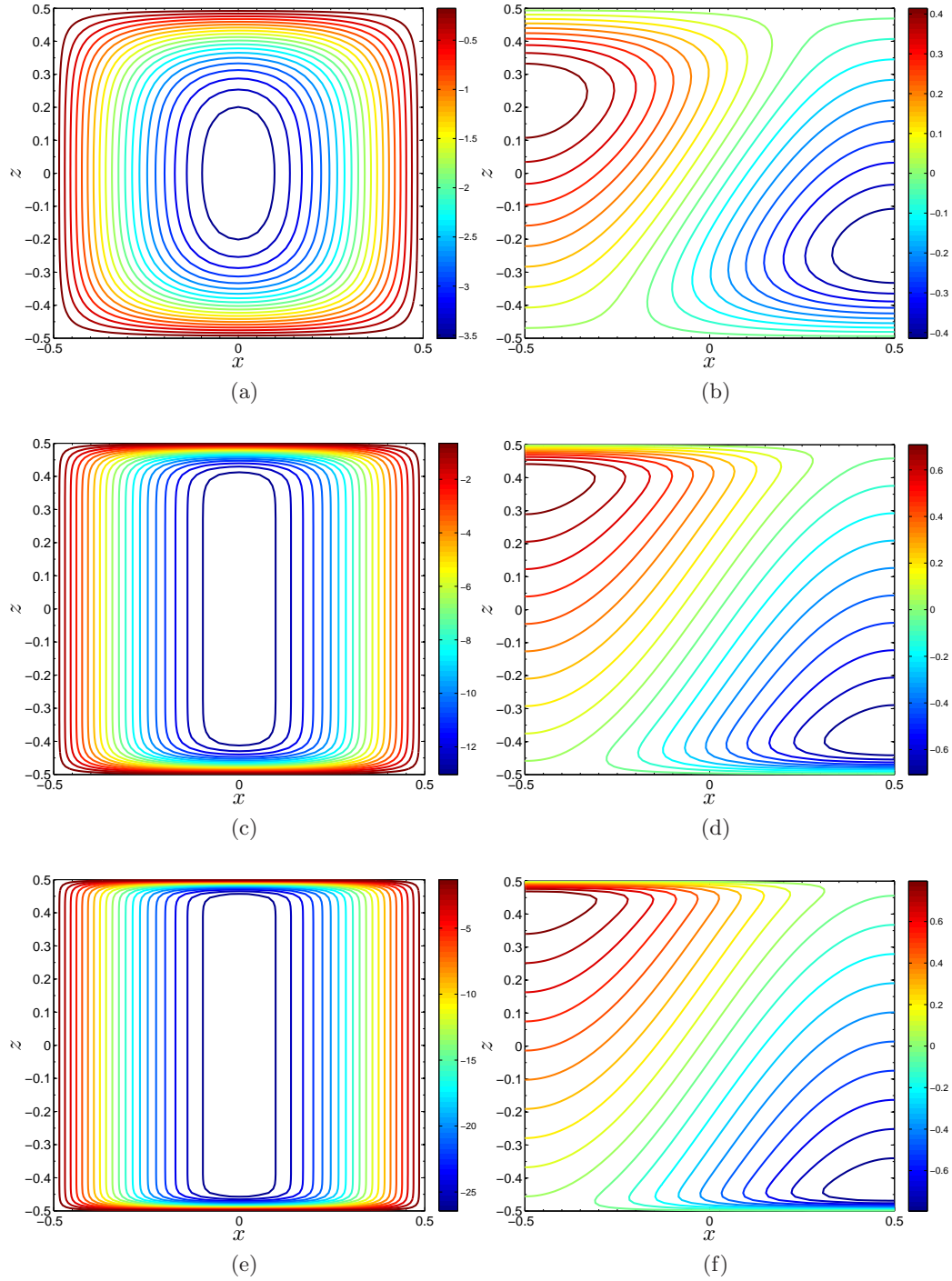


Figure 4: Evolution of the flow fields with Pe for the case with $\Gamma = 1$. Panels on the left show ψ and panels on the right show θ . (a) $Pe = 10.0$, $Nu_{\max} = 2.4$, (b) $Pe = 59.4$, $Nu_{\max} = 9.7$, (c) $Pe = 161.3$, $Nu_{\max} = 20.7$. The resolution is 61^2 .

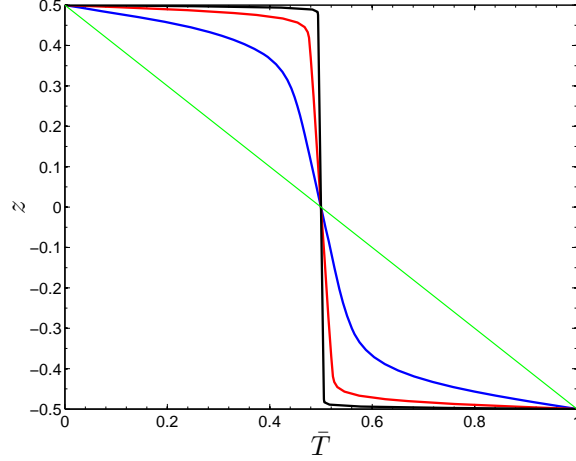


Figure 5: Vertical profiles of the horizontally averaged temperature $\bar{T}(z) = \Theta(z) + 1/\Gamma \int_0^\Gamma \theta(x, z) dx$ for $Pe = 25.6$ (blue), $Pe = 161.3$ (red), and $Pe = 1569.9$ (black). The thin green line shows $\bar{T} = \Theta$ (i.e. the purely conducting case, $Pe = 0$). $\Gamma = 1$ and $M = 61$.

changes, and also boundary layers start to develop in both ψ and θ (Figures 4c–4f). The boundary layers become thinner as Pe increases. Figure 5 clearly demonstrates the thinning of the thermal boundary layer by showing the horizontally averaged temperature $\bar{T}(z) = \Theta(z) + 1/\Gamma \int_0^\Gamma \theta(x, z) dx$ for $Pe = 0, 25.6, 161.3$ and 1569.9 . In fact, this decrease in the thermal boundary layer thickness is responsible for the increase of the vertical heat flux (and consequently Nu). This is because the thinner thermal boundary layers have larger temperature gradients (and heat fluxes) at the walls (as seen in Figure 5). Note that at the walls, $\mathbf{q}_a \cdot \mathbf{z} = -\partial T / \partial z|_{z=0,1}$ because $w = 0$. Additionally, it is easy to show that the horizontally averaged vertical flux does not vary with z , i.e. $\partial \{1/\Gamma \int_0^\Gamma (\mathbf{q}_a \cdot \mathbf{z}) dx\} / \partial z = 0$ (see e.g. [6]). Therefore, the Nusselt number can be readily calculated using the horizontally averaged vertical flux at one wall, i.e. $Nu = -1/\Gamma \int_0^\Gamma \{\partial T / \partial z|_{z=0}\} dx$. An immediate result of this analysis is that $Nu \propto 1/\delta_T$ where δ_T is the thermal boundary layer thickness.

Figure 6 presents the numerically calculated $Nu_{\max}(Pe, \Gamma)$ for several values of Γ . This figure shows that:

- The absolute upper bound (24) overpredicts the maximum possible heat transport.
- $Nu_{\max}(Pe)$ is obtained with solutions continued from linear solutions with $m = 1$. This was expected because flows with $m > 1$ produce horizontal transport in the bulk (far from the walls) which is not desired and wastes the energy of the flow. We computed several cases with $m > 1$ and a few cases with superposed solutions of two m (only one case is shown in this figure) and they all confirmed this conclusion.
- In the limit of small Pe , Nu_{\max} agrees well with the analytical bound (51).
- as Pe (and therefore nonlinearity) increases, Nu_{\max} starts to scale as $K(\Gamma) Pe^{2/3}$.
- As Pe increases, Nu_{\max} is obtained for flows with smaller Γ . This figure clearly demonstrate that Nu_{\max} plotted against Pe for different values of Γ forms an envelope

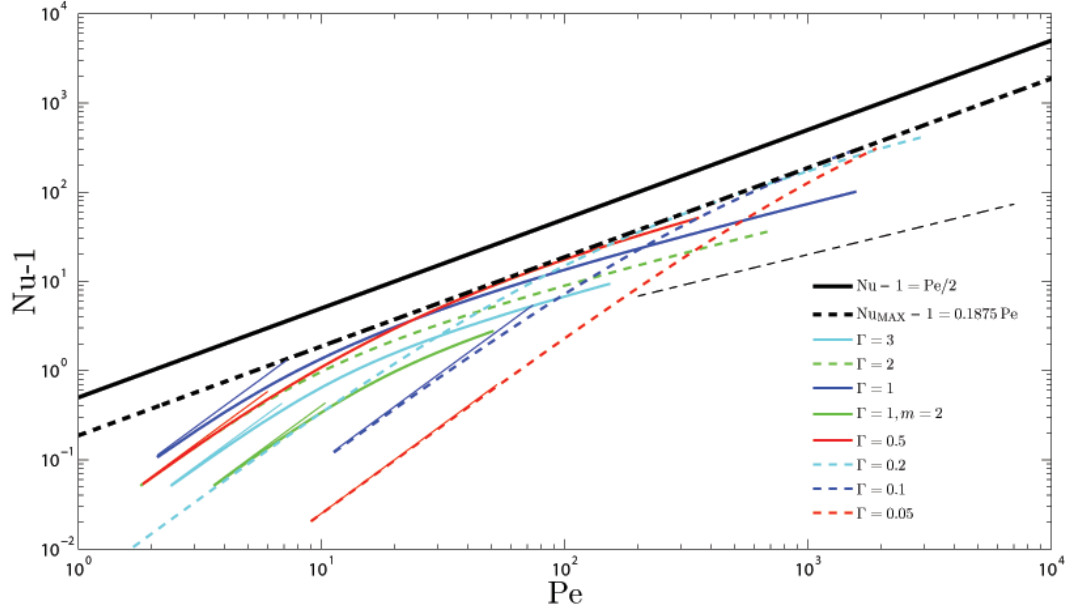


Figure 6: The non-black lines show the numerically obtained Nu_{\max} as a function of Pe for various values of Γ . For each case, the thin short line of the same color, visible for most of the cases, shows the analytical Nu_{\max} (51) in the limit of small Pe . The thick solid black line shows the absolute upper bound (24), and the thick broken black line shows the analytically obtained Nu_{MAX} (130) (see the next section). The thin broken black line indicates the $\text{Pe}^{2/3}$ slope. All numerical results started with linear solutions with $m = 1$, unless otherwise stated. All results shown here have resolution $M = 61$. Using a higher resolution $M = 91$ results in negligible difference.

which determines Nu_{MAX} . The numerical results suggests that Nu_{MAX} scales as $C \text{Pe}$ where C is a constant prefactor.

The prefactors $K(\Gamma)$ and C can be determined from the numerical results. However, this is not necessary as in the next section, guided by the numerical results, we obtain analytical solutions for (53)–(55) and hence Nu_{\max} , Nu_{MAX} , and Γ_{opt} in the limit of large Pe (the analytically obtained Nu_{MAX} is shown in Figure 6 and agrees very well with the envelope produced by the numerical results).

2.4 The Limit of Large Pe : Asymptotic Solution

The numerical results show various symmetries in ψ , θ , and ϕ in the limit of large Pe (e.g. see Figures 7 and 8). ψ is found to be nearly independent of z in the bulk and to depend on x as $\cos(\pi x/\Gamma)$ in both the bulk and boundary layers. θ and ϕ do not have such simple structure in the bulk or boundary layer. However, defining

$$\xi(x, z) \equiv \phi(x, z) + \theta(x, z), \quad (68)$$

$$\eta(x, z) \equiv \theta(x, z) - \phi(x, z), \quad (69)$$

it is observed that ξ (like ψ) is nearly independent of z except close to the top and bottom boundaries (i.e. inside the thin boundary layers), and that η is only a function of z everywhere (see Figures 7 and 8). This simple geometric structure suggests rewriting the equations for (ψ, ξ, η) and using matched asymptotic analysis to solve the resulting equations in the large-Pe (i.e. small- μ) limit.

Rewriting (53)-(55) for ψ , ξ , and η yields

$$-J(\xi, \eta) + 2\mu\Delta\psi + 2\xi_x = 0, \quad (70)$$

$$J(\psi, \xi) + \Delta\eta = 0, \quad (71)$$

$$J(\psi, \eta) + \Delta\xi - 2\psi_x = 0, \quad (72)$$

where (71) and (72) are obtained from adding and subtracting (54) and (55), respectively.

The numerical results suggest using the following ansatz:

$$\psi = \bar{\psi}(x) A(z), \quad (73)$$

$$\xi = \bar{\xi}(x) B(z), \quad (74)$$

$$\eta = \bar{\eta}(z) C(z), \quad (75)$$

where the overbar indicates the interior solution (or the so-called *outer solution*, i.e. far from the top and bottom boundary layers), and A , B , and C are equal to unity in the interior, rapidly decay close to the boundaries, and vanish at $z = \pm 0.5$. The first step in the analysis is finding the interior solution $(\bar{\psi}, \bar{\xi}, \bar{\eta})$.

2.4.1 Interior Solution

For small μ , the leading-order dominant balances in (70)–(72) in the interior are

$$2\mu\psi_{xx} - \xi_x\eta_z + \xi_z\eta_x + 2\xi_x = 0, \quad (76)$$

$$\eta_{xx} + \eta_{zz} + \psi_x\xi_z - \psi_z\xi_x = 0, \quad (77)$$

$$\xi_{xx} + \xi_{zz} + \psi_x\eta_z - \psi_z\eta_x - 2\psi_x = 0, \quad (78)$$

where the formally small $2\mu\psi_{xx}$ term has been retained to develop an asymptotic solution that remains uniformly valid in the small- μ limit even as $\Gamma \rightarrow 0$ (see below). Motivated by the numerics, we make the ansatz that $\eta(x, z) \sim \bar{\eta}(z)$ and $\psi(x, z) \sim \bar{\psi}(x)$, in the interior, in accord with (73) and (75).

Therefore, (76)–(78) reduce to

$$2\mu\bar{\psi}_{xx} + (2 - \bar{\eta}_z)\bar{\xi}_x = 0, \quad (79)$$

$$\bar{\eta}_{zz} = 0, \quad (80)$$

$$\bar{\xi}_{xx} + (\bar{\eta}_z - 2)\bar{\psi}_x = 0. \quad (81)$$

Equation (80) shows that $\bar{\eta}$ is linear in z (this could be also inferred from (79) and (81) because $\bar{\psi}$ and $\bar{\xi}$ are only functions of x). The linearity of $\bar{\eta}(z)$ along with the symmetry of the flow with respect to $z = 0$ yields

$$\bar{\eta}(z) = \bar{\eta}_o z, \quad (82)$$

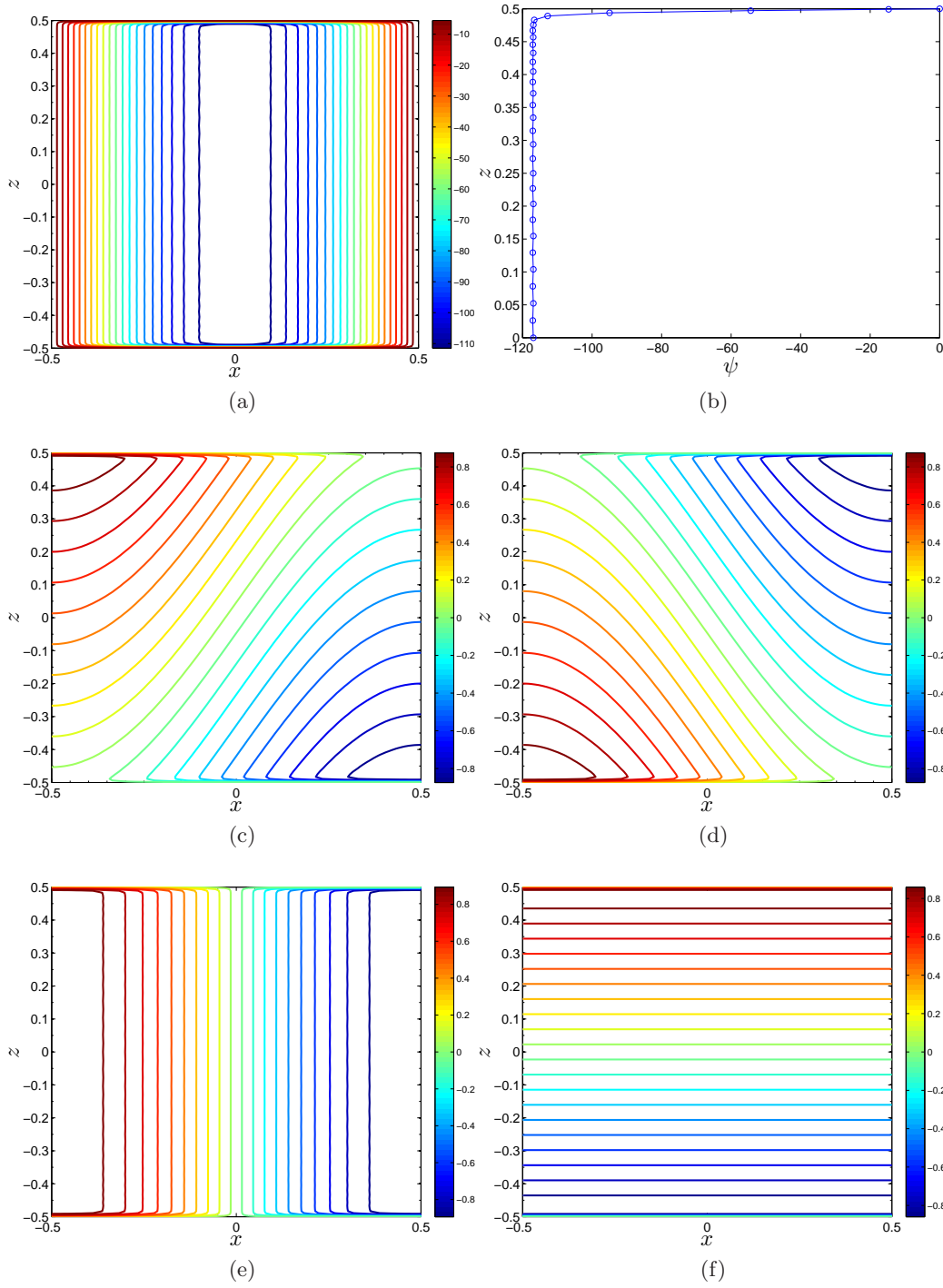


Figure 7: Flow field for $\Gamma = 1$, $\mu = 3.557 \times 10^{-5}$, $\text{Pe} = 1320.5$, and $\text{Nu}_{\max} = 90.7$. (a) ψ , (b) ψ along $x = 0$, (c) θ , (d) ϕ , (e) $\xi \equiv \theta + \phi$, and (f) $\eta \equiv \theta - \phi$. The resolution is 61^2 .

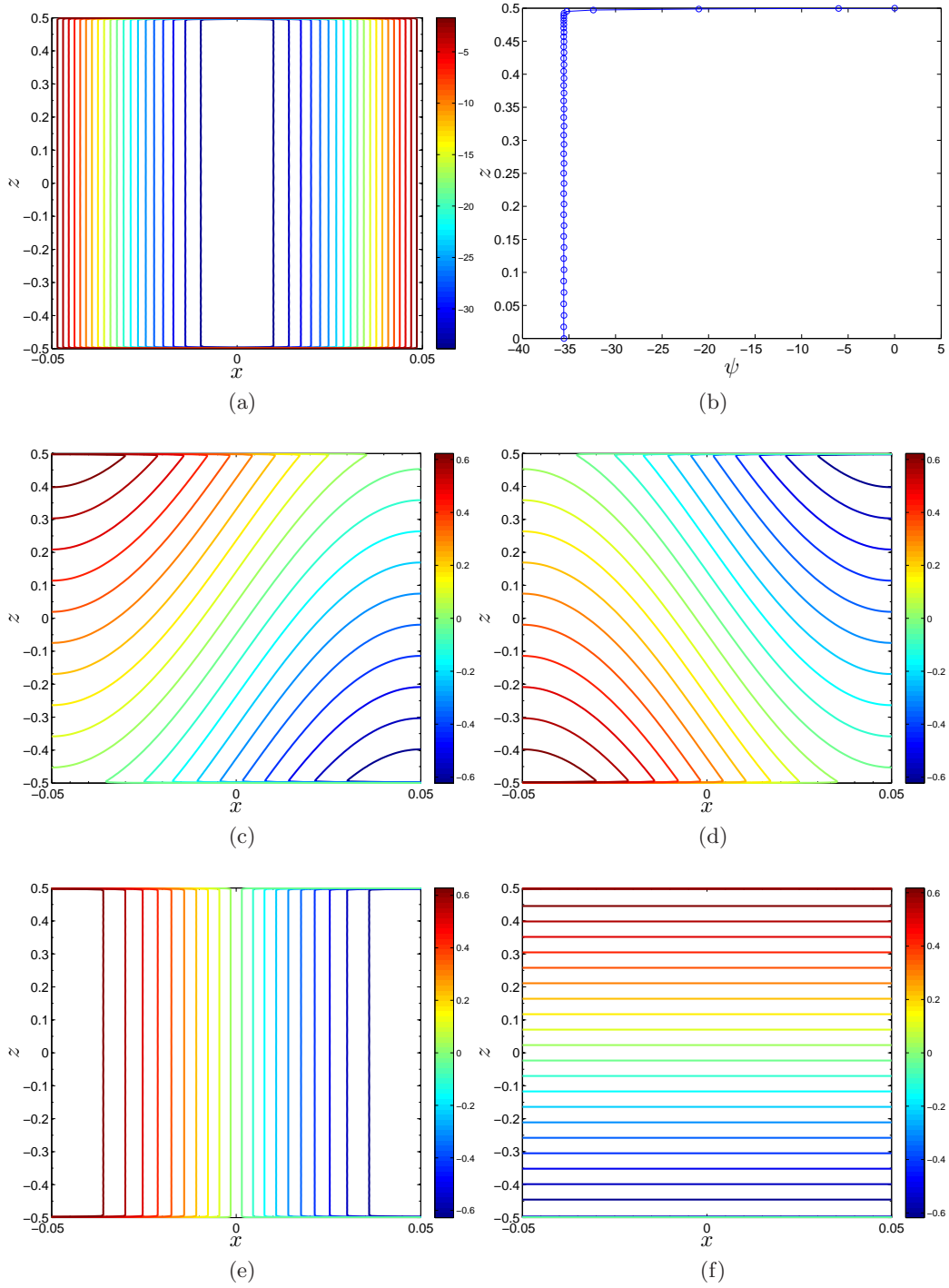


Figure 8: Flow field for $\Gamma = 0.1$, $\mu = 1.9 \times 10^{-4}$, $\text{Pe} = 1045.0$, and $\text{Nu}_{\max} = 194.0$. (a) ψ , (b) ψ along $x = 0$, (c) θ , (d) ϕ , (e) $\xi \equiv \theta + \phi$, and (f) $\eta \equiv \theta - \phi$. The resolution is 91^2 .

where $\bar{\eta}_o$ is an unknown constant. Linearity of $\bar{\eta}(z)$ can also be clearly seen from Figures 7f and 8f. Using (82) and eliminating $\bar{\psi}$ between (79) and (81) gives

$$\bar{\xi}_{xxx} + \left(\frac{\bar{\eta}_o - 2}{\sqrt{2\mu}} \right)^2 \bar{\xi}_x = 0. \quad (83)$$

Given the periodicity of 2Γ in x , and $\xi_x(\pm\Gamma/2, z) = 0$, this implies

$$\bar{\xi} = \pm \bar{\xi}_o \sin(\pi x/\Gamma), \quad (84)$$

$$\bar{\eta}_o = 2 - \frac{\pi}{\Gamma} \sqrt{2\mu}, \quad (85)$$

where $\bar{\xi}_o > 0$ is an unknown constant. Notice that there exists another possible solution $\bar{\eta}_o = 2 + (\pi/\Gamma) \sqrt{2\mu} > 2$ which is discarded here based on the numerical results. It will be shown later in section 2.4.3 that $\bar{\eta}_o$ must be ≤ 2 because of the maximum principle, confirming that (85) is the only admissible solution.

Equation (81) gives

$$\bar{\psi} = \frac{\pm \bar{\xi}_o}{\sqrt{2\mu}} \cos(\pi x/\Gamma). \quad (86)$$

Therefore, the interior flow field (i.e. outer solution) is known up to an unknown constant $\bar{\xi}_o$ (notice that in (84) and (86) either $-\bar{\xi}_o$ or $+\bar{\xi}_o$ should be chosen for both $\bar{\psi}$ and $\bar{\xi}$).

2.4.2 Boundary Layer Solution

To find the boundary layer solution (i.e. the inner solution), we rewrite (73)-(75) as

$$\psi = \bar{\psi}(x) A(Z_1), \quad (87)$$

$$\xi = \bar{\xi}(x) B(Z_2), \quad (88)$$

$$\eta = \bar{\eta}(z) C(Z_3), \quad (89)$$

where Z is the rescaled z near the boundaries at $z = \mp 0.5$:

$$Z_1 = (0.5 \pm z)/\delta_1, \quad (90)$$

$$Z_2 = (0.5 \pm z)/\delta_2, \quad (91)$$

$$Z_3 = (0.5 \pm z)/\delta_3. \quad (92)$$

For the moment we allow for the possibility that the small boundary layer thicknesses for ψ , ξ , and η are not the same. Notice that in the rescaled coordinate, $A(0) = B(0) = C(0) = 0$ and $A(+\infty) = B(+\infty) = C(+\infty) = 1$.

Focusing only on the upper boundary layer for now (i.e. close to $z = +0.5$), and using (87)-(89) and (90)-(92) in (70)-(72) gives

$$2\mu (\bar{\psi}_{xx} A + \bar{\psi} A''/\delta_1^2) + (2 - (\bar{\eta}_z C - \bar{\eta} C'/\delta_3)) \bar{\xi}_x B = 0, \quad (93)$$

$$\bar{\eta}_{zz} C - 2\bar{\eta}_z C'/\delta_3 + \bar{\eta} C''/\delta_3^2 - \bar{\psi}_x A \bar{\xi} B'/\delta_2 + \bar{\xi}_x B \bar{\psi} A'/\delta_1 = 0, \quad (94)$$

$$\bar{\xi}_{xx} B + \bar{\xi} B''/\delta_2^2 - (2 - (\bar{\eta}_z C - \bar{\eta} C'/\delta_3)) \bar{\psi}_x A = 0, \quad (95)$$

where $'$ means d/dZ (e.g. $A' \equiv dA/dZ_1$). Using the interior solution (82)-(86), and noticing that $\bar{\eta} \rightarrow \bar{\eta}_o/2$ as $z \rightarrow 0.5$, the above equations yield

$$\sqrt{2\mu} \left[-\left(\frac{\pi}{\Gamma}\right)^2 A + \frac{1}{\delta_1^2} A'' \right] + \left(\frac{\pi}{\Gamma}\right) \left[2 - \left(2 - \frac{\pi}{\Gamma} \sqrt{2\mu}\right) \left(C - \frac{1}{2\delta_3} C'\right) \right] B = 0, \quad (96)$$

$$\left(2 - \frac{\pi}{\Gamma} \sqrt{2\mu}\right) \left[-\frac{2}{\delta_3} C' + \frac{1}{2\delta_3^2} C'' \right] + \left(\frac{\pi}{2\Gamma}\right) \frac{\xi_o^2}{\sqrt{2\mu}} \left[\frac{1}{\delta_2} AB' + \frac{1}{\delta_1} BA' \right] = 0, \quad (97)$$

$$\sqrt{2\mu} \left[-\left(\frac{\pi}{\Gamma}\right)^2 B + \frac{1}{\delta_2^2} B'' \right] + \left(\frac{\pi}{\Gamma}\right) \left[2 - \left(2 - \frac{\pi}{\Gamma} \sqrt{2\mu}\right) \left(C - \frac{1}{2\delta_3} C'\right) \right] A = 0, \quad (98)$$

where (97) has been integrated over $1/\Gamma \int_0^\Gamma dx$ to eliminate the $\sin^2(\pi x/\Gamma)$ and $\cos^2(\pi x/\Gamma)$ terms.

To balance the leading order terms, we need to determine the generic boundary layer thickness δ as a function of a small parameter ϵ defined based on μ and Γ . To get to the large Pe limit, we know that $\mu \ll 1$, although from the above equations it seems that $\sqrt{\mu} \ll 1$ is a more appropriate parameter in this problem. Here we restrict our analysis to $\Gamma \leq 1$, because the numerical results of section 2.3 showed that $\Gamma > 1$ does not maximize the transport. With $\mu \ll 1$ and $\Gamma \leq 1$, we define $\lambda \equiv \Gamma\sqrt{\mu} \ll 1$. We also need to consider the magnitude of $\sigma \equiv \Gamma/\sqrt{\mu}$. If $\Gamma = \mathcal{O}(1)$, then $\sigma \gg 1$. The numerical results (Figure 6) suggest that Γ_{opt} decreases as Pe increases. Therefore, we should allow for the possibility that $\Gamma \ll 1$, i.e. $\sigma = \mathcal{O}(1)$ and $\sigma \ll 1$. However, the latter means that the cell size shrinks very fast as Pe increases, suggesting that this limit probably does not correspond to the optimal flow. A close examination of (96)-(98) reveals that $\sigma \gg 1$ and $\sigma = \mathcal{O}(1)$ give the same balance and result in the same scaling for boundary layer thicknesses. Therefore one solution covers both limits. Additionally, the distinguished limit $\sigma = \mathcal{O}(1)$ guarantees that the solution is uniformly valid in Γ . Here we focus on these two limits and exclude $\sigma \ll 1$ from our analysis (but appendix B includes a brief discussion of the scaling in this limit). Therefore, based on the above discussion, we choose the small parameter ϵ as

$$\epsilon \equiv \frac{\Gamma\sqrt{2\mu}}{\pi} \quad (99)$$

where the constants are included to simplify the algebra. Again we emphasize that we only focus on $\sigma \geq \mathcal{O}(1)$ hereafter. This will be justified later as we show that Nu_{max} for a fixed value of Γ in the limit of large Pe is obtained with $\sigma \gg 1$, and that Nu_{MAX} for large Pe is achieved when $\sigma = \mathcal{O}(1)$.

Using (99) in (96)-(98), and balancing the leading order terms gives

$$A'' + \left(1 - \frac{\pi}{\sigma\sqrt{2}}\right) B C' = 0, \quad (100)$$

$$\epsilon \delta_3 = \delta_1^2. \quad (101)$$

Notice that based on our assumption for σ , the term in the parentheses is $\mathcal{O}(1)$. The same procedure for (98) results in

$$B'' + \left(1 - \frac{\pi}{\sigma\sqrt{2}}\right) A C' = 0, \quad (102)$$

$$\epsilon \delta_3 = \delta_2^2, \quad (103)$$

showing that $\delta_1 = \delta_2 \equiv \delta$. Equation (97) yields

$$\left(1 - \frac{\pi}{\sigma\sqrt{2}}\right) C'' + \frac{\bar{\xi}_o^2}{2} (AB' + BA') = 0, \quad (104)$$

$$\epsilon \delta = \delta_3^2. \quad (105)$$

Equations (101), (103), and (105) together show that the boundary layer thicknesses are each $\mathcal{O}(\epsilon)$, i.e. $\delta_1 = \delta_2 = \delta_3 = \delta = \epsilon$. Integrating equation (104) gives

$$\left(1 - \frac{\pi}{\sigma\sqrt{2}}\right) C' = -\frac{\bar{\xi}_o^2}{2} (AB - 1), \quad (106)$$

where the constant of integration has been deduced from $C'(+\infty) = 0$ and $A(+\infty) = B(+\infty) = 1$. Substituting this equation in (100) and (102) results in the exactly the same equation for A and B , which along with the fact that they have the same boundary conditions suggests that $A = B$. Using $A = B$ in both equations (100) and (104) shows that $A = B = (1 - \pi/(\sigma\sqrt{2})) C/\bar{\xi}_o$. Boundary conditions $A(+\infty) = C(+\infty) = 1$ imply that $\bar{\xi}_o = 1 - \pi/(\sigma\sqrt{2})$. Therefore

$$A = B = C, \quad (107)$$

$$A'' + \bar{\xi}_o AA' = 0, \quad (108)$$

$$\bar{\xi}_o = \frac{\bar{\eta}_o}{2} = 1 - \frac{\pi}{2\Gamma} \sqrt{2\mu}. \quad (109)$$

Determining $\bar{\xi}_o$ completes the interior solution.

Equation (108) can be integrated once to give

$$A' + \frac{\bar{\xi}_o}{2} A^2 = \frac{\bar{\xi}_o}{2}, \quad (110)$$

where again the constant of integration comes from $A'(+\infty) = 0$ and $A(+\infty) = 1$. Equation (110) is a Riccati equation with the solution

$$A(Z) = \frac{1 - \exp(-\bar{\xi}_o Z)}{1 + \exp(-\bar{\xi}_o Z)} = \tanh \left[\frac{\bar{\xi}_o}{2} Z \right]. \quad (111)$$

2.4.3 The Complete Solution: Matching

We have found the solution for the flow field to leading order, assuming that $\Gamma\sqrt{\mu} \ll 1$ and $\Gamma/\sqrt{\mu}$ is finite or large. Including the bottom boundary layer, and matching the three regions (the interior and the two boundary layers), the complete solution is

$$\psi(x, z) = \frac{1}{\sqrt{2\mu}} \left(1 - \frac{\pi}{2\Gamma} \sqrt{2\mu}\right) \cos\left(\frac{\pi}{\Gamma} x\right) H(z), \quad (112)$$

$$\xi(x, z) = \left(1 - \frac{\pi}{2\Gamma} \sqrt{2\mu}\right) \sin\left(\frac{\pi}{\Gamma} x\right) H(z), \quad (113)$$

$$\eta(x, z) = 2 \left(1 - \frac{\pi}{2\Gamma} \sqrt{2\mu}\right) z H(z), \quad (114)$$

where

$$\begin{aligned} H(z) &= A\left(\frac{0.5-z}{\delta}\right) A\left(\frac{0.5+z}{\delta}\right) \\ &= \tanh\left[\frac{\pi}{2}\left(1 - \frac{\pi}{2\Gamma}\sqrt{2\mu}\right)\frac{z+0.5}{\Gamma\sqrt{2\mu}}\right] \tanh\left[\frac{\pi}{2}\left(1 - \frac{\pi}{2\Gamma}\sqrt{2\mu}\right)\frac{z+0.5}{\Gamma\sqrt{2\mu}}\right]. \end{aligned} \quad (115)$$

Therefore

$$u(x, z) = \frac{1}{\sqrt{2\mu}} \left(1 - \frac{\pi}{2\Gamma}\sqrt{2\mu}\right) \cos\left(\frac{\pi}{\Gamma}x\right) H'(z), \quad (116)$$

$$w(x, z) = \frac{1}{\sqrt{2\mu}} \left(\frac{\pi}{\Gamma}\right) \left(1 - \frac{\pi}{2\Gamma}\sqrt{2\mu}\right) \sin\left(\frac{\pi}{\Gamma}x\right) H(z), \quad (117)$$

$$\theta(x, z) = \frac{1}{2} \left(1 - \frac{\pi}{2\Gamma}\sqrt{2\mu}\right) \left(\sin\left(\frac{\pi}{\Gamma}x\right) + 2z\right) H(z). \quad (118)$$

This solution is compared with the numerical results in Figures 9 and 10. The agreement between the numerical and asymptotic solutions is excellent.

Note that the maximum principle requires $|\theta| \leq 1$. This means that in (118), the first term in the parentheses, i.e. $\xi_o = \bar{\eta}_o/2 = 1 - \frac{\pi}{2\Gamma}\sqrt{2\mu}$, has to be smaller than 1. This analysis justifies discarding the other solution for $\bar{\eta}_o$ in section 2.4.1.

Values of Pe and Nu_{\max} can be calculated analytically from (116)-(118):

$$\text{Pe} = \sqrt{\langle u^2 + w^2 \rangle} = \frac{1}{2\sqrt{\mu}} \left(1 - \frac{\pi}{2\Gamma}\sqrt{2\mu}\right) \sqrt{\int_{-0.5}^{0.5} \{(H')^2 + (\pi/\Gamma)^2 H^2\} dz} \quad (119)$$

$$\text{Nu}_{\max} = 1 + \langle w\theta \rangle = 1 + \frac{1}{4\sqrt{2\mu}} \left(\frac{\pi}{\Gamma}\right) \left(1 - \frac{\pi}{2\Gamma}\sqrt{2\mu}\right)^2 \int_{-0.5}^{0.5} H^2 dz \quad (120)$$

Notice that $H(z)$ depends on μ and Γ which makes it hard to find an explicit expression for $\text{Nu}_{\max}(\text{Pe}, \Gamma)$. However, (119) and (120) can be easily calculated numerically for a given pair of (μ, Γ) . Figure 11 compares the values of Pe and Nu_{\max} from the numerical solutions with the values given by (119) and (120) for $\Gamma = 0.2$ and 1. The numerical and analytical results agree well, even for relatively small values of Pe . This suggests that the higher order terms in the analytical solution may be transcendentally small in ϵ .

2.4.4 $\text{Nu}_{\max}(\text{Pe}, \Gamma)$: $\lambda \ll 1$ and $\sigma \gg 1$ Limit

In the limit of relatively small $\lambda \equiv \Gamma\sqrt{\mu}$, the integrals in (119) and (120) can be approximated as

$$\int_{-0.5}^{0.5} H^2 dz \approx 1 - \frac{4\sqrt{2}}{\pi} \frac{\lambda}{1 - \frac{\pi}{\sigma\sqrt{2}}}, \quad (121)$$

$$\int_{-0.5}^{0.5} (H')^2 dz \approx \frac{\sqrt{2}\pi}{3} \frac{1 - \frac{\pi}{\sigma\sqrt{2}}}{\lambda}, \quad (122)$$

as has been confirmed numerically (again, recall that $\sigma \equiv \Gamma/\sqrt{\mu}$ is not $\ll 1$).

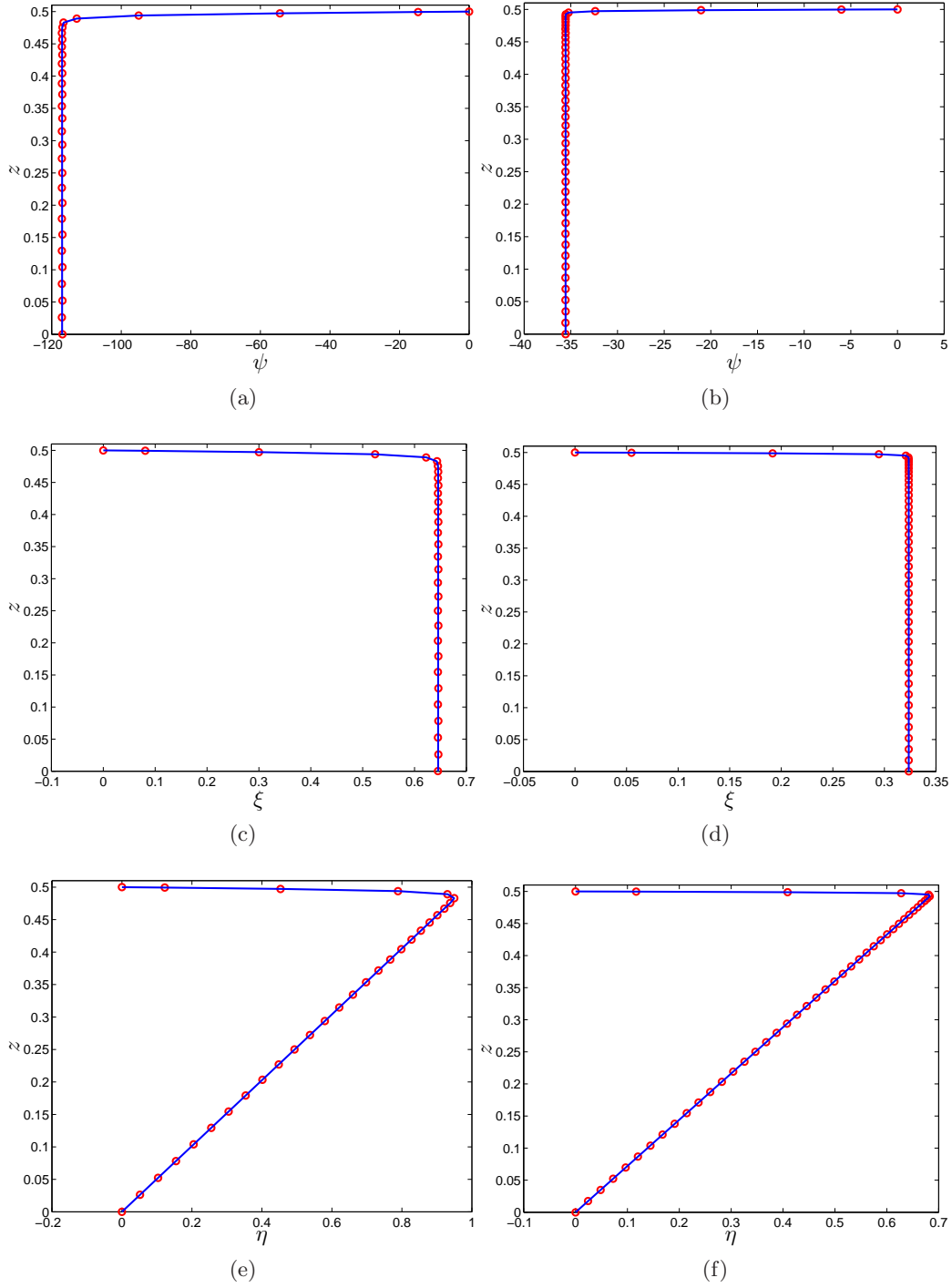


Figure 9: Comparison of the analytical (blue line) and numerical (red circles) solutions for $\Gamma = 1$ (left panels), and $\Gamma = 0.1$ (right panels). The top row is ψ along $x = 0$, the middle row is ξ along $x = -0.227$ (left) and $x = -0.0155$ (right), and the bottom row is η along $x = 0$. For $\Gamma = 1$, $Pe = 1320.5$, $Nu_{\max} = 90.7$, and $M = 61$. For $\Gamma = 0.1$, $Pe = 1045.4$, $Nu_{\max} = 194.0$, and $M = 91$.

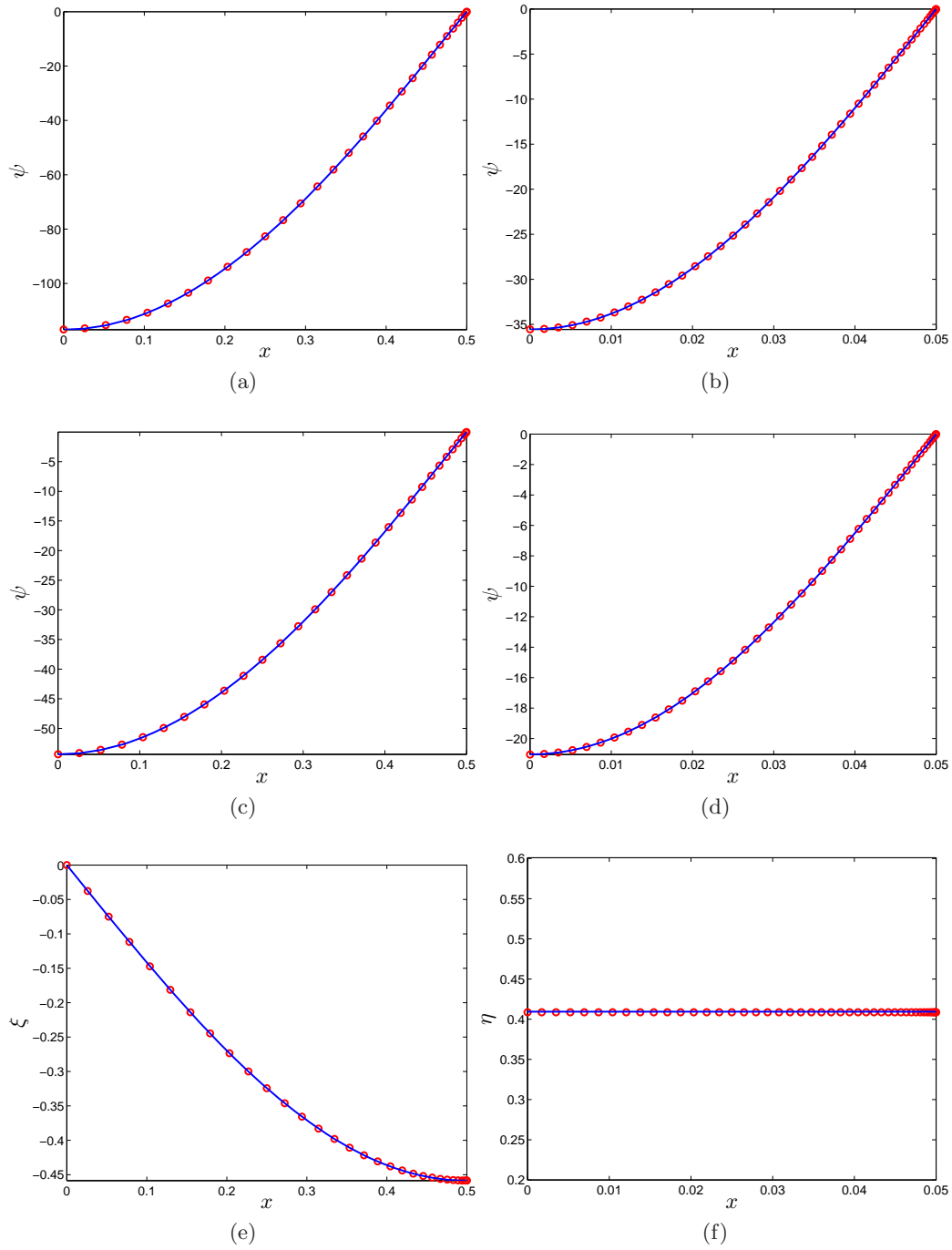


Figure 10: Comparison of the analytical (blue line) and numerical (red circles) solutions for $\Gamma = 1$ (left panels) and $\Gamma = 0.1$ (right panels) (see the caption of Figure 9 for more details). (a) and (b) ψ along $z = 0$. (c) ψ , (d) ψ , (e) ξ , and (f) η ; (c)–(f) are versus x along the third Chebyshev collocation point from the wall ($z = 0.4972$ in (c) and $z = 0.4988$ in (d)).

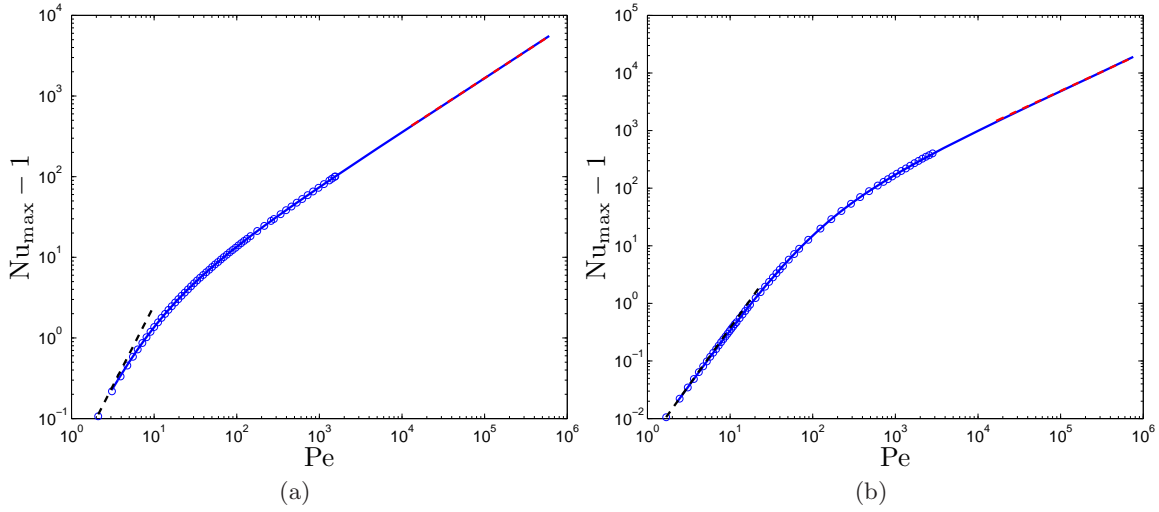


Figure 11: Nu_{\max} from the numerical solutions (blue circles), the small- Pe analytical solution (51) (dashed black lines), and the large- Pe asymptotic solution (119)-(120) (blue solid lines) for two cases: (a) $\Gamma = 1$ and (b) $\Gamma = 0.2$. The dashed red lines, which have collapsed with the blue lines in the large- Pe regime, show (125).

Here examine (119) and (120) in the limit of vanishing μ and fixed Γ , i.e. $\lambda \ll 1$ and $\sigma \gg 1$. In this limit, (121) and (122) further simplify to 1 and $\sqrt{2}\pi/(3\lambda)$, respectively. Using these limits in (119) and (120) yields

$$\text{Pe} = \frac{\pi}{2} \frac{1}{\lambda} \sqrt{\frac{\sqrt{2}}{3\pi}} \sigma, \quad (123)$$

$$\text{Nu}_{\max} - 1 = \frac{\pi}{4\sqrt{2}} \frac{1}{\lambda}. \quad (124)$$

Solving (123) for μ and using that expression in (124) gives $\text{Nu}_{\max}(\text{Pe}, \Gamma)$:

$$\text{Nu}_{\max} = 1 + \frac{1}{4} \left[\frac{3\pi^2}{\Gamma^2} \right]^{1/3} \text{Pe}^{2/3}. \quad (125)$$

The accuracy of this approximation is shown in Figure 11 for $\Gamma = 0.2$ and 1.

Equation (125) gives Nu_{\max} as a function of Pe for a fixed value of Γ , which may not be the same as Nu_{MAX} , i.e. the maximum achievable Nu_{\max} at that Pe . $\text{Nu}_{\text{MAX}}(\text{Pe})$ is found in the next section and requires letting Γ shrink as Pe increases.

2.4.5 $\text{Nu}_{\text{MAX}}(\text{Pe})$: $\lambda \ll 1$ and $\sigma = \mathcal{O}(1)$ Limit

Here we look at the limit $\sqrt{\mu} \ll 1$ and $\Gamma \ll 1$ when their ratio is finite. Physically this means that as Pe gets larger, we allow the cells to narrow. It turns out that it is in this distinguished limit that Nu_{MAX} for a given Pe , i.e. the optimal transport for a given amount of energy, is achieved.

In this limit, (121) again reduces to 1, but (122) cannot be further simplified. Using these approximations for the integrals in (119)–(120) gives

$$\text{Pe} = \frac{\pi}{2} \frac{1}{\lambda} \left(1 - \frac{\pi}{\sqrt{2}} \frac{1}{\sigma} \right) \sqrt{\frac{2}{3} + \frac{\sqrt{2}}{3\pi} \sigma}, \quad (126)$$

$$\text{Nu}_{\max} - 1 = \frac{\pi}{4\sqrt{2}} \frac{1}{\lambda} \left(1 - \frac{\pi}{\sqrt{2}} \frac{1}{\sigma} \right)^2. \quad (127)$$

By dividing (127) by (126) we eliminate λ :

$$\frac{\text{Nu}_{\max} - 1}{\text{Pe}} = \frac{1}{2\sqrt{2}} \frac{1 - \frac{\pi}{\sqrt{2}} \frac{1}{\sigma}}{\sqrt{\frac{2}{3} + \frac{\sqrt{2}}{3\pi} \sigma}}. \quad (128)$$

Thus we have obtained $\text{Nu}_{\max}(\text{Pe}, \sigma)$, which is found to be maximized at

$$\sigma_{\text{opt}} \equiv \frac{\Gamma_{\text{opt}}}{\sqrt{\mu}} = 2\sqrt{2}\pi \approx 8.885766. \quad (129)$$

This gives the aspect ratio Γ_{opt} that maximizes Nu_{\max} at a given μ . Using $\sigma = \sigma_{\text{opt}}$ in (128) gives $\text{Nu}_{\text{MAX}}(\text{Pe})$:

$$\text{Nu}_{\text{MAX}} = 1 + 0.1875 \text{Pe}. \quad (130)$$

Figure 6 shows that (130) gives the maximum possible transport with remarkable accuracy.

Combining (129) and (126) gives $\Gamma_{\text{opt}}(\text{Pe})$, i.e. the optimal cell aspect ratio at a given Pe :

$$\Gamma_{\text{opt}} = 3.8476 \text{Pe}^{-1/2} \quad (131)$$

Therefore as the Pe number increases, thinner cells provide the maximum transport.

2.5 Example: Application to Porous Media Convection

Here we show that convection in porous media is an example of transport with fixed energy. We find Nu_{\max} and Nu_{MAX} as a function of the Rayleigh number Ra and compare them with the results of previous analytical and numerical investigations.

Convection in a layer of fluid-saturated porous medium heated from below and cooled from above is often modeled by [6]

$$\nabla \cdot \mathbf{v} = 0, \quad (132)$$

$$\frac{1}{\text{Pr}} (\dot{\mathbf{v}} + \mathbf{v} \cdot \nabla \mathbf{v}) + \mathbf{v} = -\nabla p + \text{Ra} T \mathbf{z}, \quad (133)$$

$$\dot{T} + \mathbf{v} \cdot \nabla T = \Delta T, \quad (134)$$

where the first and the third equations are the incompressibility constraint and advection–diffusion equation. The second equation is the Boussinesq momentum equation where Pr is

the Prandtl–Darcy number, and Ra is the Rayleigh number. The linear velocity damping term comes from the Darcy’s law (see [6] and references therein for details).

Multiplying (133) by \mathbf{v} and integrating over long time and over the domain with impermeable walls gives

$$\langle \mathbf{v} \cdot \mathbf{v} \rangle = Ra \langle wT \rangle, \quad (135)$$

where the transient term vanishes due to long–time averaging, and the nonlinear and pressure terms vanish because of the spatial integration. Using the definition of Pe for fixed energy problems (13) and Nu (16) from section 1.1 we obtain

$$Pe^2 = Ra (Nu - 1). \quad (136)$$

The Nusselt number Nu , when calculated by long–time averaging, is just a function of Ra . As a results, in both steady and statistically–steady flows, equation (136) shows that Pe is fixed for a fixed value of Ra (note that Ra depends on the fluid properties and the imposed temperature difference between the walls; it does not depend on the flow). Therefore, convection in porous media occurs with fixed energy.

Employing (136), Pe can be replaced with Ra in (125), (130), and (131):

$$Nu_{\max}(Ra, \Gamma) = 1 + \frac{\sqrt{3}\pi}{8\Gamma} Ra^{1/2}, \quad (137)$$

$$Nu_{\text{MAX}}(Ra) = 1 + 0.0352 Ra, \quad (138)$$

$$\Gamma_{\text{opt}} = 8.89 Ra^{-0.5}. \quad (139)$$

Interestingly, $Ra^{-0.5}$ is the scaling of the smallest unstable mode in porous media convection (obtained from linear stability analysis).

Table 1 compares (137)–(139) with the results obtained using other methods in the literature. The classical argument of Malkus [14] and Howard [11], which is based on the marginal stability of the boundary layer, gives $Nu \sim Ra$ for convection in porous media [10]. The background method also gives upper bounds on Nu which scale linearly with Ra . The prefactors in the upper bounds have been improved over the years [6, 16, 19].

While we solved (132) and the steady version of (134) for one cell in the current work, we did not solve the momentum equation of porous media convection, i.e. (133) (instead we solved an Euler–Lagrange equation (26) which resembles (133) to some extent). The outcome of our analysis is the optimal steady flow, which might not satisfy (133). Solving the steady version of (132)–(134) in the limit of infinite Prandtl–Darcy number for one cell (using numerical continuation), Corson [5] has shown that $Nu \sim Ra^{2/3}$ and $\Gamma \sim Ra^{-0.5}$. Furthermore, Corson [5] shows that if Γ is fixed, Nu scales as $Ra^{1/3}$. Comparing these scalings with those obtained in the current work shows that steady convection in porous media does not transport as much as possible by a steady flow with a given amount of energy. This might be due to the fact that the flow in steady porous media convection differs significantly from the optimal steady flow (e.g. compare Figures 12b and 12a).

The latest direct numerical simulations (DNS) of (132)–(134) in the limit of infinite Prandtl–Darcy number at Ra as high as 4×10^4 show that Nu scales as Ra and that the cell aspect ratio scales as $Ra^{-0.4}$ [9]. Comparing the steady [5] and unsteady [9] solutions of (132)–(134) suggests that unsteadiness might enhance the transport.

Table 1: Comparison of the results of the current work with the scalings for porous media convection obtained using various other methods.

	Nu(Ra)	$\Gamma(\text{Ra})$	Nu(Ra, Γ_{fixed})
Boundary Layer Stability Argument Malkus [14], Howard [11], Horne & O’Sullivan [10]	$\sim C \text{Ra}$		
Upper Bounds using Background Method Doering & Constantin [6] Otero <i>et al.</i> [16] Wen <i>et al.</i> [19]	$\leq 0.035 \text{Ra}$ $\leq 0.029 \text{Ra}$ $\lesssim 0.017 \text{Ra}$		
DNS: Unsteady Simulations Otero <i>et al.</i> [16]: $\text{Ra} \leq 10^4$ Hewitt <i>et al.</i> [9]: $\text{Ra} \leq 4 \times 10^4$	$\sim C \text{Ra}^{0.9}$ $\sim 0.007 \text{Ra}$	$\sim C \text{Ra}^{-0.4}$	
Steady Unicellular Analysis Fowler [8] Corson [5]	$\sim C \text{Ra}^{2/3}$	$\sim C \text{Ra}^{-0.5}$	$\sim C(\Gamma) \text{Ra}^{1/3}$ $\sim C(\Gamma) \text{Ra}^{1/3}$
Current Work Numerical & asymptotic analyses	$\leq 1 + 0.035 \text{Ra}$	$\sim 8.89 \text{Ra}^{-0.5}$	$\leq 1 + \frac{0.68}{\Gamma} \text{Ra}^{0.5}$

Results of the current work show that the maximum possible steady transport scales linearly with Ra, which curiously agrees with the unsteady results. As shown in Figure 12, the optimal steady flow obtained here and the unsteady flow look similar to some extent. However, the unsteady transport is around 5 times smaller than the maximum possible steady transport at a given Ra, and the convection cells of the unsteady flow are wider than the optimal cells with aspect ratio Γ_{opt} .

3 Optimal Transport with Fixed Enstrophy

In the second problem, we investigate the optimal steady transport with fixed enstrophy. Therefore, equations (8)–(11) and (14) become

$$\mathbf{v} \cdot \nabla \theta = \Delta \theta + w, \quad (140)$$

$$\nabla \cdot \mathbf{v} = 0, \quad (141)$$

$$\text{Pe} = \langle |\nabla \mathbf{v}|^2 \rangle, \quad (142)$$

$$\theta(x, 0) = \theta(x, 1) = 0, \quad (143)$$

$$w(x, 0) = w(x, 1) = 0. \quad (144)$$

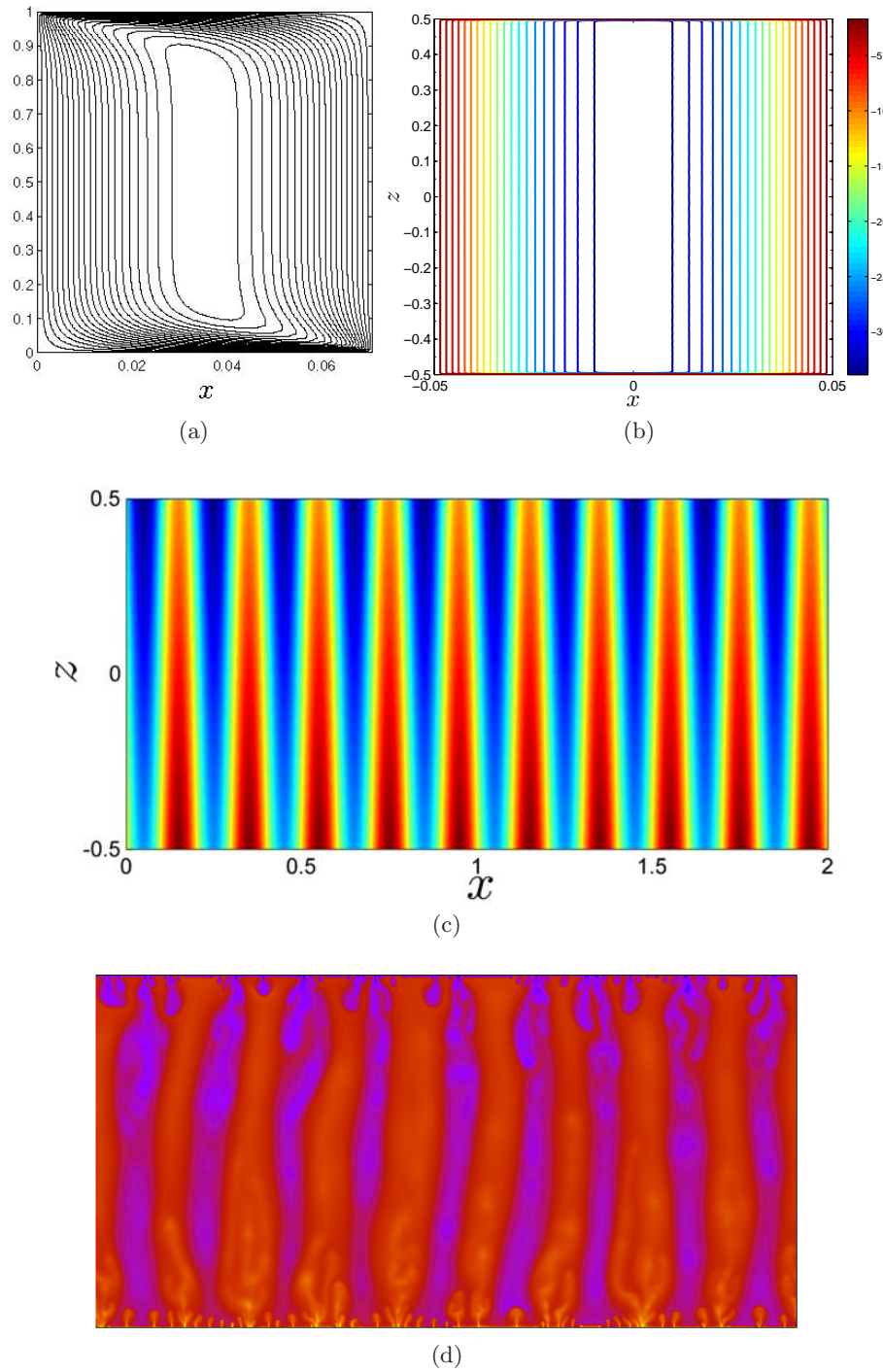


Figure 12: Streamfunction ψ for (a) steady porous media convection with $\Gamma = 0.07$ and $Ra = 9976$ [5] and (b) steady optimal flow with $\Gamma = 0.1$ and $Ra = 5658$. Temperature T in the large- Ra regime (c) steady optimal flow with $\Gamma = 0.1$ and $Ra = 4028.4$ and (d) unsteady DNS results with $Ra = 2 \times 10^4$ [9].

As for the first problem, a simple analysis gives a relatively crude upper bound of Nu. Starting from (16)

$$\begin{aligned} \text{Nu} &= 1 + \langle wT \rangle = 1 + \langle w(T - 1/2) \rangle \leq 1 + \langle |w|^2 \rangle^{1/2} \langle |T - 1/2|^2 \rangle^{1/2} \leq 1 + \frac{\langle |\mathbf{v}|^2 \rangle^{1/2}}{2} \\ &\leq 1 + \frac{\langle |\nabla \mathbf{v}|^2 \rangle^{1/2}}{2\pi} = 1 + \frac{\text{Pe}}{2\pi}, \end{aligned} \quad (145)$$

where as before, the Cauchy–Schwarz inequality and maximum principle have been used in the first line. The Poincaré inequality is applied to get the first term on the second line, and (142) is used to get the final result. This upper bound, is too high, and a full analysis of (140)–(144) is needed to obtain a better estimate. As the analysis is very similar to the first problem, many details are omitted for brevity.

3.1 Variational Formulation for Steady Flows

The variational formulation of the second problem involves maximizing equation (16) given constraints (140)–(142), and boundary conditions (143)–(144):

$$\mathcal{F} = \left\langle w\theta - \phi(x, z) (\mathbf{v} \cdot \nabla \theta - \Delta \theta - w) + p(x, z) (\nabla \cdot \mathbf{v}) + \frac{\mu}{2} (|\nabla \mathbf{v}|^2 - \text{Pe}^2) \right\rangle, \quad (146)$$

where again, $\phi(x, z)$, $p(x, z)$, and μ are Lagrange multipliers. The Euler-Lagrange equations are:

$$0 = \frac{\delta \mathcal{F}}{\delta \mathbf{v}} = (\theta + \phi) \hat{\mathbf{z}} + \theta \nabla \phi - \nabla p + \mu \Delta \mathbf{v}, \quad (147)$$

$$0 = \frac{\delta \mathcal{F}}{\delta \theta} = \mathbf{v} \cdot \nabla \phi + \Delta \phi + w, \quad (148)$$

$$0 = \frac{\delta \mathcal{F}}{\delta \phi} = \mathbf{v} \cdot \nabla \theta - \Delta \theta - w, \quad (149)$$

$$0 = \frac{\delta \mathcal{F}}{\delta p} = \nabla \cdot \mathbf{v} \quad (150)$$

$$0 = \frac{\partial \mathcal{F}}{\partial \mu} = \langle |\nabla \mathbf{v}|^2 \rangle - \text{Pe}^2, \quad (151)$$

where again it has been assumed that ϕ vanishes at $z = [0, 1]$. Also to eliminate the surface term $\nabla \cdot (\mathbf{v} \nabla \mathbf{v})$, we can use either the free-slip (i.e. $\partial u / \partial z = 0$) or no-slip (i.e. $u = 0$) boundary conditions at $z = [0, 1]$. Therefore the boundary conditions are the same as before, i.e.

$$w(x, 0) = w(x, 1) = 0, \quad (152)$$

$$\theta(x, 0) = \theta(x, 1) = 0, \quad (153)$$

$$\phi(x, 0) = \phi(x, 1) = 0, \quad (154)$$

in addition to one of

$$u(x, 0) = u(x, 1) = 0 \quad \text{no-slip} \quad (155)$$

$$\left. \frac{\partial u}{\partial z} \right|_{z=0} = \left. \frac{\partial u}{\partial z} \right|_{z=1} = 0 \quad \text{free-slip} \quad (156)$$

Here we only focus on the free-slip boundary condition and use (156).

Equations (147) and (149)-(150) look relatively similar to the Boussinesq equations (see e.g. [7]), although here, an extra field ϕ exists.

3.2 The Limit of Small Pe: Asymptotic Solution

In the limit of small Pe, $|\mathbf{v}| \ll 1$ and we can linearize equations (147)-(149):

$$-\mu \Delta \mathbf{v} + \nabla p = (\theta + \phi) \hat{\mathbf{z}} \quad (157)$$

$$\Delta \phi + w = 0, \quad (158)$$

$$\Delta \theta + w = 0, \quad (159)$$

$$\nabla \cdot \mathbf{v} = 0. \quad (160)$$

Subtracting (159) from (158) and using (153)-(154) gives $\theta = \phi$ in the small-Pe regime. Taking the divergence of equation (157) and following the same steps as before results in

$$-\mu \Delta \Delta w = 2 \theta_{xx}, \quad (161)$$

which along with equation (159), and boundary conditions (152)-(153) and (156) can be analytically solved to find (\mathbf{v}, θ) in the small-Pe limit.

A Fourier transform in the x direction, these equations become

$$(D_z^2 - k^2) \hat{\theta}_k(z) + \hat{w}_k(z) = 0, \quad (162)$$

$$-\mu(D_z^2 - k^2)^2 \hat{w}_k(z) + 2k^2 \hat{\theta}_k(z) = 0. \quad (163)$$

As before, the solution has the form

$$\hat{w}_k(z) = A_k \sin(m\pi z), \quad (164)$$

$$\hat{\theta}_k(z) = B_k \sin(m\pi z), \quad (165)$$

with unknown Fourier coefficients A_k and B_k . Substituting these equations into (162) and (163) gives

$$\mu = (2k^2)/(m^2\pi^2 + k^2)^3, \quad (166)$$

$$A_k = (m^2\pi^2 + k^2) B_k, \quad (167)$$

and equation (160), yields

$$\hat{u}_k(z) = i \frac{m\pi}{k} A_k \cos(m\pi z). \quad (168)$$

Using (168) and (164) in (151) results in

$$\langle |\nabla \mathbf{v}|^2 \rangle = \frac{1}{k^2} (m^2\pi^2 + k^2)^2 A_k^2 = \text{Pe}^2 \Rightarrow A_k = \frac{k}{(m^2\pi^2 + k^2)} \text{Pe}, \quad (169)$$

which combined with (167) yields

$$B_k = \frac{k}{(m^2\pi^2 + k^2)^2} \text{Pe}. \quad (170)$$

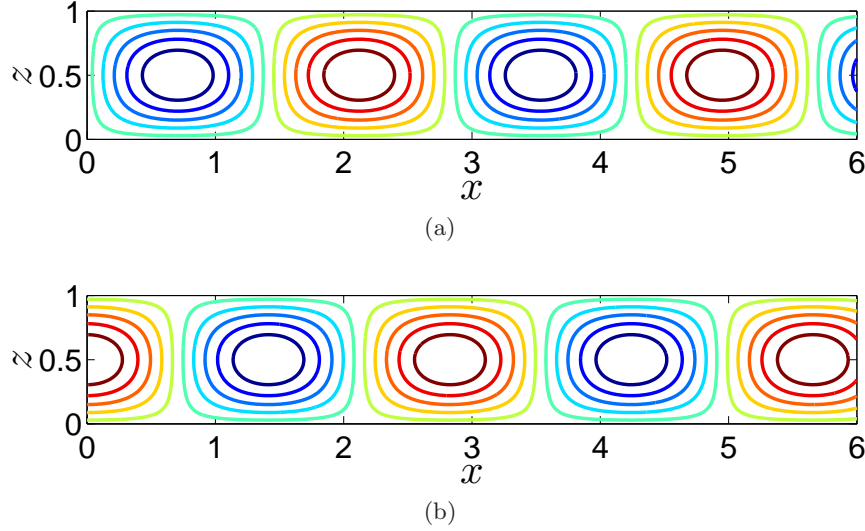


Figure 13: Optimal flow field in the small Pe limit for the fixed enstrophy problem with free-slip boundaries (a) streamlines ψ , (b) temperature θ .

Knowing A_k and B_k , Nu is obtained from (16):

$$Nu = 1 + A_k B_k = 1 + \frac{k^2}{(m^2 \pi^2 + k^2)^3} Pe^2, \quad (171)$$

which for a given $(Pe, \Gamma = \pi/k)$, is maximized at $m = 1$. As a result, using the notation defined in section 1.2:

$$Nu_{\max}(Pe, \Gamma) = 1 + \frac{\Gamma^4}{\pi^4(\Gamma^2 + 1)^3} Pe^2. \quad (172)$$

The largest value of $Nu_{\max}(Pe, \Gamma)$, i.e. Nu_{MAX} , is achieved at $\Gamma_{\text{opt}} = \sqrt{2}$:

$$Nu_{\text{MAX}}(Pe) = 1 + \frac{Pe^2}{(27\pi^4/4)}. \quad (173)$$

In the limit of small Pe , the maximum transport is achieved via an array of cells with aspect ratio $\Gamma_{\text{opt}} = \sqrt{2}$ (Figure 13). This flow field (equations (164)–(165) and (168)), and the cells of the aspect ratio of $\sqrt{2}$, closely resemble those of the Rayleigh-Bénard convection (with free-slip boundary conditions) at the onset of linear instability (see e.g. [7]). The factor $27\pi^4/4$ in (173) is in fact the critical Ra of the instability.

3.3 Small to Large Pe : Numerical Simulation

Following the same steps as before, and using $\omega = \Delta\psi$, equations (147)–(150) simplify to

$$J(\theta, \phi) - \mu \Delta\omega + (\theta + \phi)_x = 0, \quad (174)$$

$$\Delta\psi - \omega = 0, \quad (175)$$

$$-J(\psi, \theta) - \Delta\theta + \psi_x = 0, \quad (176)$$

$$-J(\psi, \phi) + \Delta\phi - \psi_x = 0, \quad (177)$$

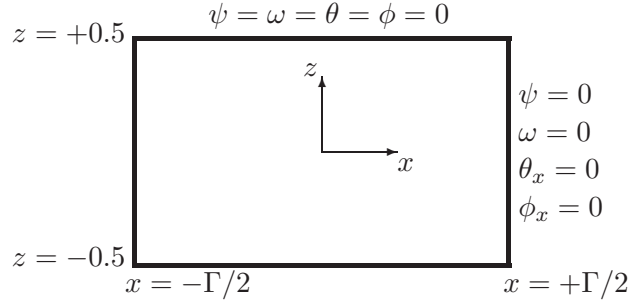


Figure 14: The fixed enstrophy problem: the geometry and boundary conditions of the computational domain which is a single 2D convection cell. Boundary conditions on the bottom (left) boundary are the same as top (right) boundary.

and boundary conditions (152)-(154) and (156) become

$$\psi(x, 0) = \psi(x, 1) = 0, \quad (178)$$

$$\omega(x, 0) = \omega(x, 1) = 0, \quad (179)$$

$$\theta(x, 0) = \theta(x, 1) = 0, \quad (180)$$

$$\phi(x, 0) = \phi(x, 1) = 0, \quad (181)$$

where ω has been introduced to avoid the occurrence fourth order derivatives and to simplify the implementation of boundary conditions.

Using the same continuation algorithm as given in section 2.3.1, and following the same steps as section 2.3.2 and appendix A, equations (174)-(177) become

$$\begin{aligned} & \begin{bmatrix} \mu\Delta & -I & O \\ O & \mu\Delta & -(I + \phi_z^N)D_x + \phi_x^N D_z \\ -(I - \theta_z^N)D_x - \theta_x^N D_z & O & \Delta - \psi_z^N D_x + \psi_x^N D_z \\ -(I + \phi_z^N)D_x + \phi_x^N D_z & O & O \end{bmatrix} \begin{bmatrix} O & -(I - \theta_z^N)D_x - \theta_x^N D_z \\ O & \Delta + \psi_z^N D_x - \psi_x^N D_z \end{bmatrix} \begin{bmatrix} \delta\psi \\ \delta\omega \\ \delta\theta \\ \delta\phi \end{bmatrix} \\ &= \begin{bmatrix} -\Delta\psi^N + \omega^N \\ -\mu\Delta\omega^N + (I + \phi_z^N)\theta_x^N + (I - \theta_z^N)\phi_x^N \\ -\Delta\theta^N + (I - \theta_z^N)\psi_x^N + \psi_z^N\theta_x^N \\ -\Delta\phi^N + (I + \phi_z^N)\psi_x^N - \psi_z^N\phi_x^N \end{bmatrix} \quad (182) \end{aligned}$$

The details of the matrix algebra and boundary condition implementation are the same as before (see section 2.3.2).

3.3.1 Numerical Results

All the results presented here are obtained using $M = 61$ or 81 . As before, the iterative solution always converged in less than 6 iterations, and the converged solution satisfies the equations and boundary conditions with the relative error of 10^{-10} or smaller.

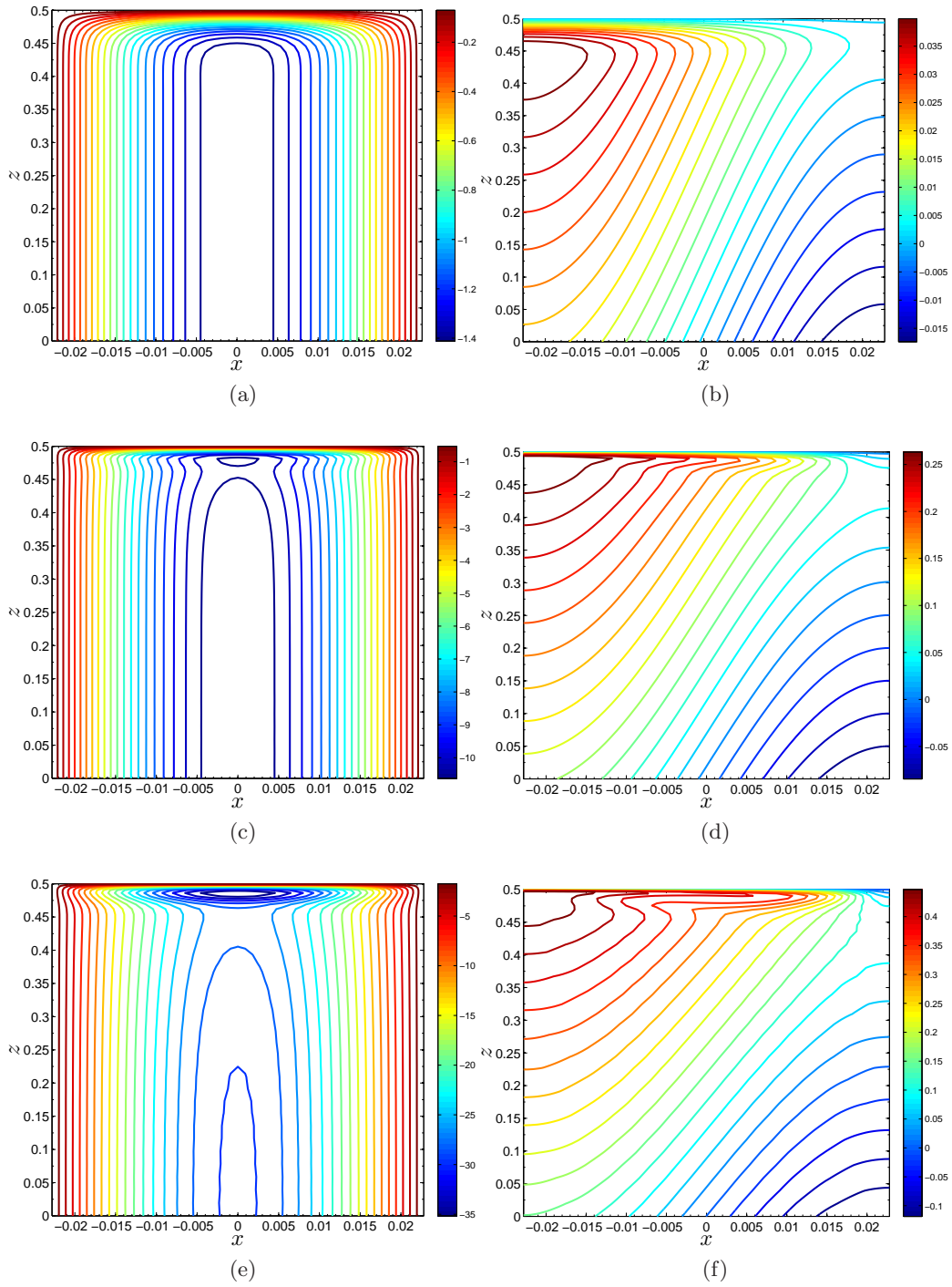


Figure 15: Evolution of the flow field with Pe for the case with $\Gamma = \sqrt{2}/\pi^3$. Panels on the left show ψ and panels on the right show θ (only the upper half of the domain is shown for better illustration of the circulation zone). (a) $Pe = 4889.1$, $Nu_{\max} = 1.98$, (b) $Pe = 3.97 \times 10^4$, $Nu_{\max} = 40.1$, (c) $Pe = 1.43 \times 10^5$, $Nu_{\max} = 175.6$. The resolution is 81^2 .

Figure 15 shows ψ and θ for the case with $\Gamma = \sqrt{2}/\pi^3$ for low to high values of Pe . Nu_{\max} increases with Pe , and the flow structure changes. The enhancement of the heat transport is associated with the development of the boundary layers: the boundary layers thin as Pe increases and result in larger Nu_{\max} . However, here we observe that for very large values of Pe , a circulation zone emerges between the boundary layers and the bulk. The circulation zone complicates the flow structure even for ξ and η . Figures 16 and 17 present $(\psi, \theta, \phi, \xi, \eta)$ for $\Gamma = \sqrt{2}/\pi^2$ and $\sqrt{2}/\pi^3$ in the limit of large Pe (the wiggles are due to the lack of numerical resolution). These results show that the optimal flow field for the fixed enstrophy problem is more complicated than the optimal flow field for the fixed energy problem, mainly due to the presence of the circulation zone. However, the bulk flows in the two problems still look rather similar: ψ and ξ are nearly independent of z and have a single mode dependence on x . η seems to be linear in z as before and nearly x -independent. Appendix C presents the interior solution for this problem:

$$\bar{\xi} = \pm \bar{\xi}_o \sin(\pi x/\Gamma), \quad (183)$$

$$\bar{\eta}_o = 2 - \left(\frac{\pi}{\Gamma}\right)^2 \sqrt{2\mu}, \quad (184)$$

$$\bar{\psi} = \frac{\pm \bar{\xi}_o}{(\pi/\Gamma)\sqrt{2\mu}} \cos(\pi x/\Gamma), \quad (185)$$

which agree with the observations of the numerical results. This solution is determined up to an unknown constant $\bar{\xi}_o$ which should be determined from the boundary layer solution. Owing to the complexity of this flow, we have not yet succeeded in solving the boundary layer equations and completing the matched asymptotic analysis.

In the absence of an analytical solution, we use the numerical results to find $\text{Nu}_{\max}(\text{Pe}, \Gamma)$ and $\text{Nu}_{\text{MAX}}(\text{Pe})$. Figure 18 shows the numerically calculated $\text{Nu}_{\max}(\text{Pe}, \Gamma)$ for several values of Γ . The first three conclusions made from the results of Figure 6 are also true for these results. However, the scalings of Nu_{\max} and Nu_{MAX} with Pe are different. For fixed Γ , we observe that

$$\text{Nu}_{\max}(\text{Pe}, \Gamma) = 1 + K(\Gamma) \text{Pe}^{1/2}, \quad (186)$$

where $K(\Gamma)$ is a prefactor that can be determined from the numerical results. A fit to the envelope made by the largest values of Nu_{\max} gives

$$\text{Nu}_{\text{MAX}}(\text{Pe}) = 1 + 0.2175 \text{Pe}^{10/17}. \quad (187)$$

The exponent we originally found by eyeballing was 0.58. However, the scaling of Nu with Ra reported by other investigators for Rayleigh–Bénard convection with stress-free boundaries (see Table 2) gives $\text{Nu} \sim \text{Ra}^{5/12}$. Interpreting their results in term of Pe (using (192) gives $\text{Nu} \sim \text{Pe}^{10/17=0.5882}$. This led us to believe that $\text{Pe}^{10/17}$ is the scaling in our problem as well. Also note that this scaling is only valid for moderate and large values of Pe ; in the limit of small Pe , (172) is the scaling of Nu_{MAX} . This explains the crossing of (187) and (145) in the limit of very small Pe .

To find $\Gamma_{\text{opt}}(\text{Pe})$ accurately from the numerical results, more data points in Γ (and especially for smaller Γ) are needed. However, using just three points in the wide range of $\text{Pe} = 1701 - 4.1 \times 10^4$, we obtain -0.361 and -0.358 as the exponent of Pe in the scaling of $\Gamma_{\text{opt}}(\text{Pe})$.

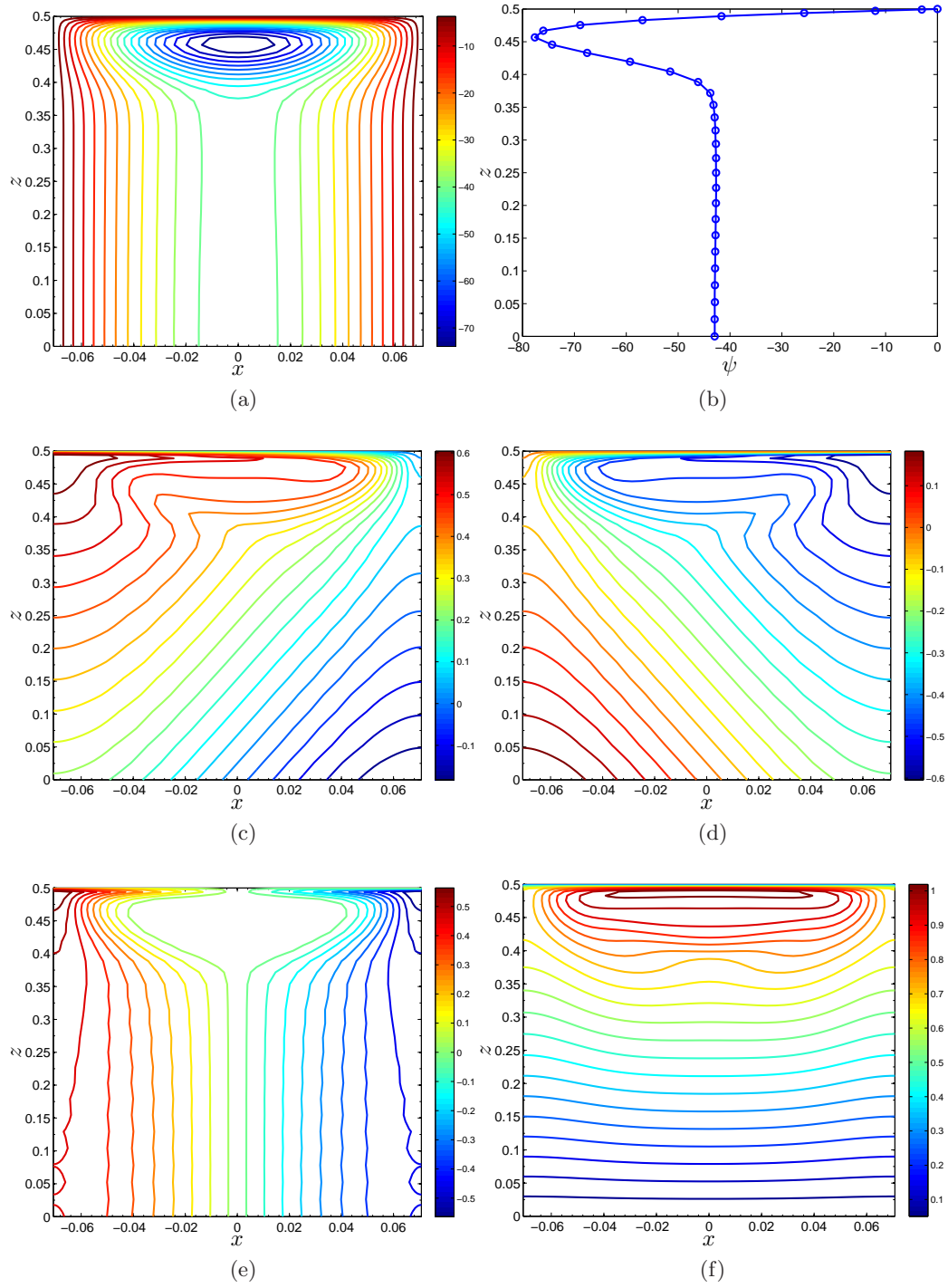


Figure 16: Flow field for $\Gamma = \sqrt{2}/\pi^2$, $\mu = 4.83 \times 10^{-8}$, $\text{Pe} = 3.57 \times 10^4$, and $\text{Nu}_{\max} = 103.3.7$. Only the upper half of the domain is shown for better illustration of the circulation zone. (a) ψ , (b) ψ along $x = 0$, (c) θ , (d) ϕ , (e) $\xi \equiv \theta + \phi$, and (f) $\eta \equiv \theta - \phi$. The resolution is 61^2 .

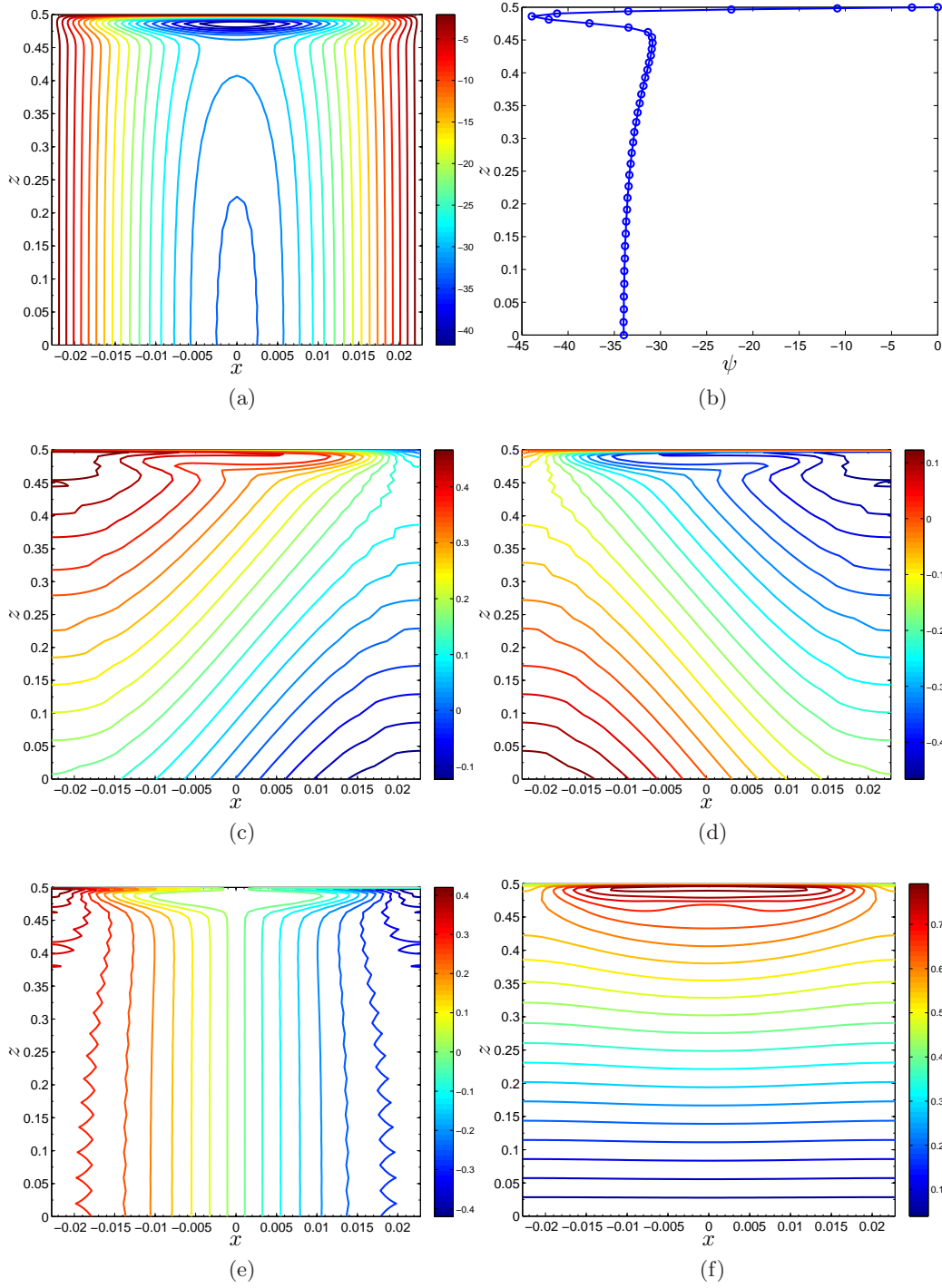


Figure 17: Flow field for $\Gamma = \sqrt{2}/\pi^3$, $\mu = 9.7 \times 10^{-9}$, $\text{Pe} = 1.2 \times 10^5$, and $\text{Nu}_{\max} = 153.1$. Only the upper half of the domain is shown for better illustration of the circulation zone. (a) ψ , (b) ψ along $x = 0$, (c) θ , (d) ϕ , (e) $\xi \equiv \theta + \phi$, and (f) $\eta \equiv \theta - \phi$. The resolution is 81^2 .

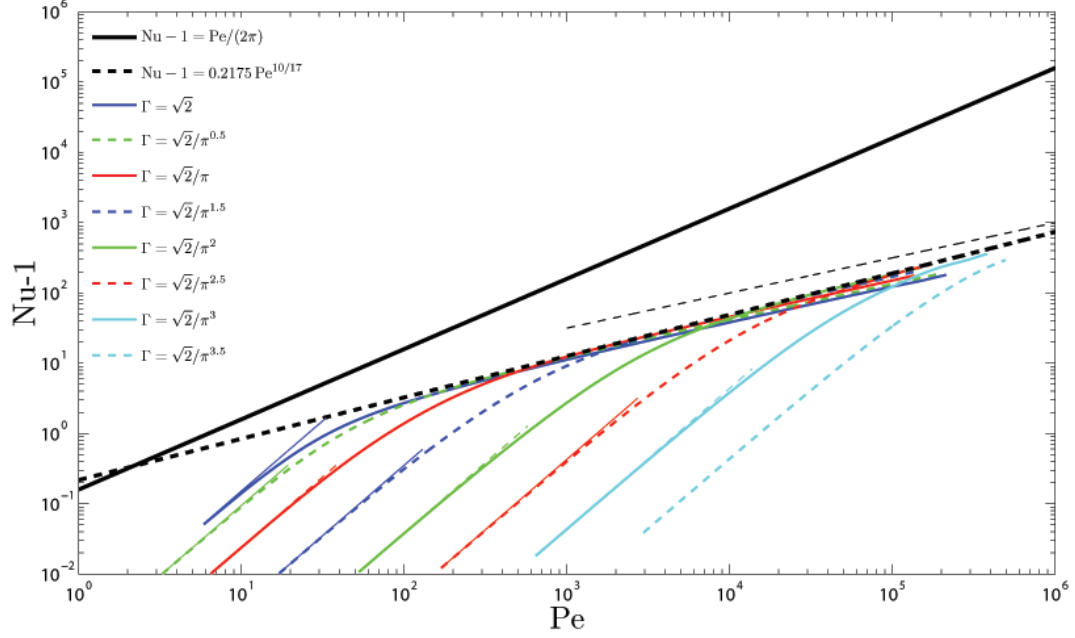


Figure 18: The non-black lines show the numerically obtained Nu_{\max} as a function of Pe for various values of Γ . For each case, the thin short line of the same color, visible for most of the cases, shows the analytical Nu_{\max} (172) in the limit of small Pe . The thick solid black line shows the absolute upper bound (145), and the thick broken black line shows a fit to the envelope (i.e. Nu_{\max}) (see equation (187)). The thin broken black line indicates the $Pe^{1/2}$ slope. All numerical results started with linear solutions with $m = 1$ and all results shown here have resolution $M = 61$. Using a higher resolution $M = 81$ results in negligible changes to the plot.

3.4 Example: Application to Rayleigh-Bénard Convection

Rayleigh-Bénard convection, i.e. convection in a layer of fluid heated from below and cooled from above, is a problem of great interest in science and engineering and has been studied extensively over the past few decades [1]. Here we show that this problem is an example of transport with fixed enstrophy. We find Nu_{max} and Nu_{MAX} as a function of the Rayleigh number Ra and compare them with the results of previous analytical and numerical analyses.

Rayleigh-Bénard convection is modeled by the Boussinesq equations [7, 20]:

$$\nabla \cdot \mathbf{v} = 0, \quad (188)$$

$$\frac{1}{\text{Pr}} (\dot{\mathbf{v}} + \mathbf{v} \cdot \nabla \mathbf{v}) = -\nabla p + \Delta \mathbf{v} + \text{Ra} T \mathbf{z}, \quad (189)$$

$$\dot{T} + \mathbf{v} \cdot \nabla T = \Delta T, \quad (190)$$

where Pr is the Prandtl number.

Multiplying (189) by \mathbf{v} and integrating over long time and over a domain with impermeable walls gives

$$0 = \langle |\nabla \mathbf{v}|^2 \rangle + \text{Ra} \langle wT \rangle, \quad (191)$$

where the left-hand side and the pressure term vanish due to the long time-space averaging. Using the definition of Pe for the fixed enstrophy problems (14) and Nu (16) from section 1.1 we obtain

$$\text{Pe}^2 = \text{Ra} (\text{Nu} - 1). \quad (192)$$

As argued before, the Nusselt number Nu , when calculated by long-time averaging, is just a function of Ra . As a result, in both steady and statistically-steady flows, equation (192) shows that Pe is fixed for a fixed value of Ra (as before Ra depends on the fluid properties and the imposed temperature difference between the walls; it does not depend on the flow). Therefore, Rayleigh-Bénard convection occurs with fixed enstrophy. Employing the analogy made before between enstrophy and viscous dissipation in (4), we can conclude that Rayleigh-Bénard convection in Newtonian fluids occurs with fixed viscous dissipation.

Employing (192), Pe can be replaced with Ra in (186) and (187):

$$\text{Nu}_{\text{max}}(\text{Ra}, \Gamma) = 1 + (K(\Gamma))^{4/3} \text{Ra}^{1/3}, \quad (193)$$

$$\text{Nu}_{\text{MAX}}(\text{Ra}) = 1 + 0.1152 \text{Ra}^{5/12}. \quad (194)$$

Also using the rather crude approximations we obtained for the exponent of Pe in $\Gamma_{\text{opt}}(\text{Pe})$,

$$\Gamma_{\text{opt}}(\text{Ra}) \sim \text{Ra}^{-0.2546}. \quad (195)$$

Curiously, $\text{Ra}^{-0.25}$ is the scaling of the smallest unstable mode for Rayleigh-Bénard convection (the same agreement was observed for porous media convection, see equation (139)).

Table 2 compares (193)–(194) with the results obtained using other methods in the literature. The classical argument of Malkus [14] and Howard [11], which is based on the marginal stability of the boundary layer, gives $\text{Nu} \sim \text{Ra}^{1/3}$ while the argument by Spiegel [17] and Kraichnan [13] gives $\text{Nu} \sim \text{Ra}^{1/2}$. These arguments are independent of the type

Table 2: Comparison of the results of the current work with the scalings for Rayleigh–Bénard convection with free-slip boundary condition obtained using various other methods.

	$\text{Nu}(\text{Ra}, \text{Pr})$	$\text{Nu}(\text{Ra}, \Gamma_{\text{fixed}})$
Classical Theories Malkus [14] & Howard [11] Spiegel [17] & Kraichnan [13]	$\sim C \text{Ra}^{1/3}$ $\sim C (\text{Pr} \text{Ra})^{1/2}$	
Upper Bounds using Background Method Ierley <i>et al.</i> [12]: Numerical with infinite Pr Otero <i>et al.</i> [15]: 2D Numerical with finite Pr Whitehead & Doering [20]: Analytical, 2D finite Pr and 3D infinite Pr)	$\leq C \text{Ra}^{5/12}$ $\leq 0.142 \text{Ra}^{5/12}$ $\leq 0.289 \text{Ra}^{5/12}$	
DNS: Unsteady Turbulent Simulations	inconclusive	
Steady Unicellular Analysis Chini & Cox [4]		$\sim C(\Gamma) \text{Ra}^{1/3}$
Current Work: Numerical	$\leq 1 + 0.115 \text{Ra}^{5/12}$	$\leq 1 + (K(\Gamma))^{4/3} \text{Ra}^{1/3}$

of boundary conditions. For free-slip boundary conditions, the background method gives $\text{Nu} \sim \text{Ra}^{5/12}$ independent of the Pr number [12, 15, 20]. DNS results of (188)–(190) for high-Ra turbulent convection with free-slip boundary conditions, conducted by several research groups, are still inconclusive.

$\text{Nu}_{\text{MAX}}(\text{Ra})$ obtained in this work has the same scaling in Ra as the upper bounds obtained using the background method. This was also the case for the fixed energy problem. For fixed Γ , Chini and Cox [4] have analyzed the steady Rayleigh–Bénard convection in one cell (in an approach very similar to the current work) and found that $\text{Nu} \sim \text{Ra}^{1/3}$, which agrees with the scaling of $\text{Nu}_{\text{max}}(\text{Ra}, \Gamma)$ with Ra obtained here. This agreement suggests that steady Rayleigh–Bénard convection transports as much as possible by a steady flow with a given amount of enstrophy, modulo a constant prefactor.

4 Concluding Remarks

How much heat can be transported by flows which have a given amount of kinetic energy or enstrophy? What the optimal velocity field look like? In this investigation, we addressed these questions for steady incompressible 2D flows. We focused on heat transport between two parallel impermeable walls. For each of the two main constraints (fixed kinetic energy and fixed enstrophy), we employed the calculus of variations to find the divergence-free velocity field that maximizes the heat transport between the walls. We solved the resulting nonlinear Euler-Lagrange equations numerically in a cell of a given aspect ratio Γ . For the problem with fixed kinetic energy, we exploited the symmetries in the flow and solved the nonlinear equations using matched asymptotic analysis as well. The analytical and numerical results agree remarkably well. The problem could be readily formulated for mass transport, or the transport of any scalar tracer.

We report our results based on Nusselt number Nu and Péclet number Pe, which

quantify the heat transport and the strength of advection, respectively. For both problems, our analysis shows that as Pe increases, the maximum possible transport Nu_{MAX} is achieved by cells of smaller aspect ratio. For the problem with fixed energy, we found that $Nu_{MAX} \sim Pe$ and $\Gamma_{opt} \sim Pe^{-0.5}$. If enstrophy is fixed, $Nu_{MAX} \sim Pe^{10/17}$ and $\Gamma_{opt} \sim Pe^{-0.36}$.

For practical purposes, we assume that the optimal velocity field can be produced by a combination of force fields, although such a flow might be linearly or nonlinearly unstable. For each of the two main constraints, we have looked into a buoyancy-driven flow which satisfies that constraint to see how the transport compares with upper bounds. For these problems we interpret the results in terms of the Ra number which is more appropriate. For convection in porous media, which occurs with fixed energy, we have found $Nu_{MAX} \sim Ra$ and $\Gamma_{opt} \sim Ra^{-0.5}$. For Rayleigh-Bénard convection, an example of fixed enstrophy transport, we found $Nu_{MAX} \sim Ra^{5/12}$ and $\Gamma_{opt} \sim Ra^{-0.25}$. Interestingly, for both problems the scalings of $\Gamma_{opt}(Ra)$ agree with the scalings of the smallest unstable mode.

The research presented in this work gives new insight into steady 2D optimal transport. There are several lines of research which should be pursued to further expand our understanding of optimal transport:

- Completing the large- Pe asymptotic solution for the fixed enstrophy problem would help in confirming and interpreting the numerical results
- Studying the fixed enstrophy problem with no-slip boundary conditions is more challenging but of great interest
- Obtaining conclusive results for the unsteady turbulent simulation and steady unicellular analysis of the Rayleigh-Bénard problem with free- and no-slip boundary conditions and for small and high values of Pr number would significantly improve our understanding of the physics of heat transport
- Investigating the transport by 3D cells, although difficult, should produce interesting results
- Finally, studying unsteady transport using optimal control is of great interest and importance and will result in much deeper insight into turbulent transport

Acknowledgments

I am deeply grateful to Charlie Doering and Greg Chini for proposing this project and for insightfully guiding me through the summer. Their devotion, patience, and support made this project a productive and enjoyable experience. I would like to express my gratitude toward the faculty, staff, and participants of the 2012 GFD program, especially George Veronis and Colm Caulfield, for the inspiring and fruitful summer. Particularly, I would like to thank all the fellows for the great time we had in Walsh Cottage, softball field, and Captain Kidd. Special thanks are extended to Duncan Hewitt for answering my questions about porous media convection, and Cédric Baume for our informative discussions about numerics. I appreciate Lindsey Corson's kind support at the beginning of the summer.

Also I would like to thank Phil Marcus for teaching me computation and analytical methods, which I used throughout this work. Furthermore, I am thankful to John Neu for his wonderful course on asymptotic analysis which I greatly benefited from during this project.

A Equations for Newton-Kantorovich Iteration Scheme

Here we present more details on how equation (67) was derived. First, we deduce from equations (53)-(55) that

$$F = \frac{1}{\mu} (-(1 + \phi_z)\theta_x + (\theta_z - 1)\phi_x), \quad (196)$$

$$G = (1 - \theta_z)\psi_x + \psi_z\theta_x, \quad (197)$$

$$Q = (1 + \phi_z)\psi_x - \psi_z\phi_x. \quad (198)$$

Calculating the Frechet derivatives, recalling the definition of $\delta(\cdot) \equiv (\cdot)^{N+1} - (\cdot)^N$, and ignoring the higher order terms, equations (64)-(66) become

$$\begin{aligned} \mu\Delta\delta\psi + (1 + \phi_z^N)\delta\theta_x - \phi_x^N\delta\theta_z + (1 - \theta_z^N)\delta\phi_x + \theta_x^N\delta\phi_z &= \\ -\mu\Delta\psi^N - [(1 + \phi_z^N)\theta_x^N + (1 - \theta_z^N)\phi_x^N] & \end{aligned} \quad (199)$$

$$\begin{aligned} \Delta\delta\theta - \psi_z^N\delta\theta_x + \psi_x^N\delta\theta_z - (1 - \theta_z^N)\delta\psi_x - \theta_x^N\delta\psi_z &= \\ -\Delta\theta^N + (1 - \theta_z^N)\psi_x^N + \psi_z^N\theta_x^N & \end{aligned} \quad (200)$$

$$\begin{aligned} \Delta\delta\phi - (1 + \phi_z^N)\delta\psi_x + \phi_x^N\delta\psi_z + \psi_z^N\delta\phi_x - \psi_x^N\delta\phi_z &= \\ -\Delta\phi^N + (1 + \phi_z^N)\psi_x^N - \psi_z^N\phi_x^N & \end{aligned} \quad (201)$$

B Limit of $\lambda \ll 1$ and $\sigma \ll 1$

To study the large Pe asymptotic solution in the case that $\sigma \ll 1$, we start from equations (96)-(98). The main difference between the current analysis and the one in section 2.4.2 is that the $(2 - \pi\sqrt{2\mu}/\Gamma)$ term is $\mathcal{O}(1/\Gamma) \gg 1$ if $\sigma \ll 1$ (as opposed to $\mathcal{O}(1)$ in section 2.4.2). Therefore, it contributes to the balancing of the leading order. Only keeping the terms which might contribute to the leading order, and rearranging a few constants, we get

$$\left[-\pi^2 A + \frac{\Gamma^2}{\delta_1^2} A'' \right] - \frac{\pi^2}{2\delta_3} C' B = 0, \quad (202)$$

$$-\frac{\mu}{\delta_3^2} C'' + \frac{\bar{\xi}_o^2}{2} \left[\frac{1}{\delta_2} AB' + \frac{1}{\delta_1} BA' \right] = 0, \quad (203)$$

$$\left[-\pi^2 B + \frac{\Gamma^2}{\delta_2^2} B'' \right] - \frac{\pi^2}{2\delta_3} C' A = 0. \quad (204)$$

The first equation shows that the same as section 2.4.2, the balance is between the A'' and $C' B$ terms and $\delta_1^2 = \Gamma^2\delta_3$. Similarly, in the third equation the balance is between B'' and $C' A$ terms and $\delta_2^2 = \Gamma^2\delta_3$, implying that $\delta_1 = \delta_2$. The balancing terms in the second equation are the same as before as well, and $\delta_3^2 = \mu\delta_1$. Combining these equalities gives

$$\delta_1 = \delta_2 = \Gamma^{4/3} \mu^{1/3}, \quad (205)$$

$$\delta_3 = \Gamma^{2/3} \mu^{2/3}. \quad (206)$$

Therefore, unlike section 2.4.2, here ψ and ξ do not have the same boundary layer thickness as η which complicates the problem as we have to deal with a nested boundary layer.

However, the $\text{Nu}_{\max}(\text{Pe})$ obtained in section 2.4.5 agrees very well with the results of the numerical simulations (see Figure 6) and shows that the optimal transport is achieved in the distinguished limit that $\sigma = \mathcal{O}(1)$. Therefore, we do not further analyze the $\sigma \ll 1$ limit.

C Interior Solution for the Fixed Enstrophy Problem

Equations (174) and (177)-(176) can be written in terms of (ψ, ξ, η)

$$-J(\xi, \eta) - 2\mu\Delta^2\psi + 2\xi_x = 0, \quad (207)$$

$$J(\psi, \xi) + \Delta\eta = 0, \quad (208)$$

$$J(\psi, \eta) + \Delta\xi - 2\psi_x = 0, \quad (209)$$

which except for $-2\mu\Delta^2$ instead of $+2\mu\Delta$ are the same as (70)-(72). However, the higher derivative is expected to result in major differences between the two problems.

The numerical results suggests

$$\psi = \bar{\psi}(x) A(x, z), \quad (210)$$

$$\xi = \bar{\xi}(x) B(x, z), \quad (211)$$

$$\eta = \bar{\eta}(z) C(x, z), \quad (212)$$

where $(\bar{\psi}, \bar{\xi}, \bar{\eta})$ constitute the outer solution.

Using $(\bar{\psi}(x), \bar{\xi}(x), \bar{\eta}(z))$ in (207)-(209) gives

$$2\mu\bar{\psi}_{xxxxx} - (2 - \bar{\eta}_z)\bar{\xi}_x = 0, \quad (213)$$

$$\bar{\eta}_{zz} = 0, \quad (214)$$

$$\bar{\xi}_{xx} - (2 - \bar{\eta}_z)\bar{\psi}_x = 0, \quad (215)$$

which again imply that

$$\bar{\eta}(z) = \bar{\eta}_o z, \quad (216)$$

where $\bar{\eta}_o$ is an unknown constant. Eliminating $\bar{\psi}$ between (213) and (215) yields

$$\bar{\xi}_{xxxxx} - \left(\frac{\bar{\eta}_o - 2}{\sqrt{2\mu}}\right)^2 \bar{\xi}_x = 0, \quad (217)$$

Given the periodicity of 2Γ in x , and $\xi_x(\pm\Gamma/2, z) = 0$, this implies

$$\bar{\xi} = \pm\bar{\xi}_o \sin(\pi x/\Gamma) \quad (218)$$

$$\bar{\eta}_o = 2 - \left(\frac{\pi}{\Gamma}\right)^2 \sqrt{2\mu}, \quad (219)$$

where $\bar{\xi}_o > 0$ is an unknown constant. Notice the difference between (219) and 85).

Equation (215) yields

$$\bar{\psi} = \frac{\pm\bar{\xi}_o}{(\pi/\Gamma)\sqrt{2\mu}} \cos(\pi x/\Gamma). \quad (220)$$

As before, the interior flow field (i.e. outer solution) is known up to an unknown constant $\bar{\xi}_o$ which shall be determined using the inner solution.

References

- [1] G. AHLERS, S. GROSSMANN, AND D. LOHSE, *Heat transfer and large scale dynamics in turbulent Rayleigh–Bénard convection*, Review of Modern Physics, 81 (2009).
- [2] G. B. ARFKEN AND H. J. WEBER, *Mathematical Methods for Physicists*, Academic Press, 6th ed., 2005.
- [3] J. P. BOYD, *Chebyshev and Fourier Spectral Methods*, Dover, 2nd ed., 2001.
- [4] G. P. CHINI AND S. M. COX, *Large Rayleigh number thermal convection: heat flux predictions and strongly nonlinear solutions*, Physics of Fluids, 21 (2009).
- [5] L. T. CORSON, *Maximizing the heat flux in steady unicellular porous media convection*, Geophysical Fluid Dynamics Program Report, Woods Hole Oceanographic Institution, (2011).
- [6] C. R. DOERING AND P. CONSTANTIN, *Bounds for heat transport in a porous layer*, Journal of Fluid Mechanics, 376 (1998).
- [7] P. G. DRAZIN AND W. H. REID, *Hydrodynamic Stability*, Cambridge University Press, 2nd ed., 2004.
- [8] A. C. FOWLER, *Mathematical Models in the Applied Sciences*, Cambridge University Press, 1st ed., 1997.
- [9] D. R. HEWITT, J. A. NEUFELD, AND J. R. LISTER, *Ultimate regime of high Rayleigh number convection in a porous medium*, Physical Review Letters, 108 (2012).
- [10] R. N. HORNE AND P. O’SULLIVAN, *Origin of oscillatory convection in a porous medium heated from below*, Physics of Fluids, 21 (1978).
- [11] L. HOWARD, *Convection at high Rayleigh numbers*, Proceedings of the 11th International Congress of Applied Mechanics, edited by H. Görtler (1964).
- [12] G. R. IERLEY, R. R. KERSWELL, AND S. C. PLASTING, *Infinite–prandtl–number convection. part 2. a singular limit of upper bound theory*, Journal of Fluid Mechanics.
- [13] R. H. KRAICHNAN, *Turbulent thermal convection at arbitrary Prandtl number*, Physics of Fluids, 5 (1962).
- [14] W. V. R. MALKUS, *The heat transport and spectrum of thermal turbulence*, Proceedings of the Royal Society of London. Series A, 225 (1954).
- [15] J. OTERO, *Bounds for the heat transport in turbulent convection*, Ph.D. Thesis, University of Michigan, 2002.
- [16] J. OTERO, L. A. DONTCHEVA, H. JOHNSTON, R. A. WORTHING, A. KURGANOV, G. PETROVA, AND C. R. DOERING, *High–Rayleigh–number convection in a fluid–saturated porous layer*, Journal of Fluid Mechanics, 500 (2004).

- [17] E. A. SPIEGEL, *Thermal turbulence at very small Prandtl number*, Journal of Geophysical Research, 67 (1962).
- [18] L. N. TREFETHEN, *Spectral Methods in MATLAB*, SIAM, 1st ed., 2001.
- [19] B. WEN, N. DIANATI, E. LUNASIN, G. P. CHINI, AND C. R. DOERING, *New upper bounds and reduced dynamical modeling for Rayleigh-Bénard convection in a fluid saturated porous layer*, Journal of Fluid Mechanics, 500 (2004).
- [20] J. P. WHITEHEAD AND C. R. DOERING, *Ultimate state of two-dimensional Rayleigh-Bénard convection between free-slip fixed-temperature boundaries*, Physical Review Letters, 106 (2011).

A reduced model for exact coherent states in high Reynolds number shear flows

Cédric Beaume

April 16, 2013

Abstract

We consider a shear flow driven in the streamwise direction by a sinusoidal body force varying in the wall normal direction and apply a lower branch scaling found by Wang *et al.* (2007) to reduce the dynamics to a set of two-dimensional PDEs valid at high Reynolds numbers. We then propose an iterative strategy to converge to lower branch exact coherent structures. This strategy only necessitates a two-dimensional projection of the streamwise velocity as initial condition and has been used to approach a stationary lower branch solution. Further strategies to find lower branch solutions are also proposed.

1 Introduction

Incompressible channel flow driven by in-plane boundary motion, referred to as plane Couette flow (figure 1), is a canonical model of a wall-bounded shear flow that is frequently used to investigate transition to turbulence. Although this flow is known to be linearly stable for all Reynolds numbers $Re = UL/\nu$, where U is the speed of the upper (or oppositely-moving lower) boundary, L is the half-channel width and ν is the kinematic viscosity [13], experiments and numerical simulations show a transition to a disordered flow state when Re exceeds a few hundred [11] (see figure 2). Theoretical progress on this transition process has been made by computing numerically exact coherent states (ECS): stationary or time-periodic solutions corresponding to fixed points in a (reduced) phase space [12, 7, 19, 4]. Analysis of a low-order model [20] and more systematic numerical studies [21, 14] reveal that these solutions seem to exist in an open interval of Reynolds number and are created through a saddle-node bifurcation. As the lower part of the branch produced by the saddle-node is not connected to the laminar solution, the mechanism underlying the existence of ECS is nonlinear. It consists in a cycle in which streamwise-invariant rolls (also called vortices) redistribute streamwise momentum by advection that leads to the creation of spanwise inhomogeneities, namely the streaks. The streaks then create wave-like structures varying in the streamwise direction that, in turn, feed the rolls to close the feedback loop. This cyclic mechanism, first articulated by Waleffe [20] is called the self-sustaining process and is illustrated in figure 3.

As the laminar profile is linearly stable at all Reynolds numbers, a finite-amplitude perturbation is necessary to trigger observable solutions such as turbulence (*cf.* diagram in figure 2). Given an appropriate spatial form for the perturbation, if the amplitude is

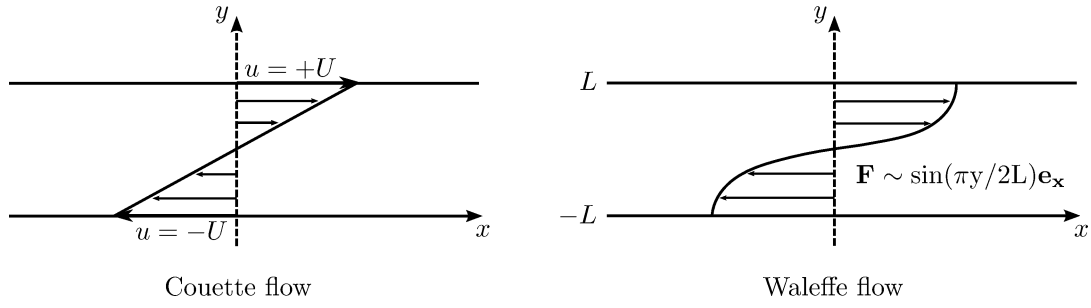


Figure 1: Sketch of plane Couette and Waleffe flows. Plane Couette flow is driven by wall motion in the x direction, the top and bottom walls moving with opposite velocities $\pm U$. Plane Waleffe flow is driven by a volume force in the x direction. The forcing is half a sine period in the y coordinate. Note that the laminar flow is stable despite the presence of an inflection point owing to the proximity of free-slip walls.

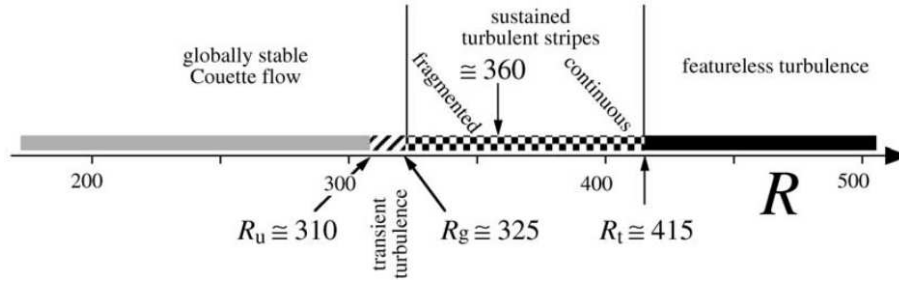


Figure 2: Behavior observed in experimental Couette flow. Once the Reynolds number (here R) is above 310, the system exhibits nonlinear dynamics. After Manneville [11].

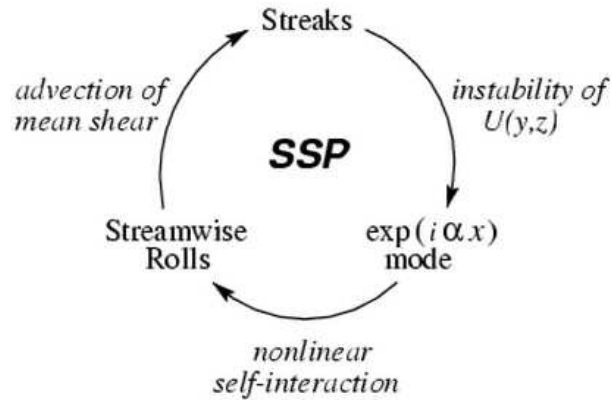


Figure 3: Self-sustaining process (SSP) sketched as a loop. After Waleffe [20].

too small, it decays. Conversely, if it is too large, the perturbation grows and a nonlinear behavior is reached. This defines a boundary between decay and growth that is called “the edge” and is populated by unstable nonlinear solutions. By studying the edge in small domains of different sizes, Schneider *et al.* [14] have obtained a family of ECS. They continued these solutions in Re to locate the saddle-nodes characteristic of these solutions and studied their stability, revealing that one of the lower branch solutions is only once unstable. It follows that lower branch ECS are likely to control some of the edge dynamics.

Wang *et al.* [21] established that lower branch solutions have an asymptotic structure as $Re \rightarrow \infty$ consisting of $\mathcal{O}(1)$ streaks and $\mathcal{O}(Re^{-1})$ rolls. They also identified that the fundamental streamwise-varying mode scales roughly as $\mathcal{O}(Re^{-1})$ and that higher harmonics are $o(Re^{-1})$. In the present study, we exploit these scalings to systematically derive a multiscale PDE model for plane parallel shear flow. The proposed reduced model appears to be conceptually simpler than a related asymptotic reduction of the Navier–Stokes equations by Hall & Sherwin [6]. Although both approaches enable the dynamics to be reduced from a 3D problem to two coupled 2D systems, the reduced formulation described here appears more straightforward. Moreover, this reduced model may be useful not only for studying large Reynolds number states, but also solutions in spatially-extended domains.

The following section introduces the new reduced model. After reviewing the asymptotic scaling observed by Wang *et al.* [21], the model is derived and interpreted. Section 3 deals with strategies for obtaining a nontrivial solution of the reduced model. In section 4, we explore the long-wavelength limit and present further reductions in this case. The last section briefly summarizes the work done and outlines work in progress.

2 Reduced model

2.1 Asymptotic law

Among the very few successful attempts to continue nonlinear solutions to relatively high Reynolds numbers (above 10^3) in plane Couette flow is a study by Wang, Gibson and Waleffe [21]. In their paper, the authors reported a computation in a box of size $2\pi \times 2 \times \pi$ where they decomposed the stationary lower branch solutions in Fourier modes in the streamwise direction,

$$\mathbf{u}(x, y, z) = \sum_{n=0}^N \mathbf{u}_n(y, z) e^{in\alpha x} + c.c., \quad (1)$$

where \mathbf{u}_n represents the n -th Fourier mode, N is the order of truncation in the expansion, α is the fundamental wavenumber in the streamwise direction and *c.c.* denotes the complex conjugate.

The result of the numerical continuation of the stationary nonlinear solution is shown in figure 4. The solution is represented by its dominant components and their amplitude is plotted as a function of the Reynolds number. The figure indicates that the amplitudes scale like powers of the Reynolds number with the higher harmonics decaying faster than the lower ones. The stationary solution of interest is represented in figure 5. It consists of streaks u_0 and streamwise rolls (v_0, w_0) representing the average behavior in the streamwise direction. In addition to these quantities, a contribution \mathbf{u}_1 that fluctuates in the streamwise direction

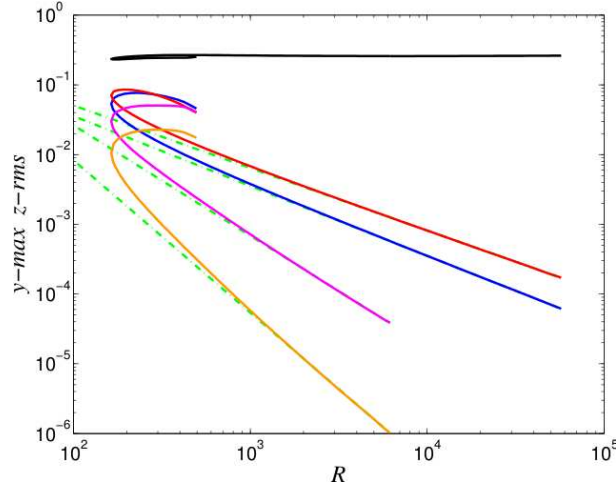


Figure 4: Results of the continuation in Reynolds number R of the stationary nonlaminar solution shown as the y -maximum of the z -root-mean-square of the leading Fourier modes. From top to bottom: the $\mathcal{O}(1)$ $n = 0$ mode u_0 (black), the $\mathcal{O}(R^{-0.9})$ fundamental mode \mathbf{u}_1 (red), the $\mathcal{O}(R^{-1})$ streamwise rolls (v_0, w_0) (blue), the $\mathcal{O}(R^{-1.6})$ second harmonics \mathbf{u}_2 (purple) and the $\mathcal{O}(R^{-2.2})$ third harmonics \mathbf{u}_3 (amber). After Wang *et al.* [21].

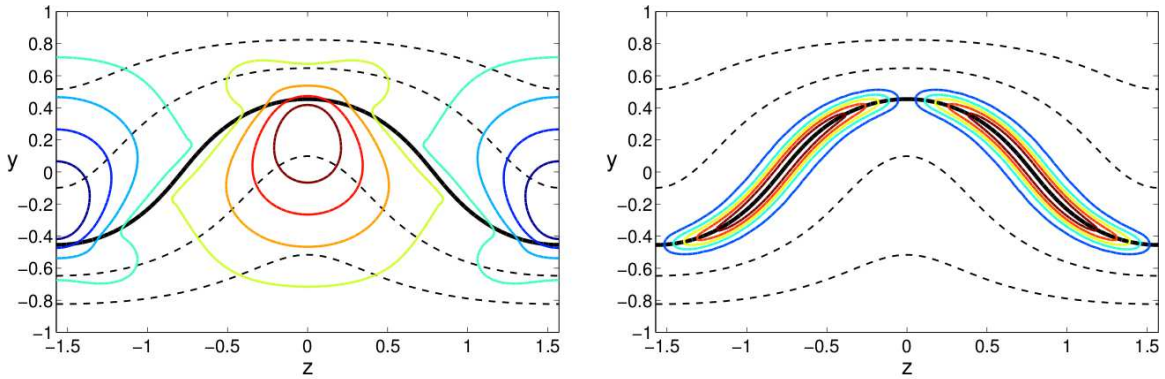


Figure 5: Representation of the solution studied by Wang *et al.* at $Re = 50171$. In both panels, the (black) open lines denotes contours of u_0 , the thick line being $u_0 = 0$. The left (right) panel represents the contours of v_0 (v_1). After Wang *et al.* [21].

is present and accumulates around $u_0 = 0$. This specifies the location of the critical layer, a strong gradient zone centered on the isosurface on which the phase speed (here 0 since the solution is stationary) matches the streamwise flow velocity. Figure 4 shows that the streaks are $\mathcal{O}(1)$ at all Reynolds numbers and that the rolls and the fundamental mode scale roughly like the inverse of the Reynolds number. Note that beyond $Re = 6168$, the second and higher harmonics have been dropped but the computation continues to be well resolved, indicating that the $n = 0$ and fundamental modes suffice to approximate the solution when the Reynolds number is large.

Consequently, the streamwise structure of this type of nonlinear solution in plane Couette flow becomes simpler and simpler when the Reynolds number is increased. However, due to gradient sharpening in the vicinity of the critical layer, the solution structure becomes more and more difficult to resolve in the y - z plane. It is therefore possible to take advantage of this emergent $1/Re$ scaling by truncating the streamwise representation of the solution to the constant and fundamental modes to derive a reduced model for lower branch ECS at high Reynolds number.

2.2 Model derivation

In this work, we do not consider plane Couette flow, but a simpler case introduced by Waleffe [20] in which the flow is driven by a streamwise body force varying sinusoidally in the wall-normal direction with free-slip boundary conditions. A sketch of this flow is also shown in figure 1. The corresponding dimensionless Navier–Stokes equation for incompressible flow is

$$\partial_t \mathbf{u} + (\mathbf{u} \cdot \nabla) \mathbf{u} = -\nabla p + \frac{1}{Re} \nabla^2 \mathbf{u} + \frac{\sqrt{2}\pi^2}{4Re} \sin(\pi y/2), \quad (2)$$

$$\nabla \cdot \mathbf{u} = 0, \quad (3)$$

where t is the time variable, $\mathbf{u} = (u, v, w)$ is the 3D velocity field with components u , v and w in the x , y and z Cartesian directions respectively, p is the pressure and $Re = UL/\nu$ is the Reynolds number where U is the root-mean-square velocity of the laminar solution ($u = \sqrt{2}\sin(\pi y/2)$, $v = w = 0$ in dimensionless form), L is half the distance between the walls and ν is the kinematic viscosity of the fluid. These equations are complemented by stress-free boundary conditions along each wall:

$$\partial_y u(y = \pm 1) = v(y = \pm 1) = \partial_y w(y = \pm 1) = 0, \quad (4)$$

as well as periodic boundary conditions in the spanwise and streamwise directions. Although inflectional, the laminar flow is stable at all Re because of wall-blocking [20]. In the following, we refer to this flow as Waleffe flow. Its advantage, compared to plane Couette flow, lies in the use of the stress-free boundary-conditions, preventing the formation of diffusive boundary layers and facilitating Fourier-type expansions in all three coordinates.

To exploit the scaling behavior discussed in section 2.1, we first introduce a reduced Reynolds number $R = \epsilon Re = \mathcal{O}(1)$. Given the small parameter ϵ , we proceed to the following asymptotic expansion:

$$u = u_0 + \epsilon u_1 + \mathcal{O}(\epsilon^2), \quad (5)$$

$$v = \epsilon v_1 + \epsilon^2 v_2 + \mathcal{O}(\epsilon^3), \quad (6)$$

$$w = \epsilon w_1 + \epsilon^2 w_2 + \mathcal{O}(\epsilon^3), \quad (7)$$

where the subscript denotes the order in the ϵ -expansion. In this new framework, the streaks are contained in the variable u_0 and the rolls *as well as* the fundamental mode in the variables u_1, v_1, w_1 as they arise at first order (for notational simplicity, the subscript has a different meaning than in the previous section and in Wang *et al.* [21]). We also introduce a long spatial scale $X = \epsilon x$ to allow for modulation in the streamwise direction together with a slow time scale $T = \epsilon t$. The variables are treated by separating the fast- (x, t) average from the fluctuations:

$$f_n = \bar{f}_n(X, y, z, T) + f'_n(x, X, y, z, t, T), \quad (8)$$

where \bar{f}_n stands for the (x, t) average of the field f_n and f'_n for its fluctuation. We then average the equations over x and t and examine the mean and fluctuation fields separately. The averaged equations read:

$$\partial_T \bar{u}_0 + \bar{u}_0 \partial_X \bar{u}_0 + \bar{v}_1 \partial_y \bar{u}_0 + \bar{w}_1 \partial_z \bar{u}_0 = \frac{1}{R} \nabla_\perp^2 \bar{u}_0 + \frac{\sqrt{2}\pi^2}{4R} \sin(\pi y/2), \quad (9)$$

$$\begin{aligned} \partial_T \bar{v}_1 + \bar{u}_0 \partial_X \bar{v}_1 + \bar{v}_1 \partial_y \bar{v}_1 + \bar{w}_1 \partial_z \bar{v}_1 + \\ \partial_y \left(\overline{v'_1 v'_1} \right) + \partial_z \left(\overline{w'_1 v'_1} \right) = -\partial_y \bar{p}_2 + \frac{1}{R} \nabla_\perp^2 \bar{v}_1, \end{aligned} \quad (10)$$

$$\begin{aligned} \partial_T \bar{w}_1 + \bar{u}_0 \partial_X \bar{w}_1 + \bar{v}_1 \partial_y \bar{w}_1 + \bar{w}_1 \partial_z \bar{w}_1 + \\ \partial_y \left(\overline{v'_1 w'_1} \right) + \partial_z \left(\overline{w'_1 w'_1} \right) = -\partial_z \bar{p}_2 + \frac{1}{R} \nabla_\perp^2 \bar{w}_1, \end{aligned} \quad (11)$$

$$\partial_X \bar{u}_0 + \partial_y \bar{v}_1 + \partial_z \bar{w}_1 = 0, \quad (12)$$

where ∇_\perp^2 is the restriction of the Laplacian operator to the y - z plane. The fluctuation equations are:

$$\partial_t u'_1 + \bar{u}_0 \partial_x u'_1 + v'_1 \partial_y \bar{u}_0 + w'_1 \partial_z \bar{u}_0 = -\partial_x p'_1, \quad (13)$$

$$\partial_t v'_1 + \bar{u}_0 \partial_x v'_1 = -\partial_y p'_1, \quad (14)$$

$$\partial_t w'_1 + \bar{u}_0 \partial_x w'_1 = -\partial_z p'_1, \quad (15)$$

$$\partial_x u'_1 + \partial_y v'_1 + \partial_z w'_1 = 0. \quad (16)$$

Equations (9) and (12)–(16) are obtained at $\mathcal{O}(\epsilon)$ while equations (10) and (11) are obtained at $\mathcal{O}(\epsilon^2)$ (at $\mathcal{O}(\epsilon)$, \bar{p}_1 must satisfy a zero-gradient condition, hence the absence of pressure term in equation (9)). Note that at leading order ($\mathcal{O}(1)$), $u'_0 = p_0 = 0$. Moreover, fluctuating terms like $v'_1 v'_1 - \overline{v'_1 v'_1}$ enter at $\mathcal{O}(\epsilon^2)$ and therefore are not present in the fluctuation equations derived at $\mathcal{O}(\epsilon)$.

Further reduction can be achieved by exploiting the simple structure in the streamwise direction noted in section 2.1. The leading order streamwise velocity is $\mathcal{O}(1)$ and independent of the fast streamwise coordinate x . In addition, the first order wall-normal and spanwise velocities involve both the zero and fundamental modes. If we further assume that the leading order streamwise velocity and the fluctuations are independent of the slow

streamwise coordinate X , we can expand as follows:

$$\bar{u}_0 \sim \bar{u}_0^0(y, z, T), \quad (17)$$

$$\bar{v}_1 \sim \bar{v}_1^0(y, z, T) + \bar{v}_1^\delta(y, z, T)e^{i\delta X} + c.c., \quad (18)$$

$$\bar{w}_1 \sim \bar{w}_1^0(y, z, T) + \bar{w}_1^\delta(y, z, T)e^{i\delta X} + c.c., \quad (19)$$

$$u'_1 \sim u'_1(y, z, t, T)e^{i\alpha x} + c.c., \quad (20)$$

$$v'_1 \sim v'_1(y, z, t, T)e^{i\alpha x} + c.c., \quad (21)$$

$$w'_1 \sim w'_1(y, z, t, T)e^{i\alpha x} + c.c., \quad (22)$$

where $\delta = \mathcal{O}(1)$ is the wavenumber in the long ($\mathcal{O}(\epsilon^{-1})$) streamwise scale, α is the wavenumber in the short ($\mathcal{O}(1)$) streamwise scale. The streamwise independent variables are noted with a 0 superscript, those varying on the long streamwise scale with a δ superscript and the fluctuations with a prime. As $\bar{u}_0 = \bar{u}_0^0(y, z, t, T) \neq f(X)$, the mean incompressibility condition (equation (12)) yields the following constraints:

$$\partial_y \bar{v}_1^0 + \partial_z \bar{w}_1^0 = 0, \quad (23)$$

$$\partial_y \bar{v}_1^\delta + \partial_z \bar{w}_1^\delta = 0. \quad (24)$$

This reduction enables us to introduce a streamfunction-vorticity formulation:

$$\bar{v}_1^0 = -\partial_z \bar{\psi}_1^0, \quad \bar{w}_1^0 = \partial_y \bar{\psi}_1^0, \quad \bar{\omega}_1^0 = \nabla_\perp^2 \bar{\psi}_1^0, \quad (25)$$

$$\bar{v}_1^\delta = -\partial_z \bar{\psi}_1^\delta, \quad \bar{w}_1^\delta = \partial_y \bar{\psi}_1^\delta, \quad \bar{\omega}_1^\delta = \nabla_\perp^2 \bar{\psi}_1^\delta. \quad (26)$$

Here, $\bar{\psi}_1^0$ ($\bar{\psi}_1^\delta$) stands for the streamfunction for the velocities with a 0 (δ) superscript and $\bar{\omega}_1^0$ ($\bar{\omega}_1^\delta$) is the associated vorticity in the y - z plane. Given these further simplifications, the system (9)–(16) can be rewritten:

$$\partial_T \bar{u}^0 + \partial_y \bar{\psi}_1^0 \partial_z \bar{u}^0 - \partial_z \bar{\psi}_1^0 \partial_y \bar{u}^0 = \frac{1}{R} \nabla_\perp^2 \bar{u}^0 + \frac{\sqrt{2}\pi^2}{4R} \sin(\pi y/2), \quad (27)$$

$$\begin{aligned} \partial_T \bar{\omega}_1^0 + J(\bar{\psi}_1^0, \bar{\omega}_1^0) + 2\mathcal{R} \left[J(\bar{\psi}_1^{\delta*}, \bar{\omega}_1^\delta) \right] + \\ 2(\partial_y^2 - \partial_z^2) \overline{\mathcal{R}(v'_1 w'^{*}_1)} + 2\partial_z \partial_y \left(\overline{w'_1 w'^{*}_1} - \overline{v'_1 v'^{*}_1} \right) = \frac{1}{R} \nabla_\perp^2 \bar{\omega}_1^0, \end{aligned} \quad (28)$$

$$\begin{aligned} \partial_T \bar{\omega}_1^\delta + i\delta \left[\bar{u}^0 \bar{\omega}_1^\delta + \partial_y \bar{u}^0 \partial_y \bar{\psi}_1^\delta + \partial_z \bar{u}^0 \partial_z \bar{\psi}_1^\delta \right] + \\ J(\bar{\psi}_1^0, \bar{\omega}_1^\delta) + J(\bar{\psi}_1^\delta, \bar{\omega}_1^0) = \frac{1}{R} \nabla_\perp^2 \bar{\omega}_1^\delta, \end{aligned} \quad (29)$$

where $J(f, g) = \partial_y f \partial_z g - \partial_z f \partial_y g$ is the Jacobian of the functions f and g , $\mathcal{R}(f)$ is the real part of the function f and the superscript $*$ indicates the complex conjugate. These equations are to be solved together with the fluctuation equations:

$$\partial_t u'_1 + i\alpha \bar{u}^0 u'_1 + v'_1 \partial_y \bar{u}^0 + w'_1 \partial_z \bar{u}^0 = -i\alpha p'_1 + \frac{\epsilon}{R} \nabla_\perp^2 u'_1, \quad (30)$$

$$\partial_t v'_1 + i\alpha \bar{u}^0 v'_1 = -\partial_y p'_1 + \frac{\epsilon}{R} \nabla_\perp^2 v'_1, \quad (31)$$

$$\partial_t w'_1 + i\alpha \bar{u}^0 w'_1 = -\partial_z p'_1 + \frac{\epsilon}{R} \nabla_\perp^2 w'_1, \quad (32)$$

$$i\alpha u'_1 + \partial_y v'_1 + \partial_z w'_1 = 0, \quad (33)$$

where the streamfunctions are determined from equations (25) and (26). In writing the fluctuation system (30)–(33), the higher order diffusion term has been retained in order to regularize the equations, hence their occurrence with an ϵ prefactor.

2.3 Discussion

A classic picture of linearly stable shear flow dynamics is the presence of three unconnected families of solutions:

- the laminar solution: here, $\bar{u}^0 = \sqrt{2}\sin(\pi y/2)$ with the other variables vanishing
- turbulent trajectories: strongly nonlinear solutions with nontrivial time behavior
- intermediate states that include the lower branch states: stationary or periodic solutions in time corresponding to fixed points in a (reduced) phase space

The model derived in section 2.2 is intended to capture lower branch ECS as well as similar states exhibiting amplitude modulation in the streamwise direction. The use of an asymptotic expansion in our derivation can be interpreted as a zoom in a particular regime in which at least one lower branch solution is present. Only solutions in this scaling regime can be captured and we anticipate the reduced model to preclude turbulent states as well as some of the fixed points.

In the usual derivation of equations for mean quantities from the Navier–Stokes equations, one ends up with products of fluctuations, namely the Reynolds stresses. The primary challenge is then to find a closure for these Reynolds stresses [18]. In the present case, the use of multiscale analysis not only allows us to study streamwise modulation but also to obtain a natural closure using the time-dependent fluctuation equations (30)–(33).

The model (27)–(33) contains the essential ingredient for the existence of nontrivial solutions: the self-sustaining process [20]. For short to moderate streamwise domains ($\bar{\omega}_1^\delta = 0$), this process is as follows:

- streamwise rolls $\bar{\omega}_1^0$ redistribute the streamwise momentum \bar{u}^0 by advection to create spanwise inhomogeneities
- spatial inhomogeneities of \bar{u}^0 generate a wave-like instability in the streamwise direction by feeding the fluctuations (u'_1, v'_1, w'_1)
- the fluctuations, through the Reynolds stresses in equation (28), reenergize the rolls $\bar{\omega}_1^0$

This cycle explains why solutions other than the base flow can persist in plane Waleffe flow and be captured in our model.

Finally note that the time separation between the mean variables evolving slowly as $T = \epsilon t$ and the fluctuations evolving on the rapid time scale t leads to the quasi-linearity of the fluctuation equations (30)–(33). Indeed, the pseudo-nonlinear terms in these equations always involve a product between one fluctuation and \bar{u}^0 . While the former variable evolves rapidly, the latter evolves far more slowly, making \bar{u}^0 roughly a constant during time scales on which the fluctuations evolve. Although this quasi-linearity can enable analytical progress, it also causes the amplitude of the fluctuations to be indeterminate. This characteristic is common in models derived using multiscale analysis and has previously been observed in multiscale models for the tropics [10] as well as the description of the interaction on time disparate scales of ocean dynamics [5] and of atmospheric flows [8]. To deal with this pathology, one needs to adapt the technique, as described in the next section.

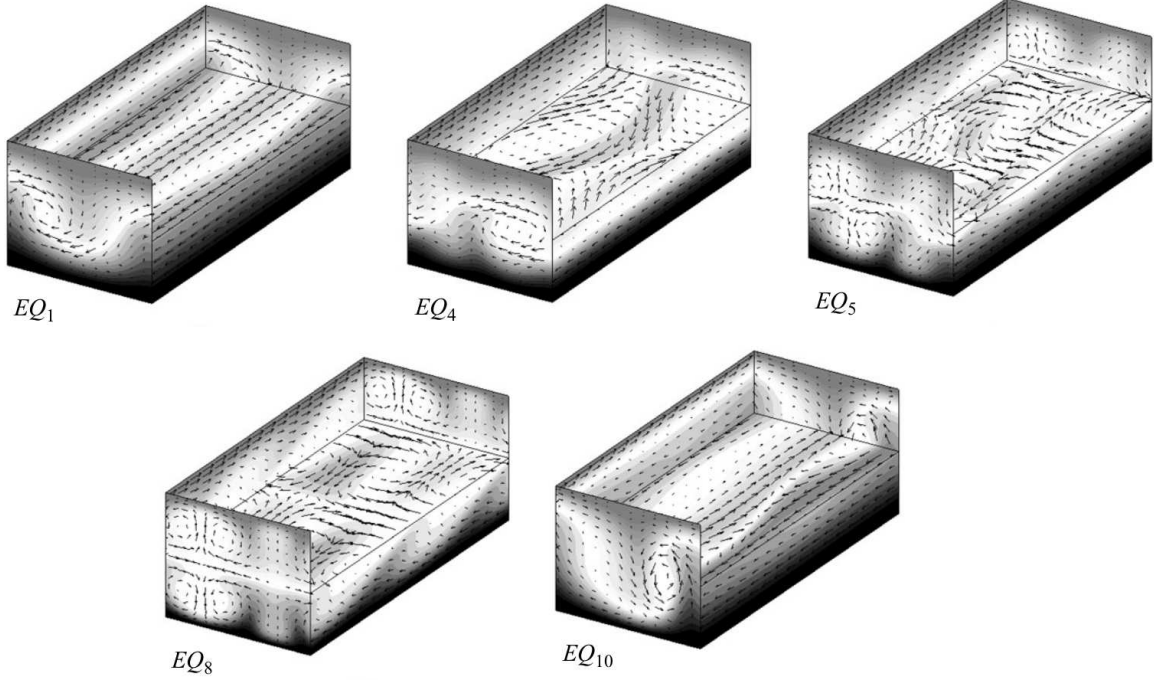


Figure 6: Equilibrium solutions of plane Couette flow in a $2\pi/1.14 \times 2 \times 2\pi/2.5$ domain at $Re = 400$. The greyscale indicates the streamwise velocity of the fluid: light (dark) grey shows fluid moving at $u = +1$ ($u = -1$). Arrows indicate in-plane velocity. The top half of the fluid is cut away to show the (u, w) velocity in the $y = 0$ midplane. Note that solution EQ_1 is a lower branch Nagata solution. After Gibson *et al.* [4].

3 Computing a lower branch exact coherent structure

We look for solutions of the same type as those computed by Gibson *et al.* [4] and shown in figure 6. As for most of those presented in the literature [21, 14, 3], these solutions have been computed in a small ($\mathcal{O}(1)$ aspect-ratio) domain. As a natural first step, we similarly restrict our search to solutions with no long-scale dynamics, for which $\overline{\psi}_1^\delta = 0$ ($\overline{\omega}_1^\delta = 0$).

By taking the divergence of the fluctuation equations (30)–(32) and applying the incompressibility condition (33), we find an equation for the pressure that does not involve u'_1 :

$$(\alpha^2 - \nabla_\perp^2)p'_1 = 2i\alpha(v'_1\partial_y\overline{u}^0 + w'_1\partial_z\overline{u}^0). \quad (34)$$

Neither equation (34) nor equations (31) and (32) for v'_1 , w'_1 involve u'_1 . As this fluctuation field is not needed to compute the Reynolds stresses in equations (28) and (29), equation

(30) does not need to be solved. Hence, the “maximally simplified” reduced model is:

$$\epsilon \partial_t \bar{u}^0 + \partial_y \bar{\psi}_1^0 \partial_z \bar{u}^0 - \partial_z \bar{\psi}_1^0 \partial_y \bar{u}^0 = \frac{1}{R} \nabla_\perp^2 \bar{u}^0 + \frac{\sqrt{2}\pi^2}{4R} \sin(\pi y/2), \quad (35)$$

$$\epsilon \partial_t \bar{\omega}_1^0 + J(\bar{\psi}_1^0, \bar{\omega}_1^0) + 2(\partial_y^2 - \partial_z^2) \overline{\mathcal{R}(v'_1 w_1'^*)} + 2\partial_z \partial_y (\overline{w'_1 w_1'^*} - \overline{v'_1 v_1'^*}) = \frac{1}{R} \nabla_\perp^2 \bar{\omega}_1^0, \quad (36)$$

$$(\alpha^2 - \nabla_\perp^2) p'_1 = 2i\alpha(v'_1 \partial_y \bar{u}^0 + w'_1 \partial_z \bar{u}^0), \quad (37)$$

$$\partial_t v'_1 + i\alpha \bar{u}^0 v'_1 = -\partial_y p'_1 + \frac{\epsilon}{R} \nabla_\perp^2 v'_1, \quad (38)$$

$$\partial_t w'_1 + i\alpha \bar{u}^0 w'_1 = -\partial_z p'_1 + \frac{\epsilon}{R} \nabla_\perp^2 w'_1, \quad (39)$$

where we have replaced T by the non-asymptotic form t/ϵ to have a single time variable.

We proceed by choosing $Re = 400$ ($\epsilon = 1/400$ and $R = 1$), the streamwise wavenumber $\alpha = 0.5$, and the spanwise extent of the domain to be π . The domain is discretized using an equispaced mesh in both the wall-normal y and the spanwise z coordinates. We used 64 points in both directions which proved sufficient for convergence when compared with a 96-point mesh. The equations are treated in spectral space, using the Fast Fourier transform in the periodic direction z and the Fast Cosine Transform-I or Fast Sine Transform-I in the y direction, depending on the boundary conditions [2]. The nonlinear products are computed in physical space, and a classic 2/3 dealiasing rule is applied before each nonlinear computation to prevent frequency folding. Spatial derivatives are computed in spectral space. Derivatives in z are computed by a multiplication of the spectral coefficients by ik where k is the wavenumber corresponding to the spectral coefficient. Derivatives in y are treated similarly, bearing in mind that differentiating a field expanded in sine functions yields cosine coefficients and *vice versa*.

3.1 Iterative algorithm

The solutions we seek to compute are unstable and cannot be reached via time-integrating the reduced equations. As shown in figures 5 and 6, they also have a non-trivial spatial structure and the absence of a very precise initial condition prevents the successful use of a fixed point method. Finally, these solutions do not bifurcate from the laminar base state, so continuation from that state is not useful. Fortunately, we can exploit the mathematical structure of the simplified reduced model (35)–(39). The mean variables \bar{u}^0 and $\bar{\omega}_1^0$ and the fluctuations p'_1 , v'_1 and w'_1 evolve over different time scales. By separating the fast fluctuation system (37)–(39) from the slow averaged one, the former becomes linear as the mean quantities do not evolve over the fast time scale. The advantage of this decoupling is that, owing to the linearity of equations (37)–(39), the fluctuations can be thought of as solutions of an eigenvalue problem with a temporal growth rate λ . The crucial observation is that if an eigenvector has a vanishing real growth rate, it is a stationary solution of equations (37)–(39). Of course, the amplitude of the fluctuations is then indeterminate and must be formally introduced as a new scalar unknown A . For such fluctuations and given A , if the mean fields \bar{u}^0 and $\bar{\omega}_1^0$ are stationary, then we have a stationary solution.

To apply this decoupling algorithm we proceed as follows:

- Choose a fluctuation amplitude A
- While the growth rate λ is not converged:

- Compute the fastest non-oscillatory growing (or most slowly decaying) fluctuation mode and its real growth rate λ using equations (37)–(39)
 - Compute the Reynolds stresses using A and the fluctuation fields so obtained
 - Time-advance \bar{u}^0 and $\bar{\omega}_1^0$ to steady state using equations (35) and (36)
- Store the converged λ and adjust A to drive λ to zero

Thus, given an initial condition for \bar{u}^0 , this algorithm requires iteration on the amplitude A . We describe the method to obtain the initial condition for \bar{u}^0 below. Solution of the fluctuation eigenvalue problem is performed using an Arnoldi iteration [9]. This computation is equivalent to finding the stability of \bar{u}^0 with respect to perturbations varying sinusoidally in the streamwise direction. In this sense, one wants to focus on the least unstable, hence more realizable and dynamically influential solutions. This is achieved by picking the fastest growing (or most slowly decaying) mode. Moreover, we choose to isolate non-oscillatory modes ($\mathcal{I}(\lambda) = 0$) to compute stationary ECS. It should be possible to find a traveling-wave ECS by choosing an oscillatory mode ($\mathcal{I}(\lambda) \neq 0$). Finally, time integration of equations (35) and (36) is carried out using a semi-implicit third order Runge–Kutta scheme [17].

3.2 Results

3.2.1 Initial condition

We describe here how we obtained an initial condition for the algorithm described in the previous section. We remind the reader that we do not need a full initial condition as only \bar{u}^0 is required to initiate the calculation of the fluctuations. We generate a physically reasonable initial profile for \bar{u}^0 by imposing faux rolls $\bar{\psi}_1^0$ and then solving for \bar{u}^0 from (35) with $\bar{\psi}_1^0$ frozen. We choose a simple shape for the rolls: $\bar{\psi}_1^0(y, z) = \Psi \sin(2z) \cos(\pi y/2)$, with Ψ an arbitrary amplitude to be tuned to get the desired initial condition. Figure 7 depicts a family of initial conditions parametrized by Ψ . In this way, we have generated a whole family of initial conditions having the characteristic u-shape of the desired ECS. Given these results, we choose to use the profile obtained for $\Psi = -20$ (figure 7(b), top right).

3.2.2 Algorithm behavior

We executed the algorithm for different values of the fluctuation amplitude A and summarize the results of the iterations in figure 8. The convergence of the leading real eigenvalue λ_{max} is monitored which allows us to identify two different regimes. For small amplitudes (figure 8(a)), the algorithm converges but λ_{max} is not necessarily 0. Figure 9 shows \bar{u}^0 at convergence for $A = 5$ to $A = 6.8$. These converged iterations indicate that for small fluctuation amplitudes, the streamwise velocity \bar{u}^0 relaxes to reach a converged state that is close to the laminar state (figure 9(a)). When the amplitude is large enough, the algorithm converges to a \bar{u}^0 that now has a pronounced u-shape (figure 9(b) and (c)). By comparing converged iterates for $A = 6.6$ and $A = 6.8$, it is evident that the increase in the fluctuation amplitude leads to a stretching of the $\bar{u}^0 = 0$ line.

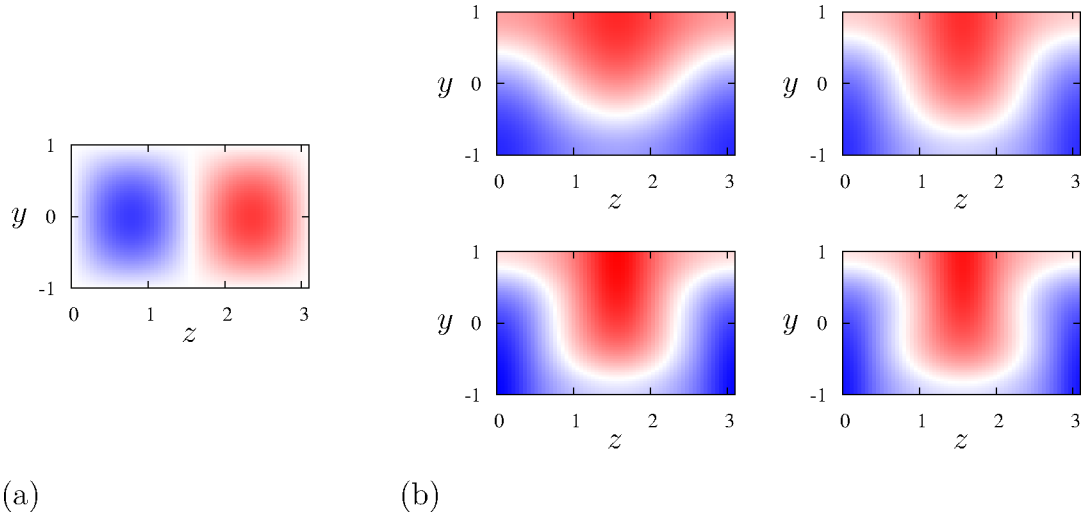


Figure 7: (a) Faux rolls $\bar{\psi}_1^0(y, z) = \Psi \sin(2z) \cos(\pi y/2)$ used to create the initial guess for \bar{u}^0 in (b). Different streak profiles are plotted in (b) corresponding to different values of Ψ , from $\Psi = -10$ (top left) to $\Psi = -40$ (bottom right) with an increment of -10 . Red indicates positive velocity, blue indicated negative velocity and white $\bar{u}^0 = 0$. The initial condition used in the following is the solution plotted in the top right panel, corresponding to $\Psi = -20$.

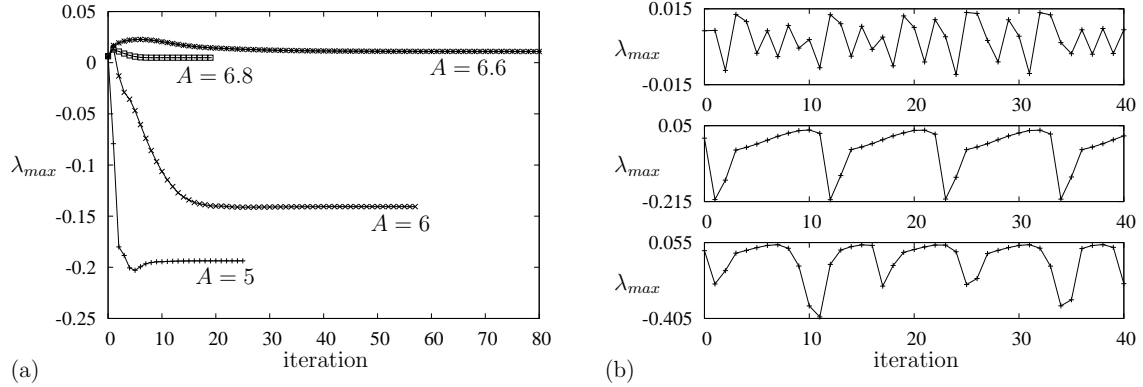


Figure 8: (a) Plot of the leading real eigenvalue λ_{max} as a function of the iteration number for different fluctuation amplitudes. The algorithm is stopped when λ_{max} is converged to the sixth digit: $\lambda_{max} = -0.19366$ for $A = 5$, $\lambda_{max} = -0.14064$ for $A = 6$, $\lambda_{max} = 0.01099$ for $A = 6.6$, $\lambda_{max} = 0.00489$ for $A = 6.8$. (b) From top to bottom, the leading real eigenvalue is shown as a function of iteration number for $A = 7$, $A = 7.5$ and $A = 8$.

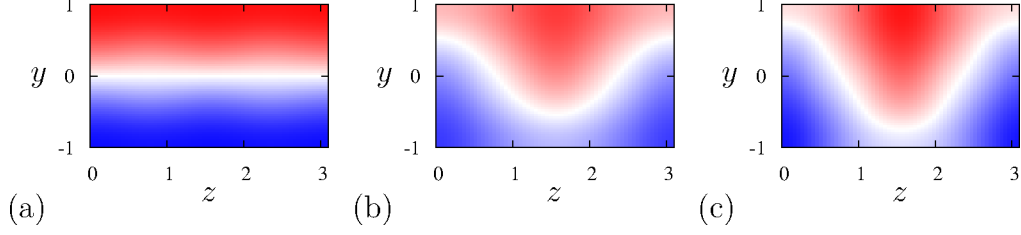


Figure 9: Converged iterations represented via \bar{u}^0 for (a) $A = 5$ (a similar solution is obtained for $A = 6$), (b) $A = 6.6$ and (c) $A = 6.8$. The color code is the same as in figure 7.

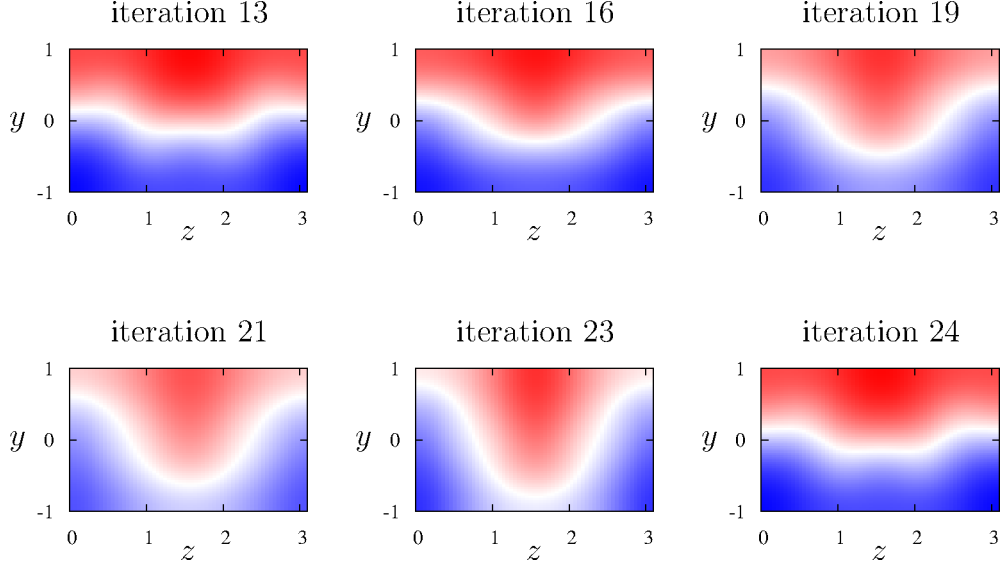


Figure 10: Streamwise mean velocity \bar{u}^0 during iterations 13, 16, 19, 21, 23 and 24 obtained with $A = 7.5$. A global view of the behavior of the algorithm for this value of the fluctuation amplitude is available in figure 8(b) center plot. The same color code is used as in figure 7.

If the amplitude of the fluctuations is increased approximately $A = 6.8$, another regime is reached. As illustrated in figure 8(b), the iterations do not converge but instead produce oscillations around $\lambda_{max} = 0$ with large excursions to negative values. The oscillations are bounded although the interval increases as A is increased with the upper bound increasing slowly while the lower bound decreases rapidly. Some iterates computed during the simulation run with $A = 7.5$ are shown in figure 10. These iterates are taken along the second “cycle” in figure 8(b) center plot. At iteration 13, \bar{u}^0 is close to the laminar profile, with the $\bar{u}^0 = 0$ isosurface rather flat. Then, until iteration 23, the streaks build progressively owing to the forcing generated by the fluctuations. The u-shape of the $\bar{u}^0 = 0$ surface becomes more and more pronounced until, at iteration 24, \bar{u}^0 becomes remarkably similar to that at iteration 13. This cycle is repeated, although with slight “phase” changes during further iterations.

Regarding the Reynolds stresses as a forcing term, we can interpret the amplitude of the fluctuations as the (square root of the) amplitude of the forcing. When A is too

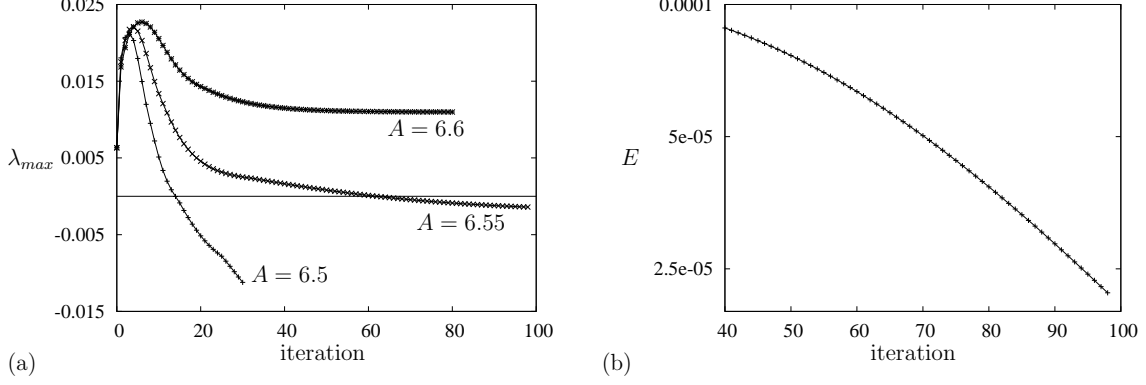


Figure 11: (a) Plot of the leading real eigenvalue λ_{max} as a function of the iteration for different amplitudes of the fluctuations. The horizontal line indicates $\lambda_{max} = 0$. Only the curve for $A = 6.6$ is stopped at convergence, that for $A = 6.5$ goes way below $\lambda_{max} = 0$ and that at $A = 6.55$ converges very slowly. (b) Evolution of the difference E between two successive iterates of λ_{max} for $A = 6.55$ on logarithmic scale.

small, the dynamics are diffusion dominated, with any initial condition relaxing to the laminar solution except for a slight perturbation that is maintained by fluctuations (that have fixed amplitude). This behavior is observed for $A \leq 6$. For sufficiently large A , the Reynolds stresses are strong enough to compete with diffusion in equation (36), and allow the fluctuations to maintain a nontrivial profile as seen for $A = 6.6$ and $A = 6.8$. Finally, if A is too large, the Reynolds stresses dominate diffusion and an oscillatory behavior sets in, as observed for $A \geq 7$ and exemplified at $A = 7.5$ in figure 10. At these large values of the fluctuation amplitude, the mean variables \bar{u}^0 and $\bar{\omega}_1^0$ over-respond to the fluctuations due to their exaggerated amplitude, and the solution oscillates around what may be the actual fixed point.

The results shown in figure 8(a) show that the converged λ_{max} first increases as A increases, eventually becoming positive. Then, at $A \approx 6.6$, λ_{max} starts decreasing before the oscillatory regime is reached. These results suggest that there is at least one value of the fluctuation amplitude A_{opt} for which $\lambda_{max} \rightarrow 0$. This amplitude lies in the range $6 < A < 6.6$ and will lead to a stationary solution of the problem (35)–(39), that is, a lower branch ECS. A second value $6.8 < A'_{opt} < 7$ may lead to a stationary solution: as A is increased above 6.6, λ_{max} decreases but is still positive for $A = 6.8$ before oscillating for $A \geq 7$. This solution, if captured by our reduced model, presumably would have the same structure and would be related to the lower branch solution found with A_{opt} .

3.2.3 Towards a solution

Given the results of the preceding section, we focus on the interval $6 < A < 6.6$. Figure 11 shows the results obtained from simulations with $A = 6.5$, $A = 6.55$ and $A = 6.6$. As in figure 8, the leading real eigenvalue converges to $\lambda_{max} = 0.01099$ for $A = 6.6$ after approximately 80 iterations. When $A = 6.5$, λ_{max} decreases quickly to converge to a negative value. This indicates that $6.5 < A_{opt} < 6.6$. A typical result for A within this interval is

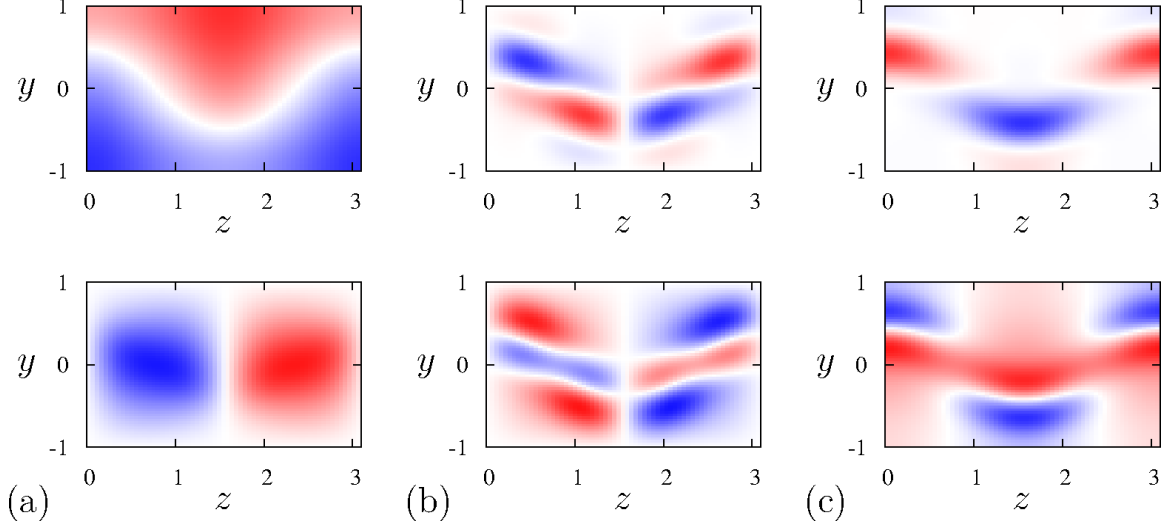


Figure 12: Flow fields at the last iteration for $A = 6.55$ (see figure 11). (a) Top: \bar{u}^0 , bottom: $\bar{\psi}_1^0$. (b) Top: $\mathcal{R}(v'_1)$, bottom: $\mathcal{I}(v'_1)$. (c) Top: $\mathcal{R}(w'_1)$, bottom: $\mathcal{I}(w'_1)$. In all cases, blue (red) represents negative (positive) values of the field.

reported in figure 11. Even after nearly 100 iterations, λ_{max} is not fully converged. The difference E between two successive iterates is plotted as a function of the iteration number in figure 11(b). The error E decreases faster than exponentially, indicating convergence is likely. However, the slope is very small and a large number of iterations is therefore required to satisfy a reasonable convergence criterion.

The converged values of λ_{max} for different A indicate that the fluctuation amplitude of the actual lower branch solution is close to 6.55. Moreover, the solutions obtained by varying A are very similar (as the reader can convince himself by comparing figures 9(b) and (c)). This suggests the state shown in figure 12, obtained at the last iteration for $A = 6.55$, is very close to the actual lower branch solution. This state is comprised of streaks \bar{u}^0 and rolls $\bar{\psi}_1^0$, with the rolls differing from the initial condition (figure 7) by a slight tilt. The fluctuations are concentrated around $\bar{u}^0 = 0$, indicating the emergence of a critical layer. This state can be used as a very good initial guess in a Newton solver to converge to the desired precision to the lower branch solution, a task we leave for future work.

4 Long-wavelength limit

It is of interest to consider the long-wavelength limit of the lower branch ECS. Indeed, Hall & Sherwin [6] have shown that the minimum drag state for lower branch ECS occurs as the fundamental streamwise wavenumber α of the fluctuation fields tends to zero. Here, we show that a further reduction of our asymptotically reduced model of plane Waleffe flow can be obtained in the limit $Re \rightarrow \infty$ and $\alpha \rightarrow 0$ with $\hat{R} \equiv \alpha Re \gg 1$. In this limit, the single streamwise scale $\chi \equiv \alpha x$ replaces the fast x scale and the modulation scale $X \equiv \epsilon x$, where, again, $\epsilon = \mathcal{O}(1/Re)$ is indicative of the amplitude of both the roll and streamwise-varying

(*i.e.* fluctuation) components of the lower-branch ECS. Two time scales are required, with the fluctuation dynamics occurring on the scale $\tau \equiv \alpha t$ and the mean fields evolving more slowly, on the scale $T \equiv \epsilon t$. It should be emphasized at the outset that the distinguished limit in which $\alpha \rightarrow 0$ with $\alpha = \mathcal{O}(1/Re)$ requires a rather different analysis in which: (i) the fluctuation dynamics are, at leading order, modified by viscous effects across the entire domain, not just within thin boundary and critical layers; and (ii) the fluctuation dynamics are fully nonlinear rather than quasi-linear, resulting in the mixing of streamwise modes. This limit, although of interest, is not pursued here.

Again motivated by the results of Wang *et al.* [21], we expand the velocity fields as

$$u \sim (\bar{u}_0 + u'_0) + \epsilon (\bar{u}_1 + u'_1) + \dots, \quad (40)$$

$$v \sim \epsilon (\bar{v}_1 + v'_1) + \epsilon^2 (\bar{v}_2 + v'_2) + \dots, \quad (41)$$

$$w \sim \epsilon (\bar{w}_1 + w'_1) + \epsilon^2 (\bar{w}_2 + w'_2) + \dots, \quad (42)$$

where generic dependent variable $f(x, y, z, t) = \bar{f}(y, z, T) + f'(\chi, y, z, \tau, T)$; that is, an overbar refers to a χ and fast time τ average and a prime to a fluctuation about that mean. Substituting into equations (2) and (3) yields $u'_0 = p_0 = p_1 = 0$ in the limit being considered. The resulting leading order mean equations can be expressed as

$$\partial_T \bar{u}_0 + J(\bar{\psi}_1, \bar{u}_0) = \frac{1}{R} \nabla_\perp^2 \bar{u}_0, \quad (43)$$

$$\partial_T \bar{\Omega}_1 + J(\bar{\psi}_1, \bar{\Omega}_1) = (\partial_z^2 - \partial_y^2) \overline{v'_1 w'_1} + \partial_z \left[\partial_y (\overline{v'_1 v'_1} - \overline{w'_1 w'_1}) \right] + \frac{1}{R} \nabla_\perp^2 \bar{\Omega}_1, \quad (44)$$

$$\nabla_\perp^2 \bar{\psi}_1 = \bar{\Omega}_1, \quad (45)$$

where $\bar{\Omega}_1 = \partial_y \bar{w}_1 - \partial_z \bar{v}_1$ is the mean vorticity with $\bar{\psi}_1$ the associated streamfunction, $R \equiv \epsilon Re = \mathcal{O}(1)$ and the Jacobian $J(a, b) \equiv \partial_y a \partial_z b - \partial_z a \partial_y b$ for fields a and b .

At $\mathcal{O}(\epsilon)$, the χ -component of the fluctuation momentum equation requires

$$J(\psi'_1, \bar{u}_0) = 0, \quad (46)$$

a key constraint that will enable significant simplifications in the following analysis. The $\mathcal{O}(\alpha\epsilon)$ y - and z - components of the fluctuation momentum equation can be combined into a single equation for the χ -component of the fluctuation vorticity:

$$\partial_\tau \Omega'_1 + \bar{u}_0 \partial_\chi \Omega'_1 = -\partial_z \bar{u}_0 \partial_\chi (\partial_z \psi'_1) - \partial_y \bar{u}_0 \partial_\chi (\partial_y \psi'_1). \quad (47)$$

Restricting attention to equilibrium lower branch ECS, we seek single χ -mode solutions of the form

$$\psi'_1 = F(\bar{u}) \cos \chi + G(\bar{u}) \sin \chi, \quad (48)$$

$$\Omega'_1 = \Omega_c(\bar{u}) \cos \chi + \Omega_s(\bar{u}) \sin \chi, \quad (49)$$

where the subscript 0 on the leading order mean streamwise velocity component has been omitted here (and will be henceforth) for brevity of notation. The Poisson equation relating the fluctuation streamfunction and vorticity yields

$$\Omega_c = |\nabla_\perp \bar{u}|^2 F'' + (\nabla_\perp^2 \bar{u}) F', \quad (50)$$

$$\Omega_s = |\nabla_\perp \bar{u}|^2 G'' + (\nabla_\perp^2 \bar{u}) G', \quad (51)$$

where a prime on $F(\bar{u})$ or $G(\bar{u})$ denotes ordinary differentiation. Finally, substituting into equation (47) gives

$$F'' + \left[\frac{\nabla_{\perp}^2 \bar{u}}{|\nabla_{\perp} \bar{u}|^2} + \frac{1}{\bar{u}} \right] F' = 0. \quad (52)$$

An analogous relation is easily derived for $G(\bar{u})$. For equation (52) to have a solution, the term in brackets must be a function only of \bar{u} :

$$\frac{\nabla_{\perp}^2 \bar{u}}{|\nabla_{\perp} \bar{u}|^2} + \frac{1}{\bar{u}} = Q(\bar{u}). \quad (53)$$

Presuming this to be the case,

$$F'(\bar{u}) = a \exp \left[- \int_0^{\bar{u}} Q(\tilde{u}) d\tilde{u} \right] \quad (54)$$

for a to-be-determined constant a .

Inspection of equations (53) and (54) shows that the fluctuation velocity field in the y - z plane, which is proportional to F' , is singular at $\bar{u} = 0$, with $F'(\bar{u}) = O(1/\bar{u})$ as $\bar{u} \rightarrow 0$. As shown in [6], this critical layer singularity is regularized by viscous forces for the lower branch ECS. Reinstating viscous diffusion in the steady version of equation (47) yields

$$\bar{u} \partial_{\chi} \Omega'_1 = -\partial_z \bar{u} \partial_{\chi} (\partial_z \psi'_1) - \partial_y \bar{u} \partial_{\chi} (\partial_y \psi'_1) + \frac{1}{\hat{R}} \nabla_{\perp}^2 \Omega'_1. \quad (55)$$

Upon substituting for ψ'_1 and Ω'_1 from equations (48) and (49), noting that the slaving relation (46) continues to be asymptotically valid within the critical layer, a pair of coupled, fourth-order ordinary differential equations (ODEs) is obtained for F and G . The ODE for F reads

$$\begin{aligned} \frac{1}{\hat{R}} \left\{ F'''' + \left(\frac{2 \nabla_{\perp} \bar{u} \cdot \nabla_{\perp} |\nabla_{\perp} \bar{u}|^2 + 2 |\nabla_{\perp} \bar{u}|^2 \nabla_{\perp}^2 \bar{u}}{|\nabla_{\perp} \bar{u}|^4} \right) F''' \right. \\ \left. + \left(\frac{2 \nabla_{\perp} \bar{u} \cdot \nabla_{\perp} (\nabla_{\perp}^2 \bar{u}) + (\nabla_{\perp}^2 \bar{u})^2 + 2 |\nabla_{\perp} (\nabla_{\perp} \bar{u})|^2 + 2 \nabla_{\perp} \bar{u} \cdot \nabla_{\perp} (\nabla_{\perp}^2 \bar{u})}{|\nabla_{\perp} \bar{u}|^4} \right) F'' \right. \\ \left. + \left(\frac{\nabla_{\perp}^4 \bar{u}}{|\nabla_{\perp} \bar{u}|^4} \right) F' \right\} - \bar{u} \left(\frac{|\nabla_{\perp} \bar{u}|^2 G'' + (\nabla_{\perp}^2 \bar{u}) G'}{|\nabla_{\perp} \bar{u}|^4} \right) - \left(\frac{|\nabla_{\perp} \bar{u}|^2}{|\nabla_{\perp} \bar{u}|^4} \right) G' = 0, \quad (56) \end{aligned}$$

with a similar equation holding for G . Within the critical layer, gradients with respect to \bar{u} are large, $\mathcal{O}(\hat{R}^{1/3})$, but \bar{u} (as a function of y and z) is smooth, implying $\bar{u} = \mathcal{O}(\hat{R}^{1/3})$. Hence, asymptotically, this ODE simplifies to

$$\frac{1}{\hat{R}} F'''' - \bar{u} \frac{|\nabla_{\perp} \bar{u}|^2}{|\nabla_{\perp} \bar{u}|^4} G'' - \frac{|\nabla_{\perp} \bar{u}|^2}{|\nabla_{\perp} \bar{u}|^4} G' = 0. \quad (57)$$

For this resulting equation to be well posed, $1/|\nabla_{\perp} \bar{u}|^2 = (Q(\bar{u}) - 1/\bar{u})/\nabla_{\perp}^2 \bar{u}$ must be a function solely of \bar{u} . In fact, consideration of other steady critical layers arising in shear flows and regularized by viscous diffusion of momentum strongly suggests that the constraint

$$|\nabla_{\perp} \bar{u}|^2 \equiv (\partial_y \bar{u})^2 + (\partial_z \bar{u})^2 = C \quad (58)$$

must be satisfied for some (to-be-determined) constant C . Presuming this to be the case, and employing the rescaling

$$\bar{u} \sim \hat{R}^{-1/3} U, \quad (59)$$

the linear, non-constant coefficient ODEs for $\mathcal{F}(U) \equiv F(\bar{u})$ and $\mathcal{G}(U) \equiv G(\bar{u})$ become

$$\mathcal{F}'''' - \frac{1}{C} U \mathcal{G}'' - \frac{1}{C} \mathcal{G}' = 0, \quad (60)$$

$$\mathcal{G}'''' + \frac{1}{C} U \mathcal{F}'' + \frac{1}{C} \mathcal{F}' = 0. \quad (61)$$

Finally, defining $\mathcal{H} \equiv \mathcal{F} + i\mathcal{G}$ and $\mathcal{J} \equiv \mathcal{H}'$, we obtain

$$\mathcal{J}'' + i \left(\frac{1}{C} \right) U \mathcal{J} = K \quad (62)$$

for some constant K . Following Hall & Sherwin (see equation (2.22) in [6]), the solution for $\mathcal{J}(U)$ that decays as $|U| \rightarrow \infty$ may be expressed in terms of Scorer functions but can be further manipulated to yield

$$\mathcal{J}(U) = -K C^{2/3} \int_0^\infty \exp \left[i \frac{1}{C^{1/3}} U s - \frac{s^3}{3} \right] ds. \quad (63)$$

As $|U| \rightarrow \infty$, the real (imaginary) part of $\mathcal{J}(U)$ matches smoothly with the solution (54) for $F'(\bar{u})$ (the corresponding solution for $G'(\bar{u})$), as $|\bar{u}| \rightarrow 0$. This asymptotic matching yields an algebraic relation between the constants K and a . Thus, apart from the constants a and C , v'_1 and w'_1 are completely determined by this analysis, at least as a function of the unknown $\bar{u}(y, z)$ – a significant simplification.

The Reynolds stress divergence across the critical layer drives a mean flow in the y – z plane; namely, the rolls. The leading-order dominant balance in equation (44) *within* the critical layer requires

$$\frac{1}{R} \nabla_\perp^2 \bar{\Omega}_1 \sim -(\partial_z^2 - \partial_y^2) \overline{v'_1 w'_1} - \partial_z \left[\partial_y \left(\overline{v'_1 v'_1} - \overline{w'_1 w'_1} \right) \right], \quad (64)$$

where it has been posited that the roll velocity is smooth but that there is a jump in the χ -component of mean vorticity $\bar{\Omega}_1$ across the critical layer, as can be verified *a posteriori*. It proves convenient to consider this equation in (\bar{u}, z) rather than Cartesian (y, z) coordinates. Specifically, we write $\bar{\Omega}_1(y, z) = \tilde{\Omega}(\bar{u}, z)$ and $\bar{\psi}_1(y, z) = \tilde{\psi}(\bar{u}, z)$, and recall $\psi'_1(\chi, y, z) = F(\bar{u}) \cos \chi + G(\bar{u}) \sin \chi$. After much algebraic manipulation, equation (64) can be expressed as

$$\begin{aligned} \frac{1}{R} |\nabla_\perp \bar{u}|^2 \partial_{\bar{u}}^2 \tilde{\Omega} \sim & \left[(F'(\bar{u}))^2 + (G'(\bar{u}))^2 \right]' \left\{ \partial_y (\partial_z \bar{u}) [(\partial_y \bar{u})^2 - (\partial_z \bar{u})^2] \right. \\ & \left. + (\partial_y \bar{u})(\partial_z \bar{u}) [\partial_z^2 \bar{u} - \partial_y^2 \bar{u}] \right\}. \end{aligned} \quad (65)$$

Integrating this equation from $\bar{u} = 0$ to $\bar{u} = \Delta$, *i.e.* from the center to the upper edge of the critical layer, yields an effective boundary condition on the “outer” mean vorticity as the critical layer is approached from above:

$$\left. \partial_{\bar{u}} \tilde{\Omega} \right|_{\bar{u} \rightarrow 0^+} \sim \frac{R}{2} \left\{ \frac{\partial_y(\partial_z \bar{u}) [(\partial_y \bar{u})^2 - (\partial_z \bar{u})^2] + (\partial_y \bar{u})(\partial_z \bar{u}) [\partial_z^2 \bar{u} - \partial_y^2 \bar{u}]}{|\nabla_{\perp} \bar{u}|^2} \right\}_{\bar{u} \rightarrow 0^+} \times \left\{ [(F'(\Delta))^2 + (G'(\Delta))^2] - [(F'(0))^2 + (G'(0))^2] \right\}. \quad (66)$$

The outer problem for the mean flow in the y - z plane *above* the critical layer (above the white region in figure 12(a) top panel for example) also requires a boundary condition on $\tilde{\psi}$. This condition is obtained by noting that $\tilde{\Omega} \sim |\nabla_{\perp} \bar{u}|^2 \partial_{\bar{u}}^2 \tilde{\psi}$ within the critical layer and, hence, that

$$\left. \partial_{\bar{u}} \tilde{\psi} \right|_{\bar{u} \rightarrow 0^+} \sim \frac{1}{|\nabla_{\perp} \bar{u}|^2} \int_{\bar{u}=0}^{\bar{u}=\Delta} \tilde{\Omega} d\bar{u}. \quad (67)$$

Note that both equations (66) and (67) implicitly enforce the symmetry conditions $\partial_{\bar{u}} \tilde{\Omega} = \partial_{\bar{u}} \tilde{\psi} = 0$ along $\bar{u} = 0$ and must satisfy the constraint (58), which applies (asymptotically) everywhere within the critical layer.

We may now summarize the algorithm for computing lower branch ECS, satisfying Wang *et al.* scalings [21], in the small- α limit with $\hat{R} \equiv \alpha Re \gg 1$ and $R = \epsilon Re = \mathcal{O}(1)$. In the limit $Re \rightarrow \infty$, the critical layer becomes infinitely thin, and we compute the solution in the non-rectangular y - z domain above the critical layer; by symmetry, we can reconstruct the solution below the critical layer. First, an initial guess for $\bar{u}(y, z)$ in this domain is required; again, it should be emphasized that this initial and all subsequent iterates must satisfy equation (58) along $\bar{u} = 0$, as noted above. We then march

$$\partial_T \tilde{\Omega} + (\partial_y \bar{u}) \left(\partial_{\bar{u}} \tilde{\psi} \partial_z \tilde{\Omega} - \partial_z \tilde{\psi} \partial_{\bar{u}} \tilde{\Omega} \right) \sim \frac{1}{R} \left[|\partial_{\perp} \bar{u}|^2 \partial_{\bar{u}}^2 \tilde{\Omega} + (\nabla_{\perp}^2 \bar{u}) \partial_{\bar{u}} \tilde{\Omega} + \partial_z^2 \tilde{\Omega} \right], \quad (68)$$

$$|\partial_{\perp} \bar{u}|^2 \partial_{\bar{u}}^2 \tilde{\psi} + (\nabla_{\perp}^2 \bar{u}) \partial_{\bar{u}} \tilde{\psi} + \partial_z^2 \tilde{\psi} = \tilde{\Omega} \quad (69)$$

to steady state on a discrete (\bar{u}, z) grid. Note that, asymptotically, the Reynolds stress terms in equation (44) are consistently omitted in equation (68). The mean flow is, instead, driven by the effective boundary conditions just above the critical layer (*i.e.* as $\bar{u} \rightarrow 0^+$): equations (66) and (67). Imposition of these boundary conditions requires evaluation of the quadrature (63) for the fluctuation fields within the critical layer. Finally, the solution for $\tilde{\psi}(\bar{u}, z)$ along with the initial iterate for $\bar{u}(y, z)$ can be used to reconstruct $\bar{\psi}_1(y, z)$ in the region above the critical layer. Then equation (43) can be marched to steady state in the discrete y - z domain (subject to $\bar{u} = 0$ at the “old” location of the critical layer), and the entire iteration repeated until convergence.

5 Discussion

In the present investigation, we have derived a model of the dynamics near lower branch ECS in plane Waleffe flow. This model is asymptotically valid in the limit of high Reynolds

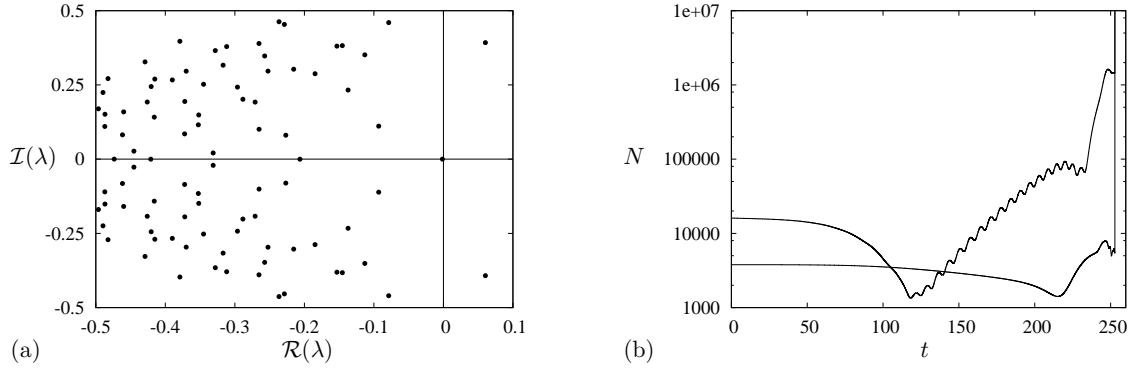


Figure 13: (a) Eigenvalues λ for the iterate shown in figure 12, with $\mathcal{R}(\lambda)$ the growth rate of the fluctuation and $\mathcal{I}(\lambda)$ the temporal pulsation. (b) Time integration of the “complete” reduced system (35)–(39) starting from this state. The solutions are represented by the 2-norm of the Fourier spectrum N for the mean variables (bottom curve) and the fluctuations (oscillating curve).

numbers. We have also developed an algorithm based on this model to obtain good estimates of lower branch solutions given only an initial profile for the streamwise averaged velocity. Using this novel iterative algorithm, we were able to compute the near lower branch flow state shown in figure 12, which, in turn, should provide an excellent first iterate for a standard Newton solver. Other solutions can easily be sought by imposing an appropriate initial condition for the streamwise averaged velocity or by using the small- α approach developed in section 4. The merit of this approach is two-fold: (i) the problem can be solved for asymptotically large Re without the need to resolve the critical layer; and (ii) the fluctuation system has been reduced to a quadrature. With a solution for asymptotically-small α available, solutions for finite α can be computed using standard numerical continuation software.

An alternative method can also be used to obtain lower branch solutions: edge-tracking [16]. Designed to find edge states, this technique involves time-stepping the governing equations for initial conditions with different amplitudes. This method exploits the fact that some edge solutions are once unstable: if the amplitude is too small, the initial condition will decay to the laminar solution; if the amplitude is too large, the initial condition will grow to reach a different state. By identifying the divergence in the decay/growth behavior, linear combinations of the diverging solutions can be formed to generate initial conditions that, when time-advanced, continue to track the edge for longer and longer durations. The edge can be followed in this way, simply using a time-stepper. The stability of the state we have found is indicated in figure 13(a). It is represented in the complex λ plane, where the real part $\mathcal{R}(\lambda)$ represents the temporal growth rate of the perturbation and the imaginary part $\mathcal{I}(\lambda)$ the temporal pulsation. There is a $\lambda \approx 0$ mode, representing the fluctuations in figure 12. In addition to this mode are modes with complex conjugate λ with positive real part. The presence of these modes indicates that the solution is unstable with respect to time-dependent fluctuations. It is therefore not an attractive edge solution, in the sense it is not strictly once unstable. Nevertheless, edge-tracking can be used to

find new solutions. We implemented a third order Runge–Kutta scheme to discretize in time [17] in the reduced system (35)–(39). A typical simulation result is plotted in figure 13(b). This simulation has been initialized using the state shown in figure 12. Initially, the dynamics are slow, owing to the fact the solution is nearly marginal. Then, oscillations, corresponding to the most unstable mode in figure 13(a), start to grow exponentially. Due to the separation in time scales, the mean variables do not respond, enabling the fluctuations to grow. At approximately $t = 200$, the fluctuations become $\mathcal{O}(1/\epsilon)$, violating the lower branch asymptotic scaling and suggesting the dynamics is moving toward upper branch solutions or turbulent states. Indeed, by continuing the computation a little bit further, the code blew up as a result of the undamped growth of the fluctuations, generating intense rolls that violated the CFL condition. This process seems unavoidable as the tests we ran with different time steps resulted in a similar blow up behavior, albeit at slightly different times despite a converged simulation until then. These simulations do however provide useful information: the quasi-linear behavior of the fluctuations and time scale separation imply that fluctuations and mean variables evolve in a rather decoupled manner. Classic edge-tracking is therefore not possible as two different amplitudes are needed (one for the fluctuations and one for the mean variables) instead of one.

To cope with these difficulties, we propose to simulate the following augmented system:

$$\zeta_1 \partial_t \bar{u}^0 + \partial_y \bar{\psi}_1^0 \partial_z \bar{u}^0 - \partial_z \bar{\psi}_1^0 \partial_y \bar{u}^0 = \frac{1}{R} \nabla_\perp^2 \bar{u}^0 + \frac{\sqrt{2}\pi^2}{4R} \sin(\pi y/2), \quad (70)$$

$$\zeta_1 \partial_t \bar{\omega}_1^0 + J(\bar{\psi}_1^0, \bar{\omega}_1^0) + 2(\partial_y^2 - \partial_z^2) \overline{\mathcal{R}(v'_1 w'^*_1)} + 2\partial_z \partial_y (\overline{w'_1 w'^*_1} - \overline{v'_1 v'^*_1}) = \frac{1}{R} \nabla_\perp^2 \bar{\omega}_1^0, \quad (71)$$

$$\partial_t u'_1 + i\alpha \bar{u}^0 u'_1 + v'_1 \partial_y \bar{u}^0 + w'_1 \partial_z \bar{u}^0 = -i\alpha p'_1 + \frac{\epsilon}{R} \nabla_\perp^2 u'_1, \quad (72)$$

$$\partial_t v'_1 + i\alpha \bar{u}^0 v'_1 + \zeta_2 (v'_1 \partial_y v'_1 + w'_1 \partial_z v'_1) = -\partial_y p'_1 + \frac{\epsilon}{R} \nabla_\perp^2 v'_1, \quad (73)$$

$$\partial_t w'_1 + i\alpha \bar{u}^0 w'_1 + \zeta_2 (v'_1 \partial_y w'_1 + w'_1 \partial_z w'_1) = -\partial_z p'_1 + \frac{\epsilon}{R} \nabla_\perp^2 w'_1, \quad (74)$$

$$i\alpha u'_1 + \partial_y v'_1 + \partial_z w'_1 = 0. \quad (75)$$

This system is a replica of equations (27)–(33) in the case of $\mathcal{O}(1)$ varying solutions in the streamwise coordinate with a few modifications. The first one concerns the occurrence of ζ_1 terms in equations (70) and (71) where ζ_1 should be ϵ . By replacing ϵ by an $\mathcal{O}(1)$ value, we eliminate the time scale separation, enabling an effective feedback from the mean variables. The second modification is the addition of the terms involving ζ_2 in equations (73) and (74). Provided $\zeta_2 = \mathcal{O}(1)$, these nonlinear terms for the fluctuations will fix their amplitude. Strictly, these terms arise at higher order and hence ζ_2 should equal ϵ to respect our model derivation. Nevertheless, the idea behind this augmented system is to compute the edge for $\zeta_1 = \mathcal{O}(1)$ and $\zeta_2 = \mathcal{O}(1)$ and then, in a process called homotopy, gradually decrease ζ_1 and ζ_2 to obtain an edge solution for $\zeta_1 = \zeta_2 = \epsilon$. At large Re (small ϵ), this solution is a solution of the system (35)–(39).

Once edge solutions are obtained, their dependence on the streamwise wavenumber α will be investigated. Indeed, the current literature has focused on finite-sized boxes, but practical applications of parallel shear flows may involve very long streamwise scales. Thus, our reduced model may provide an effective way to bridge the gap between current simulations and long domains. Another possibility is to use the model to compute more complex solutions exhibiting streamwise modulation by including $\bar{\psi}_1^\delta$ and $\bar{\omega}_1^\delta$ or to obtain localized solutions in the spanwise direction by computing in a larger domain. These lines of

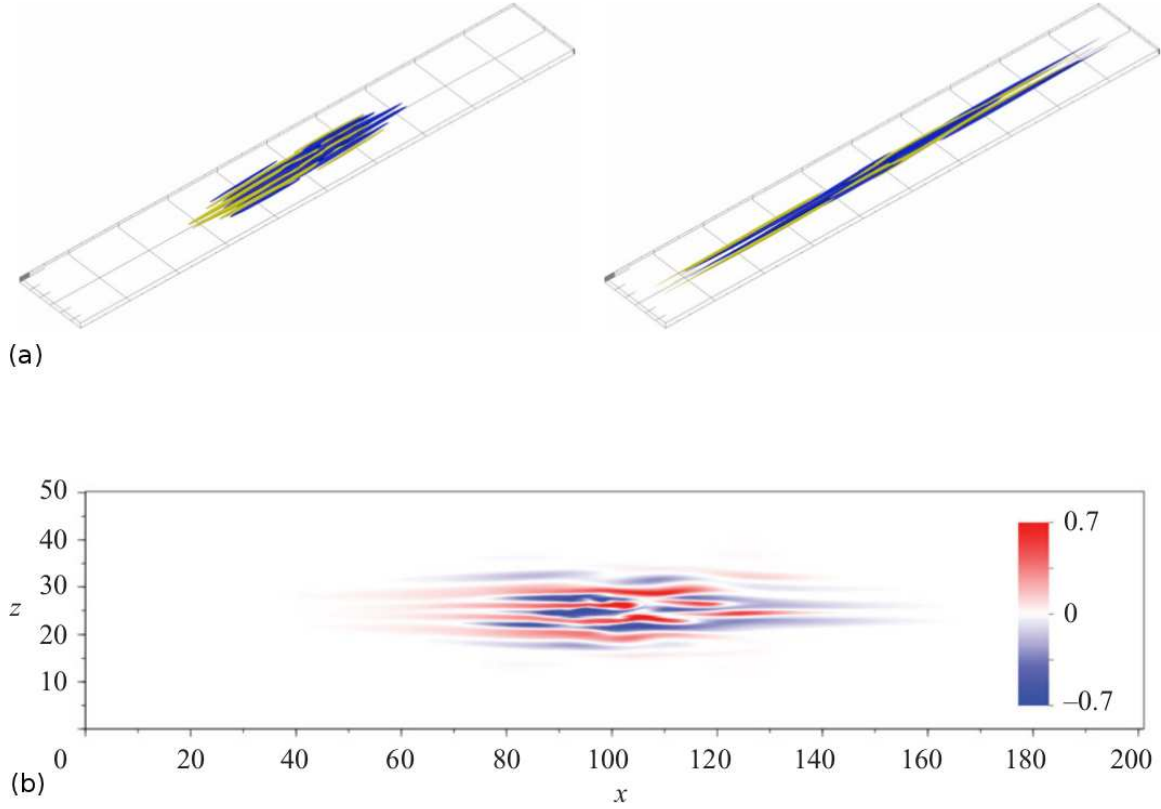


Figure 14: (a) Instantaneous snapshots of the edge state for $Re = 375$ (left) and $Re = 1000$ (right). Three-dimensional isocontours of the streamwise velocity perturbation are shown. Only part of the spanwise domain is shown here. After Duguet *et al.* [1]. (b) Localized turbulence seed at $Re = 400$ represented via the streamwise velocity in the $y = 0$ plane. After Schneider *et al.* [15].

inquiry are motivated by the edge solutions obtained by Duguet *et al.* [1] and Schneider *et al.* [15] and shown in figure 14. Computing these solutions using the reduced model would shed light on the structure of the edge at high Reynolds numbers and on various types of localization in parallel shear flows. Finally, it should be noted that although Waleffe flow has been used here as a simpler surrogate for Couette flow, there have been no systematic comparative studies of these flows. Such a comparison would inform future studies and provide important context for the current investigation.

Acknowledgments

I thank Greg Chini, Keith Julien and Edgar Knobloch for their advice and guidance throughout the program. This project greatly benefited from the unique atmosphere of Walsh Cottage, and I would like to thank all the staff members and fellows for keeping this spirit alive. Special thanks to John Gibson and Tobias Schneider for their continuous interest in the project and helpful discussions. A final thanks to Alain Bergeon and Franck Plouraboué

for their unconditional support.

References

- [1] Y. DUGUET, P. SCHLATTER, AND D. S. HENNINGSON, *Localized edge states in plane Couette flow*, Phys. Fluids, 21 (2009), p. 111701.
- [2] M. FRIGO AND S. G. JOHNSON, *The Design and Implementation of FFTW3*, Proceedings of the IEEE, 93 (2005), pp. 216–231. Special issue on “Program Generation, Optimization, and Platform Adaptation”.
- [3] J. F. GIBSON, *Channelflow: A spectral Navier-Stokes simulator in C++*, tech. rep., U. New Hampshire, 2012. Channelflow.org.
- [4] J. F. GIBSON, J. HALCROW, AND P. CVITANOVIĆ, *Equilibrium and travelling-wave solutions of plane Couette flow*, J. Fluid Mech., 638 (2009), pp. 243–266.
- [5] I. GROOMS, K. JULIEN, AND B. FOX-KEMPER, *On the interactions between planetary geostrophy and mesoscale eddies*, Dynam. Atmos. Ocean, 51 (2011), pp. 109–136.
- [6] P. HALL AND S. J. SHERWIN, *Streamwise vortices in shear flows: Harbingers of transition and the skeleton of coherent structures*, J. Fluid Mech., 661 (2010), pp. 178–205.
- [7] G. KAWAHARA AND S. KIDA, *Periodic motion embedded in plane Couette turbulence: Regeneration cycle and burst*, J. Fluid Mech., 449 (2001), pp. 291–300.
- [8] R. KLEIN, *Scale-dependent models for atmospheric flows*, Annu. Rev. Fluid Mech., 42 (2010), pp. 249–274.
- [9] R. B. LEHOUCQ, D. C. SORESENSEN, AND C. YANG, *ARPACK Users Guide: Solution of Large Scale Eigenvalue Problems by Implicitly Restarted Arnoldi Methods.*, 1997.
- [10] A. J. MAJDA AND R. KLEIN, *Systematic multiscale models for the Tropics*, J. Atmos. Sci., 60 (2003), pp. 393–408.
- [11] P. MANNEVILLE, *Spots and turbulent domains in a model of transitional plane Couette flow*, Theoret. Comput. Fluid Dynamics, 18 (2004), pp. 169–181.
- [12] M. NAGATA, *Three-dimensional finite-amplitude solutions in plane Couette flow: Bifurcation from infinity*, J. Fluid Mech., 217 (1990), pp. 519–527.
- [13] P. J. SCHMID AND D. S. HENNINGSON, *Stability and Transition in Shear Flows*, no. 142 in Applied Mathematical Sciences, Springer, 2001.
- [14] T. M. SCHNEIDER, J. F. GIBSON, M. LAGHA, F. D. LILLO, AND B. ECKHARDT, *Laminar-turbulent boundary in plane Couette flow*, Phys. Rev. E, 78 (2008), p. 037301.
- [15] T. M. SCHNEIDER, D. MARINC, AND B. ECKHARDT, *Localized edge states nucleate turbulence in extended plane Couette cells*, J. Fluid Mech., 646 (2010), pp. 441–451.

- [16] J. D. SKUFCA, J. A. YORKE, AND B. ECKHARDT, *Edge of chaos in parallel shear flow*, Phys. Rev. Lett., 96 (2006), p. 174101.
- [17] P. R. SPALART, R. D. MOSER, AND M. M. ROGERS, *Spectral methods for the Navier–Stokes equations with one infinite and two periodic boundary conditions*, J. Comp. Phys., 96 (1991), pp. 297–324.
- [18] C. G. SPEZIALE, *Analytical methods for the development of Reynolds-stress closures in turbulence*, Annu. Rev. Fluid Mech., 23 (1991), pp. 107–157.
- [19] D. VISWANATH, *Recurrent motions within plane Couette turbulence*, J. Fluid Mech., 580 (2007), pp. 339–358.
- [20] F. WALEFFE, *On a self-sustaining process in shear flows*, Phys. Fluids, 9 (1997), pp. 883–900.
- [21] J. WANG, J. GIBSON, AND F. WALEFFE, *Lower branch coherent states in shear flows: Transition and control*, Phys. Rev. Lett., 98 (2007), p. 204501.

REPORT DOCUMENTATION PAGE	1. REPORT NO. WHOI-2013-07	2.	3. Recipient's Accession No.
4. Title and Subtitle 2012 Program of Study: Coherent Structures			5. Report Date November 2013
			6.
7. Author(s) Colm-cille Caulfield and Charles Doering			8. Performing Organization Rept. No.
9. Performing Organization Name and Address Woods Hole Oceanographic Institution Woods Hole, Massachusetts 02543			10. Project/Task/Work Unit No.
			11. Contract(C) or Grant(G) No. (C)N00014-09-10844 (G)OCE-0824636
12. Sponsoring Organization Name and Address Office of Naval Research National Science Foundation			13. Type of Report & Period Covered Technical Report
			14.
15. Supplementary Notes This report should be cited as: Woods Hole Oceanographic Institution Technical Report, WHOI-2013-07.			
16. Abstract (Limit: 200 words) The 2012 GFD Program theme was Coherent structures with Professors Jeffrey Weiss of the University of Colorado at Boulder and Edgar Knobloch of the University of California at Berkeley serving as principal lecturers. Together they introduced the audience in the cottage and on the porch to a fascinating mixture of models, mathematics and applications. Deep insights snaked through the whole summer, as the principal lecturers stayed on to participate in the traditional debates and contributed stoutly to the supervision of the fellows.			
17. Document Analysis a. Descriptors coherent Structures spatial localization dynamical systems b. Identifiers/Open-Ended Terms c. COSATI Field/Group			
18. Availability Statement Approved for public release; distribution unlimited.		19. Security Class (This Report)	21. No. of Pages 445
		20. Security Class (This Page)	22. Price